frontiers | Research Topics

The use of large animal models to improve pre-clinical translational research

Edited by
Mark Gray, Abirami Kugadas and Stefano Guido

Published in
Frontiers in Veterinary Science

ISSN 1664-8714
ISBN 978-2-83251-932-5
DOI 10.3389/978-2-83251-932-5

About Frontiers

Frontiers is more than just an open access publisher of scholarly articles: it is a pioneering approach to the world of academia, radically improving the way scholarly research is managed. The grand vision of Frontiers is a world where all people have an equal opportunity to seek, share and generate knowledge. Frontiers provides immediate and permanent online open access to all its publications, but this alone is not enough to realize our grand goals.

Frontiers journal series

The Frontiers journal series is a multi-tier and interdisciplinary set of open-access, online journals, promising a paradigm shift from the current review, selection and dissemination processes in academic publishing. All Frontiers journals are driven by researchers for researchers; therefore, they constitute a service to the scholarly community. At the same time, the *Frontiers journal series* operates on a revolutionary invention, the tiered publishing system, initially addressing specific communities of scholars, and gradually climbing up to broader public understanding, thus serving the interests of the lay society, too.

Dedication to quality

Each Frontiers article is a landmark of the highest quality, thanks to genuinely collaborative interactions between authors and review editors, who include some of the world's best academicians. Research must be certified by peers before entering a stream of knowledge that may eventually reach the public - and shape society; therefore, Frontiers only applies the most rigorous and unbiased reviews. Frontiers revolutionizes research publishing by freely delivering the most outstanding research, evaluated with no bias from both the academic and social point of view. By applying the most advanced information technologies, Frontiers is catapulting scholarly publishing into a new generation.

What are Frontiers Research Topics?

Frontiers Research Topics are very popular trademarks of the *Frontiers journals series*: they are collections of at least ten articles, all centered on a particular subject. With their unique mix of varied contributions from Original Research to Review Articles, Frontiers Research Topics unify the most influential researchers, the latest key findings and historical advances in a hot research area.

Find out more on how to host your own Frontiers Research Topic or contribute to one as an author by contacting the Frontiers editorial office: frontiersin.org/about/contact

The use of large animal models to improve pre-clinical translational research

Topic editors

Mark Gray — University of Edinburgh, United Kingdom

Abirami Kugadas — Takeda, Cambridge, United States

Stefano Guido — University of Edinburgh, United Kingdom

Citation

Gray, M., Kugadas, A., Guido, S., eds. (2023). *The use of large animal models to improve pre-clinical translational research*. Lausanne: Frontiers Media SA.

doi: 10.3389/978-2-83251-932-5

Table of contents

frontiers | Frontiers in Veterinary Science

TYPE Editorial
PUBLISHED 15 November 2022
DOI 10.3389/fvets.2022.1086912

OPEN ACCESS

EDITED AND REVIEWED BY
Ali Mobasheri,
University of Oulu, Finland

*CORRESPONDENCE
Mark Gray
mgray34@ed.ac.uk

SPECIALTY SECTION
This article was submitted to Comparative and Clinical Medicine, a section of the journal Frontiers in Veterinary Science

RECEIVED 01 November 2022
ACCEPTED 03 November 2022
PUBLISHED 15 November 2022

CITATION
Gray M, Guido S and Kugadas A (2022) Editorial: The use of large animal models to improve pre-clinical translational research.
Front. Vet. Sci. 9:1086912.
doi: 10.3389/fvets.2022.1086912

Editorial: The use of large animal models to improve pre-clinical translational research

Mark Gray[1]*, Stefano Guido[1,2] and Abirami Kugadas[3]

[1]The Royal (Dick) School of Veterinary Studies, The Roslin Institute, University of Edinburgh, Edinburgh, United Kingdom, [2]Bioresearch and Veterinary Services, University of Edinburgh, Edinburgh, United Kingdom, [3]Takeda Pharmaceutical Company Limited, Cambridge, MA, United States

KEYWORDS

disease models (animal), comparative model, large animal models, translational, genetically altered animals

Editorial on the Research Topic
The use of large animal models to improve pre-clinical translational research

Drug and medical device research and development is an expensive and time-consuming process, involving *in vitro* target identification/validation, progressing through to phase 0, I, II, III, and IV clinical trials. It has been estimated that in the USA alone it costs between $1.8–2.6 billion and 13 years to develop and gain regulatory approval for a new drug. The situation is similar for medical devices, costing between $75–94 million and 4.5 years (1). In addition to these financial and time commitments, most drugs showing pre-clinical success fail to show efficacy in clinical trials, with an estimated failure rate of 86–95% (1, 2). These issues can deter drug companies from developing novel therapeutics.

While the use of live animals should be replaced wherever possible, animal models are still necessary to generate data in support of conducting human clinical trials. Pre-clinical research has historically focused upon *in vitro* (e.g., cell line) and *in vivo* rodent models for studying human conditions. Unfortunately, *in vitro* models are unable to faithfully recapitulate complex physiological environments. With a plethora of relatively low cost inflammatory, neoplastic, transgenic and knockout rodent models now available, they have become ingrained in pre-clinical research. Rodent models often fail to capture disease characteristics typically seen in humans, they fail to address translatable immune related outcomes, are not very useful to address specific toxicities and are unsuitable for the application of size-relevant clinical imaging (ultrasound, computed tomography, magnetic resonance imaging, bronchoscopy and endoscopy) and surgical techniques used in human patients. These issues will continue to hamper the development of new therapies and medical devices. To mitigate against these issues, over recent years there has been a scientific push for the development of translational pre-clinical large animal models that can more accurately represent the complex clinical and pathologic features of a variety of human diseases. Whether the model is predictive (treatment effects), isomorphic (similar symptoms but different etiology), or homologous

(same symptoms and etiology) (3), various large animal species can be used for translational research.

Pigs, and perhaps to a lesser extent sheep and goats, have gained significant scientific attention as translational models as they share important proteomic, genomic and immunologic similarities to that of humans. Each of these species have been successfully used for cardiovascular, respiratory, gastrointestinal, immune, musculoskeletal, neurological and cancer studies. The pig has also been utilized for interspecies transplantation studies and satisfies the Food and Drug Administration (FDA) evaluation requirements for pharmaceutical drugs (4). Furthermore, similarities in anatomy and physiology allow anesthetic techniques, drug administration, advanced imaging and surgical procedures to be used in large animal species as they would be used in humans. Despite these advantages, several perceived limitations have obstructed their widespread use in biomedical studies. These issues include higher costs of maintenance and the need for specialized surgical facilities and veterinary care. Although these limitations have to be considered when developing or using large animal models, the translational data they produce can overcome the issues with rodent models and enable significant advancements in the understanding and treatment of a wide variety of disease conditions to be made.

This Frontiers in Veterinary Science Research Topic presents six Original Research Articles, three Reviews, one Case Report, one Brief Research Report, and one Methods paper which span multiple large animal species including pigs, horses, goats, and sheep.

In the original research section Qi et al. investigated methods and management strategies used in an ovine veno-arterial extracorporeal membrane oxygenation model. They suggested it could be used as a platform for pathophysiology exploration and new medical device validation. Gadomski et al. developed an ovine orthopedic model, with their findings indicating that the carpometacarpal joint may be used for investigating human foot and ankle orthopedic devices. Xu et al. investigated how to enhance the ability of immunological tolerance in pig-to-human xenotransplantations through the generation of triple-gene-modified Diannan miniature pigs. Wedlich et al. described the refinement of a goat bovine tuberculosis model using a video-guided endoscopic intra-bronchial inoculation procedure which could be used for testing tuberculosis vaccine efficacy. Höglund et al. described a protocol for isolating extracellular vesicles from the bronchio-aveolar fluid (BALF) of asthmatic horses. Sper et al. generated a novel immunodeficient pig model and demonstrated successful engraftment of swine leukocyte antigen mismatched allogeneic D42 fetal liver cells and human CD34+ hematopoietic stem cells after *in utero* cell transplantation.

In the mini review and review sections, Rose et al. describes how the pig can be used as a translational gastrointestinal microbiota model for elucidating the pathogenesis of human bowel disorders. Schaaf and Gonzalez also looked at pig gastrointestinal models, but instead focused on describing gene editing technologies to advance intestinal disease research. Billings and Anderson reviewed the role of animal models (including pig, sheep, and goats) utilized for the study of bacterial osteomyelitis, and their critically important role in understanding how the models can be used to improve bacterial osteomyelitis management.

In the case report, brief research report and methods sections, Weisskopf et al. presented work elaborating the do's and don'ts in porcine models of aortic insufficiency. Furthermore, Malbon et al. described a hemodynamically, highly relevant atrial septal defect with incompetent mitral and tricuspid valves, in an asymptomatic, juvenile pig. They suggested that although not common, congenital heart defects could influence experimental variability or mortality rates. Solanes et al. looked at porcine acute myocardial infarction models and reported the differences in infarct size and cardiac function for various anesthetic protocols and pig breeds.

Author contributions

MG designed and formulated the idea for this special issue and recruited both co-authors. All authors listed have made a substantial, direct, and intellectual contribution to the work and approved it for publication.

Conflict of interest

Author AK was employed by Takeda Pharmaceutical Company Limited.

The remaining authors declare that the research was conducted in the absence of any commercial or financial relationships that could be construed as a potential conflict of interest.

Publisher's note

References

1. Schomberg DT, Tellez A, Meudt JJ, Brady DA, Dillon KN, Arowolo FK, et al. Miniature swine for preclinical modeling of complexities of human disease for translational scientific discovery and accelerated development of therapies and medical devices. *Toxicol Pathol.* (2016) 44:299–314. doi: 10.1177/0192623315618292

2. Wong CH, Siah KW, Lo AW. Estimation of clinical trial success rates and related parameters. *Biostatistics*. (2019) 20:273–86. doi: 10.1093/biostatistics/kxx069

3. Conn PM. *Animal Models for the Study of Human Disease*. London; Waltham, MA: Elsevier (2013).

4. Kano M, Mizutani E, Homma S, Masaki H, Nakauchi H. Xenotransplantation and interspecies organogenesis: current status and issues. *Front Endocrinol.* (2022) 13:963282. doi: 10.3389/fendo.2022.963282

frontiers in Veterinary Science

CASE REPORT
published: 06 December 2021
doi: 10.3389/fvets.2021.790019

Pathology and Advanced Imaging—Characterization of a Congenital Cardiac Defect and Complex Hemodynamics in a Pig: A Case Report

Alexandra J. Malbon[1†], Miriam Weisskopf[2], Lukas Glaus[3], Sebastian Neuber[4,5], Maximilian Y. Emmert[4,5,6], Christian T. Stoeck[7] and Nikola Cesarovic[2,3,4]*

[1] Institute of Veterinary Pathology, Vetsuisse Faculty, University of Zurich, Zurich, Switzerland, [2] Center for Surgical Research, University of Zurich, University Hospital of Zurich, Zurich, Switzerland, [3] Translational Cardiovascular Technologies, Department of Health Sciences and Technology, Swiss Federal Institute of Technology, ETH Zurich, Zurich, Switzerland, [4] Cardiosurgical Research Group, Department of Cardiothoracic and Vascular Surgery, German Heart Center Berlin, Berlin, Germany, [5] Translational Cardiovascular Regenerative Technologies Group, Berlin Institute of Health at Charité – Universitätsmedizin Berlin, BIH Center for Regenerative Therapies, Berlin, Germany, [6] Institute for Regenerative Medicine, University of Zurich, Zurich, Switzerland, [7] Institute for Biomedical Engineering, Department of Information Technology and Electrical Engineering, Swiss Federal Institute of Technology, ETH Zurich, Zurich, Switzerland

OPEN ACCESS

Edited by:
Abirami Kugadas, Takeda, United States

Reviewed by:
Howard H. Erickson, Kansas State University, United States
Yu Ueda, North Carolina State University, United States

***Correspondence:**
Nikola Cesarovic
nikola.cesarovic@hest.ethz.ch

†Present address:
Alexandra J. Malbon, The Royal (Dick) School of Veterinary Studies, University of Edinburgh, Edinburgh, United Kingdom

Specialty section:
This article was submitted to Comparative and Clinical Medicine, a section of the journal Frontiers in Veterinary Science

Received: *05 October 2021*
Accepted: *12 November 2021*
Published: *06 December 2021*

Citation:
Malbon AJ, Weisskopf M, Glaus L, Neuber S, Emmert MY, Stoeck CT and Cesarovic N (2021) Pathology and Advanced Imaging—Characterization of a Congenital Cardiac Defect and Complex Hemodynamics in a Pig: A Case Report. Front. Vet. Sci. 8:790019. doi: 10.3389/fvets.2021.790019

Domestic pigs are widely used in cardiovascular research as the porcine circulatory system bears a remarkable resemblance to that of humans. In order to reduce variability, only clinically healthy animals enter the study as their health status is assessed in entry examination. Like humans, pigs can also suffer from congenital heart disease, such as an atrial septal defect (ASD), which often remains undetected. Due to the malformation of the endocardial cushion during organ development, mitral valve defects (e.g., mitral clefts) are sometimes associated with ASDs, further contributing to hemodynamic instability. In this work, we report an incidental finding of a hemodynamically highly relevant ASD in the presence of incompetent mitral and tricuspid valves, in an asymptomatic, otherwise healthy juvenile pig. In-depth characterization of the cardiac blood flow by four-dimensional (4D) flow magnetic resonance imaging (MRI) revealed a prominent diastolic left-to-right and discrete systolic right-to-left shunt, resulting in a pulmonary-to-systemic flow ratio of 1.8. Severe mitral (15 mL/stroke) and tricuspid (22 mL/stroke) regurgitation further reduced cardiac output. Pathological examination confirmed the presence of an ostium primum ASD and found a serous cyst of lymphatic origin that was filled with clear fluid partially occluding the ASD. A large mitral cleft was identified as the most likely cause of severe regurgitation, and histology showed mild to moderate endocardiosis in the coaptation area of both atrio-ventricular valves. In summary, although not common, congenital heart defects could play a role as a cause of experimental variability or even intra-experimental mortality when working with apparently heathy, juvenile pigs.

Keywords: large animal models, cardiovascular imaging, congenital heart defects, cardiovascular pathology, atrial septal defect, blood flow

INTRODUCTION

Due in part to their good availability, acceptable cost, and relatively easy handling, domestic (farm) pigs are often used in research (1). The similarities between the cardiovascular anatomy and physiology of pigs and humans make them a valuable model-species in cardiovascular science projects. In order to reduce inter-animal variability, but also to exclude the effects of comorbidities on the experimental read-out, only clinically healthy animals are allowed to participate in a scientific study. However, thorough, pre-entry clinical examinations are usually focused on infectious diseases or apparent malformations. It is thereby extraordinarily challenging to ascertain the state of cardiac health in large laboratory animals such as pigs, especially during entry examination. In this context, congenital heart defects may go undetected, particularly in juvenile animals, which often show no obvious signs of distress or apparent stunted growth. Atrial septal defects (ASDs) are among the three most common types of congenital heart disease in pigs (2). The same study found a prevalence for ASD of 1.6 per 100 live births in pigs, whereas it has an estimated prevalence of 1.6 per 1,000 live births in humans (3). ASDs include several distinct types of atrial communication and allow shunting of blood between the systemic and the pulmonary circulations (4). The flow direction of the shunted blood is often determined by ventricular compliance. As the right ventricle (RV) is more compliant than the left, large ASDs are often associated with prominent left-to-right (L-R) shunting and result in right ventricular volume overload and reduced left ventricular output (4). If left untreated, patients with large ASD will gradually develop right ventricular dilatation and eventually right-sided heart failure. Mitral and/or tricuspid regurgitation has been observed in some cases, as atrioventricular valves are often malformed in the presence of ostium primum ASD (5). However, in large animals used in cardiovascular research, the presence of complex congenital cardiac malformations is rarely described.

In order to diagnose and delineate congenital heart defects in large laboratory animals as well as in the clinic, multiple imaging modalities can be used, with echocardiography as a primary screening tool (6). Furthermore, magnetic resonance imaging (MRI) is increasingly gaining acceptance and importance in ASD diagnosis and follow-up care (7). Particularly for blood flow imaging, phase contrast MRI is becoming an increasingly important method in cardiovascular medicine and research (8). However, none of these imaging techniques are routinely used in clinical pre-assessment of large laboratory animals, such as pigs. Furthermore, it is relatively rare that intravital cardiac imaging results can be correlated with pathological findings. Here, we present a case report in which detailed imaging analysis was combined with a pathological examination.

CASE DESCRIPTION

All pigs entering the research facility are provided by the same supplier and screened under the national surveillance program for classical and African swine fever, foot and mouth disease, Aujeszky's disease, porcine reproductive and respiratory syndrome (PRRS) and swine vesicular disease. While still at the supplier, piglets are vaccinated against *Glaesserella parasuis* and porcine circovirus at the age of 3 and 6 weeks, whereas sows are vaccinated against Parvovirus and *Erysipelothrix rhusiopathiae*. Additionally, sows are vaccinated against *E. coli* 5 and 3 weeks prior to giving birth. Upon arrival at our facility, all pigs are clinically assessed by observation (general behavior, posture and gait, visible injuries, color of the skin, breathing pattern, nasal and ocular discharge, appetite, defecation and urination) and only if further indicated by physical examination as it often induces additional stress to newly arrived animals. Following an unremarkable entry examination, a 30 kg female pig (Swiss White large "Edelschwein") ∼10–12 weeks old, was included in an acute study as part of a scientific project investigating the use of hyperpolarized 13C urea for magnetic resonance perfusion imaging under the license ZH152/2013. After 10 days of habituation, the animal was anesthetized for the imaging procedure as part of the experimental protocol. General anesthesia was induced by intramuscular application of ketamine (15 mg/kg), azaperone (2 mg/kg) and atropine (0.05 mg/kg), deepened with intravenous propofol (1 mg/kg) for orotracheal intubation and maintained with isoflurane (2–3%) in 100% oxygen under volume controlled, positive pressure ventilation (tidal volume 8–10 mL/kg; respiration frequency 20 bpm; PEEP 5–6 mmHg; Pmax 25 mmHg). The animal was subjected to functional and phase contrast MRI (2 × 2 × 2 mm spatial resolution, 42 ms temporal resolution) on a clinical grade 1.5 T Philips Ingenia scanner (Philips Healthcare, Best, The Netherlands). Upon completion of the imaging procedure, the animal was euthanized with an i.v. overdose of pentobarbital (150 mg/kg; Esconarkon®, Streuli Pharma AG, Uznach, Switzerland) while still in deep anesthesia; according to the study protocol. The heart was harvested and preserved in 10% neutral buffered formalin for pathological analysis. Following macroscopic examination, tissue blocks of the left and right atria, left and right ventricular free walls, and the septum were prepared and histological sections of the affected regions were made. Tissue blocks were routinely processed and embedded in paraffin wax prior to haematoxylin and eosin staining of 2 µm sections. Consecutive sections were additionally stained with reticulin, elastic van Gieson and trichrome stains or mounted onto positively charged glass slides and stained for Factor VIII-related antigen (FVIIIra) and CD31 using immunohistochemistry.

DIAGNOSTIC ASSESSMENT

Imaging Results

Functional MRI showed a clear defect in the atrial septum and a moderately enlarged right ventricle (**Figures 1A–C**). Analysis of the phase contrast MRI data performed on specialized GTFlow software (Gyrotools) revealed a diastolic L-R and a systolic right-to-left (R-L) shunt through the atrial septal defect, as well as mitral and tricuspid valve insufficiency and disturbed diastolic intra cardiac blood flow patterns. The systolic R-L shunt was discrete and had a total volume of 4.6 mL per stroke with a maximum jet velocity of 25 cm/s. Peak diastolic L-R shunt velocity through the ASD was 48 cm/s and the

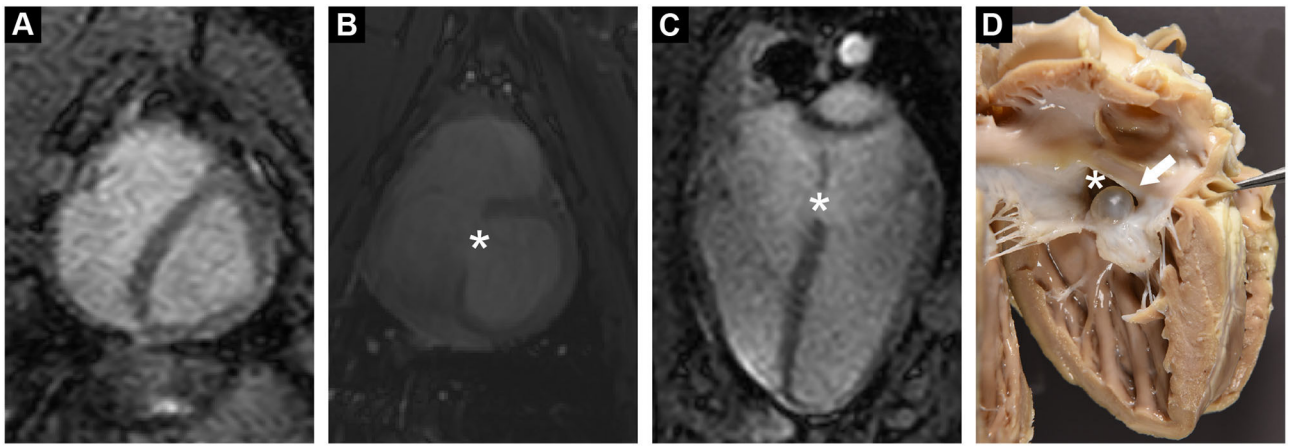

FIGURE 1 | (A) Functional cardiac MRI in short axis revealed a diastolic D-shaped left ventricle, indicating increased right ventricular pressure. **(B,C)** Cardiac MRI in short and long axis demonstrated a tissue defect in the inter-atrial septum (*). **(D)** Post mortem examination confirmed a large ASD (*). ASD was partially occluded by a serous cyst (arrow).

total volume of shunted blood was 14.1 mL per stroke. Peak velocities of mitral and tricuspid regurgitant jets were 36.4 and 46.9 cm/s, respectively, indicating a severe dysfunction of the atrioventricular (AV) valves (**Figure 2**). Surprisingly, mitral back-flow (regurgitation) was observed both during systole and diastole, with a total regurgitant volume of 15 mL per stroke (990 mL/min). Moreover, end-diastolic D-shape of the left ventricle was observed, indicating right ventricular volume overload (**Figure 1A**). Using blood particle tracking analysis, we were able to estimate that 26% of the blood volume contained in the diastolic mitral regurgitation (MR) jet directly crossed the ASD orifice and reached the RV, while only 18% of the systolic MR jet volume crossed the ASD in the subsequent diastole. Tricuspid regurgitation was limited to systole only, but was more severe with a total regurgitant volume of 22 mL per stroke (1.4 L/min).

Furthermore, MRI examination revealed an elevated ratio of pulmonary-to-systemic flow (Qp/Qs = 1.8), supporting the presence of a hemodynamically relevant ASD (area of 182 mm^2) with a diastolic L-R shunt (930 mL/min).

Pathology Results

The autopsy of the heart revealed a defect in the atrial septum in which the atrioventricular orifices remained separate, but with a continuous AV valve bridging the septum, thus creating an ostium primum ASD (**Figures 1D**, **3B**). The membranous oval fossa was prominently delineated, but the foramen ovale was not patent. The mitral valve showed a large cleft in the anterior leaflet segment A1/A2, with A1 partially connected to the ventricular wall (**Figure 3**). Both mitral leaflets, especially the anterior, were diffusely thickened. The tricuspid valve also had several mild nodular thickenings at its free margin (**Figure 3**). Histologically, these changes corresponded to a loss of valvular layer definition, with a disruption of the fibrosa and an expansion of the spongiosa. The spongiosa layer showed reduced staining uptake due to the deposition of oedematous ground substance and extracellular matrix components surrounding loosely arranged whorls of stellate cells. These findings indicate myxomatous valvular degeneration (endocardiosis) (**Figure 4C**). A serous cyst with a diameter of 1 cm protruded into and partially occluded the septal defect, extending from the septum at the exposed junction of the left and right AV valves (**Figure 4A**). Histologically, the cyst was lined by a flat endothelial cell layer. Immunohistochemical staining of the cyst revealed a positive reaction of the cyst wall with CD31 and a negative reaction with FVIIIra, which corresponds to lymphatic origin and is compatible with the clear fluid contents of the cyst (**Figure 4**).

DISCUSSION

Animal pre-selection and health screening are an essential part of every pre-clinical trial. However, health examination of farm pigs entering scientific studies are challenging to perform and are often focused on general health and preventing infectious diseases from entering the facility. As a result, some cardiac conditions might go undetected. This is especially true for congenital heart defects in juvenile farm pigs, as in this age group the heart condition can still be effectively compensated with animals displaying no obvious symptoms (9). In the present study, this was the case for a juvenile female pig with an incidental finding of ASD with highly relevant L-R shunt, severe mitral and tricuspid regurgitation, and an increased pulmonary-aortic flow ratio.

The type of ASD described in this study is part of the spectrum of atrioventricular septal defects (AVSDs) and is also known as incomplete AVSD or endocardial cushion defect.

AVSDs account for ∼3% of congenital cardiac defects in humans and are also highly associated with both Noonan and Down syndrome (10). The most common type of ASD is the ostium secundum defect, which accounts for ∼80% of ASDs seen in the clinic. This defect represents a tissue deficiency of the fossa ovalis. Ostium primum ASDs, as in our case, account for only about 10% of septal defects and develop owing to a deficiency

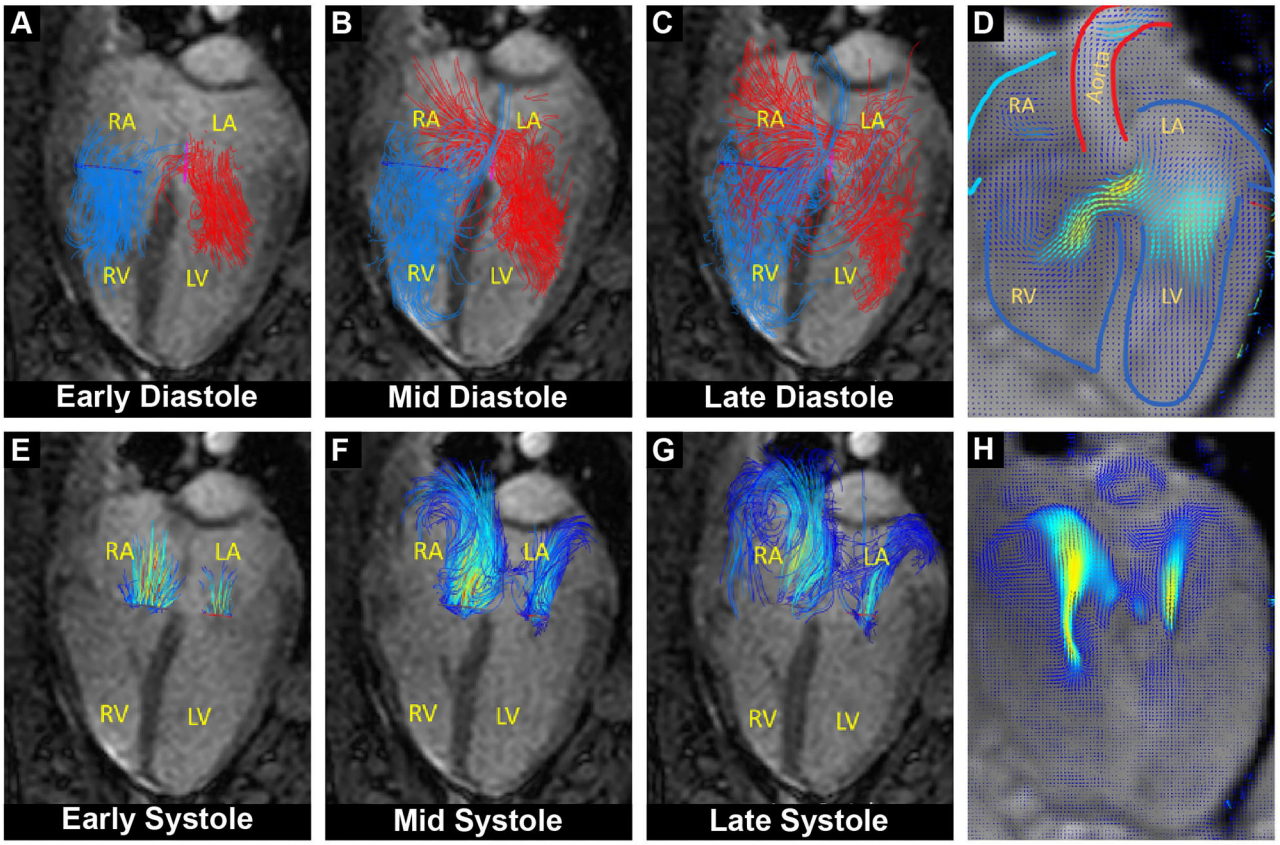

FIGURE 2 | Overlay of cardiac functional MRI and pathline visualization of blood flow during the cardiac cycle. RA, right atrium; LA, left atrium; RV, right ventricle; LV, left ventricle. **(A–C)** Pathline visualization of blood flow originating from the left (red) and from the right (blue) atrium, showing left-to-right flow across the atrial septum during diastole (L-R shunt). **(D)** Velocity field visualization focused on the diastolic shunt across the atrial septum. **(E–G)** Pathline visualization of regurgitant blood flow through the closed mitral and tricuspid valve during systole. **(H)** Velocity field visualization focused on the systolic mitral and tricuspid regurgitant flow.

in tissue near the atrioventricular valves (11). Ostium primum ASDs are often associated with clefting of the mitral valve, potentially inducing severe regurgitation. Although present at birth, ASD are often only diagnosed in adulthood as patients are frequently asymptomatic in their early life (11). Despite late development of symptoms, large ASDs induce dramatic circulatory perturbations and treatment is usually indicated (12). Conversely, it has been shown that AVSD and ASDs represent the most frequent congenital cardiac anomalies in farm pigs as well as in cloned and transgenic piglets (2, 13, 14). Moreover, heritable ventricular septal defect syndrome has been reported in Yucatan miniature swine breed for scientific purposes (15). However, little is known about the development and progression of AVSD and ASDs in farm pigs, as they are often presented as slaughter-house findings (2).

Diastolic L-R shunting as described in this case could be attributed to hemodynamic effects caused by differences in ventricular stiffness and compliance, whereas the small systolic R-L shunt could be due to pulmonary hypertension and severe tricuspid regurgitation. Diastolic MR is a rare event and often indicates diastolic left ventricular dysfunction or AV block (16). Furthermore, our case showed that the association of ostium primum ASD and mitral valve clefts seen in humans can also be applied to farm pigs. This valvular defect was probably the cause of severe mitral regurgitation that further decreased the forward cardiac output. Furthermore, myxomatous degeneration of the atrio-ventricular valves shown in the presented case, is often seen in patients with incompetent valves (17). Often described in dogs as a major contributor to mitral regurgitation, myxomatous valvular degeneration is though quite unusual in juvenile animals as in our case (18).

Cysts associated with ASD are rare but have been reported in patients previously. However, they were often either tumorous (myxoma) in origin or blood cysts usually filled with necrotic tissue and thrombus material (19, 20). Valvular cysts are relatively common in domestic farm species, particularly cattle, and are usually found as an incidental finding at slaughter (21). They may be of blood or lymphatic vascular origin. Approximately 2% of pigs may also be affected, although it rarely appears in animals under 6 months of age (22). Such valvular cysts are often filled with clear, aqueous fluid and lined with cells indistinguishable from the valvular endothelium (22). The age of the animal in our

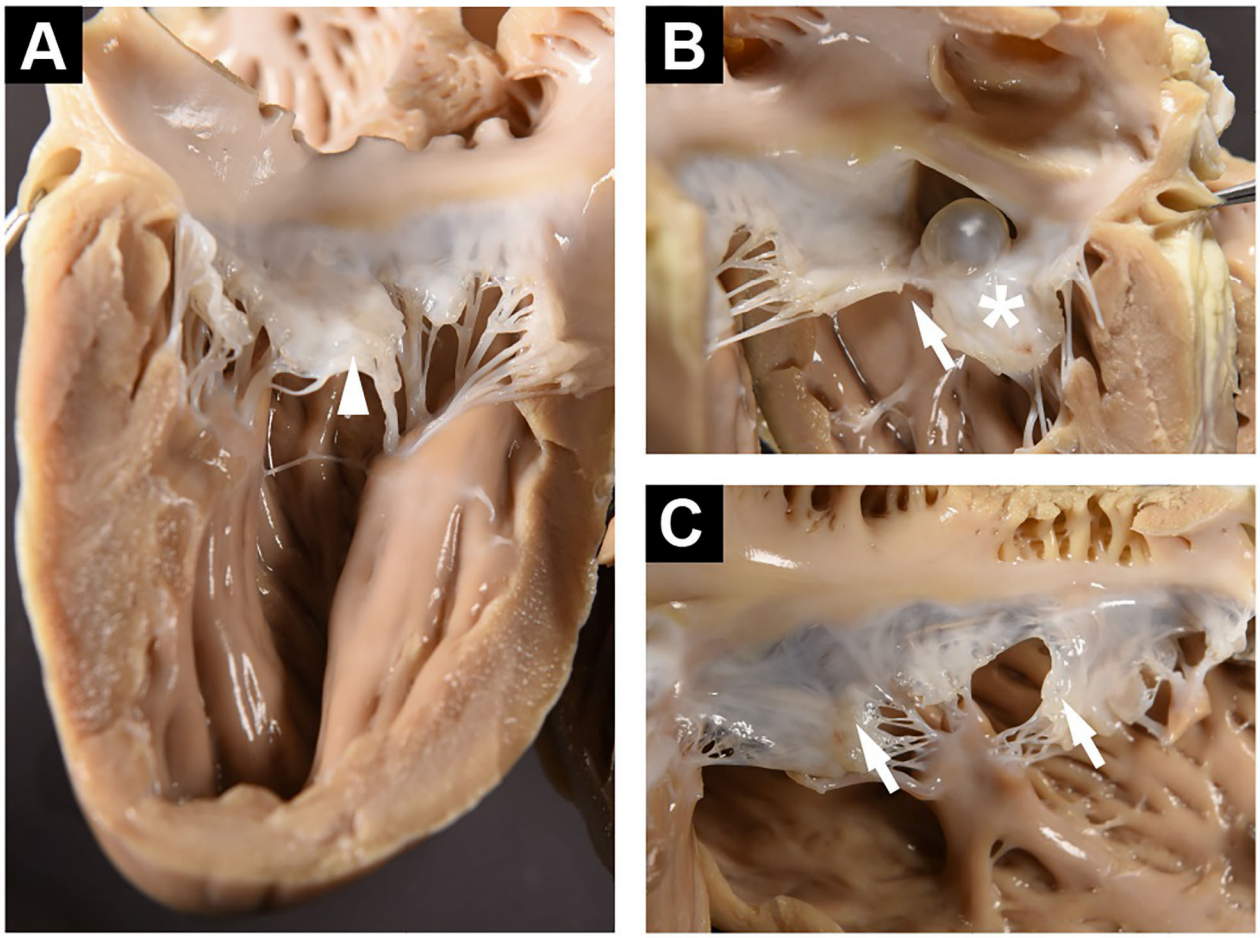

FIGURE 3 | (A) Left ventricular free wall and posterior mitral valve showing enlarged middle scallop (arrowhead). **(B)** Septum as viewed from the left ventricle showing ASD and cyst. The anterior mitral leaflet is exhibiting diffuse thickening (*), and A1/A2 clefting (arrow). **(C)** Right ventricular free wall and tricuspid valve with small nodular thickenings at the free margin (arrows).

case was unknown as only the weight was available, but can be estimated at 2–3 months.

Hence, congenital septal and related valvular defects in humans as well as in pet and farm animals are quite similar in anatomical appearance and corresponding hemodynamic effects. Although important, diagnosis of such cardiac disease could be quite challenging in large laboratory animals. Specialized imaging techniques such as functional and phase contrast MRI, besides echocardiography, can be applied. However, such MRI procedures require general anesthesia with multiple breath holds and are lengthy. Nevertheless, modern acquisition sequences and hardware are available that can significantly shorten the scan time and hence increase safety and 'comfort' of large animals used for scientific purposes (23, 24).

CONCLUSION

Domestic (i.e., farm) pigs are widely used in studies of human heart disease and therapy, mainly due to the similarity in heart development, physiology, and anatomy. These similarities also extend to congenital heart defects, such as ASD. Although having a strong impact on cardiac function, such defects are often not apparent upon clinical examination prior to the study and their diagnosis often require specialized imaging procedures like echocardiography or magnetic resonance. Easier to perform, jet less specific diagnostic methods, like cardio-pulmonary auscultation, might be successfully used with well-adapted and/or trained (mini-) pigs, however they are quite challenging in a setting of entry examination of farm pigs not used to human handling. Although echocardiographic equipment is widely available in the laboratory animal setting, examinations still require pigs to be sedated. Transthoracic as well as transoesophageal echo-imaging windows are quite restrictive in porcine and a comprehensive echocardiographic examination requires experience and adapted imaging protocols (25). On the other hand, magnetic resonance imaging of cardiac morphology, function and blood flow as well as myocardial perfusion

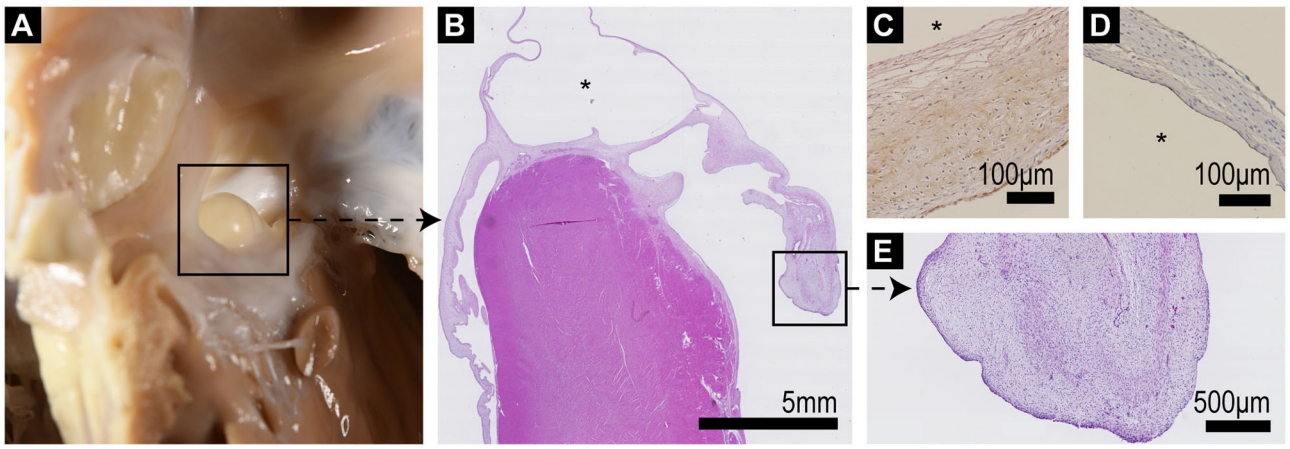

FIGURE 4 | (A) Septum with ASD and protruding serous cyst as viewed from the right ventricle. **(B)** Low power (10x) histological overview of a longitudinal section through the interventricular septum including the cyst (*) which bridges the septum and atrioventricular valves; the left AV valve is to the right of the image, exhibiting marked thickening and distortion of the valve leaflet particularly at its tip. **(C)** FXIIIra/vWF staining shows positive staining of the outer aspect of the cyst wall, which corresponds to the endocardial valve surface, with negative staining of the inner (*) lining. **(D)** CD31 (pan-endothelial marker) staining shows positive staining of both aspects of the cyst wall. **(E)** Higher power view of the thickened valve tip of the mitral valve showing loss of layering of the leaflet and expansion of the spongiosa by whorls of stellate cells within a loose pale staining proteoglycan matrix (endocardiosis).

and microstructural changes (such as fibrosis) can readily be obtained in farm pigs used for scientific purposes (26). By using standardized human-grade MRI protocols, ASD was successfully uncovered in this case. However, such protocols require specialized equipment, additional procedural handling and general anesthesia, hence are often not applicable in a routine laboratory setting.

Hence, congenital heart defects should be considered as a possible cause of inter-animal variability or even mortality when working with healthy-appearing juvenile domestic pigs in scientific projects. However, the detection of such defects is challenging and requires specialized imaging procedures *in vivo* or detailed pathological post-mortem examination.

DATA AVAILABILITY STATEMENT

The raw data supporting the conclusions of this article will be made available by the authors, without undue reservation.

ETHICS STATEMENT

The animal study was reviewed and approved by Cantonal Veterinary Office Zurich.

AUTHOR CONTRIBUTIONS

NC, MW, and CS: conceptualization, imaging procedure, animal handling, data reconstruction, data analysis, and preparation and review of manuscript. AM and LG: pathology data acquisition, data analysis, and preparation of the manuscript. SN and ME: data analysis, data interpretation, and review of manuscript. All authors contributed to the article and approved the submitted version.

FUNDING

This work was partially funded by grants from the Swiss National Science Foundation (PZ00P2_174144 and CR23I3_166485) and Olga Mayenfish foundation.

REFERENCES

1. Cesarovic N, Lipiski M, Falk V, Emmert MY. Animals in cardiovascular research. *Eur Heart J*. (2020) 41:200–3. doi: 10.1093/eurheartj/ehz933
2. Hsu FS, Du SJ. Congenital heart diseases in swine. *Vet Pathol*. (1982) 19:676–86. doi: 10.1177/030098588201900613
3. van der Linde D, Konings EE, Slager MA, Witsenburg M, Helbing WA, Takkenberg JJ, et al. Birth prevalence of congenital heart disease worldwide: a systematic review and meta-analysis. *J Am Coll Cardiol*. (2011) 58:2241–7. doi: 10.1016/j.jacc.2011.08.025
4. Le Gloan L, Legendre A, Iserin L, Ladouceur M. Pathophysiology and natural history of atrial septal defect. *J Thorac Dis*. (2018) 10(Suppl. 24):S2854–S63. doi: 10.21037/jtd.2018.02.80
5. Balchum OJ, Blount SG Jr, Gensini G. The persistent ostium primum atrial septal defect. *Circulation*. (1956) 13:499–509. doi: 10.1161/01.CIR.13.4.499
6. Faletra FF, Saric M, Saw J, Lempereur M, Hanke T, Vannan MA. Imaging for Patient's Selection and Guidance of LAA and ASD Percutaneous and Surgical Closure. *JACC Cardiovasc Imaging*. (2021) 14:3–21. doi: 10.1016/j.jcmg.2019.06.032

7. Chelu RG, Horowitz M, Sucha D, Kardys I, Ingremeau D, Vasanawala S, et al. Evaluation of atrial septal defects with 4D flow MRI-multilevel and inter-reader reproducibility for quantification of shunt severity. *Magma*. (2019) 32:269–79. doi: 10.1007/s10334-018-0702-z
8. Markl M, Frydrychowicz A, Kozerke S, Hope M, Wieben O. 4D flow MRI. *J Magn Reson Imaging*. (2012) 36:1015–36. doi: 10.1002/jmri.23632
9. Chetboul V, Gouni V, Charles V, Nicolle A, Sampedrano CC, Tissier R, et al. Atrial septal defects in dogs and cats: a retrospective study of 156 cases (2001-2005). *J Vet Intern Med*. (2006) 20:779–80. doi: 10.1111/j.1439-0442.2006.00813.x
10. Craig B. Atrioventricular septal defect: From fetus to adult. *Heart*. (2006) 92:1879–85. doi: 10.1136/hrt.2006.093344
11. Bradley EA, Zaidi AN. Atrial septal defect. *Cardiol Clin*. (2020) 38:317–24. doi: 10.1016/j.ccl.2020.04.001
12. Stout KK, Daniels CJ, Aboulhosn JA, Bozkurt B, Broberg CS, Colman JM, et al. 2018 AHA/ACC Guideline for the Management of Adults With Congenital Heart Disease: a report of the American College of Cardiology/American Heart Association Task Force on Clinical Practice Guidelines. *Circulation*. (2019) 139:e698–800. doi: 10.1161/CIR.0000000000000603
13. Schmidt M, Winther KD, Secher JO, Callesen H. Postmortem findings in cloned and transgenic piglets dead before weaning. *Theriogenology*. (2015) 84:1014–23. doi: 10.1016/j.theriogenology.2015.05.037
14. Holyoake PK, Stevenson J, Moran C, Stokes R, Kirk EP, Sugo E, et al. The occurrence of congenital heart defects in an inbred herd of pigs in Australia. *Aust Vet J*. (2006) 84:129–33. doi: 10.1111/j.1751-0813.2006.tb13395.x
15. Swindle MM, Thompson RP, Carabello BA, Smith AC, Hepburn BJ, Bodison DR, et al. Heritable ventricular septal defect in Yucatan miniature swine. *Lab Anim Sci*. (1990) 40:155–61.
16. Agmon Y, Freeman WK, Oh JK, Seward JB. Diastolic mitral regurgitation. *Circulation*. (1999) 99:e13. doi: 10.1161/01.CIR.99.21.e13
17. Neto FL, Marques LC, Aiello VD. Myxomatous degeneration of the mitral valve. *Autops Case Rep*. (2018) 8:e2018058. doi: 10.4322/acr.2018.058
18. Borgarelli M, Haggstrom J. Canine degenerative myxomatous mitral valve disease: natural history, clinical presentation and therapy. *Vet Clin North Am Small Anim Pract*. (2010) 40:651–63. doi: 10.1016/j.cvsm.2010.03.008
19. Dong D, Zhu T, Yang X, Zhu J. A patient with an unusual cyst of the inter-atrial septum and atrial sepal defect. *Echocardiography*. (2018) 35:876–9. doi: 10.1111/echo.14024
20. Turan T, Aykan AC, Akyuz AR, Gokdeniz T. Concomitant presence of blood cyst and atrial septal defect: a rare association. *Turk Kardiyol Dern Ars*. (2015) 43:577. doi: 10.5543/tkda.2015.46805
21. Marcato PS, Benazzi C, Bettini G, Masi M, DellaSalda L, Sarli G, et al. Blood and serous cysts in the atrioventricular valves of the bovine heart. *Vet Pathol*. (1996) 33:14–21. doi: 10.1177/030098589603300102
22. Jones JET. Observations on endocardial lesions in Pigs. *Res Vet Sci*. (1980) 28:281–90. doi: 10.1016/S0034-5288(18)32710-3
23. Peper ES, Gottwald LM, Zhang Q, Coolen BF, van Ooij P, Nederveen AJ, et al. Highly accelerated 4D flow cardiovascular magnetic resonance using a pseudo-spiral Cartesian acquisition and compressed sensing reconstruction for carotid flow and wall shear stress. *J Cardiovasc Magn Reson*. (2020) 22:7. doi: 10.1186/s12968-019-0582-z
24. Walheim J, Dillinger H, Kozerke S. Multipoint 5D flow cardiovascular magnetic resonance - accelerated cardiac- and respiratory-motion resolved mapping of mean and turbulent velocities. *J Cardiovasc Magn Reson*. (2019) 21:42. doi: 10.1186/s12968-019-0549-0
25. Billig S, Zayat R, Ebeling A, Steffen H, Nix C, Hatam N, et al. Transesophageal echocardiography in swine: evaluation of left and right ventricular structure, function and myocardial work. *Int J Cardiovasc Imaging*. (2021) 37:835–46. doi: 10.1007/s10554-020-02053-7
26. Stoeck CT, von Deuster C, Fuetterer M, Polacin M, Waschkies CF, van Gorkum RJH, et al. Cardiovascular magnetic resonance imaging of functional and microstructural changes of the heart in a longitudinal pig model of acute to chronic myocardial infarction. *J Cardiovasc Magn Reson*. (2021) 23:103. doi: 10.1186/s12968-021-00794-5

Conflict of Interest: The authors declare that the research was conducted in the absence of any commercial or financial relationships that could be construed as a potential conflict of interest.

Publisher's Note: All claims expressed in this article are solely those of the authors and do not necessarily represent those of their affiliated organizations, or those of the publisher, the editors and the reviewers. Any product that may be evaluated in this article, or claim that may be made by its manufacturer, is not guaranteed or endorsed by the publisher.

frontiers in Veterinary Science

ORIGINAL RESEARCH
published: 23 December 2021
doi: 10.3389/fvets.2021.809487

An Ovine Model of Awake Veno-Arterial Extracorporeal Membrane Oxygenation

*Jiachen Qi[1], Sizhe Gao[1], Gang Liu[1], Shujie Yan[1], Min Zhang[2], Weidong Yan[1], Qiaoni Zhang[1], Yuan Teng[1], Jian Wang[1], Chun Zhou[1], Qian Wang[1] and Bingyang Ji[1]**

[1] Department of Cardiopulmonary Bypass, State Key Laboratory of Cardiovascular Medicine, Fuwai Hospital, National Center for Cardiovascular Disease, Chinese Academy of Medical Science and Peking Union Medical College, Beijing, China, [2] Beijing Key Laboratory of Pre-clinical Research and Evaluation for Cardiovascular Implant Materials, State Key Laboratory of Cardiovascular Medicine, Fuwai Hospital, National Center for Cardiovascular Disease, Chinese Academy of Medical Science and Peking Union Medical College, Beijing, China

Background: Large animal models are developed to help understand physiology and explore clinical translational significance in the continuous development of veno-arterial extracorporeal membrane oxygenation (VA-ECMO) technology. The purpose of this study was to investigate the establishment methods and management strategies in an ovine model of VA-ECMO.

Methods: Seven sheep underwent VA-ECMO support for 7 days by cannulation *via* the right jugular vein and artery. The animals were transferred into the monitoring cages after surgery and were kept awake after anesthesia recovery. The hydraulic parameters of ECMO, basic hemodynamics, mental state, and fed state of sheep were observed in real time. Blood gas analysis and activated clotting time (ACT) were tested every 6 h, while the complete blood count, blood chemistry, and coagulation tests were monitored every day. Sheep were euthanized after 7 days. Necropsy was performed and the main organs were removed for histopathological evaluation.

Results: Five sheep survived and successfully weaned from ECMO. Two sheep died within 24–48 h of ECMO support. One animal died of fungal pneumonia caused by reflux aspiration, and the other died of hemorrhagic shock caused by bleeding at the left jugular artery cannulation site used for hemodynamic monitoring. During the experiment, the hemodynamics of the five sheep were stable. The animals stayed awake and freely ate hay and feed pellets and drank water. With no need for additional nutrition support or transfusion, the hemoglobin concentration and platelet count were in the normal reference range. The ECMO flow remained stable and the oxygenation performance of the oxygenator was satisfactory. No major adverse pathological injury occurred.

Conclusions: The perioperative management strategies and animal care are the key points of the VA-ECMO model in conscious sheep. This model could be a platform for further research of disease animal models, pathophysiology exploration, and new equipment verification.

Keywords: extracorporeal membrane oxygenation (ECMO), translational large animal model, critical care, cardiopulmonary support, perioperative management

OPEN ACCESS

Edited by:
Mark Gray,
University of Edinburgh,
United Kingdom

Reviewed by:
Warwick Wolf Butt,
Royal Children's Hospital, Australia
Guoping Lu,
Fudan University, China

****Correspondence:***
Bingyang Ji
jibingyang@fuwai.com

Specialty section:
This article was submitted to Comparative and Clinical Medicine, a section of the journal Frontiers in Veterinary Science

Received: *05 November 2021*
Accepted: *22 November 2021*
Published: *23 December 2021*

Citation:
Qi J, Gao S, Liu G, Yan S, Zhang M, Yan W, Zhang Q, Teng Y, Wang J, Zhou C, Wang Q and Ji B (2021) An Ovine Model of Awake Veno-Arterial Extracorporeal Membrane Oxygenation. Front. Vet. Sci. 8:809487. doi: 10.3389/fvets.2021.809487

INTRODUCTION

Veno-arterial extracorporeal membrane oxygenation (VA-ECMO) is used as a rescue therapy for patients with severe cardiopulmonary failure, and it can provide a bridge to recovery of the natural organs or transplantation (1, 2). Basic research in animals plays an important role in the continuous development of VA-ECMO technology. Small animal models are mainly used for the study of molecular biological mechanisms, whereas large animal models are developed to help understand physiology and explore clinical translational significance.

Previous studies on ECMO in large animals were mostly in the acute stage, and the survival time of large animals was within 24 h (3). Some studies have reported the use of ECMO on awake, non-intubated, spontaneously breathing large animals, as this strategy offers several benefits over mechanical ventilation (4–6). However, most awake ECMO methods focused on veno-venous modality (7, 8), and a few cases of awake VA-ECMO have been reported, especially support for up to 7 days (9). As there are some differences between large animals and clinical situations, optimized establishment methods and perioperative management strategies are still lacking in large animal models supported by VA-ECMO. Based on our previous studies on the survival rat model of cardiopulmonary support (10, 11), we aimed to establish an awake ovine VA-ECMO model that could run for 7 days and to investigate the establishment method and perioperative management using this model.

MATERIALS AND METHODS

Animals and Preparation

This experimental protocol was approved by the Institutional Animal Care and Use Committee (IACUC) of Fuwai Hospital [no. 0101-2-20-HX(X)], and all procedures were in accordance with the Guide for the Care and Use of Laboratory Animals published by the National Institutes of Health, USA (publication no. 86-23, revised 1996). The experiment was conducted at Beijing Key Laboratory of Pre-clinical Research and Evaluation for Cardiovascular Implant Materials, Animal Experimental Center of Fuwai Hospital (registration no. CNAS LA0009). The experimental animals were all healthy sheep with qualified quarantine provided by the Animal Experimental Center of Fuwai Hospital. During the whole experimental process, we strictly followed the ARRIVE (Animal Research: Reporting of *in vivo* Experiments) guidelines for pre-clinical animal studies.

Seven healthy 12- to 24-month-old adult male sheep (Small Tailed Han sheep, weight = 54–63 kg; Beijing Jinyutongfeng Trading Co., Ltd., Beijing, China) received VA-ECMO implantation (**Table 1**). Sheep received 24-h cage-side care and were monitored by a veterinarian according to the animal management protocol. The pre-operative fasting time was 48 h and the water deprivation time was 12 h.

Device

The VA-ECMO circuit consisted of an arterial cannula (18-Fr; Edwards Lifesciences, Irvine, CA, USA), a venous cannula (24-Fr; Edwards Lifesciences), a centrifugal pump drive and console (OASSIST STM001; Jiangsu STMed Technologies Co., Suzhou, China), a disposable centrifugal pump (STM CP-24 I; Jiangsu STMed Technologies Co.), and an oxygenator kit (Hilite7000LT; XENIOS, Heilbronn, Germany, or BE-PLS 2050, Maquet, Rastatt, Germany). The ECMO system was primed with 800 ml Ringer's lactate solution.

Surgical Procedure

Anesthesia was induced with propofol (3–5 mg/kg) through the auricular vein. Electrocardiogram monitoring was connected and basic hemodynamics were recorded. Tracheal intubation was conducted with a single-lumen endotracheal tube (#10). Then, the intubation was connected for mechanical ventilation. The ventilation mode was the volume control mode, the tidal volume was 8–10 ml/kg, the respiratory rate was 12–20 breaths/min, and the fraction of inspiration oxygen (FiO_2) was 60%. General anesthesia was maintained through isoflurane inhalation (2–3%) and propofol injection (8–10 mg kg^{-1} h^{-1}). Intraoperative blood pressure and heart rate were maintained within ±20% of their baseline values, and the partial pressure of end tidal carbon dioxide ($PaCO_2$) was maintained at 35–45 mmHg.

After the induction of anesthesia, the experimental sheep were immobilized on the operating table in the supine position. A single-lumen central venous catheter (18-G) was placed in the left jugular artery (arterial line) and a three-lumen central venous catheter (7-Fr) placed in the left jugular vein (venous line). These two lines were used for hemodynamic monitoring, intravenous fluids, drug injection, and blood collection.

Systemic anticoagulation was performed with a bolus of heparin (120 IU/kg) after the right jugular artery and vein were exposed. The target activated clotting time (ACT) of the cannulation was higher than 250 s. The arterial cannula (18-Fr) was inserted through the right common carotid artery, with the cannula descending 10–15 cm, while the venous cannula (24-Fr) was inserted through the right external jugular vein to the right atrium.

The centrifugal pump and a membrane oxygenator were connected and primed. The venous cannula was connected to the pump inlet, while the arterial cannula was connected to the oxygenator outlet. Extracorporeal circulation was started with a pump flow of 2.0–2.5 L/min and a rotational speed of 3,200–3,500 rpm. Then, the incision was sutured, the cannula was fixed securely, and the circuit line was half looped around the neck to avoid displacement and kinking (**Figure 1A**).

The sheep were moved into a metabolic cage and properly restrained (**Figure 1B**) after the operation was completed and vital signs were stable. Special attention was paid to the fixation of the head and shoulder of the sheep to prevent the cannula from dislocation or kinking. Then, the depth of anesthesia was gradually reduced. After the sheep recovered to spontaneous respiration and the blood gas analysis was stable, the endotracheal tube was extubated.

Post-surgical Care, Monitoring, and Data Collection

Extracorporeal circulation was maintained with a target pump flow of 2.0 L/min (30 ml kg^{-1} min^{-1}) and pump speed around

TABLE 1 | Detailed characteristics of experimental sheep.

Sheep number	Gender	Weight (kg)	Duration (days)	Termination	Cannulation site
S2020-014	M	58	7	Scheduled	Vjr (24-Fr)–Ajr (18-Fr)
S2020-038	M	57	7	Scheduled	Vjr (24-Fr)–Ajr (18-Fr)
S2020-040	M	54	7	Scheduled	Vjr (24-Fr)–Ajr (18-Fr)
S2020-041	M	55	7	Scheduled	Vjr (24-Fr)–Ajr (18-Fr)
S2020-043	M	56	7	Scheduled	Vjr (24-Fr)–Ajr (18-Fr)
S2020-042	M	63	1	Accidental death	Vjr (24-Fr)–Ajr (18-Fr)
S2020-016	M	56	2	Accidental death	Vjr (24-Fr)–Ajr (18-Fr)

M, male; Vjr, right jugular vein; Ajr, right jugular artery.

FIGURE 1 | (A) Fixation of the cannula around the neck (from *right* to *left side*). **(B)** The sheep were moved into a metabolic cage and properly restrained after the operation. **(C,D)** The sheep could eat and move freely within a certain range in the monitoring cage. They were provided with appropriate amount of hay, pellets, and water every day.

3,500 rpm during the experimental period. The sweep gas flow of the oxygenator was 1.0–1.5 L/min at a concentration of 50–80%. Dynamic adjustment was made according to the blood gas analysis, venous oxygen saturation (SvO_2), and arterial oxygen saturation (SaO_2). Heparin was infused continuously to maintain ACT in the range of 220–250 s. In the first 24 h after surgery, flurbiprofen axetil (1–2 mg/kg) and dexmedetomidine (0.2–0.3 $\mu g\ kg^{-1}\ h^{-1}$) were administered intravenously.

After the surgery, the sheep stayed awake in the monitoring cage. The animals freely ate hay and feed pellets and drank water. The daily volume load was maintained at a positive balance around 1,000 ml, while the central venous pressure was maintained at 5–12 cm H_2O. Intravenous infusion was adjusted according to the intake, urine volume, blood pressure, and mental state. After operation, antibiotics were used daily to prevent infection (cefuroxime sodium, 1.5 g, i.v., b.i.d.). The incision was disinfected daily, and the infection and bleeding signs were observed at the same time.

Basic hemodynamics (including heart rate and mean arterial pressure) of experimental sheep and the ECMO hydraulic parameters (including speed, flow rate, pre-pump pressure, post-pump pressure, and post-oxygenator pressure) were monitored in real time. Blood gas analysis (Abbott i-STAT1; Abbott Point of Care Inc., Princeton, NJ, USA) and ACT (Hemochron Signature Elite; Hemochron, Bedford, MA, USA) were tested every 6 h. Complete blood count (ADVIA 2120i; Siemens Healthcare, Erlangen, Germany), free hemoglobin (fHb) (DiaSpect T Low Hemoglobin Analyzer; DiaSpect Medical GmbH, Sailauf, Germany), blood chemistry (Catalyst One; IDEXX Laboratories, Inc., Westbrook, MA, USA), and coagulation test (Fully

Automated Coagulation Analyzer SF-8050; Beijing Succeeder Technology Inc., Beijing) were monitored daily. After 168 h (7 days), the ECMO system was removed and the sheep were euthanized by venous administration of potassium chloride (100 mg/kg) under the sedation of propofol (20 mg/kg). Necropsy was conducted by two pathologists to visualize the cannula position *in vivo* and to examine cannulation-related injury and thrombus formation. The main organs (heart, lung, kidney, liver, brain, and intestine) were removed for further histopathological evaluation.

Histological Analysis

Specimens of the main organs and blood vessels obtained through pathological anatomy were cut into small pieces and fixed with 10% neutral fumarin fix solution (Yili Fine Chemical Co., Ltd., Beijing, China). The fixed tissues were embedded in paraffin and hematoxylin–eosin staining (hematoxylin; Yili Fine Chemical Co., Ltd.; eosin; Sigma-Aldrich Trading Co., Ltd., Shanghai, China) was performed on 5-μm-thick samples. Histological analysis was performed under a light microscope and evaluated by two pathologists.

Data Analysis

Data were analyzed using SPSS software (version 26.0; IBM Corp., Chicago, IL, USA) and GraphPad Prism 8 (version 8.4.0; San Diego, CA, USA). Continuous variables were presented as the mean ± standard deviation (SD), and significant differences at various time points were determined with one-way analysis of variance with *post-hoc* multiple comparisons. A $p < 0.05$ was considered statistically significant.

RESULTS

Seven sheep survived surgery and recovered from anesthesia. Five sheep survived and successfully weaned from ECMO. Two sheep died within 24–48 h of ECMO support. One animal (no. S2020-016) suffered low partial pressure of arterial oxygen (PaO_2, 62 mmHg), while the oxygenation performance of the oxygenator decreased (PaO_2 after the oxygenator was 85 mmHg) after 6 h of ECMO support. After continuous liquid therapy and application of vasoactive drugs (epinephrine and norepinephrine), the blood pressure of the sheep continued to decrease. The sheep finally died of respiratory and circulatory failure after 48 h of ECMO support. The other animal developed neck swelling after 8 h of ECMO support, and then the hemoglobin decreased continuously. Although we performed a second operation to explore the bleeding point and remove the hematoma, the sheep still died of hemorrhagic shock after 24 h of ECMO support. These two sheep were not included in our subsequent data and histological analysis.

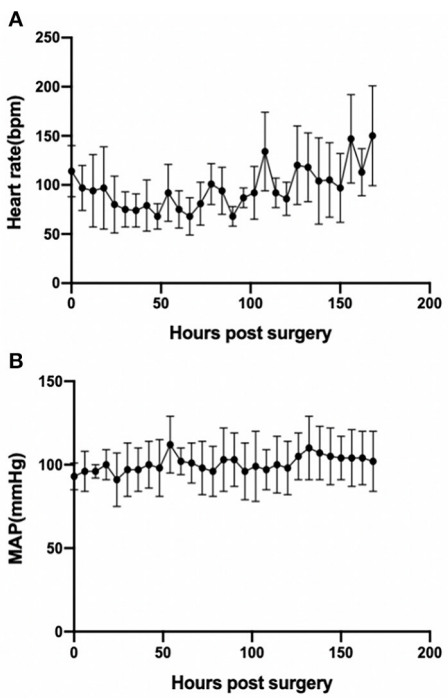

FIGURE 2 | Basic hemodynamics as assessed by heart rate ($p < 0.001$) **(A)** and MAP ($p > 0.05$) **(B)** during the experimental period. *Error bars* show the standard deviation. *MAP*, mean arterial pressure.

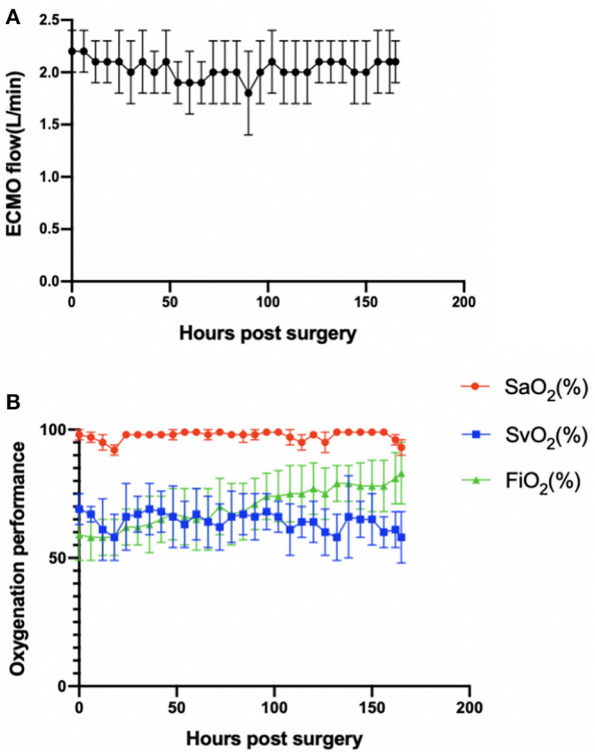

FIGURE 3 | (A) ECMO flow was stable ($p > 0.05$). **(B)** Oxygenation performance of the oxygenator was good ($p > 0.05$). *Error bars* show the standard deviation. *ECMO*, extracorporeal membrane oxygenation; SaO_2, oxygen saturation after the oxygenator; SvO_2, oxygen saturation before the oxygenator; FiO_2, fraction of inspiration oxygen.

TABLE 2 | Main hematology, hemolysis, coagulation, and biochemical results.

Variable[a]	Pre-surgical	Hours after surgery							
		6 h	24 h	48 h	72 h	96 h	120 h	144 h	168 h
Main hematology, hemolysis and coagulation results									
Hb (g/L)	102 ± 15	104 ± 22	112 ± 9	106 ± 10	103 ± 11	113 ± 10	101 ± 12	102 ± 8	102 ± 13
PLT ($\times 10^9$/L)	162 ± 85	166 ± 82	138 ± 58	130 ± 53	142 ± 52	182 ± 98	222 ± 191	275 ± 200*	276 ± 157*
WBC ($\times 10^9$/L)	6.63 ± 0.81	7.20 ± 4.23	7.20 ± 4.23	14.66 ± 5.73*	9.17 ± 1.18*	6.88 ± 3.11	7.96 ± 1.77	9.54 ± 2.58*	14.23 ± 6.34*
hsCRP (mg/L)	0.28 ± 0.10	0.19 ± 0.13	0.21 ± 0.12	0.12 ± 0.14	0.19 ± 0.10	0.19 ± 0.14	0.06 ± 0.03	0.10 ± 0.10	0.18 ± 0.09
fHb (g/L)	0.28 ± 0.07	0.12 ± 0.16	0.24 ± 0.05	0.20 ± 0.11	0.14 ± 0.12	0.24 ± 0.05	0.14 ± 0.12	0.20 ± 0.00	0.16 ± 0.08
ACT (s)	165 ± 20	252 ± 40	273 ± 24	233 ± 27	226 ± 32	249 ± 22	231 ± 13	242 ± 14	230 ± 9
Main biochemical indicators									
TP (g/L)	68.8 ± 10.2	64.2 ± 7.9	65.2 ± 6.8	65.8 ± 6.0	67.8 ± 5.9	69.4 ± 5.3	71.7 ± 2.7	69.8 ± 5.3	73.7 ± 7.2
ALB (g/L)	27.0 ± 3.4	25.4 ± 1.7	25.8 ± 2.6	26.3 ± 2.5	26.4 ± 2.3	27.0 ± 2.3	27.6 ± 2.7	26.6 ± 3.2	27.8 ± 3.3
Cr (μmol/L)	135.7 ± 15.4	134.5 ± 25.1	128.1 ± 20.5	109.2 ± 16.2	114.6 ± 20.2	110.8 ± 15.5	110.6 ± 14.3	115.4 ± 24.8	109.7 ± 27.6

Hb, hemoglobin; PLT, platelet; WBC, white blood cells; hsCRP, high-sensitivity C-reactive protein; fHb, plasma-free hemoglobin; ACT, activated clotting time; TP, total protein; ALB, albumin; Cr, creatinine.

**$p < 0.05$ (compared with pre-surgical baseline).*

[a]Data are shown as the mean ± SD.

Hemodynamics and ECMO Performance

The animals stayed awake and freely ate hay and feed pellets and drank water (**Figures 1C,D**). Hemodynamics were in the normal physiological range throughout the experimental period (**Figure 2**), with no need of inotropic medicine. During the experiment, the ECMO flow was stable ($p > 0.05$; **Figure 3A**) and the oxygenation performance of the oxygenator was good ($p > 0.05$; **Figure 3B**).

Hematology, Hemolysis, and Coagulation Results

Table 2 summarizes the changes of the main hematology, hemolysis, and coagulation results. Considering the basic physiological values of hematology in sheep (12), the hemoglobin levels remained stable with no blood transfusion ($p > 0.05$), and the platelet counts were within the physiologic range, although slightly decreased, and then increased after surgery. White blood cell (WBC) counts increased at 48, 72, 144, and 168 h after surgery, while high-sensitivity C-reactive protein (hsCRP) was still within normal ranges ($p > 0.05$). The fHb concentration was kept at a low level after surgery ($p > 0.05$). The ACT was maintained at the target level by dynamically adjusting the heparin dosage.

Blood Gas Parameters, Blood Chemistry, and Fluid Volume

The variety of main blood gas parameters is shown in **Figure 4**. Arterial blood pH, PaO_2, and $PaCO_2$ were maintained at relatively normal levels. Important biochemical indicators are also summarized in **Table 2**. The levels of total protein (TP) and albumin (ALB) were relatively stable ($p > 0.05$). The creatinine levels during VV-ECMO support and after weaning were lower than those of the baseline ($p > 0.05$). The daily volume load was maintained at a positive balance (1,096 ± 654 ml/day).

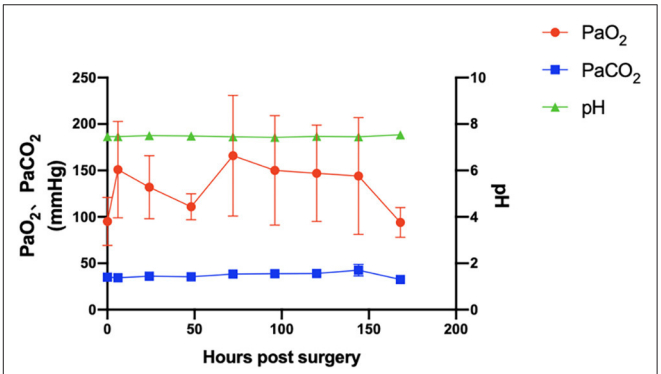

FIGURE 4 | The main blood gas parameters of arterial blood pH, PaO_2, and $PaCO_2$ ($p > 0.05$) were maintained at normal levels. *Error bars* show the standard deviation. *PaO_2*, partial pressure of arterial oxygen; *$PaCO_2$*, partial pressure of arterial carbon dioxide.

Pathological Analysis

Two animals died within 24–48 h of ECMO support. According to the necropsy, one sheep died of respiratory and circulatory

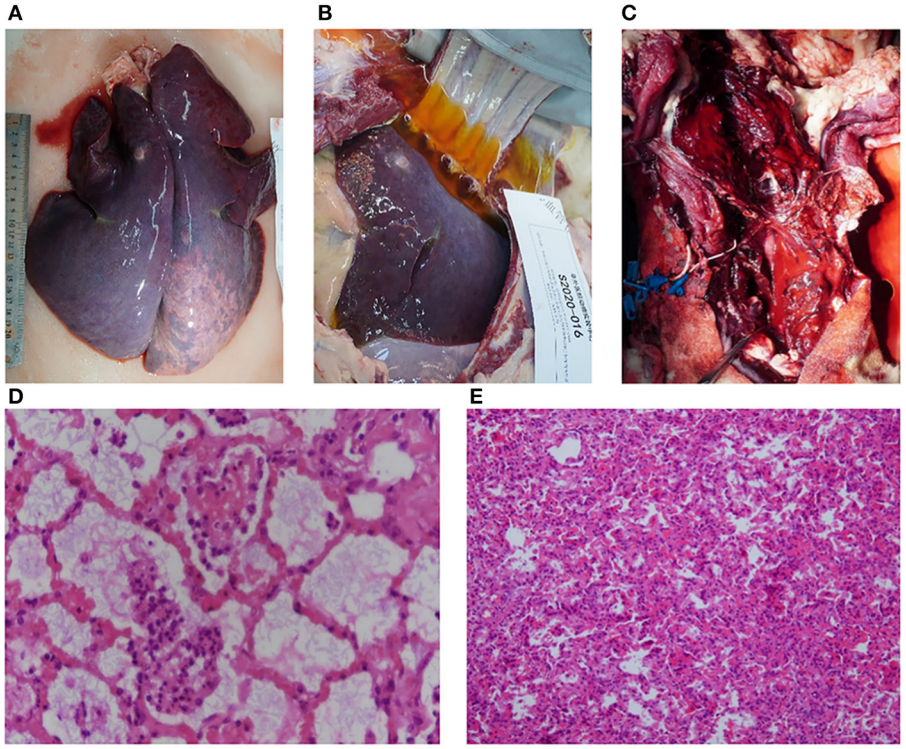

FIGURE 5 | Pathological evaluation of dead animals. **(A)** Pulmonary edema, congestion, and consolidation were observed in both lungs (animal no. S2020-016). **(B)** A large amount of pleural effusion was observed (animal no. S2020-016). **(C)** Extensive hemorrhage and hematoma formation around the neck (animal no. S2020-042). **(D)** Inflammatory cells and fungal hyphae could be seen in the alveoli and bronchium under a light microscope (stained with hematoxylin and eosin, ×100 magnification) (animal no. S2020-016). **(E)** Atelectasis caused by hemothorax was observed under a light microscope (stained with hematoxylin and eosin, ×200 magnification) (animal no. S2020-042).

TABLE 3 | Main pathological findings.

Sheep number	Cannulation position	Vascular injury at cannulation site	Cardiac findings	Pulmonary changes	Other changes
S2020-014	Correct	None	Myocarditis	None	None
S2020-038	Correct	Thrombosis	None	None	Small focal renal infarction
S2020-040	Correct	None	None	None	Hepatic cyst
S2020-041	Correct	Thrombosis	Small calcification	None	None
S2020-043	Correct	Thrombosis	None	None	None

failure caused by fungal pneumonia within 48 h (no. S2020-016). Pulmonary edema, congestion, and consolidation occurred in both lungs accompanied by a large amount of pleural effusion (**Figures 5A,B**). Food fibers could be seen in the small airway, while a large number of fungal hyphae with suppurative inflammation in the alveoli were observed (**Figure 5D**). The other sheep died in the first 24 h of hemorrhagic shock caused by bleeding at the left jugular artery cannulation site, which was used for hemodynamic monitoring (no. S2020-042). Gross anatomy showed massive acute bleeding (mainly blood clots) in the neck and superior mediastinum on the opposite side (left) of the ECMO cannulation (**Figure 5C**). At the same time, hemothorax led to atelectasis (**Figure 5E**). There was an obvious edema and a small amount of bleeding at the cannulation site of the right jugular artery and vein.

Five sheep survived and were successfully weaned from ECMO. Pathological anatomy showed that the position of the cannula was correct and there were no subcutaneous hematoma or other bleeding signs (**Table 3**; **Figure 6**). Thrombosis at the cannulation site occurred in three cases (3/5 cases; **Table 3**), but there was no vascular occlusion or stenosis. According to the histopathological evaluation, the organ infarction rate was low (1/5 cases; **Table 3**), and the infarct focal size was small (<5% surface areas, with no obvious clinical effect). Focal lymphocytic myocarditis near the epicardium was observed under a light microscope in one sheep (no. S2020-014; **Table 3**; **Figure 6**), but the size of the lesion was small (<5% surface areas) and there was no obvious clinical effect. Multiple small myocardial calcifications were observed under a light microscope in one sheep (no. S2020-041; **Table 3**; **Figure 6**), but were of no

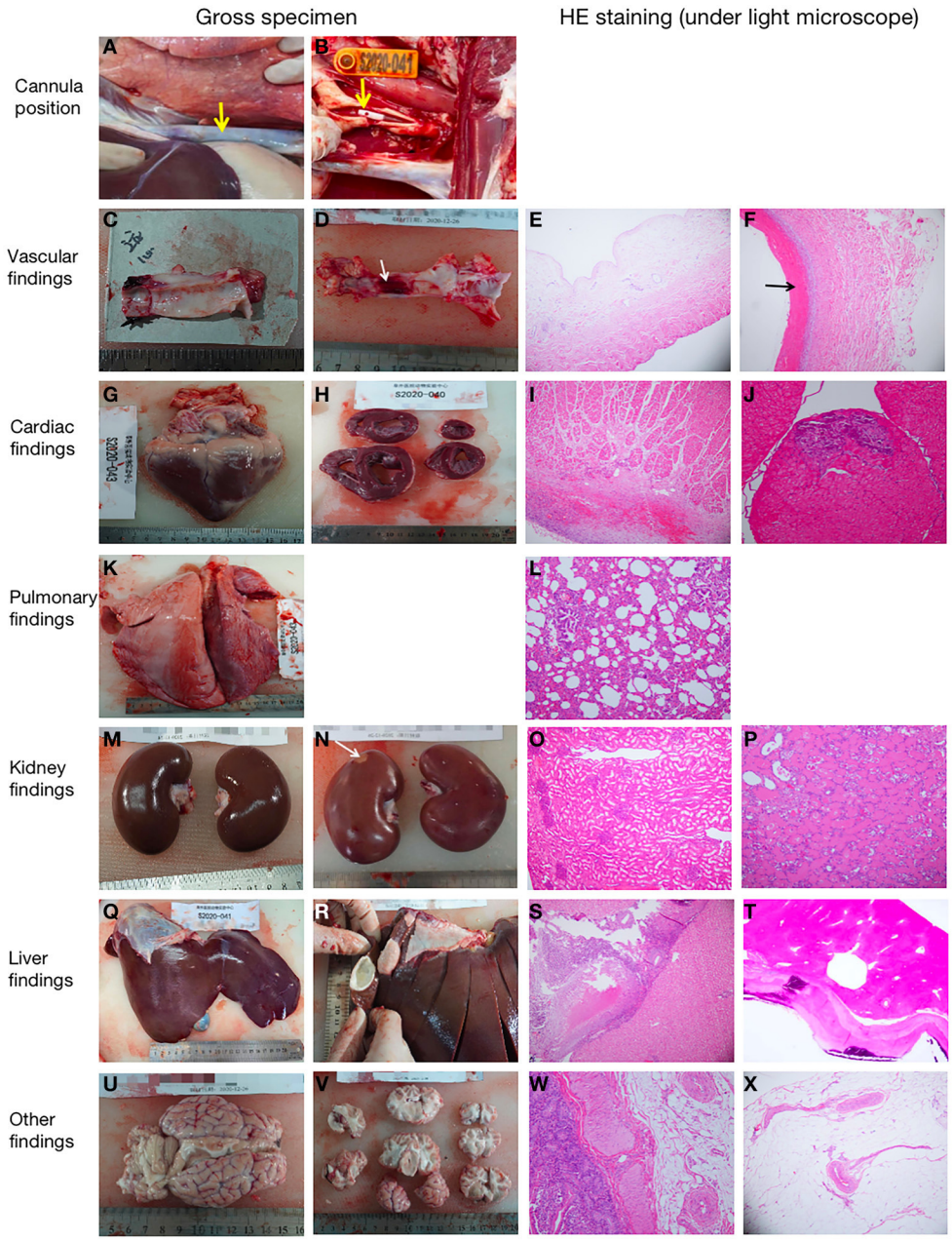

FIGURE 6 | Representative pathological pictures. **(A)** The internal thoracic segment of the jugular vein cannula was observed *in situ*. The superior vena cava was not dissected (as shown by the *arrow*), and there was no cannulation displacement (animal no. S2020-038). **(B)** The tip of the cannula (as shown by the *arrow*) could be seen in the jugular artery (animal no. S2020-041). **(C)** Normal gross specimen of the right jugular intima (animal no. S2020-040). **(D)** Thrombus (as shown by the *arrow*) was seen in the middle intima of the right jugular vein (animal no. S2020-038). **(E)** The normal jugular vein was observed under a light microscope [stained with hematoxylin and eosin (HE), ×10 magnification] (animal no. S2020-014). **(F)** There was a small amount of thrombosis in the jugular vein at the cannulation site (as shown by the *arrow*) (HE, ×100 magnification) (animal no. S2020-038). **(G,H)** Normal gross specimens of the heart (animal nos. S2020-043 and S2020-040). **(I)** Normal myocardial tissue of the right atrium (HE, ×10 magnification) (animal no. S2020-038). **(J)** Small myocardial calcification (HE, ×20 magnification) (animal no. S2020-041). **(K)** Normal lung specimen (animal no. S2020-043). **(L)** Normal lung tissue (HE, ×20 magnification) (animal no. S2020-038). **(M)** Gross specimen of normal kidney (animal no. S2020-043). **(N)** Gross specimen of small renal infarction (as shown by the *arrow*) (animal no. S2020-038). **(O)** Normal kidney tissue (HE, ×10 magnification) (animal no. S2020-043). **(P)** Small infarct (HE, ×20 magnification) was observed in the kidney (animal no. S2020-038). **(Q)** Normal liver specimen (animal no. S2020-041). **(R)** Cyst was found in the liver (animal no. S2020-040). **(S)** Normal liver tissue (HE, ×10 magnification) (animal no. S2020-038). **(T)** Spontaneous cyst with calcification (HE, ×20 magnification) was found in the liver, (animal no. S2020-040). **(U,V)** Gross specimens of the brain. There was no hemorrhage or infarction (animal no. S2020-038). **(W)** Normal intestine tissue (HE, ×20 magnification) (animal no. S2020-043). **(X)** Normal mesentery tissue (HE, ×10 magnification) (animal no. S2020-014).

clinical significance. In addition, no major adverse pathological injury occurred.

DISCUSSION

We established an awake VA-ECMO ovine model that achieved both respiratory and circulatory support for 7 days. By using the portable OASSIST ECMO system that has shown satisfactory safety and biocompatibility during the 7-day pre-clinical evaluation (13), 5 of the 7 sheep survived and were successfully weaned from ECMO. During the experiment, hemodynamics were in the normal physiological range, and no serious bleeding or coagulation events occurred. The animals obtained adequate nutrition from normal eating and maintained a satisfactory hemoglobin level, with no need of additional artificial nutritional support or blood transfusion. The ECMO flow remained stable, plasma fHb was maintained at a low level, and the oxygenation performance of the oxygenator was satisfactory. No major adverse pathological injury occurred.

In this study, extracorporeal circulation was maintained with a target rotational speed of 3,200–3,500 rpm and a pump flow of 2.0 L/min. Although the JACC Scientific Expert Panel stated that the flow of VA-ECMO could reach 4–6 L/min (50–70 ml kg^{-1} min^{-1}) when supporting human patients with heart failure (14), a target pump flow of 2.0 L/min could satisfy the hemodynamic needs in our healthy sheep model with a functional native heart. As the healthy sheep has a functional native heart, a higher pump speed will increase the pre-pump pressure, resulting in blood damage. Besides, Iizuka et al. tested a novel centrifugal pump (CAPIOX SL) in chronic large animal (healthy sheep) experiments, with target pump flow of 2.0–3.0 L/min during the experimental period (9). Akiyama et al. also evaluated an ultra-compact durable ECMO system in healthy sheep, and the flow rate ranged from 2.2 $\pm$ 0.7 to 2.5 $\pm$ 0.1 L/min under a pump speed higher than 4,000 rpm (15). In our experiment, the speed was set at 3,200–3,500 rpm. The ECMO flow ranged from 1.8 $\pm$ 0.1 to 2.4 $\pm$ 0.14 L/min. This range can provide sufficient hemodynamic support comparable to that in previous animal studies. Further research on establishing a large animal disease model should dynamically adjust the target rotational speed and flow rate of VA-ECMO according to the specific situation.

At the beginning of our experiment, two sheep died of fungal pneumonia or hemorrhagic shock within 24–48 h after ECMO support. According to the necropsy, sheep no. S2020-016 died of respiratory and circulatory failure caused by fungal pneumonia within 48 h. Food fibers could be seen in the small airway, while a large number of fungal hyphae with suppurative inflammation in the alveoli were also observed. Therefore, we inferred that the fungal pneumonia was caused by reflux aspiration. At the same time, the anesthesia induction and the endotracheal intubation process of the experimental sheep were smooth, and oxygenation was normal during the maintenance of anesthesia. Therefore, we considered that it is highly possible that the reflux aspiration occurred in the period of anesthesia recovery (recovery to spontaneous respiration) after ECMO implantation. During the recovery period, the sheep did not fully recover muscle strength and manifested active cough and swallowing reflex, resulting in gastroesophageal reflux. To avoid the occurrence of reflux aspiration, the sheep should be fasted for at least 48 h and the endotracheal tube should be extubated when the sheep recovered spontaneous breathing, swallowing reflex, or airway protective reflex. Besides, we should pay more attention to cannulation. Effective hemostasis is required during cannulation, and observation for serious bleeding or thrombotic events is also needed during ECMO support. In addition, these adverse events indicate that the cannulation approach, perioperative management, and animal care are the key to the success of this model.

Sheep can be used to establish an awake ECMO model because they are docile and more conducive to perioperative management than are other large animals such as pigs and oxen. Different from the femoro-femoral cannulation approach often used in adult VA-ECMO patients, the femoral artery and vein of sheep are relatively thin, while the neck vessels are thick, and mobility is relatively fixed. In order to ensure the target flow and flow stability, we selected the neck vessels of sheep as the cannulation vessel. Besides, the upper-body cannulation approach is often preferred when mobility is of sufficiently high priority (16). In our model, the common carotid artery and external jugular vein were chosen to conduct the autonomous activity. The advantage of ambulation was obvious. Firstly, sheep breathed and coughed spontaneously, which might reduce pulmonary infection. Secondly, no intubation allowed independent feed for sheep to get adequate nutrition, contributing to appropriate hemoglobin, TP and ALB levels, and no need for blood transfusion. However, caring conscious and ambulatory sheep supported by ECMO met some difficulties. We paid attention to avoid the occurrence of reflux aspiration, as mentioned before. To ensure stable ECMO flow and avoid cannula dislocation or kinking, the cannula was fixed securely while the line was half looped around the neck. Special attention was paid to the fixation of the head and shoulder of the sheep using a "sling" (**Figure 1B**) to prevent the cannula from kinking.

Anticoagulant management is an important part of the perioperative management. In our preliminary experiment, the ACT was set at 180–220 s according to clinical situations and previous studies in sheep (7–9, 17, 18). However, fibrinogen accumulated and thrombus formed in the oxygenator within 48 h, indicating that sheep needed higher anticoagulant conditions. Therefore, we adjusted the target ACT to 220–250 s, while there was no serious bleeding or coagulation events occurred. The ACT should be monitored every 6 h throughout the experiment to detect the potential risk of heparin insufficiency or overdose.

Some retrospective studies have reported that fluid overload commonly occur in patients supported with ECMO (19). Progressive fluid overload during ECMO is associated with acute kidney injury, higher mortality, prolonged mechanical ventilation, and ECMO duration (20). Therefore, the daily fluid balance of the experimental sheep should be focused on. Unlike in clinical practice where patients tend to have cardiac failure, a negative fluid balance does not need to be controlled as healthy sheep have normal cardiac function. At the same time, excessive

fluid negative balance can affect the performance of ECMO and lead to blood damage. Considering the insensible water loss (such as salivation) and the reduced food intake of sheep during ECMO support, the daily volume was maintained at positive balance around 1,000 ml (1,096 ± 654 ml/day). Intravenous infusion was adjusted properly according to the fluid balance. The creatinine levels during ECMO support were lower than those at baseline, and no pathological changes were found in the kidney, indicating that the fluid management was appropriate and the renal function was maintained within the normal range.

One advantage of this study is that it is the first to focus on the perioperative management and animal care in large animal models of awake VA-ECMO. Further studies should be conducted based on this model. Firstly, the interaction between cardiopulmonary support and natural perfusion should be explored. Besides, detailed hemodynamic analysis (such as cardiac output) is expected during awake VA-ECMO support. In addition, further studies on the establishment of a disease model in large animals and related pathophysiology exploration are also expected.

CONCLUSIONS

We established a VA-ECMO ovine model by cannulation *via* the jugular vein and artery, which could achieve both respiratory and circulatory support for 7 days. The perioperative management strategies and animal care are the key points of this model. This model could be a platform for further research on disease animal models, hemodynamic analysis, pathophysiology exploration, and new equipment verification.

DATA AVAILABILITY STATEMENT

The raw data supporting the conclusions of this article will be made available by the authors, without undue reservation.

ETHICS STATEMENT

The animal study was reviewed and approved by Institutional Animal Care and Use Committee (IACUC) of Fuwai Hospital.

AUTHOR CONTRIBUTIONS

BJ conceived and originally designed the research and approved the final manuscript. JQ conducted the experiment and wrote the draft of the manuscript. JQ and SG analyzed the data. JQ, SG, WY, and QZ extracted data from the electronic and paper databases. GL, SY, and MZ conducted the experiment and revised the section Discussion of the manuscript. JW, YT, CZ, and QW conducted the experiment and revised the section Materials and Methods of the manuscript. All authors contributed to the article and approved the submitted version.

REFERENCES

1. Karagiannidis C, Brodie D, Strassmann S, Stoelben E, Philipp A, Bein T, et al. Extracorporeal membrane oxygenation: evolving epidemiology and mortality. *Intensive Care Med.* (2016) 42:889–96. doi: 10.1007/s00134-016-4273-z
2. Muller G, Flecher E, Lebreton G, Luyt CE, Trouillet JL, Bréchot N, et al. The encourage mortality risk score and analysis of long-term outcomes after VA-ECMO for acute myocardial infarction with cardiogenic shock. *Intensive Care Med.* (2016) 42:370–8. doi: 10.1007/s00134-016-4223-9
3. Heinsar S, Rozencwajg S, Suen J, Bassi GL, Malfertheiner M, Vercaemst L, et al. Heart failure supported by veno-arterial extracorporeal membrane oxygenation (ECMO): a systematic review of pre-clinical models. *Intensive Care Med Exp.* (2020) 8:16. doi: 10.1186/s40635-020-00303-5
4. Langer T, Santini A, Bottino N, Crotti S, Batchinsky AI, Pesenti A, et al. "Awake" extracorporeal membrane oxygenation (ECMO): pathophysiology, technical considerations, and clinical pioneering. *Crit Care.* (2016) 20:150. doi: 10.1186/s13054-016-1329-y
5. Deng L, Xia Q, Chi C, Hu G. Awake veno-arterial extracorporeal membrane oxygenation in patients with perioperative period acute heart failure in cardiac surgery. *J Thorac Dis.* (2020) 12:2179–87. doi: 10.21037/jtd.2020.04.38
6. Abrams D, Garan AR, Brodie D. Awake and fully mobile patients on cardiac extracorporeal life support. *Ann Cardiothorac Surg.* (2019) 8:44–53. doi: 10.21037/acs.2018.08.03
7. Zhou X, Wang D, Sumpter R, Pattison G, Ballard-Croft C, Zwischenberger JB. Long-term support with an ambulatory percutaneous paracorporeal artificial lung. *J Heart Lung Transplant.* (2012) 31:648–54. doi: 10.1016/j.healun.2012.02.007
8. Karagiannidis C, Joost T, Strassmann S, Weber-Carstens S, Combes A, Windisch W, et al. Safety and efficacy of a novel pneumatically driven extracorporeal membrane oxygenation device. *Ann Thorac Surg.* (2020) 109:1684–91. doi: 10.1016/j.athoracsur.2020.01.039
9. Iizuka K, Katagiri N, Takewa Y, Tsukiya T, Mizuno T, Itamochi Y, et al. Evaluation of the novel centrifugal pump, CAPIOX SL, in chronic large animal experiments. *Artif Organs.* (2018) 42:835–41. doi: 10.1111/aor.13100
10. Liu M, Zeng Q, Li Y, Liu G, Ji B. Neurologic recovery after deep hypothermic circulatory arrest in rats: a description of a long-term survival model without blood priming. *Artif Organs.* (2019) 43:551–60. doi: 10.1111/aor.13407
11. Liu M, Li Y, Liu Y, Yan S, Liu G, Zhang Q, et al. Cold-inducible RNA-binding protein as a novel target to alleviate blood-brain barrier damage induced by cardiopulmonary bypass. *J Thorac Cardiovasc Surg.* (2019) 157:986–96.e5. doi: 10.1016/j.jtcvs.2018.08.100
12. Wilhelmi MH, Tiede A, Teebken OE, Bisdas T, Haverich A, Mischke R. Ovine blood: establishment of a list of reference values relevant for blood coagulation in sheep. *ASAIO J.* (2012) 58:79–82. doi: 10.1097/MAT.0b013e31823a5414
13. Gao S, Wang W, Qi J, Liu G, Wang J, Yan S, et al. Safety and efficacy of a novel centrifugal pump and driving devices of the OASSIST ECMO system: a preclinical evaluation in the ovine model. *Front Med.* (2021) 8:712205. doi: 10.3389/fmed.2021.712205
14. Guglin M, Zucker MJ, Bazan VM, Bozkurt B, El Banayosy A, Estep JD, et al. Venoarterial ECMO for adults: JACC scientific expert panel. *J Am Coll Cardiol.* (2019) 73:698–716. doi: 10.1016/j.jacc.2018.11.038
15. Akiyama D, Katagiri N, Mizuno T, Tsukiya T, Takewa Y, Tatsumi E. Preclinical biocompatibility study of ultra-compact durable ECMO system in chronic animal experiments for 2 weeks. *J Artif Organs.* (2020) 23:335–41. doi: 10.1007/s10047-020-01180-1
16. Yu X, Gu S, Li M, Zhan Q. Awake extracorporeal membrane oxygenation for acute respiratory distress syndrome: which clinical issues should be taken into consideration. *Front Med.* (2021) 8:682526. doi: 10.3389/fmed.2021.682526
17. Kocyildirim E, Cárdenes N, Ting A, Cáceres E, BermUdez C, Rojas M. The use of GMP-produced bone marrow derived stem cells in combination with extra corporeal membrane oxygenation in ARDS -an animal model. *ASAIO J.* (2017) 63:324–32. doi: 10.1097/MAT.0000000000000566
18. Langer T, Vecchi V, Belenkiy SM, Cannon JW, Chung KK, Cancio LC, et al. Extracorporeal gas exchange and spontaneous breathing for the treatment of

acute respiratory distress syndrome: an alternative to mechanical ventilation? *Crit Care Med.* (2014) 42:e211–20. doi: 10.1097/CCM.0000000000000121
19. McCanny P, Smith MW, O'Brien SG, Buscher H, Carton EG. Fluid balance and recovery of native lung function in adult patients supported by venovenous extracorporeal membrane oxygenation and continuous renal replacement therapy. *ASAIO J.* (2019) 65:614–9. doi: 10.1097/MAT.0000000000000860
20. Anton-Martin P, Quigley R, Dhar A, Bhaskar P, Modem V. Early fluid accumulation and intensive care unit mortality in children receiving extracorporeal membrane oxygenation. *ASAIO J.* (2021) 67:84–90. doi: 10.1097/MAT.0000000000001167

Conflict of Interest: The authors declare that the research was conducted in the absence of any commercial or financial relationships that could be construed as a potential conflict of interest.

Publisher's Note: All claims expressed in this article are solely those of the authors and do not necessarily represent those of their affiliated organizations, or those of the publisher, the editors and the reviewers. Any product that may be evaluated in this article, or claim that may be made by its manufacturer, is not guaranteed or endorsed by the publisher.

frontiers in Veterinary Science

ORIGINAL RESEARCH
published: 03 February 2022
doi: 10.3389/fvets.2022.816529

A Large Animal Model for Orthopedic Foot and Ankle Research

Benjamin C. Gadomski[1], Kevin M. Labus[1], Holly L. Stewart[2], Katie T. Bisazza[2], Brad B. Nelson[2], Christian M. Puttlitz[1], Kirk C. McGilvray[1], Daniel P. Regan[3] and Jeremiah T. Easley[2]*

[1] Orthopedic Bioengineering Research Laboratory, Department of Mechanical Engineering and School of Biomedical Engineering, Colorado State University, Fort Collins, CO, United States, [2] Preclinical Surgical Research Laboratory, Department of Clinical Sciences, Colorado State University, Fort Collins, CO, United States, [3] Department of Microbiology, Immunology, and Pathology, Colorado State University, Fort Collins, CO, United States

Trauma to the soft tissues of the ankle joint distal syndesmosis often leads to syndesmotic instability, resulting in undesired movement of the talus, abnormal pressure distributions, and ultimately arthritis if deterioration progresses without treatment. Historically, syndesmotic injuries have been repaired by placing a screw across the distal syndesmosis to provide rigid fixation to facilitate ligament repair. While rigid syndesmotic screw fixation immobilizes the ligamentous injury between the tibia and fibula to promote healing, the same screws inhibit normal physiologic movement and dorsiflexion. It has been shown that intact screw removal can be beneficial for long-term patient success; however, the exact timing remains an unanswered question that necessitates further investigation, perhaps using animal models. Because of the sparsity of relevant preclinical models, the purpose of this study was to develop a new, more translatable, large animal model that can be used for the investigation of clinical foot and ankle implants. Eight (8) skeletally mature sheep underwent stabilization of the left and right distal carpal bones following transection of the dorsal and interosseous ligaments while the remaining two animals served as un-instrumented controls. Four of the surgically stabilized animals were sacrificed 6 weeks after surgery while the remaining four animals were sacrificed 10 weeks after surgery. Ligamentous healing was evaluated using radiography, histology, histomorphometry, and histopathology. Overall, animals demonstrated a high tolerance to the surgical procedure with minimal complications. Animals sacrificed at 10 weeks post-surgery had a slight trend toward mildly decreased inflammation, decreased necrotic debris, and a slight increase in the healing of the transected ligaments. The overall degree of soft tissue fibrosis/fibrous expansion, including along the dorsal periosteal surfaces/joint capsule of the carpal bones was very similar between both timepoints and often exhibited signs of healing. The findings of this study indicate that the carpometacarpal joint may serve as a viable location for the investigation of human foot and ankle orthopedic devices. Future work may include the investigation of orthopedic foot and ankle medical devices, biologic treatments, and repair techniques in a large animal model capable of providing translational results for human treatment.

Keywords: foot and ankle, sheep, carpus, fixation, syndesmosis

OPEN ACCESS

Edited by:
Abirami Kugadas, Cambridge, United States

Reviewed by:
Christian Peham, University of Veterinary Medicine Vienna, Austria
Laura Mercedes Riggs, Louisiana State University, United States

****Correspondence:***
Benjamin C. Gadomski
Ben.Gadomski@colostate.edu

Specialty section:
This article was submitted to Comparative and Clinical Medicine, a section of the journal Frontiers in Veterinary Science

Received: *16 November 2021*
Accepted: *04 January 2022*
Published: *03 February 2022*

Citation:
Gadomski BC, Labus KM, Stewart HL, Bisazza KT, Nelson BB, Puttlitz CM, McGilvray KC, Regan DP and Easley JT (2022) A Large Animal Model for Orthopedic Foot and Ankle Research. Front. Vet. Sci. 9:816529. doi: 10.3389/fvets.2022.816529

INTRODUCTION

The foot is a highly complex portion of the human anatomy, consisting of 28 bones, 33 joints, and over 100 ligaments (1, 2). The foot articulates with long bones of the tibia and fibula via the ankle joint, with multiple tendons and muscles traversing the bones of the foot and ankle allowing for propulsion and balance. The ankle joint consists of the tibia, fibula and talus. The "distal syndesmosis" of the ankle joint is made up of the articulation of the distal tibia and fibula, held together by the anterior inferior tibiofibular ligament (AITFL), posterior inferior tibiofibular ligament (PITFL), interosseous ligament (IOL), and interosseous membrane (IOM). Trauma to these soft tissues often leads to syndesmotic instability, resulting in undesired movement of the talus, abnormal pressure distributions, and ultimately arthritis if deterioration progresses without treatment (3).

Amongst weight-bearing joints, ankle fractures are the most common with an estimated total of 673,214 ankle fractures occurring between 2012 and 2016 (3, 4). At the beginning of this period, the total estimated economic burden of foot and ankle procedures was ∼$11 billion in the United States, up 38% from the previous decade (5). It has been reported that between 13 and 23% of all ankle fractures will have an associated syndesmosis injury (6–9). Typically, in ankle fractures, the AITFL, PITFL, IOL and a portion of the IOM are often torn in combination with the fracture. It also can occur as part of a "high ankle sprain" where one or more of the above ligaments are torn. Historically, syndesmotic injuries have been repaired by placing a screw across the distal syndesmosis to provide rigid fixation. While syndesmotic injuries are relatively common, questions remain about the most effective course of treatment, specifically if or when fixation screws should be removed (7). Trans-syndesmotic fixation with rigid metal screws has been accepted as the gold-standard of treatment. While rigid syndesmotic screw fixation immobilizes the ligamentous injury between the tibia and fibula to promote healing, the same screws inhibit normal physiologic movement and dorsiflexion (7), thus screw breakage is seen in many of these rigid constructs as a result of the physiologic motion that occurs across this joint once weight-bearing is restored (10, 11). Several studies have shown that intact screw removal can be beneficial for long-term patient success; however, the exact timing remains an unanswered question that necessitates further investigation, perhaps using animal models (7).

Use of animal models in foot and ankle research has been sparse. Though the findings related to basic science in small animal healing models for long bones and spine allow for insight into healing, they are not analogous to healing that may take place in different anatomic areas, such as the foot and ankle, due to differences in vascularity, soft tissue enclosure, and local biology (12). Lewis rats have been used to study fusion across the tibiotalar joint, which is believed to be the first dependable model of small animal ankle arthrodesis (12). C57BL/6J mice have been used as a model to study the effect of Metformin injection in the prevention of Achilles tendinopathy (13). Sprague-Dawley rats were used to study the injection of autologous adipose tissue-derived mesenchymal stem cells into their foot fat pad (14). While these animal studies have provided valuable insights, there remains a paucity of relevant animal models available for foot and ankle research. This is particularly true for large animal models, where appropriately sized implants and fixation devices may be investigated with more direct translation to human clinical practice. Sheep are commonly used in bone and joint research due to the similarities they share with humans as well as ease of handling and care (15–17). More specifically, in the context of syndesmosis, the front limb carpal bones of sheep share similar anatomy to humans because of the common anterior/dorsal, posterior/ventral, and interosseous ligamentous attachments between bones, similar morphometry of the medial/lateral distal carpal bones of the sheep to the human fibula/tibia, and a cartilage zone lining the respective bones in the interosseous region (**Figure 1**) (18). Due to these similarities and the need for relevant preclinical models, the purpose of this study was to develop a new, more translatable, large animal model that can be used for the investigation of clinical foot and ankle implants.

METHODS

Surgical Procedure

This study was performed under the approval of Colorado State University's Animal Care and Use Committee (IACUC). Eight (8) skeletally mature female Rambouillet Cross sheep underwent stabilization of the left and right distal carpal bones (fused $2^{nd}/3^{rd}$ and 4^{th}) following transection of the dorsal intercarpal ligament (**Figure 2**) while the remaining two animals served as un-instrumented controls. Fentanyl patches (150 mcg) were placed transdermally on all animals 24 h prior to surgery. Additionally, all animals received florfenical (20 mg/kg, subcutaneous (SQ)) every 48 h for a total of 3 doses and Phenylbutazone (1 g, oral (PO)) every 24 h for a total of 7 doses starting 24 h prior to surgery. The auricular vein and artery were catheterized and anesthesia was induced with a combination of ketamine (3.3 mg/kg, intravenous (IV)) and diazepam (0.1 mg/kg, IV). Following anesthetic induction, the sheep were intubated with a cuffed endotracheal tube and maintained on isoflurane (1.5–3%) with 100% oxygen using positive pressure ventilation (20 cm H_2O) for the duration of the procedure. Animals were placed under general anesthesia. Each animal was positioned in dorsal recumbency with the left front limb fully extended. The surgical site was clipped and aseptically prepared using chlorhexidine and isopropyl alcohol. Surgery was performed using sterile drapes and instruments and was performed aseptically. A single intraoperative dose of cefazolin (1 gram, IV) was administered within the first 15 min of the surgical procedure. Under fluoroscopic guidance via stab incisions only, the distal most row of carpal bones ($2^{nd}/3^{rd}$ carpal and 4^{th} carpal) were "stabilized" together using a cannulated screw. Prior to implanting the screws, the dorsal (anterior) ligaments were transected using a beaver blade by needle guidance determined with fluoroscopy, specifically, the dorsal ligament connecting the $2^{nd}/3^{rd}$ carpal to the 4^{th} carpal bone. The two aforementioned bones in the distal row were connected by drilling a 1.2 mm K-wire into the medial aspect of the limb into the fused $2^{nd}/3^{rd}$

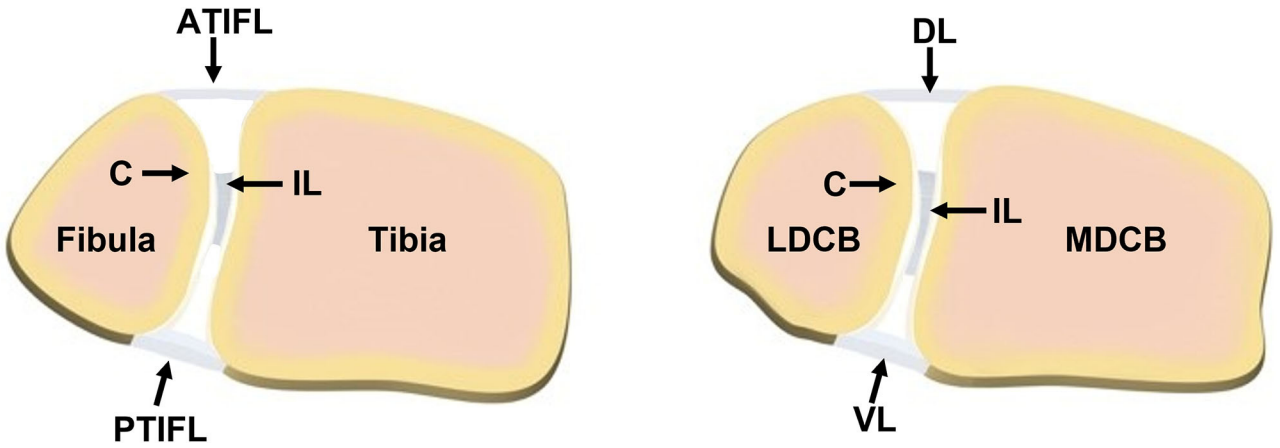

FIGURE 1 | Comparison of the (left) human syndesmotic structure and the (right) sheep distal carpal bones. (Left) The human structure contains the fibula and tibia joined anteriorly by the anterior tibiofibular ligament (ATIFL), posteriorly by the posterior tibiofibular ligament (PTIFL), and centrally by an interosseous ligament (IL) located between a layer of cartilage (C) on the two bones. (Right) The distal carpal bones of the sheep (MDCB, medial distal carpal bone; LDCB, lateral distal carpal bone) share similar cross-sectional morphometry as the human fibula and tibia, ligamentous attachments (DL, dorsal ligament; VL, ventral ligament; IL, interosseous ligament) and cartilage (C) zone as the human syndesmotic complex. Illustration courtesy of Kelsea Erickson, DVM.

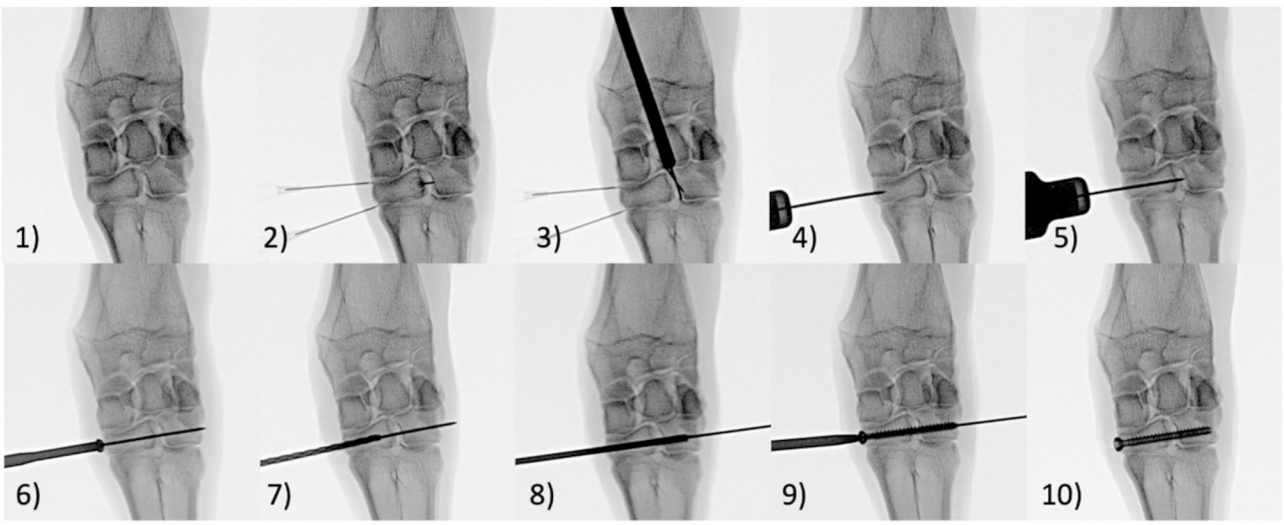

FIGURE 2 | Step **(1)** An Anterior-posterior fluoroscopic image of the carpus was taken. Step **(2)** 22-gauge needles were placed within the carpometacarpal joint and the middle carpal joint as well as the intercarpal joint between the 2nd/3rd and 4th Carpal bones to aid in alignment. Step **(3)** A beaver blade was placed within the 2nd/3rd and 4th inter carpal bone to transect the anterior inter carpal ligament. Step **(4)** A 1.2mm K-wire was placed midway between the carpometacarpal joint and middle carpal joint. Step **(5)** The 1.2mm K-wire was inserted from the medial aspect of the fused 2nd/3rd carpal bone across the intercarpal joint and through the 4th carpal bone. The K-wire angled in ∼15 degrees anteromedial to posterolateral direction in order to stay central within the 2nd/3rd and 4th carpal bones in both the dorsal and transverse planes. Step **(6)** A cannulated countersink tool was placed over the K-wire to countersink the medial edge of 2nd/3rd carpal bone. Step **(7)** The K-wire distance was measured and a 2.6mm cannulated drill bit was used to drill a hole of matching length. Step **(8)** A 4.0mm tap is placed over the K-wire to thread the drill hole. Step **(9)** A 4.0 mm cannulated screw was placed over the K-wire and driven across the fused 2nd/3rd and 4th carpal bones in a neutral position to stabilize the intercarpal joint. Step **(10)** The K-wire was removed from the cannulated screw.

carpal bones and extending into and through the 4th carpal bone. A cannulated countersink was then created to accommodate the screw head. The k-wire distance was measured, and a 2.6 mm cannulated drill bit was used to drill a hole of matching length. The hole was then threaded using a 4.0 mm tap, and a 4.0 mm cannulated screw (Mini-Monster® Screw, Paragon 28®, Inc.) was driven across two distal carpal bones to stabilize the joint. The procedure was then repeated on the distal most row of carpal bones on the animal's contralateral limb. The stab incision was closed with 2–0 Nylon in a single horizontal mattress. A thick bandage with roll cotton, brown gauze and Elastkon was placed across both carpi to provide additional support and coverage to

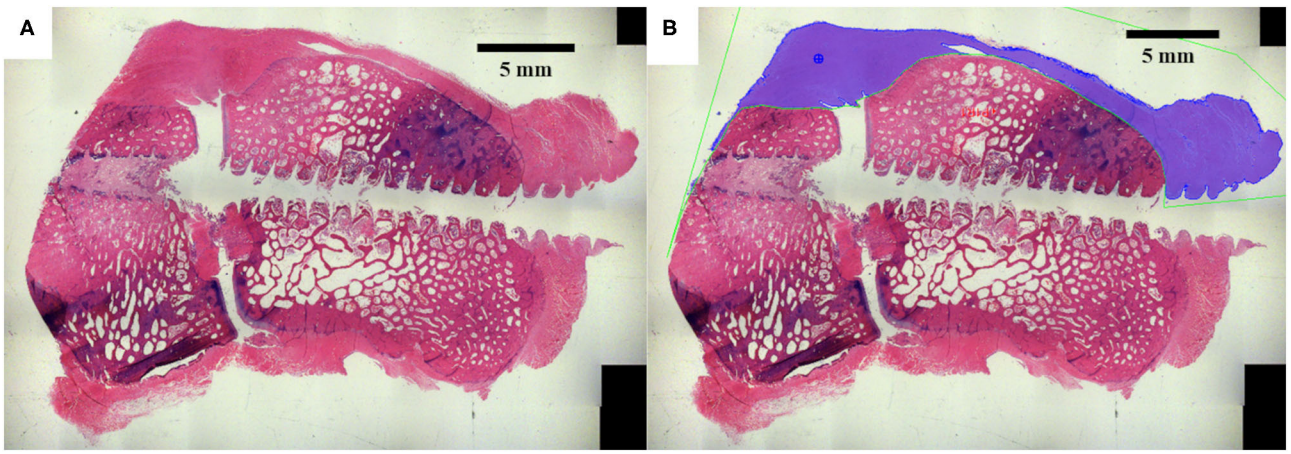

FIGURE 3 | The dorsal ligament area was histomorphometrically analyzed. **(A)** Original histology section. **(B)** The dorsal ligament area was quantified around the dorsal peripheral surface of the carpal bones.

the carpus in the immediate recovery period. Following surgery and recovery, animals were allowed to roam freely and feed *ad libitum*. Four of the surgically stabilized animals were sacrificed 6 weeks after surgery (eight total 6-week Group specimens) while the remaining four animals were sacrificed 10 weeks after surgery (eight total 10-week Group specimens). The distal row of carpal bones were collected from the left and right limbs of two animals from an unrelated study and served as un-instrumented controls (four total Control group specimens). The distal row of carpal bones was carefully dissected from the left and right front limbs of each animal and high-resolution digital images and radiographs were taken of each specimen.

Histological Preparation

The distal carpal bone specimen from each limb was sectioned into a block of tissue ∼1 cm thick to display the bone-ligament-bone construct in the transverse plane using an irrigated band saw. This section region of interest (ROI) displayed the ligament, soft tissue, and surrounding bone. Samples were fixed in 10% neutral buffered formalin until fixation was complete. After fixation, tissue was decalcified in 8% trifluoroacetic acid and the decalcification end point was determined by daily radiographic assessment. Each sample was processed for decalcified histology using standard paraffin techniques and sectioned at 5 μm thickness. Slides were stained with Hematoxylin and Eosin (H&E). Two slides were cut through each joint ROI.

Histomorphometry Analysis

High-resolution digital images were acquired for all surgical site slides using a Nikon E800 microscope (AG Heinze, Lake Forest, CA), a Spot digital camera (Diagnostic Instruments, Sterling, Heights, MI), and ImagePro Premier Software (Media Cybernetics, Silver Spring, MD). The dorsal ligament area around the perimeter of the carpal bones was quantitatively assessed for all timetpoints (**Figure 3**) based on tissue stain color within the analyzed region (ImagePro Premier Software, Media Cybernetics, Silver Spring, MD). Statistical comparisons of histomorphometry data between treatment groups was performed using a one-way analysis of variance (ANOVA) with an alpha value of 0.05 and a Tukey *post-hoc* test (Minitab 17, Minitab Inc., State College PA).

Histopathology

Histology slides were reviewed by a board-certified veterinary pathologist for analysis of cellular constituents and response using the ISO 10993-6 Annex E criteria for the biological evaluation of local effects following the implantation of a medical device. The outcome data included a quantitative scoring of the parameters listed in **Table 1**. The pathologist was initially blinded to the treatment parameters of each site and was unblinded following scoring of all the slides to draw conclusions between treatment groups.

RESULTS

Surgical Procedure

All animals recovered well from surgery. Five of eight animals (63%) that underwent stabilization of the distal carpal bones showed mild to moderate, intermittent, shifting forelimb lameness that was managed with intermittent administration of Meloxicam (75 mg PO SID). Lameness was more prominent immediately after rising from lying down. No other postoperative complications were noted throughout the study and all sheep survived to their designated sacrifice timepoints. Procedural time for both carpi averaged 43 min from incision to closure (range 26–70 min). Surgery time decreased from an average of 53 min for the first 4 animals down to 31 min for the remaining animals. A total of 6/16 screws utilized measured 30 mm in length, 5/16 measured 32 mm in length and 5/16 measured 34 mm in length. Fluoroscopic guidance was highly valuable to the successful placement of the stabilizing screws.

TABLE 1 | Semi-quantitative histopathology scoring parameters for the distal carpal bone histology slide sections. Scoring parameters are referenced from the ISO 10993-6 Annex E standards for the biological evaluation of local effects after implantation of medical devices.

	Score				
Cell type/response	**0**	**1**	**2**	**3**	**4**
Polymorphonuclear cells (PMNs)	None	Rare, 1–5/HPF*	5–10/HPF	Heavy infiltrate	Packed
Lymphocytes	None	Rare, 1–5/HPF	5–10/HPF	Heavy infiltrate	Packed
Plasma cells	None	Rare, 1–5/HPF	5–10/HPF	Heavy infiltrate	Packed
Macrophages (Mϕ)	None	Rare, 1–5/HPF	5–10/HPF	Heavy infiltrate	Packed
Giant cells	None	Rare, 1–2/HPF	3–5/HPF	Heavy infiltrate	Sheets
Necrosis	None	Minimal	Mild	Moderate	Severe
Neovascularization	None	Minimal	Mild	Moderate	Severe
Fibrosis	None	Minimal	Mild	Moderate	Severe
Collagen Fiber Organization	None	Very Loose	Moderate	Dense/Mature	N/A

**HPF – per high powered field.*

Radiographic Interpretation

Post-surgery radiographs revealed appropriate placement across the fixed $2^{nd}/3^{rd}$ and 4^{th} carpal bones. Radiographs from explanted limbs and following disarticulation of the carpometacarpal joint revealed appropriate placement across both bones. All screws were placed from medial in a dorsolateral direction. This resulted in screws engaging more of the central portion of the fixed $2^{nd}/3^{rd}$ carpal bones compared to the 4^{th} carpal bones. None of the screws bent or broke throughout the study period.

In 6-week radiographs, signs of severe arthritic changes (osteophyte formation, nonuniform joint space loss) were noted on dorsopalmar or lateromedial views in 1 of 8 (12.5%) carpi. This animal showed the most significant lameness of all animals on the study. 10-week radiographs noted 2 of 12 carpi (17% of carpi) with mild arthritic changes within the carpometacarpal joints. These two animals were also mildly lame on the arthritic limb.

Histomorphometry

Mean dorsal ligament area around the periphery of the carpal bones was similar between 6-week and 10-week specimens (**Figure 4**). There was no statistically different change in mean dorsal ligament area in 6-week and 10-week groups as compared to the Control group. Bridging and reconnection of the severed dorsal ligament was observed in many of the specimens, with 62.5% (5 of 8 samples) demonstrating dorsal ligament bridging at 6 weeks and 87.5% (7 of 8 samples) demonstrating bridging at 10 weeks.

Histopathology

All evaluated histopathological parameters were predominately similar in composition and severity across all study animals and timepoints (**Table 2**). Representative histologic images of each timepoint are presented in **Figure 5**. Overall, animals sacrificed at 10 weeks post-surgery had a slight trend toward mildly decreased inflammation, decreased necrotic debris, and a slight increase in the healing and organization of the reactive fibrous tissue surrounding the interosseous ligament. Mean (±standard deviation) cumulative inflammation scores (the sum of polymorphonuclear cells, lymphocytes, plasma cells, macrophages, and giants cells) were 5(±3) and 4(±2) for the 6 and 10-week groups, respectively, with 0 being the lowest and 20 being the highest possible scores. The carpal joint of the 6-week group that displayed severe arthritic changes had a cumulative inflammation score of 12. The two animals that showed mild arthritic changes at 10 weeks had cumulative inflammation scores of 3 and 8. Several carpal joints from both timepoints showed cumulative inflammation scores as great as 6 with no apparent signs of arthritic progression. The overall degree of soft tissue fibrosis/fibrous expansion, including along the dorsal periosteal surfaces/joint capsule of the carpal bones was very similar between both timepoints.

The primary histological changes within the tissues of animals from both timepoints were most evident in the void space left at the site of screw placement. This void space bisected both carpal bones, traversed articular surfaces, and spanned the intraarticular space. While not factored into the overall histological score for each section, the host tissue response within this screw void space almost always communicated with either or both the interosseous ligament present between the carpal bones, as well as the fibrous periosteum/joint capsule/ligaments along the dorsal (cranial) periosteal surface of the carpal bones. Thus, the nature of the tissue response within this screw placement space often extended to characterize that present within the tissue regions-of-interest (ROI) of the intra-articular space, interosseous ligament, and soft tissues along the dorsal aspect of the carpal bones.

Regarding the interosseous ligament and the associated soft tissue response surrounding it and filling the intra-articular space, this response was again typically an extension of the fibrous tissue which surrounded the site of the screw placement. In the majority of animals and sites, the interosseous ligament was intact and primarily retained its native structure, with the majority of the ligamentous structure appearing histologically normal, and the only host tissue response occurring along the peripheral/lateral margins of the ligament.

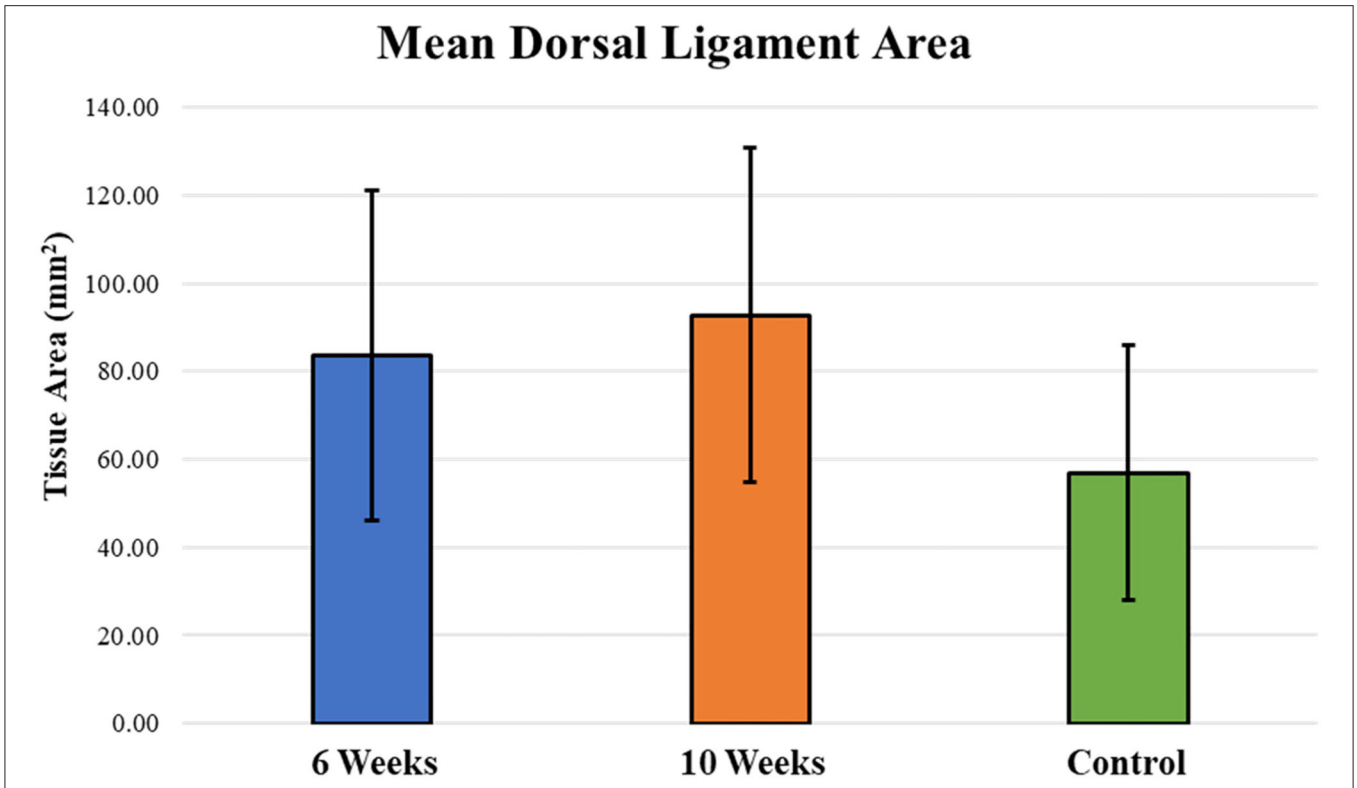

FIGURE 4 | Mean dorsal ligament area around the periphery of the carpal bones was similar between 6-week and 10-week specimens and increased as compared to the Control group; however, those differences were not statistically significant between groups.

TABLE 2 | Mean and (standard deviation) histopathologic scores for Control, 6-week, 10-week specimens. PMN indicates polymorphonuclear cells, lymphs indicates lymphocytes, Mj indicates macrophage cell presence, neovasc indicates neovascularization.

Timepoint	PMNs	Lymphs	Plasma cells	Mj	Giant cells	Cumulative inflammation score	Osteoblast activity	Osteoclast Activity	Necrosis	Neovasc	Fibrosis	Collagen fiber organization
Control	0 (0)	0 (0)	0 (0)	0 (0)	0 (0)	0 (0)	0 (0)	0 (0)	0 (0)	0 (0)	0 (0)	3 (0)
6 Weeks	1 (1)	1 (1)	1 (1)	1 (0)	0 (0)	5 (3)	1 (1)	1 (1)	2 (1)	2 (1)	2 (1)	1 (1)
10 Weeks	0 (0)	1 (0)	1 (1)	1 (1)	1 (1)	4 (2)	2 (1)	1 (1)	1 (1)	2 (1)	2 (1)	2 (1)

DISCUSSION

In many situations, *in vitro* and cadaveric investigations may be sufficient to answer the relevant research questions of the particular study, however, limitations exist in these methods, and live animal research becomes necessary to elucidate translational, physiologically accurate responses. In translational orthopedic research, these physiologic responses may include inflammatory reactions as a result of device or drug safety, bone remodeling, cartilage generation/degeneration, and the overall healing response in a complex, multivariable systemic environment. Furthermore, live animal models that are clinically and anatomically relevant, especially in larger species, are vital to the regulatory approval and commercialization process of orthopedic medical devices. To date, relevant animal models for orthopedic foot and ankle research have been scarce. Small animal models, specifically mice and rats, have been the historical gold standard in this field. While insights gained using these animal models have been valuable, these small animal foot and ankle models possess shortcomings that prevent meaningful translation to the human clinical setting including vastly different metabolic rates, healing rates, bone structures, and perhaps most importantly, extremely different physical sizes from humans that prevent the direct investigation of implants designed for human use (19). This study sought to develop a new, large animal model for foot and ankle research leveraging the orthopedic resemblances between sheep and humans. Sheep are commonly used in bone and joint research due to the similarities they share

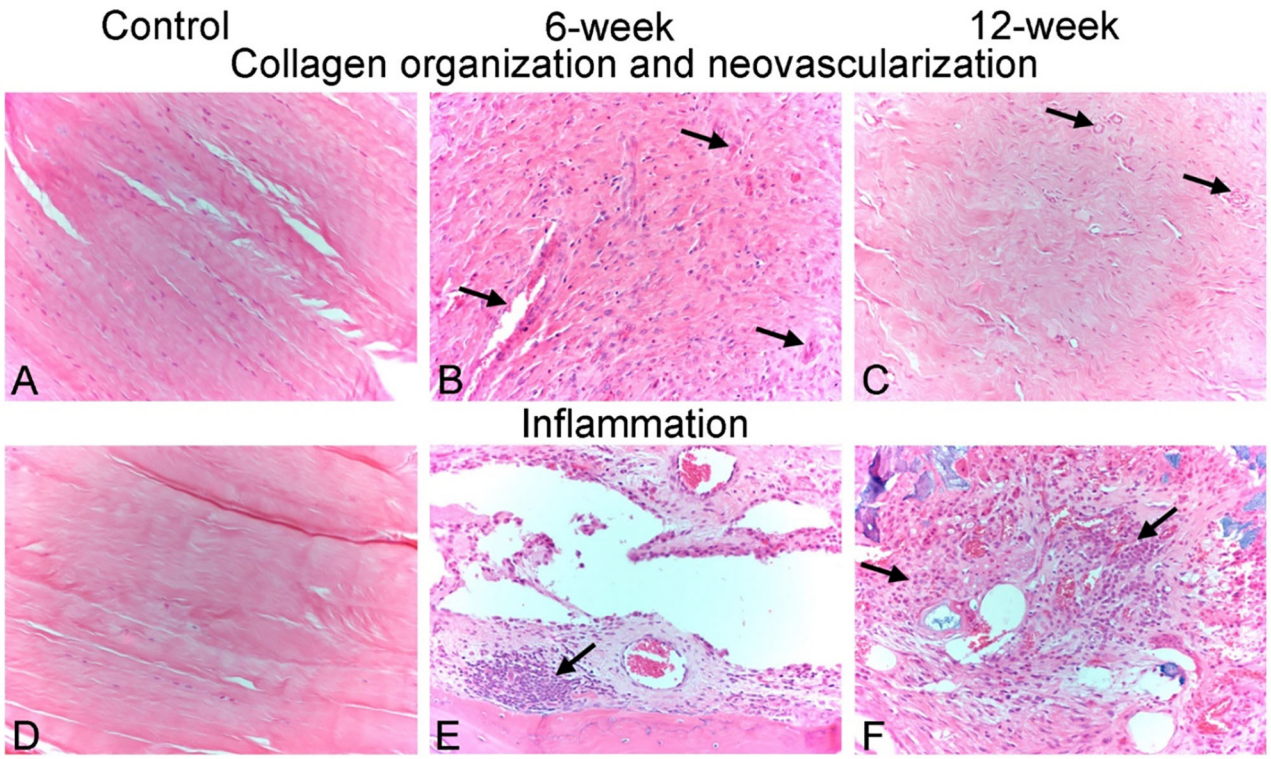

FIGURE 5 | Representative photomicrographs of histological scoring parameters. **(A–C)** Collagen organization and neo-vascularization scoring. **(A)** Control animal 1 - left. Photomicrograph demonstrating a collagen fiber organization score of 3 (dense/mature) and a neovascularization score of 0 (none). Interosseous ligament collagen is comprised entirely of bundles of densely packed collagen fibers with a crimped appearance and which contain few flattened, hyperchromatic nuclei of ligament fibroblasts. No blood vessels are observed within this ligament tissue. **(B)** Animal PG04 - right, 6-week timepoint. Photomicrograph demonstrating a collagen fiber organization score of 0 (none/no organization) and a neovascularization score of 2 (mild). Newly produced fibrous tissue surrounding carpal bones is characterized by reactive and disorganized fibroplasia with haphazardly intersecting collagen bundles, and numerous plump reactive fibroblasts. 3–5 capillary-sized neo-vessels per high powered (400x magnification) field are present throughout this fibrous tissue (arrows). **(C)** Animal PG07 - right, 12-week timepoint. Photomicrograph demonstrating a collagen fiber organization score of 2 (moderate) and a neovascularization score of 2 (mild). Newly produced fibrous tissue is being progressively re-organized into more parallel and tightly packed bundles of collagen fibers, similar to native interosseous ligament observed in healthy control animals. Similar to the 6-week animal shown in **(B)**, 3–5 capillary-sized neo-vessels per high powered (400x magnification) field remain present throughout this fibrous tissue (arrows). **(D–F)** Inflammation scoring. **(D)** Control animal 4 - left. Photomicrograph demonstrating a cumulative inflammation score 0. No inflammatory cells were observed in the carpal ligament tissues of any healthy control animals. **(E)** Animal PG06 – right, 6-week timepoint. Photomicrograph demonstrating a cumulative inflammation score of 6/20. Multifocal nodular clusters of predominately lymphocytes and fewer plasma cells (arrow), as well as scattered individual infiltrating macrophages, were observed throughout the newly produced fibrous tissue. **(F)** Animal PG05 – left, 12-week timepoint. Photomicrograph demonstrating a cumulative inflammation score of 8/20. Similar to animal PG06-right, clusters of infiltrating lymphocytes, plasma cells and macrophages (arrows) are multifocally present throughout the newly produced fibrous tissue. All images are 20x magnification.

with humans, specifically similar weight, metabolic rates, healing rates, bone microarchitecture, and anatomical size, as well as ease of handling and care (15–17, 19). Importantly, the anatomical size of sheep allows for the direct investigation of orthopedic devices that are sized specifically for human clinical use. This study presents the first large animal (sheep) model for foot and ankle research using orthopedic hardware sized for human use in the distal carpal bones of the sheep forelimb.

There is limited description of sheep carpal anatomy specifically in the literature (20). However, the carpal anatomy of sheep is similar to that of the cow. There are three joints within the sheep carpus, consisting of the: (1) antebrachial joint between the radius/ulna and proximal carpal bones, (2) middle carpal joint between the two rows of carpal bones and (3) the carpometacarpal joint between the distal carpal bones and the proximal metacarpals. The proximal row of carpal bones consists of the medially located radial carpal bone, the centrally located intermediate carpal bone and the laterally located ulnar and accessory carpal bones. The distal row of carpal bones consists of a medially located fused 2nd and 3rd carpal bones and a laterally located 4th carpal bone. The 1st carpal bone and 5th carpal bone are not present. While the carpal anatomy of the sheep does not mimic the carpal or tarsal anatomy of humans, carpal and tarsal joints of both species consist of cuboid bones or squared shaped bones. These cuboid bones are commonly stabilized or fused with internal screw fixation in people in a similar fashion to

the procedure described herein. In this current study, the carpal bones in the sheep model were selected because they mimic the general structure and axial loading pattern of the syndesmosis. Specifically, ligaments are present anterior and posterior to the joint, as well as having an interosseous ligament. The sizes of the bones are similar to that of the short bones of the foot, allowing for implants manufactured for foot and ankle procedures to be used in this region.

The animals of this study demonstrated high tolerance to the surgical procedure with only mild, intermittent lameness in the operated limbs. The orthopedic hardware used in this study, a 4.0 mm cannulated screw, was a commercially available device used in human foot and ankle procedures. The screw was sized appropriately for the anatomy of the sheep carpometacarpal bones, and hardware failure was not experienced at the surgical site. The ability to directly investigate the effects of orthopeadic devices designed specifically for human use is a distinct advantage of this new sheep model.

In terms of the overall healing response, similarities were observed between the animals in this study and what has been documented in human patients that underwent trans-syndesmotic fixation. First, more than half of the animals in this study demonstrated bridging and reconnection of the transected dorsal ligament at the 6-week timepoint, and all but one specimen demonstrated reconnection of the dorsal ligament at the 10-week timepoint. The soft tissues surrounding the dorsal perimeter of the carpal bones in the animals of this study generally displayed well-organized collagen structures despite the inflammatory response induced by the surgical procedure and ligament transection. This organization tended to decrease toward the intra-articular space between the carpal bones. This healing ability has also been shown to be characteristic of the anterior tibiofibular ligament in human patients with acute syndesmotic injuries as trans-fixation screws are often removed post-operatively following a recovery period without concomitant widening of the syndesmosis (21). Arthritic changes were observed in 1 of 8 (12.5%) carpi at the shorter timepoint (6 weeks) and 2 of 12 carpi (17%) at the 10-week timepoint. This also is not unlike the human clinical presentation of syndesmotic instability and fixation, and trans-syndesmotic fixation has been shown to be a risk factor associated with human synostosis (22). Further, while related but not directly investigated in this animal study, it is well known that malreduction of the syndesmosis can play a major role in ankle joint arthritis in humans (23). Overall inflammation scores decreased in the areas around the stabilization screw and dorsal ligaments over time from 6 to 10 weeks in the animals of this study, and while it is impossible to directly compare these results to histopathological inflammatory response of human patients, it is likely that arthritic changes are also associated with some level of inflammatory response.

There are, of course, inherent limitations when using animals as a surrogate for clinical human research. These shortcomings include postural (quadruped vs. biped) and healing differences. Perhaps most importantly, the constraints of human clinical research prevent the direct histological comparison of the healing response of the ligaments in the human syndesmosis to the histopathological observations from this study. Despite these limitations, numerous similarities between sheep and humans, including anatomical characteristics (similar bone sizes), *in vivo* biomechanical loads, bone composition, bone macro and micro architecture, and ligamentous healing characteristics, make the sheep model one of the most translatable for orthopedic research.

In conclusion, the findings of this study indicate that the carpometacarpal joint may serve as a viable location for the investigation of human foot and ankle orthopedic devices. Future work may include the investigation of orthopedic foot and ankle medical devices, biologic treatments, and repair techniques in a large animal model capable of providing translational results for human treatment.

DATA AVAILABILITY STATEMENT

The raw data supporting the conclusions of this article will be made available by the authors, without undue reservation.

ETHICS STATEMENT

The animal study was reviewed and approved by Colorado State University Institutional Animal Care and Use Committee.

AUTHOR CONTRIBUTIONS

BG participated in conceptual design of the study, data acquisition, analysis, interpretation, manuscript drafting, and final approval. KL participated in data acquisition, analysis, interpretation, manuscript drafting, and final approval. HS, KB, and BN participated in data acquisition, manuscript drafting, and final approval. CP participated in conceptual design of the study, manuscript drafting, and final approval. KM participated in conceptual design of the study, manuscript drafting, and final approval. DR participated in data acquisition, analysis, interpretation, manuscript drafting, and final approval. JE participated in conceptual design of the study, data acquisition, analysis, interpretation, manuscript drafting, and final approval. All authors agree to be accountable for this work and ensure its integrity.

FUNDING

This work was funded by a research grant from Paragon 28, LLC., Englewood, CO.

ACKNOWLEDGMENTS

Special thanks to Cecily Broomfield and Lucas Nakamura from the Colorado State University Orthopedic Bioengineering Research Laboratory for sample histological preparation.

REFERENCES

1. Bonnel FBM, Canovas F, Chamoun M, Bouysset M. Anatomy of the foot and ankle. Bouysset M, editors. *Bone and Joint Disorders of the Foot and Ankle Berlin*, Heielberg: Springer. (1998). doi: 10.1007/978-3-662-06132-9_1
2. Lang LMG. The anatomy of the foot. *Bailliere Clin Rheum.* (1987) 1:215–40. doi: 10.1016/S0950-3579(87)80001-8
3. Bava E, Charlton T, Thordarson D. Ankle fracture syndesmosis fixation and management: the current practice of orthopedic surgeons. *Am J Orthop (Belle Mead NJ).* (2010) 39:242–6.
4. Scheer RC, Newman JM, Zhou JJ, Oommen AJ, Naziri Q, Shah NV, et al. Ankle fracture epidemiology in the united states: patient-related trends and mechanisms of injury. *J Foot Ankle Surg.* (2020) 59:479–83. doi: 10.1053/j.jfas.2019.09.016
5. Belatti DA, Phisitkul P. Economic burden of foot and ankle surgery in the US medicare population. *Foot Ankle Int.* (2014) 35:334–40. doi: 10.1177/1071100713519777
6. Dattani R, Patnaik S, Kantak A, Srikanth B, Selvan TP. Injuries to the tibiofibular syndesmosis. *J Bone Joint Surg Br.* (2008) 90b:405–10. doi: 10.1302/0301-620X.90B4.19750
7. Walley KC, Hofmann KJ, Velasco BT, Kwon JY. Removal of hardware after syndesmotic screw fixation: a systematic literature review. *Foot Ankle Spec.* (2017) 10:252–7. doi: 10.1177/1938640016685153
8. Egol KA, Pahk B, Walsh M, Tejwani NC, Davidovitch RI, Koval KJ. Outcome after unstable ankle fracture: effect of syndesmotic stabilization. *J Orthop Trauma.* (2010) 24:7–11. doi: 10.1097/BOT.0b013e3181b1542c
9. Sagi HC, Shah AR, Sanders RW. The functional consequence of syndesmotic joint malreduction at a minimum 2-year follow-up. *J Orthop Trauma.* (2012) 26:439–43. doi: 10.1097/BOT.0b013e31822a526a
10. Hsu YT, Wu CC, Lee WC, Fan KF, Tseng IC, Lee PC. Surgical treatment of syndesmotic diastasis: emphasis on effect of syndesmotic screw on ankle function. *Int Orthop.* (2011) 35:359–64. doi: 10.1007/s00264-010-1147-9
11. Wang C, Yang J, Wang S, Ma X, Wang X, Huang J, et al. Three-dimensional motions of distal syndesmosis during walking. *J Orthop Surg Res.* (2015) 10. doi: 10.1186/s13018-015-0306-5
12. Kadakia RJ, Devereaux EJ, Ahn H, Traub BC, Kephart D, Willett NJ, et al. Development of a small animal ankle arthrodesis model. *Foot Ankle Int.* (2020) 41:101–8. doi: 10.1177/1071100719873900
13. Zhang P, Liang Y, He JS, Fang YC, Chen PT, Wang JC. A systematic review of suture-button versus syndesmotic screw in the treatment of distal tibiofibular syndesmosis injury. *BMC Musculoskel Dis.* (2017) 18. doi: 10.1186/s12891-017-1645-7
14. Molligan J, Mitchell R, Bhasin P, Lakhani A, Schon L, Zhang ZJ. Implantation of autologous adipose tissue-derived mesenchymal stem cells in foot fat pad in rats. *Foot Ankle Int.* (2015) 36:1344–51. doi: 10.1177/1071100715591092
15. Potes JC, Reis J, Capela e Silva F, Relvas C, Cabrita AS, Simões JA. The sheep as an animal model in orthopaedic research. *Exp Pathol Health Sci.* (2008) 2:29–32.
16. Turner AS. Experiences with sheep surgery: Strengths and as an animal model for shoulder shortcomings. *J Shoulder Elb Surg.* (2007) 16:158s—63s. doi: 10.1016/j.jse.2007.03.002
17. Wancket LM. Animal models for evaluation of bone implants and devices: comparative bone structure and common model uses. *Vet Pathol.* (2015) 52:842–50. doi: 10.1177/0300985815593124
18. Hermans JJ, Beumer A, de Jong TA, Kleinrensink GJ. Anatomy of the distal tibiofibular syndesmosis in adults: a pictorial essay with a multimodality approach. *J Anat.* (2010) 217:633–45. doi: 10.1111/j.1469-7580.2010.01302.x
19. Gadomski BC, McGilvray KC, Easley JT, Palmer RH, Ehrhart EJ, Haussler K, et al. An *in vivo* ovine model of bone tissue alterations in simulated microgravity conditions. *J Biomech Eng.* (2014) 136:021020. doi: 10.1115/1.4025854
20. Saber AS, Bolbol AE, Schenksaber B. A radiographic study of the development of the sheep carpus from birth to 18 months of age. *Vet Radiology.* (1989) 30:189–92. doi: 10.1111/j.1740-8261.1989.tb00775.x
21. Kwon JY, Stenquist D, Ye M, Williams C, Giza E, Kadakia AR, et al. Anterior syndesmotic augmentation technique using nonabsorbable suture-tape for acute and chronic syndesmotic instability. *Foot Ankle Int.* (2020) 41:1307–15. doi: 10.1177/1071100720951172
22. Hinds RM, Lazaro LE, Burket JC, Lorich DG. Risk factors for posttraumatic synostosis and outcomes following operative treatment of ankle fractures. *Foot Ankle Int.* (2014) 35:141–7. doi: 10.1177/1071100713510913
23. Ray R, Koohnejad N, Clement ND, Keenan GF. Ankle fractures with syndesmotic stabilisation are associated with a high rate of secondary osteoarthritis. *Foot Ankle Surg.* (2019) 25:180–5. doi: 10.1016/j.fas.2017.10.005

Conflict of Interest: The authors declare that the research was conducted in the absence of any commercial or financial relationships that could be construed as a potential conflict of interest.

frontiers in Veterinary Science

MINI REVIEW
published: 25 March 2022
doi: 10.3389/fvets.2022.834598

Porcine Models of the Intestinal Microbiota: The Translational Key to Understanding How Gut Commensals Contribute to Gastrointestinal Disease

*Elizabeth C. Rose, Anthony T. Blikslager and Amanda L. Ziegler**

Department of Clinical Sciences, College of Veterinary Medicine, North Carolina State University, Raleigh, NC, United States

In the United States, gastrointestinal disorders account for in excess of $130 billion in healthcare expenditures and 22 million hospitalizations annually. Many of these disorders, including necrotizing enterocolitis of infants, obesity, diarrhea, and inflammatory bowel disease, are associated with disturbances in the gastrointestinal microbial composition and metabolic activity. To further elucidate the pathogenesis of these disease syndromes as well as uncover novel therapies and preventative measures, gastrointestinal researchers should consider the pig as a powerful, translational model of the gastrointestinal microbiota. This is because pigs and humans share striking similarities in their intestinal microbiota as well as gastrointestinal anatomy and physiology. The introduction of gnotobiotic pigs, particularly human-microbial associated pigs, has already amplified our understanding of many gastrointestinal diseases that have detrimental effects on human health worldwide. Continued utilization of these models will undoubtedly inform translational advancements in future gastrointestinal research and potential therapeutics.

Keywords: intestinal microbiota, translational models, pig models, gut commensals, gastrointestinal disease

OPEN ACCESS

Edited by:
Mark Gray,
University of Edinburgh,
United Kingdom

Reviewed by:
Bert Devriendt,
Ghent University, Belgium
Harry D. Dawson,
Agricultural Research Service (USDA),
United States

****Correspondence:***
Amanda L. Ziegler
Amanda_ziegler@ncsu.edu

Specialty section:
This article was submitted to Comparative and Clinical Medicine, a section of the journal Frontiers in Veterinary Science

Received: *13 December 2021*
Accepted: *28 February 2022*
Published: *25 March 2022*

Citation:
Rose EC, Blikslager AT and Ziegler AL (2022) Porcine Models of the Intestinal Microbiota: The Translational Key to Understanding How Gut Commensals Contribute to Gastrointestinal Disease. Front. Vet. Sci. 9:834598. doi: 10.3389/fvets.2022.834598

THE RISE AND PLATEAU OF GUT MICROBIOTA RESEARCH

Over the first few days of life, the neonatal gut is rapidly populated by a diverse population of microorganisms that exponentially expands to a number exceeding that of the total host cells (1). Interestingly, a recently-proposed paradigm shift suggests that the gut microbiota begins to develop *in utero* rather than during birth (2–5). Such findings are pivotal to our understanding of the gut microbiota given that microbes support vital physiologic processes including production of volatile fatty acids and vitamin K as well as transportation of electrolytes and water across the mucosal surface. The presence of gut commensals is particularly crucial in developing neonates, the developing immune system of which is stimulated by indigenous microflora. Furthermore, the absence of certain gut commensals has been associated with increased risk for lifelong autoimmune diseases (6, 7).

Paralleling increased interest in the gut bacterial microbiota, herein referred to as the gut microbiota, there have been robust advancements in laboratory technologies able to characterize such populations. Increased accessibility to 16S rRNA and next-generation DNA sequencing has permitted detailed characterization of the gastrointestinal microbiota in numerous species. Furthermore, "-omics" laboratory techniques have informed investigations into the systemic impact of gut microbial communities. These communities are now heavily linked with the development of several intestinal and multisystemic diseases in humans including obesity and inflammatory bowel disease (IBD).

Despite instrumental advances in microbial identification, establishing association between variations in microbial diversity and disease phenotypes is continuously challenged by sampling limitations within humans. Subsequently, gastrointestinal research has experienced drastic drops in the development of new pharmaceuticals and diagnostics despite large monetary investments by public and private institutions. This decelerated translation of basic research to clinical practice is colloquially referred to as the "pipeline problem" (8). This problem is attributable, at least in part, to the historic use of inappropriate animal models, frequently rodents, that do not adequately emulate the human patient. Consequently, gastrointestinal research has steadily turned toward pig models given their anatomic and physiologic similarities with humans (9). This review examines these similarities and summarizes recently-characterized parallels between the pig and human gut microbiota, thereby advocating for the pig as an unequaled model of the human gut microbiota and a powerful tool to break through current plateaus in exploring disease association with the gut microbiota.

ANATOMIC AND PHYSIOLOGICAL SIMILARITIES BETWEEN THE HUMAN AND PIG OUTWEIGH DIFFERENCES

Nutritionists around the world continue to preach that we are what we eat. In the realm of gastroenterology, this proverb can be interpreted literally given that gastrointestinal morphology is directly associated with meal frequency, type of food from which nutrients are extracted and composition of the gut microbiota (10, 11). Unlike rats and other domestic animals, the pig and human are both true omnivores (12). Therefore, it comes as no surprise that their gastrointestinal tracts share many macroscopic and microscopic features (**Figure 1**).

Pigs, rodents and humans all have a "simple" stomach comprised of one compartment. While the entirety of the human stomach and majority of the pig stomach are glandular, the rodent stomach is divided into a glandular portion and non-glandular portion. This non-glandular portion, which is used for food storage and digestion, defines nearly 50% of the gastric mucosal surface area in rodents, therefore complicating the use of rodent models for human gastric studies. In all three species, the glandular section is composed of cardiac, gastric and pyloric mucosa. The pig stomach contains significantly more cardiac mucosa than the human stomach. This cardiac mucosa creates a pseudo-diverticulum for food storage as well as digestion and is a proposed site of microbial metabolism. Furthermore, cardiac epithelial cells are mainly mucus-secreting while parietal and chief cells of the gastric and pyloric mucosa secrete hydrochloric acid and pepsinogen, respectively. Taking these physiochemical differences into account, the relatively large size of the cardiac mucosa in pigs may support a unique, physiologic niche for microbes that is not mirrored in the human. Therefore, caution is urged when making comparisons between human and pig gastric microbiota. Researchers should be aware of this anatomic variation and consider sampling protocols that emphasize collection from the shared gastric and pyloric mucosa rather than the cardiac mucosa.

Aboard to the stomach, porcine and human intestines are strikingly similar. The ratio of total intestinal length per kilogram bodyweight is $\sim$ 0.1 in both pigs and humans, meaning both species share a similar relative length of their intestinal tract (14, 15). The small intestines of both species are macroscopically similar, characterized by a linear, continuous tube anchored to the peritoneum by intricately-vascularized mesentery. This linear morphology is retained in the human large intestines but disrupted in the pig by the formation of a spiral colon that coils into itself. The pig colon is additionally slightly larger than the human colon; the pig colon accounts for approximately 46% of total intestinal tract weight while the human colon accounts for approximately 36% of total intestinal tract weight (14). Despite this discrepancy in shape and relative size, however, the large intestines in both species are functionally similar and house the body's largest population of microbes. Notably, the large intestinal microbiota in both species is responsible for synthesizing volatile fatty acids, which are absorbed through the intestinal mucosa (16). Sacculations and tenia within the human and pig colon additionally provide similar physiologic and anatomic niches for gut commensals and thereby may encourage similar microbial populations.

The colon is also the primary site for ingesta fermentation in both pigs and humans. Rodents, however, are cecal fermenters. Given that intestinal fermentation is primarily regulated by luminal microbes, its anatomic localization directly affects the constituents of the gut microbiota. Therefore, given that rodents ferment within their cecum, the constituents of their large intestinal microbiota will significantly vary from that of colon fermenters, namely pigs and humans. The pig and human ceca do diverge with respect to their size; the pig cecum is relatively large and grossly demarcated from the remainder of the large intestines compared to the human cecum. Therefore, similar to the gastric cardia, the study of the pig cecum as a model for humans must be regarded with caution.

Mucosal Peyer's patches are another anatomic feature that distinguishes the pig and human gastrointestinal tract, specifically the small intestines, from one another. Pig and human Peyer's patches intestines diverge with respect to the cellular composition, development, distribution and number (12, 17, 18). In fact, organogenesis research suggests that pigs develop two distinct types of Peyer's patches, jejunal and ileal, while humans develop only one (19). Given that one of the

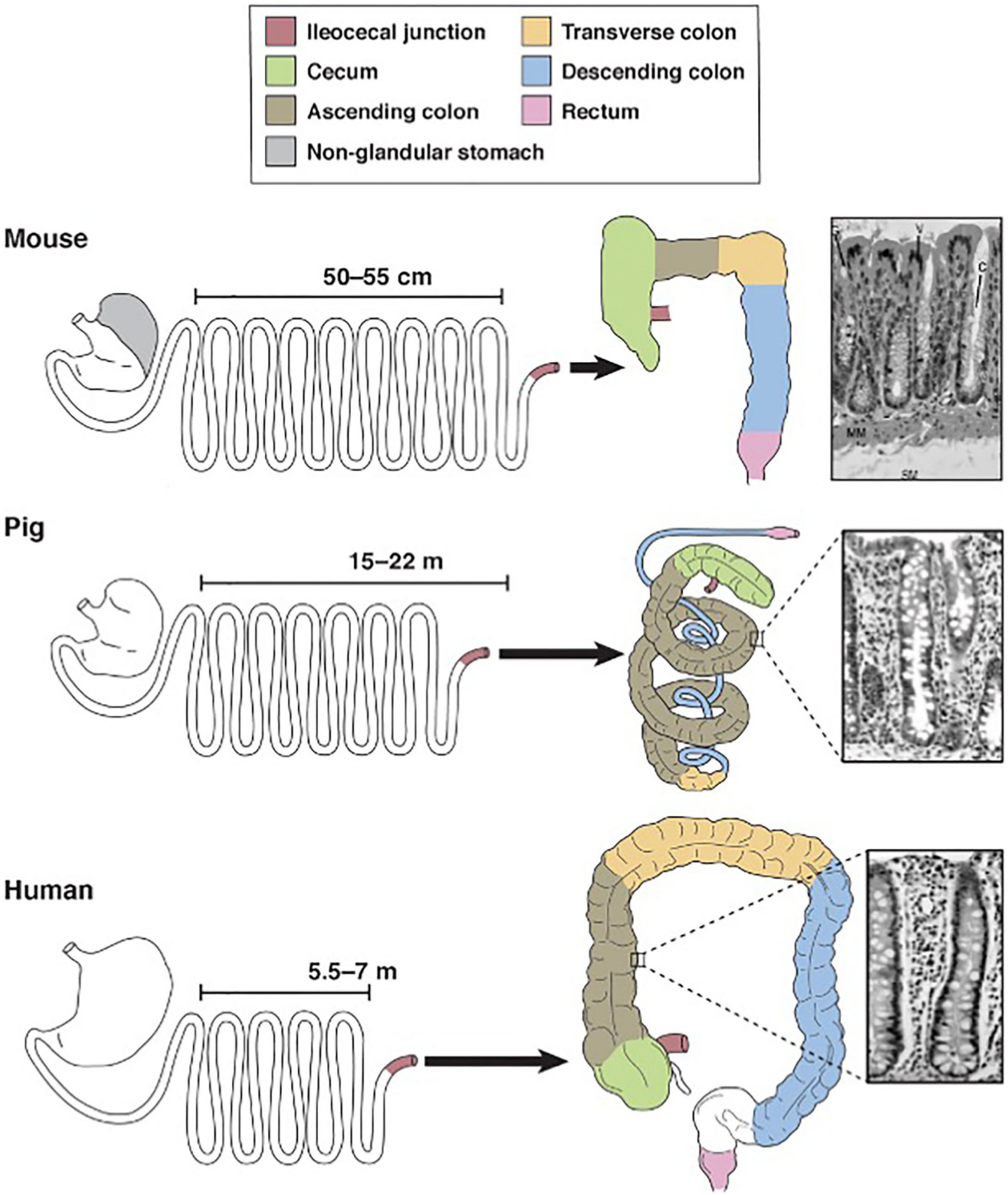

FIGURE 1 | Schematic diagram for comparison of mouse, pig and human gastrointestinal tract anatomy. Derived from Ziegler et al. (13).

Peyer's patches many functions is to discriminate between pathogenic and commensal bacteria, we can speculate that this interspecies variability may provoke distinct host perception of and interaction with gut commensals. Conversely, several researchers argue that these differences between pig and human Peyer's patches are of limited significance because pigs and

humans demonstrate similar immunologic responses to various gastrointestinal insults (12, 20, 21).

The anatomic similarities between the pig and human gastrointestinal tracts translate to comparable intestinal motility, referring to the contraction and relaxation of the muscularis layers, as well as similar ingesta transit time, referring to the time ingesta takes to travel from the esophagus to the rectum (22). Significant alterations in the gut microbiota are regularly detected in individuals with altered intestinal mobility, such as surgery patients with postoperative ileus. Therefore, similar ingesta transit times between pigs and humans may facilitate similar populations of gut microbiota by discouraging colonization by pathogenic or non-commensal organisms.

COMPARING THE NEONATAL AND ADULT INTESTINAL MICROBIOTA OF PIGS AND HUMANS REVEALS IMPORTANT SIMILARITIES AND DIFFERENCES

Many studies have made impactful comparisons between the intestinal microbiota of pigs and humans (23–25). Although the intestinal microbiota in healthy adults and mature pigs is relatively stable, it fluctuates widely over the first year of life for both species (26–28). One study has demonstrated that piglets from the same litter as well as newborn human twins can differ with respect to their intestinal microbiota (29). Furthermore, adult humans and pigs demonstrate similar alterations to their gut microbiota in response to environmental stressors and antibiotics (30–35). This suggests that the pig is a powerful model of pathologic disturbances in the intestinal microbiota, such as those elicited by antibiotic-induced dysbiosis and IBD.

Notably, most studies on the intestinal microbiota are based primarily on fecal samples due to limitations in sample acquisition. Sampling the human gastrointestinal microbiota is particularly challenging given that elective surgeries to obtain such samples are costly, time-consuming, and simply unappealing to most individuals. Elective surgeries in laboratory animals are certainly more feasible but still elicit a systemic stress response, which may compromise the microbiota and consequently the study's integrity. Therefore, very few studies have provided direct, interspecies comparisons of microbial populations across specific sites of the gastrointestinal tract.

Given this sampling limitation, most comparative studies have been limited to the large intestines, namely the colon (**Figure 2**). Under natural conditions, more than 90% of the bacteria in the colon of adult humans and pigs are within one of two phyla: Firmicutes or Bacteroidetes (27, 30, 31, 33, 34, 38). Although there is slight variation in bacterial genus and species due to species specificity, shared bacterial physiology and metabolism within these phyla solidify the adult pig as a feasible model of the human colonic microbiota in health.

Species divergence becomes more readily apparent when considering the large intestinal microbiota of neonatal pigs and human infants. Large intestinal content and feces isolated from adults and infants contain significantly more Actinobacteria than adult or neonatal pigs (33, 39). In fact, the large intestines of formula- and breast-fed infants are dominated by Actinobacteria. This discrepancy between wildtype neonatal pigs and human infants can be mitigated through the use of increasingly-available, gnotobiotic animals, which will be further discussed in subsequent sections. Wildtype piglets may remain relevant models of the infant gut microbiota, however, given their shared alternations in the intestinal microbiota following the introduction of solid food (40). Therefore, wildtype neonatal pigs can be used to examine the pathogenesis and potential therapies for dietary and environmental perturbations on the intestinal microbiota of infants as long as relative alterations in specific bacterial genera and species are interpreted with care.

Although the large intestines of adults and mature pigs are dominated by the same two phyla, interspecies variability is further elucidated by comparing the bacterial genera isolated from those phyla. Within Bacteroidetes, the most abundant genus in the human intestines is *Bacteroides* while that in pig intestines is *Prevotella* (26). At 10 weeks-of-age, *Prevotella* represents up to 30% of the microbiota of the pig colon. As the pig reaches 22-weeks-old, however, relative numbers of *Prevotella* species drop to 4% and relative numbers of Anaerobacter sp., which are in the Firmicutes phylum, increase (33, 41). This steady decline in Bacteroidetes and increase in Firmicutes is mirrored in human infants over their first 4 months of life (41, 42). Therefore, although there are select differences in bacterial genera and species between pig and human intestines, shared bacterial phyla likely trigger comparable physiologic developments and establish similar symbiotic relationships.

One of the most conspicuous dissimilarities between the human and pig microbiota is the presence of specific microorganisms that are unique to pigs. In fact, both sow-reared and formula-fed piglets have greater intestinal microbial diversity than human infants (39). Low numbers of *Fusobacterium* are detected in the feces of neonatal pigs but not breast-fed infants (39). Significantly more *Lactobacilli*, *Spirochetes* and *Streptococci* are isolated from the porcine intestines than the human intestines at any age (26, 33, 41). A high percentage of the porcine ileal microbiota is represented by Proteobacterium, which is not reported in the human ileum (30). However, large numbers of Proteobacteria have be isolated from the feces of breast-fed infants (39). This being said, aforementioned limitations on sample collection presumably limit researchers' ability to fully characterize every bacterium within the human intestines. Identification of certain gastrointestinal commensals in pigs but not humans may be attributable to sampling techniques that are feasible in the former but not the latter.

The stark differences among the environments of humans, pigs and rodents must also be considered as a potential driver of these variations. Coprophagy is considered to be normal behavior of pigs and rodents. In piglets, the influence of sanitary conditions and coprophagia on the gastrointestinal microbiota has been well established (43, 44). Coprophagia of the sow's feces may in fact benefit piglets as a source for commensal microbes that foster the development of the piglet's microbiome. Considering the commonality of coprophagia in pigs, many researchers have turned to germ free, gnotobiotic or even humanized pigs, all of which are further discussed below.

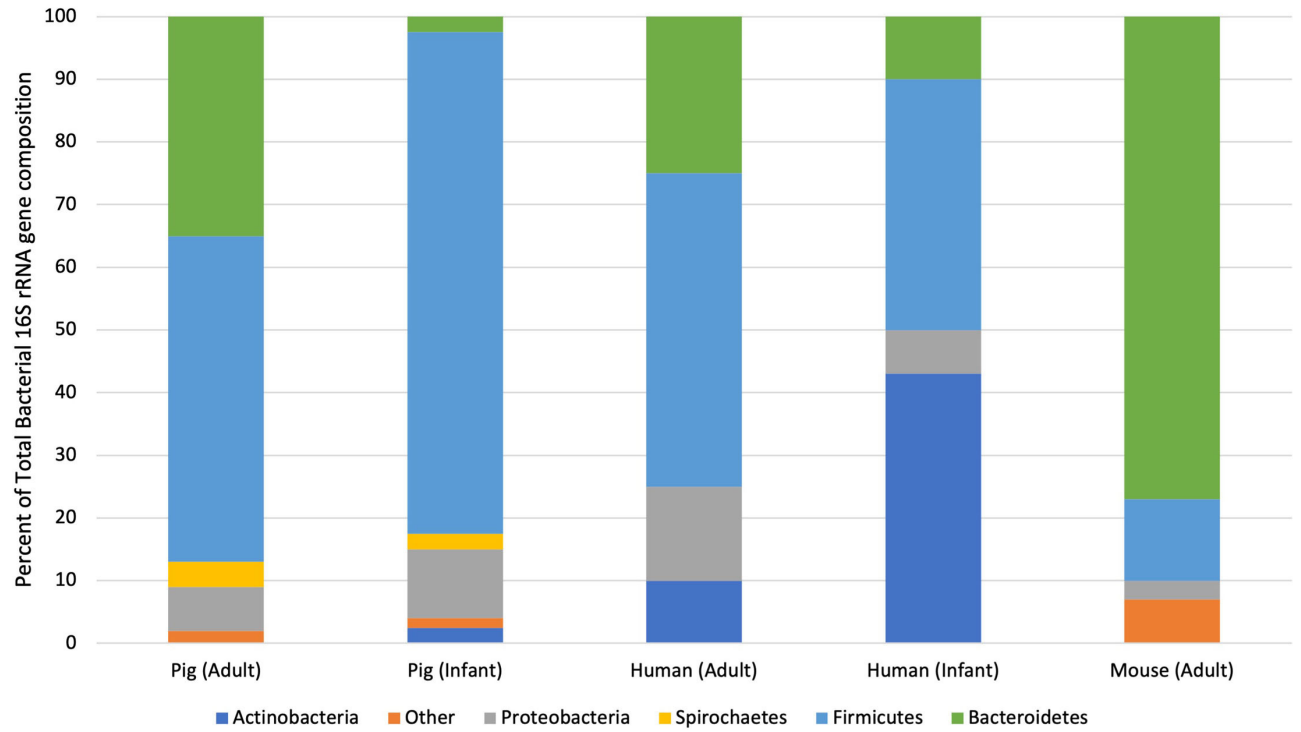

FIGURE 2 | Taxonomic distribution of bacterial phyla from pigs, humans and mice at different life stages. This graph illustrates the percent of sequences assigned to each bacterial phylum isolated through 16S rRNA sequencing of pooled fecal samples isolated from healthy individuals of each species (33, 36, 37).

Despite select dissimilarities in the intestinal microbiota of pigs and humans, the alluring nature of the pig as a model for the human intestinal microbiota is largely attributable to the fact that the pig is the best model we currently have. While the laboratory animal population across the world remains dominated by rodents, anatomic and physiologic dissimilarities between the human and rodent gastrointestinal tracts promote significant interspecies variation in the gut microbiota (23, 45). Nearly 85% of the bacteria genera isolated from the mouse gut is not present within the human, which immensely overshadows aforementioned variations in intestinal microbiota of pigs and humans (46).

CUTTING-EDGE TECHNIQUES ARE AVAILABLE IN PIG MODELS

The pig's potential for high impact, translational research is further exemplified by the vast number of laboratory techniques that have been adapted to the pig. One of the biggest advantages of pig is its relative size compared to other traditional laboratory animals such as mice and rats. The pig's large gastrointestinal tract equates to increased surgical access and manipulation as well as experimental tissue volume. Furthermore, standardization of pig care and surgery permits even a novice researcher to easily expand their studies to include pig models (47–50).

Paralleling this expanse in laboratory techniques, there has been a sharp rise in the type of available pig models. The pig genome has been fully sequenced, leading to the emergence of genetically-modified pigs. Genetically-modified pigs are stronger translational models than rodents given that the human genome is more closely related to the pig than to the mouse or rat (51–53). Such models can strengthen our understanding of disease pathogenesis by introducing the ability to knock-down or knock-out genes as well as artificially tag specific cell populations and proteins so that they can be traced along the course of disease. Therefore, observations elucidated from these pigs can better inform putative disease therapies in human medicine.

In addition to genetically-modified pigs, many researchers are introducing germ-free, gnotobiotic and human-microbial associated (HMA) pigs to their experimental design. Through elimination of the intestinal microbiota in germ-free pigs, investigators may track variances in disease pathogenesis and consequently infer disease association or correlation with specific gut commensals. This being said, germ-free pigs have shorter small intestines, shorter crypts, longer villi and smaller Peyer's patches compared to conventionally-raised pigs (39). These anatomic variances, along with associated alterations in intestinal physiology and immunology, force researchers to question the translatability of germ-free pigs. Gnotobiotic pigs are arguably more powerful models of gastrointestinal

disease because they permit direct manipulation of the intestinal microbiota such that investigators can characterize disease progression in the presence of select microbes. One emerging subset of gnotobiotic pigs, HMA pigs, are exceptionally noteworthy and will be discussed further within the following section.

IMPORTANT DIFFERENCES BETWEEN THE HUMAN AND PORCINE INTESTINAL MICROBIOTA MAY BE SURPASSED THROUGH HUMAN-MICROBIAL ASSOCIATED PIGS

Several laboratories have successfully "humanized" the intestinal microbiota of animal models by inoculating germ-free animals with microorganisms isolated from the human intestines (11). Human microbiota-associated piglets have been established using inocula from infants, children and adults (40, 54, 55). The gut microbiota from these recipient HMA piglets is more similar to that of the human donor than that of conventionally-raised piglets. Furthermore, age-related microbial succession in HMA piglets mirrors that observed within the human donors (40).

Notably, bacteria from the Actinobacteria phyla, namely *Bifidobacteria*, successfully colonize HMA piglets and reach population densities similar to those in humans (40). Therefore, although the intestinal microbiota of conventionally-raised piglets diverges from that of infants due to the absence of naturally occurring Acintobacteria, the intestinal microbiota of HMA-piglets can be manipulated such that it closely emulates that of humans. Attempts to create HMA models in other animal species have not been as fruitful. The predominant bacterial genera of the human intestines, including Lactobacillus and Bifidobacterium, do not successfully colonize the gut of mice and zebrafish following inoculation (56–58). Therefore, not all HMA animals are powerful models of the human intestinal microbiota and something within the pig, perhaps the similarities in gastrointestinal anatomy and physiology, supports successful colonization of human bacteria.

The strength in the HMA pig model stems from the vast number of questions that can be gleaned through its integration in experimental design. As probiotics and prebiotics continue to gain momentum while synbiotics and postbiotics gain traction in the world of dietary supplementation, HMA pig models may be key to evaluating the impact of these compounds on the microbiota (59–61). Long-term studies of HMA pigs can therefore overcome the limitations in sample collection from the intestinal lumen of humans, thereby allowing further study of microbial community succession and biogeography in infants to adults. Additionally, it will be interesting to use HMA pigs to investigate whether key microbial activities can be transferred to recipient animals. This may inform future treatment modalities for gastrointestinal disorders that are associated with microbiota derangements.

WITH IMPACTFUL MODELS COMES IMPACTFUL COSTS

One of the biggest limitations of pig models is their relative cost of model acquisition and maintenance. In the Unites States, the *per diem* housing cost for rodents typically ranges between $1-3 USD while for a pig is up to $19 USD depending on the facility[1]. Given that the lifespan of most laboratory rodents is around 2–3 years and that of pigs is around 20 years, accruing costs of pig colony management may limit the feasibility of long-term, prospective studies. Even a single finishing pig, which is between 4-months and 1-year-old, is up to 30 times the cost of an adult laboratory mouse or rat (personal communication with Dr. Jack Odle, North Carolina State University). Despite the previously discussed power of gnotobiotic and HMA pig models, the limited number of laboratory facilities that can house large animals significantly potentiates costs. One litter of gnotobiotic pigs is estimated to cost around $25,000 and the cost of a 9-month study on 2 gnotobiotic litters is around $350,000 (personal communication with Dr. Michael Oglesbee, The Ohio State University). While gnotobiotic mice are certainly not cheap at $500 each, they are significantly less expensive than their porcine counterpart[2].

CONCLUDING REMARKS AND FUTURE DIRECTIONS

As gastrointestinal researchers continue to embrace the pig model and HMA pigs become increasingly accessible, emerging translational studies will divulge the pathogenesis of and putative therapies for diseases characterized by or associated with intestinal dysbiosis. Pig models have already proven advantageous in the study of microbiota-associated diseases such as necrotizing enterocolitis of infants, which is a complication of preterm, very-low birth weight infants that has been associated with bacterial colonization of the intestines (62–70). Particularly now that the porcine intestinal microbiota has been fully characterized through multiple life stages, gastrointestinal researchers can easily track changes in the microbial composition and make direct associations between these changes and disease (28, 38, 41, 71). Compounding these studies with investigations into potential preventative and therapeutic interventions will undoubtedly uncover exciting, translational advances that will benefit humans and animals alike.

AUTHOR CONTRIBUTIONS

ER: manuscript generation. AB and AZ: editing and revising. All authors contributed to the article and approved the submitted version.

FUNDING

ER was supported by a COHA Translational Fellowship funded by U01 TR002953.

[1]NCSU CVM Laboratory Animal Resources. https://cvm.ncsu.edu/lar-cost/

[2]Taconic Biosciences Inc. https://www.taconic.com/mouse-model/black-6-b6ntac

REFERENCES

1. Backhed F, Ley RE, Sonnenburg JL, Peterson DA, Gordon JI. Host-bacterial mutalism in the human intestine. *Science.* (2005) 307:1104816. doi: 10.1126/science.1104816
2. Collado MC, Rautava S, Aakko J, Isolauri E, Salminen S. Human gut colonisation may be initiated in utero by distinct microbial communities in the placenta and amniotic fluid. *Sci Rep.* (2016) 6:23129. doi: 10.1038/srep23129
3. Hansen R, Scott KP, Khan S, Martin JC, Berry SH, Stevenson M, et al. First-pass meconium samples from healthy term vaginally-delivered neonates: an analysis of the microbiota. *PLoS ONE.* (2015) 10:e0133320. doi: 10.1371/journal.pone.0133320
4. Aagaard K, Ma J, Antony KM, Ganu R, Petrosino J, Versalovic J. The placenta harbors a unique microbiome. *Sci Transl Med.* (2014) 6, 237ra265. doi: 10.1126/scitranslmed.3008599
5. Stinson LF, Boyce MC, Payne MS, Keelan JA. The not-so-sterile womb: evidence that the human fetus is exposed to bacteria prior to birth. *Front Microbiol.* (2019) 10:1124. doi: 10.3389/fmicb.2019.01124
6. Savage DC. Microbial ecology of the gastrointestinal tract. *Ann Rev Microbiol.* (1977) 31:543. doi: 10.1146/annurev.mi.31.100177.000543
7. Leslie M. Gut microbes keep rare immune cells in line. *Science.* (2012) 335:1428. doi: 10.1126/science.335.6075.1428
8. Phillips KVBS, Issa A. Diagnostics and biomarker development: priming the pipeline. *Nat Rev Drug Discov.* (2006) 5:nrd2033. doi: 10.1038/nrd2033
9. Lunney JK, Van Goor A, Walker KE, Hailstock T, Franklin J, Dai C. Importance of the pig as a human biomedical model. *Sci Transl Med.* (2021) 13:abd5758. doi: 10.1126/scitranslmed.abd5758
10. Foong JPP, Hung LY, Poon S, Savidge TC, Bornstein JC. Early life interaction between the microbiota and the enteric nervous system. *Am J Physiol Gastrointest Liver Physiol.* (2020) 319:G541–8. doi: 10.1152/ajpgi.00288.2020
11. Yu Y, Lu L, Sun J, Petrof EO, Claud EC. Preterm infant gut microbiota affects intestinal epithelial development in a humanized microbiome gnotobiotic mouse model. *Am J Physiol Gastrointest Liver Physiol.* (2016) 311:G521–32. doi: 10.1152/ajpgi.00022.2016
12. Kararli TT. Comparison of the gastrointestinal anatomy, physiology, and biochemistry of humans and commonly used laboratory animals. *Biopharm Drug Dispos.* (1995) 16:351–80. doi: 10.1002/bdd.2510160502
13. Ziegler A, Gonzalez L, Blikslager A. Large animal models: the key to translational discovery in digestive disease research. *Cell Mol Gastroenterol Hepatol.* (2016) 2:6. doi: 10.1016/j.jcmgh.2016.09.003
14. Gonzalez LM, Moeser AJ, Blikslager AT. Porcine models of digestive disease: the future of large animal translational research. *Transl Res.* (2015) 166:12–27. doi: 10.1016/j.trsl.2015.01.004
15. Hatton GB, Yadav V, Basit AW, Merchant HA. Animal farm: considerations in animal gastrointestinal physiology and relevance to drug delivery in humans. *J Pharm Sci.* (2015) 104:2747–76. doi: 10.1002/jps.24365
16. Stevens C. Physiologicla implications of microbial digestion in the large intestine of mammals: relation to dietary factors. *Am J Clin Nutr.* (1978) 10:S161–8. doi: 10.1093/ajcn/31.10.S161
17. Maroilley T, Berri M, Lemonnier G, Esquerre D, Chevaleyre C, Melo S, et al. Immunome differences between porcine ileal and jejunal Peyer's patches revealed by global transcriptome sequencing of gut-associated lymphoid tissues. *Sci Rep.* (2018) 8:9077. doi: 10.1038/s41598-018-27019-7
18. Burkey TE, Skjolaas KA, Minton JE. Board-invited review: porcine mucosal immunity of the gastrointestinal tract. *J Anim Sci.* (2009) 87:1493–501. doi: 10.2527/jas.2008-1330
19. Furukawa M, Ito S, Suzuki S, Fuchimoto D, Onishi A, Niimi K, et al. Organogenesis of ileal Peyer's patches is initiated prenatally and accelerated postnatally with comprehensive proliferation of B cells in pigs. *Front Immunol.* (2020) 11:604674. doi: 10.3389/fimmu.2020.604674
20. Swindle MM, Makin A, Herron AJ, Clubb FJ, Frazier KS. Swine as models in biomedical research and toxicology testing. *Vet Pathol.* (2012) 49:344–56. doi: 10.1177/0300985811402846
21. Swindle MM. Comparative anatomy and physiology of the pig. *Scand J Lab Anim Sci.* (1998) 25:11–21.
22. Graham H, Aman P. The pig as a model in dietary fibre digestion studies. *Scand J Gastroenterol Suppl.* (1987) 129:55–61. doi: 10.3109/00365528709095851
23. Li X, Liang S, Xia Z, Qu J, Liu H, Liu C, et al. Establishment of a Macaca fascicularis gut microbiome gene catalog and comparison with the human, pig, and mouse gut microbiomes. *Gigascience.* (2018) 7. doi: 10.1093/gigascience/giy100
24. Xiao L, Estelle J, Killerich P, Ramayo-Caldas Y, Zia Z, Feng Q, et al. A reference gene catalogue of the pig gut microbiome. *Nat Microbiol.* (2016) 1:16161. doi: 10.1038/nmicrobiol.2016.161
25. Chen C, Zhou Y, Fu H, Xiogn X, Fang S, Jiang H, et al. Expanded catalog of microbial genes and metagenome-assembled genomes from the pig gut microbiome. *Nat Commun.* (2021) 12. doi: 10.1038/s41467-021-21295-0
26. Roura E, Koopmans SJ, Lalles JP, Le Huerous-Luron I, de Jager N, Schuurman T, et al. Critical review evaluating the pig as a model for human nutritional physiology. *Nutr Res Rev.* (2016) 29:60–90. doi: 10.1017/S0954422416000020
27. Gao S, Yan L, Wang R, Li J, Yong J, Zhou X, et al. Tracing the temporal-spatial transcriptome landscapes of the human fetal digestive tract using single-cell RNA-sequencing. *Nat Cell Biol.* (2018) 20:721–34. doi: 10.1038/s41556-018-0105-4
28. Chen L, Xu Y, Chen X, Fang C, Zhao L, Chen F. The maturing development of gut microbiota in commercial piglets during the weaning transition. *Front Microbiol.* (2017) 8:1688. doi: 10.3389/fmicb.2017.01688
29. Koo H, Hakim JA, Crossman DK, Lefkowitz EJ, Morrow CD. Sharing of gut microbial strains between selected individual sets of twins cohabitating for decades. *PLoS ONE.* (2019) 14:e0226111. doi: 10.1371/journal.pone.0226111
30. Isaacson R, Kim HB. The intestinal microbiome of the pig. *Anim Health Res Rev.* (2012) 13:100–9. doi: 10.1017/S1466252312000084
31. Looft T, Johnson A, Allen HK, Bayles DO, Alt DP, Stedtfeld RD, et al. In-feed antibiotic effects on the swine intestinal microbiome. *Proc Nat Acad Sci.* (2012) 109:1691–6. doi: 10.1073/pnas.1120238109
32. Dethlefsen L, Huse S, Sogin ML, Relman DA. The pervasive effects of an antibiotic on the human gut microbiota, as revealed by deep 16S rRNA sequencing. *PLoS Biol.* (2008) 6:e280. doi: 10.1371/journal.pbio.0060280
33. Lamendella R, Santo Domingo JW, Ghosh S, Martinson J, Oerther DB. Comparative fecal metagenomics unveils unique functional capacity of the swine gut. *BMC Microbiol.* (2011) 11:103. doi: 10.1186/1471-2180-11-103
34. Guo X, Xia X, Tang R, Zhou J, Zhao H, Wang K, et al. Development of a real-time PCR method for Firmicutes and Bacteroidetesin faeces and its application to quantify intestinal population of obese and lean pigs. *Lett Appl Microbiol.* (2008) 47:367–73. doi: 10.1111/j.1472-765X.2008.02408.x
35. Borewicz KA, Kim HB, Singer RS, Gabhart CJ, Sreevatsan S, Johnson T, et al. Changes in the porcine intestinal microbiome in response to infection with *Salmonella enterica* and *Lawsonia intracellularis*. *PLoS ONE.* (2015) 10:e0139106. doi: 10.1371/journal.pone.0139106
36. Schokker D, Zhang J, Zhang L-L, Vastenhouw HG, Heilig HJ, Smidt H, et al. Early-life environmental variation affects intestinal microbiota and immune development in new-born piglets. *PLoS ONE.* (2014) 9:e100040. doi: 10.1371/journal.pone.0100040
37. Yang Y-W, Chen M-K, Yang B-Y, Huang X-J, Zhang X-R, He L-Q, et al. Use of 16S rRNA gene-targeted group-specific primers for real-time pcr analysis of predominant bacteria in mouse feces. *Appl Environ Microbiol.* (2015) 81:6749–56. doi: 10.1128/AEM.01906-15
38. Crespo-Piazuelo D, Migura-Garcia L, Estelle J, Criado-Mesas L, Revilla M, Castello A, et al. Association between the pig genome and its gut microbiota composition. *Sci Rep.* (2019) 9:8791. doi: 10.1038/s41598-019-45066-6
39. Wang M, Donovan SM. Human microbiota-associated swine: current progress and future opportunities. *ILAR J.* (2015) 56:63–73. doi: 10.1093/ilar/ilv006
40. Pang X, Hua X, Yang Q, Ding D, Che C, Cui L, et al. Inter-species transplantation of gut microbiota from human to pigs. *ISME J.* (2007) 1:156–62. doi: 10.1038/ismej.2007.23
41. Kim H B, Borewicz K, White BA., Singer RS., Sreevatsan S, Tu ZJ, et al. Longitudinal investigation of the age-related bacterial diversity in the feces of commercial pigs. *Vet Microbiol.* (2011) 153:124–33. doi: 10.1016/j.vetmic.2011.05.021

42. Vaiserman A, Romanenko M, Piven L, Moseiko V, Lushchak O, Kryzhanovska N, et al. Differences in the gut firmicutes to bacteroidetes ratio across age groups in healthy Ukrainian population. *BMC Microbiol.* (2020) 20:1–8. doi: 10.1186/s12866-020-01903-7
43. Montagne L, Arturo-Schaan M, Le Floc'h N, Guerra L, Le Gall M. Effect of sanitary conditions and dietary fibre on the adaptation of gut microbiota after weaning. *Livestock Sci.* (2010) 133:113–6. doi: 10.1016/j.livsci.2010.06.039
44. Schmidt B, Mulder IE, Musk CC, Aminov RI, Lewis M, Stokes CR, et al. Establishment of normal gut microbiota is compromised under excessive hygiene conditions. *PLoS ONE.* (2011) 6:e28284. doi: 10.1371/journal.pone.0028284
45. Xiao L, Feng Q, Liang S, Sonne SB, Xia Z, Qiu X, et al. A catalog of the mouse gut metagenome. *Nat Biotechnol.* (2015) 33:1103–8. doi: 10.1038/nbt.3353
46. Nguyen TLA, Vieira-Silva S, Liston A, Raes J. How informative is the mouse for human gut microbiota research? *Disease Models Mechanisms.* (2015) 8:1–16. doi: 10.1242/dmm.017400
47. Rehbinder C, Baneux P, Forbes D, Van Herck H, Nicklas W, Rugaya Z, et al. FELASA recommendations for the health monitoring of breeding colonies and experimental units of cats, dogs and pigs: Report of the Federation of European Laboratory Animal Science Associations (FELASA) Working Group on Animal Health. *Lab Anim.* (1998) 32:1–17. doi: 10.1258/002367798780559428
48. Marchant-Forde JN, Herskin MS. Pigs as laboratory animals. In: *Advances in Pig Welfare*. WoodHead Publishing (2018). p. 445–75.
49. Smith AC, Swindle MM. Preparation of swine for the laboratory. *ILAR J.* (2006) 47:358–63. doi: 10.1093/ilar.47.4.358
50. Swindle M. *Swine in the Laboratory. Surgery, Anaesthesia, Imaging and Experimental Techniques*. Boca Raton: CRC Press/Taylor and Friends (2007).
51. Wernersson R, Schierup MH., Jorgensen FG., Gorodkin J, Panitz F, Staerfeldt H-H, et al. Pigs in sequence space: A 0.66X coverage pig genome survey based on shotgun sequencing. *BMC Genom.* (2005) 6:1–7. doi: 10.1186/1471-2164-6-70
52. Jørgensen F, Hobolth A, Hornshoj H, Bendizen C, Fredhold M, Schierup M. Comparative analysis of protein coding sequences from human, mouse and the domestic pig. *BMC Biol.* (2005) 3:2. doi: 10.1186/1741-7007-3-2
53. Walters EM, Wolf E, Whyte JJ, Mao J, Renner S, Nagashima H, et al. Completion of the swine genome will simplify the production of swine as a large animal biomedical model. *BMC Med Genomics.* (2012) 5:55. doi: 10.1186/1755-8794-5-55
54. Zhang H, Wang H, Shepherd M, Wen K, Li G, Yang X, et al. Probiotics and virulent human rotavirus modulate the transplanted human gut microbiota in gnotobiotic pigs. *Gut Pathog.* (2014) 6:1–7. doi: 10.1186/s13099-014-0039-8
55. Zhang Q, Widmer G, Tzipori S. A pig model of the human gastrointestinal tract. *Gut Microbes.* (2013) 4:193–200. doi: 10.4161/gmic.23867
56. Rawls JF, Mahowald MA, Ley RE, Gordon JI. Reciprocal gut microbiota transplants from zebrafish and mice to germ-free recipients reveal host habitat selection. *Cell.* (2006) 127:423–33. doi: 10.1016/j.cell.2006.08.043
57. Imaoka A, Setoyama H, Takagi A, Matsumoto S, Umesaki Y. Improvement of human faecal flora-associated mouse model for evaluation of the functional foods. *J Appl Microbiol.* (2004) 96:656–63. doi: 10.1111/j.1365-2672.2004.02189.x
58. Raibaud P, Ducluzeau R, Dubos F, Hudault S, Bewa H, Muller MC. Implantation of bacteria from the digestive tract of man and various animals into gnotobiotic mice. *Am J Clin Nutr.* (1980) 33:2440. doi: 10.1093/ajcn/33.11.2440
59. Scarpellini E, Rinninella E, Basillico M, Colomier E, Rasetti C, Larussa T, et al. From pre- and probiotics to post-biotics: a narrative review. *Int J Environ Res Public Health.* (2021) 19:37. doi: 10.3390/ijerph19010037
60. Salminen S, Collado MC, Endo A, Hill C, Lebeer S, Quigley EMM, et al. The international scientific association of probiotics and prebiotics (ISAPP) consensus statement on the definition and scope of postbiotics. *Nat Rev Gastroenterol Hepatol.* (2021) 18:649–67. doi: 10.1038/s41575-021-00440-6
61. Li H-Y, Zhou D-D, Gan R-Y, Huang S-Y, Zhao C-N, Shang A, et al. Effects and mechanisms of probiotics, prebiotics, synbiotics, and postbiotics on metabolic diseases targeting gut microbiota: a narrative review. *Nutrients.* (2021) 13:3211. doi: 10.3390/nu13093211
62. Bjornvad CR, Thymann T, Deutz NE, Burrin DG, Jensen SK, Jensen BB, et al. Enteral feeding induces diet-dependent mucosal dysfunction, bacterial proliferation, and necrotizing enterocolitis in preterm pigs on parenteral nutrition. *Am J Physiol Gastrointest Liver Physiol.* (2008) 295:G1092–1103. doi: 10.1152/ajpgi.00414.2007
63. Sangild PT, Siggers RH, Schmidt M, Elnif J, Bjornvad CR, Thymann T, et al. Diet- and colonization-dependent intestinal dysfunction predisposes to necrotizing enterocolitis in preterm pigs. *Gastroenterology.* (2006) 130:1776–92. doi: 10.1053/j.gastro.2006.02.026
64. Mendez YS, Khan FA, Perrier GV, Radulescu A. Animal models of necrotizing enterocolitis. *World J. Pediatric Surg.* (2020) 3:e000109. doi: 10.1136/wjps-2020-000109
65. Fitzgibbons SC, Ching Y, Yu D, Carpenter J, Kenny M, Weldon C, et al. Mortality of necrotizing enterocolitis expressed by birth weight categories. *J Pediatr Surg.* (2009) 44:1072–6. doi: 10.1016/j.jpedsurg.2009.02.013
66. Krediet T, Lelyveld N, Vijibrief D, Brouwers H, Kramer W, Fleer A, et al. (2007). Microbiological factors associated with neonatal necrotizing enterocolitis: protective effect of early antibiotic treatment. *Acta Paediatr.* 92:1180–2. doi: 10.1111/j.1651-2227.2003.tb02481.x
67. Ladd N, Ngo T. The use of probiotics in the prevention of necrotizing enterocolitis in preterm infants. *Baylor University Medical Center Proc.* (2009) 22:287–91. doi: 10.1080/08998280.2009.11928535
68. Jiang YN, Muk T, Stensballe A, Nguyen DN, Sangild PT, Jiand PP. Early protein markers of necrotizing enterocolitis in plasma of preterm pigs exposed to antibiotics. *Front Immunol.* (2020) 11:565862. doi: 10.3389/fimmu.2020.565862
69. Brunse A, Peng Y, Li Y, Lykkesfeldt J, Sangild PT. Co-bedding of preterm newborn pigs reduces necrotizing enterocolitis incidence independent of vital functions and cortisol levels. *Front Pediatr.* (2021) 9:636638. doi: 10.3389/fped.2021.636638
70. Birck MM, Nguyen DN, Ciliebord MS, Kamal SS, Nielson DS, Dambord P, et al. Enteral but not parenteral antibiotics enhance gut function and prevent necrotizing enterocolitis in formula-fed newborn preterm pigs. *Am J Physiol Gastrointest Liver Physiol.* (2016) 310:G323–333. doi: 10.1152/ajpgi.00392.2015
71. Gresse CD, Dunière B, Forano D. Microbiota composition and functional profiling throughout the gastrointestinal tract of commercial weaning piglets. *Microorganisms.* (2019) 7:343. doi: 10.3390/microorganisms7090343

Conflict of Interest: The authors declare that the research was conducted in the absence of any commercial or financial relationships that could be construed as a potential conflict of interest.

Publisher's Note: All claims expressed in this article are solely those of the authors and do not necessarily represent those of their affiliated organizations, or those of the publisher, the editors and the reviewers. Any product that may be evaluated in this article, or claim that may be made by its manufacturer, is not guaranteed or endorsed by the publisher.

frontiers | Frontiers in Veterinary Science

REVIEW
published: 26 April 2022
doi: 10.3389/fvets.2022.879630

Role of Animal Models to Advance Research of Bacterial Osteomyelitis

Caroline Billings and David E. Anderson*

Large Animal Clinical Sciences, University of Tennessee College of Veterinary Medicine, Knoxville, TN, United States

Osteomyelitis is an inflammatory bone disease typically caused by infectious microorganisms, often bacteria, which causes progressive bone destruction and loss. The most common bacteria associated with chronic osteomyelitis is *Staphylococcus aureus*. The incidence of osteomyelitis in the United States is estimated to be upwards of 50,000 cases annually and places a significant burden upon the healthcare system. There are three general categories of osteomyelitis: hematogenous; secondary to spread from a contiguous focus of infection, often from trauma or implanted medical devices and materials; and secondary to vascular disease, often a result of diabetic foot ulcers. Independent of the route of infection, osteomyelitis is often challenging to diagnose and treat, and the effect on the patient's quality of life is significant. Therapy for osteomyelitis varies based on category and clinical variables in each case. Therapeutic strategies are typically reliant upon protracted antimicrobial therapy and surgical interventions. Therapy is most successful when intensive and initiated early, although infection may recur months to years later. Also, treatment is accompanied by risks such as systemic toxicity, selection for antimicrobial drug resistance from prolonged antimicrobial use, and loss of form or function of the affected area due to radical surgical debridement or implant removal. The challenges of diagnosis and successful treatment, as well as the negative impacts on patient's quality of life, exemplify the need for improved strategies to combat bacterial osteomyelitis. There are many *in vitro* and *in vivo* investigations aimed toward better understanding of the pathophysiology of bacterial osteomyelitis, as well as improved diagnostic and therapeutic strategies. Here, we review the role of animal models utilized for the study of bacterial osteomyelitis and their critically important role in understanding and improving the management of bacterial osteomyelitis.

Keywords: osteomyelitis, bone, *in vivo*, animal model, *Staphylococcus aureus*

OPEN ACCESS

Edited by:
Mark Gray,
University of Edinburgh,
United Kingdom

Reviewed by:
Chao Xie,
University of Rochester, United States
Elysia A. Masters,
United States Food and Drug Administration, United States

****Correspondence:***
Caroline Billings
cbilli10@vols.utk.edu

Specialty section:
This article was submitted to Comparative and Clinical Medicine, a section of the journal Frontiers in Veterinary Science

Received: *20 February 2022*
Accepted: *05 April 2022*
Published: *26 April 2022*

Citation:
Billings C and Anderson DE (2022) Role of Animal Models to Advance Research of Bacterial Osteomyelitis. Front. Vet. Sci. 9:879630. doi: 10.3389/fvets.2022.879630

INTRODUCTION: CLINICAL DISEASE AND PATIENT IMPACT

Osteomyelitis is an inflammatory bone disease that results in progressive bone destruction and bone loss and is typically caused by infectious microorganisms (1–4). The most common causative organisms are bacteria (1), specifically Gram-positive Staphylococci such as *Staphylococcus aureus* (*S. aureus*) (1–3, 5–8). There are three main etiologies of osteomyelitis: hematogenous, trauma or surgery associated, and secondary to vascular disease. Hematogenous osteomyelitis is most common among pediatric patients (5, 7, 8). Injury associated osteomyelitis may be spread from

a contiguous focus of infection, may be secondary to trauma, or may be associated with surgery, especially where implanted medical devices are used. This may occur in individuals of any age (2, 3, 5–7). Osteomyelitis also commonly occurs secondary to vascular insufficiency and is often a result of diabetic foot ulcers (DFU) (2, 6, 7). The annual incidence rate of osteomyelitis in the United States is not precisely known. In 1999, the incidence was reported to be as high as one out of every 675 hospital admissions, which translates to approximately 50,000 cases annually (9). Since that time, the incidence of osteomyelitis cases of all categories has been increasing (8). The rise in caseload is partially due to increases in cases of diabetes (8), trauma (10), numbers of reconstructive orthopedic procedures and implanted prosthetic materials (6, 11–13), and also may be associated with improvements in diagnosis (2).

Clinical presentation of patients suffering from osteomyelitis is variable. Acute osteomyelitis may present with fever, redness, pain and draining lesions. Symptoms of chronic osteomyelitis may be vague, with a wide array of clinical features which may be as subtle as simple focal swelling and tenderness on physical examination (2, 6, 7, 11, 14, 15). Nonspecific clinical presentation necessitates a thorough patient workup for successful diagnosis (16). Diagnostic testing often includes physical examination, hematology and biochemistry panels, measurement of C-reactive protein (CRP), culture and sensitivity testing of bone and wound samples, and imaging such as radiographs and ultrasound. Radiographic evidence of boney changes lag behind pathologic changes, so early disease may not be apparent on standard radiographs (7, 11, 17). Advanced imaging can be helpful, and magnetic resonance imaging (MRI) or computed tomography (CT) (1, 11, 16) may be required. Despite the abundance of available tests that may be employed, there are few early pathognomonic findings for osteomyelitis (7, 18, 19). Therefore, while osteomyelitis may be suspected, the gold standard of diagnosis requires a bone biopsy for culture (2, 5, 11, 18–20) and histopathologic examination (7, 11, 18–21).

Osteomyelitis results in significant morbidity and mortality to the patient (6, 10, 14, 22, 23), and expedient, intensive treatment is indicated. The most common clinical approach to treatment of bacterial osteomyelitis involves a combination of medical and surgical management (4, 6, 11, 18, 24, 25). Systemic antibiotic therapy should be guided by microbial cultures whenever possible (11). In the absence of culture and sensitivity results, empirical, broad-spectrum antibiotics are usually administered (4, 5, 18). Antimicrobial therapy is typically administered for a minimum of 4–6 weeks (2, 19, 20, 24, 26) and is often continued for longer periods of time in an attempt to mitigate risks of chronic osteomyelitis (20). Some clinicians advocate treatment for up to six months after diagnosis (19, 20, 26). Local antibiotic therapy may be instituted to complement systemic antimicrobial therapy (27). Surgical debridement of affected tissue is routine treatment in conjunction with medical management (2, 15, 18, 19). A hallmark of osteomyelitis is the presence of necrotic bone (2, 6, 15), which is readily colonized and surrounded by biofilm (11, 28). Biofilms often result in persistence of bacterial infection. Persistence is multifactorial and is partially due to the protective slime matrix that provides a physical barrier between immune cells and bacterial cells (6, 11, 14) and can impair diffusion of antibacterial substances (29). Persistence also results from the physiologic environment of biofilms, which allows for enhanced antimicrobial resistance through creation and persistence of immense phenotypic diversity, including metabolically inactive bacteria and subpopulations of "persisters" or phenotypically resistant bacteria (30–33). Debridement of necrotic bone should be thorough, with the goal of reaching healthy, viable tissue and removing sources of biofilm. This often includes removing implanted hardware (2, 5). While this approach sounds straightforward and reasonable to accomplish, there are many challenges in the treatment of osteomyelitis which often leave patients suffering relapses or struggling with chronic infections (11, 34–36). Particular challenges include inadequate debridement (2, 15, 19, 30), metabolically inactive bacteria or bacteria embedded in biofilm (2, 12, 30), inadequate antimicrobial penetration to infected tissues (37), antimicrobial resistant bacterial species (2, 25), and loss of tissue or organ function to the patient during treatment (12, 38). Challenges are augmented by the negative impact of treatment on patient quality of life (25), increased risk of bacterial infection upon hardware reimplantation (39), and the ability of *S. aureus* to evade the host immune system (30, 40).

Bacterial osteomyelitis has a progressively increasing incidence, and it is important to reduce morbidity and mortality to patients while concurrently reducing the burden on the healthcare system (11). Continued improvements in the understanding, diagnosis, and therapy of bacterial osteomyelitis are necessary to accomplish these goals. As a result of variable patient population, case presentation and disease management, clinical osteomyelitis research has proven difficult (38). A major step in achieving improved diagnostic and therapeutic methods lies within animal modeling of this disease. *In vivo* models facilitate groundbreaking research by allowing scientists to expand upon promising *in vitro* discoveries and utilize research findings to improve the lives of patients suffering from osteomyelitis. Ultimately, animal models promise to speed advances in modern medicine. The purpose of this review is to highlight a range of animal models used to study bacterial osteomyelitis. While it is not possible to present all of the features for each individual model, this review will emphasize the limitations and benefits of the most common animal models used to investigate the pathogenesis, diagnostic methods, and therapeutic strategies to better understand and combat bacterial osteomyelitis.

MODEL DEVELOPMENT

There are many approaches to inducing bacterial osteomyelitis in animal models. This review will focus on two main categories of bacterial osteomyelitis induction: surgical and hematogenous.

Authors have chosen to exclude detailed discussion of *in vivo* modeling of osteomyelitis secondary to DFU. There are reports of modeling bacterial infection with diabetic rodent strains, however, osteomyelitis resulting from DFU is a multifactorial, chronic condition and the complexity of

modeling and translational healing differences raise concerns regarding reliable *in vivo* models (41–44). To surgically induce bacterial osteomyelitis in any species, there are a few necessary components. An injury to bone tissue (45) is required, and typically stems from mechanical trauma with or without the addition of a sclerosing agent (22, 46). A foreign body or medical device may be used to serve as a nidus for bacterial colonization (47). Bacterial inoculation is necessary and may be accomplished *via* direct administration of a bacterial inoculum (48), soaking of a foreign object or hardware in a bacterial suspension, creating a biofilm on a piece of hardware for implantation (49), or by intravenous (IV) administration of bacterial suspension (hematogenous seeding) (50). Many investigators choose to seal the bone defect, e.g. using sterile bone wax to ensure local containment of the bacteria and minimize undesired concomitant soft tissue infections (51). Induction of hematogenous bacterial osteomyelitis typically carries the advantage no required surgical manipulations or placement of foreign materials (52, 53). Hematogenous models are designed to closely mimic the acute hematogenous osteomyelitis that most commonly occurs in pediatric patients (52, 54).

Within these two categories, many differences exist in model design. Differences include the type of bone injury and surgical approach, bacterial strain and colony forming unit (CFU) count, administration vehicle and quantity of bacterial inoculum, as well as length of study and monitoring techniques. It is crucial to consider the bacterial species and strain that will be utilized in animal modeling. During initial model establishment, it is recommended to utilize a bacterial strain with well documented behavior within the chosen animal species. After confirming that osteomyelitis can be established in the selected model, the bacterial species, strain, dose, and even delivery vehicle may be altered to best accomplish the research objectives. On that token, investigators should consider the species-specificity, antimicrobial sensitivity profile, and clinical relevance of the chosen pathogen. These pillars of model development are highlighted by Laratta et al. (55) and commented on by Johansen et al. (56). Markers of success within model development typically include clinical manifestation of disease, evidence of osteomyelitis on histopathology, and positive bone cultures upon study completion. Most investigators elect to pulverize bone samples and perform bacterial culture from the pulverized samples. Confirmation of bacterial cultures using polymerase chain reaction (PCR) has become routine since the method was described in 1999 (54).

SMALL ANIMAL MODELS

Mouse Models

Model Development

There are many surgical models of bacterial osteomyelitis performed in murine models. Models typically utilize long bones, although alternatives such as vertebral models are also reported (57). An extensive review of murine models, including the goal, method, and bacterial inoculum used in each study, was recently published by Guarch-Pérez et al. (58). One approach used by multiple investigators was described in 2008 as a model to assess intramedullary response to titanium particles (59). This surgical approach is accomplished by creating a medial parapatellar arthrotomy to access the femur. Once accessed, a defect extending to the medullary cavity of the femur is created. Kirschner wire (K-wire) is inserted into the femoral medullary canal and penetrated into the patellofemoral joint space. Bacterial inoculation occurs *via* direct application of a bacterial suspension and the surgical site is closed (48, 60, 61). This model was recently adapted and modified to model shoulder implant infections (62). In this study, investigators were able to reliably induce bacterial osteomyelitis using a bioluminescent strain of *S. aureus* and were able to track infection with radiographs and bioluminescent imaging (BLI). Another surgical approach that is utilized in various forms by many investigators is described well by Funao et al. (63). Much of this approach is similar to that described above; the distal portion of the femur is exposed surgically, and a 0.5 mm drill hole is created to expose the medullary canal of the femur. Rather than placing an implant, bioluminescent *S. aureus* is inoculated directly into the defect. The defect is then sealed with bone wax and the surgical site is closed. Another unique model of murine bacterial osteomyelitis is the hematogenous model described by Horst et al. (52). This model does not involve surgical manipulation or placement of foreign material. Instead, mice received one injection of *S. aureus* in phosphate-buffered saline (PBS) *via* the lateral tail vein. This model was created to closely mimic both acute and chronic hematogenous bacterial osteomyelitis and is unique in that it does not require additional bone injury. These approaches highlight the various methods available to induce bacterial osteomyelitis and the subtleties between the various models.

Insights Into Pathogenesis

While arguably each investigation into bacterial osteomyelitis provides information on pathogenesis, there are experiments designed to evaluate specific questions regarding the pathogenesis of bacterial osteomyelitis (64). One such experiment, described by De Mesy Bentley et al. (65), utilized two murine long bone infection models and captured groundbreaking transmission electron microscopy (TEM) images of *S. aureus* invading and residing within the osteocyte lacuno-canalicular network (OLCN) of live bone. *Staphylococcus aureus* cells are thought to be protected while within the canaliculi system, as immune cells are likely too large to successfully access this area of the body. Therefore, these findings offer insight into the ability of *S. aureus* to evade the host immune system and cause latent and recurrent osteomyelitis. Zoller et al. (40), established and utilized a murine model of bulk allograft infection to expand upon the findings of de Mesy Bentley et al. by investigating the mechanisms of immune system evasion by *S. aureus*, specifically microarchitecture of implant surfaces as a potential factor in increased bacterial colonization. *Staphylococcus aureus* was discovered within allograft cortical haversian canals and submicron canaliculi within the native mouse femur. Results indicated that bulk allograft implant material was more susceptible to bacterial infection even at low bacterial inoculums compared to stainless steel implants. This finding suggests that implant microarchitecture is incredibly

important and may offer bacteria a submicron reservoir to evade clearance by the immune system. The work of Masters et al. (66) expanded upon these findings by investigating the role of *S. aureus* cell wall synthesis machinery and surface adhesins in OLCN invasion. The authors established a model of bacterial osteomyelitis by placing stainless steel pins inoculated with various mutant strains of *S. aureus* into the medial tibia of mice. Results showed significant changes in OLCN invasion, abscess formation and pathogenic bone loss with the deletions of penicillin binding protein 3 and 4 (PBP3, PBP4) and autolysin (Atl), indicating that cell wall synthesis machinery can modulate *S. aureus*' pathogenesis in osteomyelitis.

Improvements in Diagnostic Capabilities

While there are multiple reports of utilizing BLI and *in vivo* micro-CT in murine models (63, 67, 68), these reports are often geared toward improving the *in vivo* modeling system rather than improving diagnostic capabilities for clinical patients (63). Recently, however, Isogai et al. (69) performed plasma metabolome analysis in a model of murine osteomyelitis caused by *S. aureus* and identified 12 metabolites as candidate positive biomarkers and two candidate negative biomarkers for osteomyelitis. Novel plasma biomarkers are aimed to improve the early diagnosis of osteomyelitis. Improvement in the early diagnosis of osteomyelitis is of great interest, as there are currently many challenges in obtaining a swift and specific diagnosis in clinical patients.

Investigations Into Therapeutic Strategies

A major goal of *in vivo* osteomyelitis work is to evaluate novel treatment strategies and investigate potential efficacy for clinical use. There are many investigations focused on various combinations or applications of antibiotics for clearance of osteomyelitis (48, 70–72). Jørgensen et al. modeled the particularly challenging situation of biofilm presence upon orthopedic implants. They investigated the efficacy of rifampicin-containing combinations of antimicrobials compared with non-rifampicin-containing combinations of antimicrobials in reducing bacterial counts or clearing infection. Results indicated that combinations of antimicrobials that included rifampicin, as well as the combination of daptomycin and linezolid, were more effective in reducing bacterial burden than combinations not containing rifampicin (70). There are also many investigations into novel therapeutics (73–75). Wang et al. utilized a model of *S. aureus* hematogenous orthopedic implant infection to identify specific virulence factors to be translated into therapeutic targets. This work identified two key pathogenic factors, anti-α-toxin (AT) and anti-clumping factor A (ClfA) and demonstrated markedly improved efficacy in infection treatment utilizing human anti-AT/anti-ClfA combination therapy (50). Similarly, Yokogawa et al. (76) created a novel murine one-stage revision model of methicillin-resistant *S. aureus* (MRSA) implant-associated osteomyelitis. This model facilitated discovery of synergistic activity of vancomycin and anti-glucosaminidase (Gmd). Identification of alternative therapeutics is important, as medical device implantation continues to increase and antimicrobial resistance (AMR) is becoming increasingly prevalent.

Conclusion

Murine models are particularly helpful to researchers investigating bacterial osteomyelitis. Main attractions of the mouse model include the small size, economics, and genetic and molecular tools that are available to tailor murine strains and facilitate a wide array of investigations. Indeed, mouse strain selection is of paramount importance as strains contain significant differences from one another. Investigators should consider the primary research objective of the model to guide strain selection and ensure research objectives can be accomplished appropriately. This pillar of model development is highlighted nicely by Dworsky et al. (57). These advantages make mice attractive for investigations into pathogenesis and proof of concept models (58, 72). Also, mice allow for certain longitudinal monitoring techniques, such as BLI and *in vivo* microCT. Longitudinal monitoring is an asset that adds strength and clarity to data collection as individuals can be compared to themselves over multiple timepoints. While mice can mimic the human inflammatory response of osteomyelitis (58), their bone structure and bone remodeling process is less similar to humans than other animal models provide (77). As a result of the mouse's small size, complex and multi-stage surgical procedures are not impossible, but are challenging to perform. This small size also prohibits the investigation and translation of implants intended for human use. Additionally, serial blood collection is limited by volume and frequency. When considering the benefits and limitations of murine models, it can be concluded that mice are an excellent tool for early investigations from *in vitro* to *in vivo* modeling and proof of concept work.

Rat Models

Model Development

Rats provide a variety of models that produce well-characterized and reliable bacterial osteomyelitis. Significant historical developments have previously been described (36, 64, 78, 79). Currently, the most popular rat models are of long bone osteomyelitis and most often utilize the tibia (17, 22, 80–83) or femur (84–90). Long bone models rely on mechanical trauma, placement of foreign bodies, or creation of fractures, all typically with concurrent sealing of the defect area with bone wax to contain bacterial inoculums and prevent concomitant soft tissue infection. Alternative models include mandibular models (91), vertebral models (92), joint prosthesis models (93), and hematogenous models (94, 95). Hematogenous models required additional surgical manipulations to successfully establish osteomyelitis. This may be a result of the rat's ability to respond to acute infection, which can rapidly clear peripheral infection and may complicate infection models (78). Although reports of rat osteomyelitis models exist, a comprehensive review of these models is lacking. In this review, we present a detailed summary of rat osteomyelitis models that were utilized to inform this review (**Table 1**).

TABLE 1 | Rat models of osteomyelitis.

Reference	Title	Sex, strain	Age, weight	Study endpoint(s)	Bacterial strain, inoculum size and volume	Inoculation method	Brief description of procedure	Evaluation methods
*Rissing et al. (96)	Model of experimental chronic osteomyelitis in rats	Albino Sprague-Dawley	300–400 g	35 and 70 days	*Staphylococcus aureus* 52/52A/80 and OM-1. 3×10^6 CFU/5 μl	Injection into intramedullary canal	Defect to tibial metaphysis, with medullary exposure, either *via* drill or needle. Application of sclerosing agent. Sealed with bone wax.	Histology, pathology, microbiology, radiographs, blood analyses
Spagnolo et al. 1993 (97)	Chronic *Staphylococcal* osteomyelitis: a new experimental rat model	Male, Wistar	250–350 g	30, 60, 90 and 180 days	*Staphylococcus aureus* (clinical isolate), 2×10^6 CFU/5 μl	Injection into defect	Defects to tibial metaphyses bilaterally. Fibrin glue placed in defect. Sealed with bone wax	Radiographs, microbiology, histology, pathology
*Hienz et al. (95)	Development and characterization of a new model of hematogenous osteomyelitis in the rat	Female, Wistar	200 g	14 days	*Staphylococcus aureus* Phillips (clinical isolate), 1 ml of 5×10^4-10^8 CFU/ml	Intravenous injection *via* femoral vein	Drill defects to mandibular ramus and tibial metaphysis. Application of sclerosing agent.	Radiographs, microbiology, histology
Lucke et al. (22)	A new model of implant-related osteomyelitis in rats	Female, Sprague-Dawley	5 months	28 days	*Staphylococcus aureus* ATCC 49230, 10^2, 10^3, 10^6 CFU/10 μl	Injection into intramedullary canal	Burr defect into tibial metaphysis, placement of K-wire	Radiographs, blood and serum analyses, microbiology, histology
*Fukushima et al. (81)	Establishment of rat model of acute *Staphylococcal* osteomyelitis: relationship between inoculation dose and development of osteomyelitis	Male, Wistar	200–270 g	7 days	*Staphylococcus aureus* BB – Bovine mastitis, 6×10–10^5/5 μl	Injection into intramedullary canal	Drill defect into tibial metaphysis, sealed with bone wax	Microbiology, pathology, histology
Makinen et al. (51)	Comparison of ^{18}F-FDG and ^{68}Ga PET imaging in the assessment of experimental osteomyelitis due to *Staphylococcus aureus*	Male, Sprague-Dawley	380 g	2 weeks	*Staphylococcus aureus* 52/52A/80, 0.05 ml of 3×10^8 CFU/ml	Injection into intramedullary canal	Drill defect into tibial metaphysis, application of sclerosing agent, sealed with bone wax	PET, pQCT, microbiology, histology, radiology
Bisland et al. (13)	Pre-clinical *in vitro* and *in vivo* studies to examine the potential use of photodynamic therapy in the treatment of osteomyelitis	Female, Sprague-Dawley	250–300 g	At least 14 days	*Staphylococcus aureus* Xen29, 10^6 CFU/ml	*Via* biofilm coating on K-wire	Bilateral defects to tibial metaphyses with medullary cavity exposure. K-wire inserted into medullary cavity. Sclerosing agent applied shortly after. Sealed with bone wax	Fluoroscopy, BLI
Aktekin et al. (17)	A different perspective for radiological evaluation of experimental osteomyelitis	Female, Wistar albino	6 months, 250 g	3 and 6 weeks	*Staphylococcus aureus* ATCC 25923, 10^5 CFU/0.05 ml	Injection into intramedullary canal	Tibial intramedullary aperture by 19G needle and application of sclerosing agent. Sealed with bone wax	Radiographs, CT, DEXA scans
Ofluoglu et al. (92)	Implant-related infection model in rat spine	Male, Sprague-Dawley	6 months, 300–350 g	15 days	*Staphylococcus aureus*, 10 μl of 10^2, 10^3, or 10^6 CFU	Injection into surgical site	Reaming of junction between vertebral lamina and facet joint, placement of titanium microscrew.	Microbiology, histology

(Continued)

TABLE 1 | Continued

Reference	Title	Sex, strain	Age, weight	Study endpoint(s)	Bacterial strain, inoculum size and volume	Inoculation method	Brief description of procedure	Evaluation methods
Robinson et al. (84)	Development of a Fracture osteomyelitis model in the rat femur	Male, Sprague-Dawley	250–300 g	3 weeks	*Staphylococcus aureus* (clinical isolate), 10^4 CFU/50 μl	Injection into intramedullary canal	Defect to distal femur with medullary exposure. Stainless steel pin insertion. Sealed with bone wax	Radiographs, microbiology, histology
Vergidis et al. (98)	Treatment with linezolid or vancomycin in combination with rifampin is effective in an animal model of methicillin-resistant *Staphylococcus aureus* foreign body osteomyelitis	Male, Wistar	215–475 g	7 weeks	MRSA (clinical isolate IDRL 6169), 50 μl of 5×10^5 CFU/ml	Injection into intramedullary canal	Drill defect into tibial metaphysis with medullary cavity exposure. Placement of wire into canal. Sealed with dental gypsum	Microbiology
Hamza et al. (10)	Intra-cellular *Staphylococcus aureus* alone causes infection *in vivo*	Male, Sprague-Dawley	400–450 g	3 weeks	*Staphylococcus aureus* ATCC 25923, 5×10^8 CFU/ml	*Via* inclusion into osteoblasts (UMR-106) and application to fracture site, or osteoblast preparation with extracellular *Staphylococcus aureus* inoculum applied to fracture site	Mid-shaft femoral fracture created *via* custom device. Fracture stabilized with K-wire	Blood analyses, radiographs, microbiology
Sanchez et al. (85)	Effects of local delivery of D-amino acids from biofilm-dispersive scaffolds on infection in contaminated rat segmental defects	Sprague-Dawley	N/A	2 weeks	*Staphylococcus aureus* UAMS-1 and Xen36, 10^2 CFU	*Via* soaked type I bovine collagen	6 mm segmental femoral defect, stabilized with polyacetyl plate and K-wires	Microbiology
Søe et al. (93)	A novel knee prosthesis model of implant-related osteomyelitis in rats	Male, Sprague-Dawley	6–9 weeks, 300 g	42 days	*Staphylococcus aureus* MN8 and UAMS-1, 10 μl of 10^{2-5} CFU	Injection into intramedullary canals	Non-constrained knee prosthesis	Radiographs, microbiology, histology, biochemical analysis
Fölsch et al. (86)	Coating with a novel gentamicinpalmitate formulation prevents implant-associated osteomyelitis induced by methicillin-susceptible *Staphylococcus aureus* in a rat model	Male, Sprague-Dawley	5 months	42 days	*Staphylococcus aureus* subsp. *aureus Rosenbach*, 10^2 CFU	Injection into intramedullary canal	Reaming of femoral intramedullary cavity *via* a stifle approach. Placement of K-wire	Blood analyses, radiographs, microbiology

(Continued)

TABLE 1 | Continued

Reference	Title	Sex, strain	Age, weight	Study endpoint(s)	Bacterial strain, inoculum size and volume	Inoculation method	Brief description of procedure	Evaluation methods
Stadelmann et al. (99)	*In vivo* microCT monitoring of osteomyelitis in a rat model	Female, Wistar	15 weeks, 276 g	28 days	*Staphylococcus aureus* (clinical isolate JAR 06.01.31), 3.3×10^7 CFU/ml	*Via* soaking of experimental implant	Drill defect into tibial metaphysis. Placement of experimental implant	*In vivo* microCT, histology, microbiology
Vergidis et al. (100)	Comparative activities of vancomycin, tigecycline and rifampin in a rat model of methicillin-resistant *Staphylococcus aureus* osteomyelitis	Male, Wistar	250–350 g	7 and 9 weeks	MRSA (clinical isolate IDRL-6169), 5×10^5 CFU/ml	Injection into intramedullary canal	Drill defect into tibial metaphysis with medullary cavity exposure. Placement of wire into canal. Sealed with dental gypsum	Microbiology
Avdeeva et al. (101)	Experimental simulation of traumatic osteomyelitis in rats	Male, Albino	200–250 g	21 days	*Staphylococcus aureus*	Injection into intramedullary canal	Defect to distal femoral metaphysis with thick needle	Blood analyses, histology
Fölsch et al. (102)	Systemic antibiotic therapy does not significantly improve outcome in a rat model of implant-associated osteomyelitis induced by Methicillin susceptible *Staphylococcus aureus*	Male, Sprague-Dawley	5 months	42 days	*Staphylococcus aureus* subsp. *aureus Rosenbach*, 10^2 CFU	Injection into intramedullary canal	Reaming of femoral intramedullary cavity *via* a stifle approach. Placement of K-wire	Blood analyses, radiographs, microbiology
Harrasser et al. (82)	A new model of implant-related osteomyelitis in the metaphysis of rat tibiae	Male, Wistar	5 months, 350–400 g	42 days	*Staphylococcus aureus* ATCC 25923, 10^2 or 10^3 CFU/10 µl	Injection into intramedullary canal	Unicortical tibial metaphyseal defect with placement of experimental implant	Radiographs, microbiology, histology
Oh et al. (88)	Antibiotic-eluting hydrophilized PMMA bone cement with prolonged bactericidal effect for the treatment of osteomyelitis	Sprague-Dawley	250–300 g	4 and 8 weeks	*Staphylococcus aureus* (clinical isolate KCTC1621) 100 µl of 10^4 CFU/ml	Injection into intramedullary canal	Defect to distal femur with medullary exposure. Sealed with bone wax	MicroCT, blood analysis
Park et al. (103)	Activity of tedizolid in methicillin-resistant *Staphylococcus aureus* experimental foreign body-associated osteomyelitis	Male, Wistar	250–350 g	7 weeks	MRSA (clinical isolate IDRL-6169), 50 µl of 10^6 CFU/ml	Injection into intramedullary canal	Drill defect into tibial metaphysis with medullary cavity exposure. Placement of wire into canal. Sealed with dental gypsum	Microbiology
Hassani Besheli et al. (80)	Sustainable release of vancomycin from silk fibroin nanoparticles for treating severe bone infection in rat tibia osteomyelitis model	Male, Wistar	260–330 g	3 weeks	MRSA, ATCC 43300, 40 µl of 1–2 $\times 10^8$ CFU/ml	Injection into intramedullary canal	Burr defect into tibial metaphysis, placement of K-wire	Blood analysis, histology

(Continued)

TABLE 1 | Continued

Reference	Title	Sex, strain	Age, weight	Study endpoint(s)	Bacterial strain, inoculum size and volume	Inoculation method	Brief description of procedure	Evaluation methods
Cui et al. (104)	Masquelet induced membrane technique for treatment of rat chronic osteomyelitis	Male, Sprague-Dawley	8 week, 190–220 g	20 weeks	*Staphylococcus aureus*, 0.3 ml	Injection into intramedullary canal	Modified blunt trauma method (101)	Blood analyses
Kussman et al. (105)	Dalbavancin for treatment of implant-related methicillin-resistant *Staphylococcus aureus* osteomyelitis in an experimental rat model	Male, Sprague-Dawley	260–330 g	3 weeks	MRSA ATCC 43300, 40 µl of 1–2 × 10^8 CFU/ml	Injection into intramedullary canal	Burr defect into tibial metaphysis, placement of K-wire	Blood analysis, histology
Melicherčík et al. (89)	Testing the efficacy of antimicrobial peptides in the topical treatment of induced osteomyelitis in rats	Male, Wistar	250 g	17 days	*Staphylococcus aureus* CNCTC 6271 (ATCC 43300; MRSA). 100 µl of 10^8 CFU/ml	Injection into intramedullary canal	Reaming of femoral intramedullary cavity *via* a stifle approach	Radiographs
Neyisci et al. (83)	Treatment of implant-related methicillin- resistant *Staphylococcus aureus* osteomyelitis with vancomycin-loaded VK100 silicone cement: An experimental study in rats	Female, Sprague-Dawley	18–20 weeks	4 weeks	MRSA N315 (NBCI Taxonomy ID: 158879), 10^8 CFU/ml	Injection into intramedullary canal	Reaming of tibial intramedullary canal with K-wire. Insertion of needle into canal. Sealed with bone wax. Implant removal at 2 weeks	Radiographs, microbiology, histology
Cobb et al. (106)	CRISPR-Cas9 modified bacteriophage for treatment of *Staphylococcus aureus* induced osteomyelitis and soft tissue infection	Female, Sprague-Dawley	13 weeks	8 days	*Staphylococcus aureus* ATCC 6538-GFP	*Via* soaked implant. Avg CFU: 5 × 10^4	Bicortical drill defect to mid-femoral diaphysis. Placement of contaminated screws	Radiographs with fluorescent overlays, microbiology, histology, SEM
Jung et al. (87)	*In situ* gelling hydrogel with anti-bacterial activity and bone healing property for treatment of osteomyelitis	Sprague-Dawley	N/A	3 and 6 weeks	*Staphylococcus aureus*, 100 µl of 10^4 CFU/ml	Injection into intramedullary canal	Defect to distal femur with medullary exposure. Sealed with bone wax	MicroCT, microbiology
Wu et al. (107)	Virulence of methicillin-resistant *Staphylococcus aureus* modulated by the YycFG two-component pathway in a rat model of osteomyelitis	Female, Sprague-Dawley	260–280 g	4 weeks	MRSA (clinical strain) and ASyycG over-expression MRSA clinical strain (ASyycG mutant). 40 µl of mid-exponential phase	Injection into intramedullary canal	Drill defect to antero-medial tibia with medullary cavity exposure	*In vivo* microCT, histology, SEM, rtPCR
Zhou et al. (108)	The synergistic therapeutic efficacy of vancomycin and omega-3 fatty acids T alleviates *Staphylococcus aureus*-induced osteomyelitis in rats	Male, Albino	180–200 g	At least 7 days	MRSA 1 × 10^6 CFU/ml	Injection into intramedullary canal	Defect to tibial metaphysis, with medullary exposure, *via* dental burr. Reaming of medullary cavity with K-wire	Biochemical markers, histology, microbiology

(Continued)

TABLE 1 | Continued

Reference	Title	Sex, strain	Age, weight	Study endpoint(s)	Bacterial strain, inoculum size and volume	Inoculation method	Brief description of procedure	Evaluation methods
Deng et al. (109)	Extracellular Vesicles: A potential biomarker for quick identification of infectious osteomyelitis	Male, Wistar	8–10 weeks, 300–350 g	At least 3 days	*Staphylococcus aureus, Staphylococcus epidermidis, Pseudomonas aeruginosa*, and *Escherichia coli* (clinical isolates), 100 μl of 10^8 CFU/ml	Injection into intramedullary canal	Defect to tibial metaphysis, with medullary exposure, *via* needle. Needle tip indwelling within medullary canal. Sealed with bone wax	Serum extracellular vesicles
Sahukhal et al. (110)	The role of the msaABCR operon in implant-associated chronic osteomyelitis in *Staphylococcus aureus* USA300 LAC	Sprague-Dawley	250–300 g	4, 8 and 15 days	*Staphylococcus aureus* USA300 LAC, msaABCR mutant, and msaABCR complementation	*Via* biofilm coating on K-wire. Avg. CFU: 6.09 × 10^5	K-wire pin insertion into tibial metaphysis	MicroCT, microbiology, histology, cytokine analysis
Qu et al. (90)	Zinc alloy-based bone internal fixation screw with antibacterial and anti-osteolytic properties	Male, Sprague-Dawley	3 months	3 and 6 weeks	MRSA ATCC 43300, 10^7 CFU	*Via* soaked experimental implant	Defect between distal femoral condyles with medullary exposure. Contaminated implant placed. Sealed with bone wax.	Radiographs, microbiology, histology, blood analyses,
Sodnomi-Ish et al. (91)	Decompression effects on bone healing in rat mandible osteomyelitis	Male, Sprague-Dawley	8 week, 230 g	4 weeks	*Staphylococcus aureus* ATCC 29213, 20 μl of 10^7 CFU/ml	Injection into defect	4 mm defect to mandibular ramus, sealed with fibrin glue	MicroCT, histology, immunohisto chemistry, blood analyses

Asterisks denote papers deemed by the authors to be seminal to rat osteomyelitis modeling.

Insights Into Pathogenesis

Similar to murine models, rat models can be utilized for investigations into pathogenesis. Rat models have facilitated valuable discoveries, including investigations of virulence factors associated with *S. aureus* biofilms and the ability of *S. aureus* to function as an intracellular pathogen. Biofilms are well recognized as a source of recalcitrant bacteria that can impair antibiotic treatment of osteomyelitis and cause persistent or recurrent osteomyelitis, particularly when orthopedic implants are in place (13, 31, 111). Two studies that have pursued the *in vivo* investigation of biofilm virulence factors and genetic components in rats include the investigation by Wu et al. (107), which demonstrated that overexpression of AS*yycG* led to a reduction in biofilm formation and *in vivo* pathogenicity of MRSA in a model of rat tibial osteomyelitis; as well as the investigation by Sahukhal et al. (110) who utilized a model of implant-associated osteomyelitis. This investigation demonstrated that deletion of the *msaABCR* operon of *S. aureus* (USA300 LAC) resulted in defective biofilm production and reduced severity of bacterial osteomyelitis. The capability of *S. aureus* to function as an intracellular pathogen is considered to be a mechanism of immune system evasion and a source of recurrent, persistent osteomyelitis (31) and is supported by *in vitro* evidence (112, 113). Based on that *in vitro* evidence, Hamza et al. investigated and confirmed the ability of purely intracellular *S. aureus* to induce osteomyelitis in a rat model (10).

Improvements in Diagnostic Capabilities

Similar to murine models, rat models have allowed for improvements in diagnostic or longitudinal monitoring capabilities in experimental models. Examples of these improvements include the findings of Stadelmann et al. (99), who demonstrated the use of *in vivo* microCT to longitudinally monitor bacterial osteomyelitis in a rat tibial model, thus offering a method to limit numbers of animals needed for experiments and to add strength to collected data. Also, Aktekin et al. evaluated the utility of available scoring systems for the radiographic evaluation of experimental osteomyelitis. Authors utilized a tibial model of osteomyelitis and evaluated serial radiographs throughout their study period, ultimately concluding that it is best to evaluate and report each radiograph individually, rather than appointing a numerical grade from a previously published grading scale (17). This is a valuable report for experimental studies, and with appropriate radiographic interpretation, is likely to add strength to radiograph assessments. An improvement to *in vivo* studies that holds potential to translate into human medicine is the investigation into various tracers for positron emission tomography (PET) to successfully image osteomyelitis and differentiate between bone infection and bone healing (51). The work investigating PET tracers indicated that Gallium-68 (^{68}Ga), did not accumulate in healing bone, only infected bone. This work brings interest to the use of ^{68}Ga and PET for clinical patients, although further work is needed to clarify use and safety concerns. Another interesting foray into improving diagnostics for clinical patients was completed by Deng et al. who described the potential use of extracellular vesicles (EVs) as a diagnostic marker for acute osteomyelitis (109).

Investigations Into Therapeutic Strategies

Rats are recognized to be more resilient than mice and therefore are well suited to investigations into therapeutic strategies, such as antibiotic trials. Indeed, there are many investigations into antibiotic therapies. These include therapeutic efficacy assessments of systemic antibiotics administered solo or in combination (98, 100, 103, 105), investigations of local antibiotic delivery systems (80, 83, 88) and antibiotics in combination with alternative therapies such as omega-3 fatty acid supplementation (108). There also are investigations into novel therapeutic strategies such as the use of photodynamic therapy (PDT) to treat contaminated orthopedic implants and minimize reliance on antibiotic therapy to clear implant associated bacterial osteomyelitis (13). Recently, Cobb et al. (106) investigated the feasibility of utilizing a bacteriophage to mitigate bacterial osteomyelitis, biofilm, and soft tissue infection.

Conclusion

Rat models are a valuable animal resource in the study of osteomyelitis. They provide similar benefits to mice, including small size, economics, ease of housing and handling, and well-characterized strains that provide appropriate uniformity and enable study of disease pathophysiology relevant to that seen in people (97). Rats have the ability to tolerate sustained, high dose antibiotic therapy (97). While larger than mice, rats remain too small for assessment of orthopedic hardware for human use, and multi-step revision procedures, although not impossible, remain challenging. Uniquely, the rat is one of few ideal species for modeling of mandibular osteomyelitis (91, 95) because of their size, anatomy, and general hardiness. Therefore, the strength of rat models lies within the ability to investigate pathogenesis and pursue initial investigations into therapeutic strategies to further understand *in vitro* data and gain *in vivo* knowledge prior to utilizing a larger animal model.

Rabbit Models

Model Development

Rabbits provide many useful and reliable models of bacterial osteomyelitis. The systematic review by Reizner et al. (78) details significant historical developments and the review by Bottagisio et al. provides a thorough overview of model development and utility (114). Historically and currently, the most utilized models are long bone models, including tibial (115–121), femoral (49, 122–124), and radial (125–129). Alternative models such as joint prostheses (130, 131), mandibular defects (132), vertebral models (133–136) and implant infection *via* hematogenous seeding (137) exist. Induction of osteomyelitis among these various models can be accomplished *via* mechanical trauma, either defect (117) or fracture (49) creation and bacterial contamination with or without application of a sclerosing agent or foreign body placement (115), or through placement of contaminated implants (49, 129). Bone wax may be used to seal defect areas and prevent bacterial leakage and concomitant soft tissue infection (116). A benefit of rabbits compared to smaller models such as mice and

rats is the improved ability to model chronic osteomyelitis (138) and perform revision procedures such as debridement (23, 116), which improves the capabilities of modeling human osteomyelitis and therapy. Rabbits offer a distinct advantage in studying bone disease because full segmental defects of the radius can be created without the need to stabilize the bone using orthopedic implants.

Insights Into Pathogenesis

Majority of reports into pathogenesis utilize well-characterized and reproducible rabbit models and are related to the capabilities of various bacterial species and strains (117, 121, 128) to induce osteomyelitis, as opposed to mechanistic work that more often is performed in murine and rat models. For example, Gahukamble et al. (117) describe an investigation into the abilities of *Staphylococcus lugdunensis* (*S. lugdunensis*) and *Propionibacterium acnes* (*P. acnes*) to establish osteomyelitis in a model that was previously characterized with a strain of *S. aureus* isolated from an infected human hip prosthesis (139). Results indicated that both organisms could induce osteomyelitis and described varying severity and clinical presentation. This work again emphasizes the importance of considering model development and bacterial strain selection during experimental design.

Improvements in Diagnostic Capabilities

Similar to murine and rodent models, there are studies aimed to improve the longitudinal monitoring of experimental osteomyelitis in rabbit models (21, 115) to improve utility of animal modeling and reduce required animal numbers. Odekerken et al., demonstrated that ^{18}F-FDG micro-PET is a sensitive diagnostic tool for detecting early bone pathology, including early osteomyelitis (21), even in the presence of titanium implants (118). This method of imaging could differentiate between aseptic and infected bone as early as three weeks post-operatively and post-infection. Authors suggest that ^{18}F-FDG PET carries potential as an early detector of clinical osteomyelitis cases, which is further confirmed by a retrospective analysis of clinical osteomyelitis cases performed by Wenter et al. (140). An important investigation geared toward improving available diagnostics was performed in a rabbit model of chronic osteomyelitis. In this study, the capability of PCR to return positive results was compared with traditional osteomyelitis diagnosis *via* radiographs and bacterial cultures of bone biopsies taken *via* different methods. Results indicated that PCR was a sensitive diagnostic tool and described techniques to determine species identification (23). It deserves recognition that while PCR is a strong tool to detect low bacterial burdens or metabolically inactive bacteria that may not yield positive bacterial culture, PCR results will not provide antibiotic susceptibility data. The described PCR techniques are useful for experimental models and also offer utility for clinical cases.

Investigations Into Therapeutic Strategies

Rabbits are widely utilized to test therapeutic strategies for the clearance of bacterial osteomyelitis. Rabbits are hindgut fermenters, which means that they may process oral antibiotics differently than humans (64). Nonetheless, rabbits have been widely utilized for evaluation of systemic and locally delivered antibiotic therapies (114, 123, 141). Rabbits also are a useful modeling system for evaluation of antibacterial coatings upon implants and local drug delivery systems (114, 129), as demonstrated by the use of silver ion doped calcium phosphate beads (120). There have also been investigations into alternative therapies for osteomyelitis, including the work performed by Kishor et al., investigating the use of bacteriophages to clear chronic osteomyelitis (142). In this study, *S. aureus* specific phages were purified, characterized, and utilized as a therapeutic in a model of acute and chronic femoral osteomyelitis. High doses of phage cocktail were found to be effective to clear *S. aureus* infection. This work presents an intriguing consideration for specific therapy of bacterial osteomyelitis. Another interesting study investigated the use of locally applied ozonated oxygen in a rabbit femoral model. While this treatment did not eliminate osteomyelitis, it did seem to lessen the clinical and radiographic markers of disease (122).

Conclusion

Rabbits fill a unique niche in *in vivo* osteomyelitis research. They are often utilized when the research goal involves assessment of orthopedic hardware or locally applied therapeutics and a small animal is needed, whether that need is dictated by animal housing limitations or by stage of research development. Rabbits provide a more relevant size to evaluate some human orthopedic implants, as well as an appropriate size to be maintained long-term so that revision procedures can be performed. Rabbits also provide a more similar immune system and long bone density to humans than mice and rats provide (143, 144). Despite these benefits, rabbit models are accompanied by more complex challenges including respiratory depression under anesthesia, hindgut fermentation, which impacts the ability to assess oral antibiotic therapies, and variation in bone healing response of young rabbits compared to humans. Most rabbit modeling should be performed in mature rabbits to maximize translation of results to clinical patients.

LARGE ANIMAL MODELS

Pig Models

Model Development

Pigs are not as widely utilized to model bacterial osteomyelitis, but the models that are available are effective, well-characterized, and have seen logical progression. Studies may utilize either mini-pigs or commercial pigs. Perhaps the most widely utilized model of porcine osteomyelitis is a hematogenous model (56, 145–149). Alternative models include mandibular osteomyelitis (46, 150), tibial implant-related osteomyelitis (151–154), and traumatic tibial osteomyelitis (155). When the hematogenous model of osteomyelitis was initially introduced, an inoculum of *S. aureus* (S54F9) was administered IV through a lateral ear vein without any additional trauma. This IV inoculation resulted in acute, suppurative pneumonic and osteomyelitic lesions. Lesions of osteomyelitis were found primarily in the long bones, but also in the costochondral junctions of ribs (147). This model has been modified and is most frequently used by administering bacterial

inoculums into the femoral artery (145, 146, 148, 149). Femoral artery inoculation is reliable in inducing osteomyelitis localized to the injected limb. This technique may produce concurrent soft tissue infections, injection site abscesses, and the degree of disease during the study may be variable (148, 156). However, this remains a strong technique for modeling acute hematogenous (juvenile) osteomyelitis.

Insights Into Pathogenesis

Pigs have not been utilized as widely as mice and rats to investigate pathogenesis of osteomyelitis, but there are a few interesting reports. One such study was carried out in a hematogenous model of osteomyelitis to determine the infection potential and disease characterization of three different strains of *S. aureus* (56). This work compared the typically utilized strain of porcine *S. aureus* (SF549) with two human strains of *S. aureus* (UAMS-1 and NCTC-8325-4). Results indicated that UAMS-1 and NCTC-8325-4 were less successful in establishing osteomyelitis than the porcine specific strain. Authors hypothesize that this may be due to increased host specificity, in contrast to rodent models, and that inoculation dose may play a role, which again brings attention to the importance of model and bacterial strain selection during experimental design. Additionally, an interesting discovery of biofilm within bone lesions shortly after infection was made and raises the concern that biofilms may form quite early on in disease. Jødal et al. investigated blood perfusion using [^{15}O]water PET, and confirmed their hypothesis that blood perfusion would be increased in osteomyelitis-diseased bone as compared to healthy bone. While blood perfusion was increased in diseased bone as compared to healthy bone, blood perfusion was four-fold greater in areas of soft tissue infection than diseased bone (156).

Improvements in Diagnostic Capabilities

Afzelius et al. (149, 157) have made multiple investigations involving ideal tracing agents for diagnosing osteomyelitis. They investigated the use of more specific radiotracers, including: ^{68}Ga-labeled DOTA-K-A9, DOTA-GSGK-A11, [^{18}F]NaF, [^{68}Ga]Ga Ubiquicidin, and [^{68}Ga]Ga-DOTA-Siglec-9, and compared them to the use of [^{18}F]FDG. This study demonstrated no accumulation of the more specific radiotracers, but positive accumulation of [^{18}F]FDG (149). Investigators also compared [^{99m}Tc]Interleukin-8 (IL-8) scintigraphy with [^{18}F]FDG PET/CT in a hematogenous porcine model of osteomyelitis and found that [^{99m}Tc]IL-8 was simple to prepare and use, and that it was capable of detecting 70% of lesions compared with 100% sensitivity of [^{18}F]FDG PET/CT. This makes [^{99m}Tc]IL-8 scintigraphy a promising candidate for further investigation for use in children, to decrease the radiation exposure, as compared to utilizing [^{18}F]FDG PET/CT (157). Another interesting study was performed by Lüthje et al., who investigated the regulation of various acute phase proteins during osteomyelitis and found a significant pro-inflammatory local response to osteomyelitis, with limited systemic response. These findings confirm that osteomyelitis remains challenging to diagnose based on systemic findings and adds to the understanding that local investigation is necessary (153).

Investigations Into Therapeutic Strategies

Most porcine studies thus far have been accomplishing model development, pharmacokinetic work (152) and diagnostic methods. There is even one investigation into bone regeneration techniques in the face of osteomyelitis (46). Hill et al. (155) completed a study utilizing tibial implant-associated osteomyelitis and found that they could prevent osteomyelitis by administering combination antibiotic therapy every 6 h for 7 days. Jensen et al. (154) comment that pigs provide an ideal model for investigation into implant surface coatings, medical and surgical treatment regimes, and vaccination against *S. aureus*.

Conclusion

Pigs, particularly mini-pigs, offer many benefits, including size that is appropriate for complex or multi-stage procedures and for assessments of orthopedic hardware for human use. Porcine bone possesses similar fracture stress to human bone (158), hematogenous modeling creates a very similar situation to juvenile hematogenous osteomyelitis, and the gastrointestinal system of pigs is appropriate to receive oral antibiotics. There are many challenges when using pig models, including rapid growth and excessive mature body weight when utilizing commercial pigs (159), shorter long bones than found in people (154), the greater expense associated with a large animal model, variation in degree of disease manifestation, as well as a generally fractious demeanor. Porcine models are not currently as widely utilized as small animal models of osteomyelitis but provide an ideal model for the study of hematogenous osteomyelitis, offer great capabilities into investigation of imaging techniques, and are an area of interest for further development in the modeling of osteomyelitis. In general, commercial pigs are suitable for proof of concept and model development work, as they are less expensive than mini-pigs, but for longer-term studies and more appropriate translational work, mini-pigs should be utilized.

Sheep Models

Model Development

Kaarsemaker et al. (160) initiated development of ovine models of osteomyelitis *via* creation of a tibial defect and subsequent bacterial inoculum injection into the medullary cavity of adult sheep. This study provided valuable information, including the ability to establish osteomyelitis in sheep and also the requirement for peri-operative systemic antibiotics to lessen the risk of fatal sepsis. Since then, a variety of long bone models have been developed, focused on the tibia (161, 162) or the femur (163), and often involving hardware infected with biofilm or planktonic bacteria (164) with or without revision procedures (162, 165). There remain a variety of techniques of creating bone injury, from unicortical defects and medullary canal inoculation (165) to osteotomies stabilized with experimental hardware (166). Recently, Moriarty et al. (162) established a model to replicate a failed two-stage revision procedure utilizing a MRSA infected intramedullary nail. This will likely be a valuable model to evaluate therapeutic strategies moving forward.

Investigations Into Therapeutic Strategies

Most investigations into therapeutics in ovine models have been centered upon experimental implants, systemic or local antibiotic therapies, and the ability to replicate the multi-stage revision procedures utilized in human medicine. There have been multiple investigations into local drug delivery devices to clear osteomyelitis. Boot et al. performed a multi-stage revision procedure and compared an injectable hydrogel impregnated with gentamicin and vancomycin to an antibiotic-loaded bone cement impregnated with gentamicin and vancomycin. Investigators were able to clear significantly more cases of osteomyelitis in the experimental hydrogel group, compared to the bone cement group, thereby presenting this material as a promising candidate for further exploration (165). Stewart et al. investigated another concept in local drug delivery by creating a vancomycin-modified titanium plate that demonstrated decreased clinical signs of infection, prevented biofilm formation and promoted bone healing in an infected tibial osteotomy model (166).

Conclusion

Currently, sheep are most often utilized for investigations into therapeutics utilizing long bone models. As such, sections regarding pathogenesis and diagnostic innovations were not included. Regardless, sheep are a valuable animal resource for the modeling of bacterial osteomyelitis, particularly focused on long bones. Sheep provide an ideal long bone size to perform complex procedures, replicate the treatment strategies utilized in clinical cases such as multiple revision procedures, and assess orthopedic hardware and devices for human use. Many characteristics of ovine bone are similar to that of humans, including torsional stiffness and osteogenesis (64), which adds to the strength of ovine modeling. Challenges associated with ovine modeling include the risk of sepsis, which may require peri-operative antibiotics, as well as the cost of housing and maintaining a large animal.

Goat Models

Model Development

Most caprine models of osteomyelitis utilize the tibia, although models have variable approaches. Salgado et al. described a unicortical tibial defect with concurrent application of a sclerosing agent. *Staphylococcus aureus* was inoculated into the medullary canal and the defect was sealed with bone wax. In this model, goats received a perioperative dose of IV antibiotics. Induction of osteomyelitis was successful and no goats suffered from fatal sepsis (167). In an adaptation of this model, the sclerosing agent and perioperative antibiotics were omitted, and osteomyelitis was successfully induced, again with no reported sepsis (168). Other tibial models include the internal fixation of a tibial osteotomy (169) and percutaneous pin placement throughout the tibia (170). Through these investigations, researchers have also proposed histology scoring systems, to aid in the evaluation of model development (169).

Investigations Into Therapeutic Strategies

Similar to sheep, goats serve as viable translational models for investigations into therapeutic strategies. Wenke et al. utilized a similar model to that of Salgado et al. to investigate the efficacy of tobramycin-loaded calcium sulfate pellets compared to the efficacy of tobramycin-loaded antibiotic beads to treat bacterial osteomyelitis. Calcium sulfate and bone cement formulations loaded with tobramycin performed well, raising interest into the use of calcium sulfates for local drug delivery, as they do not require an additional procedure for removal (168). Tran et al. (169) investigated a silver-based antibacterial coating on intramedullary nails. In an experiment utilizing two goats, the goat that received the experimental implant displayed less severe signs of osteomyelitis than the control goat. An interesting experiment was performed to investigate the utility of a directly applied electric current to eliminate osteomyelitis over the course of 3 weeks. Authors found that electric currents were able to prevent signs of infection and suggest that this would be effective in clinical situations (170). Salgado et al. also reported an investigation of muscle vs. non-muscle flaps for reconstruction of defects and effective clearance of osteomyelitis. This study was designed as a result of discrepancies in the literature, with some reports of muscle flaps being superior and vice versa. This study found no difference between muscle and non-muscle flaps and re-emphasized that the most critical factor in treatment of bacterial osteomyelitis is thorough debridement (38).

Conclusion

Similar to sheep, goats possess great utility in modeling bacterial osteomyelitis, and this utility lies primarily within the size and composition of the caprine long bones, specifically the tibia. Long bone size and composition makes goats ideal for complex procedures and multi-stage surgeries. Goats provide an excellent model for assessment of orthopedic hardware intended for human use, as well as examination of local drug delivery devices and experimental coatings. Goats have not suffered from the reported sepsis that affected sheep when receiving intramedullary bacterial inoculation, which may aid researchers when selecting either sheep or goats as a model. Similar to any large animal model, goats are accompanied by greater costs than small animal models. As the majority of caprine modeling has been performed to either establish a reliable model or assess treatment options, the sections for pathogenesis and diagnostic investigations were omitted.

Dog Models

Model Development

Canine models have been used in the past to model osteomyelitis, although today they are not widely utilized. Similar to caprine and ovine models, canine models have primarily utilized long bones, specifically the tibia (53, 171, 172) and the femur (47, 173, 174), although a vertebral model has also been described (175). Models vary in approach. Deysine et al. described an injection of bacterial inoculum into the tibial nutrient artery without any additional trauma. This approach was effective in establishing osteomyelitis, but also resulted in the loss of three dogs from septicemia (53). Most other models report bone trauma and

bacterial inoculation of the medullary canal, whether that is by direct inoculation or placement of an infected implant (47, 171, 174). Khodaparast et al. had success in establishing osteomyelitis *via* application of a penetrating captive bolt device to the tibia of dogs to create an open fracture. This approach was selected in order to mimic traumatic osteomyelitis. This model involved the placement of microdialysis probes for sample collection, which is a valuable tool (172) when investigating the dynamics of local environments, whether that is physiologic dynamics or drug delivery profiles.

Investigations Into Pathogenesis

As described above, Khodaparast et al. (172) established a tibial fracture model of canine osteomyelitis and placed microdialysis probes with the goal of exploring the role of vascular endothelial growth factor (VEGF) as a rate-limiting step in wound healing. This was investigated by measuring VEGF mRNA levels in response to *S. aureus* osteomyelitis and *S. aureus* osteomyelitis treated with a rotational gastrocnemius muscle flap. The muscle flap was investigated because wound healing is accelerated in the presence of well-vascularized tissue. VEGF mRNA levels were found to be greater in the animals with osteomyelitis that received the rotational muscle flap as compared to those who did not. This finding suggests that type of surgical closure impacts specific biological signals and cellular pathways, and may add strength to the recommendation for utilizing muscle flaps for improved wound healing in reconstructive surgeries. Another investigation into pathogenesis was performed by Chen et al. (175) who aimed to investigate the presence, type, and origin of bacteria adjacent to metal implants utilized in the surgical management of pyogenic vertebral osteomyelitis. Investigators found that bacteria were retrieved not only from metal implants, but also from surrounding bone, despite the lack of radiographic signs of infection. These findings suggest that metallic implants are not necessarily the source of persistent or recurrent bacterial infection in vertebral osteomyelitis.

Investigations Into Therapeutic Strategies

Despite there being few reports, there are canine models of osteomyelitis that investigate treatment strategies. Two models focused on the prevention of osteomyelitis, and found that the placement of gentamicin impregnated bone cement could prevent the development of osteomyelitis in the experimental models (171, 173). Similarly, Huneault et al. (174) investigated the ability of cross-linked high amylose starch (CLHAS) implants loaded with ciprofloxacin to prevent and cure chronic femoral osteomyelitis. This study demonstrated strong preventative efficacy of the ciprofloxacin loaded implants, and also showed that ciprofloxacin loaded implants and oral ciprofloxacin had similar efficacy in clearing bacterial osteomyelitis.

Conclusion

Dogs provide strong models for long bone osteomyelitis. Benefits include appropriate size to perform complex and multi-stage procedures, bone composition and density that is most similar to humans out of the available species (158), temperament that is amenable to handling, as well as well-characterized anesthetic and imaging protocols. Despite these strengths, canine models are no longer frequently utilized for osteomyelitis research. Osteomyelitis research is terminal, and ethical concerns are raised when considering these companion animals as research models. Therefore, despite the provided benefits, it is unlikely that dogs will have a resurgence in popularity for osteomyelitis modeling.

CONCLUSIONS AND FUTURE DIRECTIONS

Through the currently available reports of advancements in the management and understanding of osteomyelitis that animal models have facilitated, it is clear that animal models are vital in osteomyelitis research. With the plethora of available species and approaches to model bacterial osteomyelitis, it is also clear that each species provides specific strengths and certain shortcomings, as is highlighted in this review. Based on current information, we suggest an approach where proof of concept work is performed in small mammal models, either a mouse or a rat model. Advanced pathogenesis investigations can also be carried out in small mammal models, either a mouse, rat, or rabbit model. Complex treatment strategies, whether local or systemic, are best suited for large animal models, either mini-pigs, sheep, or goats, to mimic the human response as closely as possible. Improvements to diagnostic procedures may be performed in a variety of models; initial investigations, especially into novel imaging techniques, are best suited for rodent models. Ideally, imaging techniques would be validated in large animal models before preclinical testing. Regardless of the specific indication and utility, the knowledge we gain from animal models of osteomyelitis is an essential asset to the understanding, diagnosis and treatment of bacterial osteomyelitis, and animal modeling is a crucial step toward improving the lives of patients suffering from this life-altering disease.

AUTHOR CONTRIBUTIONS

CB: conceptualization, writing, and editing. DA: conceptualization, editing, and supervision. All authors contributed to the article and approved the submitted version.

REFERENCES

1. Kavanagh N, Ryan E, Widaa A. *Staphylococcal* osteomyelitis: disease progression, treatment, challenges and future directions. *Clin Microbiol Rev.* (2018) 31. doi: 10.1128/CMR.00084-17
2. Conterno LO, Turchi MD. Antibiotics for treating chronic osteomyelitis in adults. *Cochrane Database Syst Rev.* (2013) CD004439. doi: 10.1002/14651858.CD004439.pub3
3. Garcia Del Pozo E, Collazos J, Carton JA, Camporro D, Asensi V. Factors predictive of relapse in adult bacterial osteomyelitis of

long bones. *BMC Infect Dis.* (2018) 18. doi: 10.1186/s12879-018-3550-6
4. Dinh P, Hutchinson BK, Zalavras C, Stevanovic MV. Reconstruction of osteomyelitis defects. *Semin Plast Surg.* (2009) 23:108–18. doi: 10.1055/s-0029-1214163
5. Fritz JM, McDonald JR. Osteomyelitis: approach to diagnosis and treatment. *Phys Sportsmed.* (2008) 36:nihpa116823. doi: 10.3810/psm.2008.12.11
6. Lew DP, Waldvogel FA. Osteomyelitis. *Lancet.* (2004) 364:369–79. doi: 10.1016/S0140-6736(04)16727-5
7. Calhoun JH, Manring MM, Shirtliff M. Osteomyelitis of the long bones. *Semin Plast Surg.* (2009) 23:59–72. doi: 10.1055/s-0029-1214158
8. Kremers HM, Nwojo ME, Ransom JE, Wood-Wentz CM, Melton LJ, Huddleston PM. Trends in the epidemiology of osteomyelitis. *J Bone Joint Surg.* (2015) 97:837–45. doi: 10.2106/JBJS.N.01350
9. Rubin RJ, Harrington CA, Poon A, Dietrich K, Greene JA, Moiduddin A. The economic impact of *Staphylococcus aureus* infection in new york city hospitals. *Emerg Infect Dis.* (1999) 5:9–17. doi: 10.3201/eid0501.990102
10. Hamza T, Dietz M, Pham D, Clovis N, Danley S, Li B. Intra-cellular *Staphylococcus aureus* alone causes infection *in vivo*. *Eur Cell Mater.* (2013) 25:341–50. Discussion: 50. doi: 10.22203/eCM.v025a24
11. Panteli M, Giannoudis PV. Chronic osteomyelitis: what the surgeon needs to know. *EFORT Open Rev.* (2016) 1:128–35. doi: 10.1302/2058-5241.1.000017
12. Zimmerli W. Clinical presentation and treatment of orthopaedic implant-associated infection. *J Intern Med.* (2014) 276:111–9. doi: 10.1111/joim.12233
13. Bisland SK, Chien C, Wilson BC, Burch S. Pre-clinical *in vitro* and *in vivo* studies to examine the potential use of photodynamic therapy in the treatment of osteomyelitis. *Photochem Photobiol Sci.* (2006) 5:31–8. doi: 10.1039/B507082A
14. Urish KL, Cassat JE. *Staphylococcus aureus* osteomyelitis: bone, bugs, and surgery. *Infect Immun.* (2020) 88:e00932-19. doi: 10.1128/IAI.00932-19
15. Gallie WE. First recurrence of osteomyelitis eighty years after infection. *J Bone Joint Surg Br.* (1951) 33:110–1. doi: 10.1302/0301-620X.33B1.110
16. Tiemann A, Hofmann GO, Krukemeyer MG, Krenn V, Langwald S. Histopathological Osteomyelitis Evaluation Score (HOES) – an innovative approach to histopathological diagnostics and scoring of osteomyelitis. *GMS Interdiscip Plast Reconstr Surg DGPW.* (2014) 3:Doc08. doi: 10.3205/iprs000049
17. Aktekin CN, Ozturk AM, Tabak AY, Altay M, Korkusuz F, A. Different perspective for radiological evaluation of experimental osteomyelitis. *Skeletal Radiol.* (2007) 36:945–50. doi: 10.1007/s00256-007-0342-2
18. Hatzenbuehler J, Pulling TJ. Diagnosis and management of osteomyelitis. *Am Fam Physician.* (2011) 84:1027–33.
19. Lima AL, Oliveira PR, Carvalho VC, Cimerman S, Savio E, Diretrizes Panamericanas para el Tratamiento de las Osteomielitis e Infecciones de Tejidos Blandos Group. Recommendations for the treatment of osteomyelitis. *Braz J Infect Dis.* (2014) 18:526–34. doi: 10.1016/j.bjid.2013.12.005
20. Trampuz A, Zimmerli W. Diagnosis and treatment of infections associated with fracture-fixation devices. *Injury.* (2006) 37(Suppl 2):S59–66. doi: 10.1016/j.injury.2006.04.010
21. Odekerken JC, Walenkamp GH, Brans BT, Welting TJ, Arts JJ. The longitudinal assessment of osteomyelitis development by molecular imaging in a rabbit model. *Biomed Res Int.* (2014) 2014:424652. doi: 10.1155/2014/424652
22. Lucke M, Schmidmaier G, Sadoni S, Wildemann B, Schiller R, Stemberger A, et al. A new model of implant-related osteomyelitis in rats. *J Biomed Mater Res B Appl Biomater.* (2003) 67:593–602. doi: 10.1002/jbm.b.10051
23. Mariani BD, Martin DS, Chen AF, Yagi H, Lin SS, Tuan RS. Polymerase chain reaction molecular diagnostic technology for monitoring chronic osteomyelitis. *J Exp Orthop.* (2014) 1:9. doi: 10.1186/s40634-014-0009-6
24. Darouiche R. Treatment of infections associated with surgical implants. *N Engl J Med.* (2004) 350:1422–9. doi: 10.1056/NEJMra035415
25. Ellington JK, Harris M, Hudson MC, Vishin S, Webb LX, Sherertz R. Intracellular *Staphylococcus aureus* and antibiotic resistance: implications for treatment of *Staphylococcal* osteomyelitis. *J Orthop Res.* (2006) 24:87–93. doi: 10.1002/jor.20003
26. Roblot F, Besnier JM, Juhel L, Vidal C, Ragot S, Bastides F, et al. Optimal duration of antibiotic therapy in vertebral osteomyelitis. *Semin Arthritis Rheum.* (2007) 36:269–77. doi: 10.1016/j.semarthrit.2006.09.004
27. Gomes D, Pereira M, Bettencourt AF. Osteomyelitis: an overview of antimicrobial therapy. *Braz J Pharm Sci.* (2013) 49:13–27. doi: 10.1590/S1984-82502013000100003
28. Cobb LH, McCabe EM, Priddy LB. Therapeutics and delivery vehicles for local treatment of osteomyelitis. *J Orthop Res.* (2020) 38:2091–103. doi: 10.1002/jor.24689
29. Sankaran J, Tan NJHJ, But KP, Cohen Y, Rice SA, Wohland T. Single microcolony diffusion analysis in *Pseudomonas aeruginosa* biofilms. *NPJ Biofilms Microbiomes.* (2019) 5:35. doi: 10.1038/s41522-019-0107-4
30. Masters EA, Trombetta RP, de Mesy Bentley KL, Boyce BF, Gill AL, Gill SR, et al. Evolving concepts in bone infection: redefining "biofilm", "acute vs. chronic osteomyelitis", "the immune proteome" and "local antibiotic therapy". *Bone Res.* (2019) 7:20. doi: 10.1038/s41413-019-0061-z
31. Muthukrishnan G, Masters EA, Daiss JL, Schwarz EM. Mechanisms of immune evasion and bone tissue colonization that make *Staphylococcus aureus* the primary pathogen in osteomyelitis. *Curr Osteoporos Rep.* (2019) 17:395–404. doi: 10.1007/s11914-019-00548-4
32. Savage VJ, Chopra I, O'Neill AJ. *Staphylococcus aureus* biofilms promote horizontal transfer of antibiotic resistance. *Antimicrob Agents Chemother.* (2013) 57:1968–70. doi: 10.1128/AAC.02008-12
33. Hall-Stoodley L, Costerton JW, Stoodley P. Bacterial biofilms: from the natural environment to infectious diseases. *Nat Rev Microbiol.* (2004) 2:95–108. doi: 10.1038/nrmicro821
34. Al-Mayahi M, Hemmady MV, Shoaib A, Morgan-Jones RL. Recurrence of chronic osteomyelitis in a regenerated fibula after 65 years. *Orthopedics.* (2007) 30:403–4. doi: 10.3928/01477447-20070501-12
35. Libraty DH, Patkar C, Torres B. *Staphylococcus aureus* reactivation osteomyelitis after 75 years. *N Engl J Med.* (2012) 366:481–2. doi: 10.1056/NEJMc1111493
36. O'Reilly T, Mader JT. Rat model of bacterial osteomyelitis of the tibia. In: Zak O, Sande MA, editors. *Handbook of Animal Models of Infection: Experimental Models in Antimicrobial Chemotherapy*. San Diego, CA: Academic Press. (1999), p. 561–75. doi: 10.1016/B978-012775390-4/50205-0
37. Ford CA, Cassat JE. Advances in the local and targeted delivery of anti-infective agents for management of osteomyelitis. *Expert Rev Anti Infect Ther.* (2017) 15:851–60. doi: 10.1080/14787210.2017.1372192
38. Salgado CJ, Mardini S, Jamali AA, Ortiz J, Gonzales R, Chen HC. Muscle versus nonmuscle flaps in the reconstruction of chronic osteomyelitis defects. *Plast Reconstr Surg.* (2006) 118:1401–11. doi: 10.1097/01.prs.0000239579.37760.92
39. Darouiche R. Device-associated infections: a macroproblem that starts with microadherence. *Healthc Epidemiol.* (2001) 33:1567–72. doi: 10.1086/323130
40. Zoller SD, Hegde V, Burke ZDC, Park HY, Ishmael CR, Blumstein GW, et al. Evading the host response: *Staphylococcus* "Hiding" in cortical bone canalicular system causes increased bacterial burden. *Bone Res.* (2020) 8:43. doi: 10.1038/s41413-020-00118-w
41. Zomer HD, Trentin AG. Skin wound healing in humans and mice: challenges in translational research. *J Dermatol Sci.* (2018) 90:3–12. doi: 10.1016/j.jdermsci.2017.12.009
42. Phang SJ, Arumugam B, Kuppusamy UR, Fauzi MB, Looi ML. A review of diabetic wound models-novel insights into diabetic foot ulcer. *J Tissue Eng Regen Med.* (2021) 15:1051–68. doi: 10.1002/term.3246
43. Mendes JJ, Leandro CI, Bonaparte DP, Pinto AL. A rat model of diabetic wound infection for the evaluation of topical antimicrobial therapies. *Comp Med.* (2012) 62:37–48.
44. Ortines RV, Liu H, Cheng LI, Cohen TS, Lawlor H, Gami A, et al. Neutralizing alpha-toxin accelerates healing of *Staphylococcus aureus*-infected wounds in nondiabetic and diabetic mice. *Antimicrob Agents Chemother.* (2018) 62:e02288-17. doi: 10.1128/AAC.02288-17
45. Mader JT. Animal models of osteomyelitis. *Am J Med.* (1985) 78:213–7. doi: 10.1016/0002-9343(85)90387-0
46. Hwang SC, Hwang DS, Kim HY, Kim MJ, Kang YH, Byun SH, et al. Development of bone regeneration strategies using human periosteum-derived osteoblasts and oxygen-releasing microparticles in mandibular

osteomyelitis model of miniature pig. *J Biomed Mater Res A*. (2019) 107:2183–94. doi: 10.1002/jbm.a.36728
47. Petty W, Spanier S, Shuster J, Silverthorne C. The influence of skeletal implants on incidence of infection experiments in a canine model. *J Bone Joint Surg.* (1985) 67:1236–44. doi: 10.2106/00004623-198567080-00015
48. Niska JA, Shahbazian JH, Ramos RI, Francis KP, Bernthal NM, Miller LS. Vancomycin-rifampin combination therapy has enhanced efficacy against an experimental *Staphylococcus aureus* prosthetic joint infection. *Antimicrob Agents Chemother.* (2013) 57:5080–6. doi: 10.1128/AAC.00702-13
49. Zhang X, Ma YF, Wang L, Jiang N, Qin CH, Hu YJ, et al. A rabbit model of implant-related osteomyelitis inoculated with biofilm after open femoral fracture. *Exp Ther Med.* (2017) 14:4995–5001. doi: 10.3892/etm.2017.5138
50. Wang Y, Cheng LI, Helfer DR, Ashbaugh AG, Miller RJ, Tzomides AJ, et al. Mouse model of hematogenous implant-related *Staphylococcus aureus* biofilm infection reveals therapeutic targets. *Proc Natl Acad Sci USA*. (2017) 114:E5094–102. doi: 10.1073/pnas.1703427114
51. Makinen TJ, Lankinen P, Poyhonen T, Jalava J, Aro HT, Roivainen A. Comparison of 18f-Fdg and 68ga pet imaging in the assessment of experimental osteomyelitis due to *Staphylococcus aureus*. *Eur J Nucl Med Mol Imaging.* (2005) 32:1259–68. doi: 10.1007/s00259-005-1841-9
52. Horst SA, Hoerr V, Beineke A, Kreis C, Tuchscherr L, Kalinka J, et al. A novel mouse model of *Staphylococcus aureus* chronic osteomyelitis that closely mimics the human infection: an integrated view of disease pathogenesis. *Am J Pathol.* (2012) 181:1206–14. doi: 10.1016/j.ajpath.2012.07.005
53. Deysine M, Isenberg H, Steiner G. Chronic haematogenous osteomyelitis; studies on an experimental model. *Int Orthop.* (1983) 7:69–78. doi: 10.1007/BF00266454
54. Chadha HS, Fitzgerald RH, Wiater P, Sud S, Nasser S, Wooley PH. Experimental acute hematogenous osteomyelitis in mice I histopathological and immunological findings. *J Orthop Res.* (1999) 17:376–81. doi: 10.1002/jor.1100170312
55. Laratta JL, Shillingford JN, Hardy N, Lehman RA, Lenke LG, Riew KD. A dose-response curve for a gram-negative spinal implant infection model in rabbits. *Spine.* (2017) 42:E1225–30. doi: 10.1097/BRS.0000000000002205
56. Johansen LK, Koch J, Frees D, Aalbæk B, Nielsen OL, Leifsson PS, et al. Pathology and biofilm formation in a porcine model of *Staphylococcal* osteomyelitis. *J Comp Path.* (2012) 147:343–53. doi: 10.1016/j.jcpa.2012.01.018
57. Dworsky EM, Hegde V, Loftin AH, Richman S, Hu Y, Lord E, et al. Novel *in vivo* mouse model of implant related spine infection. *J Orthop Res.* (2017) 35:193–9. doi: 10.1002/jor.23273
58. Guarch-Pérez C, Riool M, Zaat S. Current osteomyelitis mouse models, a systematic review. *Eur Cells Mater.* (2021) 42:334–74. doi: 10.22203/eCM.v042a22
59. Bragg B, Epstein NJ, Ma T, Goodman S, Smith RL. Histomorphometric analysis of the intramedullary bone response to titanium particles in wild-type and Il-1r1 Knock-out mice: a preliminary study. *J Biomed Mater Res B Appl Biomater.* (2008) 84:559–70. doi: 10.1002/jbm.b.30904
60. Pribaz JR, Bernthal NM, Billi F, Cho JS, Ramos RI, Guo Y, et al. Mouse model of chronic post-arthroplasty infection: noninvasive *in vivo* bioluminescence imaging to monitor bacterial burden for long-term study. *J Orthop Res.* (2012) 30:335–40. doi: 10.1002/jor.21519
61. Bernthal NM, Stavrakis AI, Billi F, Cho JS, Kremen TJ, Simon SI, et al. A Mouse model of post-arthroplasty *Staphylococcus aureus* joint infection to evaluate *in vivo* the efficacy of antimicrobial implant coatings. *PLoS ONE.* (2010) 5:e12580. doi: 10.1371/journal.pone.0012580
62. Sheppard WL, Mosich GM, Smith RA, Hamad CD, Park HY, Zoller SD, et al. Novel *in vivo* mouse model of shoulder implant infection. *J Shoulder Elb Surg.* (2020) 29:1412–24. doi: 10.1016/j.jse.2019.10.032
63. Funao H, Ishii K, Nagai S, Sasaki A, Hoshikawa T, Aizawa M, et al. Establishment of a real-time, quantitative, and reproducible mouse model of *Staphylococcus* osteomyelitis using bioluminescence imaging. *Infect Immun.* (2012) 80:733–41. doi: 10.1128/IAI.06166-11
64. Roux KM, Cobb LH, Seitz MA, Priddy LB. Innovations in osteomyelitis research: a review of animal models. *Animal Model Exp Med.* (2021) 4:59–70. doi: 10.1002/ame2.12149
65. De Mesy Bentley KL, Trombetta R, Nishitani K, Bello-Irizarry SN, Ninomiya M, Zhang L, et al. Evidence of *Staphylococcus aureus* deformation, proliferation, and migration in canaliculi of live cortical bone in murine models of osteomyelitis. *J Bone Miner Res.* (2017) 32:985–90. doi: 10.1002/jbmr.3055
66. Masters EA, Muthukrishnan G, Ho L, Gill AL, de Mesy Bentley KL, Galloway CA, et al. *Staphylococcus aureus* cell wall biosynthesis modulates bone invasion and osteomyelitis pathogenesis. *Front Microbiol.* (2021) 12:723498. doi: 10.3389/fmicb.2021.723498
67. Bernthal NM, Taylor BN, Meganck JA, Wang Y, Shahbazian JH, Niska JA, et al. Combined *in vivo* optical and microct imaging to monitor infection, inflammation, and bone anatomy in an orthopaedic implant infection in mice. *J Vis Exp.* (2014) doi: 10.3791/51612
68. Avci P, Karimi M, Sadasivam M, Antunes-Melo WC, Carrasco E, Hamblin MR. In-vivo monitoring of infectious diseases in living animals using bioluminescence imaging. *Virulence.* (2018) 9:28–63. doi: 10.1080/21505594.2017.1371897
69. Isogai N, Shiono Y, Kuramoto T, Yoshioka K, Ishihama H, Funao H, et al. Potential osteomyelitis biomarkers identified by plasma metabolome analysis in mice. *Sci Rep.* (2020) 10:839. doi: 10.1038/s41598-020-57619-1
70. Jørgensen NP, Skovdal SM, Meyer RL, Dagnæs-Hansen F, Fuursted K, Petersen E. Rifampicin-containing combinations are superior to combinations of vancomycin, linezolid and daptomycin against *Staphylococcus aureus* biofilm infection*in vivo*and*in vitro*. *Pathog Dis.* (2016) 74:ftw019. doi: 10.1093/femspd/ftw019
71. Inzana J, Trombetta R, Schwarz E, Kates S, Awad H. 3D printed bioceramics for dual antibiotic delivery to treat implant-associated bone infection. *Eur Cells Mater.* (2015) 30:232–47. doi: 10.22203/eCM.v030a16
72. Trombetta R, Ninomiya M, El-Atawneh I, Knapp E, De Mesy Bentley K, Dunman P, et al. Calcium phosphate spacers for the local delivery of sitafloxacin and rifampin to treat orthopedic infections: efficacy and proof of concept in a mouse model of single-stage revision of device-associated osteomyelitis. *Pharmaceutics.* (2019) 11:94. doi: 10.3390/pharmaceutics11020094
73. Lindsay SE, Lindsay HG, Kallet J, Weaver MR, Curran-Everett D, Crapo JD, et al. Mnte-2-pyp disrupts *Staphylococcus aureus* biofilms in a novel fracture model. *J Orthop Res.* (2021) 39:2439–45. doi: 10.1002/jor.24967
74. Büren C, Lögters T, Oezel L, Rommelfanger G, Scholz AO, Windolf J, et al. Effect of hyperbaric oxygen therapy (Hbo) on implant-associated osteitis in a femur fracture model in mice. *PLoS ONE.* (2018) 13:e0191594. doi: 10.1371/journal.pone.0191594
75. Johnson CT, Sok MCP, Martin KE, Kalelkar PP, Caplin JD, Botchwey EA. Lysostaphin and Bmp-2 co-delivery reduces *S. aureus* infection and regenerates critical-sized segmental bone defects. *Sci Adv.* (2019) 5: eaaw1228. doi: 10.1126/sciadv.aaw1228
76. Yokogawa N, Ishikawa M, Nishitani K, Beck CA, Tsuchiya H, Mesfin A, et al. Immunotherapy synergizes with debridement and antibiotic therapy in a murine 1-stage exchange model of MRSA implant-associated osteomyelitis. *J Orthop Res.* (2018) 36:1590–8. doi: 10.1002/jor.23801
77. Muschler GF, Raut VP, Patterson TE, Wenke JC, Hollinger JO. The design and use of animal models for translational research in bone tissue engineering and regenerative medicine. *Tissue Eng Part B Rev.* (2010) 16:123–45. doi: 10.1089/ten.teb.2009.0658
78. Reizner W, Hunter JG, O'Malley NT, Southgate RD, Schwarz EM, Kates SL, et al. Systematic review of animal models for *Staphylococcus aureus* osteomyelitis. *Eur Cell Mater.* (2015) 27:196–212. doi: 10.22203/eCM.v027a15
79. An YH, Kang QK, Arciola CR. Animal models of osteomyelitis. *Int J Artif Organs.* (2006) 29:407–20. doi: 10.1177/039139880602900411
80. Hassani Besheli N, Mottaghitalab F, Eslami M, Gholami M, Kundu SC, Kaplan DL, et al. Sustainable release of vancomycin from silk fibroin nanoparticles for treating severe bone infection in rat tibia osteomyelitis model. *ACS Appl Mater Interfaces.* (2017) 9:5128–38. doi: 10.1021/acsami.6b14912
81. Fukushima N, Yokoyama K, Sasahara T, Dobashi Y, Itoman M. Establishment of rat model of acute *Staphylococcal* osteomyelitis: relationship between inoculation dose and development of osteomyelitis. *Arch Orthop Trauma Surg.* (2005) 125:169–76. doi: 10.1007/s00402-004-0785-z

82. Harrasser N, Gorkotte J, Obermeier A, Feihl S, Straub M, Slotta-Huspenina J, et al. A new model of implant-related osteomyelitis in the metaphysis of rat tibiae. *BMC Musculoskelet Disord.* (2016) 17:152. doi: 10.1186/s12891-016-1005-z
83. Neyisci C, Erdem Y, Bilekli AB, Demiralp B, Kose O, Bek D, et al. Treatment of implant-related methicillin-resistant *Staphylococcus aureus* osteomyelitis with vancomycin-loaded Vk100 silicone cement: an experimental study in rats. *J Orthop Surg.* (2018) 26:2309499017754093. doi: 10.1177/2309499017754093
84. Robinson DA, Bechtold JE, Carlson CS, Evans RB, Conzemius MG. Development of a fracture osteomyelitis model in the rat femur. *J Orthop Res.* (2011) 29:131–7. doi: 10.1002/jor.21188
85. Sanchez CJ Jr., Prieto EM, Krueger CA, Zienkiewicz KJ, Romano DR, Ward CL, et al. Effects of local delivery of D-amino acids from biofilm-dispersive scaffolds on infection in contaminated rat segmental defects. *Biomaterials.* (2013) 34:7533–43. doi: 10.1016/j.biomaterials.2013.06.026
86. Fölsch C, Federmann M, Kuehn KD, Kittinger C, Kogler S, Zarfel G, et al. Coating with a novel gentamicinpalmitate formulation prevents implant-associated osteomyelitis induced by methicillin-susceptible *Staphylococcus aureus* in a rat model. *Int Orthop.* (2015) 39:981–8. doi: 10.1007/s00264-014-2582-9
87. Jung SW, Oh SH, Lee IS, Byun JH, Lee JH. *In situ* gelling hydrogel with anti-bacterial activity and bone healing property for treatment of osteomyelitis. *Tissue Eng Regen Med.* (2019) 16:479–90. doi: 10.1007/s13770-019-00206-x
88. Oh EJ, Oh SH, Lee IS, Kwon OS, Lee JH. Antibiotic-eluting hydrophilized PMMA bone cement with prolonged bactericidal effect for the treatment of osteomyelitis. *J Biomater Appl.* (2016) 30:1534–44. doi: 10.1177/0885328216629823
89. Melicherčík P, Cerovský V, Nešuta O, Jahoda D, Landor I, Ballay R, et al. Testing the efficacy of antimicrobial peptides in the topical treatment of induced osteomyelitis in rats. *Folia Microbiol.* (2018) 63:97–104. doi: 10.1007/s12223-017-0540-9
90. Qu X, Yang H, Jia B, Wang M, Yue B, Zheng Y, et al. Zinc alloy-based bone internal fixation screw with antibacterial and anti-osteolytic properties. *Bioact Mater.* (2021) 6:4607–24. doi: 10.1016/j.bioactmat.2021.05.023
91. Sodnom-Ish B, Eo MY, Oh JH, Seo MH, Yang HJ, Lee JH, et al. Decompression effects on bone healing in rat mandible osteomyelitis. *Sci Rep.* (2021) 11:11673. doi: 10.1038/s41598-021-91104-7
92. Ofluoglu EA, Zileli M, Aydin D, Baris YS, Kuçukbasmaci O, Gonullu N, et al. Implant-related infection model in rat spine. *Arch Orthop Trauma Surg.* (2007) 127:391–6. doi: 10.1007/s00402-007-0365-0
93. Søe NH, Jensen NV, Nürnberg BM, Jensen AL, Koch J, Poulsen SS, et al. A novel knee prosthesis model of implant-related osteo- myelitis in rats. *Acta Orthop.* (2013) 84:92–7. doi: 10.3109/17453674.2013.773121
94. Shiels SM, Bedigrew KM, Wenke JC. Development of a hematogenous implant-related infection in a rat model. *BMC Musculoskelet Disord.* (2015) 16. doi: 10.1186/s12891-015-0699-7
95. Hienz SA, Sakamoto H, Flock JI, Mörner AC, Reinholt FP, Heimdahl A, et al. Development and characterization of a new model of hematogenous osteomyelitis in the rat. *J Infect Dis.* (1995) 171:1230–6. doi: 10.1093/infdis/171.5.1230
96. Rissing JP, Buxton TB, Weinstein RS, Shockley RK. Model of experimental chronic osteomyelitis in rats. *Infect Immun.* (1985) 47:581–6. doi: 10.1128/iai.47.3.581-586.1985
97. Spagnolo N, Greco F, Rossi A, Ciolli L, Teti A, Posteraro P. Chronic *Staphylococcal* osteomyelitis: a new experimental rat model. *Infect Immun.* (1993) 61:5225–30. doi: 10.1128/iai.61.12.5225-5230.1993
98. Vergidis P, Rouse MS, Euba G, Karau MJ, Schmidt SM, Mandrekar JN, et al. Treatment with linezolid or vancomycin in combination with rifampin is effective in an animal model of methicillin-resistant *Staphylococcus aureus* foreign body osteomyelitis. *Antimicrob Agents Chemother.* (2011) 55:1182–6. doi: 10.1128/AAC.00740-10
99. Stadelmann VA, Potapova I, Camenisch K, Nehrbass D, Richards RG, Moriarty TF. *In vivo* microct monitoring of osteomyelitis in a rat model. *Biomed Res Int.* (2015) 2015:1–12. doi: 10.1155/2015/587857
100. Vergidis P, Schmidt-Malan SM, Mandrekar JN, Steckelberg JM, Patel R. Comparative activities of vancomycin, tigecycline and rifampin in a rat model of methicillin-resistant *Staphylococcus aureus* osteomyelitis. *J Infect.* (2015) 70:609–15. doi: 10.1016/j.jinf.2014.12.016
101. Avdeeva EY, Slizovsky GV, Skorokhodova MG, Fomina TI, Zorkaltsev MA, Zavadovskaya VD, et al. Experimental simulation of traumatic osteomyelitis in rats. *Bull Exp Biol Med.* (2016) 161:137–40. doi: 10.1007/s10517-016-3364-8
102. Fölsch C, Federmann M, Lakemeier S, Kuehn KD, Kittinger C, Kerwat M, et al. Systemic antibiotic therapy does not significantly improve outcome in a rat model of implant-associated osteomyelitis induced by methicillin susceptible *Staphylococcus aureus*. *Arch Orthop Trauma Surg.* (2016) 136:585–92. doi: 10.1007/s00402-016-2419-7
103. Park KH, Greenwood-Quaintance KE, Mandrekar J, Patel R. Activity of tedizolid in methicillin-resistant *Staphylococcus aureus* experimental foreign body-associated osteomyelitis. *Antimicrob Agents Chemother.* (2016) 60:6568–72. doi: 10.1128/AAC.01248-16
104. Cui T, Li J, Zhen P, Gao Q, Fan X, Li C. Masquelet induced membrane technique for treatment of rat chronic osteomyelitis. *Exp Ther Med.* (2018) doi: 10.3892/etm.2018.6573
105. Kussmann M, Obermueller M, Berndl F, Reischer V, Veletzky L, Burgmann H, et al. Dalbavancin for treatment of implant-related methicillin-resistant *Staphylococcus aureus* osteomyelitis in an experimental rat model. *Sci Rep.* (2018) 8:9661. doi: 10.1038/s41598-018-28006-8
106. Cobb LH, Park J, Swanson EA, Beard MC, McCabe EM, Rourke AS, et al. Crispr-Cas9 modified bacteriophage for treatment of *Staphylococcus aureus* induced osteomyelitis and soft tissue infection. *PLoS ONE.* (2019) 14:e0220421. doi: 10.1371/journal.pone.0220421
107. Wu S, Liu Y, Lei L, Zhang H. Virulence of methicillin-resistant *Staphylococcus aureus* modulated by the YycFG two-component pathway in a rat model of osteomyelitis. *J Orthop Surg Res.* (2019) 14:433. doi: 10.1186/s13018-019-1508-z
108. Zhou P, Wu J, Wang Y, Zhang H, Xia Y, Zhang Y, et al. The synergistic therapeutic efficacy of vancomycin and omega-3 fatty acids alleviates *Staphylococcus aureus* -induced osteomyelitis in rats. *Biomed Pharmacother.* (2019) 111:1228–33. doi: 10.1016/j.biopha.2018.12.125
109. Deng S, Wang Y, Liu S, Chen T, Hu Y, Zhang G, et al. Extracellular vesicles: a potential biomarker for quick identification of infectious osteomyelitis. *Front Cell Infect Microbiol.* (2020) 10:323. doi: 10.3389/fcimb.2020.00323
110. Sahukhal GS, Tucci M, Benghuzzi H, Wilson G, Elasri MO. The role of the msaabcr operon in implant-associated chronic osteomyelitis in *Staphylococcus aureus* Usa300 Lac. *BMC Microbiol.* (2020) 20:324. doi: 10.1186/s12866-020-01964-8
111. Schierholz JM, Beuth J. Implant infections: a haven for opportunistic bacteria. *J Hosp Infect.* (2001) 49:87–93. doi: 10.1053/jhin.2001.1052
112. Hudson MC, Ramp WK, Nicholson NC, Williams AS, Nousiainen MT. Internalization of *Staphylococcus aureus* by cultured osteoblasts. *Microb Pathog.* (1995) 19:409–19. doi: 10.1006/mpat.1995.0075
113. Tucker KA, Reilly SS, Leslie CS, Hudson MC. Intracellular *Staphylococcus aureus* induces apoptosis in mouse osteoblasts. FEMS *Microbiol Lett.* (2000) 186:151–6. doi: 10.1111/j.1574-6968.2000.tb09096.x
114. Bottagisio M, Coman C, Lovati AB. Animal models of orthopaedic infections. A review of rabbit models used to induce long bone bacterial infections. *J Med Microbiol.* (2019) 68:506–37. doi: 10.1099/jmm.0.000952
115. Odekerken JC, Arts JJ, Surtel DA, Walenkamp GH, Welting TJ, et al. A rabbit osteomyelitis model for the longitudinal assessment of early post-operative implant infections. *J Orthop Surg Res.* (2013) 8:38. doi: 10.1186/1749-799X-8-38
116. Yan L, Wu J, Jiang D, Wu J, Wang X, Wang Z-L, et al. Treatment of *Staphylococcus aureus* -induced chronic osteomyelitis with bone-like hydroxyapatite/poly amino acid loaded with rifapentine microspheres. *Drug Des Devel Ther.* (2015) 9:3665–76. doi: 10.2147/DDDT.S84486
117. Gahukamble AD, McDowell A, Post V, Salavarrieta Varela J, Rochford ET, Richards RG, et al. *Propionibacterium acnes* and *Staphylococcus lugdunensis* cause pyogenic osteomyelitis in an intramedullary nail model in rabbits. *J Clin Microbiol.* (2014) 52:1595–606. doi: 10.1128/JCM.03197-13
118. Odekerken JC, Brans BT, Welting TJ, Walenkamp GH. (18)F-Fdg micropet imaging differentiates between septic and aseptic wound healing after orthopedic implant placement: a longitudinal study of an

implant osteomyelitis in the rabbit tibia. *Acta Orthop.* (2014) 85:305–13. doi: 10.3109/17453674.2014.900894
119. Zahar A, Kocsis G, Citak M, Puskás G, Domahidy M, Hajdú M, et al. Use of antibiotic-impregnated bone grafts in a rabbit osteomeylitis model. *Technol Health Care.* (2017) 25:929–38. doi: 10.3233/THC-170869
120. Kose N, Asfuroglu ZM, Kose A, Sahinturk V, Gurbuz M, Dogan A. Silver ion-doped calcium phosphate-based bone-graft substitute eliminates chronic osteomyelitis: an experimental study in animals. *J Orthop Res.* (2021) 39:1390–401. doi: 10.1002/jor.24946
121. Yin L-Y, Manring MM, Calhoun JH, A. Rabbit osteomyelitis model to simulate multibacterial war wound infections. *Mil Med.* (2013) 178:696–700. doi: 10.7205/MILMED-D-12-00550
122. Steinhart H, Schulz S, Mutters R. Evaluation of ozonated oxygen in an experimental animal model of osteomyelitis as a further treatment option for skull-base osteomyelitis. *Eur Arch Otorhinolaryngol.* (1999) 256:153–7. doi: 10.1007/s004050050130
123. Moskowitz JS, Blaisse MR, Samuel RE, Hsu H-P, Harris MB, Martin SD, et al. The effectiveness of the controlled release of gentamicin from polyelectrolyte multilayers in the treatment of *Staphylococcus aureus* infection in a rabbit bone model. *Biomaterials.* (2010) 31:6019–30. doi: 10.1016/j.biomaterials.2010.04.011
124. Inceoglu S, Botimer G, Maskiewicz VK. Novel microcomposite implant for the controlled delivery of antibiotics in the treatment of osteomyelitis following total joint replacement. *J Orthop Res.* (2021) 39:365–75. doi: 10.1002/jor.24919
125. Jones-Jackson L, Walker R, Purnell G, McLaren SG, Skinner RA, Thomas JR, et al. Early detection of bone infection and differentiation from post-surgical inflammation using 2-deoxy-2-[18F]-fluoro-D-glucose positron emission tomography (FDG-PET) in an animal model. *J Orthop Res.* (2005) 23:1484–9. doi: 10.1016/j.orthres.2005.03.010.1100230635
126. Overstreet D, McLaren A, Calara F, Vernon B, McLemore R. Local gentamicin delivery from resorbable viscous hydrogels is therapeutically effective. *Clin Orthop Relat Res.* (2015) 473:337–47. doi: 10.1007/s11999-014-3935-9
127. Munoz NM, Minhaj AA, Dupuis CJ, Ensor JE, Golardi N, Jaso JM, et al. What are the effects of irreversible electroporation on a *Staphylococcus aureus* rabbit model of osteomyelitis? *Clin Orthop Relat Res.* (2019) 477:2367–77. doi: 10.1097/CORR.0000000000000882
128. Smeltzer MS, Thomas JR, Hickmon SG, Skinner RA, Nelson CL, Griffith D, et al. Characterization of a rabbit model of *Staphylococcal* osteomyelitis. *J Orthop Res.* (1997) 15:414–21. doi: 10.1002/jor.1100150314
129. Ambrose CG, Clyburn TA, Mika J, Gogola GR, Kaplan HB, Wanger A, et al. Evaluation of antibiotic-impregnated microspheres for the prevention of implant-associated orthopaedic infections. *J Bone Joint Surg Am.* (2014) 96:128–34. doi: 10.2106/JBJS.L.01750
130. Saleh-Mghir A, Muller-Serieys C, Dinh A, Massias L, Cremieux AC. Adjunctive rifampin is crucial to optimizing daptomycin efficacy against rabbit prosthetic joint infection due to methicillin-resistant *Staphylococcus aureus*. *Antimicrob Agents Chemother.* (2011) 55:4589–93. doi: 10.1128/AAC.00675-11
131. Nielsen NHS, Renneberg J, Nürnberg BM, Torholm C. Experimental implant-related osteomyelitis induced with *Staphylococcus aureus*. *Eur J Orthop Surg Traumatol.* (1996) 6:97–100. doi: 10.1007/BF00568321
132. Lan Y, Xie H, Shi Y, Jin Q, Zhang X, Wang Y, et al. Nemobinding domain peptide ameliorates inflammatory bone destruction in a *Staphylococcus aureus* induced chronic osteomyelitis model. *Mol Med Rep.* (2019) 19:3291–7. doi: 10.3892/mmr.2019.9975
133. Liu G, Chen S, Fang J, Xu B, Li S, Hao Y, et al. Vancomycin microspheres reduce postoperative spine infection in an *in vivo* rabbit model. *BMC Pharmacol Toxicol.* (2016) 17:61. doi: 10.1186/s40360-016-0105-6
134. Elgazzar AH, Dannoon S, Sarikaya I, Farghali M, Junaid TA. Scintigraphic patterns of indium-111 oxine-labeled white blood cell imaging of gram-negative versus gram-positive vertebral osteomyelitis. *Med Princ Pract.* (2017) 26:415–20. doi: 10.1159/000480083
135. Shiels SM, Raut VP, Patterson PB, Barnes BR, Wenke JC. Antibiotic-loaded bone graft for reduction of surgical site infection in spinal fusion. *Spine J.* (2017) 17:1917–25. doi: 10.1016/j.spinee.2017.06.039
136. Bierry G, Jehl F, Boehm N, Robert P, Dietemann J-L, Kremer S. Macrophage imaging by USPIO-enhanced MR for the differentiation of infectious osteomyelitis and aseptic vertebral inflammation. *Eur Radiol.* (2009) 19:1604–11. doi: 10.1007/s00330-009-1319-4
137. Poultsides LA, Papatheodorou LK, Karachalios TS, Khaldi L, Maniatis A, Petinaki E, et al. Novel model for studying hematogenous infection in an experimental setting of implant-related infection by a community-acquired methicillin-resistant *S. aureus* strain. *J Orthop Res.* (2008) 26:1355–62. doi: 10.1002/jor.20608
138. Schulz S, Steinhart H, Mutters R. Chronic osteomyelitis in a new rabbit model. *J Invest Surg.* (2001) 14:121–31. doi: 10.1080/08941930152024246
139. Moriarty TF, Campoccia D, Nees SK, Boure LP, Richards RG. *In vivo* evaluation of the effect of intramedullary nail microtopography on the development of local infection in rabbits. *Int J Artif Organs.* (2010) 33:667–75. doi: 10.1177/039139881003300913
140. Wenter V, Müller J-P, Albert NL, Lehner S, Fendler WP, Bartenstein P, et al. The diagnostic value of [18f]Fdg pet for the detection of chronic osteomyelitis and implant-associated infection. *Eur J Nucl Med Mol Imaging.* (2016) 43:749–61. doi: 10.1007/s00259-015-3221-4
141. Lazzarini L, Overgaard KA, Conti E, Shirtliff ME. Experimental osteomyelitis: what have we learned from animal studies about the systemic treatment of osteomyelitis? *J Chemother.* (2006) 18:451–60. doi: 10.1179/joc.2006.18.5.451
142. Kishor C, Mishra RR, Saraf SK, Kumar M, Srivastav AK, Nath G. Phage therapy of *Staphylococcal* chronic osteomyelitis in experimental animal model. *Indian J Med Res.* (2016) 143:87–94. doi: 10.4103/0971-5916.178615
143. Graur D, Duret L, Gouy M. Phylogenetic position of the order lagomorpha (rabbits, hares and allies). *Nature.* (1996) 379:333–5. doi: 10.1038/379333a0
144. Mäkitaipale J, Sievänen H, Laitinen-Vapaavuori O. Tibial bone density, cross-sectional geometry and strength in finnish pet rabbits: a peripheral quantitative computed tomography study. *Vet Rec.* (2018) 183:382. doi: 10.1136/vr.104419
145. Nielsen OL, Afzelius P, Bender D, Schønheyder HC, Leifsson PS, Nielsen KM, et al. Comparison of autologous (111)In-leukocytes, (18)F-FDG, (11)C-methionine, (11)C-PK11195 and (68)Ga-citrate for diagnostic nuclear imaging in a juvenile porcine haematogenous *Staphylococcus aureus* osteomyelitis model. *Am J Nucl Med Mol Imaging.* (2015) 5:169–82.
146. Johansen LK, Svalastoga EL, Frees D, Aalbaek B, Koch J, Iburg TM, et al. A new technique for modeling of hematogenous osteomyelitis in pigs: inoculation into femoral artery. *J Invest Surg.* (2013) 26:149–53. doi: 10.3109/08941939.2012.718043
147. Jensen EH, Nielsen OL, Agerholm JS, Iburg T, Johansen LK, Johannesson E, et al. A non-traumatic *Staphylococcus aureus* osteomyelitis model in pigs. *In Vivo.* (2010) 24:257–64.
148. Jødal L, Roivainen A, Oikonen V, Jalkanen S, Hansen SB, Afzelius P, et al. Kinetic modelling of [68ga]Ga-dota-siglec-9 in porcine osteomyelitis and soft tissue infections. *Molecules.* (2019) 24:4094. doi: 10.3390/molecules24224094
149. Afzelius P, Alstrup A, Nielsen O, Nielsen K, Jensen S. Attempts to target *Staphylococcus aureus* induced osteomyelitis bone lesions in a juvenile pig model by using radiotracers. *Molecules.* (2020) 25:4329. doi: 10.3390/molecules25184329
150. Patterson AL, Galloway RH, Baumgartner JC, Barsoum IS. Development of chronic mandibular osteomyelitis in a miniswine model. *J Oral Maxillofac Surg.* (1993) 51:1358–62. doi: 10.1016/S0278-2391(10)80142-9
151. Jensen LK, Koch J, Aalbaek B, Moodley A, Bjarnsholt T, Kragh KN, et al. Early implant-associated osteomyelitis results in a peri-implanted bacterial reservoir. *APMIS.* (2017) 125:38–45. doi: 10.1111/apm.12597
152. Bue M, Hanberg P, Koch J, Jensen LK, Lundorff M, Aalbaek B, et al. Single-dose bone pharmacokinetics of vancomycin in a porcine implant-associated osteomyelitis model. *J Orthop Res.* (2017) 36:1093–8. doi: 10.1002/jor.23776
153. Lüthje FL, Blirup-Plum SA, Moller NS, Heegaard PMH, Jensen HE, Kirketerp-Moller K, et al. The host response to bacterial bone infection involves a local upregulation of several acute phase proteins. *Immunobiology.* (2020) 225:151914. doi: 10.1016/j.imbio.2020.151914
154. Jensen LK, Koch J, Dich-Jorgensen K, Aalbaek B, Petersen A, Fuursted K, et al. Novel porcine model of implant-associated osteomyelitis: a

comprehensive analysis of local, regional, and systemic response. *J Orthop Res.* (2017) 35:2211–21. doi: 10.1002/jor.23505
155. Hill PF, Watkins PE. The prevention of experimental osteomyelitis in a model of gunshot fracture in the pig. *Eur J Orthop Surg Traumatol.* (2001) 11:237–41. doi: 10.1007/BF01686897
156. Jødal L, Nielsen OL, Afzelius P, Alstrup AKO, Hansen SB. Blood perfusion in osteomyelitis studied with [15o]water pet in a juvenile porcine model. *EJNMMI Research.* (2017) 7:4. doi: 10.1186/s13550-016-0251-2
157. Afzelius P, Heegaard PM, Jensen SB, Alstrup AKO, Schønheyder HC, Eek A, et al. [^{99m} Tc]-labelled interleukin-8 as a diagnostic tool compared to [^{18} F]FDG and CT in an experimental porcine osteomyelitis model. *Am J Nucl Med Mol Imaging.* (2020) 10:32–46.
158. Aerssens J, Boonen S, Lowet G, Dequeker J. Interspecies differences in bone composition, density, and quality: potential implications for *in vivo* bone research*. *Endocrinology.* (1998) 139:663–70. doi: 10.1210/endo.139.2.5751
159. Mullender MG, Huiskes R, Versleyen H, Buma P. Osteocyte density and histomorphometric parameters in cancellous bone of the proximal femur in five mammalian species. *J Orthop Res.* (1996) 14:972–9. doi: 10.1002/jor.1100140618
160. Kaarsemaker S, Walenkamp GH, Bogaard AE. New model for chronic osteomyelitis with *Staphylococcus aureus* in sheep. *Clin Orthop Relat Res.* (1997) 339:246–52. doi: 10.1097/00003086-199706000-00033
161. Klein K, Schweizer TA, Siwy K, Lechmann B, Karol A, von Rechenberg B, et al. Establishment of a localized acute implant-associated *Staphylococcus aureus* bone infection model in sheep. *Pathog Dis.* (2021) 79:ftab032. doi: 10.1093/femspd/ftab032
162. Moriarty TF, Schmid T, Post V, Samara E, Kates S, Schwarz EM, et al. A large animal model for a failed two-stage revision of intramedullary nail-related infection by methicillin-resistant *Staphylococcus aureus*. *Eur Cell Mater.* (2017) 34:83–98. doi: 10.22203/eCM.v034a06
163. McLaren JS, White LJ, Cox HC, Ashraf W, Rahman CV, Blunn GW, et al. A biodegradable antibiotic-impregnated scaffold to prevent osteomyelitis in a contaminated *in vivo* bone defect model. *Eur Cell Mater.* (2014) 27:332–49. doi: 10.22203/eCM.v027a24
164. Williams DL, Haymond BS, Woodbury KL, Beck JP, Moore DE, Epperson RT, et al. Experimental model of biofilm implant-related osteomyelitis to test combination biomaterials using biofilms as initial inocula. *J Biomed Mater Res A.* (2012) 100A:1888–900. doi: 10.1002/jbm.a.34123
165. Boot W, Schmid T, D'Este M, Guillaume O, Foster A, Decosterd L, et al. A hyaluronic acid hydrogel loaded with gentamicin and vancomycin successfully eradicates chronic methicillin- resistant *Staphylococcus aureus* orthopedic infection in a sheep model. *Antimicrob Agents Chemother.* (2021) 65:e01840-20. doi: 10.1128/AAC.01840-20
166. Stewart S, Barr S, Engiles J, Hickok NJ, Shapiro IM, Richardson DW, et al. Vancomycin-modified implant surface inhibits biofilm formation and supports bone-healing in an infected osteotomy model in sheep. *J Bone Joint Surg.* (2012) 94:1406–15. doi: 10.2106/JBJS.K.00886
167. Salgado CJ, Jamali AA, Mardini S, Buchanan K, Veit B, A. Model for chronic osteomyelitis using *Staphylococcus aureus* in goats. *Clin Orthop Relat Res.* (2005) (436):246–50. doi: 10.1097/01.blo.0000159154.17131.bf
168. Wenke JC, Owens BD, Svoboda SJ, Brooks DE. Effectiveness of commercially-available antibiotic-impregnated implants. *J Bone Joint Surg Br.* (2006) 88:1102–4. doi: 10.1302/0301-620X.88B8.17368
169. Tran N, Tran PA, Jarrell JD, Engiles JB, Thomas NP, Young MD, et al. *In vivo* caprine model for osteomyelitis and evaluation of biofilm-resistant intramedullary nails. *Biomed Res Int.* (2013) 2013:674378. doi: 10.1155/2013/674378
170. van der Borden AJ, Maathuis PG, Engels E, Rakhorst G, van der Mei HC, Busscher HJ, et al. Prevention of pin tract infection in external stainless steel fixator frames using electric current in a goat model. *Biomaterials.* (2007) 28:2122–6. doi: 10.1016/j.biomaterials.2007.01.001
171. Fitzgerald RH. Experimental osteomyelitis: description of a canine model and the role of depot administration of antibiotics in the prevention and treatment of sepsis. *J Bone Joint Surg.* (1983) 65:371–80. doi: 10.2106/00004623-198365030-00013
172. Khodaparast O, Coberly DM, Mathey J, Rohrich RJ, Levin LS, Brown SA. Effect of a transpositional muscle flap on VEGF mRNA expression in a canine fracture model. *Plast Reconstr Surg.* (2003) 112:171–6. doi: 10.1097/01.PRS.0000066170.56389.27
173. Petty W, Spanier S, Shuster J. Prevention of infection after total joint replacement. *J Bone Joint Surg.* (1988) 70:536–9. doi: 10.2106/00004623-198870040-00009
174. Huneault LM, Lussier B, Dubreuil P, Chouinard L, Désévaux C. Prevention and treatment of experimental osteomyelitis in dogs with ciprofloxacin-loaded crosslinked high amylose starch implants. *J Orthop Res.* (2004) 22:1351–7. doi: 10.1016/j.orthres.2004.04.007
175. Chen WH, Kang YJ Dai LY, Wang B, Lu C, Li J, et al. Bacteria detected after instrumentation surgery for pyogenic vertebral osteomyelitis in a canine model. *Eur Spine J.* (2014) 23:838–45. doi: 10.1007/s00586-013-3061-5

Conflict of Interest: The authors declare that the research was conducted in the absence of any commercial or financial relationships that could be construed as a potential conflict of interest.

frontiers | Frontiers in Veterinary Science

ORIGINAL RESEARCH
published: 28 April 2022
doi: 10.3389/fvets.2022.848833

Production of Triple-Gene (GGTA1, B2M and CIITA)-Modified Donor Pigs for Xenotransplantation

Kaixiang Xu[1,2,3†], *Honghao Yu*[4†], *Shuhan Chen*[1,2,5†], *Yaxuan Zhang*[1,2,5†], *Jianxiong Guo*[1,2], *Chang Yang*[1,2], *Deling Jiao*[1,2,3], *Tien Dat Nguyen*[1,2,3], *Heng Zhao*[1,2,5], *Jiaoxiang Wang*[1,2,3], *Taiyun Wei*[1,2], *Honghui Li*[1,2,3], *Baoyu Jia*[1,2,5], *Muhammad Ameen Jamal*[1,2,3], *Hong-Ye Zhao*[1,2*], *Xingxu Huang*[6*] and *Hong-Jiang Wei*[1,2,3,5*]

[1] Yunnan Province Key Laboratory for Porcine Gene Editing and Xenotransplantation, Yunnan Agricultural University, Kunming, China, [2] Yunnan Province Xenotransplantation Research Engineering Center, Yunnan Agricultural University, Kunming, China, [3] Faculty of Animal Science and Technology, Yunnan Agricultural University, Kunming, China, [4] College of Biotechnology, Guilin Medical University, Guilin, China, [5] College of Veterinary Medicine, Yunnan Agricultural University, Kunming, China, [6] School of Life Science and Technology, ShanghaiTech University, Shanghai, China

OPEN ACCESS

Edited by:
Abirami Kugadas,
Takeda, United States

Reviewed by:
Megan Sykes,
Columbia University, United States
Sen Yan,
Jinan University, China

***Correspondence:**
Hong-Jiang Wei
hongjiangwei@126.com
Hong-Ye Zhao
hyzhao2000@126.com
Xingxu Huang
huangxx@shanghaitech.edu.cn

[†]These authors have contributed equally to this work

Specialty section:
This article was submitted to Comparative and Clinical Medicine, a section of the journal Frontiers in Veterinary Science

Received: 05 January 2022
Accepted: 28 March 2022
Published: 28 April 2022

Citation:
Xu K, Yu H, Chen S, Zhang Y, Guo J, Yang C, Jiao D, Nguyen TD, Zhao H, Wang J, Wei T, Li H, Jia B, Jamal MA, Zhao H-Y, Huang X and Wei H-J (2022) Production of Triple-Gene (GGTA1, B2M and CIITA)-Modified Donor Pigs for Xenotransplantation. Front. Vet. Sci. 9:848833. doi: 10.3389/fvets.2022.848833

Activation of human immune T-cells by swine leukocyte antigens class I (SLA-I) and class II (SLA-II) leads to xenograft destruction. Here, we generated the GGTA1, B2M, and CIITA (GBC) triple-gene-modified *Diannan* miniature pigs, analyzed the transcriptome of GBC-modified peripheral blood mononuclear cells (PBMCs) in the pig's spleen, and investigated their effectiveness in anti-immunological rejection. A total of six cloned piglets were successfully generated using somatic cell nuclear transfer, one of them carrying the heterozygous mutations in triple genes and the other five piglets carrying the homozygous mutations in GGTA1 and CIITA genes, but have the heterozygous mutation in the B2M gene. The autopsy of GBC-modified pigs revealed that a lot of spot bleeding in the kidney, severe suppuration and necrosis in the lungs, enlarged peripulmonary lymph nodes, and adhesion between the lungs and chest wall were found. Phenotyping data showed that the mRNA expressions of triple genes and protein expressions of B2M and CIITA genes were still detectable and comparable with wild-type (WT) pigs in multiple tissues, but α1,3-galactosyltransferase was eliminated, SLA-I was significantly decreased, and four subtypes of SLA-II were absent in GBC-modified pigs. In addition, even in swine umbilical vein endothelial cells (SUVEC) induced by recombinant porcine interferon gamma (IFN-γ), the expression of SLA-I in GBC-modified pig was lower than that in WT pigs. Similarly, the expression of SLA-II DR and DQ also cannot be induced by recombinant porcine IFN-γ. Through RNA sequencing (RNA-seq), 150 differentially expressed genes were identified in the PBMCs of the pig's spleen, and most of them were involved in immune- and infection-relevant pathways that include antigen processing and presentation and viral myocarditis, resulting in the pigs with GBC modification being susceptible to pathogenic microorganism. Furthermore, the numbers of human IgM binding to the fibroblast cells of GBC-modified pigs were obviously reduced. The GBC-modified porcine

PBMCs triggered the weaker proliferation of human PBMCs than WT PBMCs. These findings indicated that the absence of the expression of α1,3-galactosyltransferase and SLA-II and the downregulation of SLA-I enhanced the ability of immunological tolerance in pig-to-human xenotransplantation.

Keywords: GGTA1, B2M, CIITA, major histocompatibility complex, pig

INTRODUCTION

Worldwide, there is an increasing number of patients with end-stage organ failure in urgent need of transplants, but the number of organs or tissues available from deceased or living human donors is limited (1). Xenotransplantation using genetically modified pig organs or tissues is increasingly close to the clinic. The inactivation of the GGTA1 gene effectively prevents hyperacute rejection (HAR and FDA recently approved that the α-Gal-free pig could potentially be used as a biomedical source) (https://www.fda.gov/news-events/press-announcements/fda-approves-first-its-kind-intentional-genomic-alteration-line-domestic-pigs-both-human-food). Currently, the porcine kidney with α-Gal-free was performed with a short-term *ex vivo* perfusion of a brain-dead patient's blood, indicating no signs of immediate rejection (2). However, other immunological rejection, such as human adaptive immune response, is also important for the long-term survival of xenografts, which can be overcome by the overexpression of other humanized genes and/or deficiency of other porcine endogenous genes. Furthermore, it has been suggested that prolonged survival of xenografts in xenotransplantation needs more genetic modifications under the background of GGTA1 knockout (3, 4).

T-cell-mediated immune responses belong to adaptive immune response and are closely related to the expression of major histocompatibility complex (MHC) genes, including MHC class I, class II, and class III (5, 6). MHC class I and class II proteins share the task of presenting antigens on the cell surface for recognition by $CD8^+$ and $CD4^+$ T-cells, respectively (7). It has been reported that porcine MHC molecules, including MHC class I and class II, known as swine leukocyte antigen class I and class II (SLA-I and SLA-II), can cross-react with anti-human leukocyte antigen antibodies and trigger human T-cell responses after xenotransplantation (8, 9). The SLA-I is a heterotrimeric complex composed of a heavy α-chain, a light β-chain, and a variable short peptide, expressing on all nucleated cells. The porcine β2-microglobulin (B2M) is a highly conserved gene encoding the β-chain of SLA-I and thus is a potential target for reducing or eliminating the SLA-I expression on the cell surface (10). The SLA-II had high homology with humans and expressed a variety of subtypes on the cell membrane, including SLA-II DRA, DRB1, DQA, and DQB1 (11). Additionally, their expression on spatiotemporal and quantitative aspects is highly governed by the MHC class II transactivator, the CIITA gene (12, 13).

To alleviate the adaptive immune response for xenotransplantation, the pigs carrying B2M-null (14) or expressing human dominant-negative CIITA (hCIITA-DN) (15) have been produced, which significantly diminished the expression of SLA-I or SLA-II. These porcine xenografts can escape from the human T cell-mediated immune response to some extent, resulting in the prolonged survival of xenografts. Therefore, the deletion of GGTA1, B2M, and CIITA genes in pigs could further improve the immune compatibility between humans and pigs more effectively to prolong graft survival.

In this study, to provide an available donor pig for xenotransplantation research, we simultaneously targeted the porcine GGTA1, B2M, and CIITA genes by the CRISPR/Cas9 system and generated the α-Gal, SLA-II-deficient and SLA-I low *Diannan* miniature pigs by somatic cell nuclear transfer (SCNT). We performed RNA sequencing (RNA-seq) of PBMCs in the pig's spleen and analyzed the effects of gene modifications on pig health. We further assessed their effectiveness in anti-immunological rejection by an antibody-antigen-binding assay and mixed lymphocyte reaction (MLR). These results suggested that, although these gene modifications impaired pig health, the pigs were helpful for protecting from human antibody-binding cytotoxicity and cellular immune responses in xenotransplantation.

MATERIALS AND METHODS

Animals and Chemicals

Pigs used in this study were approved by the Animal Care and Use Committee of Yunnan Agricultural University (permission code: YAUACUC01; publication date: 10 July 2013). All chemicals were purchased from Sigma-Aldrich (St. Louis, MO, USA) unless otherwise stated.

Design of sgRNA Targeting GGTA1, B2M, and CIITA Genes and Construction of Plasmid Vectors

The specific sgRNAs targeting GGTA1, B2M, and CIITA were designed as follows: GGTA1-sgRNA, GCTACAGGC CTGGTGGTACA; B2M-sgRNA, GAAGGTTCAGGTTTACTC AC; and CIITA-sgRNA, TCAACTGCGAACAGTTCAGC. A total of two complementary DNA oligos for generating sgRNAs were annealed. Subsequently, these double-strand DNAs were subcloned into the pGL3-U6-sgRNA (Addgene no.: 51133) vector to generate the reconstructed plasmid vectors. The reconstructed pGL3-U6-GGTA1-sgRNA, pGL3-U6-B2M-sgRNA, and pGL3-U6-CIITA-sgRNA plasmids were confirmed by sequencing. Then, a high concentration (∼2,000 ng/μl) of sgRNA and pST1374-NLS-flag-linker-Cas9 (Addgene no.: 44758) plasmids was prepared for cell transfection.

Cell Culture, Transfection, Selection, and Identification

Pig fetal fibroblasts (PFFs) were prepared as previously described (16). The day before cell transfection, PFFs were thawed and cultured in DMEM supplemented with 10% fetal bovine serum (FBS). Approximately 7×10^5 cells suspended in the electro-transfection buffer containing pGL3-U6-GGTA1-sgRNA (5 μg), pGL3-U6-B2M-sgRNA (5 μg), pGL3-U6-CIITA (5 μg), and pST1374-NLS-flag-linker-Cas9 (5 μg) were electroporated at 250 V for 20 ms with a Gene Pulser Xcell electroporator (Bio-Rad Gene Pulser Xcell, USA).

After electroporation, the cells were plated into a T25 flask for 24 h in DMEM supplemented with 10% FBS. Then, 3 μg/ml Puromycin and 5 μg/ml Blasticidin S were added into the medium for 24—48 h to select successfully transfected cells. Subsequently, the survived cells were digested and about 80 cells were seeded into 100-mm-diameter culture dish for 8 days. At last, the cell colonies were seeded individually into 48-well plates to isolate single-cell colonies. Single-cell-derived colonies were harvested after 3 days of culture, and the colonies were genotyped by PCR, T7 endonuclease I cleavage assay (T7EI), and sequencing. The biallelic GGTA1, B2M, and CIITA knockout (GTKO/B2MKO/CIITAKO) cell colonies were selected as the donor cell for SCNT.

SCNT and Embryo Transfer

Oocyte collection, *in vitro* maturation, SCNT and embryo transfer were performed as described in our previous studies (17). Briefly, the cultured cumulus oocyte complex (COCs) were freed of cumulus cells by treatment with 0.1% (w/v) hyaluronidase. The first polar body contained in the oocytes and the adjacent cytoplasm was enucleated *via* gentle aspiration using a beveled pipette in TLH-PVA. Donor cells from a GTKO/B2MKO/CIITAKO-positive fibroblast cell line were inserted into the perivitelline space of an enucleated oocyte. The reconstructed embryos were fused with a single direct current pulse of 200 V/mm for 20 μs using the Electro Cell Fusion Generator (LF201, NEPA GENE Co., Ltd., Japan) in fusion medium. Then, the embryos were cultured for 0.5–1 h in PZM-3 and were activated with a single pulse of 150 V/mm for 100 ms in the activation medium. The embryos were equilibrated in PZM-3 supplemented with 5 μg/ml cytochalasin B for 2 h at 38.5°C in a humidified atmosphere with 5% CO_2, 5% O_2, and 90% N_2 (APM-30D, ASTEC, Japan) and then cultured in PZM-3 medium with the same culture conditions described above until embryo transfer. The SCNT embryos were surgically transferred into the oviducts of the recipients.

Identification of GBC-Modified Piglets

After birth of cloned piglets, their ear tissues were collected, and DNA was extracted using a Tissue DNA Kit (TaKaRa, Japan). The GBC-modified piglets and wild-type cloned piglets were identified by assessing the GGTA1 (Forward primer: 5'-ACAGCAACAGACGTCTCTCATC-3' Reverse primer: 5'-CTTGAAGCACTCCTGAGTGATG-3'), B2M (Forward primer: 5'-GGAAACGAATCCGACTGGTAAC-3' Reverse primer: 5'-GTGGACCAGAAGGTAGAAAGAC-3'), and CIITA (Forward primer: 5'-GATGGACCTGGCTGGAGAAGAAGAG-3' Reverse primer: 5'-CGTGGTTACTCGTCAGGGTTGTTAC-3') genes by RT-PCR, T7EI digestion, and Sanger sequencing.

Quantitative Polymerase Chain Reaction

The heart, liver, kidney, spleen, and lung tissues were collected from GBC-modified pigs, including pigs P1, P3, P4, and P5 provided in **Supplementary Table 1**, and WT pigs. Total RNAs were isolated using the TRIzol reagent (Transgen Up, China) according to the manufacturer's instructions. Complementary DNA (cDNA) was synthesized from total RNA using a PrimeScript RT reagent Kit (TaKaRa, Japan) and was used as a template to perform qPCR in SYRB green-based qPCR instrument (CFX-96, Bio-Rad, USA). The reaction was performed in a 20 μl reaction mixtures comprising 10 μl of 2× SYBR (TaKaRa, Japan), 1 μl of cDNA, 1 μl of forward primer, 1 μl of reverse primer, and 7 μl of ddH_2O. The reaction program is as follows: 95°C for 30 s, followed by 40 cycles of 95°C for 10 s, and 62°C for 45 s. The relative expression levels of target genes were quantified by 2–ΔΔCt. The primers are listed in **Supplementary Table 2**.

CFSE-Based Mixed Lymphocyte Reaction

The human blood was collected from a healthy volunteer. The peripheral blood mononuclear cells (PBMCs) of WT, GBC-modified piglet P4P3 (**Supplementary Table 1**), and humans were isolated from heparinized blood using the PBMC separation medium kit (Cat# LTS1110, TBD science, China). The PBMCs of WT and GBC-modified pigs, respectively, were treated with 30 μg/ml mitomycin C as stimulator cells. In addition, the human's PBMCs were labeled with 2.5 μm CFSE (Cat# 65-0850-84, Invitrogen) as the responder cells. Then, the 2×10^4 porcine PBMCs per well treated with mitomycin C and 1×10^5 CFSE-labeled human PBMCs were co-cultured in 200 μl RPMI-1640 medium containing 10% FBS at 37°C and in dark conditions. Then, 1.2×10^5 stimulator cells per well were cultured as the negative control and 1.2×10^5 responder cells per well were cultured as the positive control. After 3 days of culture, cells were harvested and performed flow cytometry using a CytoFLEX flow cytometer (Beckman Coulter). The cell proliferation rate was calculated according to the following formula:

$$\text{Cell proliferation rate} = \left(\frac{\text{NPCMC}}{\frac{1}{1.2} * \text{NPCPC} + \frac{0.2}{1.2} * \text{NPCNC}} - 1 \right) * 100\%.$$

NPCMC, numbers of progeny cells of mixed culture; NPCPC, numbers of progeny cells of positive control; NPCNC, numbers of progeny cells of the negative control. Progeny cells refer to proliferating cells with a decreased CFSE-labeled fluorescence intensity during cell culture.

Immunohistochemistry of Tissue Sections

The kidney tissues from GBC-modified pig, P4 (**Supplementary Table 1**) and WT pig were excised and fixed in 4% paraformaldehyde for 24 h. The tissues were embedded with paraffin and cut into 5 μm. After dewaxing and hydration,

sections were incubated in 3% H_2O_2 solution for 30 min and washed with phospate-buffered solution (PBS) for three times (each time 3 min). After that, the sections were blocked in PBS containing 5% BSA for 15 min at room temperature. Finally, the tissue sections were incubated with 5 μg/ml anti-gal antibody (ALX-801–090, Abcam, UK) at 4°C overnight. After washing with PBS for three times, sections were incubated with 5 μg/ml HRP-conjugated goat anti-rabbit or -mouse IgG antibody (KIT-9901, Elivision TM plus Polyer HRP IHC Kit, Fuzhou, China) for 20 min. After washing three times again, sections were stained with fresh DAB (KIT-9901, Elivision TM plus Polyer HRP IHC Kit, Fuzhou, China) solution in dark for 5 min. Then, sections were washed with PBS for 3 min for three times, stained with hematoxylin, and imaged by OLYMPUS BX53 fluorescence microscope.

Immunofluorescence

The paraffin-embedded tissue blocks from GBC-modified pig, P4P3 (**Supplementary Table 1**), and WT pigs were cut into 5 μm, transferred to glass slides, dewaxed using xylene and gradient alcohol, put into a microwave oven to retrieve antigens with EDTA buffer (pH 8.0; Servicebio Bio, China) at 92–98°C for 15 min, and cooled at room temperature. Then, sections were washed with PBS for three times (each time 3 min), incubated with autofluorescence quencher A (Servicebio Bio, China) at room temperature in dark for 15 min, washed with PBS for three times again, incubated with FBS at room temperature for 30 min, and dried. The dried sections were incubated with the corresponding antibodies.

For detection of SLA-I and SLA-II molecules, FITC-conjugated anti-SLA-I (Cat# MCA2261GA, Bio-rad) and anti-SLA-II DR (Cat# MCA2314GA, Bio-Rad) antibodies were diluted with PBS containing 10% FBS (v/v = 1:200) and used to incubate sections at 4°C in dark for 2 h, and a negative control was incubated with PBS containing 10% FBS.

For detection of B2M and CIITA protein, 1% Triton X-100 was used to punch cell membrane of tissues for 15 min after retrieving antigens. The primary antibodies of anti-B2M (Cat# abs126086a, Absin Bioscience) and anti-CIITA (Cat# sc-13556, Santa Cruz Biotechnology) were diluted with PBS containing 10% FBS (v/v = 1:200) and used to incubate sections at 4°C overnight. Then, sections were washed with PBS for three times, and CY3-conjugated goat anti-rabbit IgG antibodies (Servicebio Bio, China) were diluted with PBS (v/v = 1:200) and used to incubate sections in dark for 2 h.

Then, sections were washed with PBS three times and stained with DAPI (Servicebio Bio, China) for 3 min. After washing with PBS for 1 min, autofluorescence quencher B (Servicebio Bio, China) was added for 5 min and washed three times again. Finally, sections were mounted with antifluorescence quencher (Servicebio Bio, China) and imaged using an OLYMPUS BX53 fluorescence microscope.

Human Serum-Mediated Antibody-Binding Assay

The mixed human serum (Cat# HSER-P50ML) was purchased from ZenBio, Inc., USA. The serum was inactivated at 56°C for 30 min and was diluted at 1:4 in staining buffer (PBS containing 1% FBS). In addition, porcine fibroblasts derived from the GBC pig, P4P3 (**Supplementary Table 1**), and WT and human fibroblasts were collected, washed two times, and resuspended in staining buffer. Then, 1×10^5 cells were incubated with 100 μl inactive human serum (test group) or 100 μl PBS (negative control) for 45 min at room temperature. Then, cells were washed with cold staining buffer to terminate reaction and incubated with goat anti-human IgM-FITC (Cat# 2020-02, 1:100 dilution, SouthernBiotech) and goat anti-human IgG Alexa Fluor 647 (Cat# A21249, 1:200 dilution, Invitrogen) for 30 min at 4°C. Finally, cells were washed with cold staining buffer for two times, centrifuged at 400 × g for 4 min, and resuspended with 200 μl PBS for a CytoFLEX flow cytometer (Beckman Coulter, USA).

Flow Cytometry

All flow cytometry assays were performed by CytoFLEX flow cytometer (Beckman Coulter, USA). For detection of SLA-I, SLA-II DQ, and SLA-II DR surface molecules on porcine umbilical vein endothelial cells derived from the GBC pig, P4P3 (**Supplementary Table 1**) and WT, cells were cultured in the cell medium (Cat# TM002, abmGood) containing 10% FBS (Cat# VS500T, Ausbian) and 1% Pen-Strep solution (Cat# 03-031-1BCS, Biological Industries) with or without 100 ng/ml of recombinant pig interferon-gamma (IFN-γ; Cat# PPP022, Bio-rad) for 3 days. After collection, 1×10^5 cells were incubated with mouse anti-pig SLA class I (Cat# MCA2261GA, 1:100, Bio-Rad), mouse anti-pig SLA class II DQ (Cat# MCA1335GA, 1:100, Bio-rad), and mouse anti-pig SLA class II DR (Cat# MCA2314GA, 1:100, Bio-rad) for 1 h at 4°C, respectively. After that, cells were washed two times with PBS and centrifuged at 1,400 rpm for 5 min. Then, cells were labeled with the secondary antibody FITC goat anti-mouse IgG (Cat# AS001, ABclonal) for 1 h at room temperature.

For detection of CD4 and CD8 T-cell subtypes in PBMCs derived from the blood of WT and GBC-modified pigs by flow cytometry, PBMCs were isolated from whole blood with the porcine PBMC separation medium kit (Cat# LTS1110, TBD science, China). Then, 2×10^5 cells per sample were incubated with anti-CD3 antibody conjugated with FITC (Cat# 559582, 1:40, BD Pharmingen), anti-CD4 antibody conjugated with PE-Cy7 (Cat# 561473, 1:40, BD Pharmingen), and anti-CD8 antibody conjugated with APC (Cat# 561475, 1:40, BD Pharmingen) individually and in combination in dark for 2 h at 4°C. All data acquired from flow cytometry were analyzed using FlowJo VX software.

Transcriptome Profiling of PBMC in Pig's Spleen

The three GBC-modified piglets, namely, GBC_1, GBC_2, and GBC_3, were generated by recloning from the piglet named P4P1 (**Supplementary Table 1**) and sacrificed for sample collection at 6, 32, and 34 days after birth. In addition, three WT piglets, namely, WT_1, WT_2, and WT_3, were sacrificed at 6, 19, and 34 days after birth. The PBMCs of the pig's spleen were isolated and extracted using the PBMC separation medium kit (Cat# LTS1110P, TBD science, China) according to the manufacturer's instructions. Total RNAs were extracted using

TRIzol reagent (Invitrogen, USA) following the manufacturer's procedure. The total RNA quantity and purity were quantified using NanoDrop ND-1000 (NanoDrop, USA). The RNA integrity was assessed by Bioanalyzer 2100 (Agilent, USA) and confirmed by electrophoresis with denaturing agarose gel. The high-quality RNA samples with RIN number >7.0 were used to construct the sequencing library. Poly (A) RNA was purified from 1 μg total RNA using Dynabeads Oligo (dT) 25-61005 (Thermo Fisher, USA) using two rounds of purification. Then, the poly(A) RNA was fragmented into small pieces using Magnesium RNA Fragmentation Module (NEB, Cat# e6150, USA) under 94°C for 5–7 min. Then, the cleaved RNA fragments were reverse-transcribed to create the cDNA by SuperScript™ II Reverse Transcriptase (Invitrogen, Cat# 1896649, USA), which were next used to synthesize U-labeled second-stranded DNAs with *Escherichia coli* DNA polymerase I (NEB, Cat# m0209, USA), RNase H (NEB, Cat# m0297, USA), and dUTP solution (Thermo Fisher, Cat# R0133, USA). An A-base was then added to the blunt ends of each strand, preparing them for ligation to the indexed adapters. Each adapter contains a T-base overhang for ligating the adapter to the A-tailed fragmented DNA. Single- or dual-index adapters are ligated to the fragments, and size selection was performed with AMPureXP beads. After the heat-labile UDG enzyme (NEB, Cat# m0280, USA) treatment of the U-labeled second-stranded DNAs, the ligated products were amplified with PCR by the following conditions: initial denaturation at 95°C for 3 min; eight cycles of denaturation at 98°C for 15 s, annealing at 60°C for 15 s, and extension at 72°C for 30 s; and then final extension at 72°C for 5 min. The average insert size for the final cDNA library was 300 ± 50 bp. At last, we performed the 2 × 150 bp paired-end sequencing (PE150) on an Illumina Novaseq™ 6000 (LC-Bio Technology CO., Ltd., Hangzhou, China) following the vendor's recommended protocol.

Fastp software (http://opengene.org/fastp/fastp) was used to obtain the clean reads by removing the reads that contained adaptor contamination, low-quality bases, and undetermined bases with default parameters. Then, clean reads were mapped using the Sus scrofa genome 11.1 as a reference with HISAT2 (https://ccb.jhu.edu/software/hisat2). The fragments per kilobase of transcript per million fragments mapped (FPKM) value of each gene was calculated using StringTie (https://ccb.jhu.edu/software/stringtie) with default parameters. The differentially expressed genes (DEGs) were selected with fold change >2 or fold change <0.5 and with parametric *F*-test comparing nested linear models (*P*-value < 0.05) by R package edgeR (https://bioconductor.org/packages/release/bioc/html/edgeR.html). The DEGs were annotated by Gene Ontology (GO) functional enrichment and Kyoto Encyclopedia of Genes and Genomes (KEGG) pathway analysis using the topGO package (http://www.geneontology.org) and the online website tool at https://www.kegg.jp/, respectively.

Statistical Analysis

All data were expressed as mean ± standard error (SE). Independent sample unpaired *t*-test was performed with SPSS 22.0 software package (IBM Crop, Armonk, NY) for the data of qPCR, relative median fluorescence intensity (MFI), and cell proliferation rate. Statistical significance was defined as $^{*}P < 0.05$, **, $^{\#\#}P < 0.01$.

RESULTS

Generation and Identification of GTKO/B2MKO/CIITAKO Donor Cells and Piglets

We designed the sgRNAs targeting the GGTA1, B2M, and CIITA genes (**Figure 1A**). Then, these sgRNA plasmids and Cas9 plasmids were co-transfected into PFFs, and a total of 10 single-cell colonies were obtained after puromycin and Blasticidin S selection. The PCR and T7EI cleavage showed that the colony C9 was confirmed as GTKO/B2MKO/CIITAKO modification (**Figures 1B,C**). In addition, Sanger sequencing further indicated that the genotypes of GGTA1, B2M, and CIITA at the target sites were WT/+1 bp, WT/−1 bp/−3 bp, and WT/−1 bp/−10 bp in the colony C9, respectively (**Figure 1D**). Therefore, the cell colony C9 was used as the donor cells for SCNT. The reconstructed embryos were transferred into 13 recipient gilts, five of whom became pregnant, and three delivered, yielding six piglets (P1–P6; **Table 1**). All these piglets were confirmed by PCR and T7EI cleavage of the target site as the GTKO/B2MKO/CIITAKO-modified individuals (**Figures 1E,F**). In addition, the Sanger sequencing analysis indicated that the genotypes of the GGTA1 gene were +1 bp/+1 bp in all piglets except in piglet P2 (WT/+1 bp), of the B2M gene were WT/−1 bp/−3 bp in all piglets, and of the CIITA gene were −1 bp/−10 bp in all piglets except in piglet P2 (WT/−10 bp) (**Figure 1G**). Considering that the B2M gene was not completely knocked out, thereafter, we named our GTKO/B2MKO/CIITAKO pigs as GBC-modified pigs.

Autopsy of GBC-Modified Pigs

We observed that the birth weight of GBC-modified piglets except for piglet P4 was lower than WT piglets, and the birth weight of the smallest piglets only was 147 g (**Figure 2A**). The piglet P4 survived for 19 days but other piglets died soon after birth. Next, we recloned the GBC-modified pigs using the fibroblast cells of piglet P4 for donor cells, obtained three live piglets, namely, P4P1, P4P2, and P4P3, and they survived for 93, 13, and 12 days, respectively. We performed the autopsy of piglets P4P1 and P4P2 and found a lot of spot bleeding in the kidney of the piglet P4P2 (**Figures 2B,C**) and severe suppuration and necrosis in the upper part of the lungs (**Figure 2D**), enlarged the peripulmonary lymph nodes (**Figure 2E**) and adhesion between the lungs and chest wall (**Figure 2F**) in the piglet P4P1, and suspected severe respiratory pathogen infection. These issues suggested that the modification of B2M and CIITA genes affected these procine's health and made them susceptible to pathogenic microorganisms.

Functional Identification of GGTA1, B2M, and CIITA Genes in GBC-Modified Pigs

To verify that the three genes are functionally inactive or impaired in GBC-modified pigs, we first detected their mRNA

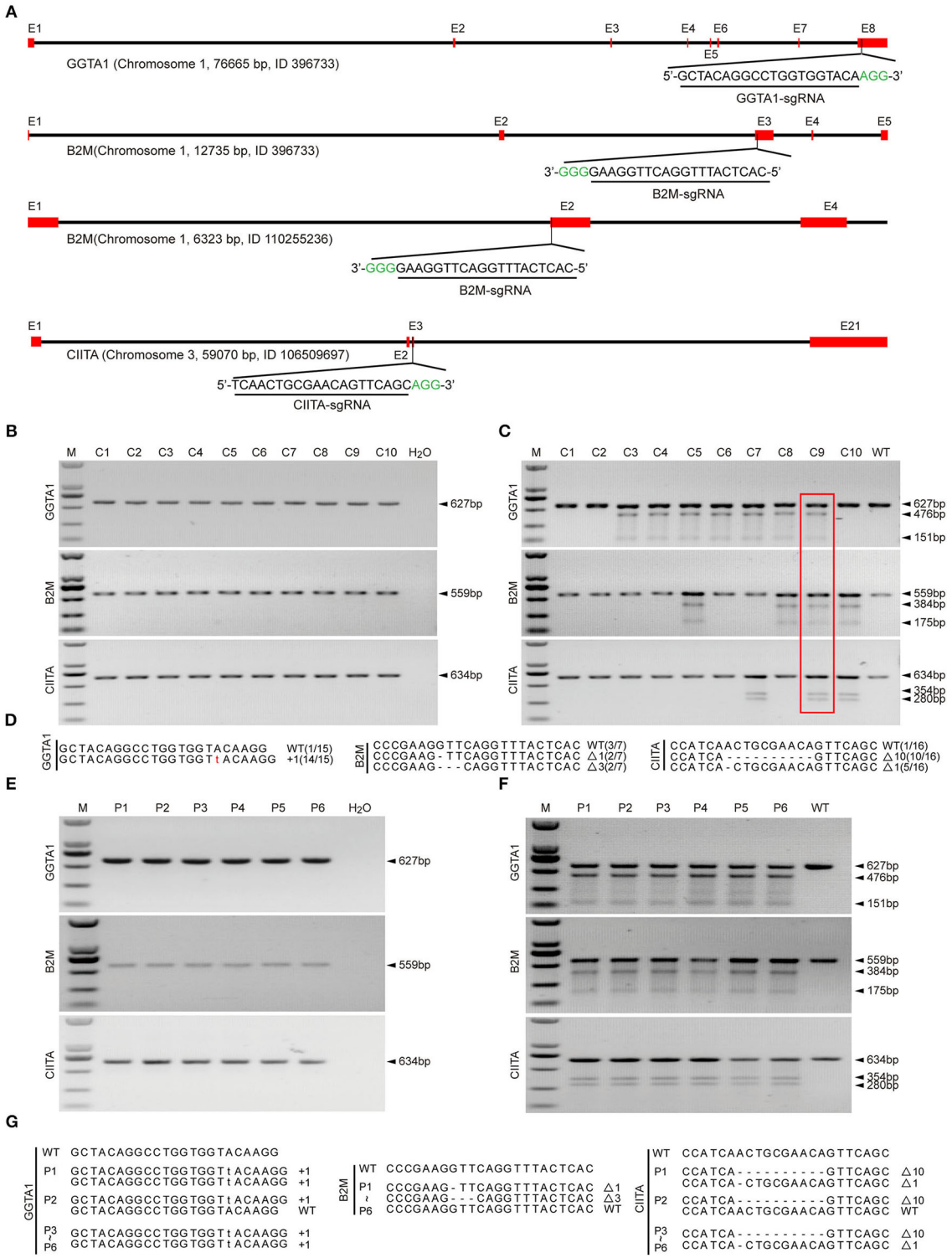

FIGURE 1 | Establishment of GBC-modified cell colonies and generation of GBC-modified pigs. **(A)** Schematic diagram of targeting to porcine GGTA1, B2M, and CIITA genes by the CRISPR/Cas9 system. **(B)** PCR products harboring the targeting regions of GGTA1, B2M, and CIITA genes from cell colonies (M, DNA maker DL2000; C, colony). **(C)** Identification of postive cell colonies by T7EI cleavage assay. The colony C9 is positive for triple-gene modification. **(D)** Genotypes of colony C9 by Sanger sequencing. **(E)** PCR products harboring the targeting regions of GGTA1, B2M, and CIITA genes from cloned pigs (P, pig). **(F)** Identification of cloned pigs by T7EI cleavage assay. **(G)** Genotypes of cloned pigs by Sanger sequencing.

TABLE 1 | The embryo transfer and generation of GBC-modified piglets.

Recipients	Donor cells	No. of transferred embryos	Pregnancy (%)	Days of pregnancy	No. of offspring (alive)
1	Colony C9	210	–	–	–
2		205	+	119	1(1)
3		300	+	117	1 (Stillborn)
4		280	–	–	–
5		300	–	–	–
6		270	+	129	2(1)
7		270	+	118	1 (Stillborn)
8		280	–	–	–
9		280	–	–	–
10		223	–	–	–
11		300	–	–	–
12		241	+	114	1(1)
13		220	–	–	–
Total		3,379	5(38.5%)		6(3)

expression level in tissues. As a result, GGTA1 mRNA expression level was significantly decreased in the heart and the lungs, but that was greatly increased in the liver and was comparable in the kidney when compared to the wild type. Meanwhile, the mRNA expression levels of the B2M and CIITA genes were either elevated or comparable in GBC-modified pigs to WT pigs (**Figure 3A**). These results indicated that the mutated three genes still can be transcribed into mRNA.

Given that the mRNA cannot reflect whether the mutated B2M and CIITA genes were knocked out, we further detect the protein expression levels of the three genes by immunohistochemistry or immunofluorescence on a tissue level. As a result, the GGTA1 gene was dysfunctional (**Figure 3B**), but B2M and CIITA proteins still were obviously detected in GBC-modified pigs (**Figure 3C**). Therefore, we speculated that the B2M and CIITA genes with short-fragment insertion or deletion will accelerate the upregulation of nonsense mRNA and protein expression levels. Given the above results, we directly analyzed the mRNA expression levels of SLA-I and four isoforms of SLA-II (SLA-II DOB, SLA-II DQB1, SLA-II DRA, and SLA-II DRB1) in GBC-modified pigs. The result showed that the heart, liver, spleen, and kidney of GBC-modified pigs had decreased expression levels of SLA-I and SLA-II mRNA than those of WT pigs (**Figure 4A**). Consistently, the protein expression levels of SLA-I and SLA-II DR in the liver were significantly decreased compared with WT (**Figure 4B**). We also detected the percentage of CD4 and CD8 T-cells from CD3-positive PBMCs derived from WT and GBC-modified pigs. The result showed that the percentage of CD8-positive cells was decreased compared with WT pigs, demonstrating that the mutation of B2M and CIITA genes led to the impaired CD8 T-cell development in GBC-modified pigs (**Figure 4C**). Moreover, the SLA-I had a significantly lower level in umbilical vein endothelial cells (UVECs) of GBC-modified pigs than those of WT pigs. After treatment with IFN-γ, SLA-I levels were significantly upregulated in both WT and GBC UVECs, but the higher upregulated SLA-I level of WT UVECs than that of GBC UVECs (**Figures 5A,B**), suggesting that B2M in CBG pigs was not completely deleted. Although the SLA-II DR and SLA-II DQ had a similar level between WT and GBC UVECs when untreated with IFN-γ, their levels were significantly upregulated in WT UVECs but not in GBC UVECs when treated with IFN-γ (**Figures 5A,C**), suggesting that the CIITA gene cannot effectively transactivate the expression of SLA-II molecules in GBC UVECs, even with IFN-γ treatment. Therefore, these results finally determined that B2M and CIITA genes in our GBC-modified pigs were dysfunctional or functionally impaired.

Transcriptome Analysis of PBMC of the Spleen in GBC-Modified Pigs

To further investigate the effects of GBC modification on the porcine immune system, we performed RNA-seq and analyzed the transcriptional profile of the spleen PBMC of GBC-modified pigs. The high Pearson correlation coefficient (**Supplementary Figure 1A**) and no significant differences in the gene expression among the biological replicates (**Supplementary Figure 1B**) showed that the RNA-seq data were reliable and met the conditions for differential expression analysis. Using the *P*-value ($P < 0.05$) and fold change (FC > 2) as the different standards for analysis, a total of 150 differential expression genes (DEGs) were detected between WT and GBC-modified pig's spleen PBMCs, including 68 upregulated genes and 82 downregulated genes (**Figures 6A,B**). Notably, a cluster of SLA genes was significantly downregulated in GBC-modified pigs, including SLA-DRB1, SLA-DQA1, SLA-DRA, SLA-DQB1, SLA-DOA, SLA-DMA, SLA-DMB, and SLA-DOB. Additionally, the expression of GGTA1, B2M, and CIITA genes in GBC-modified pig's spleen PBMCs also had no significant change compared with WT (**Supplementary Figure 2**). These findings were consistent with our qPCR results. Furthermore, the GO analysis of 150 DEGs revealed enrichment of 365 GO terms ($P < 0.05$). The top 20 significant enrichments indicated that

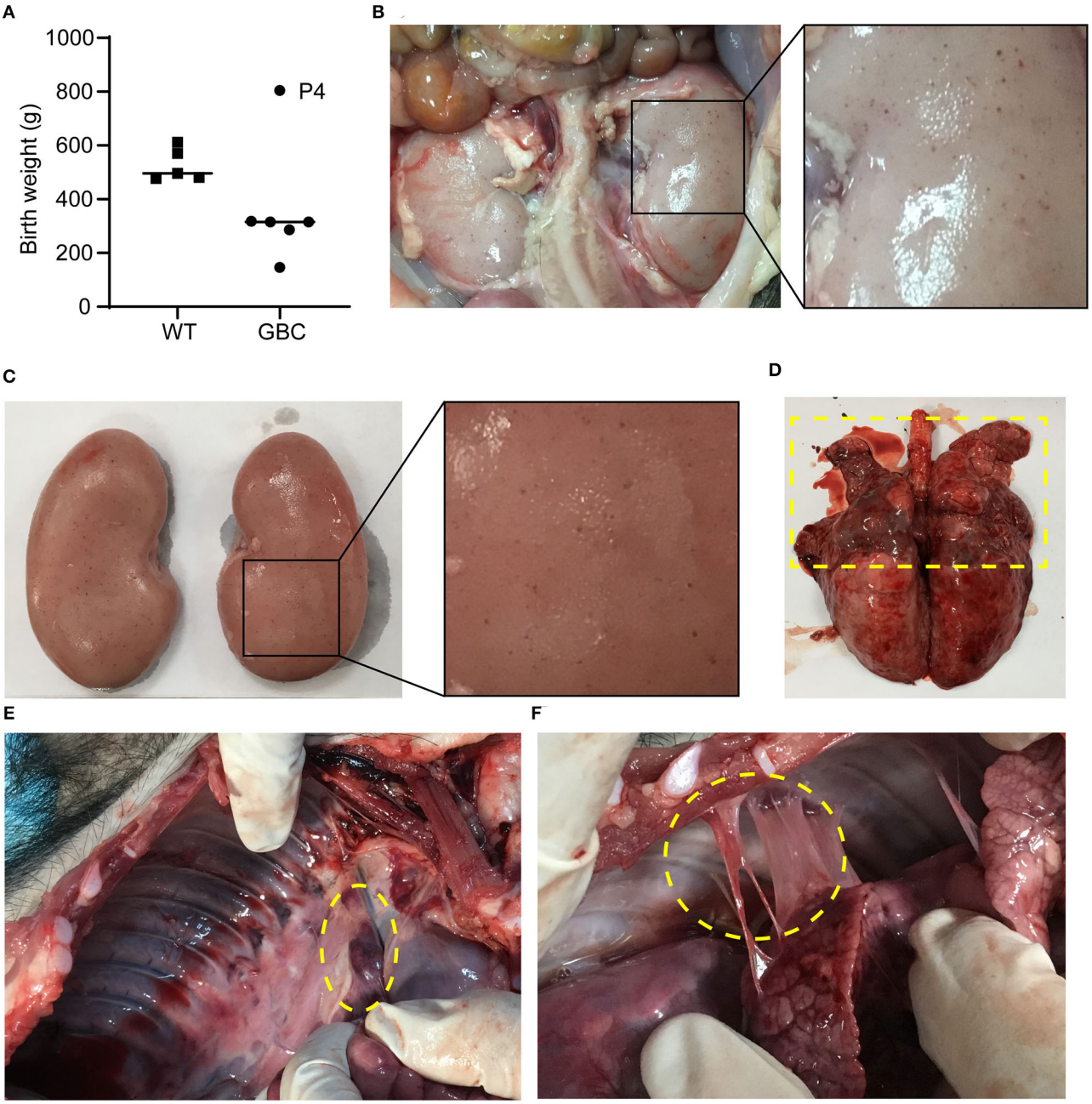

FIGURE 2 | Autopsy of GBC-modified pigs. **(A)** Birth weight of GBC-modified piglets. **(B,C)** A lot of spot bleeding in the kidney of GBC-modified pig P4P2 (13 days). **(D)** The lungs of GBC-modified pig P4P1 (93 days), indicating severe suppuration and necrosis in the upper part. **(E)** Enlarged peripulmonary lymph nodes in pig P4P1. **(F)** Adhesion between the lungs and the chest wall in pig P4P1.

CIITA knockout caused a severely impaired immune system, especially in antigen processing and presentation (**Figure 6C**). The pathway analysis based on the KEGG database revealed that many immune-related and infection-related pathways were enriched (**Figure 6D**), also suggesting that insufficiency of B2M and CIITA genes may make pigs susceptible to pathogenic microorganisms.

Immune Response of GBC-Modified Porcine Cells to Mixed Human Serum and Human PBMC

To investigate whether GBC-modified pigs had a weakened xenotransplantation rejection, we performed the IgG and IgM antibody-binding assays of mixed human serum and the mixed lymphocyte reaction between pigs and humans. As a result, the

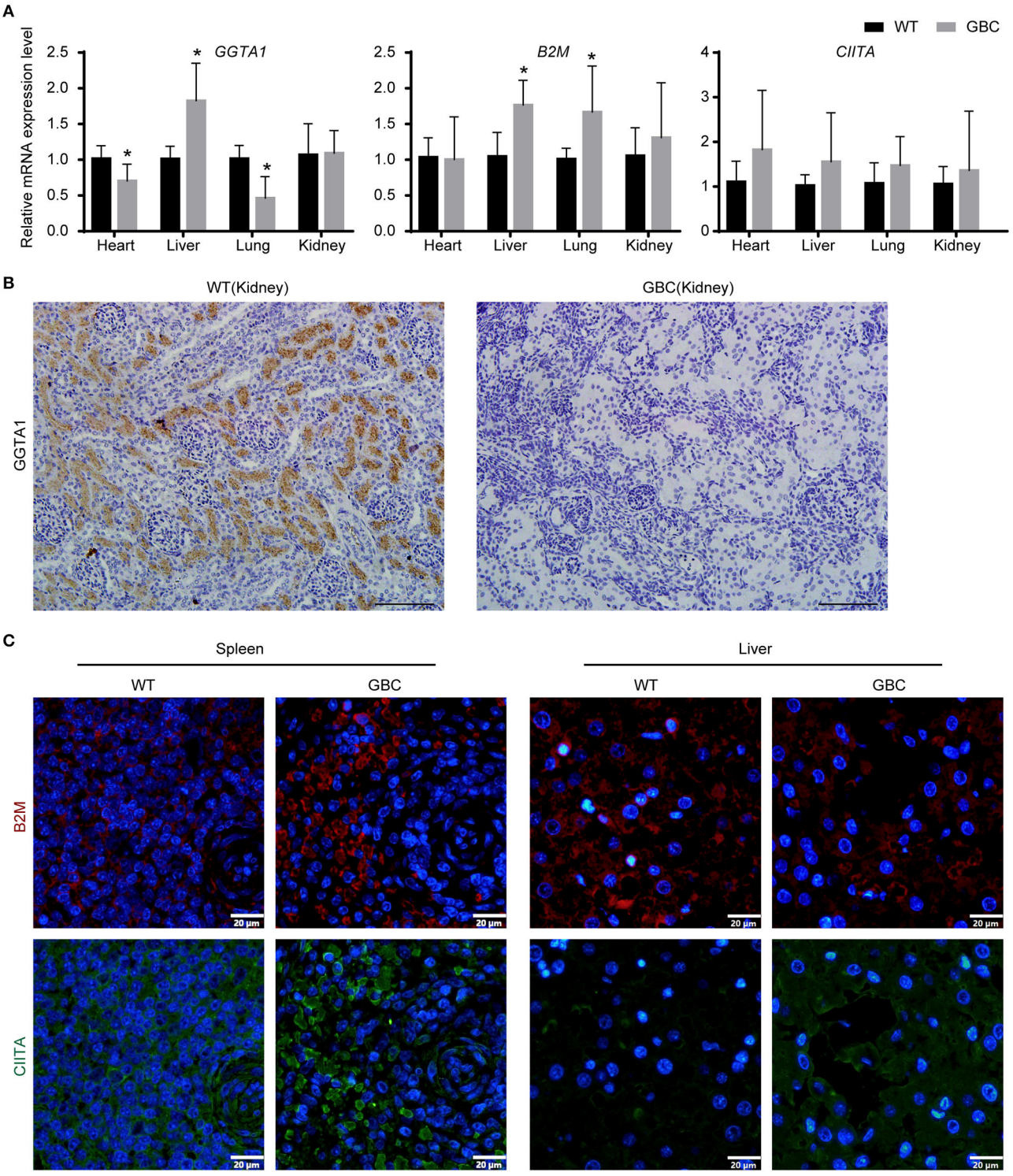

FIGURE 3 | Expression of GGTA1, B2M, and CIITA genes in GBC-modified pigs. **(A)** The mRNA expression levels of GGTA1, B2M, and CIITA genes in the heart, the liver, the lungs, and the kidney (*$P < 0.05$ vs. WT). **(B)** Immunohistochemical staining of αGal in the kidney (scale bar = 100 μm). **(C)** Immunofluorometric analysis of B2M and CIITA proteins in the spleen and the liver (scale bar = 20 μm).

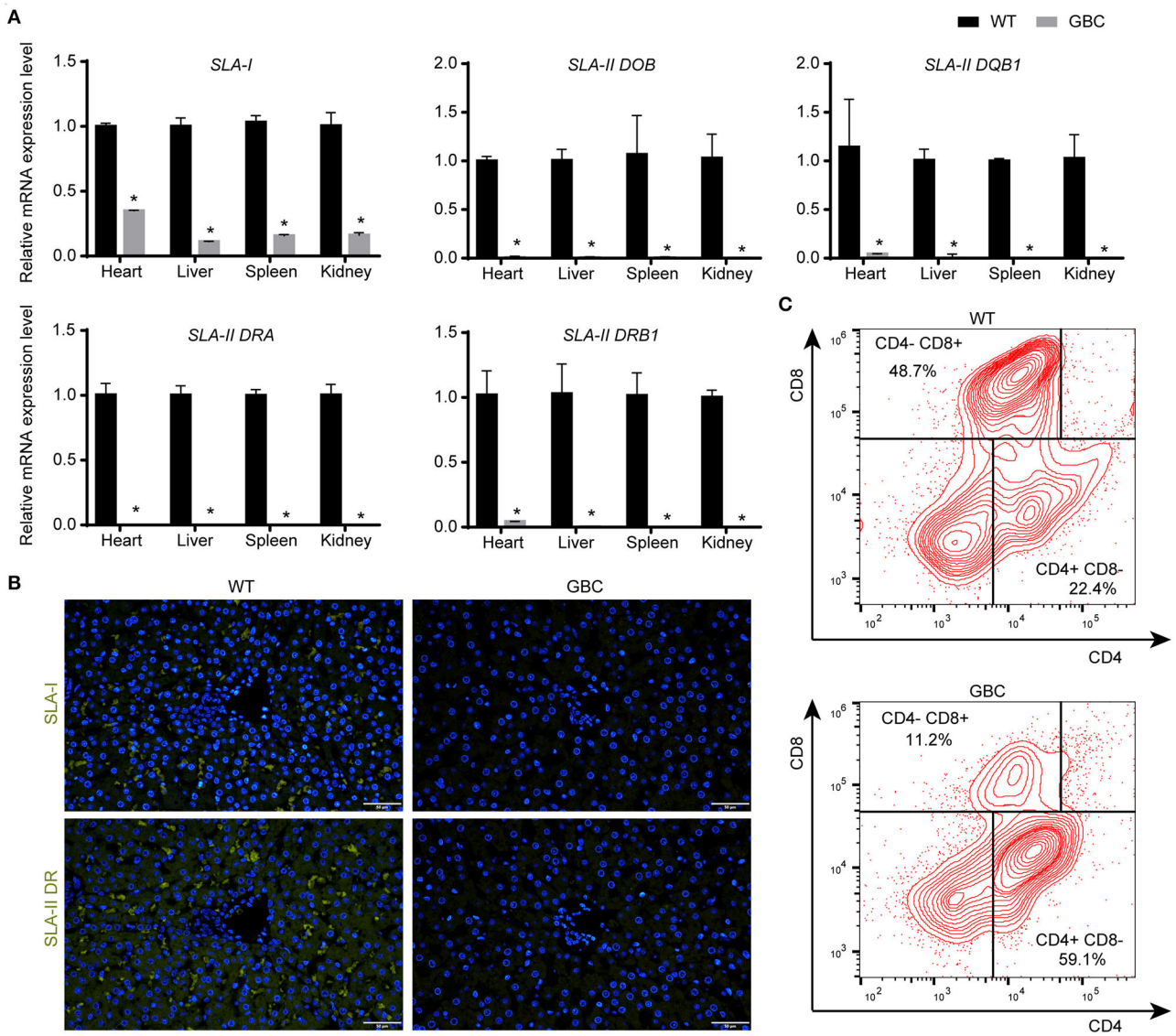

FIGURE 4 | Expression of SLA-I and SLA-II genes, and alteration of T-cell subtype (CD4 and CD8) in GBC-modified pigs. **(A)** The mRNA expression levels of SLA-I and four isoforms of the SLA-II gene in the heart, liver, lung, and kidney (*$P < 0.05$ vs. WT). **(B)** Immunofluorometric analysis of SLA-I and SLA-II DR molecules in the liver (scale bar = 50 μm). **(C)** The percentage of $CD4^+/CD8^-$ and $CD4^-/CD8^+$ T-cells in PBMCs derived from WT and GBC-modified pigs.

human antibodies IgM but not IgG binding to GBC-modified porcine fibroblasts were obviously decreased compared with WT (**Figures 7A,B**). After the co-culture of porcine and human PBMCs, the proliferation rate of the human PBMC mixed with GBC porcine PBMCs as the stimulators was significantly lower than that of the human PBMC mixed with WT porcine PBMCs (**Figures 7C,D**). Therefore, our GBC-modified pigs can attenuate xenogeneic immune rejection.

DISCUSSION

The development of CRISPR/Cas9 systems makes porcine genome engineering to be simple, accompanied with the increasingly multiple genetically modified pigs available for xenotransplantation research, and xenotransplantation is more likely to be close to the clinic. Here, we generated the GGTA1, B2M, and CIITA triple-gene-modified *Diannan* miniature pigs with CRISPR/Cas9 system in combination with SCNT. Recently, Fu et al. (18) also obtained the pigs with the knockout of GGTA1, B2M, and CIITA genes using the same technology. Differently, they applied the multiple sgRNAs to target each gene, which cloud increase the editing efficiency but simultaneously increased the risk of off-targets. Peng et al. (19) deemed it necessary to minimize the number of sgRNAs for reducing the negative effects caused by the off-target editing when a pool of sgRNAs was used simultaneously. In this study, we only selected one sgRNA for each target gene, aiming to decrease

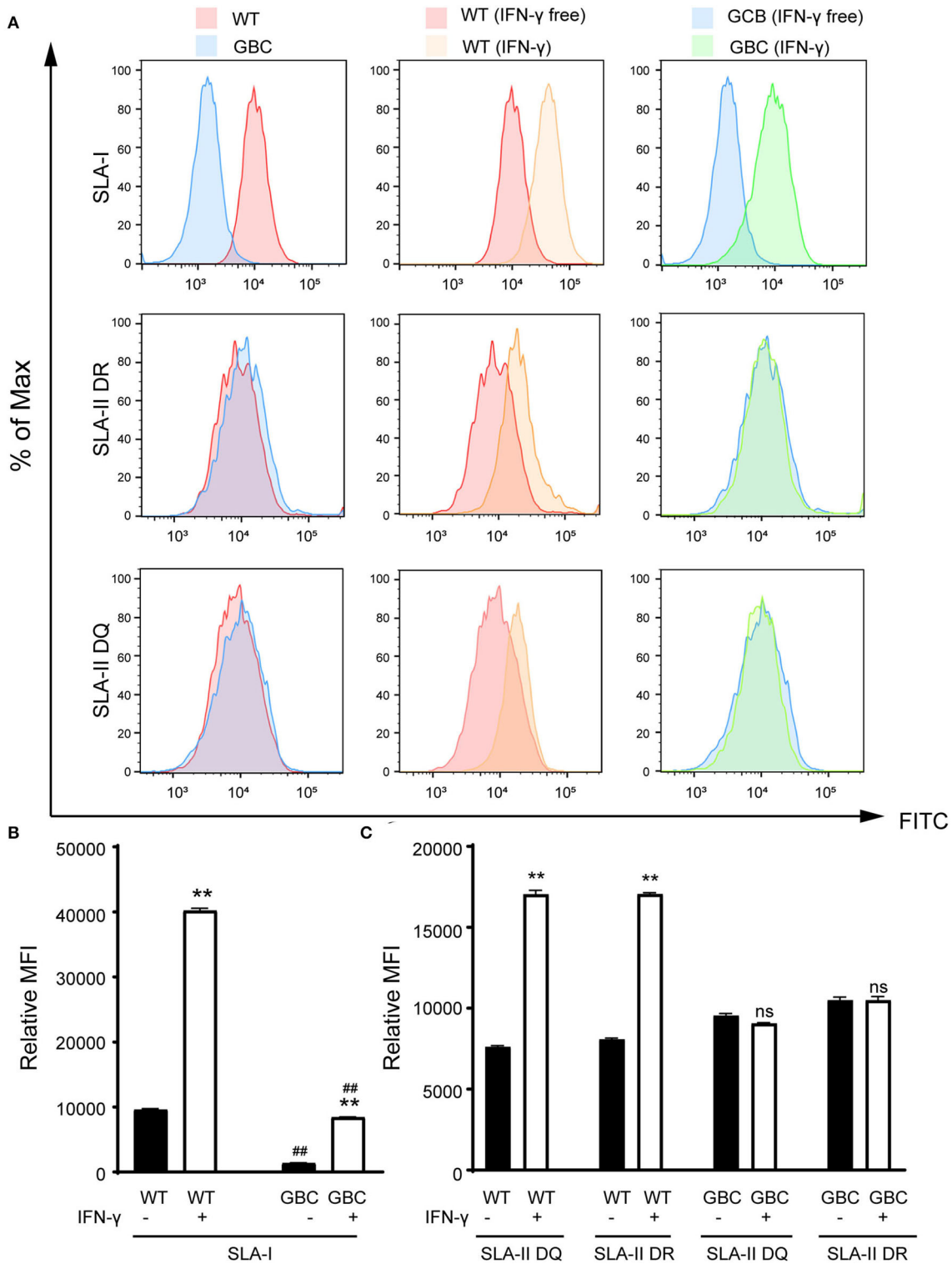

FIGURE 5 | Flow cytometry analysis of expression of SLA-I, SLA-II DR, and SLA-II DQ molecules in the umbilical vein endothelial cells (UVECs) of GBC-modified pigs. **(A)** The expression of the SLA-I molecule is lower in GBC-modified pigs than WT pigs. Additionally, interferon-γ treatment caused an increase in the number of SLA-I molecules in both GBC-modified and WT pig UVECs, but WT had a higher increase than the other. The expression of SLA-II DR and DQ molecules was comparable between GBC-modified and WT pig UVECs. After interferon-γ treatment, the expression of SLA-II DR and DQ molecules was increased in WT pig UVECs but not changed in GBC-modified pig UVECs. **(B,C)** Relative mean immunofluorescence intensity (MFI) of SLA-I **(B)**, SLA-II DR, and SLA-II DQ **(C)** in WT and GBC-modified pig UVECs treated with or without IFN-γ. Data of three dependent experiments are presented. $^{**}P < 0.01$ vs. IFN-γ-free; $^{\#\#}P < 0.01$ vs. WT.

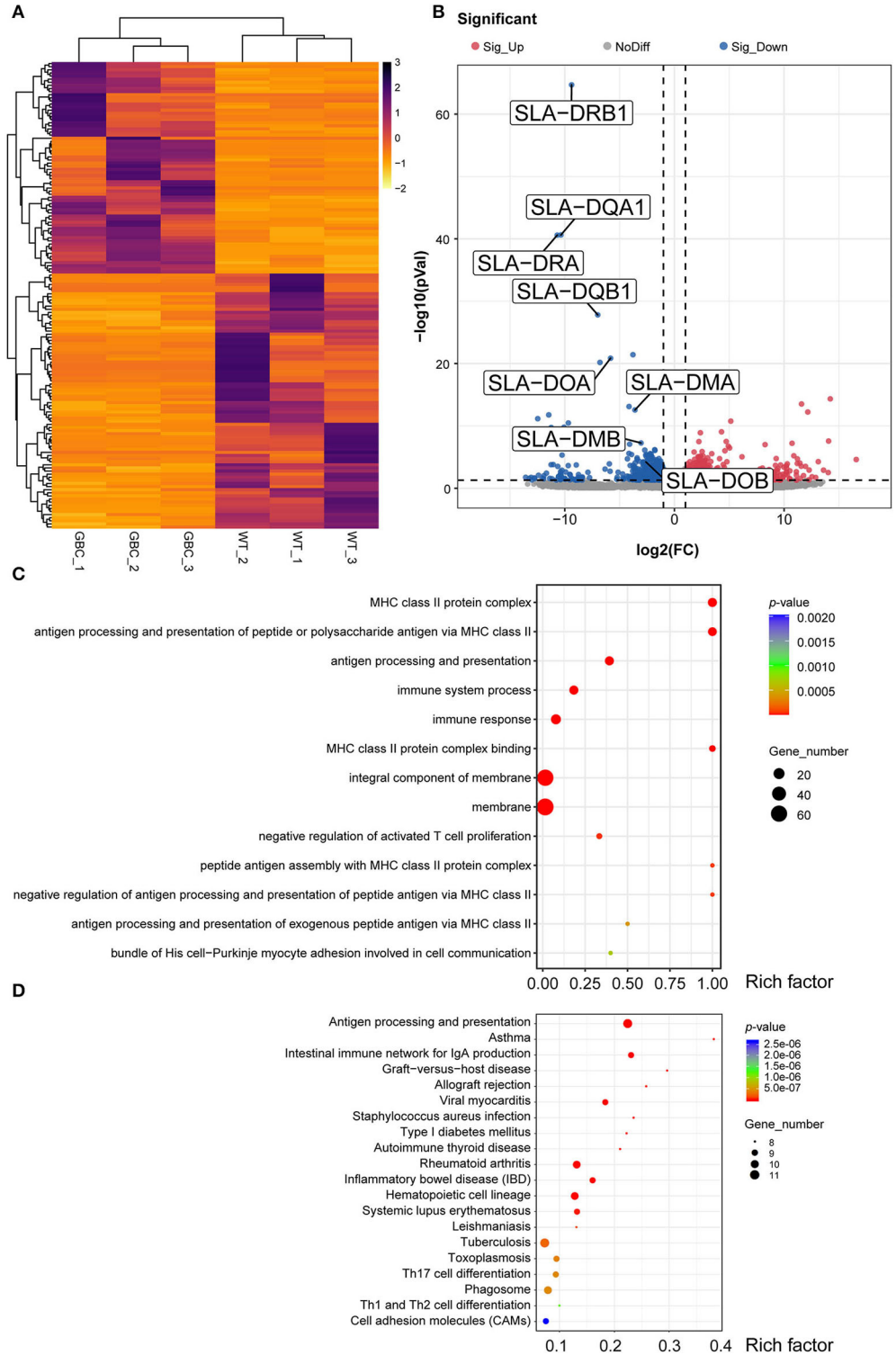

FIGURE 6 | Transcriptome profiling of PBMCs in GBC-modified pig's spleen. **(A)** Heatmap of 150 significant DEGs ($P < 0.05$) between GBC-modified and WT pigs. **(B)** A volcano plot between GBC modified and WT pigs, including 68 upregulated genes and 82 downregulated genes. **(C)** The top 13 Gene Ontology (GO) enrichments of DEGs. The *y*-axis is the name of each category, the *x*-axis is their rich factor. Rich factor = numbers of genes at a category/total numbers of genes at GO analysis. **(D)** The top 20 Kyoto Encyclopedia of Genes and Genomes (KEGG) pathways of DEGs. The *y*-axis is the name of each category, and the *x*-axis is their rich factor. Rich factor = numbers of genes at a pathway/total numbers of genes at KEGG analysis. The number of genes enriched in each category was shown at the size of each circular.

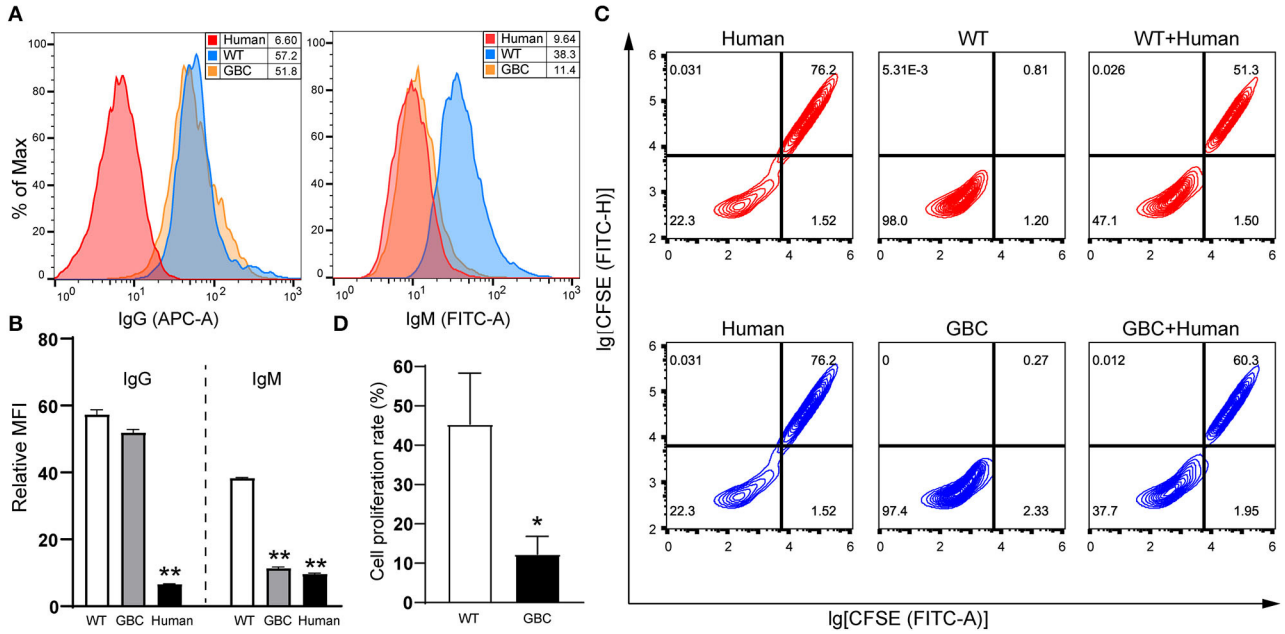

FIGURE 7 | Evaluation of anti-immunological rejection effectiveness of GBC-modified pigs. **(A)** Reduction of human IgM binding to GBC-modified pig fibroblast cells. **(B)** Relative mean immunofluorescence intensity (MFI) of IgG and IgM antibodies binding to WT, GBC-modified, and human fibroblast cells treated with mixed human serum. Data of three dependent experiments are presented (**$P < 0.01$ vs. WT). **(C)** Proliferation analysis of human peripheral blood mononuclear cells (PBMCs) after stimulation with porcine PBMCs by flow cytometry, and human PBMCs were labeled with CFSE. **(D)** Quantification of the proliferation rate of human PBMCs stimulated with porcine PBMCs (*$P < 0.05$ vs. WT).

the risk of off-targets. It has been known that there were at least two copies of the B2M gene in the pig genome. For the B2M gene, we designed the single sgRNA for targeting its two copies. Unfortunately, only one copy of the B2M gene was mutated in our GBC-modified pigs, resulting in the reduction of SLA-I expression rather than deficiency. In addition, GGTA1, B2M, and CIITA genes appeared two genotypes of WT and 1-bp insertion (+1/WT), three genotypes of WT, 1- and 3-bp deletion (Δ1/Δ3/WT), and three genotypes of WT, 1- and 10-bp deletion (Δ1/Δ10/WT) in the single-cell colony C9, respectively. Correspondingly, our GBC-modified pigs also showed two genotypes, the pig P2 carrying the genotypes of +1/WT, Δ1/Δ3/WT, and Δ10/WT and the others carrying the genotypes of +1/+1, Δ1/Δ3/WT, and Δ1/Δ10 in GGTA1, B2M, and CIITA genes, respectively. Therefore, we speculated that the colony C9 did not grow from a single cell but rather formed from a mixed cell population in the cell culture.

In the GBC-modified pigs, we found that the mRNA expression levels of GGTA1, B2M, and CIITA genes in some tissues were comparable or upregulated compared with WT pigs. Recently, a similar phenomenon was also reported in zebrafish and mice, in which the short insertions or deletions in some genes triggered genetic compensation that pretends that these mutant mRNAs have no function, thus leading them to transcribe more mRNAs for genetic compensation (20). However, the α1,3-galactosyltransferase was undetectable, and thus, we speculated that the mRNA of the mutated GGTA1 gene was degraded by a nonsense-mediated mRNA decay pathway (21). In addition, the fluorescence intensity of B2M and CIITA was comparable with WT. It might be either due to alternative splicing that produced an isoform protein in the mRNA maturation process or due to translation that might be reinitiated at exons after the modified site to form a truncated protein after mRNA maturation (22, 23). Nevertheless, these isoforms or truncated proteins were dysfunctional, resulting from the reduced SLA-I and SLA-II molecules in GBC-modified pigs. In **Figure 5**, we found that the expression levels of SLA-II DR and DQ in the GBC UVECs without IFN-γ induction were similar to WT. After treatment with IFN-γ, the expression levels of SLA-II DR and DQ in WT UVECs were upregulated, but no changes were observed in GBC UVECs. The SLA-II molecules were mainly expressed in primarily antigen-presenting cells such as macrophages, dendritic cells, and B cells and often do not express in endothelial cells but can be induced by IFN-γ (24). Based on our results, we suspect that IFN-γ hardly induces SLA-II expression in UVECs porcine, thus leading to minor changes between WT and GBC UVECs. Importantly, the GBC modification can alleviate the immune response to human serum antibodies and PBMCs and contributed to the survival of porcine skin in pig-to-non-human primate xenotransplantation (data not shown). Therefore, we believe that the skin of GBC-modified pigs is valuable for patients with severe burns, especially for patients that are highly sensitized to HLA-I and II.

In pig-to-human xenotransplantation, porcine xenoantigens, including αGal epitopes, can initiate the binding of human

natural antibodies, IgG and IgM, thus leading to complement activation and cause HAR. It has been demonstrated that the knockout of the GGTA1 gene can alleviate effectively HAR (25). Here, we also confirmed that the inactivation of the GGTA1 gene can attenuate HAR because the ratio of human IgM binding to fibroblast cells of the GBC-modified pigs was decreased (**Figure 7A**). In our previous study, simultaneous knockout of GGTA1, CMAH, and β4GalNT2 genes reduced the binding ability of human IgG and IgM by 90% (26), which essentially overcome HAR. Therefore, we suggested that multiple genetically modified donor pigs for xenotransplantation should be considered to delete the two other xenoantigens Neu5Gc and SDa, except αGal epitopes.

The SLA molecules play an important role in cellular immune response in pig-to-human xenotransplantation. To ensure the long-term survival of xenografts, the SLA molecules could be considered for knockout or knockdown. The donor pigs carrying B2M null or SLA-I deficiency had been generated and demonstrated that these genetic modifications can effectively improve the survival of xenografts (14, 27). However, several studies indicated that the inactivation of SLA-I molecules impaired the porcine immune system and led them to susceptibility to infection. In addition, these pigs need to be kept under strict hygienic housing conditions to maintain their healthy growth (22, 28). Our results of the autopsy and transcriptome profiling also demonstrated that B2M and CIITA knockout destroyed the porcine immune system, resulting in susceptibility to pathogenic microorganisms. It has been reported that the survival times of the pigs with SLA-I inactivation did not exceed 4 weeks (28). In this study, the longest survival of a GBC-modified pig (P4P1) with the decreased SLA-I expression was up to 93 days and it grew up to 6.8 kg when reaching sexual maturity. Therefore, we suggested that knockdown rather than knockout of B2M may be more conducive to the survival and breeding process of donor pigs. Of course, we may also consider the overexpression of human HLA molecules instead of deleting SLA molecules to weaken the response of human immune cells (29). On the other hand, the inactivation of CIITA abolished the expression of SLA-II molecules, seriously impaired the differentiation and maturation of porcine CD4 lymphocytes, and was likely to cause pigs to suffer from the bare lymphocyte syndrome (30). Therefore, it seemed more reasonable to knockdown SLA-II molecules by overexpressing the human dominant-negative CIITA gene (15). In summary, we believe that the knockout of B2M and CIITA had advantages and disadvantages: the advantages were that it prolonged the survival of xenografts and reduced the intensity of the immuno-suppressive regimen in xenotransplantation, and the disadvantages were that it harmed the health of pigs and increased the difficulty of breeding. Currently, although the CRISPR/Cas9 technology is simple and versatile for editing the pig genome, the goal of developing genetically modified donor pigs for xenotransplantation is to enable pigs to be used in the clinic. Therefore, to generate the tailored xenotransplantation donor pigs, we strongly suggest that we should carefully consider which genes are essential and non-essential for modification and formulate accurate gene-editing strategies for specific tissues or organs so that the CRISPR/Cas9 technology can more effectively serve the development of donor pigs.

CONCLUSIONS

In conclusion, we successfully generated the triple-gene (GGTA1, B2M, and CIITA)-modified pigs by the CRISPR/Cas9 system and SCNT. These pigs presented the absence of the expression of α1,3-galactosyltransferase and SLA-II and the downregulation of the expression of SLA-I, which can enhance the ability of immunological tolerance in pig-to-human xenotransplantation. However, CIITA knockout caused a significant decrease in a cluster of SLA-II molecules, involved in immune- and infection-relevant pathways, including antigen processing and presentation and viral myocarditis, and made these pigs susceptible to pathogenic microorganisms.

DATA AVAILABILITY STATEMENT

The datasets presented in this study can be found in online repositories. The names of the repository/repositories and accession number(s) can be found at: https://ngdc.cncb.ac.cn/gsub/submit/gsa/subCRA008147/finishedOverview, CRA005606.

ETHICS STATEMENT

The animal study was reviewed and approved by Animal Care and Use Committee of Yunnan Agricultural University (permission code: YAUACUC01). Written informed consent was obtained from the owners for the participation of their animals in this study.

AUTHOR CONTRIBUTIONS

H-JW, H-YZ, HY, and KX designed the research. SC, KX, HY, YZ, CY, JW, HL, and BJ performed the molecular experiments and analyzed data. DJ transfected the cell and performed a cell culture. JG, H-JW, HZ, TN, and TW carried out SCNT and embryo transfer. KX wrote the manuscript. H-YZ, XH, MAJ, and H-JW revised the manuscript and validated the data. All authors contributed to the article and approved the submitted version.

FUNDING

The work was supported by the grants from the National Key R&D Program of China (grant no. 2019YFA0110700), the Major Science and Technology Project of Yunnan Province (grant no. 202102AA310047), and the Innovative Research Team of Science and Technology in Yunnan Province.

ACKNOWLEDGMENTS

We thank the Ministry of Science and Technology of the People's Republic of China and the Yunnan Provincial Science

and Technology Department for the support provided for this research.

SUPPLEMENTARY MATERIAL

The Supplementary Material for this article can be found online at: https://www.frontiersin.org/articles/10.3389/fvets.2022.848833/full#supplementary-material

Supplementary Figure 1 | Verification of RNA-seq data quality. **(A)** The Pearson correlation coefficient between GBC-modified and WT pigs. **(B)** Boxplots of the gene expression distributions.

Supplementary Figure 2 | Expression levels of GGTA1, B2M, and CIITA genes analyzed by RNA-seq in the PBMCs of the pig's spleen.

Supplementary Table 1 | Sample information.

Supplementary Table 2 | The primers of qPCR.

REFERENCES

1. Lu T, Yang B, Wang R, Qin C. Xenotransplantation: current status in preclinical research. *Front Immunol.* (2019) 10:3060. doi: 10.3389/fimmu.2019.03060
2. Choi A, Han JJ. First porcine to human kidney transplantation performed in the United States. *Artif Organs.* (2021) 46:178–9. doi: 10.1111/aor.14139
3. Ekser B, Kumar G, Veroux M, Cooper DK. Therapeutic issues in the treatment of vascularized xenotransplants using gal-knockout donors in nonhuman primates. *Curr Opin Organ Transplant.* (2011) 16:222–30. doi: 10.1097/MOT.0b013e3283446c3c
4. Cooper DKC, Hara H, Iwase H, Yamamoto T, Li Q, Ezzelarab M, et al. Justification of specific genetic modifications in pigs for clinical organ xenotransplantation. *Xenotransplantation.* (2019) 26:e12516. doi: 10.1111/xen.12516
5. Lunney JK, Ho CS, Wysocki M, Smith DM. Molecular genetics of the swine major histocompatibility complex, the SLA complex. *Dev Comp Immunol.* (2009) 33:362–74. doi: 10.1016/j.dci.2008.07.002
6. Yang JY, Sarwal MM. Transplant genetics and genomics. *Nat Rev Genet.* (2017) 18:309–26. doi: 10.1038/nrg.2017.12
7. Wieczorek M, Abualrous ET, Sticht J, Álvaro-Benito M, Stolzenberg S, Noé F, et al. Major histocompatibility complex (MHC) class I and MHC class II proteins: conformational plasticity in antigen presentation. *Front Immunol.* (2017) 8:292. doi: 10.3389/fimmu.2017.00292
8. Martens GR, Reyes LM Li P, Butler JR, Ladowski JM, Estrada JL, et al. Humoral reactivity of renal transplant-waitlisted patients to cells from GGTA1/CMAH/B4GalNT2, and SLA class I knockout pigs. *Transplantation.* (2017) 101:e86–92. doi: 10.1097/TP.0000000000001646
9. Ladowski JM, Reyes LM, Martens GR, Butler JR, Wang ZY, Eckhoff DE, et al. Swine leukocyte antigen class II Is a xenoantigen. *Transplantation.* (2018) 102:249–54. doi: 10.1097/TP.0000000000001924
10. Qi P, Liu K, Wei J, Li Y, Li B, Shao D, et al. Nonstructural protein 4 of porcine reproductive and respiratory syndrome virus modulates cell surface swine leukocyte antigen class I expression by downregulating β2-microglobulin transcription. *J Virol.* (2017) 91:e01755–01716. doi: 10.1128/JVI.01755-16
11. Smith DM, Lunney JK, Ho CS, Martens GW, Ando A, Lee JH, et al. Nomenclature for factors of the swine leukocyte antigen class II system, 2005. *Tissue Antigens.* (2005) 66:623–39. doi: 10.1111/j.1399-0039.2005.00492.x
12. Masternak K, Muhlethaler-Mottet A, Villard J, Peretti M, Reith W. Molecular genetics of the Bare lymphocyte syndrome. *Rev Immunogenet.* (2000) 2:267–82.
13. Masternak K, Muhlethaler-Mottet A, Villard J, Zufferey M, Steimle V, Reith W, et al. is a transcriptional coactivator that is recruited to MHC class II promoters by multiple synergistic interactions with an enhanceosome complex. *Genes Dev.* (2000) 14:1156–66. doi: 10.1101/gad.14.9.1156
14. Wang Y, Du Y, Zhou X, Wang L, Li J, Wang F, et al. Efficient generation of B2m-null pigs via injection of zygote with TALENs. *Sci Rep.* (2016) 6:38854. doi: 10.1038/srep38854
15. Hara H, Witt W, Crossley T, Long C, Isse K, Fan L, et al. Human dominant-negative class II transactivator transgenic pigs - effect on the human anti-pig T-cell immune response and immune status. *Immunology.* (2013) 140:39–46. doi: 10.1111/imm.12107
16. Yu H, Long W, Zhang X, Xu K, Guo J, Zhao H, et al. Generation of GHR-modified pigs as Laron syndrome models via a dual-sgRNAs/Cas9 system and somatic cell nuclear transfer. *J Transl Med.* (2018) 16:41. doi: 10.1186/s12967-018-1409-7
17. Wei H, Qing Y, Pan W, Zhao H, Li H, Cheng W, et al. Comparison of the efficiency of Banna miniature inbred pig somatic cell nuclear transfer among different donor cells. *PLoS One.* (2013) 8:e57728. doi: 10.1371/journal.pone.0057728
18. Fu R, Fang M, Xu K, Ren J, Zou J, Su L, et al. Generation of GGTA1-/-β2M-/-CIITA-/- pigs using CRISPR/Cas9 technology to alleviate xenogeneic immune reactions. *Transplantation.* (2020) 104:1566–73. doi: 10.1097/TP.0000000000003205
19. Peng H, Zheng Y, Zhao Z, Li J. Multigene editing: current approaches and beyond. *Brief Bioinform.* (2021). doi: 10.1093/bib/bbaa396
20. El-Brolosy MA, Kontarakis Z, Rossi A, Kuenne C, Günther S, Fukuda N, et al. Genetic compensation triggered by mutant mRNA degradation. *Nature.* (2019) 568:193–7. doi: 10.1038/s41586-019-1064-z
21. Kurosaki T, Popp MW, Maquat LE. Quality and quantity control of gene expression by nonsense-mediated mRNA decay. *Nat Rev Mol Cell Biol.* (2019) 20:406–20. doi: 10.1038/s41580-019-0126-2
22. Hein R, Sake HJ, Pokoyski C, Hundrieser J, Brinkmann A, Baars W, et al. Triple (GGTA1, CMAH, B2M) modified pigs expressing an SLA class I(low) phenotype-effects on immune status and susceptibility to human immune responses. *Am J Transplant.* (2020) 20:988–98. doi: 10.1111/ajt.15710
23. Yang L, Church G, Zhao HY, Huang L, Gao Y, Wei HJ, et al. Porcine germline genome engineering. *Proc Natl Acad Sci USA.* (2021) 118:e2004836117. doi: 10.1073/pnas.2004836117
24. Chang CH, Fontes JD, Peterlin M, Flavell RA. Class II transactivator (CIITA) is sufficient for the inducible expression of major histocompatibility complex class II genes. *J Exp Med.* (1994) 180:1367–74. doi: 10.1084/jem.180.4.1367
25. Cooper DK, Ekser B, Ramsoondar J, Phelps C, Ayares D. The role of genetically engineered pigs in xenotransplantation research. *J Pathol.* (2016) 238:288–99. doi: 10.1002/path.4635
26. Yue Y, Xu W, Kan Y, Zhao HY, Zhou Y, Song X, et al. Extensive germline genome engineering in pigs. *Nat Biomed Eng.* (2021) 5:134–43. doi: 10.1038/s41551-020-00613-9
27. Fischer K, Rieblinger B, Hein R, Sfriso R, Zuber J, Fischer A, et al. Viable pigs after simultaneous inactivation of porcine MHC class I and three xenoreactive antigen genes GGTA1, CMAH and B4GALNT2. *Xenotransplantation.* (2020) 27:e12560. doi: 10.1111/xen.12560
28. Sake HJ, Frenzel A, Lucas-Hahn A, Nowak-Imialek M, Hassel P, Hadeler KG, et al. Possible detrimental effects of beta-2-microglobulin knockout in pigs. *Xenotransplantation.* (2019) 26:e12525. doi: 10.1111/xen.12525

29. Abicht JM, Sfriso R, Reichart B, Langin M, Gahle K, Puga Yung GL, et al. Multiple genetically modified GTKO/hCD46/HLA-E/hbeta2-mg porcine hearts are protected from complement activation and natural killer cell infiltration during ex vivo perfusion with human blood. *Xenotransplantation.* (2018) 25:e12390. doi: 10.1111/xen.12390
30. Reith W, Mach B. The bare lymphocyte syndrome and the regulation of MHC expression. *Annu Rev Immunol.* (2001) 19:331–73. doi: 10.1146/annurev.immunol.19.1.331

Conflict of Interest: The authors declare that the research was conducted in the absence of any commercial or financial relationships that could be construed as a potential conflict of interest.

Publisher's Note: All claims expressed in this article are solely those of the authors and do not necessarily represent those of their affiliated organizations, or those of the publisher, the editors and the reviewers. Any product that may be evaluated in this article, or claim that may be made by its manufacturer, is not guaranteed or endorsed by the publisher.

frontiers | Frontiers in Veterinary Science

ORIGINAL RESEARCH
published: 03 May 2022
doi: 10.3389/fvets.2022.877322

Video Endoscopy-Guided Intrabronchial Spray Inoculation of *Mycobacterium bovis* in Goats and Comparative Assessment of Lung Lesions With Various Imaging Methods

Nadine Wedlich[1], Julia Figl[1†], Elisabeth M. Liebler-Tenorio[1*], Heike Köhler[1], Kerstin von Pückler[2], Melanie Rissmann[3†], Stefanie Petow[4], Stefanie A. Barth[1], Petra Reinhold[1], Reiner Ulrich[3†], Leander Grode[5], Stefan H. E. Kaufmann[6,7,8] and Christian Menge[1]

[1] *Institute of Molecular Pathogenesis, Friedrich-Loeffler-Institute (FLI), Jena, Germany,* [2] *Clinic for Small Animals – Radiology, Justus-Liebig-University Giessen, Giessen, Germany,* [3] *Department of Experimental Animal Facilities and Biorisk Management, Friedrich-Loeffler-Institute, Greifswald-Insel Riems, Germany,* [4] *Institute for Animal Welfare and Animal Husbandry, Friedrich-Loeffler-Institute, Celle, Germany,* [5] *Vakzine Projekt Management GmbH, Hannover, Germany,* [6] *Director Emeritus, Max Planck Institute for Infection Biology, Berlin, Germany,* [7] *Emeritus Group for Systems Immunology, Max Planck Institute for Multidisciplinary Sciences, Göttingen, Germany,* [8] *Hagler Institute for Advanced Study, Texas A&M University, College Station, TX, United States*

Bovine tuberculosis (bTB) not only poses a zoonotic threat to humans but also has a significant economic impact on livestock production in many areas of the world. Effective vaccines for humans, livestock, and wildlife are highly desirable to control tuberculosis. Suitable large animal models are indispensable for meaningful assessment of vaccine candidates. Here, we describe the refinement of an animal model for bTB in goats. Intrabronchial inoculation procedure *via* video-guided endoscopy in anesthetized animals, collection of lungs after intratracheal fixation *in situ*, and imaging of lungs by computed tomography (CT) were established in three goats using barium sulfate as surrogate inoculum. For subsequent infection experiments, four goats were infected with 4.7×10^2 colony-forming units of *M. bovis* by intrabronchial inoculation using video-guided endoscopy with spray catheters. Defined amounts of inoculum were deposited at five sites per lung. Four age-matched goats were mock-inoculated. None of the goats developed clinical signs until they were euthanized 5 months post infection, but simultaneous skin testing confirmed bTB infection in all goats inoculated with *M. bovis*. In tissues collected at necropsy, *M. bovis* was consistently re-isolated from granulomas in lymph nodes, draining the lungs of all the goats infected with *M. bovis*. Further dissemination was observed in one goat only. Pulmonary lesions were quantified by CT and digital 2D radiography (DR). CT revealed mineralized lesions in all the infected goats ranging from <5 mm to >10 mm in diameter. Small lesions <5 mm predominated. The DR failed to detect small lesions and to determine the exact location of lesions because of overlapping of pulmonary lobes. Relative volume of pulmonary lesions was low in three but high in one goat that also had extensive cavitation.

OPEN ACCESS

Edited by:
Mark Gray,
University of Edinburgh,
United Kingdom

Reviewed by:
Eduard Otto Roos,
Clinomics, South Africa
Ana Cláudia Coelho,
University of Trás-os-Montes and Alto Douro, Portugal

****Correspondence:***
Elisabeth M. Liebler-Tenorio
elisabeth.liebler-tenorio@fli.de

†Present addresses:
Julia Figl,
Institut für veterinär medizinische Untersuchungen, Austrian Agency for Health and Food Safety, Mödling, Austria
Melanie Rissmann,
Department of Viroscience, Erasmus Medical Centre, Rotterdam, Netherlands
Reiner Ulrich,
Institut für Veterinär-Pathologie, Fakultät für Veterinärmedizin, Leipzig University, Leipzig, Germany

Specialty section:
This article was submitted to Comparative and Clinical Medicine, a section of the journal Frontiers in Veterinary Science

Received: *16 February 2022*
Accepted: *01 April 2022*
Published: *03 May 2022*

Citation:
Wedlich N, Figl J, Liebler-Tenorio EM, Köhler H, von Pückler K, Rissmann M, Petow S, Barth SA, Reinhold P, Ulrich R, Grode L, Kaufmann SHE and Menge C (2022) Video Endoscopy-Guided Intrabronchial Spray Inoculation of Mycobacterium bovis in Goats and Comparative Assessment of Lung Lesions With Various Imaging Methods. Front. Vet. Sci. 9:877322. doi: 10.3389/fvets.2022.877322

CT lesions could be correlated to gross pathologic findings and histologic granuloma types in representative pulmonary lobes. In conclusion, video-guided intrabronchial inoculation with spray catheters, mimicking the natural way of infection, resulted in pulmonary infection of goats with *M. bovis*. CT, but not DR, presented as a highly sensitive method to quantify the extent of pulmonary lesions. This goat model of TB may serve as a model for testing TB vaccine efficacy.

Keywords: tuberculosis, *Mycobacterium bovis*, goat, inoculation, spray catheter, imaging, CT, histology

INTRODUCTION

Infections of ruminants with *M. bovis* and its close relative *M. caprae* have a significant economic impact on livestock production in many areas of the world (1–3), threaten wildlife populations (4), and cause zoonotic infections (5). Human tuberculosis (1) is predominantly associated with *Mycobacterium* (*M.*) *tuberculosis* infections and caused an estimated 1.5 million deaths in 2020 (4). Preventive measures in human medicine still mostly rely on vaccination with *Bacille Calmette-Guérin* (BCG), a vaccine developed almost a century ago. Intense efforts are ongoing to develop improved vaccines, specifically designed for certain age groups, individuals with co-infections, or distinct routes of application (6–8).

Appropriate, standardized animal models are indispensable to evaluate and compare the efficacy of new vaccines and immunization regimens. Information derived from laboratory rodent models allow for only limited translational extrapolation because of differences in respiratory anatomy and physiology, as well as immunologic features (9–11). Optimal non-human primate models have limited availability, as well as significant ethical and financial constraints (12). Goats are a well-suited model species for mycobacterial infections in both humans and ruminants (6, 13–15). The anatomy of their respiratory tract resembles more closely that of humans than that of rodents with regard to complex branching airways (16), vascularization (5, 17), and distribution of mucosa-associated lymphoid tissues (18). The size and body weight of goats are in the range of those of humans. This is advantageous, since the diameter of airways correlates with body weight (16). Goats are susceptible to natural infection with *M. bovis* and *M. caprae* and develop tuberculosis (19, 20). The disease takes a chronic course resulting in pulmonary lesions comparable to those in humans, e.g., granulomas and caverns (14, 20). Tuberculous granulomas in goats are fibrotic like in human TB which impedes the penetration of anti-TB drugs and efficacy of chemotherapy. This is difficult to reproduce in other animal models (21).

Goat models, however, are more difficult to standardize compared to laboratory rodent models, since goats are an outbread species resulting in higher individual variation. High numbers of experimental animals, on the other hand, are generally not feasible for practical reasons. Therefore, it is important that variables, like route of inoculation and read-out parameters, are standardized. Inoculation must be practicable, reproducible, and safe in terms of both unwanted adverse effects in the animals hampering the development of natural disease progression, and work safety for the experimenter. Different routes of inoculation, e.g., intratracheal, transthoracic, and endobronchial, using low doses of *M. bovis* or *M. caprae* have been successfully used (13, 15, 22, 23). These applications have in common that bacterial suspensions are administered as a bolus. The most common source of natural TB infection, however, are aerosolized bacteria which are inhaled and deposited in the respiratory tract of the recipient (24). This prompted the establishment of a caprine aerosol *M. bovis* infection model (21). Unfortunately, the model required high inoculation doses and did not result in the formation of cavernous lung lesions. Frequent development of such lesions is one of the peculiarities observed in caprine TB infection studies and an additional advantage of goats as human TB models. The seeder animal approach, e.g., exposure to infected goats by close contact, mimics natural infection most closely and is effective (25, 26). However, it suffers from the significant disadvantage that the exact time of infection and the infectious dose for individual animals remain unknown. High-definition video endoscopy and application *via* spray catheter to ensure optimal distribution have been used for other purposes, e.g., to distribute dyes throughout the colon resulting in higher detection rate of intraepithelial neoplasia in clinical oncology (27). Spray catheters have also been suggested as devices for intrathoracic aerosol chemotherapy (28). The use of spray catheters in respiratory infection studies would allow for aerosolizing the inoculum at defined sites in the bronchial tree while, at the same time, avoiding the disadvantages of aerosol application.

Current anti-TB vaccines only ameliorate lesion formation and bacterial load (29), making quantitative evaluation of lesions at high resolution indispensable to reliably unveil differences in vaccine efficacy. For large animal TB models, slicing of the entire lungs and semiquantitative scoring are commonly used, but imaging technologies like radiography (30), magnetic resonance imaging (31), and computed tomography (32) have also been assessed (13, 33, 34). A comparative evaluation of semiquantitative scoring of thinly sliced lungs and CT demonstrated superior quality of CT (13) and the latter technique was successfully applied in a series of TB studies on goats (23, 35). A limitation of this approach is, however, that the lungs have to be removed from infected animals, conserved, and treated to be no longer infectious, as CT devices are not regularly available in high containment animal facilities. This prevents the use of CT to monitor the development of TB lesions *intra vitam* during the course of the experiment. This could be more easily achieved by classical or digital 2D radiography (DR).

The aim of this study was further refinement of the infection model for *M. bovis* in goats. The endoscopy-guided deposition of a suspension at defined sites of the respiratory tract of young goats was established. Distribution of the inoculum in the lungs was investigated, and parameters for pulmonary CT analysis were defined. Lungs were fixed *in situ* to retain the original size of the lungs, thereby avoiding artifacts and leveraging objective determination of lesion sizes. The protocol applied for inoculation with *M. bovis via* spray catheter was used for this purpose for the first time to the best of our knowledge. Number, size, and spatial distribution of pulmonary lesions were assessed by CT imaging and digital radiography, and were compared to macroscopic and histological findings.

MATERIALS AND METHODS

Establishment of Intrabronchial Application Procedure and Pulmonary CT Imaging (Trial 1)

Animals

Three male castrated goats of the breed German Improved White were purchased from a conventional farm. They were transferred at the age of 3 months to the animal facility at Friedrich-Loeffler-Institut, Jena, Germany (FLI Jena). The goats were kept as one group on straw bedding, had access to hay and water *ad libitum*, and received age-adjusted quantities of concentrated feed. They had been vaccinated against *Clostridium* spp., *Mannheimia haemolytica*, and *Pasteurella trehalosi* in their herd of origin. Upon arrival at FLI Jena, they were screened for bacterial infections with *Salmonella* spp., *Mycoplasma* spp., *Pasteurella* spp., *Mycobacterium* spp., *Coxiella burnetti*, and *Chlamydia* spp. as well as for ecto- and endoparasites. They were negative for bacterial infections, but all the goats were infected with *Eimeria* spp. They were treated with antibiotics for 5 days [Baytril 10%; Bayer, Leverkusen, Germany; 2.5 mg/kg body weight (BW), s.c.] as a preventive measure and with a single dose of antiparasitics (Baycox; Bayer; 20 mg/kg BW, oral) within the first 2 weeks at FLI Jena. They were examined daily for general behavior, appetite, clinical symptoms, and rectal temperature. Their health status was documented using a scoring system.

Legislation and Ethical Approval

This study was carried out in strict accordance with European and National Law for the Care and Use of Animals. The protocol was reviewed by the Committee on the Ethics of Animal Experiments of the State of Thuringia, Germany, and approved by the competent authority (permit number: 22-2684-04-04-101/16, date of permission 20.04.2016). Every effort was made to minimize the suffering of the animals during the entire study. The stables were equipped with enrichments for activity, e.g., chains and different equipment for climbing.

Intrabronchial Application of Barium Sulfate

The goats were healthy, notably free of respiratory disease, and weighed ∼30 kg at the time of intrabronchial application. The animals were sedated with midazolam (Midazolam-ratiopharm© 15 mg/ml; Ratiopharm, Ulm, Germany; 0.5 mg/kg BW) and ketamine (Ketamin 10%, WDT, Garbsen, Germany; 10 mg/kg BW) intramuscularly. Then, they were transferred to an examination room and anesthetized intravenously (IV) with midazolam (Midazolam-ratiopharm© 15 mg/ml; 0.1 mg/kg BW) and ketamine (Ketamin 10%; 5 mg/kg BW). The pharynx was locally anesthetized by spraying with 2% lidocaine (Betapharm Arzneimittel, Augsburg, Germany).

For guided intrabronchial application of liquids, a technique described by Prohl et al. (36) for calves was adapted. The anesthetized goats were positioned in sternal recumbency on an examination table. In this trial, the 5.2 mm diameter of the bronchoscope was too big for the nasal passage of the goats and had to be inserted orally. A plastic tube (diameter: 2 cm, length: 20 cm) was placed into the goat's mouth, and a flexible video endoscope of 85 cm working length and outer diameter of 5.2 mm (Veterinary Video Endoscope 60001 VL 1, Storz, Tuttlingen, Germany) was inserted through the mouth into the trachea. To be able to immediately control the distribution of the inocula, a barium sulfate suspension (1 g $BaSO_4$ in 2.5 ml H_2O; WDT, Garbsen, Germany) was applied as radiography dense reference liquid. Aliquots of 1 ml of the barium sulfate suspension were placed at the *bronchus (b.) tracheobronchialis*, *b. principalis dexter*, and *b. principalis sinister* (**Figure 1**). Because of its viscosity, the suspension was applied through a standard catheter.

Necropsy

The goats were euthanized with pentobarbital-sodium (Release©, WDT; 150 mg/kg BW, IV) immediately after intrabronchial application while still in deep anesthesia. The lungs were fixed by intratracheal instillation with 4% neutral buffered formalin (NBF). For this, the goats were positioned on their back. The trachea was exposed and cut caudal of the larynx. A flexible tube attached to a container with 4% NBF located 30 cm above the

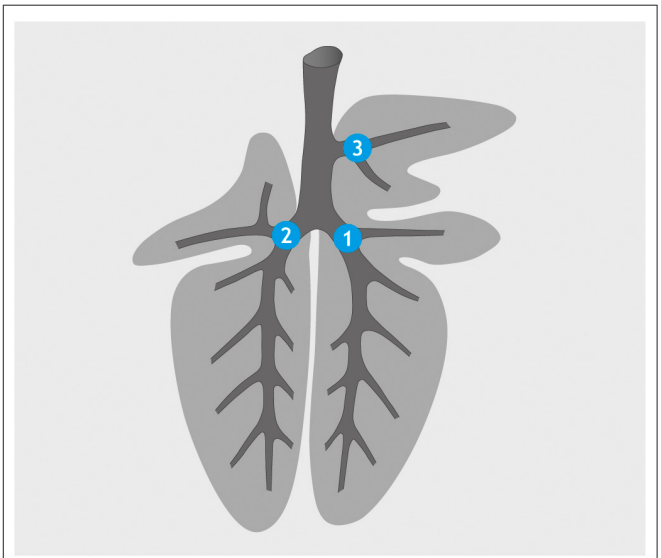

FIGURE 1 | Application sites for barium sulfate suspension (standard catheter): *bronchus* (*b.*) *principalis dexter* (1), *b. principalis sinister* (2), and *b. tracheobronchialis* (3).

thorax (for a pressure of about 30 mbar) was inserted into the trachea and 1.5 l of fixative allowed to fill the lungs. After 15 min, the trachea was closed, the thoracic cavity was opened, and the lungs were carefully removed. Mediastinal lymph nodes, the heart, and the esophagus were detached. The pulmonary surface was visually inspected, and gross lesions were documented. The lungs were stored in 4% NBF at 4°C.

Radiological Examination by Computed Tomography

For CT, the lungs were removed after 2 weeks from NBF and placed into two plastic bags inside a plastic container. The optimal settings for scanning were evaluated in this trial. The lungs were scanned in a position corresponding to sternal recumbency in a computer tomograph (Brilliance 16; Phillips, Hamburg, Germany) at 120 kV and 0.8 mm slice thickness and the use of the lung algorithm. Virtual slices were analyzed with Synedra personal view© (www.synedra.com). Initially, the lungs were scanned in plastic bags with a minute volume of formalin around the tissue. Since the intrapulmonary fixative obscured the airways, liquids were drained as much as possible from the lungs in the following scans.

Inoculation of Goats With *M. bovis*, *intra vitam*, and *post mortem* Studies (Trial 2)

Animals

For the infection experiment, eight male goats were obtained from the same source as in trial 1 and transferred to FLI Jena at an average age of 24 days. The nutrition regime was changed from milk replacer to a diet with concentrated feed, hay or hay cobs, and water *ad libitum* during the 1st weeks of life. The goats were kept in two groups in separate rooms on straw bedding. They had been vaccinated, were screened for infections, and received treatment as described for trial 1. They were castrated at the age of 3 months under sedation and local as well as systemic analgesia using a Burdizzoe emasculatome. At the age of 6 months, the goats were transferred to the biosafety level three animal facility at FLI in Greifswald–Insel Riems, Germany (FLI Riems). Air-conditioned rooms were located in the center of an experimental animal facility with several layers of negative air-pressure to prevent any release of pathogens. Rooms used to keep the animals for this study had an overall negative air pressure of 120 Pa relative to the outside environment and an air exchange rate of 9 times/h. The outgoing air was passed through HEPA filters. The rooms had artificial light for 12 h a day and were equipped with rubber mattresses. Chains, platforms for climbing, branches, and balls served as enrichment as described for trial 1.

Legislation and Ethical Approval

This study was carried out in strict accordance with European and National Law for the Care and Use of Animals. The protocol was reviewed by the Committee on the Ethics of Animal Experiments of the State of Mecklenburg-Western Pomerania, Germany and approved by the competent authority (permit number: 7221.3-1-084/16, date of permission: 08.02.2017). The infection experiment was conducted in a contained area at biosafety level 3 under supervision of the authorized institutional Agent for Animal Protection. Bronchoscopy was strictly performed under general anesthesia as described above. During the entire study, every effort was made to minimize the suffering of the animals.

Inoculum

Strain *M. bovis* SB0989 [collection of the German National Reference Laboratory for Bovine Tuberculosis, FLI Jena (37)] was cultured in Middlebrook 7H9 (MB) bouillon for 4 months, characterized by real-time PCR targeting IS*1081* (38), and colony count was determined. The bacterial suspension was cryo-conserved in MB bouillon supplemented with glycerin and an antibiotic mixture containing polymyxin B, amphotericin B, nalidixic acid, trimethoprim, and azlocillin, and stored at −80°C. For inoculation, the strain was defrosted and transferred into phosphate-buffered saline (PBS). In brief, the suspension was centrifuged at 4,000 × *g* for 10 min at 20°C, and the pellet was resuspended in 1 ml sterile PBS. Based on colony counts of the cryo-conserved stock, the inoculation dose was adjusted to achieve ∼5 × 10^2 cfu per animal.

Quantitative re-assessment of the remaining inoculum yielded 4.7 × 10^2 cfu per animal. In the preceding experiment (data not shown), the colony count of the bacterial suspension before and after passage through a spray catheter had been determined to ascertain that there was no marked loss of bacteria. Quality control of the inoculum after use by endpoint and real-time PCR using the targets IS*1081* (38) and RD4 (32), as well as by spoligotyping (39) and MIRU-VNTR (40, 41) confirmed that the inoculum contained *M. bovis* Lineage BOV_1 SB0989, MIRU-24 profile 222324253322645431223433. However, low-level contamination by *M. caprae* Lineage BOV_4 SB0418, MIRU-24 profile 235424253422435222423421 was discovered. The proportion of the copy number of *M. caprae* in the inoculum amounted to 0.1% of the copy number of *M. bovis* as estimated by quantitative real-time PCR. From the data gathered in this study, particularly the fact that only *M. bovis* was retrieved by culturing samples and tissues from the inoculated animals, we have no reason to suspect that this contamination negatively impacts the interpretation of the data presented.

Intrabronchial Inoculation

Inoculation was performed as established in trial 1 but using a spray catheter (Storz). Depending on the size of the individual animal (30–50 kg BW), access to the airways was accomplished *via* the ventral nasal passage (**Figure 2**) or the oral cavity while using a biting protector. Goats in the infection group ($n = 4$) received a 2.5-ml suspension containing 4.7 × 10^2 cfu of *M. bovis*. Goats in the control group ($n = 4$) were mock-inoculated with 2.5 ml PBS. Aliquots of 500 µl were deposited at five sites, *b. trachealis*, *b. principales dexter and sinister*, *b. lobaris cranialis*, and *b. lobaris medialis* (**Figure 3**). The goats were observed after inoculation until they regained full awareness. Nasal swabs were taken from each goat within 30 min after bronchoscopy. Thereafter, nasal swabs and feces were collected daily for 14 days to monitor a potential excretion of *M. bovis*.

FIGURE 2 | Intrabronchial application of *Mycobacterium bovis* suspension under biosafety level 3 conditions. **(A)** Bronchoscope inserted through the nose of an anesthetized goat in sternal recumbency. **(B)** Bronchoscopic view of the trachea of the goat.

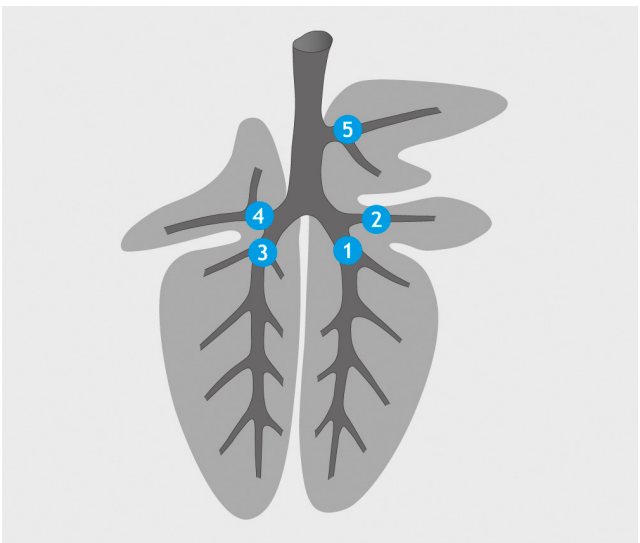

FIGURE 3 | Application sites for *M. bovis* suspension/PBS (spray catheter): *bronchus* (*b.*) *principalis dexter* (1), *b. lobaris medialis* (2), *b. principalis sinister* (3), *b. lobaris cranialis sinister* (4), and *b. tracheobronchialis* (5).

Single Intradermal Cervical Comparative Tuberculin (SICCT) Test

SICCT test was performed 137 days post inoculation (dpi, 72 h before necropsy). The goats were injected intradermally with 1 ml of a solution containing either 2,500 IE avian PPD (aPPD; WDT) at the left side and 5,000 IE bovine PPD (bPPD; WDT) at the right side of the neck. Skin fold thickness was measured with a caliper prior and 72 h after injection. Positive response was defined as difference in the increase in skin fold thickness of more than 4 mm between the bPPD and aPPD injection sites, redness or edema at the bPPD injection site, and/or systemic reactions like fever 72 h after injection. Negative response was defined as difference in the increase in skin fold thickness of <2 mm between the bPPD and aPPD injection sites and absence of clinical signs.

Necropsy

At the end of the observation period (>140 dpi), the goats were tranquilized with xylacine (Rompun® 2%; Bayer; 0.2 mg/kg BW, IV) followed by euthanasia with pentobarbital-sodium (Release©, WDT; 150 mg/kg BW, IV). At first, the lungs were fixed intratracheally as described above followed by complete necropsy. Different tissues were collected for histological examination and cultural isolation of mycobacteria. Sampled tissues were: injection sites of PPDa and PPDb, *lymphonodus* (*LN*) *cervicalis superficialis sinister et dexter*, *LN mandibularis sinister et dexter*, *LN parotideus sinister et dexter*, tonsils, *LN retropharyngealis medius sinister et dexter*, *LN tracheobronchialis sinister*, *LNN mediastinales*, thymus, heart, liver, spleen, kidney, *LNN renales*, bone marrow, Peyer's patches in jejunum and ileum, *LNN ileocolici*, and *LNN mesenteriales*. Samples for bacterial culture were collected under aseptic conditions. Tissues for histological examination were fixed in 4% NBF. Lungs and tissues for histological examination were stored in the fixative that was renewed after 1 week and after 2 months, and for >2 months at 4°C in the necropsy facility to make sure that *M. bovis* was inactivated.

Histology and Ziehl-Neelsen Staining

The right cranial lobe (RCL), right basal lobe (RBL), and accessory lobe (AL) of the lungs of one of the infected goats without superficial lesions and the infected goats with macroscopically visible superficial lesions were cut in 1- (RCL, AL) or 2-cm (RBL) thick slices. Lesions visible on cut surfaces were dissected, and up to five sites per pulmonary lobe were embedded in paraffin. Representative sites, preferentially with macroscopic lesions, of the other sampled tissues were embedded in paraffin.

Paraffin sections were stained with hematoxylin and eosin (H&E) for evaluation of lesions. Granulomas were graded according to a modified scheme from Wangoo et al.

(42) (see **Supplementary Table 1**). Sections from the lungs, tracheobronchial LN, mediastinal LNN, and other sites with granulomas were stained in addition to the Ziehl-Neelsen (ZN) staining protocol for acid-fast bacilli (AFB). AFB numbers were classified as none, single (+, 1 to 10 AFB/section), few (++, 11-50 AFB/section), or many (+ + +, >50 AFB/section) (43).

Microbiological Cultivation

From each tissue sample, 1 g was placed into 10 ml PBS and homogenized with a stomacher device (Interscience, Saint Nom, France) for 6 min at room temperature. Then, 10 ml of NALC-NaOH solution containing 2.9% natrium-citrat-dihydrat and 0.5% N-acetyl-L-cystein was added, and the sample was agitated for 25 min at 300 rpm in a shaker. After addition of 20 ml PBS, the sample was vortexed and centrifuged for 20 min at 3,800 × *g*. The supernatant was discarded, 10 ml PBS was added, and the sample was centrifuged as before. The supernatant was discarded, and the pellet was resuspended in 1 ml PBS and homogenized thoroughly by vortexing. Of the resuspended pellet, 200 µl was transferred to one slant of Löwenstein-Jensen medium with polymyxin B, amphotericin B, carbenicillin, trimethoprim (PACT), and glycerin, and to two slants of a Coletsos medium with PACT (both Artelt Enclit GmbH, Wyhra, Germany). Tubes were incubated for 1 week in horizontal position, afterward in upright position for up to 12 weeks. Cultures were examined every 2 weeks for colony growth. Once visible colonies appeared, presence of *M. bovis* was confirmed by real-time PCR targeting IS*1081* (44) and by endpoint PCR targeting RD4 (33). Nasal swabs and feces were examined in the same way.

Radiological Examination by Computed Tomography (CT) and Digital 2D Radiography (DR)

For CT scanning, lungs were placed into two plastic bags inside a plastic container. The lungs were scanned as described for trial 1, and data were analyzed with Synedra personal view© and 3D Slicer© (https://www.slicer.org/). Synedra was used to count lesions in the slices and record their size. Every slice was examined, and larger lesions were followed from beginning to end to avoid re-counting the same lesion in consecutive sections. Round and polygonal lesions could be distinguished. The largest diameter of each lesion was used as parameter for lesion size. The lesions were categorized into three classes: (I) small mineralized lesions <5 mm in diameter, (II) mineralized lesions more than 5 mm in diameter, and (III) partially mineralized confluent lesions >10 mm in diameter and containing several mineralized nuclei. The volume of the altered lung tissue was determined, both automatically and with the free hand tool of the 3D Slicer software. For automatic measurement, the threshold function was used with the range set from 250 to maximum Hounsfield units (HUs). Free-hand measurement was conducted for small or less mineralized lesions, which were not completely recognized by the threshold function. These lesions were marked with the free hand tool in every slice. The software allowed for adding up the lesion volume of the automatic and freehand measurements.

Later, digital 2D radiography images were taken of each lung using a Blueline-Ultra-1040HF x-ray apparatus (WDT) with Leonardo-Thales-DR-Kofferset wireless devices. The settings were 60 kV and 2.5 mAs exposure with a distance of 70 cm between the x-ray tube and the detector. The right and left lung were x-rayed separately in the dorsoventral and latero-lateral orientations. Four images per lung were analyzed with the Dicom PACS® software (Oehm and Rehbein, Rostock, Germany).

RESULTS

Establishment of the Intrabronchial Application Procedure (Trial 1)

The anesthesia achieved with the protocol applied was found to be superficial, with the animals responding to external stimuli, but sufficiently deep to prevent defensive movements. The 85-cm working length of the bronchoscope allowed for access to all three sites selected for application. Correct positioning of the catheter for the applications was fast and easy to find with the help of the video image of the bronchoscope. The *bronchus (b.) tracheobronchialis*, which is the first diversion on the right side of the trachea, was used for orientation. The 1:2.5 dilution of barium sulfate suspension in water was easily applicable using a standard catheter and viscous enough to adhere to the mucosa, and 1-ml boli were deposited at the entrances to the *b. trachealis,* the right main bronchus, and the left main bronchus under visual control. Further distribution of the contrast medium could not be followed by bronchoscopy, because it completely filled the bronchial lumina and obscured the view.

Examination of lungs following euthanasia of the goats and intratracheal fixation of the lungs 30 min after deposition of the contrast medium did not reveal macroscopic lesions (**Figure 4**). Subsequent CT scans showed contrast medium in left and right lung lobes and in the accessory lobe. It had accumulated around the three application sites and extended further down the respective airways (**Figure 5**). The amount of barium sulfate suspension was not evenly distributed among the sites.

Inoculation of Goats With *M. bovis* and *intra vitam* Assessment (Trial 2)

Based on experiences from trial 1, the number of application sites was increased from three to five, adding *b. lobaris cranialis* and *b. lobaris medialis* as application sites for the *M. bovis* suspension (**Figure 3**). The increased number of inoculation sites was compensated for by reducing the volume of inoculum deposited at each site to 500 µl. The *M. bovis* inoculum was more liquid than the barium sulfate suspension allowing for the use of a spray catheter to achieve a more even distribution of the inoculum. All the five sites selected for inoculation could be reached with the bronchoscope, and correct positioning of the catheter was fast and easy under video guidance. The spray catheter allowed for the application of the inoculums at all sites from a single syringe, step-by-step, with little pressure.

The goats remained clinically healthy and in good general condition from the time of inoculation to the time of SICCT testing. They were blithely and intent, and had an undisturbed appetite and an average rectal temperature of 38.9 ± 0.3°C (mean ± SD of all daily measurements over time; $n = 4$ animals). Cultures of nasal swabs and fecal samples taken for mycobacterial

FIGURE 4 | Lung after intratracheal fixation: voluminous, not collapsed parenchyma because of the instilled NBF. Dark red areas indicate retained blood, light areas indicate retained air. The distinctive distribution is caused by the position of the goats, lying on their back, during instillation of NBF.

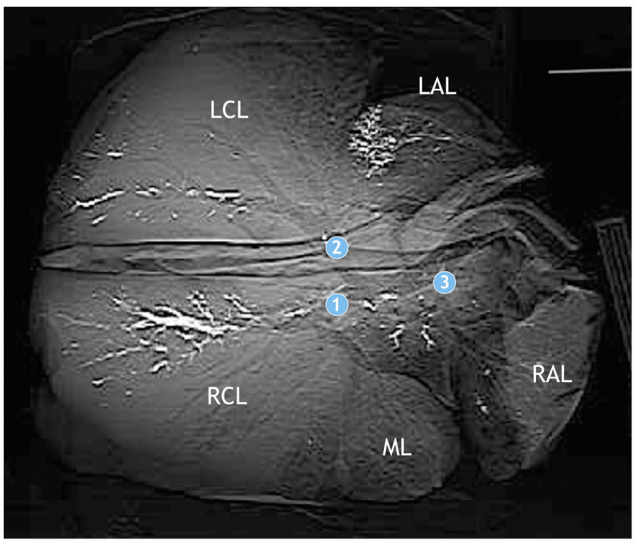

FIGURE 5 | Computed tomography of the lung of a goat after application of barium sulfate suspension. Application sites are indicated by circles with numbers as in **Figure 1**. Barium sulfate (white) is present in the bronchial system of the left and right apical lobes (LAL, RAL), the accessory lobe, and the left and right caudal lobes (LCL, RCL), but not the middle lobe (ML). The amount varies among the lobes.

growth on the day of inoculation and then daily from 1 dpi until 13 dpi and 21, 28, 56, 84, 112, and 140 dpi did not yield positive results throughout. All goats inoculated with *M. bovis* presented clearly positive SICCT 137 dpi, indicating a 100% infection rate. The control goats developed neither local nor systemic reactions in response to SICCT.

Comparative Computed Tomography (CT) and 2D Digital Radiography (DR) Imaging of Lungs From *M. bovis*-Inoculated Goats

CT allowed to identify the different lung lobes based on branching of the bronchial tree and to distinguish different types of lesions in the lungs of the goats inoculated with *M. bovis* (**Figure 6**; see **Supplementary Table 1**). Most lesions presented as small, round hyperdense foci with smooth borders. They had a density of more than 250 HU, indicating that they were mineralized. The diameter of these lesions was below 5 mm. The pulmonary tissue surrounding the mineralization did not present with increased density. The second category consisted of larger round or pleomorphic lesions with a diameter of more than 5 mm and significant variation in density. Most of the lesions were mineralized or partly mineralized. Sometimes, a fine dust of mineralization was present in the center. These lesions were surrounded by a tissue of higher density than the lung tissue. Lesions of the third category had a diameter of more than 1 cm. Some had multiple foci of mineralization and were of irregular shape. They were interpreted as result of confluent lesions. Most of the granulomas were located at the application sites of the inoculum and in proximity to bronchi. Frequency and distribution of the types of lesions varied among individual animals (**Table 1**), but small, mineralized lesions were detected most frequently. CT allowed to determine total numbers of lesions, total lung volume, total lesion volume, and, thus, percentage of lung volume affected by the lesions (**Table 2**). The percentage of affected lung volume was low in three animals, but reached 34% in one goat.

DR imaging gave a distinct outline of the lung tissue. The airways presented as hypodense structures. The identification of pulmonary lobes (left and right apical lobes, middle lobe, left and right caudal lobes, and accessory lobe) was based on their outline and branching of airways. The lungs of all the goats inoculated with *M. bovis* had tuberculous lesions, i.e., mineralized and partly mineralized foci of >1 cm size (**Figure 7A**). The cavernous lesion of goat #436 was clearly outlined by mineralization along the edges. Even though right and left lung lobes were dissected at the *bifurcatio tracheae* and, hence, separately radiographed, and images were taken in two orientations (dorsoventral and latero-lateral), overlapping of the pulmonary lobes hampered the identification of the exact location of lesions and assignment to lobes, as well as the determination of number and size of lesions (**Figure 7B**).

Nevertheless, comparison of lesions detected by adspection, by CT, and by DR in the control goats and individual goats inoculated with *M. bovis* unveiled some degree of correlation. CT of the lungs of control goats that had no macroscopic lesions (**Figure 8A**) revealed homogeneous lung parenchyma with a density of below 250 HU (**Figures 8C,D**). There were no hyperdense areas indicative of pulmonary lesions. This was confirmed by the x-ray images (**Figure 8B**).

The numerous lesions counted in goat #418 by CT were located deep within the parenchyma and not detected by adspection (**Figure 9A**). The lesions were predominantly <5 mm in diameter and mineralized (**Figures 9C,D**), but several lesions

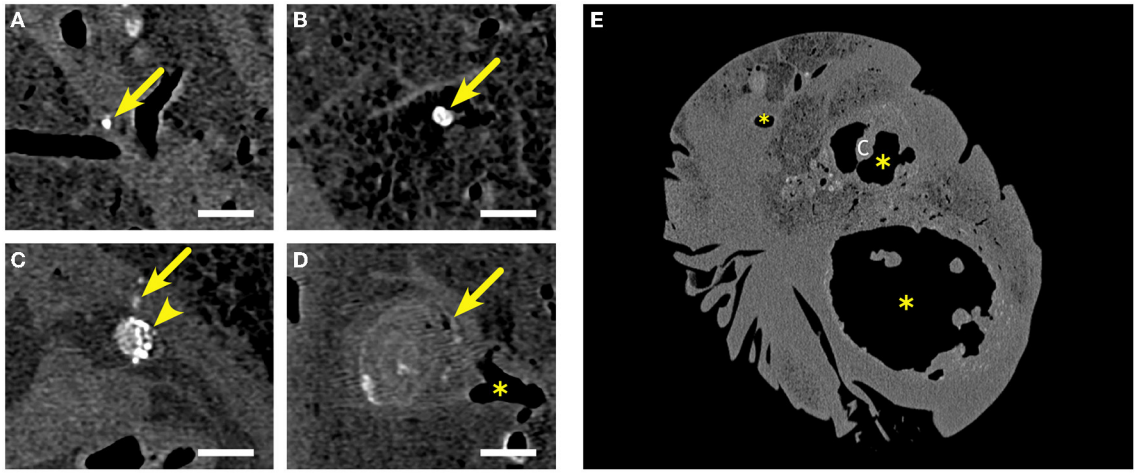

FIGURE 6 | Examples of lesions detected by computed tomography in the fixed lungs of goats inoculated with *M. bovis*. **(A,B)** Small lesions <5 mm in diameter (arrows), mineralized (indicated by the white color) and with a density of >250 HU. **(C)** Lesion between 5 and 10 mm in diameter, mostly mineralized (arrowhead) next to a small lesion <5 mm diameter, mineralized (arrow). **(D)** Lesion exceeding 10 mm in diameter with multiple small foci of mineralization (arrow) located at a bronchial branching (*). **(E)** Several caverns (*) of variable sizes with highly variable outline and protruding *cristae* (c). Walls of the caverns are of variable thickness with multifocal mineralization (density >250 HU). Lumina are hypodense, indicating that they are filled with air. Caverns are surrounded by numerous mostly mineralized lesions of variable sizes. Bars in **(A–D)** = 10 mm.

TABLE 1 | Frequency and distribution of types of lesion detected by computed tomography (CT) in *Mycobacterium bovis*-inoculated goats.

Location of lesions (lung lobe)		Lesions <5 mm, mineralized				Lesions >5 mm, mineralized				Lesions >10 mm, irregular mineralization			
		Goat #418	Goat #423	Goat #428	Goat #436	Goat #418	Goat #423	Goat #428	Goat #436	Goat #418	Goat #423	Goat #428	Goat #436
Right lung	*L. apicalis*	8	5		10	1	1		3		2		2
	L. medialis	1		1									
	L. caudalis	15	2	2	2	5			1	2			
	L. access.		27	2									1
Left lung	*L. apicalis*			4	17				1				
	L. caudalis	10			4	1		1		1		1	
Total number of lesions (by size)		34	34	9	33	7	1	1	5	3	2	1	3

TABLE 2 | Number and volume of pulmonary lesions and percentage of affected lung tissue in *M. bovis*-inoculated goats.

	Goat #418	Goat #423	Goat #428	Goat #436
Lesions <5 mm	34	34	9	33
Lesions >5 mm	7	1	1	5
Lesions >10 mm	3	2	1	3
Caverns detected by CT	0	0	0	2
Total number of lesions	44	37	10	43
Total lung volume in cm^3	2415.64	2499.78	2695.32	3255.08
Total lesion volume in cm^3	9.78	33.68	7.61	1116.99
Lesion volume (%)	0.41	1.35	0.28	34.31

>5 mm in diameter and larger confluent lesions were also detectable. The majority of the lesions was located in close association to the bronchi, especially the ventral segmental bronchi of the right and left caudal lobes (**Figure 9C**). Some lesions were found in the apical lobe of the right lung. By radiography, only a few hyperdense lesions were detected in the left lung and in the caudal and accessory lobes of the right lung (**Figure 9B**). As observed by CT, they were located close to the bronchi. The numerous small lesions (<5 mm) revealed by CT could not be identified by DR.

In goat #423, predominantly small mineralized lesions <5 mm were detected by CT. They were most numerous in the right lung and the accessory lobe. Larger lesions were present in the right apical lobe. The left lung was free of lesions. Most of the lesions were located around the bronchi, but two lesions were close to the pleura. Corresponding round hyperdense structures were detected in DR radiographs of the right lung, although lesions in the cranial lung could not be assigned to distinct lobes.

In goat #428, the smallest number of lesions was detected by CT. Small mineralized lesions were rather evenly distributed in

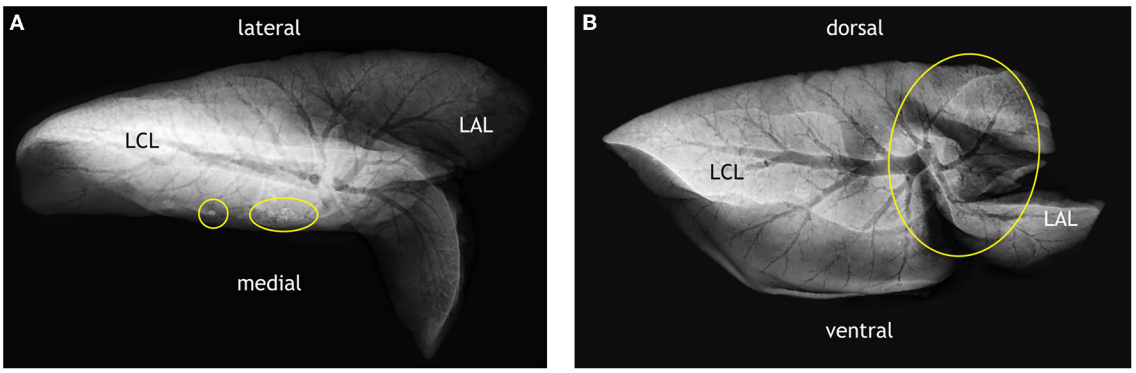

FIGURE 7 | Examples of lesions detected by 2D radiography in the fixed lungs of goats inoculated with *M. bovis*. **(A)** Radiograph of the left lung of goat #428 in a dorsoventral view (lateral and medial sites indicated). Several mineralized and partly mineralized lesions (circles) are present in the left caudal lobe (LCL). **(B)** Radiograph of the left lung of goat #436 in a latero-lateral view (dorsal and ventral sites indicated). Caudal lung lobe (LCL) and apical lung lobe (LAL) are overlapping as indicated by the circle.

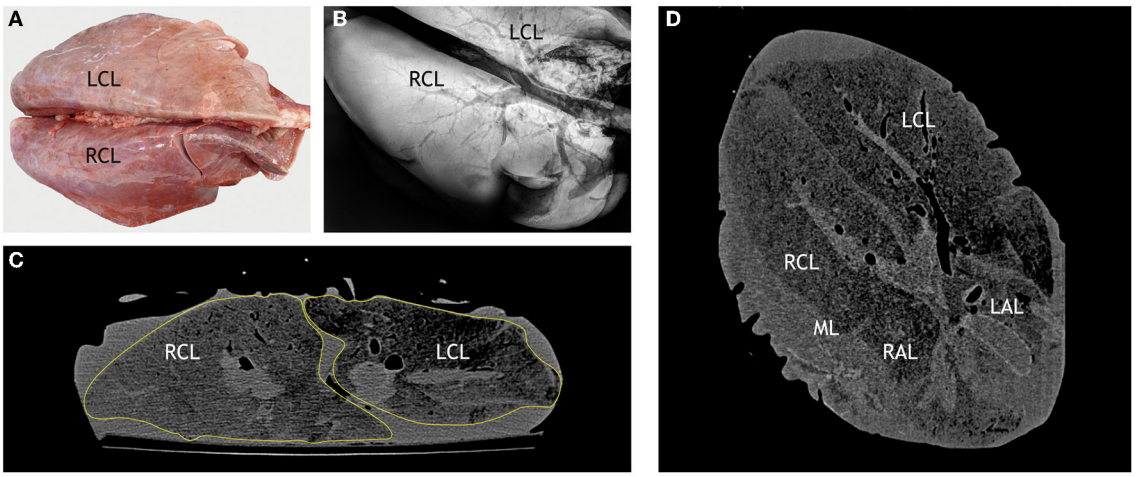

FIGURE 8 | Correlation of macroscopic, radiographic, and computed tomography (CT) findings in a control goat. **(A)** Dorsal view of a lung without lesions after intratracheal instillation with NBF, right and left caudal lobes (RCL, LCL) are indicated. **(B)** Dorsoventral radiographic view of the same lung lobe: distinct outline of the homogenous pulmonary parenchyma (RCL, LCL indicated) and hypodense airways. **(C)** CT scan in transversal plane through the right and left caudal lobes (RCL, LCL). Pulmonary parenchyma is outlined by a yellow line. **(D)** CT scan in dorsal plane through the right and left caudal lobes (RCL, LCL), right and left apical lobes (RAL, LAL) and middle lobe (ML). Control goat #417 was inoculated with PBS.

the middle, caudal, and accessory lobes of the right lung and in the apical and caudal lobe of the left lung. They were located near the bronchi, especially at their ventral aspect. A larger, irregular shaped hyperdense structure was present in the left caudal lobe 2 cm beneath the lung surface. DR radiographs revealed irregular hyperdense structures in the lobar bronchi of the bifurcation. Two hyperdense areas with irregular outline were present in the left caudal lobe close to the surface. The small lesions (<5 mm) revealed by CT could not be identified by DR.

Lesions were most extensive in goat #436 (**Figure 10**). Numerous small mineralized lesions were detected in the left and right apical lobes by CT. A large cavern extended throughout most of the right lung (**Figures 10C,D**). The cavern was outlined by an irregularly shaped, hyperdense wall which varied in thickness (up to 1 cm) and had multiple mineralized foci (>250 HU). Many hyperdense *cristae* and *septae* extended into the cavern and subdivided it. Its center was hypodense, indicating that it was filled with air. The cavern was surrounded by numerous mineralized lesions of variable size. Size difference between the left and right lungs was also evident by DR imaging. The right lung was distended by the large cavern with features comparable to those described by CT (**Figure 10B**). Distinct mineralized structures were present in the cranial part of the right lung without connection to the cavern.

Pathological Findings in the Lungs of *M. bovis*-Inoculated Goats

Gross examination was initially limited to external inspection to keep the lungs intact for subsequent CT and DR examination. Macroscopic lesions were detected in none of the controls

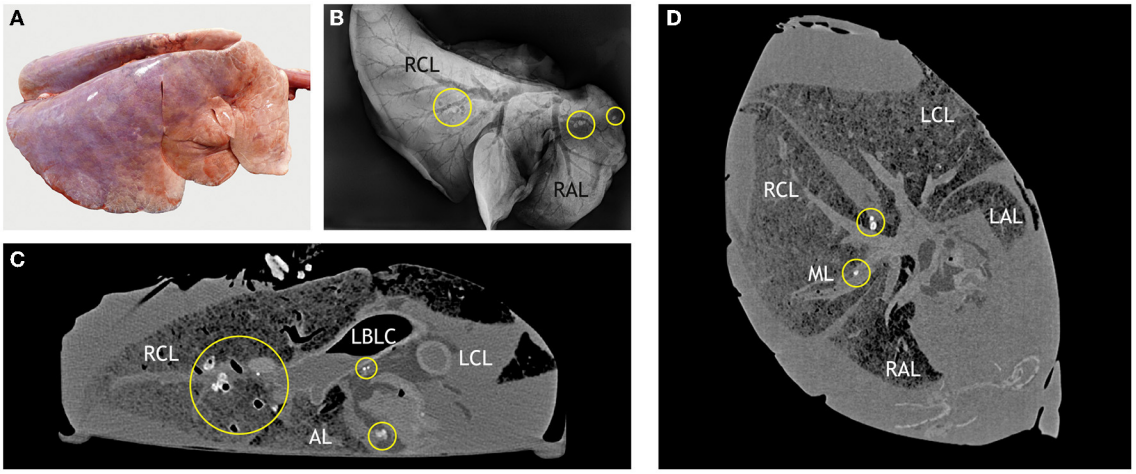

FIGURE 9 | Correlation of macroscopic, radiographic, and computed tomography (CT) findings in a goat inoculated with *M. bovis* that developed no superficial lesions. **(A)** Macroscopic findings comparable to those in control goats (**Figure 8A**). **(B)** Dorsoventral radiographic view of the right lung reveals multiple mineralized lesions (indicated by circles) in the right caudal lobe (RCL) in close association to a ventral segmental bronchus (hypodense) and in the cranial part of the apical lobe (RAL) in close association to a segmental bronchus. **(C)** CT scan in transversal plane through the right and left caudal lobes (RCL, LCL) and accessory lobe (AL) shows mineralized lesions in the RCL and in the LCL (indicated by circles). The lesions are associated with the bronchial tree (left *bronchus lobaris caudalis*, LBLC, as example). **(D)** CT scan in dorsal plane through the right and left caudal lobes (RCL, LCL) and right and left apical lobes (RAL, LAL) shows lesions (indicated by circles) near the main bronchus of the RCL and one small lesion near the main bronchus of the medial lobe. Goat #418, inoculated with *M. bovis*.

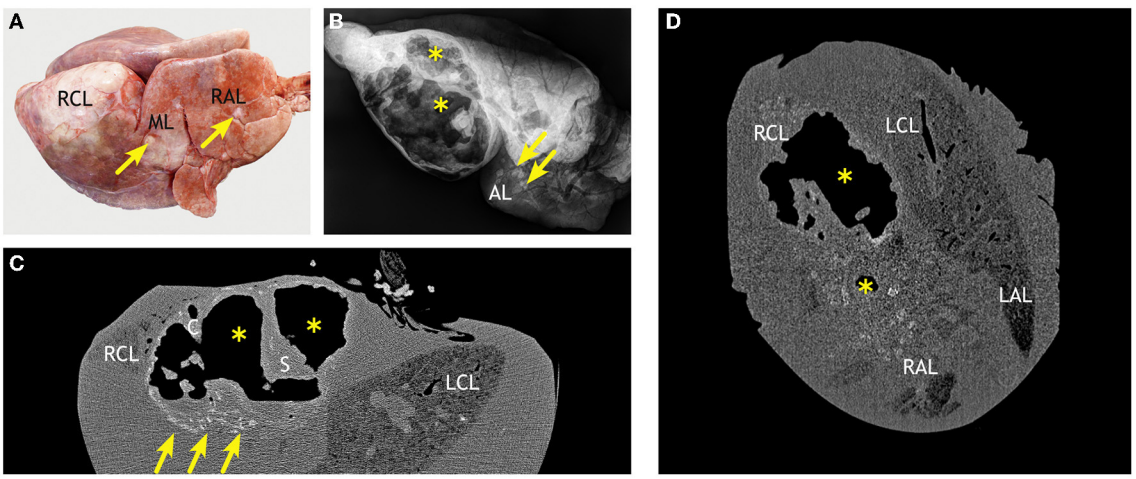

FIGURE 10 | Correlation of macroscopic, radiographic, and computed tomography (CT) findings in a goat inoculated with *M. bovis* that developed severe lesions and extensive caverns. **(A)** Markedly enlarged right caudal lobe (RCL) and multiple white nodules in the middle (ML) and apical (RAL) lobes (arrows, examples). **(B)** Latero-lateral radiographic view of the right lung reveals large caverns (*) and mineralized lesions (arrows, examples) in the accessory lobe (AL). **(C)** CT scan in transversal plane shows that the air-filled caverns (*) with *septae* (S) and *cristae* (C) are predominantly located in the right caudal lobe (RCL) and cause its dorsal protrusion. Multiple mineralized lesions are prominent at the ventral aspect of the caverns (arrows). **(D)** The dorsal plane of CT scans through the caudal lobes (RCL, LCL) and apical lobes (RAL, LAL) confirm the irregular outline of the air-filled caverns (*) and reveal the extension of confluent partly mineralized lesions in the adjacent pulmonary parenchyma. Goat #436, inoculated with *M. bovis*.

and only in the lungs of one of the goats inoculated with *M. bovis* (goat #436). Here, the lesions presented as chronic fibrous pleuritis of the right basal lobe with a circumscribed adhesion between the visceral and parietal serosa. The lung was asymmetric with a markedly enlarged right caudal lobe (**Figure 10A**). Multiple white to yellow nodules, 1–15 cm in diameter, were irregularly distributed throughout the right apical, middle, and caudal lobes.

Based on CT findings, the lungs of one goat without superficial macroscopic lesions (goat #418, **Figure 11**) and of the goat with lesions (goat #436) were dissected (**Figure 12**). Macroscopic examination of the dissected lung without superficial lesions revealed nine caseous granulomas (1–4 mm in diameter) in the proximal half of the right apical lobe. In the right caudal lobe, multiple granulomas (2–11 mm in diameter) and caverns (2–13 mm in diameter) were located proximal to the ventral

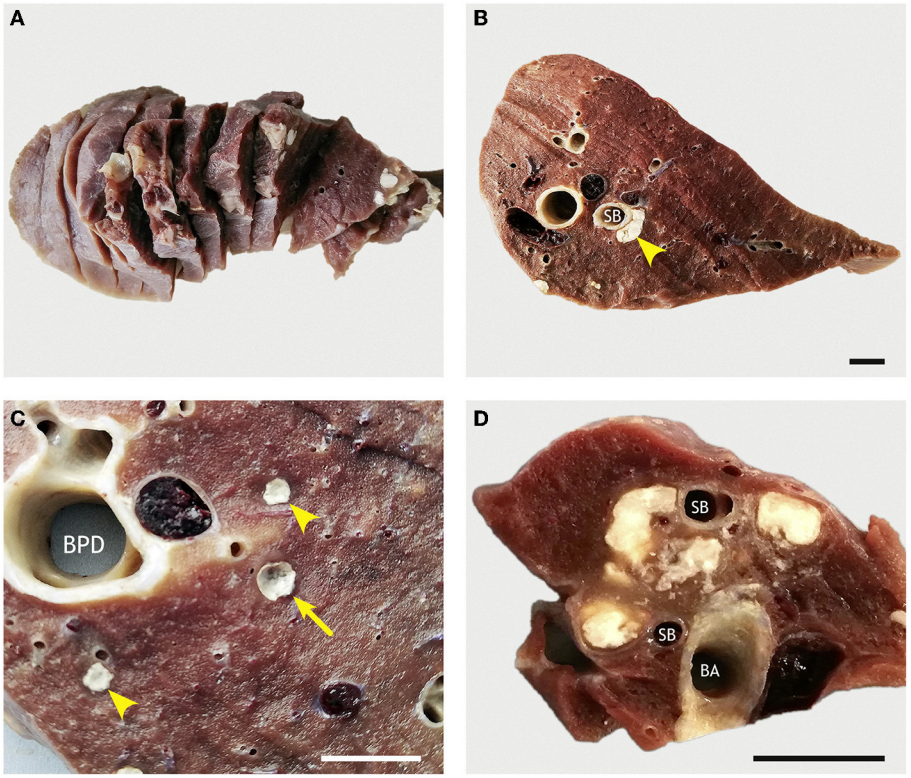

FIGURE 11 | Sliced lung of a goat inoculated with *M. bovis* that developed no superficial lesions. **(A)** Pulmonary lobes (accessory lobe) were completely sliced at 1-cm thickness. **(B)** Section of the RCL with confluent granulomas (arrowhead) surrounding the ventral aspect of a ventral segmental bronchus (SB). **(C)** Higher magnification of pulmonary tissue next to the *bronchus principalis dexter* (BPD) reveals two small caseous granulomas (arrowheads) and one small cavern (arrow). **(D)** Multiple confluent caseous granulomas located between *bronchus accessorius* (BA) and branching segmental bronchi (SB) in the accessory lobe. Goat #418, inoculated with *M. bovis.* Bars = 1 cm.

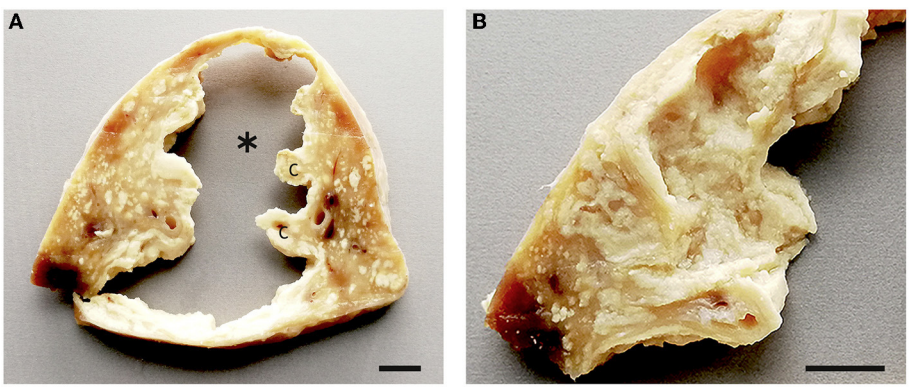

FIGURE 12 | Sliced lung of a goat inoculated with *M. bovis* that developed severe lesions and extensive caverns. **(A)** Section through the extensive polygonal cavern (*) with multiple *cristae* (C) in the RCL. The surrounding pulmonary tissue is replaced by confluent caseous granulomas with multiple foci of mineralization. **(B)** Higher magnification of the highly corrugated lining of the cavern (*). Goat #436, inoculated with *M. bovis.* Bars = 1 cm.

segmental bronchi and smaller medio-ventral airways. Larger confluent granulomas were located at the ventral aspect of the bronchi (**Figure 11B**). The granulomas were filled with a white caseous material (**Figure 11C**). The caverns had empty centers surrounded by irregularly thickened walls of the white caseous material. In the accessory lobe, multiple confluent granulomas (10 × 10 × 16–30 mm^3) were present in the proximal part of the branching segmental bronchi (**Figure 11D**), and there was a medium-sized cavern (10 × 16 × 5 mm^3).

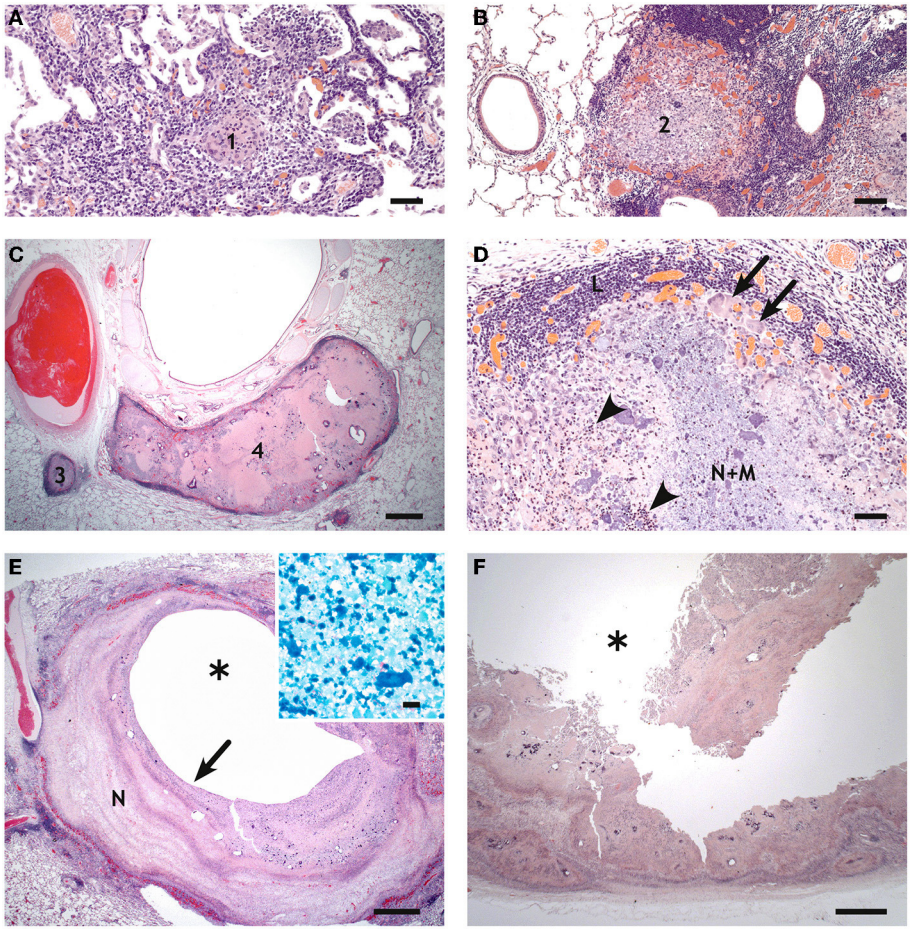

FIGURE 13 | Histology of pulmonary lesions in goats inoculated with *M. bovis*. **(A)** Type 1 granuloma (1) consisting of epitheloid cells in the accessory lobe of goat #418, bar = 50 μm. **(B)** Type 2 granuloma (2) with predominantly epitheloid cells and minimal necrosis in the apical lobe of goat #418, bar = 100 μm. **(C)** Type 3 (3) and type 4 (4) granulomas in the caudal lobe of goat #418, bar = 1,000 μm. **(D)** Higher magnification of the type 3 granuloma in **(C)** shows central necrosis and mineralization (N+M), neutrophils (arrowheads, examples), epithelioid cells and multinucleated giant cells (arrows, examples), and a lymphocytic infiltrate (L), bar = 50 μm. **(E)** Small cavern (*) in the caudal lobe of goat #418. The central cavity is surrounded by multiple layers of necrosis (N), bar = 1,000 μm; inset: a few AFBs in the necrotic wall (site indicated by arrow), bar = 10 μm. **(F)** Highly corrugated wall of the large cavern (*) of goat #436. The pulmonary tissue is replaced by confluent granulomas. Bar = 1,000 μm.

The macroscopic examination of the dissected lung with superficial lesions (goat #436) revealed that most of the pulmonary tissue was replaced by a large polygonal cavern of ∼70 mm diameter. The cavern had a highly irregular outline and multiple protruding *cristae* (**Figure 12**), and was surrounded by confluent granulomas with discrete foci of caseous necrosis.

By histology, small granulomas in both lungs were classified as type 1, 2, or 3, larger granulomas as type 3 or 4, sometimes with type 1 satellite granulomas (**Figures 13A–D**). The granulomas were not well-demarcated, and inflammatory cells including epitheloid cells were present in surrounding alveoli. The caverns resembled the granulomas, with most of the central necrotic material missing (**Figures 13E,F**). A part of the wall was lined by bronchial epithelium in some of the caverns. No AFB was present in any of the granulomas, but a few (++) AFBs were present in the necrotic material around one of the smaller caverns (**Figure 13E** inset).

Pathological Findings and Cultural Isolation of *M. bovis* From Other Tissues of *M. bovis*-Inoculated Goats

All the inoculated goats, but none of the controls, presented granulomas in the LNN *tracheobronchiales* or LNN *mediastinales* (see **Supplementary Table 2**). In three goats, macroscopic lesions presented as multiple, caseous granulomas. Histologically, all types of granulomas were seen, but types 3 and 4 granulomas were more frequent. AFBs were not detected in any of these granulomas. In the goat with severe pulmonary lesions (goat #436), LNN *tracheobronchiales* and LNN *mediastinales* were almost completely replaced by confluent caseous granulomas. Histologically, these were categorized as multicentric type 4 granulomas with satellite granulomas in the periphery. Single AFBs were present in a few multinucleated giant cells. In goat #436, type 1 granulomas were detected in the mucosa-associated lymphoid tissue at the ileocecal entrance and types 1, 2, and

3 granulomas in the LNN *mesenteriales* and *ileocolici*. These granulomas were negative for AFBs.

The *M. bovis*-inoculated goats had severe reactions characterized by necrotizing vasculitis, lymphohistiocytic perivasculitis, microabscesses, and severe edema in the dermis and subcutis at the site where bPPD had been injected. Alterations were associated with swelling, edema, and activation of the draining LNN *cervicalis superficialis*. The reactions at the injection site of aPPD were mild. No reactions were observed in the mock-inoculated control goats.

In tissues collected at necropsy, mycobacterial growth was detected in one or more tissues of all the goats inoculated with *M. bovis*, but none in those of the mock-inoculated control animals (see **Supplementary Table 2**). All positive cultures were confirmed to be *M. bovis*. *M. caprae* was not identified.

DISCUSSION

Compared to cattle, the main natural host of *M. bovis*, goats qualify as experimental animal species, particularly for infection experiments under high containment conditions, because of lower maintenance cost and easier handling by experimenters. The size of most goat breeds is favorable for the application of different imaging techniques to live animals or extirpated organs, and handling of the organs (fixation, transport, scanning) is easier than in cattle. Notably, goats are also natural hosts for members of the *M.tuberculosis* complex (MTC), namely, *M. bovis*, *M. caprae*, and *M. tuberculosis* (45). The combination of these factors makes these animals highly suitable models for TB research, for studying both the disease and effects of new vaccines (13, 45).

Different routes of infection have been successfully applied, but pathomorphological manifestations varied with inoculation procedure (13, 15, 21–23). This is particularly critical when minute differences in the virulence of bacterial strains, in the efficacy of vaccine candidates, or in the individual susceptibility of animals to tuberculosis morbidity and mortality shall be unveiled (46). As all inoculation procedures have their advantages and disadvantages, this study assessed a novel inoculation technique based on endobronchial administration but replacing the classical bolus application at the *bifurcatio tracheae* with a visually controlled application of a spray. The results of the different microbiological, immunological, pathological, and imaging methods indicate that this inoculation protocol produced disease in all inoculated animals and is at least equivalent to published protocols.

Experimental infection of cattle with *M. tuberculosis* isolates documents the attenuation of the human tubercle bacillus for cattle (47). Goats challenged by the transthoracic route with different members of the MTC displayed different clinical signs (45). Highest lesion scores were observed in *M. bovis*-challenged goats, followed by those challenged with *M. caprae*. Differences in the proportion of animals with viable bacteria in tissues and in response to the intradermal and gamma-interferon (IFN-γ) tests imply that *M. bovis* and *M. caprae* differ in their virulence and capability of activating host response (45). Even though *M. caprae* dominates endemic bTB infections in the alpine region in Europe affecting cattle and red deer (48), *M. caprae* is mostly recognized as a goat pathogen. Nevertheless, given the recognized heterogeneity of *M. caprae* strains circulating in animal populations (49, 50), we considered it favorable to use an *M. bovis* isolate as inoculum for the improvement of the caprine TB infection model. Once established, it would be highly intriguing to apply the model to unveil differences in the degree of virulence and host adaptation of *M. caprae* isolates.

It is generally accepted that, with some exceptions, cattle become infected with *M. bovis* by either the oral or the respiratory route (51). The oral route is most important in calves nursed by tuberculous cows, while the respiratory route is most common in adult cattle and facilitated by the animals' natural behavior. Using the oral, subcutaneous, or intravenous route of infection for experimental inoculation requires higher doses, lesions are frequently atypical, and animals show systemic reactions (52). Like in experimental TB infection of cattle (53–55), studies on goats have mostly mimicked the respiratory route by intratracheal, transthoracic, and endobronchial inoculation. Low doses (10^2-10^3cfu) of *M. bovis* or *M. caprae* reportedly resulted in 100% infection rates with lesions in the lower respiratory tract and systemic dissemination (13, 15, 22, 23). A caprine aerosol *M. bovis* infection model required high inoculation doses and did not result in the formation of cavernous lung lesions (21). Non-quantifiable, partial losses of the inoculum due to adherence to the surface of the endotracheal tube used for delivery of aerosolized bacteria, as well as due to the HEPA filter indispensable for clearing exhaled air, likely account for these deviations. Indeed, studies with *Burkholderia pseudomallei* indicated that only an estimated 10% of nebulized bacteria were deposited in the lungs (56). Applying for the first time a combination of video-guided bronchoscopy and spray application of an inoculum to several defined sites, we demonstrate that intrabronchial inoculation can be achieved with minimal technical effort in a more natural manner than bolus application.

All the goats inoculated in this study with a minute dose of *M. bovis* (4.7×10^2 cfu) became infected, as deduced from the positive IGRA results and eventually confirmed by re-isolation of the inoculated strain from the mediastinal lymph nodes of all the inoculated goats. Installing the inoculum as spray, the liquid volume administered to a given area of the mucosal surface will be comparably higher than after aerosol inoculation, particularly as we flushed the catheter with 1 ml NaCl after installation of the inoculum. Physiological mechanisms comprising a retrograde movement of mucus by ciliated epithelia of airways and coughing may theoretically lead to removal of a part of the inoculum before *M. bovis* can enter cells and tissues on site. However, repeated sampling on the days after inoculation of nasal secretion and feces of the goats yielded negative results throughout. This strongly indicates that the effective infectious dose closely corresponds to bacterial titers in the inoculum. This finding is in positive contrast to studies deploying aerosol and seeder animal approaches that resulted in low estimated portions of the inoculum deposited in the respiratory tract and an incomplete infection rate of co-housed goats, respectively (21).

Aerogenic infection with *M. bovis* in goats resulted in lesions to similar those described for pulmonary disease in natural caprine TB (15). Researchers conducting endobronchial inoculation at the *bifurcatio tracheae* of goats in the right decubitus position experienced that the intrapulmonary extension of lesions to one or more lobes and, subsequently, the spread of mycobacteria to the draining lymph nodes was strongly influenced by the inoculation procedure (13). In our study, sedated animals were placed in sternal position for inoculation, which placed the thorax in a position comparable to an animal standing upright. With endoscopic-guided inoculation of the goats and deposition of several small aliquots of the inoculum, we achieved a wider and more even distribution than inoculation without a visible control (13, 45). The application of a contrast medium in a pre-study (trial 1) indicated that the procedure led to the inclusion of major sections of the bronchial tree, even when the medium was applied with a regular rather than a spray catheter and by approaching only three sites of the bronchial tree.

Endoscopy is instrumental for purposeful placing of inocula at pre-defined sites of the airways but requires special handling of animals, which poses a problem under high containment conditions. To ensure that the animals tolerate the procedure without defensive movements, the goats were subjected to anesthesia with midazolam and ketamine. Using midazolam instead of the commonly used xylazine led to reduced salivation and improved the bronchoscopic view (data not shown). The goats tolerated this procedure well, even though some of them needed a prolonged time for regaining consciousness. Other anesthesia protocols may be even more convenient (57). Alternatively, pushing the catheter *via* the nasal route could be applied with sedation and good fixation only, if the experimental animals are of appropriate size or age (58).

Application of CT scanning and analysis has been introduced to TB research on a goat model by de Val Perez et al. (13). In their protocol, the lungs and heart are removed at necropsy, lung gross lesions were recorded first by palpation of the different lobes, and then the whole lungs are fixed with formalin by pouring the fixative into the trachea while holding the lungs in a vertical position until the trachea is filled with fixative. The authors stressed the importance of instillation of the lungs with formalin to distend the lungs to approximately the same volume they would have in the pulmonary cavity. This renders the ratio of the lesion volume to the total lung volume comparable between different experiments and research groups. The use of this ratio also corrects for slight differences that could exist in sizes of animals and lungs, even in age-matched animals. Taken this recommendation into account, the protocol was modified in such a way that the lungs were instilled with a fixative solution before opening the thoracic cavity and consequently without squeezing the tissue by palpation to retain the original shape and size of the lung lobes as much as possible.

CT scanning is a highly sensitive and quantitative method for evaluation of pulmonary lesions, which allows to detect TB lesions $<1\,mm^3$ that would be difficult to find by direct macroscopic evaluation (35). To obtain a reasonable resolution of CT images, we faced the issue of density of the formalin solution. The lungs had to be immersed in formalin for >2 months for biosafety reasons before they could be transferred to the CT device located outside the high containment facility. The software deployed for the image analysis insufficiently differentiated the margin of the lungs because the attenuation value of formalin was very similar to the attenuation of the lung tissue. Therefore, the formalin solution was drained from the lungs as much as possible. In some cases, it was still unavoidable to mark the volume of the lung tissue on the digital image by hand. Although this was time-intensive, it guaranteed a detailed analysis of every virtual slice and, consequently, of every part of the lungs.

Perez de Val et al. (35) distinguished four different kinds of lesions (calcified, cavitary, solid, and complex) by CT and calculated the total pulmonary volume and the volume of lesions. Solid lesions with less calcification or caverns are difficult to detect automatically with the analysis software, and it is necessary to observe every slice to characterize and measure the TB lesions. While this is tedious, it bears the capacity to detect small changes in density patterns due to inflammatory reactions around granulomas that may not be visible by direct macroscopic observation. Granulomas classified as multicentric by histology often comprise multiple foci of mineralization. Some of them may have been identified as separate small granulomas <5 mm by CT. Multicentric granulomas could result from fusion of monocentric granulomas that have developed in close proximity. It was difficult to decide by CT whether some granulomas around the bronchial system and deeper in the lung tissue that were located very close to each other represented separate granulomas or one large confluent lesion. Comparison of CT and histologic findings of the same area, however, revealed that the granulomas were mostly separate entities.

The use of CT has several advantages compared to radiography. A three-dimensional view that can be reconstructed *in silico* by employing different programs for analyses allows for a more detailed evaluation of TB lesions. However, CT instruments are rarely available in high-containment facilities. Scanning of extirpated and fixated organs is a suitable workaround but only applicable for end-point determinations, as this depends on sacrifice of experimental animals. In contrast, digital radiography devices are rather small in size and weight, have comparably low investment needs, and come with surfaces that, at least in part, can be subjected to appropriate disinfection procedures. Thus, this technology offers an excellent opportunity to monitor the development of TB organ lesions *intra vitam* and over time. Therefore, we evaluated the applicability and resolution of a digital and portable radiography system for the infection model in goats. To mitigate an overlap of the lung tissue, which impedes the exact evaluation of lung lesions, especially regarding numbers and sizes, and to detect less mineralized granulomas, the left and right lungs were imaged separately. However, even this measure was insufficient to prevent a significant overlap. Furthermore, it was difficult to place the lungs always in the same position to allow for standardized evaluation. These problems do t arise in living animals. Therefore, digital radiography is an intriguing option to identify animals that develop lesions after inoculation and follow the development of TB lung lesions *intra vitam*.

Cavitary lesions are common features in advanced stages of human and caprine TB. Despite the severe necrosis found

in some lesions, cavitary lesions were not detected in studies deploying aerosol inoculation (21). The authors speculated that, because of the progressive worsening of the animals' condition, they had to be sacrificed very early at 12 weeks p.i. Other studies that have applied the inoculum endobronchially in goats (13, 35) left the animals for 14 weeks and observed large cavitary lesions in the majority of the animals by then. In trials carried out on other species like badgers (59) and calves (60), using the endobronchial route of infection, lesions progressed slowly, resembling what is observed in natural cases of TB in these species (13). Particularly in low challenge-dose experiments in calves, large coalescent lesions were usually not found. Goats seem to show a faster progression of lesions, which can be considered advantageous for experimental conditions (13). We necropsied animals 20 weeks pi. Given the sizes of the lesions observed including a huge cavern in one animal, it is likely that, similar to the endobronchial application (13), the spray catheter application results in cavernous lesions early on.

DATA AVAILABILITY STATEMENT

The raw data supporting the conclusions of this article will be made available by the authors, without undue reservation.

ETHICS STATEMENT

The animal study was reviewed and approved by Committee on the Ethics of Animal Experiments of the State of Thuringia, Germany; Committee on the Ethics of Animal Experiments of the State of Mecklenburg-Western Pomerania, Germany. Written informed consent was obtained from the owners for the participation of their animals in this study.

AUTHOR CONTRIBUTIONS

SK, LG, and CM coordinated the research project. HK conceived the study and planned and supervised the animal experiment, bacterial culture, and immunological experiments. EL-T and RU performed the necropsies. EL-T conducted macroscopic and histologic assessments of the lesions. SB supervised the molecular typing of the inoculum. NW, JF, and MR performed the animal experiments and analyzed the data. KP and NW analyzed the radiological data. SP made the radiographs. NW, CM, and EL-T drafted the manuscript. All the authors discussed the results, commented on the manuscript, and read and approved the final version of the manuscript.

FUNDING

The project Innovative Vaccines against *Mycobacterium tuberculosis* complex (MTC) and *Staphylococcus aureus* for application in veterinary and human medicine (funding code 03ZZ0806C) was funded by the German Ministry for Education and Research (BMBF) as part of the consortium InfectControl 2020–Novel Anti-Infective Strategies.

ACKNOWLEDGMENTS

The authors sincerely thank Diana Tiesel, Michelle Fischer, Christopher Sust, Lisa-Marie Karnbach, Lisa Wolf, and Wolfram Maginot (Friedrich-Loeffler-Institute, Institute for Molecular Pathogenesis) for their excellent technical assistance. We appreciate the valuable support by Charlotte Schröder, Bärbel Hammerschmidt, and the staff of the experimental animal facilities of the Jena and the Isle of Riems sites of the Friedrich-Loeffler-Institute, and Ella Wenz, Clinic for Small Animals, Radiology, Justus-Liebig-University Giessen, for the technical support by scanning the goats' lungs.

SUPPLEMENTARY MATERIAL

The Supplementary Material for this article can be found online at: https://www.frontiersin.org/articles/10.3389/fvets.2022.877322/full#supplementary-material

REFERENCES

1. Herzmann C, Sotgiu G, Bellinger O, Diel R, Gerdes S, Goetsch U, et al. Risk for latent and active tuberculosis in Germany. *Infect*. (2017) 45:283–90. doi: 10.1007/s15010-016-0963-2
2. Caminiti A, Pelone F, LaTorre G, De Giusti M, Saulle R, Mannocci A, et al. Control and eradication of tuberculosis in cattle: a systematic review of economic evidence. *Vet Rec*. (2016) 179:70–5. doi: 10.1136/vr.103616
3. Thomas J, Balseiro A, Gortazar C, Risalde MA. Diagnosis of tuberculosis in wildlife: a systematic review. *Vet Res*. (2021) 52:31. doi: 10.1186/s13567-020-00881-y
4. World Health Organization. *Global Tuberculosis Report 2020*. Geneva: WHO (2020).
5. Taye H, Alemu K, Mihret A, Wood JLN, Shkedy Z, Berg S, et al. Global prevalence of *Mycobacterium bovis* infections among human tuberculosis cases: systematic review and meta-analysis. *Zoonoses Public Health*. (2021) 68:704–18. doi: 10.1111/zph.12868
6. Buddle BM, Parlane NA, Wedlock DN, Heiser A. Overview of vaccination trials for control of tuberculosis in cattle, wildlife and humans. *Transbound Emerg Dis*. (2013) 60(Suppl.1):136–46. doi: 10.1111/tbed.12092
7. Kaufmann SH. Tuberculosis vaccines: time to think about the next generation. *Semin Immunol*. (2013) 25:172–81. doi: 10.1016/j.smim.2013.04.006
8. Vordermeier HM, Perez de Val B, Buddle BM, Villarreal-Ramos B, Jones GJ, Hewinson RG, et al. Vaccination of domestic animals against tuberculosis: review of progress and contributions to the field of the TBSTEP project. *Res Vet Sci*. (2014) 97:S53–60. doi: 10.1016/j.rvsc.2014.04.015
9. Kaufmann SH. Immune response to tuberculosis: experimental animal models. *Tuberculosis*. (2003) 83:107–11. doi: 10.1016/S1472-9792(02)00063-X
10. Cardona PJ, Prats C. The small breathing amplitude at the upper lobes favors the attraction of polymorph nuclear neutrophils to *Mycobacterium tuberculosis* lesions and helps to understand the evolution toward active disease in an individual-based model. *Front Microbiol*. (2016) 7:354. doi: 10.3389/fmicb.2016.00354
11. Cardona PJ. Pathogenesis of tuberculosis and other mycobacteriosis. *EnfermInfecc Microbiol Clin*. (2018) 36:38–46. doi: 10.1016/j.eimce.2017.10.009
12. Scanga CA, Flynn JL. Modeling tuberculosis in nonhuman primates. *Cold Spring HarbPerspect Med*. (2014) 4:018564. doi: 10.1101/cshperspect.a018564
13. de Val Perez B, Lopez-Soria S, Nofrarias M, Martin M, Vordermeier HM, Villarreal-Ramos B, et al. Experimental model of tuberculosis in the domestic

goat after endobronchial infection with *Mycobacterium caprae*. *Clin Vaccine Immunol*. (2011) 18:1872–81. doi: 10.1128/CVI.05323-11
14. Domingo M, Vidal E, Marco A. Pathology of bovine tuberculosis. *Res Vet Sci*. (2014) 97:S20–9. doi: 10.1016/j.rvsc.2014.03.017
15. Ramirez IC, Santillan MA, Dante V. The goat as an experimental ruminant model for tuberculosis infection. *Small Ruminant Res.* (2003) 47:113–6. doi: 10.1016/S0921-4488(02)00243-2
16. McLaughlin RF, Tyler WS, Canada RO. A study of the subgross pulmonary anatomy in various mammals. *Am J Anat*. (1961) 108:149–65 doi: 10.1002/aja.1001080203
17. Magno M. Comparative anatomy of the tracheobronchial circulation. *Eur Respir J*. (1990) 12:557s−63s.
18. Liebler-Tenorio EM, Pabst R. MALT structure and function in farm animals. *Vet Res*. (2006) 37:257–80. doi: 10.1051/vetres:2006001
19. Seva J, Hernández D, Bernabé A, Pallarés FJ, Navarro JA. Immunophenotypical characterization of the lymphocyte infiltrate in caprine pulmonary tuberculosis. *J Comp Pathol*. (2000) 123:96–103. doi: 10.1053/jcpa.2000.0397
20. Sanchez J, Tomas L, Ortega N, Buendia AJ, del Rio L, Salinas J, et al. Microscopical and immunological features of tuberculoid granulomata and cavitary pulmonary tuberculosis in naturally infected goats. *J Comp Pathol*. (2011) 145:107–17. doi: 10.1016/j.jcpa.2010.12.006
21. Gonzalez-Juarrero M, Bosco-Lauth A, Podell B, Soffler C, Brooks E, Izzo A, et al. Experimental aerosol *Mycobacterium bovis* model of infection in goats. *Tuberculosis*. (2013) 93:558–64. doi: 10.1016/j.tube.2013.05.006
22. Bezos J, de Juan L, Romero B, Alvarez J, Mazzucchelli F, Mateos A, et al. Experimental infection with *Mycobacterium caprae* in goats and evaluation of immunological status in tuberculosis and paratuberculosis co-infected animals. *Vet Immunol Immunopathol*. (2010) 133:269–75. doi: 10.1016/j.vetimm.2009.07.018
23. Perez de Val B, Vidal E, Villarreal-Ramos B, Gilbert SC, Andaluz A, Moll X, et al. A multi-antigenic adenoviral-vectored vaccine improves BCG-induced protection of goats against pulmonary tuberculosis infection and prevents disease progression. *PLoS ONE*. (2013) 8:e81317. doi: 10.1371/journal.pone.0081317
24. Herfst S, Bohringer M, Karo B, Lawrence P, Lewis NS, Mina MJ, et al. Drivers of airborne human-to-human pathogen transmission. *Curr Opin Virol*. (2017) 22:22–9. doi: 10.1016/j.coviro.2016.11.006
25. Bezos J, Casal C, Alvarez J, Roy A, Romero B, Rodriguez-Bertos A, et al. Evaluation of the Mycobacterium tuberculosis SO_2 vaccine using a natural tuberculosis infection model in goats. *Vet J*. (2017) 223:60–7. doi: 10.1016/j.tvjl.2017.04.006
26. Roy A, Tome I, Romero B, Lorente-Leal V, Infantes-Lorenzo JA, Dominguez M, et al. Evaluation of the immunogenicity and efficacy of BCG and MTBVAC vaccines using a natural transmission model of tuberculosis. *Vet Res*. (2019) 50:82. doi: 10.1186/s13567-019-0702-7
27. Bojarski C, Waldner M, Rath T, Schürmann S, Neurath MF, Atreya R, et al. Innovative diagnostic endoscopy in inflammatory bowel diseases: from high-definition to molecular endoscopy. *Front Med*. (2021) 8:655404. doi: 10.3389/fmed.2021.655404
28. Khosrawipour V, Mikolajczyk A, Paslawski R, Plociennik M, Nowak K, Kulas J, et al. Intrathoracic aerosol chemotherapy *via* spray-catheter. *Mol Clin Oncol*. (2020) 12:350–4. doi: 10.3892/mco.2020.1999
29. Arrieta-Villegas C, Perálvarez T, Vidal E, Puighibet Z, Moll X, Canturri A, et al. Efficacy of parenteral vaccination against tuberculosis with heat-inactivated *Mycobacterium bovis* in experimentally challenged goats. *PLoS ONE*. (2018) 13:e0196948. doi: 10.1371/journal.pone.0196948
30. Maue AC, Waters WR, Palmer MV, Whipple DL, Minion FC, Brown WC, et al. CD80 and CD86, but not CD154, augment DNA vaccine-induced protection in experimental bovine tuberculosis. *Vaccine*. (2004) 23:769–79. doi: 10.1016/j.vaccine.2004.07.019
31. Sharpe AH. Mechanisms of costimulation. *Immunol Rev*. (2009) 229:5–11. doi: 10.1111/j.1600-065X.2009.00784.x
32. Warren RM, Gey van Pittius NC, Barnard M, Hesseling A, Engelke E, de Kock M, et al. Differentiation of *Mycobacterium tuberculosis* complex by PCR amplification of genomic regions of difference. *Int J Tuberc Lung Dis*. (2006) 10:818–22.
33. Ohlerth S, Becker-Birck M, Augsburger H, Jud R, Makara M, Braun U. Computed tomography measurements of thoracic structures in 26 clinically normal goats. *Res Vet Sci*. (2012) 92:7–12. doi: 10.1016/j.rvsc.2010.10.019
34. Balseiro A, Thomas J, Gortázar C, Risalde MA. Development and challenges in animal tuberculosis vaccination. *Pathogens*. (2020) 9:472. doi: 10.3390/pathogens9060472
35. Perez de Val B, Villarreal-Ramos B, Nofrarias M, Lopez-Soria S, Romera N, Singh M, et al. Goats primed with Mycobacterium bovis BCG and boosted with a recombinant adenovirus expressing Ag85A show enhanced protection against tuberculosis. *Clin Vaccine Immunol*. (2012) 19:1339–47. doi: 10.1128/CVI.00275-12
36. Prohl A, Ostermann C, Lohr M, Reinhold P. The bovine lung in biomedical research: visually guided bronchoscopy, intrabronchial inoculation and in vivo sampling techniques. *J Vis Exp*. (2014) 89:51557. doi: 10.3791/51557
37. Kohl TA, Utpatel C, Niemann S, Moser I. 2018 *Mycobacterium bovis* persistence in two different captive wild animal populations in Germany: a longitudinal molecular epidemiological study revealing pathogen transmission by whole-genome sequencing. *J Clin Microbiol*. (2018) 56:e00302–18. doi: 10.1128/JCM.00302-18
38. Taylor GM, Worth DR, Palmer S, Jahans K, Hewinson RG. Rapid detection of *Mycobacterium bovis* DNA in cattle lymph nodes with visible lesions using PCR. *BMC Vet Res*. (2007) 3:12. doi: 10.1186/1746-6148-3-12
39. Ruettger A, Nieter J, Skrypnyk A, Engelmann I, Ziegler A, Moser I, et al. Rapid spoligotyping of *Mycobacterium tuberculosis* complex bacteria by use of a microarray system with automatic data processing and assignment. *J Clin Microbiol*. (2012) 50:2492–5. doi: 10.1128/JCM.00442-12
40. Frothingham R, Meeker-O'Connell WA. Genetic diversity in the *Mycobacterium tuberculosis* complex based on variable numbers of tandem DNA repeats. *Microbiology*. (1998) 144:1189–96. doi: 10.1099/00221287-144-5-1189
41. Supply P, Allix C, Lesjean S, Cardoso-Oelemann M, Rüsch-Gerdes S, Willery E, et al. Proposal for standardization of optimized mycobacterial interspersed repetitive unit-variable-number tandem repeat typing of *Mycobacterium tuberculosis*. *J Clin Microbiol*. (2006) 44:4498–510. doi: 10.1128/JCM.01392-06
42. Wangoo A, Johnson L, Gough J, Ackbar R, Inglut S, Hicks D, et al. Advanced granulomatous lesions in *Mycobacterium bovis*-infected cattle are associated with increased expression of type I procollagen, gammadelta (WC1+) T cells and CD 68+ cells. *J Comp Pathol*. (2005) 133:223–34. doi: 10.1016/j.jcpa.2005.05.001
43. Garcia-Jimenez WL, Fernandez-Llario P, Gomez L, Benitez-Medina JM, Garcia-Sanchez A, Martinez R, et al. Histological and immunohistochemical characterisation of *Mycobacterium bovis* induced granulomas in naturally infected fallow deer (*Damadama*). *Vet Immunol Immunopathol*. (2021) 149:66–75. doi: 10.1016/j.vetimm.2012.06.010
44. Openagrar.de. Tuberkulose der Rinder: *Mycobacterium bovis* und *Mycobacterium caprae*. In: AmtlicheMethode und Falldefinition, Friedrich-Loeffler-Institut, Federal Research Institute for Animal Health. (2021). Available online at: https://www.openagrar.de/receive/openagrar_mods_00054079 (accessed January 25, 2022).
45. Bezos J, Casal C, Diez-Delgado I, Romero B, Liandris E, Alvarez J, et al. Goats challenged with different members of the *Mycobacterium tuberculosis* complex display different clinical pictures. *Vet Immunol Immunopathol*. (2015) 167:185–9. doi: 10.1016/j.vetimm.2015.07.009
46. Holder A, Garty R, Elder C, Mesnard P, Laquerbe C, Bartens MC, et al. Analysis of genetic variation in the bovine SLC11A1 gene, its influence on the expression of NRAMP1 and potential association with resistance to bovine tuberculosis. *Front Microbiol*. (2020) 11:1420. doi: 10.3389/fmicb.2020.01420
47. Metcalfe HJ, Biffar L, Steinbach S, Guzman E, Connelley T, Morrison I, et al. Ag85A-specific CD4(+) T cell lines derived after boosting BCG-vaccinated cattle with Ad5-85A possess both mycobacterial growth inhibition and anti-inflammatory properties. *Vaccine*. (2018) 36:2850–4. doi: 10.1016/j.vaccine.2018.03.068
48. Prodinger WM, Eigentler A, Allerberger F, Schönbauer M, Glawischnig W. Infection of red deer, cattle, and humans with *Mycobacterium bovis* subsp. caprae in western Austria. *J Clin Microbiol*. (2002) 40:2270–2. doi: 10.1128/JCM.40.6.2270-2272.2002

49. Domogalla J, Prodinger WM, Blum H, Krebs S, Gellert S, Müller M, et al. Region of difference 4 in alpine *Mycobacterium caprae* isolates indicates three variants. *J Clin Microbiol.* (2013) 51:1381–8. doi: 10.1128/JCM.02966-12
50. Rettinger A, Broeckl S, Fink M, Prodinger WM, Blum H, Krebs S, et al. The region of difference four is a robust genetic marker for subtyping *Mycobacterium caprae* isolates and is linked to spatial distribution of three subtypes. *Transbound Emerg Dis.* (2017) 64:782–92. doi: 10.1111/tbed.12438
51. El-Sayed A, El-Shannat S, Kamel M, Castañeda-Vazquez MA, Castañeda-Vazquez H. Molecular epidemiology of *Mycobacterium bovis*in humans and cattle. *Zoonoses Public Health.* (2016) 63:251–64. doi: 10.1111/zph.12242
52. Rodgers JD, Connery NL, McNair J, Welsh MD, Skuce RA, Bryson DG, et al. Experimental exposure of cattle to a precise aerosolized challenge of *Mycobacterium bovis*: a novel model to study bovine tuberculosis. *Tuberculosis.* (2007) 87:405–14. doi: 10.1016/j.tube.2007.04.003
53. Buddle BM, Keen D, Thomson A, Jowett G, McCarthy AR, Heslop J, et al. Protection of cattle from bovine tuberculosis by vaccination with BCG by the respiratory or subcutaneous route, but not by vaccination with killed *Mycobacterium vaccae*. *Res Vet Sci*. (1995) 59:10–6. doi: 10.1016/0034-5288(95)90023-3
54. Cassidy JP. The pathogenesis and pathology of bovine tuberculosis with insights from studies of tuberculosis in humans and laboratory animal models. *Vet Microbiol*. (2006) 112:151–61. doi: 10.1016/j.vetmic.2005.11.031
55. Buddle BM, Vordermeier HM, Hewinson RG. Experimental infection models of tuberculosis in domestic livestock. *Microbiol Spectr*. (2016) 4:2016. doi: 10.1128/microbiolspec.TBTB2-0017-2016
56. Soffler C, Bosco-Lauth AM, Aboellail TA, Marolf AJ, Bowen RA. Development and characterization of a caprine aerosol infection model of melioidosis. *PLoS ONE.* (2012) 7:e43207. doi: 10.1371/journal.pone.0043207
57. Dzikiti TB. Intravenous anaesthesia in goats: a review. *J South African Vet Assoc.* (2013) 84:E1–8. doi: 10.4102/jsava.v84i1.499
58. Stierschneider M, Franz S, Baumgartner W. Endoscopic examination of the upper respiratory tract and oesophagus in small ruminants: technique and normal appearance. *Vet J.* (2007) 173:101–8. doi: 10.1016/j.tvjl.2005.09.002
59. Corner LA, Costello E, Lesellier S, O'Meara D, Gormley E. Experimental tuberculosis in the European badger (*Melesmeles*) after endobronchial inoculation with *Mycobacterium bovis*: II. Progression of infection. *Res Vet Sci.* (2008) 85:481–90. doi: 10.1016/j.rvsc.2008.03.003
60. Vordermeier HM, Villarreal-Ramos B, Cockle PJ, McAulay M, Rhodes SG, Thacker T, et al. Viral booster vaccines improve *Mycobacterium bovis* BCG-induced protection against bovine tuberculosis. *Infect Immun.* (2009) 77:3364–73. doi: 10.1128/IAI.00287-09

Conflict of Interest: LG was employed by Vakzine Projekt Management GmbH.

The remaining authors declare that the research was conducted in the absence of any commercial or financial relationships that could be construed as a potential conflict of interest.

Publisher's Note: All claims expressed in this article are solely those of the authors and do not necessarily represent those of their affiliated organizations, or those of the publisher, the editors and the reviewers. Any product that may be evaluated in this article, or claim that may be made by its manufacturer, is not guaranteed or endorsed by the publisher.

frontiers | Frontiers in Veterinary Science

REVIEW
published: 20 May 2022
doi: 10.3389/fvets.2022.878952

Use of Translational, Genetically Modified Porcine Models to Ultimately Improve Intestinal Disease Treatment

*Cecilia R. Schaaf and Liara M. Gonzalez**

Department of Clinical Sciences, College of Veterinary Medicine, North Carolina State University, Raleigh, NC, United States

For both human and veterinary patients, non-infectious intestinal disease is a major cause of morbidity and mortality. To improve treatment of intestinal disease, large animal models are increasingly recognized as critical tools to translate the basic science discoveries made in rodent models into clinical application. Large animal intestinal models, particularly porcine, more closely resemble human anatomy, physiology, and disease pathogenesis; these features make them critical to the pre-clinical study of intestinal disease treatments. Previously, large animal model use has been somewhat precluded by the lack of genetically altered large animals to mechanistically investigate non-infectious intestinal diseases such as colorectal cancer, cystic fibrosis, and ischemia-reperfusion injury. However, recent advances and increased availability of gene editing technologies has led to both novel use of large animal models in clinically relevant intestinal disease research and improved testing of potential therapeutics for these diseases.

Keywords: cystic fibrosis, colorectal cancer, ischemia-reperfusion injury, genetically altered models, intestinal disease, translational porcine model, stem cell reporter model

OPEN ACCESS

Edited by:
Stefano Guido,
University of Edinburgh,
United Kingdom

Reviewed by:
Christopher K. Tuggle,
Iowa State University, United States
François J. M. A. Meurens,
Agroalimentaire et de l'alimentation de Nantes-Atlantique (Oniris), France

****Correspondence:***
Liara M. Gonzalez
lmgonza4@ncsu.edu

Specialty section:
This article was submitted to Comparative and Clinical Medicine, a section of the journal Frontiers in Veterinary Science

Received: *18 February 2022*
Accepted: *27 April 2022*
Published: *20 May 2022*

Citation:
Schaaf CR and Gonzalez LM (2022) Use of Translational, Genetically Modified Porcine Models to Ultimately Improve Intestinal Disease Treatment. Front. Vet. Sci. 9:878952. doi: 10.3389/fvets.2022.878952

INTRODUCTION

Gastrointestinal disease accounts for over 3.0 million hospitalizations and over $135.9 billion in health care expenditures per year (1). To lessen this incredible burden to patients and our healthcare system, animal models play a critical role in discovery of intestinal disease pathogenesis and therapeutic innovation. For successful clinical translation, it is critical that animal models are properly validated. The criteria used to validate an animal model include certifying similarity in biology and clinical presentation between model and human disease (face validity), confirming that clinical interventions produce similar effects (predictive ability), and demonstrating that the target under investigation has a similar role in the model compared to human clinical disease (target validity) (2). Of intestinal disease animal models, rodents are historically preferred for use due to their low cost and maintenance, rapid reproduction, and readily available rodent-specific reagents. However, it is now widely recognized that rodents do not fully mimic human disease, physiology, immunology, or drug metabolism, thus limiting their use as pre-clinical models for disease treatment (3–7). For example, despite promising pre-clinical murine anti-cancer therapeutic studies, success rate of these therapeutics in human clinical trial is only around 5% (4, 8). Furthermore, the small size of rodents makes it difficult to model and advance surgical and endoscopic techniques. The differences between rodents and humans have left gaps in both basic science research and pre-clinical model development for intestinal diseases.

To better represent both human physiology and disease, and aid in the discovery of new treatments, porcine models are gaining popularity. With similar genome, size and architecture of the intestine, omnivorous diet, microbiome, immunology, and physiology to humans, pigs are increasingly the preferred model of enteric diseases (**Table 1**) (3, 6, 13, 17–23). The large size of the pig allows for multiple, longitudinal sampling from the same individual. Their large litter size of around 12 piglets allows for ease of gender and sibling matching. These attributes reduce both experimental variation as well as overall animal use. Additionally, for toxicology and drug discovery testing, pigs have oral and parenteral dosing rates similar to humans as well as similar responses to a variety of drug classes (24).

Grossly, both human and porcine adult intestine are at a ratio of 0.1 length per kilogram of body weight (25). The anatomy of the small intestine is similar between pig and human, though the large intestine varies slightly in the pig due to a larger cecum, lack of appendix, and the presence of the spiral colon (**Figure 1**) (3). Microscopically, for both species, the small and large intestine are comprised of a single layer of epithelial cells, interspersed with intra-epithelial lymphocytes, to serve as a barrier between luminal contents and systemic circulation. The single layer epithelium covers villus projections (present only in small intestine) and extends down into the crypts of Lieberkuhn. Located at the crypt-base are the intestinal epithelial stem cells (ISCs), which are responsible for renewing the epithelial cell populations on a continuous 3–5 day cycle (17, 27–29). In the human, the ISCs are interspersed with Paneth cells, a specialized secretory cell type that both supports ISC function and releases antimicrobial factors into the intestinal lumen (30, 31). While a similar cell population expressing the same biomarkers and intracellular structures has been identified in the pig, the porcine Paneth cell has yet to be fully defined (15, 32).

Beneath the epithelial barrier is the lamina propria compartment. While the lamina propria is made up of a mix of structural elements including blood and lymph vessels, connective tissue, and mesenchymal cells, immune cells constitute a major population, including dendritic cells and lymphocytes. These immune cells are responsible for discriminating between harmless luminal antigens and potential enteropathogens (33–35). Some differences exist between the immunologic organization between human and pig intestine such as the distribution and frequency of lamina propria and intraepithelial lymphocyte populations, the inverted structure of porcine peripheral and gut-associated lymph nodes, and the aggregated lymphoid follicles (Peyer's patches) which form one long continuous band in the porcine ileum (22, 29, 35). However, despite these differences, pigs are still recognized as useful models in several enteric immunologic studies including infectious disease, oral vaccination, small bowel transplantation, food hypersensitivity, and immune development (13, 22, 36–39).

With these similarities in both physiology and architecture between human and porcine intestine (**Table 1**), porcine models of various intestinal injuries such as ischemia-reperfusion injury, intestinal transplantation, short gut syndrome, and necrotizing enterocolitis have progressed the field of gastroenterology (37, 40–44). Furthermore, *in vitro* advancements continue to broaden the utility of porcine enteric disease models. These advancements include an increase in porcine specific reagents and the use of primary intestinal epithelial cell culture in 2-D monolayers, 3-D organoid culture, and co-culture with microbes and lamina-propria derived cells to better understand intestinal barrier function (15, 16, 19, 20, 40, 41, 45). However, for more mechanistic studies and to better understand human genetic diseases in the wide array of intestinal maladies, advancements in porcine gene-edited models are needed. Fortunately, enhanced strategies to edit the porcine genome and develop transgenic models, as well as approaches to genetically modify porcine-derived intestinal organoids, have increased the availability of pre-clinical modeling for Cystic Fibrosis (CF), colorectal cancer (CRC), and ischemia-reperfusion injury (**Table 2**). This review summarizes the current use of pre-clinical, gene edited porcine intestinal disease and injury models and evaluates future additional needs to ultimately improve treatment of intestinal disease.

TABLE 1 | Summary of comparisons between human and porcine intestinal physiology and anatomy as well as advantages and disadvantages of porcine models.

Porcine intestine similarities to human	Porcine intestine differences from human
• Intestinal length • Omnivorous diet • Microbiome (9) • Immune response resembles human in 80% of analyzed parameters (10) • High genome homology (11, 12)	• Presence of spiral colon • Inverted lymph node structure • Distribution and frequency of intestinal lymphocyte populations • Continuous ileal Peyer's patch
Porcine model advantages	**Porcine model disadvantages**
• Husbandry well understood • Outbred breeds better mimic variation between human individuals (13) • Large litters for gender/sibling matching • Large animal size allows for improving surgical/endoscopy techniques using human equipment for diseases like Cystic Fibrosis and colorectal cancer • Longer lifespan permits longitudinal studies • Oral/parenteral dosing and responses to many drug classes similar to humans (14) • More accepted on ethical basis compared to non-human primates or other large animals • Numerous *in vitro* applications such as advanced 3D organoid cultures (15, 16)	• Necessitate large, specialized housing facilities • More expensive than mice • Not as many species-specific reagents as mice

GENE THERAPY IN PORCINE CYSTIC FIBROSIS MODELS TO ALLEVIATE INTESTINAL OBSTRUCTION

Cystic Fibrosis (CF) is a life-threatening disease due to various mutations in the CF transmembrane conductance regulator (*CFTR*) gene (57). This critical gene encodes for an anion channel widely expressed in epithelium including lung, pancreas, kidney, and intestine; its loss of function inhibits chloride

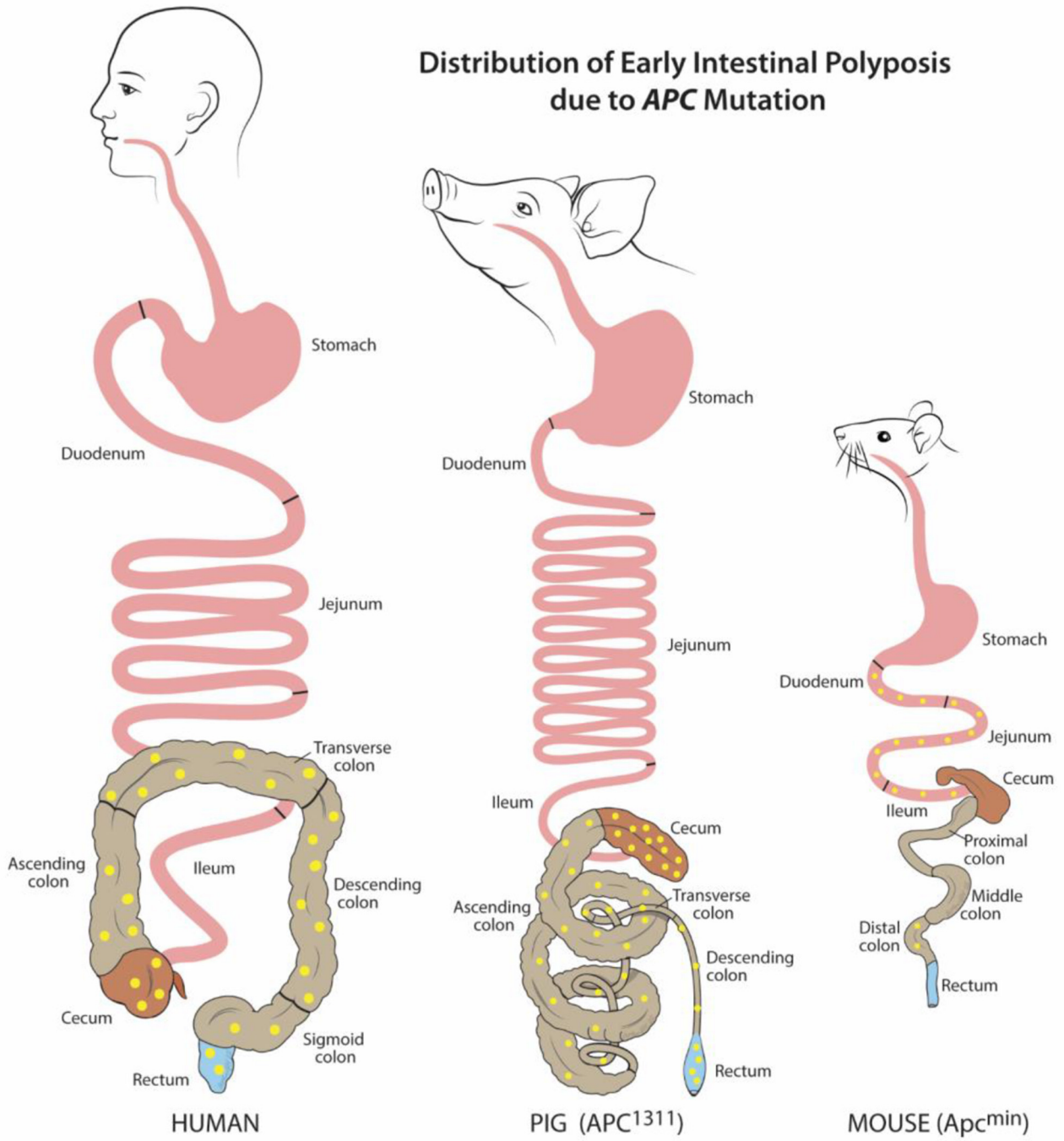

FIGURE 1 | Distribution of early intestinal polyposis due to *APC* mutation. Human and porcine (*APC*^{1311}) early adenoma/polyp distribution is similar within the colon and rectum, while murine (Apc^{min}) is mostly localized to the small intestine. Adenoma/polyps shown in yellow. Figure adapted from Gonzalez et al. and Flisikowska et al. (21, 26).

and bicarbonate transport across cell membranes. This leads to thick mucoid secretions with low pH, subsequent pathogen colonization, and dysregulated inflammation (57, 58). While cause of death in patients afflicted with CF is primarily due to respiratory failure, intestinal disease also contributes significantly to patient morbidity (59). Up to 20% of infants with CF suffer from meconium ileus at birth, followed by distal intestinal obstructive syndrome due to intestinal atresia, diverticulosis, and microcolon (46, 57). While genetically modified murine models of CF assisted in basic understanding of *CFTR* functions, these

TABLE 2 | Summary of findings from gene-edited porcine models of non-infectious intestinal disease.

Gene-edited porcine model	Key findings for intestinal disease	Sources
Cystic fibrosis		
CFTR$^{-/-}$	Intestinal gene editing to correct cystic fibrosis transmembrane conductance regulator (CFTR) expression alleviates Cystic Fibrosis induced obstructions	(46)
Colorectal cancer		
APC^{1311}	Adenomatous polyposis coli (*APC*) mutation model reproduces colonic and rectal polyps as seen in familial adenomatous polyposis (FAP)	(26)
	Identification of gene expression, micro-RNAs associated with FAP	(47–50)
	Development of nanoparticles to improve endoscopic identification of dysplastic lesions and adenomas	(51, 52)
TP53^{R167H}	Porcine TP53 isoforms expressed similarly to humans; TP53 variants and circular RNA overexpressed in colon	(53, 54)
KRAS^{G12D} *TP53*^{R167H}	Cre-recombinase inducible *TP53* and Kirsten rat sarcoma viral oncogene homolog (*KRAS*) mutation model leads to intestinal carcinoma development	(55)
Ischemia-reperfusion injury		
Enteroid culture	*In vitro* gene-editing of ischemic injured intestinal epithelium identifies cellular mechanisms of repair	(41)
Future directions: stem cell reporter		
LGR5-H2B-GFP	*In vivo* and *in vitro* tracking of LGR5^{+} intestinal stem cells, further model validation necessary	(56)

mice fail to fully recreate human clinical disease (59). These limitations in the mouse models impeded further discovery of disease pathogenesis and potential therapeutics.

In 2008, in an effort to develop an animal model that better represents CF clinical disease, Rogers et al. utilized recombinant adeno-associated virus (rAAV) vectors to create the first *CFTR*-null piglets (*CFTR*$^{-/-}$). These piglets also demonstrated immediate clinical signs of intestinal obstruction similar to that in human infants with CF (60). These clinical signs include intestinal atresia, microcolon, and diverticulosis (57). Other gene editing strategies have since been used to generate *CFTR*$^{-/-}$ pigs including bacterial artificial chromosome vectors (61) as well as rAAVs to introduce a point mutation within the *CFTR* gene, *CFTR*-ΔF508 mutation (59, 62). This specific *CFTR* mutation is the most common CF-causing mutation in human patients – it accounts for about 70% of CF alleles (62). Murine models with this same induced point mutation fail to develop airway disease, pushing the need for a porcine model of this common mutation. While *CFTR*-ΔF508 porcine models display the same features of human disease in the lung and intestine, the rate of meconium ileus is 100% in the newborn pigs, in contrast to a rate of 20% in human infants (46). As in humans, meconium ileus requires immediate medical and/or surgical correction, which inhibited the use of the porcine model due to cost and complexity. These factors pushed researchers to utilize additional gene editing techniques to alleviate meconium ileus in the porcine model. Stoltz et al. were able to correct this phenotype by inducing *CFTR* expression under the control of intestinal fatty acid-binding protein (*iFABP*) in *CFTR*$^{-/-}$ pig fibroblasts (46). These findings indicated that correcting the expression of *CFTR* by gene editing in the intestine is sufficient to prevent intestinal obstruction. Further work in the porcine CF models is necessary to identify exactly how much *CFTR* function is required for proper intestinal function. With these findings, novel gene therapy approaches can be developed such as somatic tissue gene editing to restore endogenous *CFTR* function. It is critical that this research is done in a porcine model, similarly sized to humans, so that delivery of therapeutics can be modeled using human equipment such as endoscopy. The information gained from a translational porcine model of CF will lead to the development of innovative gene therapy treatment approaches to alleviate CF-induced intestinal obstruction.

IMPROVED MODELING AND DETECTION OF COLORECTAL CANCER IN GENE EDITED PIGS

As of 2020 in the US, colorectal cancer (CRC) is the second leading cause of cancer related deaths for men and women combined (63). For many patients, including those with precursor familial adenomatous polyposis condition (FAP), CRC begins with germline or somatic mutations in the tumor-suppressor, adenomatous polyposis coli (*APC*) gene. This key driver mutation initiates polyp formation in the colonic epithelium. Subsequent compounding epigenetic changes and genetic mutations progresses tumorigenesis through the adenoma-carcinoma sequence, often culminating in metastatic cancer (64). For reasons unknown, CRC incidence has recently risen for young and middle-aged adults. Furthermore, many CRC tumor subtypes exist which remain without treatments (63). Without a doubt, there is a critical need for animal models to better understand CRC pathogenesis and develop targeted therapies. Attempts to recreate the polyp-adenoma-carcinoma pathogenesis sequence by mutating *Apc* (*Apc*$^{+/\min}$) in the mouse usually only leads to non-invasive, non-metastatic neoplasia. Furthermore, this neoplasia only typically occurs in the murine small intestine instead of the colon (**Figure 1**) (26, 65–67). Moreover, the small size of mice and critical differences in drug metabolism make these mice impractical for development of human CRC drug therapies, progress in endoscopic imaging techniques, or improving surgical interventions.

To overcome these barriers and create an improved, human-scale CRC model, the first gene-targeted APC mutated pig line was developed by inserting a translational stop signal at codon 1311 (*APC*^{1311}). This mutation is orthologous to the germline mutations in patients with familial adenomatous polyposis condition (FAP) (26). In these genetically modified pigs, colonic, and rectal polyps and adenomas develop such as

those found in human FAP and CRC patients (**Figure 1**) (68). Since their development, these pigs have contributed greatly to the discovery of epigenetic modifications, dysplastic polyp premalignant progression, and the function of genes other than *APC* that contribute to the varying severity and progression of disease in patients with FAP (47–49, 69). One pivotal study by Stachowiak et al., using APC^{1311} pigs, was the first to reveal that microRNAs are associated with premalignant transformation of colon polyps and can serve as potential useful biomarkers of disease development (50). Tan et al. attempted to replicate the *APC* mutation porcine model by transcription activator-like effector nucleases (TALENs) introduction of a stop signal at codon 902; however, these pigs have yet to develop CRC phenotype (70).

In addition to the APC^{1311} line, other mutated tumor suppressor gene porcine models are now available to study tumorigenesis. One such group carries a latent Cre-activated tumor protein *p53* gene (*TP53*) mutated allele ($TP53^{R167H}$) (53). This mutation is orthologous to the oncogenic human mutant *TP53* allele that plays a role in numerous human cancers including CRC. Previously, studies using the APC^{1311} pigs reported that in severe cases of polyposis, there is an increase in expression of polymorphic *TP53* (49). A more recent study using the $TP53^{R167H}$ pig demonstrated that these pigs express *TP53* isoforms in a more similar manner to humans, further underscoring the benefits of porcine cancer models compared to murine. The $TP53^{R167H}$ porcine model showed that *TP53* variants and circular RNA are overexpressed in the colon, indicating likely oncogenic function (54). These findings highlight the important role of porcine oncogenic models to improve our understanding of the genetic and epigenetic changes that contribute to CRC pathogenesis. Further developments on the $TP53^{R167H}$ model include the addition of inducible Kirsten rat sarcoma viral oncogene homolog (*KRAS*) mutation (55, 71). Mutated *KRAS* is present in over 25% of human tumors, including CRC, and is one of the more commonly activated oncogenes (72). Schook et al. showed that these Cre recombinase inducible $KRAS^{G12D}$ $TP53^{R167H}$ transgenic pigs developed rapid and reproducible mesenchymal tumors. For more specific study of intestinal cancer, Callesen et al. refined the combined *KRAS* and *TP53* mutation model by directing the control of the inducible recombination events under an intestinal epithelial specific gene promoter, which led to development of duodenal carcinoma. Further model establishment studies using the $KRAS^{G12D}$ $TP53^{R167H}$ pigs are warranted to establish carcinoma development in the lower intestine in order to better understand CRC carcinogenesis in a translational large animal model.

While these gene-targeted porcine CRC models have served an important role for cellular mechanistic studies, they can also afford clinicians and researchers opportunities to improve endoscopy skills for minimally invasive surgery, conduct longitudinal sampling and monitoring during treatment, and enhance detection systems for pre-malignancies in a human-sized animal model. In general, porcine models have been popular for testing and advancing endoscopic techniques, particularly for colonoscopy (73–75). Early diagnostic detection of colon dysplasia and adenomas typically relies on white-light endoscopy (76). However, due to the subtle appearance of adenomas *in situ*, early-stage CRC lesions are often missed, especially in patients with abnormal colonic mucosa due to inflammatory bowel disease (51, 52). To improve real-time detection of colorectal adenomas, one group developed biodegradable near-infrared fluorescent silica nanoparticles (FSNs) (52). These FSNs, administered intravascularly, permeate into cancerous tissue and 'mark' a lesion because tumor and dysplasia-associated blood and lymph vessels are typically leaky (52, 77). Additionally, development of these biodegradable FSNs ensured no long-term sequestration within the body, as is typical of traditional nanoparticles (52). In that study, nanoparticle application was tested by administering FSNs to APC^{1311} pigs intravenously. Twenty-four hours later, colons were surveyed using near-infrared fluorescence-assisted white light endoscopy and adenomas were successfully highlighted by the FSNs (52). Since this study, additional work has successfully tested other probes in the APC^{1311} pigs to serve as CRC polyp markers (51). This pre-clinical application testing made possible by the APC^{1311} pigs was critical to develop new techniques to accurately identify clinically significant colorectal dysplasia in human patients.

GENE EDITING IN PORCINE *IN VITRO* MODELS OF ISCHEMIA-REPERFUSION INJURY

Ischemic injury occurs when there is reduction or complete loss of blood flow to an organ. In the intestine, ischemic events can occur due to numerous pathologic events including thrombi, emboli, shock, cardiac insult, mechanical obstruction such as a hernia or intussusception, or necrotizing enterocolitis (21). In all of these disease states, the decrease in blood flow to the intestine diminishes the oxygen supply necessary for normal cellular metabolism. Cell damage and apoptosis quickly follows, particularly within the intestinal epithelium that is responsible for maintaining a critical barrier between harmful luminal microbes and systemic vasculature. Microbial translocation across a compromised epithelial barrier can develop into systemic inflammatory response syndrome, intestinal necrosis, and remote organ failure. Ultimately, this disease progression results in over 50% patient mortality (78). To lessen the high mortality rate, intestinal ischemia animal models are critical to better understand the pathophysiology of ischemic injury, identify factors driving epithelial repair, and develop potential therapeutics (40–42, 79).

The process of ischemia-induced epithelial cell loss, as described in numerous animal models, begins at the villus tip and progressively extends down to the crypt-base intestinal epithelial stem cell (ISC) compartment with increasing durations of ischemia (40, 80–83). In the ISC compartment, two populations of ISCs exist: active, proliferating ISCs that are sensitive to injury (aISCs) and quiescent, reserve ISCs that are injury resistant (rISCs). These two populations were first described using murine models (84, 85). However, small rodent models are unable to

accurately represent severe human ischemic injury, likely due to differences in intestinal microvascular anatomy and overall small intestinal size (17). Thus, the impact of ischemic injury on these two ISC populations was largely undescribed until the introduction of a porcine surgical model of mesenteric vascular occlusion (16, 17). With similar sized intestine and more similar microvascular anatomy as humans, pigs make for a better model of intestinal ischemia (17, 86). Using the surgical porcine model of mesenteric vascular occlusion, researchers identified that severe ischemic injury differentially impacts the two known ISC populations: aISCs undergo apoptosis while rISCs are preserved and are likely responsible for epithelial recovery after injury (40). In this model, rISCs were identified *in vivo* by expression of the known ISC biomarker homeodomain only protein X (HOPX) (85). When ischemic-injured tissue, initially enriched in $HOPX^+$ rISCs, was recovered *in vivo* for up to 3 days post injury, increased signs of crypt-base epithelial regeneration corresponded to a decrease in HOPX expression (41). Until this point, HOPX, a known tumor-suppressor gene in other cell types, had served as merely a biomarker of rISCs (87). To clarify the potential role of HOPX as a controller of ISC proliferation after severe ischemia, genetic modification of the porcine ischemic injury model was necessary.

Whole animal, genetically-modified porcine models have yet to be used in intestinal ischemia-reperfusion studies. However, recent advances in genetic modification of porcine intestinal crypt culture are a promising first step for more mechanistic studies. Culture techniques for porcine enteroids, 3D organoids derived from intestinal stem cells that recapitulate the intestinal epithelium, have been well described (15, 16, 28). Using lentivirus, Khalil et al. were the first group to genetically modify uninjured porcine intestinal crypts to create GFP expressing enteroids (88). To better understand epithelial recovery after ischemic injury and the specific role of HOPX function in epithelial crypt cells, Stewart et al. utilized adenovirus mediated transduction of short hairpin RNA to silence *HOPX* within ischemic injured crypt epithelium and showed that HOPX serves to suppress cellular proliferation in resultant enteroids (41). This novel advancement in porcine enteroids encourages future experiments of *in vitro* gene editing to improve our understanding of repair mechanisms in clinically relevant intestinal ischemia.

FUTURE DIRECTIONS: DEVELOPMENT OF TRANSGENIC PORCINE INTESTINAL STEM CELL REPORTER MODELS

To improve studies of the cellular mechanisms involved in various types of intestinal injury and cancer, transgenic reporter porcine models are warranted for *in vivo* and *in vitro* cell tracking of intestinal cell populations. Intestinal epithelial stem cell reporter pigs are of particular interest as ISCs play critical roles in both the generation of colorectal cancer and in epithelial barrier regeneration during homeostasis and disease (89–91). With the development of high efficiency genome editing tools, one group generated a novel porcine cell reporter model *via* CRISPR-Cas9 insertion of fused histone 2B (H2B) to green fluorescent protein (GFP) under the *ACTB* locus (92). With successful ubiquitous nuclear expression of GFP demonstrated within these pigs, the same group went on to insert the H2B-GFP sequence under control of leucine-rich repeat-containing G protein-coupled receptor 5 (*LGR5)*, a known biomarker expressed by ISCs (LGR5-H2B-GFP) (56, 84). Histologic sections of colon demonstrated nuclear GFP in the crypt base cell populations in this novel model. However, to truly utilize this translational model and isolate ISCs for study of intestinal disease, further work is necessary to conclude that these GFP expressing cells are in fact $LGR5^+$ ISCs. With this information, researchers would then have access to the first ever large animal ISC reporter, making way for improved translational studies of colorectal cancer development and intestinal barrier function and repair.

FUTURE DIRECTIONS: TRANSGENIC PORCINE MODELS OF INFLAMMATORY BOWEL DISEASE

Inflammatory Bowel Disease (IBD) is a multifactorial disease that is typically categorized as Crohn's Disease (CD) or Ulcerative Colitis (UC). These syndromes are characterized by inflammation of the intestinal mucosa, influx of immune cells, and dysregulated cytokine production. Subsequently, patients suffer from episodes of abdominal pain, diarrhea, bloody stools, and weight loss (93). Historically, gene edited rodent models have been used to determine underlying etiologies and test therapeutic targets (94). Murine models of IBD include knock-outs of cytokines such as IL-10, TGF-β, IL-2, and IL-23. Loss of these cytokines disrupts regulation of inflammation in the intestine, leading to intestinal lesions similar to those seen in IBD (95–98). Mice have also been engineered to over express signals such as IL-7 or STAT4 to upregulate immune cell activity and induce IBD (99, 100). However, given the immunological differences known between man and mouse (5, 7), alternative models that better emulate human immune physiology are needed to test surgical interventions and pharmaceutical therapeutics. A host of factors have been identified to contribute to IBD including gut microbiota, environmental factors, and abnormal innate and adaptive immune responses (93). Pigs, with similar intestinal microbiota, immunology, and anatomy to humans, are the clear choice for IBD models (3, 6, 13, 18–23). Chemical-induction of IBD by dextran sulfate sodium (DSS) or trinitrobenzenesulfonic acid (TNBS) has been shown to reproduce intestinal lesions in the pig similar to those found in UC and CD, respectively (101–105). These models have been used to test advanced endoscopic techniques to correct strictures and supplemental amino acid therapy. To study IBD on a more mechanistic level within a translationally relevant large animal model, transgenic induced IBD porcine models, parallel to the IBD murine models, are needed to mimic the specific immune cell dysregulations seen with IBD.

CONCLUSIONS

The need for large animal models, particularly porcine, to improve pre-clinical intestinal disease translational research is well known. As described in this review, innovative applications of gene-edited porcine models of Cystic Fibrosis, colorectal cancer, and ischemia-reperfusion injury have progressed both the mechanistic understanding of disease pathophysiology as well as led to novel therapeutic treatment development. With continued improvement of gene-editing systems such as CRISPR/Cas, additional porcine models to track intestinal stem cells or simulate disorders such as Inflammatory Bowel Disease can be made available to further progress translational intestinal disease research.

AUTHOR CONTRIBUTIONS

CS drafted and edited the manuscript. LG edited and revised the manuscript. CS and LG approved the final version of the manuscript.

REFERENCES

1. Peery AF, Crockett SD, Murphy CC, Lund JL, Dellon ES, Williams JL, et al. Burden and cost of gastrointestinal, liver, and pancreatic diseases in the United States: update 2018. *Gastroenterology*. (2019) 156:254–72.e11. doi: 10.1053/j.gastro.2018.08.063
2. Denayer T, Stöhr T, Van Roy M. Animal models in translational medicine: Validation and prediction. *New Horiz. Transl Med.* (2014) 2:5–11. doi: 10.1016/j.nhtm.2014.08.001
3. Kararli TT. Comparison of the gastrointestinal anatomy, physiology, and biochemistry of humans and commonly used laboratory animals. *Biopharm Drug Dispos.* (1995) 16:351–80. doi: 10.1002/bdd.2510160502
4. Mak IW, Evaniew N, Ghert M. Lost in translation: animal models and clinical trials in cancer treatment. *Am J Transl Res.* (2014) 6:114–8.
5. Mestas J, Hughes CCW. Of mice and not men: differences between mouse and human immunology. *J Immunol.* (2004) 172:2731. doi: 10.4049/jimmunol.172.5.2731
6. Lunney Joan K, Van Goor A, Walker Kristen E, Hailstock T, Franklin J, Dai C. Importance of the pig as a human biomedical model. *Sci Transl Med.* (2021) 13:eabd5758. doi: 10.1126/scitranslmed.abd5758
7. Seok J, Warren HS, Cuenca AG, Mindrinos MN, Baker HV, Xu W, et al. Genomic responses in mouse models poorly mimic human inflammatory diseases. *Proc Natl Acad Sci USA.* (2013) 110:3507–12. doi: 10.1073/pnas.1222878110
8. Hutchinson L, Kirk R. High drug attrition rates—where are we going wrong? *Nat Rev Clin Oncol.* (2011) 8:189–90. doi: 10.1038/nrclinonc.2011.34
9. Heinritz SN, Mosenthin R, Weiss E. Use of pigs as a potential model for research into dietary modulation of the human gut microbiota. *Nutr Res Rev.* (2013) 26:191–209. doi: 10.1017/S0954422413000152
10. Dawson HD, Reece JJ, Urban JF Jr. A comparative analysis of the porcine, murine, and human immune systems. *Vet Immunol Immunopathol.* (2009) 128:309. doi: 10.1016/j.vetimm.2008.10.211
11. Hart EA, Caccamo M, Harrow JL, Humphray SJ, Gilbert JGR, Trevanion S, et al. Lessons learned from the initial sequencing of the pig genome: comparative analysis of an 8 Mb region of pig chromosome 17. *Genome Biol.* (2007) 8:R168. doi: 10.1186/gb-2007-8-8-r168
12. Malkas LH, Herbert BS, Waleed A, Dobrolecki LE, Liu Y, Agarwal B, et al. A cancer-associated PCNA expressed in breast cancer has implications as a potential biomarker. *Proc Natl Acad Sci.* (2006) 103:19472–7. doi: 10.1073/pnas.0604614103
13. Meurens F, Summerfield A, Nauwynck H, Saif L, Gerdts V. The pig: a model for human infectious diseases. *Trends Microbiol.* (2012) 20:50–7. doi: 10.1016/j.tim.2011.11.002
14. Schelstraete W, Clerck LD, Govaert E, Millecam J, Devreese M, Deforce D, et al. Characterization of porcine hepatic and intestinal drug metabolizing cyp450: comparison with human orthologues from a quantitative, activity and selectivity perspective. *Sci Rep.* (2019) 9:9233. doi: 10.1038/s41598-019-45212-0
15. van der Hee B, Loonen LMP, Taverne N, Taverne-Thiele JJ, Smidt H, Wells JM. Optimized procedures for generating an enhanced, near physiological 2D culture system from porcine intestinal organoids. *Stem Cell Res.* (2018) 28:165–71. doi: 10.1016/j.scr.2018.02.013
16. Stewart AS, Freund JM, Blikslager AT, Gonzalez LM. Intestinal stem cell isolation and culture in a porcine model of segmental small intestinal ischemia. *J Vis Exp.* (2018) 135:57647. doi: 10.3791/57647
17. Nejdfors P, Ekelund M, Jeppsson B, Westrom BR. Mucosal *in vitro* permeability in the intestinal tract of the pig, the rat, and man: species- and region-related differences. *Scand J Gastroenterol.* (2000) 35:501–7. doi: 10.1080/003655200750023769
18. Käser T. Swine as biomedical animal model for T-cell research—Success and potential for transmittable and non-transmittable human diseases. *Mol Immunol.* (2021) 135:95–115. doi: 10.1016/j.molimm.2021.04.004
19. Dawson HD, Lunney JK. Porcine cluster of differentiation (CD) markers 2018 update. *Res Vet Sci.* (2018) 118:199–246. doi: 10.1016/j.rvsc.2018.02.007
20. Dawson HD, Sang Y, Lunney JK. Porcine cytokines, chemokines and growth factors: 2019 update. *Res Vet Sci.* (2020) 131:266–300. doi: 10.1016/j.rvsc.2020.04.022
21. Gonzalez LM, Moeser AJ, Blikslager AT. Porcine models of digestive disease: the future of large animal translational research. *Transl Res.* (2015) 166:12–27. doi: 10.1016/j.trsl.2015.01.004
22. Mair KH, Sedlak C, Käser T, Pasternak A, Levast B, Gerner W, et al. The porcine innate immune system: an update. *Dev Comp Immunol.* (2014) 45:321–43. doi: 10.1016/j.dci.2014.03.022
23. Nguyen TLA, Vieira-Silva S, Liston A, Raes J. How informative is the mouse for human gut microbiota research? *Dis Model Mech.* (2015) 8:1–16. doi: 10.1242/dmm.017400
24. Walters EM, Prather RS. Advancing swine models for human health and diseases. *Mo Med.* (2013) 110:212–5.
25. Patterson JK, Lei XG, Miller DD. The pig as an experimental model for elucidating the mechanisms governing dietary influence on mineral absorption. *Exp Biol Med.* (2008) 233:651–64. doi: 10.3181/0709-MR-262
26. Flisikowska T, Merkl C, Landmann M, Eser S, Rezaei N, Cui X, et al. A porcine model of familial adenomatous polyposis. *Gastroenterology.* (2012) 143:1173–5.e7. doi: 10.1053/j.gastro.2012.07.110
27. Marshman E, Booth C, Potten CS. The intestinal epithelial stem cell. *Bioessays.* (2002) 24:91–8. doi: 10.1002/bies.10028
28. Gonzalez LM, Williamson I, Piedrahita JA, Blikslager AT, Magness ST. Cell lineage identification and stem cell culture in a porcine model for the study of intestinal epithelial regeneration. *PLoS ONE.* (2013) 8:e66465. doi: 10.1371/journal.pone.0066465
29. Vega-López MA, Arenas-Contreras G, Bailey M, González-Pozos S, Stokes CR, Ortega MG, et al. Development of intraepithelial cells in the porcine small intestine. *Dev Immunol.* (2001) 8:147–58. doi: 10.1155/2001/25301
30. Sato T, van Es JH, Snippert HJ, Stange DE, Vries RG, van den Born M, et al. Paneth cells constitute the niche for Lgr5 stem cells in intestinal crypts. *Nature.* (2011) 469:415–8. doi: 10.1038/nature09637
31. Wehkamp J, Chu H, Shen B, Feathers RW, Kays RJ, Lee SK, et al. Paneth cell antimicrobial peptides: topographical distribution and quantification in human gastrointestinal tissues. *FEBS Lett.* (2006) 580:5344–50. doi: 10.1016/j.febslet.2006.08.083
32. Dekaney CM, Bazer FW, Jaeger LA. Mucosal morphogenesis and cytodifferentiation in fetal porcine small intestine. *Anat Rec.* (1997) 249:517–23.

33. Hunyady B, Mezey E, Palkovits M. Gastrointestinal immunology: cell types in the lamina propria–a morphological review. *Acta Physiol Hung.* (2000) 87:305–28. Available online at: http://europepmc.org/article/MED/11732886
34. Powell Anne E, Wang Y, Li Y, Poulin Emily J, Means Anna L, Washington Mary K, et al. The Pan-ErbB negative regulator lrig1 is an intestinal stem cell marker that functions as a tumor suppressor. *Cell.* (2012) 149:146–58. doi: 10.1016/j.cell.2012.02.042
35. Burkey TE, Skjolaas KA, Minton JE, Board-Invited Review. Porcine mucosal immunity of the gastrointestinal tract1. *J Anim Sci.* (2009) 87:1493–501. doi: 10.2527/jas.2008-1330
36. Helm RM, Furuta GT, Stanley JS, Ye J, Cockrell G, Connaughton C, et al. A neonatal swine model for peanut allergy. *J Allergy Clin Immunol.* (2002) 109:136–42. doi: 10.1067/mai.2002.120551
37. Gruessner RWG, Nakhleh RE, Benedetti E, Pirenne J, Belani KG, Beebe D, et al. Combined liver—total bowel transplantation has no immunologic advantage over total bowel transplantation alone: a prospective study in a porcine model. *Arch Surg.* (1997) 132:1077–85. doi: 10.1001/archsurg.1997.01430340031004
38. Azevedo MP, Vlasova AN, Saif LJ. Human rotavirus virus-like particle vaccines evaluated in a neonatal gnotobiotic pig model of human rotavirus disease. *Expert Rev Vaccines.* (2013) 12:169–81. doi: 10.1586/erv.13.3
39. Stokes CR, Bailey M, Wilson AD. Immunology of the porcine gastrointestinal tract. *Vet Immunol Immunopathol.* (1994) 43:143–50. doi: 10.1016/0165-2427(94)90130-9
40. Gonzalez LM, Stewart AS, Freund J, Kucera CR, Dekaney CM, Magness ST, et al. Preservation of reserve intestinal epithelial stem cells following severe ischemic injury. *Am J Physiol-Gastrointest Liver Physiol.* (2019) 316:G482–G94. doi: 10.1152/ajpgi.00262.2018
41. Stewart AS, Schaaf CR, Luff JA, Freund JM, Becker TC, Tufts SR, et al. HOPX+ injury-resistant intestinal stem cells drive epithelial recovery after severe intestinal ischemia. *Am J Physiol-Gastrointest Liver Physiol.* (2021) 321:G588–602. doi: 10.1152/ajpgi.00165.2021
42. Yandza T, Tauc M, Saint-Paul MC, Ouaissi M, Gugenheim J, Hebuterne X. The pig as a preclinical model for intestinal ischemia-reperfusion and transplantation studies. *J Surg Res.* (2012) 178:807–19. doi: 10.1016/j.jss.2012.07.025
43. Llanos JC, Bakonyi Neto A, Lerco MM, Clark RMO. Polachini do Valle A, Sousa MMF. Induction of short gut syndrome and transplantation in a porcine model. *Transplant Proc.* (2006) 38:1855–6. doi: 10.1016/j.transproceed.2006.06.085
44. Sangild PT, Siggers RH, Schmidt M, Elnif J, Bjornvad CR, Thymann T, et al. Diet- and colonization-dependent intestinal dysfunction predisposes to necrotizing enterocolitis in preterm pigs. *Gastroenterology.* (2006) 130:1776–92. doi: 10.1053/j.gastro.2006.02.026
45. Cui T, Theuns S, Desmarets LMB, Xie J, De Gryse GMA, Yang B, et al. Establishment of porcine enterocyte/myofibroblast co-cultures for the growth of porcine rota- and coronaviruses. *Sci Rep.* (2018) 8:15195. doi: 10.1038/s41598-018-33305-1
46. Stoltz DA, Rokhlina T, Ernst SE, Pezzulo AA, Ostedgaard LS, Karp PH, et al. Intestinal CFTR expression alleviates meconium ileus in cystic fibrosis pigs. *J Clin Invest.* (2013) 123:2685–93. doi: 10.1172/JCI68867
47. Sikorska A, Stachowiak M, Flisikowska T, Stachecka J, Flisikowski K, Switonski M. Polymorphisms of CSF1R and WISP1 genes are associated with severity of familial adenomatous polyposis in APC(1311) pigs. *Gene.* (2020) 759:144988. doi: 10.1016/j.gene.2020.144988
48. Perkowska A, Flisikowska T, Perleberg C, Flisikowski K, Stachowiak M, Nowacka-Woszuk J, et al. The expression of TAP1 candidate gene, but not its polymorphism and methylation, is associated with colonic polyp formation in a porcine model of human familial adenomatous polyposis. *Anim Biotechnol.* (2020) 31:306–13. doi: 10.1080/10495398.2019.1590377
49. Sikorska A, Flisikowska T, Stachowiak M, Kind A, Schnieke A, Flisikowski K, et al. Elevated expression of p53 in early colon polyps in a pig model of human familial adenomatous polyposis. *J Appl Genet.* (2018) 59:485–91. doi: 10.1007/s13353-018-0461-6
50. Stachowiak M, Flisikowska T, Bauersachs S, Perleberg C, Pausch H, Switonski M, et al. Altered microRNA profiles during early colon adenoma progression in a porcine model of familial adenomatous polyposis. *Oncotarget.* (2017) 8:96154–60. doi: 10.18632/oncotarget.21774
51. Yim JJ, Harmsen S, Flisikowski K, Flisikowska T, Namkoong H, Garland M, et al. A protease-activated, near-infrared fluorescent probe for early endoscopic detection of premalignant gastrointestinal lesions. *Proc Nat Acad Sci.* (2021) 118:e2008072118. doi: 10.1073/pnas.2008072118
52. Rogalla S, Flisikowski K, Gorpas D, Mayer AT, Flisikowska T, Mandella MJ, et al. Biodegradable fluorescent nanoparticles for endoscopic detection of colorectal carcinogenesis. *Adv Funct Mater.* (2019) 29:1904992. doi: 10.1002/adfm.201904992
53. Leuchs S, Saalfrank A, Merkl C, Flisikowska T, Edlinger M, Durkovic M, et al. Inactivation and inducible oncogenic mutation of p53 in gene targeted pigs. *PLoS ONE.* (2012) 7:e43323. doi: 10.1371/journal.pone.0043323
54. Niu G, Hellmuth I, Flisikowska T, Pausch H, Rieblinger B, Carrapeiro A, et al. Porcine model elucidates function of p53 isoform in carcinogenesis and reveals novel circTP53 RNA. *Oncogene.* (2021) 40:1896–908. doi: 10.1038/s41388-021-01686-9
55. Callesen MM, Árnadóttir SS, Lyskjær I, Ørntoft M-BW, Høyer S, Dagnæs-Hansen F, et al. A genetically inducible porcine model of intestinal cancer. *Mol Oncol.* (2017) 11:1616–29. doi: 10.1002/1878-0261.12136
56. Polkoff KM, Chung J, Simpson SG, Gleason K, Piedrahita JA. *In vitro* validation of transgene expression in gene-edited pigs using CRISPR transcriptional activators. *CRISPR J.* (2020) 3:409–18. doi: 10.1089/crispr.2020.0037
57. Yan Z, Stewart ZA, Sinn PL, Olsen JC, Hu J, McCray PB, et al. Ferret and pig models of cystic fibrosis: prospects and promise for gene therapy. *Hum Gene Ther Clin Dev.* (2014) 26:38–49. doi: 10.1089/humc.2014.154
58. Zhou ZP, Yang LL, Cao H, Chen ZR, Zhang Y, Wen X-Y, et al. *In vitro* validation of a CRISPR-mediated CFTR correction strategy for preclinical translation in pigs. *Hum Gene Ther.* (2019) 30:1101–16. doi: 10.1089/hum.2019.074
59. Rogers CS, Hao Y, Rokhlina T, Samuel M, Stoltz DA Li Y, et al. Production of CFTR-null and CFTR-ΔF508 heterozygous pigs by adeno-associated virus–mediated gene targeting and somatic cell nuclear transfer. *J Clin Invest.* (2008) 118:1571–7. doi: 10.1172/JCI34773
60. Meyerholz DK, Stoltz DA, Pezzulo AA, Welsh MJ. Pathology of gastrointestinal organs in a porcine model of cystic fibrosis. *Am J Pathol.* (2010) 176:1377–89. doi: 10.2353/ajpath.2010.090849
61. Klymiuk N, Mundhenk L, Kraehe K, Wuensch A, Plog S, Emrich D, et al. Sequential targeting of CFTR by BAC vectors generates a novel pig model of cystic fibrosis. *J Mol Med.* (2012) 90:597–608. doi: 10.1007/s00109-011-0839-y
62. Ostedgaard Lynda S, Meyerholz David K, Chen J-H, Pezzulo Alejandro A, Karp Philip H, Rokhlina T, et al. The ΔF508 mutation causes CFTR misprocessing and cystic fibrosis–like disease in pigs. *Sci Transl Med.* (2011) 3:74ra24. doi: 10.1126/scitranslmed.3001868
63. Siegel RL, Miller KD, Goding Sauer A, Fedewa SA, Butterly LF, Anderson JC, et al. Colorectal cancer statistics, 2020. *CA Cancer J Clin.* (2020) 70:145–64. doi: 10.3322/caac.21601
64. Huang D, Sun W, Zhou Y, Li P, Chen F, Chen H, et al. Mutations of key driver genes in colorectal cancer progression and metastasis. *Cancer Metastasis Rev.* (2018) 37:173–87. doi: 10.1007/s10555-017-9726-5
65. Boivin GP, Washington K, Yang K, Ward JM, Pretlow TP, Russell R, et al. Pathology of mouse models of intestinal cancer: consensus report and recommendations. *Gastroenterology.* (2003) 124:762–77. doi: 10.1053/gast.2003.50094
66. Stastna M, Janeckova L, Hrckulak D, Kriz V, Korinek V. Human colorectal cancer from the perspective of mouse models. *Genes.* (2019) 10:788. doi: 10.3390/genes10100788
67. Su L-K, Kinzler KW, Vogelstein B, Preisinger AC, Moser AR, Luongo C, et al. Multiple intestinal neoplasia caused by a mutation in the murine homolog of the APC gene. *Science.* (1992) 256:668–70. doi: 10.1126/science.1350108
68. Cancer Genome Atlas N. Comprehensive molecular characterization of human colon and rectal cancer. *Nature.* (2012) 487:330–7. doi: 10.1038/nature11252

69. Flisikowska T, Stachowiak M, Xu H, Wagner A, Hernandez-Caceres A, Wurmser C, et al. Porcine familial adenomatous polyposis model enables systematic analysis of early events in adenoma progression. *Sci Rep.* (2017) 7:6613. doi: 10.1038/s41598-017-06741-8
70. Tan W, Carlson Daniel F, Lancto Cheryl A, Garbe John R, Webster Dennis A, Hackett Perry B, et al. Efficient nonmeiotic allele introgression in livestock using custom endonucleases. *Proc Nat Acad Sci.* (2013) 110:16526–31. doi: 10.1073/pnas.1310478110
71. Schook LB, Collares TV, Hu W, Liang Y, Rodrigues FM, Rund LA, et al. A Genetic Porcine Model of Cancer. *PLoS ONE.* (2015) 10:e0128864. doi: 10.1371/journal.pone.0128864
72. Beganoyic S. Clinical significance of the kras mutation. *Bosn J Basic Med Sci.* (2009) 9:S17–20. doi: 10.17305/bjbms.2009.2749
73. Obstein KL, Valdastri P. Advanced endoscopic technologies for colorectal cancer screening. *World J Gastroenterol.* (2013) 19:431–9. doi: 10.3748/wjg.v19.i4.431
74. Choi WJ, Moon J-H, Min JS, Song YK, Lee SA, Ahn JW, et al. Real-time detection system for tumor localization during minimally invasive surgery for gastric and colon cancer removal: *in vivo* feasibility study in a swine model. *J Surg Oncol.* (2018) 117:699–706. doi: 10.1002/jso.24922
75. Ciuti G, Skonieczna-Zydecka K, Marlicz W, Iacovacci V, Liu H, Stoyanov D, et al. Frontiers of robotic colonoscopy: a comprehensive review of robotic colonoscopes and technologies. *J Clin Med.* (2020) 9:1648. doi: 10.3390/jcm9061648
76. Winawer S, Fletcher R, Rex D, Bond J, Burt R, Ferrucci J, et al. Colorectal cancer screening and surveillance: clinical guidelines and rationale-update based on new evidence. *Gastroenterology.* (2003) 124:544–60. doi: 10.1053/gast.2003.50044
77. Jiang T, Jin K, Liu X, Pang Z. 8-Nanoparticles for tumor targeting. In: Jana S, Maiti S, Jana S, editors. *Biopolymer-Based Composites*. Cambridge, MA: Woodhead Publishing (2017). p. 221–67.
78. Reginelli A, Genovese EA, Cappabianca S, Iacobellis F, Berritto D, Fonio P, et al. Intestinal ischemia: US-CT findings correlations. *Crit Ultrasound J.* (2013) 5:S7. doi: 10.1186/2036-7902-5-S1-S7
79. Nolan LS, Wynn JL, Good M. Exploring clinically-relevant experimental models of neonatal shock and necrotizing enterocolitis. *Shock.* (2020) 53:596–604. doi: 10.1097/SHK.0000000000001507
80. Chiu C-J, McArdle AH, Brown R, Scott HJ, Gurd FN. Intestinal Mucosal Lesion in Low-Flow States: I. A morphological, hemodynamic, and metabolic reappraisal. *Arch Surg.* (1970) 101:478–83. doi: 10.1001/archsurg.1970.01340280030009
81. Park PO, Haglund U, Bulkley GB, Fält K. The sequence of development of intestinal tissue injury after strangulation ischemia and reperfusion. *Surgery.* (1990) 107:574–80.
82. Parks DA, Granger DN. Ischemia-induced vascular changes: role of xanthine oxidase and hydroxyl radicals. *Am J Physiol Gastrointest Liver Physiol.* (1983) 245:G285–G9. doi: 10.1152/ajpgi.1983.245.2.G285
83. Robinson JW, Mirkovitch V, Winistörfer B, Saegesser F. Response of the intestinal mucosa to ischaemia. *Gut.* (1981) 22:512–27. doi: 10.1136/gut.22.6.512
84. Barker N, van Es JH, Kuipers J, Kujala P, van den Born M, Cozijnsen M, et al. Identification of stem cells in small intestine and colon by marker gene Lgr5. *Nature.* (2007) 449:1003–7. doi: 10.1038/nature06196
85. Takeda N, Jain R, LeBoeuf MR, Wang Q, Lu MM, Epstein JA. Interconversion between intestinal stem cell populations in distinct niches. *Science.* (2011) 334:1420. doi: 10.1126/science.1213214
86. Bellamy JE, Latshaw WK, Nielsen NO. The vascular architecture of the porcine small intestine. *Can J Comp Med.* (1973) 37:56–62.
87. Katoh H, Yamashita K, Waraya M, Margalit O, Ooki A, Tamaki H, et al. Epigenetic silencing of HOPX promotes cancer progression in colorectal cancer. *Neoplasia.* (2012) 14:55971. doi: 10.1593/neo.12330
88. Khalil HA, Lei NY, Brinkley G, Scott A, Wang J, Kar UK, et al. A novel culture system for adult porcine intestinal crypts. *Cell Tissue Res.* (2016) 365:123–34. doi: 10.1007/s00441-016-2367-0
89. Potten CS, Hume WJ, Reid P, Cairns J. The segregation of DNA in epithelial stem cells. *Cell.* (1978) 15:899–906. doi: 10.1016/0092-8674(78)90274-X
90. Barker N, Ridgway RA, van Es JH, van de Wetering M, Begthel H, van den Born M, et al. Crypt stem cells as the cells-of-origin of intestinal cancer. *Nature.* (2009) 457:608–11. doi: 10.1038/nature07602
91. Baker A-M, Graham TA, Elia G, Wright NA, Rodriguez-Justo M. Characterization of LGR5 stem cells in colorectal adenomas and carcinomas. *Sci Rep.* (2015) 5:8654. doi: 10.1038/srep08654
92. Sper RB, Koh S, Zhang X, Simpson S, Collins B, Sommer J, et al. Generation of a stable transgenic swine model expressing a porcine histone 2B-eGFP fusion protein for cell tracking and chromosome dynamics studies. *PloS ONE.* (2017) 12:e0169242–e. doi: 10.1371/journal.pone.0169242
93. Fiocchi C. Inflammatory bowel disease: etiology and pathogenesis. *Gastroenterology.* (1998) 115:182–205. doi: 10.1016/S0016-5085(98)70381-6
94. Prattis S, Jurjus A. Spontaneous and transgenic rodent models of inflammatory bowel disease. *Lab Anim Res.* (2015) 31:47–68. doi: 10.5625/lar.2015.31.2.47
95. Lees CW, Barrett JC, Parkes M, Satsangi J. New IBD genetics: common pathways with other diseases. *Gut.* (2011) 60:1739. doi: 10.1136/gut.2009.199679
96. Baumgart DC, Olivier W-A, Reya T, Peritt D, Rombeau JL, Carding SR. Mechanisms of intestinal epithelial cell injury and colitis in interleukin 2 (IL2)-deficient mice. *Cell Immunol.* (1998) 187:52–66. doi: 10.1006/cimm.1998.1307
97. Shull MM, Ormsby I, Kier AB, Pawlowski S, Diebold RJ, Yin M, et al. Targeted disruption of the mouse transforming growth factor-β1 gene results in multifocal inflammatory disease. *Nature.* (1992) 359:693–9. doi: 10.1038/359693a0
98. Berg DJ, Davidson N, Kühn R, Müller W, Menon S, Holland G, et al. Enterocolitis and colon cancer in interleukin-10-deficient mice are associated with aberrant cytokine production and CD4(+) TH1-like responses. *J Clin Invest.* (1996) 98:1010–20. doi: 10.1172/JCI118861
99. Simpson SJ, Shah S, Comiskey M, de Jong YP, Wang B, Mizoguchi E, et al. T Cell–mediated pathology in two models of experimental colitis depends predominantly on the interleukin 12/signal transducer and activator of transcription (Stat)-4 Pathway, but is not conditional on interferon γ expression by T cells. *J Exp Med.* (1998) 187:1225–34. doi: 10.1084/jem.187.8.1225
100. Watanabe M, Ueno Y, Yajima T, Okamoto S, Hayashi T, Yamazaki M, et al. Interleukin 7 transgenic mice develop chronic colitis with decreased interleukin 7 protein accumulation in the colonic mucosa. *J Exp Med.* (1998) 187:389–402. doi: 10.1084/jem.187.3.389
101. Lukas M, Kolar M, Ryska O, Juhas S, Juhasova J, Kalvach J, et al. Novel porcine model of Crohn's disease anastomotic stricture suitable for evaluation and training of advanced endoscopic techniques. *Gastrointest Endosc.* (2021) 93:250–6. doi: 10.1016/j.gie.2020.05.063
102. Ziv Y, Nevler A, Willenz E, Doron O, Zbar A, Shperber A, et al. A novel porcine model for chemically inducible Crohn's-like reaction. *Isr Med Assoc J.* (2015) 17:19–23. Available online at: http://europepmc.org/abstract/MED/25739171
103. Kim CJ, Kovacs-Nolan J, Yang C, Archbold T, Fan MZ, Mine Y. L-cysteine supplementation attenuates local inflammation and restores gut homeostasis in a porcine model of colitis. *Biochim Biophys Acta.* (2009) 1790:1161–9. doi: 10.1016/j.bbagen.2009.05.018
104. Kim CJ, Kovacs-Nolan JA, Yang C, Archbold T, Fan MZ, Mine Y. l-Tryptophan exhibits therapeutic function in a porcine model of dextran sodium sulfate (DSS)-induced colitis. *J Nutr Biochem.* (2010) 21:468–75. doi: 10.1016/j.jnutbio.2009.01.019
105. Negaard A, Loberg EM, Naess PA, Eriksen M, Klow N-E. Feasibility of MRI in experimentally induced inflammatory small bowel

disease: a pilot study in a porcine model. *Dig Dis Sci.* (2010) 55:14–20. doi: 10.1007/s10620-008-0707-y

Conflict of Interest: The authors declare that the research was conducted in the absence of any commercial or financial relationships that could be construed as a potential conflict of interest.

Publisher's Note: All claims expressed in this article are solely those of the authors and do not necessarily represent those of their affiliated organizations, or those of the publisher, the editors and the reviewers. Any product that may be evaluated in this article, or claim that may be made by its manufacturer, is not guaranteed or endorsed by the publisher.

frontiers | Frontiers in Veterinary Science

ORIGINAL RESEARCH
published: 21 June 2022
doi: 10.3389/fvets.2022.894189

Isolation of Extracellular Vesicles From the Bronchoalveolar Lavage Fluid of Healthy and Asthmatic Horses

Nina Höglund[1], Ninna Koho[1], Heini Rossi[1], Jenni Karttunen[1], Anne-Mari Mustonen[2,3], Petteri Nieminen[2], Kirsi Rilla[2], Sanna Oikari[2] and Anna Mykkänen[1]*

[1] Department of Equine and Small Animal Medicine, Faculty of Veterinary Medicine, University of Helsinki, Helsinki, Finland, [2] Institute of Biomedicine, School of Medicine, Faculty of Health Sciences, University of Eastern Finland, Kuopio, Finland, [3] Department of Environmental and Biological Sciences, Faculty of Science and Forestry, University of Eastern Finland, Joensuu, Finland

Extracellular vesicles (EVs) are membrane-bound particles that engage in inflammatory reactions by mediating cell–cell interactions. Previously, EVs have been isolated from the bronchoalveolar lavage fluid (BALF) of humans and rodents. The aim of this study was to investigate the number and size distribution of EVs in the BALF of asthmatic horses (EA, $n = 35$) and healthy horses ($n = 19$). Saline was injected during bronchoscopy to the right lung followed by manual aspiration. The retrieved BALF was centrifuged twice to remove cells and biological debris. The supernatant was concentrated and EVs were isolated using size-exclusion chromatography. Sample fractions were measured with nanoparticle tracking analysis (NTA) for particle number and size, and transmission electron microscopy and confocal laser scanning microscopy were used to visualize EVs. The described method was able to isolate and preserve EVs. The mean EV size was 247 ± 35 nm (SD) in the EA horses and 261 ± 47 nm in the controls by NTA. The mean concentration of EVs was $1.38 \times 10^{12} \pm 1.42 \times 10^{12}$ particles/mL in the EA horses and $1.33 \times 10^{12} \pm 1.07 \times 10^{12}$ particles/mL in the controls with no statistically significant differences between the groups. With Western blotting and microscopy, these particles were documented to associate with EV protein markers (CD63, TSG101, HSP70, EMMPRIN, and actin) and hyaluronan. Equine BALF is rich in EVs of various sizes, and the described protocol is usable for isolating EVs. In the future, the role of EVs can be studied in horses with airway inflammation.

Keywords: airway disease, bronchoalveolar lavage fluid (BALF), equine asthma, extracellular vesicle (EV), inflammation, size-exclusion chromatography

OPEN ACCESS

Edited by:
Mark Gray,
University of Edinburgh,
United Kingdom

Reviewed by:
Gabriel Moran,
Austral University of Chile, Chile
Guy Lester,
University of Florida, United States

****Correspondence:***
Nina Höglund
nina.m.hoglund@helsinki.fi

Specialty section:
This article was submitted to Comparative and Clinical Medicine, a section of the journal Frontiers in Veterinary Science

Received: *11 March 2022*
Accepted: *27 May 2022*
Published: *21 June 2022*

Citation:
Höglund N, Koho N, Rossi H, Karttunen J, Mustonen A-M, Nieminen P, Rilla K, Oikari S and Mykkänen A (2022) Isolation of Extracellular Vesicles From the Bronchoalveolar Lavage Fluid of Healthy and Asthmatic Horses. Front. Vet. Sci. 9:894189. doi: 10.3389/fvets.2022.894189

INTRODUCTION

Equine asthma (EA) is a common inflammatory disease of the lower airways. The equine condition resembles human non-allergic asthma in many ways, and horses can, thus, provide a naturally occurring translational model for asthma (1). Extracellular vesicles (EVs) are bioactive particles that have recently been associated with many pathological conditions. The number of EVs isolated from bronchoalveolar lavage fluid (BALF) increases in human asthma, and the potential role of EVs as

drivers of inflammation in asthmatic airways provides an interesting research premise (2, 3). Better understanding of the role of EVs in asthma pathogenesis may reveal new diagnostic possibilities and novel treatment options to alleviate inflammation and to prevent remodeling of the airways.

EA is caused by an immunological reaction triggered by external factors, such as airborne antigens. Hyperresponsive airways give rise to inflammation of the bronchi, excess airway mucus accumulation, airway wall remodeling, and bronchoconstriction (4). EA can be classified as mild/moderate or severe. Horses suffering from mild to moderate asthma often have poor performance but do not necessarily show overt clinical signs, such as cough and respiratory distress, which are present in the severe form. Currently, the asthma diagnosis is obtained through physical examination, blood analysis, bronchoscopy, and airway cytology, with BALF collection remaining the standard sampling method for lower airway diagnostics. However, all horses with clinical signs do not show marked alterations in inflammatory cell counts in their airway samples, or abnormalities in physical examination and airway endoscopy, and the correlation between parameters varies (5).

EVs are phospholipid bilayer-covered particles that are released from cells to the local environment and circulation (6). They are mainly categorized into three groups: exosomes, microvesicles, and apoptotic bodies. However, the groups overlap in size with each other, and the precise morphological identification, labeling, and isolation of EVs are challenging. EVs are released from multivesicular bodies or by outward budding from the plasma membrane, and they are associated with proteins derived from the lipid bilayer and the cytosol (7, 8). They play a crucial role in cell–cell communication and organization of the extracellular matrix and are present in all body fluids (6). EVs carry diverse cargos that include nucleic acids, proteins, lipids, and signaling molecules, and they can induce both protective and pathologic effects (9). EV communication occurs through EV surface receptors and endocytosis by the cells or by fusion of the EV and cell membranes (6). In a recent study by Nirujogi et al. (2022) on mice BALF, acute lung injury increased the release of EVs (10). In asthma, EVs are mostly recognized to promote remodeling and to disseminate inflammation by upregulating and activating proinflammatory responses, however, there are also research data supporting anti-inflammatory activity of EVs (11, 12). Additionally, EVs originate from different cells, such as eosinophils, mast cells, and neutrophils, according to disease type (10, 12). EVs have potential as biomarkers for diseases and as therapeutic agents due to their proinflammatory and immune system triggering properties (13–15).

Abbreviations: AUC, Area under curve; BALF, Bronchoalveolar lavage fluid; CD63, Cluster of differentiation 63; CLSM, Confocal laser scanning microscopy; EA, Equine asthma; EMMPRIN, Extracellular matrix metalloproteinase inducer; EV, Extracellular vesicle; HA, Hyaluronan; HSP70, Heat shock protein 70; NTA, Nanoparticle tracking analysis; r_p, Pearson's correlation coefficient; SD, Standard deviation; SEC, Size-exclusion chromatography; TBST, Tris buffered saline solution with 0.1% Tween; TEM, Transmission electron microscopy; TOMM20, Translocase of outer mitochondrial membrane 20; TSG101, Tumor susceptibility gene 101; WB, Western blotting.

TABLE 1 | General characteristics of enrolled asthmatic and control horses (mean ± SD).

	Asthma ($n = 35$)	Control ($n = 19$)	*P*
Age (years)	14 ± 5	10 ± 4	0.01
Body weight (kg)	492 ± 131	492 ± 106	0.83
Sex			0.68
Mare (*n*)	5 (14%)	5 (26%)	
Stallion (*n*)	2 (6%)	1 (5%)	
Gelding (*n*)	28 (80%)	13 (69%)	

Among bioactive molecules transported by EVs is hyaluronan (HA) (16), a non-sulfated glycosaminoglycan that is a constituent of the extracellular matrix participating in cell proliferation, inflammatory processes, and in the regulation of fluid balance in the interstitium (17, 18). High-molecular-weight HA is considered to have anti-inflammatory action, while low-molecular-weight HA can induce proinflammatory effects (19). Earlier data have shown increased amounts of lower-molecular-weight HA fragments in airways of asthma patients that could contribute to chronic inflammation and remodeling of airways (20).

The complexity of biological fluids and the nature of EVs pose the main challenges to their isolation. Therefore, a combination of several methods is necessary for successful EV extraction (13, 21). Gel chromatography, or size-exclusion chromatography (SEC), has become a popular method for EV extraction. It is based on the technique where a resin-packed column, which does not absorb or react with the fluid, separates molecules according to size. Molecules smaller than the determined size enter resin matrix pores, which results in the delayed passage of smaller particles through the column. The technique cleans soluble non-EV proteins from the sample but preserves EV functionality (13, 22). Nanoparticle tracking analysis (NTA) is a widely used method to determine the size and concentration of small particles, and transmission electron microscopy (TEM) and confocal laser scanning microscopy (CLSM) can be used to directly visualize EVs (23–25). In horses, EVs have been successfully isolated from plasma, synovial fluid, uterus, bone marrow, and adipose tissue-derived cells (26–31). However, EVs have not been previously isolated from equine BALF, and the types and content of EVs produced in equine lungs remain unknown.

We aimed to isolate EVs from equine BALF and to investigate their numbers, size distribution, and content in horses suffering from naturally occurring asthma. We hypothesized that (i) EA horses would have increased levels of EVs compared to controls, (ii) EV size distribution would differ between EA horses and healthy horses, and (iii) BALF EVs would transport HA with potential to affect airway inflammation. This study provides new insight to the role of EVs in the pathophysiology of EA and an additional method for EA diagnostics and research. This knowledge may be applicable to other species and contribute to translational asthma research.

MATERIALS AND METHODS

Sample Collection

This was a prospective clinical case-control study conducted at the Department of Equine and Small Animal Medicine, Faculty of Veterinary Medicine, University of Helsinki. The Project Authorization Board in the Regional State Administrative Agency accepted the experimental animal license (ESAVI/3285/2020), and horse owners provided informed consent to allow the participation of their animals in the study.

A total of 54 privately-owned adult horses or ponies were recruited for the study, 35 of which had chronic or recurrent signs of asthma (cough >4 months at rest or when exercised, bilateral nasal discharge, poor performance, abdominal breathing pattern) and 19 were clinically healthy controls. Inclusion criteria were an age >5 years, no signs of infection during the previous 2 months, and no medication during the past month. Exclusion criteria included findings in blood analyzes or examinations suggestive of infection or other respiratory tract diseases, such as laryngeal dysfunction, arytenoid chondropathy, infectious bronchopneumonia, interstitial pneumonia, or neoplasia. The control horses were preferably recruited from the same stables as the asthmatic horses to minimize any environmental bias caused by the stabling conditions.

The examination and sample collection procedures included a physical examination and blood sampling for hematology and biochemistry, after which the horses were sedated intravenously with a combination of detomidine (0.01 mg/kg, Domosedan, Orion, Espoo, Finland) and butorphanol (0.005–0.01 mg/kg, Butordol, Intervet, Boxmeer, the Netherlands) for airway endoscopy and bronchoalveolar lavage. A video endoscope (Pentax EC3870, Tokyo, Japan, length 170 cm, diameter 11 mm) was used to visualize the airways and to transendoscopically

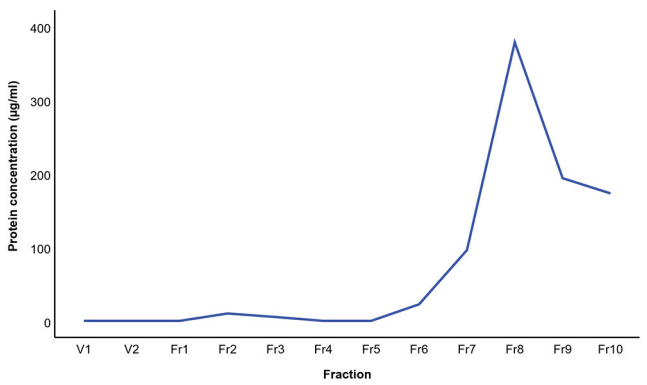

FIGURE 1 | Mean protein concentration in extracellular vesicle sample fractions from three horses isolated by size-exclusion chromatography. The protein concentration was analyzed with the bicinchoninic acid assay.

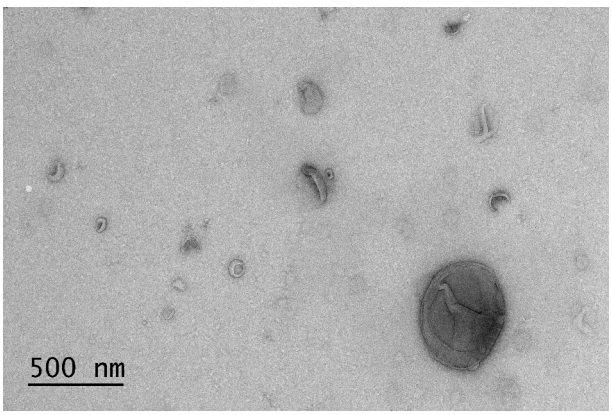

FIGURE 3 | Transmission electron microscopy image of extracellular vesicles isolated by size-exclusion chromatography from the bronchoalveolar lavage fluid of an asthmatic horse.

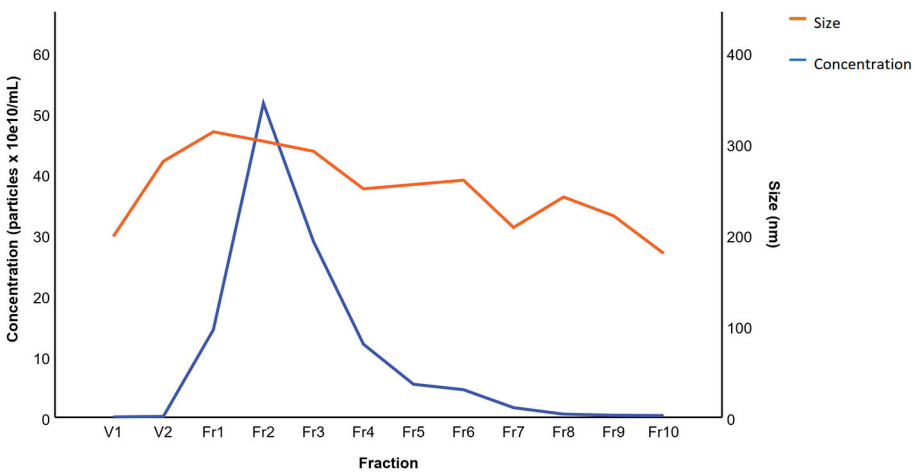

FIGURE 2 | Mean particle concentration and size in extracellular vesicle sample fractions from five horses isolated by size-exclusion chromatography. The fractions were analyzed by nanoparticle tracking analysis.

collect BALF. Prior to BALF sampling, the airways were locally anesthetized with 1% lidocaine solution (40 mL for horses and 20 mL for ponies, Lidocain, Orion). BALF collection was performed with sterile 0.9% saline (360 mL for horses and 240 mL for ponies) injected in one aliquot and manually aspirated from the right lung with 40–70% of the injected volume retrieved. The BALF samples were placed on ice and processed within 60 min of collection.

BALF Cytology, EV Isolation, and Visualization

The BALF sample syringes of each horse were pooled, 20 mL was stored at −20°C, 45 mL was prepared for EV isolation, and the remaining fluid was cytocentrifuged and stained with May–Grünwald–Giemsa stain for the differential counts of inflammatory cells performed by an experienced investigator by counting 300 cells. For EV isolation, BALF was centrifuged using polypropylene Falcon centrifuge tubes (Thermo Fisher Scientific, Waltham, MA, USA) at 4°C, first at 300 × *g* for 10 min followed by supernatant centrifugation at 3000 × *g* for 20 min to remove cells and debris. To concentrate the samples, the supernatant was centrifuged at 3800 × *g* for 90–150 min with a 10K MWCO filter (#88528, Thermo Fisher Scientific). The samples were stored at −80°C in LowBind tubes (Eppendorf, Hamburg, Germany).

EV isolation was implemented with 10 mL SEC columns with a 70 nm pore size (#ICO-70, qEVoriginal, Izon Science, Medford, MA, USA). The columns were taken to room temperature 40 min prior to use and flushed with 16 mL PBS (137 mM sodium chloride, 2.7 mM potassium chloride, and 10 mM phosphate buffer) to remove sodium azide. The samples were thawed and centrifuged at 4°C, 2000 × *g* for 10 min. First, 0.5 mL SEC fractions were collected from samples of five horses, and the particle concentration of each fraction was analyzed with NTA. The protein content of the 0.5 mL SEC fractions from three horses was measured with the bicinchoninic acid assay (#23227, Thermo Fisher Scientific) to ensure the purification of EVs. Based on the initial NTA results, the remaining samples were run through the SEC column and collected as follows: 3 mL (void), 2 mL (EV sample), 2 mL (fractions 5–8), and 5 mL (proteins). One SEC column was used for five samples. For subsequent analyses, the EV samples were concentrated to 300 μL using 10K MWCO filters (#88517, Thermo Fisher Scientific). The samples were frozen and stored at −80°C in LowBind tubes (Eppendorf).

The particles were characterized with the Nanosight LM14C (*v*3.1, Malvern Panalytical, Malvern, UK) with the camera level set at 14, and the detection threshold at 4. EVs were visualized and verified with the TEM Jeol JEM-1400 (Jeol, Tokyo, Japan) operating at 80 kV, staining was performed as described by Puhka et al. (2017) (32). TEM images were captured with the Gatan Orius SC 1000B CCD-camera (Gatan, Pleasanton, CA, USA) with 4008 × 2672 px image size and no binning. EVs were also visualized by the Zeiss Axio Observer inverted microscope equipped with the Zeiss LSM 800 confocal module (Carl Zeiss MicroImaging, Jena, Germany) as outlined previously (25). The samples were stained with CellMask Deep Red plasma membrane stain (Thermo Fisher Scientific) soluted together with Alexa Fluor 568-labeled HA binding complex (33) to double-label the EVs simultaneously with HA. In addition, CellMask Deep Red plasma membrane stain was utilized with Alexa Fluor 594-labeled phalloidin-iFluor (Abcam, Cambridge, UK) to detect cytosolic F-actin in EVs.

Western Blotting (WB)

WB was used for protein assessment from BALF of four horses to confirm the presence of EVs. For positive controls, 0.5 μg and 2 μg of homogenized equine lung tissue (obtained from an euthanized horse donated for research purposes) was used and, for the BALF EV samples, a concentration of 1.0×10^{13} particles/well in sample buffer (Laemmli, Bio-Rad, Hercules, CA, USA) with 10% β-mercaptoethanol. Samples were loaded in a volume of 20 μL/well. A molecular weight ladder (Precision Plus Protein, Dual Color standard, Bio-Rad) was used. The samples were thawed and heated at 100°C for 5 min before loading to the electrophoresis gel (SDS-PAGE Mini-Protean TGX gel, Bio-Rad). Proteins were separated on gels for 40–70 min at 150–200 V in buffer (Tris/glycine/SDS, Bio-Rad) and subsequently transferred to a nitrocellulose transfer membrane (Protran 0.2 μm, Perkin Elmer, Boston, MA, USA) by running a semi-dry transfer system in 15 V for 60 min.

An antibody produced against the C-terminus of equine extracellular matrix metalloproteinase inducer (EMMPRIN, also known as CD147, neurothelin, and basigin, generated in rabbits, purified with affinity chromatography, sequence GHHVNDKDKNVRQRNAS, GenBank accession No. ABQ53583.1) was used as an inflammatory protein marker, and antibodies against anti-human cluster of differentiation 63 protein (CD63, #bs-1523R, Bioss, Boston, MA, USA), anti-human heat shock protein 70 (HSP70, #ADI-SPA-812, Stressgen Biotechnologies, Victoria, BC, Canada), and anti-human tumor susceptibility gene 101 (TSG101, #612696, BD Transduction Laboratories, San Diego, CA, USA) as positive protein markers. Anti-human translocase of outer mitochondrial membrane 20 (TOMM20, #PA5-52843, Thermo Fisher Scientific) was used as a negative protein marker and horse serum albumin antibody (#PA5-97419, Thermo Fisher Scientific) as an EV purity control. Membranes were blocked with 5% dry milk powder in Tris-Buffered Saline with Tween (TBST, 20 mM Tris, 150 mM NaCl, 0.05% Tween-20) for 60 min followed by incubation with primary antibodies with a 1:1000 dilution in 5% milk with TBST at 4°C overnight. Excess primary antibodies were washed off the membranes in TBST initially for 10 min followed by two 5-min washes.

For secondary antibodies, 1:2000 dilutions were prepared with 2.5% dry milk powder in TBST and incubated for 60 min. Secondary antibodies were polyclonal goat anti-mouse (#P0447, Agilent, Santa Clara, CA, USA) for TSG101 and polyclonal goat anti-rabbit (#P0448, Agilent) for EMMPRIN, CD63, HSP70, TOMM20, and albumin. Excess secondary antibodies were washed off the membranes in TBST for 10 min and twice for 5 min. The membranes were incubated

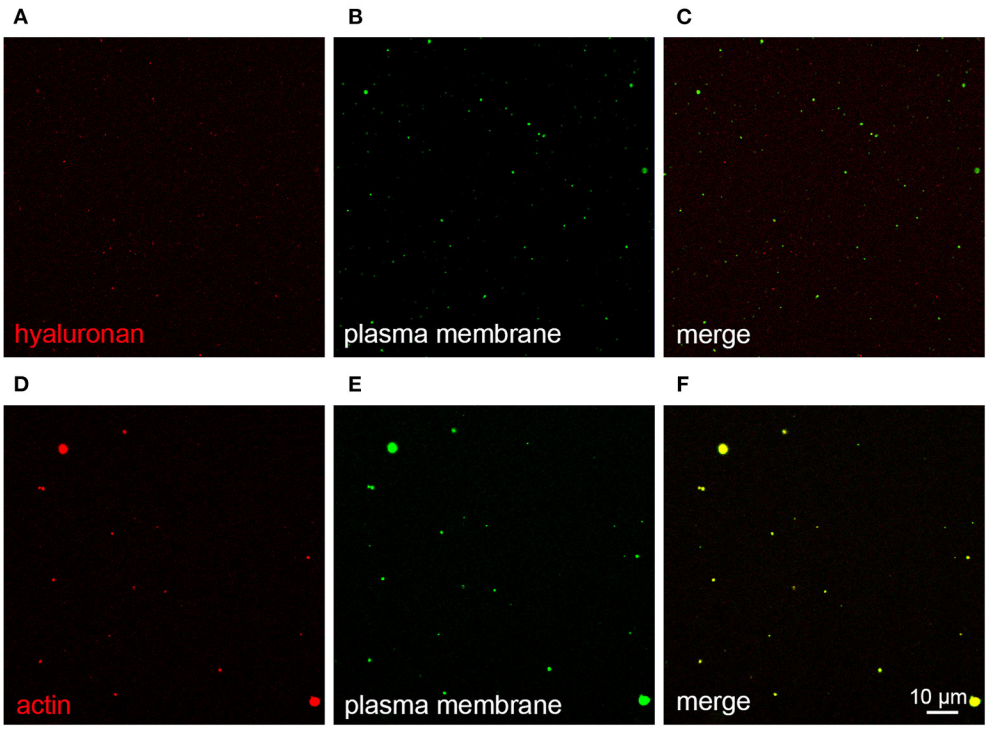

FIGURE 4 | Extracellular vesicles (EVs) from bronchoalveolar lavage fluid (BALF) stained with CellMask Deep Red plasma membrane stain (pseudocolored green, **B,E**), combined with Alexa Fluor 568-labeled hyaluronan binding complex **(A)** or 594-labeled phalloidin to detect F-actin **(D)**, both pseudocolored red. Merged images are shown in **C,F**, respectively. EVs in panels A–C were isolated by size-exclusion chromatography from BALF of a control horse. EVs in **D–F** were obtained by centrifugation and concentration of BALF of an asthmatic horse.

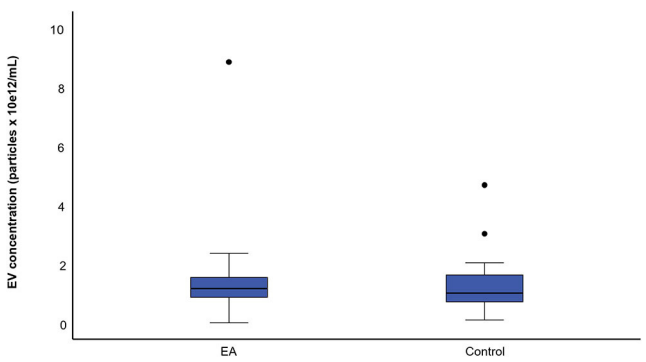

FIGURE 5 | Boxplots of mean particle concentration for the asthmatic (EA) (n = 35) and control horses (n = 19). The samples were analyzed by nanoparticle tracking analysis. Each box represents the interquartile range. The horizontal line in the box represents the median, the whiskers the range, and the circles the outliers. There was no significant difference between the groups.

in Chemiluminescence reagent West Atto Ultimate Sensitivity Substrate (Thermo Fisher Scientific) for 2 min and visualized using the luminescent image analyzer (LAS-3000, Fujifilm Life Science, Düsseldorf, Germany) with incremental exposure times.

Statistical Analyses

Sample size was calculated with the number of EVs as a primary outcome, an estimated difference of three between the groups, an expected standard deviation (SD) of five, a power of 80%, and significance at <0.05. A sufficient sample size for a paired t-test was calculated to be 25 pairs using a previous study from a similar population of horses as a reference (34). The statistical analyses were performed using the IBM SPSS $v25$ software (IBM, Armonk, NY, USA). To compare particle concentration over the different EV sizes between the groups, the AUC (area under curve) for each horse was calculated for the interval of 50–700 nm using the trapezoid method. The effects of health status on AUC adjusted for age were determined with the analysis of covariance. The model included health status as the fixed effect and age as the continuous covariate. Normality assumptions of the analysis model were tested with residual diagnostics. A square root transformation was used for the AUC to normalize the distribution. Two outliers were detected, and as they caused skewness to the distribution, the analyses were also performed excluding the outliers. The sex distribution in the study groups was tested with the Fisher's exact test and the differences in age and body weight with the Mann–Whitney U test. The association of age to EV concentration and size was tested with the Pearson's correlation coefficient (r_p). A p-value <0.05 was considered statistically significant. The results are expressed as mean ± SD.

RESULTS

Clinical Findings

The recruited horses represented several breeds (17 warmbloods, 18 coldbloods, 11 ponies, 3 standardbreds, 5 other breeds) and all sexes (41 geldings, 10 mares, 3 stallions). Out of 54 horses, 35 were included in the EA group, with owners reporting poor performance ($n = 16$), abdominal breathing pattern ($n = 11$), and nasal discharge ($n = 9$) as clinical signs in addition to cough. None of the EA horses displayed respiratory distress during clinical examinations, and there were no horses with signs of any other disease or abnormality that could potentially have caused respiratory symptoms. The control horses ($n = 19$) had no signs of respiratory disease in their medical histories or during examinations. The characteristics of the enrolled horses are described in **Table 1**. There were no differences in the sex ratios or body weights between the groups, but the EA horses were older than the controls ($p = 0.01$).

BALF Cytology, EV Isolation, and Characterization

The results of BALF cytology are presented in **Supplementary Material 1**. The 0.5 mL SEC fractions were collected and analyzed with NTA from five horses. The protein measurement of the 0.5 mL SEC fractions from three horses showed a low soluble non-EV protein content (**Figure 1**). The highest particle concentrations were observed in fractions 1–4 (**Figure 2**) and, therefore, in the remaining samples these fractions were pooled into a single sample/animal with a total volume of 2 mL (EV sample) that was concentrated to 300 μL and used for further analyses. TEM imaging from pooled fractions 1–4 verified the presence of various-sized EVs up to 1000 nm, while non-EV material, such as cell debris, was also detected in the samples (**Figure 3**). CLSM visualized EVs that transported HA and cytosolic F-actin (**Figure 4**). The positive EV protein markers CD63, TSG101, HSP70, the inflammatory protein marker EMMPRIN, and the purity control marker albumin were present in the EV and lung tissue samples (**Supplementary Material 2**). The negative EV protein marker TOMM20 was not detected in the EV samples.

EV Number and Size

The mean concentration of EVs was $1.38 \times 10^{12} \pm 1.42 \times 10^{12}$ particles/mL in the EA horses and $1.33 \times 10^{12} \pm 1.07 \times 10^{12}$ particles/mL in the control group determined by NTA (**Figure 5**). The mean size of EVs was 247 ± 35 nm in the EA horses and 261 ± 47 nm in the controls. The diameters of most EVs were between 100–350 nm (**Figure 6**), while TEM and CLSM visualized EV diameters up to 1,000 nm (**Figure 4**). There were no significant differences in the particle concentrations over the different EV sizes between the groups when tested with ($p = 0.745$) or without the outliers ($p = 0.613$). Age did not correlate significantly with the EV concentration ($r_p = -0.194$) or EV size ($r_p = -0.154$).

DISCUSSION

The present study describes a novel method for EV isolation from equine BALF and compares the size and particle concentration of EVs between horses with naturally occurring EA and healthy controls. The lack of a universal EV isolation protocol is a key challenge for EV research. Earlier studies have shown successful isolation of EVs from human and mouse BALF with ultrafiltration and ultracentrifugation (15, 35–37). Recently, SEC has become a popular method for isolating EVs because of the relatively pure and intact EVs that it can produce. However, the total separation of non-vesicular material from EVs remains impossible with currently available methods (35, 38, 39). Dilute samples are another potential downside of SEC, caused by the separation of the EVs into several fractions, but this can be avoided by pooling and by performing an additional concentration step. In the present study, the extraction method resulted in an EV concentration sufficient to be used in subsequent laboratory analyses, such as WB.

We analyzed the EVs isolated from BALF according to the MISEV 2018 guidelines (21) and demonstrated the presence of EVs in all main analyses. NTA and CLSM showed the presence of EV-sized particles in the samples, and TEM confirmed the presence of particles with cup-shaped morphology that is characteristic to EVs (23, 39). For WB, the MISEV 2018 guidelines (21) recommend analyzing proteins from three groups: (1). positive transmembrane protein markers, (2). positive cytosolic protein markers, and (3). negative protein markers. We detected CD63 (group 1), TSG101 (group 2), and HSP70 (group 2) from the EV preparations and lung tissue control samples. By using fluorescent phalloidin, the presence of actin (group 2) was also demonstrated in EVs with CLSM. TOMM20 (group 3) was detected by WB in 2 μg lung tissue but not in the EV samples. A plausible explanation for the absence of TOMM20 in the 0.5 μg lung tissue sample is the very low amount of the protein in equine lung tissue. TOMM20 is present in mitochondria, and an earlier study on different animal species has found that mitochondrial volume density decreases with increasing alveolar diameter (40). EMMPRIN was used as an inflammatory protein marker, as our group has previously found increased expression of matrix metalloproteinase-9 and its regulator EMMPRIN in the BALF of asthmatic horses (34). EMMPRIN, TSG101, CD63, and HSP70 proteins assessed with WB showed relatively low-intensity staining in the EV samples but high-intensity staining in the lung tissue samples (**Supplementary Figure 2**). This was likely caused by a low soluble protein content that is typical for samples isolated with SEC (38).

At present, there are no EV extraction methods that could purify biological fluid samples from all cell debris and proteins (35) and, in our study, TEM, CLSM, and WB analyses showed potential sample contamination. EV surface proteins are attached to the EV membrane with a smooth diffuse manner that forms a protein corona for the EV. In addition to EV proteins, other proteins and aggregates without any direct connection to EV function can attach tightly to the EV protein corona (8). This

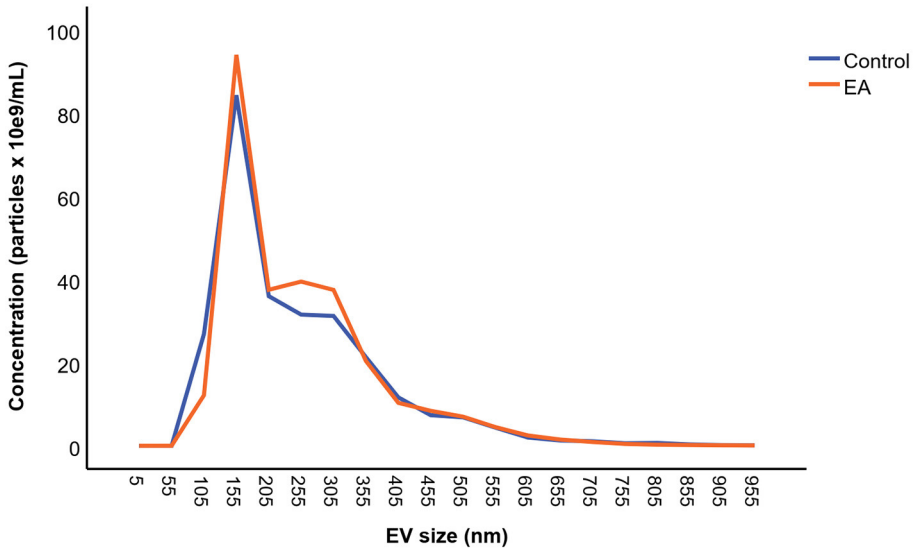

FIGURE 6 | Mean particle concentration and extracellular vesicle (EV) size distribution for the asthmatic (EA) ($n = 35$) and control horses ($n = 19$). The samples were analyzed by nanoparticle tracking analysis. There was no significant difference between the groups.

results in the co-extraction of non-EV origin proteins, which may explain the detected albumin that was used as a purity control in the EV samples. Furthermore, EV concentration measurements can be influenced by non-EV materials. The use of detergents prior to EV isolation could be a useful tactic to remove albumin from the EV samples, although EV components and subsequent analysis methods may be affected by detergent use (21, 41).

Altered concentrations of HA have been observed in several inflammatory diseases, such as asthma, rheumatoid arthritis, vascular diseases, and inflammatory bowel disease (17, 42, 43). The function of HA is dependent on its molecular weight and mechanisms of interaction, such as the access to multiple HA-binding proteins (42). We observed with CLSM that BALF EVs transported HA similar to synovial fluid EVs (25) and that the samples also contained free HA unbound to EVs. As asthma can be associated with increased secretion of HA with lower molecular size in humans (20), the potential roles of HA–EVs in its inflammatory and fibrotic processes warrant further studies to be revealed. Previously, a pretreatment with hyaluronidase led to improved recovery of EVs from equine synovial fluid with a high HA concentration (27) but, at the same time, the potentially significant physical association of EVs and HA would be lost.

Unlike in human subjects (2), the EV concentration and size did not increase in asthmatic horses. In concert with our results, the EV size distribution in humans was similar between asthmatic patients and controls (2). The particles isolated by differential centrifugation from human BALF ranged from 50 to 150 nm in size, which is less than the mean diameter in our EV samples. However, the particle count for certain-sized EVs should be interpreted cautiously because the chosen isolation method, such as the pore size in SEC, can affect the concentrations of particles by eliminating EVs of a particular diameter. As we used a pore size of 70 nm in our study, we expected that particles larger than this would leach out into the first fractions, leaving the smaller particles in the subsequent ones. The variation in the retrieved BALF volume and subsequently in the concentration of epithelial lining fluid in the samples increases sample variability, which may have an effect on the results. This can be further affected by the concentration step in the isolation protocol, and lead to large inter-individual variations observed in the NTA results.

EA prevalence varies depending on the climate and stabling conditions. Mild/moderate EA is common and reaches a prevalence of up to 66–80% (44, 45), while severe EA has a lower prevalence of 14–17% in stabled horses in the Northern hemisphere (45, 46). The milder forms have received increasing interest in recent years, as mild and moderate asthma cause economic losses worldwide due to reduced performance, which could be ameliorated through early diagnosis and treatment. The horses in our study represent a natural horse population for EA research that could also contribute to translational asthma research. However, because the symptoms were relatively mild at the time of sample collection, the low level of airway inflammation may explain why there were no statistically significant differences in the EV variables between the groups. According to a study by Moon et al. (2015) (11) on mice, the numbers of BALF EVs originating from lung epithelial cells increased in the presence of inflammation while the amount of EVs derived from other cells, such as alveolar macrophages, interstitial macrophages, or dendritic cells, remained unchanged. The clinical significance of EVs in horses with severe asthma and their relation to the extent of increase in BALF inflammatory cell counts require further studies to discover the most promising targets for translational

research. Another study limitation was the age difference between the EA and control horses. However, the age did not show significant association with the concentration or size of EVs. In addition, the data from the older horses yielded clinically relevant information about the biology of asthma in this age group.

In conclusion, the results of the present study support the study hypotheses with some exceptions. Membrane-bound particles were successfully isolated from equine BALF, and the presence of positive protein markers as well as an inflammatory protein marker verified them as EVs. Moreover, EVs were observed to carry HA with potential to influence the inflammatory or fibrotic nature of asthma. However, the count and size distribution of EVs did not differ between the horses with mild/moderate asthma and the healthy controls and, therefore, the roles of EVs of various origin and cargo in airway inflammation warrant further study.

DATA AVAILABILITY STATEMENT

The original contributions presented in the study are included in the article/**Supplementary Material**, further inquiries can be directed to the corresponding author/s.

ETHICS STATEMENT

The animal study was reviewed and approved by the Project Authorization Board in the Regional State Administrative Agency (ESAVI/3285/2020). Written informed consent was obtained from the owners for the participation of their animals in this study.

AUTHOR CONTRIBUTIONS

NH has taken part in study design, sample collection, laboratory analyses, analysis of the results, and manuscript preparation, with input from all authors. AM, HR, and NK contributed to the design and implementation of the research, to the analysis of the results, and to the writing of the manuscript. NK and JK took part in the developing of the laboratory analyses and manuscript preparation together with AM and NH. PN, A-MM, KR, and SO performed the confocal laser scanning microscopy. AM, HR, PN, A-MM, and JK were involved in the supervising of the work. All authors contributed to the article and approved the submitted version.

FUNDING

Funds were received from the Finnish Veterinary Foundation, the Finnish Foundation of Veterinary Research, and the Academy of Finland (grant #322429 to PN).

ACKNOWLEDGMENTS

We kindly thank Merja Ranta and Taija Hukkanen for their expertise in laboratory work and the EV Core Viikki (Molecular Medicine Finland, Department of Biosciences/Faculty of Pharmacy, University of Helsinki) for providing NTA and TEM laboratory facilities. We thank Karina Barreiro and Ileana Quintero for TEM analyses, Rosabella Hartman for performing NTA analyses, and Mari Palviainen and Maija Puhka for their expert advice on the field.

SUPPLEMENTARY MATERIAL

The Supplementary Material for this article can be found online at: https://www.frontiersin.org/articles/10.3389/fvets.2022.894189/full#supplementary-material

Supplementary Material 1 | Boxplots of bronchoalveolar lavage fluid (BALF) cell percentage among the control horses ($n = 19$) and horses with equine asthma (EA; $n = 35$). Each box represents the interquartile range. The horizontal line in the box represents the median, the whiskers the range, and the black points the outliers.

Supplementary Material 2 | Western blot membranes depicting the expressions of proteins EMMPRIN, CD63, HSP70, TSG101, TOMM20, and horse serum albumin in equine lung tissue and extracellular vesicles from asthmatic (EV1) and control (EV2) bronchoalveolar lavage fluids.

REFERENCES

1. Bullone M, Lavoie J-P. The equine asthma model of airway remodeling: from a veterinary to a human perspective. *Cell Tissue Res.* (2020) 380:223–36. doi: 10.1007/s00441-019-03117-4
2. Hough KP, Wilson LS, Trevor JL, Strenkowski JG, Maina N, Kim Y-I, et al. Unique lipid signatures of extracellular vesicles from the airways of asthmatics. *Sci Rep.* (2018) 8:10340. doi: 10.1038/s41598-018-28655-9
3. Nagano T, Katsurada M, Dokuni R, Hazama D, Kiriu T, Umezawa K, et al. Crucial role of extracellular vesicles in bronchial asthma. *Int J Mol Sci.* (2019) 20:2589. doi: 10.3390/ijms20102589
4. Bond S, Léguillette R, Richard EA, Couëtil L, Lavoie J-P, Martin JG, et al. Equine asthma: integrative biologic relevance of a recently proposed nomenclature. *J Vet Intern Med.* (2018) 32:2088–98. doi: 10.1111/jvim.15302
5. Simões J, Luís JS, Tilley P. Contribution of lung function tests to the staging of severe equine asthma syndrome in the field. *Res Vet Sci.* (2019) 123:112–7. doi: 10.1016/j.rvsc.2018.12.014
6. Rilla K, Mustonen A-M, Arasu UT, Härkönen K, Matilainen J, Nieminen P. Extracellular vesicles are integral and functional components of the extracellular matrix. *Matrix Biol.* (2019) 75–76:201–19. doi: 10.1016/j.matbio.2017.10.003
7. Akers JC, Gonda D, Kim R, Carter BS, Chen CC. Biogenesis of extracellular vesicles (EV): exosomes, microvesicles, retrovirus-like vesicles, and apoptotic bodies. *J Neurooncol.* (2013) 113:1–11. doi: 10.1007/s11060-013-1084-8
8. Tóth EÁ, Turiák L, Visnovitz T, Cserép C, Mázló A, Sódar BW, et al. Formation of a protein corona on the surface of extracellular vesicles in blood plasma. *J Extracell Vesicles.* (2021) 10:e12140. doi: 10.1002/jev2.12140
9. Battistelli M, Falcieri E. Apoptotic bodies: particular extracellular vesicles involved in intercellular communication. *Biology.* (2020) 9:21. doi: 10.3390/biology9010021
10. Nirujogi TS, Kotha SR, Chung S, Reader BF, Yenigalla A, Zhang L, et al. Lipidomic profiling of bronchoalveolar lavage fluid extracellular vesicles indicates their involvement in lipopolysaccharide-induced acute lung

injury. *J Innate Immun.* (2022). doi: 10.1159/000522338. [Epub ahead of print].
11. Moon HG, Cao Y, Yang J, Lee JH, Choi HS, Jin Y. Lung epithelial cell-derived extracellular vesicles activate macrophage-mediated inflammatory responses via ROCK1 pathway. *Cell Death Dis.* (2015) 6:e2016. doi: 10.1038/cddis.2015.282
12. Sangaphunchai P, Todd I, Fairclough L. Extracellular vesicles and asthma: a review of the literature. *Clin Exp Allergy.* (2020) 50:291–307. doi: 10.1111/cea.13562
13. Konoshenko MY, Lekchnov EA, Vlassov AV, Laktionov PP. Isolation of extracellular vesicles: general methodologies and latest trends. *Biomed Res Int.* (2018) 2018:8545347. doi: 10.1155/2018/8545347
14. Lee H, Abston E, Zhang D, Rai A, Jin Y. Extracellular vesicle: an emerging mediator of intercellular crosstalk in lung inflammation and injury. *Front Immunol.* (2018) 9:924. doi: 10.3389/fimmu.2018.00924
15. Papadopoulos S, Kazepidou E, Antonelou MH, Leondaritis G, Tsapinou A, Koulouras VP, et al. Secretory phospholipase A2-IIA protein and mRNA pools in extracellular vesicles of bronchoalveolar lavage fluid from patients with early acute respiratory distress syndrome: a new perception in the dissemination of inflammation? *J Pharm.* (2020) 13:415. doi: 10.3390/ph13110415
16. Mustonen A-M, Nieminen P, Joukainen A, Jaroma A, Kääriäinen T, Kröger H, et al. First in vivo detection and characterization of hyaluronan-coated extracellular vesicles in human synovial fluid. *J Orthop Res.* (2016) 34:1960–8. doi: 10.1002/jor.23212
17. Garantziotis S, Brezina M, Castelnuovo P, Drago L. The role of hyaluronan in the pathobiology and treatment of respiratory disease. *Am J Physiol Lung Cell Mol Physiol.* (2016) 310:L785–95. doi: 10.1152/ajplung.00168.2015
18. Allegra L, Patrona SD, Petrigni G. Hyaluronic acid: perspectives in lung diseases. *Handb Exp Pharmacol.* (2012) 207:385–401. doi: 10.1007/978-3-642-23056-1_17
19. Deed R, Rooney P, Kumar P, Norton JD, Smith J, Freemont AJ, et al. Early-response gene signalling is induced by angiogenic oligosaccharides of hyaluronan in endothelial cells. Inhibition by non-angiogenic, high-molecular-weight hyaluronan. *Int J Cancer Res.* (1997) 71:251–6. doi: 10.1002/(SICI)1097-0215(19970410)71:2<251::AID-IJC21>3.0.CO;2-J
20. Liang J, Jiang D, Jung Y, Xie T, Ingram J, Church T, et al. Role of hyaluronan and hyaluronan-binding proteins in human asthma. *J Allerg Clin Immunol.* (2011) 128:403–11. doi: 10.1016/j.jaci.2011.04.006
21. Théry C, Witwer KW, Aikawa E, Alcaraz MJ, Anderson JD, Andriantsitohaina R, et al. Minimal information for studies of extracellular vesicles 2018 (MISEV2018): a position statement of the International Society for Extracellular Vesicles and update of the MISEV2014 guidelines. *J Extracell Vesicles.* (2018) 7:1535750. doi: 10.1080/20013078.2018.1535750
22. Mol EA, Goumans M-J, Doevendans PA, Sluijter JPG, Vader P. Higher functionality of extracellular vesicles isolated using size-exclusion chromatography compared to ultracentrifugation. *Nanomed: Nanotechnol Biol Med.* (2017) 13:1627–36. doi: 10.1016/j.nano.2017.03.011
23. Chuo ST-Y, Chien JC-Y, Lai CP-K. Imaging extracellular vesicles: current and emerging methods. *J Biomed Sci.* (2018) 25:91. doi: 10.1186/s12929-018-0494-5
24. Dragovic RA, Gardiner C, Brooks AS, Tannetta DS, Ferguson DJP, Hole P, et al. Sizing and phenotyping of cellular vesicles using Nanoparticle Tracking Analysis. *Nanomed: Nanotechnol Biol Med.* (2011) 7:780–8. doi: 10.1016/j.nano.2011.04.003
25. Mustonen A-M, Capra J, Rilla K, Lehenkari P, Oikari S, Kääriäinen T, et al. Characterization of hyaluronan-coated extracellular vesicles in synovial fluid of patients with osteoarthritis and rheumatoid arthritis. *BMC Musculoskelet Disord.* (2021) 22:247. doi: 10.1186/s12891-021-04115-w
26. Almiñana C, Vegas AR, Tekin M, Hassan M, Uzbekov R, Fröhlich T, et al. Isolation and characterization of equine uterine extracellular vesicles: a comparative methodological study. *Int J Mol Sci.* (2021) 22:979. doi: 10.3390/ijms22020979
27. Boere J, van de Lest CHA, Libregts SFWM, Arkesteijn GJA, Geerts WJC, Nolte-'t Hoen ENM, et al. Synovial fluid pretreatment with hyaluronidase facilitates isolation of CD44+ extracellular vesicles. *J Extracell Vesicles.* (2016) 5:31751. doi: 10.3402/jev.v5.31751
28. Hotham WE, Thompson C, Szu-Ting L, Henson FMD. The anti-inflammatory effects of equine bone marrow stem cell-derived extracellular vesicles on autologous chondrocytes. *Vet Rec Open.* (2021) 8:e22. doi: 10.1002/vro2.22
29. Klymiuk MC, Balz N, Elashry MI, Heimann M, Wenisch S, Arnhold S. Exosomes isolation and identification from equine mesenchymal stem cells. *BMC Vet Res.* (2019) 15:42. doi: 10.1186/s12917-019-1789-9
30. Maredziak M, Marycz K, Lewandowski D, Siudzińska A, Smieszek A. Static magnetic field enhances synthesis and secretion of membrane-derived microvesicles (MVs) rich in VEGF and BMP-2 in equine adipose-derived stromal cells (EqASCs)—a new approach in veterinary regenerative medicine. *In Vitro Cell Dev Biol Anim.* (2015) 51:230–40. doi: 10.1007/s11626-014-9828-0
31. Springer NL, Smith E, Brooks MB, Stokol T. Flow cytometric detection of circulating platelet-derived microparticles in healthy adult horses. *Am J Vet Res.* (2014) 75:879–85. doi: 10.2460/ajvr.75.10.879
32. Puhka M, Takatalo M, Nordberg ME, Valkonen S, Nandania J, Aatonen M, et al. Metabolomic profiling of extracellular vesicles and alternative normalization methods reveal enriched metabolites and strategies to study prostate cancer-related changes. *Theranostics.* (2017) 7:3824–41. doi: 10.7150/thno.19890
33. Rilla K, Tiihonen R, Kultti A, Tammi M, Tammi R. Pericellular hyaluronan coat visualized in live cells with a fluorescent probe is scaffolded by plasma membrane protrusions. *J Histochem Cytochem.* (2008) 56:901–10. doi: 10.1369/jhc.2008.951665
34. Rossi H, Rajamäki M, Koho N, Ilves M, Mykkänen A.. Expression of extracellular matrix metalloproteinase inducer and matrix metalloproteinase-2 and -9 in horses with chronic airway inflammation. *Am J Vet Res.* (2017) 78:1329–37. doi: 10.2460/ajvr.78.11.1329
35. Dlugolecka M, Szymanski J, Zareba L, Homoncik Z, Domagala-Kulawik J, Polubiec-Kownacka M, et al. Characterization of extracellular vesicles from bronchoalveolar lavage fluid and plasma of patients with lung lesions using fluorescence nanoparticle tracking analysis. *Cell J.* (2021) 10:3473. doi: 10.3390/cells10123473
36. Mahida RY, Matsumoto S, Matthay MA. Extracellular vesicles: a new frontier for research in acute respiratory distress syndrome. *Am J Respir Cell Mol.* (2020) 63:15–24. doi: 10.1165/rcmb.2019-0447TR
37. Martin-Medina A, Lehmann M, Burgy O, Hermann S, Baarsma HA, Wagner DE, et al. Increased extracellular vesicles mediate WNT5A signaling in idiopathic pulmonary fibrosis. *Am J Respir Crit Care Med.* (2018) 198:1527–38. doi: 10.1164/rccm.201708-1580OC
38. Brennan K, Martin K, FitzGerald SP, O'Sullivan J, Wu Y, Blanco A, et al. A comparison of methods for the isolation and separation of extracellular vesicles from protein and lipid particles in human serum. *Sci Rep.* (2020) 10:1039. doi: 10.1038/s41598-020-57497-7
39. Lobb RJ, Becker M, Wen SW, Wong CSF, Wiegmans AP, Leimgruber A, et al. Optimized exosome isolation protocol for cell culture supernatant and human plasma. *J Extracell Vesicles.* (2015) 4:27031. doi: 10.3402/jev.v4.27031
40. Massaro GD, Gail DB, Massaro D. Lung oxygen consumption and mitochondria of alveolar epithelial and endothelial cells. *J Appl Physiol.* (1975) 38:588–59. doi: 10.1152/jappl.1975.38.4.588
41. Osteikoetxea X, Sódar B, Németh A, Szabó-Taylor K, Pálóczi K, Vukman KV, et al. Differential detergent sensitivity of extracellular vesicle subpopulations. *Org Biomol Chem.* (2015) 13:9775–82. doi: 10.1039/C5OB01451D
42. Lennon FE, Singleton PA. Role of hyaluronan and hyaluronan-binding proteins in lung pathobiology. *Am J Physiol Lung Cell Mol Physiol.* (2011) 301:L137–47. doi: 10.1152/ajplung.00071.2010
43. Petrey AC, de la Motte CA. Hyaluronan, a crucial regulator of inflammation. *Front Immunol.* (2014) 5:101. doi: 10.3389/fimmu.2014.00101

44. Ivester KM, Couëtil LL, Moore GE. An observational study of environmental exposures, airway cytology, and performance in racing thoroughbreds. *J Vet Intern Med*. (2018) 32:1754–62. doi: 10.1111/jvim.15226
45. Wasko AJ, Barkema HW, Nicol J, Fernandez N, Logie N, Léguillette R. Evaluation of a risk-screening questionnaire to detect equine lung inflammation: results of a large field study. *Equine Vet J.* (2011) 43:145–52. doi: 10.1111/j.2042-3306.2010.00150.x
46. Hotchkiss JW, Reid SWJ, Christley RM. A survey of horse owners in Great Britain regarding horses in their care. Part 2: Risk factors for recurrent airway obstruction. *Equine Vet J.* (2007) 39:301–8. doi: 10.2746/042516407X180129

Conflict of Interest: The authors declare that the research was conducted in the absence of any commercial or financial relationships that could be construed as a potential conflict of interest.

frontiers | Frontiers in Veterinary Science

TYPE Methods
PUBLISHED 02 September 2022
DOI 10.3389/fvets.2022.949410

OPEN ACCESS

EDITED BY
Stefano Guido,
University of Edinburgh,
United Kingdom

REVIEWED BY
Michel R. Labrosse,
University of Ottawa, Canada
Kelly Yamada,
Icahn School of Medicine at Mount Sinai, United States

*CORRESPONDENCE
Nikola Cesarovic
Nikola.Cesarovic@hest.ethz.ch

†These authors have contributed equally to this work

SPECIALTY SECTION
This article was submitted to Comparative and Clinical Medicine, a section of the journal Frontiers in Veterinary Science

RECEIVED 20 May 2022
ACCEPTED 22 July 2022
PUBLISHED 02 September 2022

CITATION
Weisskopf M, Glaus L, Trimmel NE, Hierweger MM, Leuthardt AS, Kukucka M, Stolte T, Stoeck CT, Falk V, Emmert MY, Kofler M and Cesarovic N (2022) Dos and don'ts in large animal models of aortic insufficiency. *Front. Vet. Sci.* 9:949410. doi: 10.3389/fvets.2022.949410

Dos and don'ts in large animal models of aortic insufficiency

Miriam Weisskopf[1†], Lukas Glaus[2†], Nina E. Trimmel[1], Melanie M. Hierweger[1], Andrea S. Leuthardt[1], Marian Kukucka[3], Thorald Stolte[2], Christian T. Stoeck[1,4], Volkmar Falk[2,3,5], Maximilian Y. Emmert[3,5], Markus Kofler[3] and Nikola Cesarovic[2,3]*

[1]Center for Surgical Research, University Hospital Zurich, University of Zurich, Zurich, Switzerland, [2]Department of Health Sciences and Technology, Swiss Federal Institute of Technology, Zurich, Switzerland, [3]Department of Cardiothoracic and Vascular Surgery, German Heart Center Berlin, Berlin, Germany, [4]Institute for Biomedical Engineering, University and ETH Zurich, Zurich, Switzerland, [5]Department of Cardiovascular Surgery, Charité-Universitätsmedizin Berlin, Berlin, Germany

Aortic insufficiency caused by paravalvular leakage (PVL) is one of the most feared complications following transcatheter aortic valve replacement (TAVI) in patients. Domestic pigs (*Sus scrofa domestica*) are a popular large animal model to study such conditions and develop novel diagnostic and therapeutic techniques. However, the models based on prosthetic valve implantation are time intensive, costly, and often hamper further hemodynamic measurements such as PV loop and 4D MRI flow by causing implantation-related wall motion abnormalities and degradation of MR image quality. This study describes in detail, the establishment of a minimally invasive porcine model suitable to study the effects of mild-to-moderate "paravalvular" aortic regurgitation on left ventricular (LV) performance and blood flow patterns, particularly under the influence of altered afterload, preload, inotropic state, and heart rate. Six domestic pigs (Swiss large white, female, 60–70 kg of body weight) were used to establish this model. The defects on the hinge point of aortic leaflets and annulus were created percutaneously by the pierce-and-dilate technique either in the right coronary cusp (RCC) or in the non-coronary cusp (NCC). The hemodynamic changes as well as LV performance were recorded by PV loop measurements, while blood flow patterns were assessed by 4D MRI. LV performance was additionally challenged by pharmaceutically altering cardiac inotropy, chronotropy, and afterload. The presented work aims to elaborate the dos and don'ts in porcine models of aortic insufficiency and intends to steepen the learning curve for researchers planning to use this or similar models by giving valuable insights ranging from animal selection to vascular access choices, placement of PV Loop catheter, improvement of PV loop data acquisition and post-processing and finally the induction of paravalvular regurgitation of the aortic valve by a standardized and reproducible balloon induced defect in a precisely targeted region of the aortic valve.

KEYWORDS

large animal model, aortic valve, paravalvular leakage, aortic insufficiency (AI), Minimally invasive, PV loop, MRI, pig

Introduction

Background

New onset of aortic regurgitation is considered one of the major complications following aortic valve replacement interventions. Regurgitant flow between the prosthetic valve and native aortic tissue is termed paravalvular leakage (PVL), and it is often caused by malapposition of the two structures and consequent insufficient sealing. Even with new generation transcatheter heart valves, implanted in patients with favorable device landing zone (tricuspid aortic valve, no severe calcification of the left ventricular outflow tract) the rate of at least mild PVL is still around 30% (1) and increases to almost 60% for patients with less favorable landing zones. In patients, most PVLs are considered hemodynamically insignificant; however, contemporary literature suggests that even mild PVL is associated with worse postoperative survival (2). Experimentally it could be shown that already a mild-to-moderate PVL alters intraventricular blood flow patterns by disturbing physiologic vortex formation thereby causing a potential increase in dissipation of left ventricular energy (3). All circumstances altering the cardiac output need to be interpreted in the light of the ongoing trend to use transcatheter heart valves in younger and physically more active patients. High fidelity animal models with mild-to-moderate PVL are an unmet need to provide evidence for the significance of such fluid dynamic alteration in relation to reduced cardiac function.

Rosa et al. previously described a porcine model of PVL created by replacing the native aortic valve with a lab-fabricated one, while intentionally leaving space for regurgitant flow between the valve and the aortic wall (4). Although the model appears to offer opportunities to develop and test therapeutic approaches to reduce or eliminate regurgitant flow, the model is not only difficult to reproduce but also hampers the assessment of blood flow characteristics in detail with 4D flow MRI, as image quality is degraded, dependent on the stent type and stent orientation relative to the magnetic field (5). To overcome this limitation, we developed a large animal model of mild PVL by transcatheter piercing of the aortic valve at the hinge point of the annulus and leaflet (3). Following the selection of appropriately sized animals free from pathogens that could influence cardiac health, aortic valve defects are created in a percutaneous, transcatheter fashion using the pierce-and-dilate technique. In detail, under fluoroscopic and echocardiographic guidance, a steerable sheath is navigated to either the non-coronary (NCC) or right-coronary cusp (RCC) of the aortic valve. Once in position, a stiff coronary guide wire is used to pierce the leaflet-annulus hinge point. A coronary balloon is then passed over the wire and inflated to produce a standardized defect causing aortic regurgitation (i.e., PVL). For a successful assessment of the effects on left ventricular (LV) performance, it is paramount to establish a stable position of the PV loop catheter resistant to the manipulations during PVL creation, enabling direct comparison between the healthy state and immediate hemodynamic effects of PVL. Moreover, drugs can be used to alter the hemodynamic parameters, such as cardiac afterload (i.e., aortic pressure and resistance), heart rate, and contractility, known to influence the severity and negative effects of aortic regurgitation. The animal model thereby simulates also hypertensive and/or tachycardiac patients suffering from aortic regurgitation, potentially leading to a better understanding of underlying processes responsible for adverse cardiac remodeling in this population.

Patients suffering from severe PVL display clear symptoms and can benefit from the guideline directed therapy. However, for those patients displaying only mild-to-moderate PVL the situation is less clear. This population displays a wide variety of symptoms and a therapeutic spectrum ranging from disease monitoring to invasive interventions. Moreover, currently, the influence of the PVL jet origin and its effects on left ventricular flow and function are largely left unconsidered. Hence, the main purpose of this model is to provide a reproducible, cost-effective, and ethically justifiable translational large animal platform to investigate the fluid dynamic and energetic effects of mild-to-moderate aortic PVL originating from the areas of the aortic valve clinically associated with the presentation of PVL namely the right- or the non-coronary cusp.

The presented work aims to elaborate on the dos and don'ts when establishing an aortic insufficiency/PVL model for hemodynamic studies. Benefitting from each other's learning curves will reduce redundancy in animal research and improve data quality in accordance with the 3R principles established worldwide as the ethical approach to regulating the use of animals for scientific purposes (6).

Selection of appropriately sized animals free of cardiac pathogens is a key prerequisite

The use of the domestic pig (*Sus Scrofa Domestica*) in preclinical studies plays an important role in the evaluation of efficacy and safety of new cardiac medical devices before their use in human clinical trials (7–9). However, when planning and executing porcine trials, a variety of aspects should be taken into consideration. The health status of domestic pigs varies greatly depending on their origin; thus, a rigorous pre-screening for diseases affecting cardiac health and function should be performed. A multitude of infectious diseases and nutritional deficiencies can alter cardiovascular health in commercial pigs. Among the most important infectious agents are thereby the *Porcine Circovirus type 2 (PCV2),* which has previously been associated with heart failure in young pigs due to acute necrotizing or chronic fibrosing myocarditis, and chronic vasculitis in multiple organs (10). The *Encephalomyocarditis Virus* (EMCV) causing acute myocarditis and sudden death in preweaned pigs and reproductive failure

in sows (11) has become of recent concern in the context of xenotransplantation. Although it is described as asymptomatic in older pigs, the virus appears to persist in the myocardium over a prolonged period (11). *Hemophilus parasuis*, the cause of Glasser's disease, commonly causes serofibrinous pleuritis, pericarditis, peritonitis, and arthritis (12). Porcine endocarditis is another well-known disease entity, with *Streptococcus suis* and *Erysipelothrix rhusiopathiae* being the dominant bacteria isolated from infected heart valves (13). Mulberry heart disease in pigs is characterized by lesions of acute hemorrhagic myocarditis and myocardial necrosis and has been associated with vitamin E/selene deficiency (14), recent studies further suspect viral association in the disease (15).

Anatomical differences between pigs and humans are a further aspect to consider when using this animal model. Most differences thereby arise from pigs being quadruped, hence having a narrower thorax in latero-lateral rather than in dorso-ventral orientation, unlike humans that feature a dorso-ventrally "compressed" chest (16). Consequently, the major cardiac axis of the porcine heart is tipped ventro-caudally and forms a steeper angle. Nonetheless, a vast majority of cardiac dimensions in pigs appear to correlate well with the average adult human (16), though left atrial volume and dimensions can be smaller in pigs than equivalent mitral annulus size seen in humans (17). Furthermore, the relative cardiac mass in certain breeds of pigs appears to decrease significantly from 5 gr/kg BW to just 2.3–2.9 gr/kg BW, as maturity is reached (18). As pre-experimental selection of pigs is commonly based on body weight, this nonlinear correlation between body mass and cardiac size needs to be considered. In general, in trans-catheter aortic valve implantations (TAVI) in pigs, complications are often associated with over- or undersizing of the valve and are comparable to those seen in humans, namely, coronary occlusion, rupture of the aortic root or annulus post-implantation, PVL or transcatheter valve migration (19, 20). Cardiac valve, in particular, aortic valve sizing in preclinical trials requires a different approach than typically used in clinics. Compared to the diseased calcified annulus of patients, the annulus of a healthy pig is more dynamic during the cardiac cycle demanding appropriate oversizing to avoid migration and stability issues hampering sufficient sealing between the prosthetic valve and the aortic wall (21).

Combination of fluoroscopy and ultrasound imaging is necessary to guide PVL creation and clinically assess its position and severity

Fluoroscopy was used to image the position of the steerable sheath, however, as it does not allow visualization of cardiac soft-tissue structures, which is needed to provide adequate visualization of the targeted cardiac anatomy necessary for the successful PVL creation, fluoroscopy is best complemented with ultrasound. While transthoracic echocardiography (TTE) in pigs is technically challenging by the previously mentioned keel-shaped thorax and by narrowly spaced ribs (22), a three-chamber view, showing a long axis of the left ventricle and the aortic valve can be obtained by placing a trans-esophageal echo (TEE) probe in the mid-esophageal position in an ante-flexed and latero-flexed position and plane rotating the transducer between 90 and 130° (23, 24), adjusting rotation as needed to account for individual anatomy of the animal. To obtain a simultaneous short axis view of the left ventricular outflow tract and the aortic valve, an intracardiac echocardiography (ICE) probe can be introduced through the femoral vein and placed at a low RA location in a postero-flexed position followed by counterclockwise rotation by 60–100° (25). Combining these imaging modalities allows for a precise and reproducible aortic valvular leaflet piercing.

4D MRI is best complemented by PV loop analysis to assess the effects of PVL on LV function

For a comprehensive evaluation of PVL on left ventricular hemodynamics, 4D MRI flow data is best complemented with left ventricular PV loop analysis, which is considered to be the gold standard for assessing cardiac function during each cardiac cycle (26). PV loops offer invaluable insights into the pathophysiology of PVL in the porcine model. However, PV loop analysis not only requires knowledge of the pig's anatomical and physiological particularities but comprehensive analytical skills for adequate data processing. Hence, comprehensive preclinical studies highly benefit from interdisciplinary collaborations of veterinarians, physicians, and engineers, to ensure animal welfare, translatability of the study, and reproducibility by high-quality data.

Materials and equipment

Animals

- Large white pigs, female, 60–70-kg body weight

Drugs

- **Ketamine** (Ketasol®-100 ad us.vet.; Dr. E. Graeub AG, Berne, Switzerland; 15-mg/kg body weight).
- **Azaperon** (Stresnil® ad us.vet.; Elanco Tiergesundheit AG, Basel, Switzerland; 2-mg/kg body weight).
- **Atropin 1%** (Atropinsulfat KA vet 0.1%; Kantonsapotheke, Switzerland; 0.05-mg/kg body weight).
- **Vitamin A Eye Ointment** (Vitamin A Blache Augensalbe, Bausch & Lomb Swiss AG, Zug, Switzerland).

- **Propofol** (Propofol ® Lipuro 1%, B. Braun Medical AG; Sempach, Switzerland; 1–2 mg/kg body weight (bolus), 3–5 mg/kg/h continuous infusion).
- **Isoflurane** (Attane™ Isoflurane ad.us.vet., Piramal Enterpr. India, Lyssach, Switzerland, 1–2%).
- **Buprenorphine** (Temgesic®; Indivior Schweiz AG, Baar, Switzerland; 0.01 mg/kg).
- **Amiodarone** (Cordarone®, Sanofi-Aventis (Suisse) SA, Vernier, Switzerland, 150 mg/100 ml 5% glucose, slow drip to effect).
- **Ringer's solution** (Ringerfundin®, B. Braun Medical AG, Sempach, Switzerland, 5 ml/kg/h).
- **Sodium-Heparin** (Na-Heparin, B. Braun Medical AG, Sempach, Switzerland).
- **Dobutamine** (Dobutrex®, Teva Pharma AG, Basel, Switzerland, 2.5 mg/ml, continuous infusion to effect).
- **Phenylephrine** (Neo-Synephrine HCl, Ospedialia AG, Hünenberg, Switzerland, 0.1 mg/ml, continuous infusion to effect).
- **Hypertonic Saline** (Natrium Chloratum Sintetica 25%, Sintetica S.A., Mendrisio, Switzerland,0.25 ml/kg 15% hypertonic NaCl).

Materials

- **Intravenous catheter** (BD Venflon ™ Pro Safety, Becton Dickinson Infusion Therapy, Helsingborg, Sweden, 18G).
- **Endotracheal tube** (Bivona®, ID: 9 mm, OD: 12.4 mm, 37FR, Length: 56 cm, Balloon: 5 cm).
- **Urinary balloon catheter** (Rüsch®, Ch 12, Teleflex Medical GmbH, Belp, Switzerland).
- **Vascular access sheath** (Avanti®+ Introducer,6–10 F, Cordis®, Miami Lakes FL, USA).
- **Intra-cardiac echocardiography (ICE) probe** (ViewFlex™ Xtra ICE Catheter, St.Jude Medical, Minnesota, USA).
- **Transesophageal echo probe** (X7-2T TEE Transducer, Philips, Amsterdam, The Netherlands).
- **Bidirectional steerable guiding sheath** (Agilis™ EPI Steerable Sheath, 8.5F, St. Jude Medical, Minnetonka, MN, USA, Or DESTINO™ Reach 8.5F ID, usable length 77cm, curve 17mm, Oscor®, Florida, USA).
- **PV loop catheter** (Ventri-Cath Catheter; 5F, 12E, 10 mm, DField, Pigtail, 122 cm; ADInstruments Limited, Oxford, United Kingdom).
- **Pig-tail catheter** (Infiniti 5F PIG 145.038 125 cm, Cordis Corporation, Miami Lakes, USA).
- **J-tip Guide Wire** (Rosen, Heavy-Duty Corewire J-tip, 0.035", 180 cm, Cordis®, Miami Lakes FL, USA).
- **Extra-Stiff guide wire** (Lunderquist®, 0.035"260 cm, Cook Medical, Bjaeverskov, Denmark).
- **Coronary guide wire** (IRON MAN Guide Wire, 0.014″ 190 cm, Abbott Vascular, Santa Clara CA, USA).
- **PTCA balloon** (NC Emerge MONORAIL™ PTCA Dilation Balloon 5 × 12 mm, Boston Scientific Corporation, Marlborough, MA, USA).

Equipment

- **Anesthesia machine** (Dräger Fabius GS, Dräger Medical, Lübeck, Germany).
- **Anesthetic monitoring** (Dräger Infinity, Dräger Medical, Lübeck, Germany).
- **Fluoroscopy C-Arm** (Allura Xper FD20, Philips Healthcare, Horgen, Switzerland).
- **Ultrasound machine** (TEE) (iE33, Philips Healthcare, Horgen, Switzerland).
- **Ultrasound machine** (ICE) (CX50, Philips Healthcare, Horgen, Switzerland).
- **DSI Ponemah System** (DataScience International, St. Paul, Minnesota, USA).
- Millar Mikro-Tip® Pressure Volume System (MPVS) Ultra Foundation Systems (AD Instruments, Oxford, United Kingdom).
- **Powerlab 16/35 Acquisition Unit** (AD Instruments, Oxford, United Kingdom).
- **Clinical 3T MR Scanner** (Ingenia, Philips Healthcare, Best, the Netherlands).

Methods

Animal acquisition, health check, and anesthesia

Six domestic pigs (n = 6; Swiss large white, intact females, 60–70 kg of body weight) were included in this study approved by the local Committee for Experimental Animal Research (Cantonal Veterinary Office Zurich, Switzerland) under the License numbers ZH213/2019. Animal housing and all experimental procedures were in accordance with the Swiss animal welfare protection law and conformed to the European Directive 2010/63/EU of the European Parliament and the Council on the Protection of Animals used for Scientific Purposes, and to the Guide for the Care and Use of Laboratory Animals. The pigs used in this study were all screened under the national surveillance program for Classical and African Swine fever, Foot and Mouth disease, Aujeszky's disease, Porcine reproductive and respiratory syndrome (PRRS), and Swine vesicular disease. Piglets are vaccinated against *H. parasuis* and *Porcine Circovirus* at the age of 3 weeks and 6 weeks. Sows are vaccinated at the age of 5–7 months and repeatedly prior to giving birth against Parvovirus and *E. rhusiopathiae*. Additionally, sows are vaccinated against *Escherichia coli* at 5

and 3 weeks prior to giving birth. Upon arrival, all pigs should be clinically assessed by observation (general behavior, posture and gait, visible injuries, color of the skin, breathing pattern, appetite, defecation, and urination) and if further indicated by physical examination.

Cardiopulmonary auscultation in the awake pig is not feasible as restraining the animal is stressful and will cause loud vocalization. The pigs used in this study were premedicated with an intramuscular injection of ketamine (Ketasol®-100 ad us.vet.; Dr. E. Graeub AG, Berne, Switzerland; 15 mg/kg body weight), azaperone (Stresnil® ad us.vet.; Elanco Tiergesundheit AG, Basel, Switzerland; 2 mg/kg body weight), and atropine (Atropinsulfat KA vet 0.1%; Kantonsapotheke, Switzerland; 0.05 mg/kg body weight). Anesthesia was induced by an intravenous administration of propofol (Propofol ® Lipuro 1%, B. Braun Medical AG; Sempach, Switzerland; 1–2 mg/kg body weight) to achieve relaxation and swallow-reflex diminishment sufficient for intubation. Anesthesia was then maintained with Isoflurane (Attane™ Isoflurane ad.us.vet., Piramal Enterpr. India; Lyssach, Switzerland, 1.5–3 vol%) in combination with 50% oxygen under spontaneous respiration, and in combination with a constant rate infusion of propofol (Propofol ® Lipuro 1%, B. Braun Medical AG; Sempach, 5–10 mg/kg/h). For the pain medication, buprenorphine (Temgesic®; Indivior Schweiz AG, Baar, Switzerland; 0.01 mg/kg) was administered. All pigs received amiodarone (Cordarone, Sanofi-Aventis (Suisse) SA, Vernier, Switzerland, 150 mg/100 ml 5% Glucose) as an antiarrhythmic agent, already prior to instrumentalization. Ringer's solution (Ringerfundin®, B. Braun Medical AG, Sempach, Switzerland, 5 ml/kg BW/h) was infused throughout the experiment. A blood gas analysis was performed regularly and urinary output was monitored to be between 0.5 and 1 ml/kg BW/h and fluid substitution adjusted accordingly.

Animal instrumentalization

Ultrasound-guided percutaneous placement of a femoral arterial introducer sheath (Avanti®+ Introducer, 6F, Cordis®, Miami Lakes FL, USA), a femoral venous introducer sheath (Avanti®+ Introducer, 10F, Cordis®, Miami Lakes FL, USA), and a left-sided carotid artery introducer sheath (Avanti®+ Introducer,6F, Cordis®, Miami Lakes FL, USA) was performed using the Seldinger method.

PV loop preparation, placement, and data optimization

Bench preparation of the catheter

Prior to the experiment, the PV loop catheter and the rho calibration cuvette were placed into warm water (37°C) for 30 min. Placing the PV loop catheter in a long vascular access sheath thereby prevents misshaping of the catheter prior to use. During this period a 15% hypertonic saline solution for parallel conductance correction can be prepared, based on the recommendation of AD Instruments. By using a 15% hypertonic solution, a good calibration is achieved without adverse effects on the animal.

After the required immersion, a small amount of arterial blood (<1 ml) was drawn to measure resistivity, conductivity, and blood temperature with the rho cuvette. The final measurement should be taken when the temperature matches the expected core temperature of the animal. Major changes in blood composition or body temperature may warrant repeated intraprocedural rho cuvette measurements. The pressure sensor of the PV loop catheter is zeroed at body temperature by submerging the tip just below the surface of a physiological saline solution.

Catheter placement and *in-situ* calibration

Stonko et al. (27) previously described the optimal access point for the PV Loop catheter advancement in pigs to be through the right brachial artery, or either of the carotid arteries, with each of these access routes, the catheter can be naturally steered into the ascending aortic arch. However, as the carotid artery was used in our setting to introduce the steerable sheath for aortic leaflet piercing, we used the left femoral artery to insert the PV loop catheter. The lack of a guide wire lumen has shown to make PV loop catheter placement more challenging, as it needs to be navigated over the aortic arch to cross the aortic valve. To facilitate PV loop catheter steering over the arch and through the aortic valve a pigtail catheter can be placed in the aortic sinus to improve orientation during fluoroscopy. After positioning the PV loop catheter in the left ventricle, it needs to be ensured that there is no saturation of the segmental volume readings, which would present itself as maximal, horizontal lines and would require an increase of the volume gain in the MPVS software. In order to generate meaningful cumulative PV loops, the relevant intraventricular volume segments need to be determined. The pigtail catheter in the aortic sinus thereby helps visualize the level of the aortic valve, hence the number of PV loop catheter segments below the aortic valve can be easily determined in fluoroscopy (Figures 1A,B). Within LabChart, non-relevant segments can be recognized as crossing loops with the shape of the number 8 (Figure 1C).

By launching the large animal PV Loop workflow within LabChart, a 2-point calibration for pressure and volume can be performed by setting fixed voltages within the Millar MPVS Ultra software. The minimal and maximal volumes can be calculated by multiplying the number of segments with the minimal and maximal segment volume seen within MPVS Ultra. If the resulting cumulative PV loop of all segments shows skewed shapes like non-vertical isovolumetric contractions or relaxations, the positioning of the PV loop catheter is not ideal and should be adjusted (Figure 1D), ensuring that the catheter

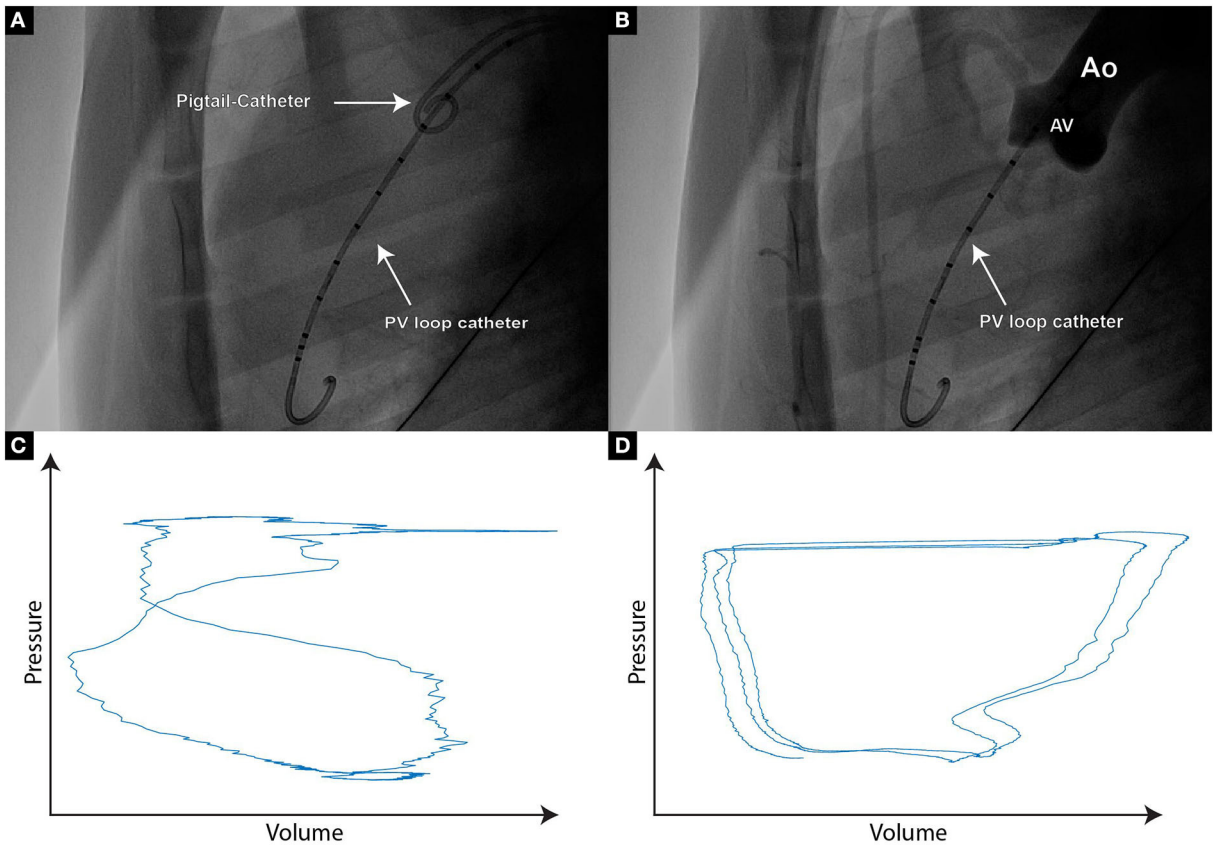

FIGURE 1
(A) Fluoroscopic image of a PigTail catheter which is positioned in the aortic valve cusp, hence enabling the assessment of PV loop catheter segments that are reliably positioned within the left ventricle; **(B)** If uncertainty regarding the PV loop segments within the left ventricle persists, contrast agent can be delivered through the PigTail catheter, hence providing an aortographic image clearly demonstrating the separation between the aorta and the left ventricle; **(C)** Typical "figure of 8" PV signal originating from the segment placed at the level of the aortic valve or above. Such segments should not be taken into further analysis; **(D)** Paradox composite PV loop curves demonstrating volume increase during systole and volume decrease during diastole. If such curves occur, re-positioning of the PV loop catheter needs to be considered.

is in a steady position within the ventricle, without interfering with the chordae or the papillary muscles. Strong movements of the PV loop catheter might also indicate entanglement and thus require repositioning as well. A minor oscillation between the two end-diastolic volumes can be observed due to respiration and is generally accepted. Due to the constant cardiac contractions, the position of the PV loop catheter can change over time. Such position changes can cause changes in the measured parameters (particularly in LV volume) and make comparisons over time quite challenging. Hence, the catheter should be secured in place. We suggest that the fixation of the PV loop catheter is ensured with a generic soldering clamp clip that is placed in close proximity to the arterial access point.

The removal of parallel conductance volume originating from the myocardium can be achieved by rapid intravenous injection of the hypertonic saline solution according to the large animal PV workflow. To eliminate artifacts induced by respiration, mechanical ventilation is stopped for the duration of approximately five loops prior to injection and held for an additional five loops after returning to baseline intraventricular volume. High R^2 values should be obtained with little variance in function of chosen loops, in order to obtain a robust parallel volume.

As a last calibration step, the measurements of the PV loop catheter are corrected for electrical field inhomogeneity by applying the alpha-correction, where the measured stroke volume of the PV loop catheter is compared with another type of measurement, such as echocardiography or MRI. In our case, we relied on TEE measurements for a simultaneous comparison. The integrity of the valves and cardiac movements are also verified by a TEE analysis.

Baseline measurements

In order to measure congruent loops without respiratory artifacts, 20 PV loops are recorded without respiration, typically in the end-inspiratory position, allowing the plotting of the central 10 loops. For the derivation of hemodynamic parameters, such as stroke work, stroke volume, or cardiac output, we recommend acquiring loops over 1 min under mechanical ventilation, thus allowing averaging over a large number of loops.

Interventions

Step 1: Placement of ICE and TEE probe

An intracardiac echocardiography (ICE) probe (ViewFlex™ Xtra ICE Catheter, St.Jude Medical, Minnesota, USA) was placed through the femoral venous access sheath, images were acquired on a Philips CX50 ultrasound machine (Philips, Amsterdam, the Netherlands). Furthermore, a transesophageal echo probe (X7-2T TEE Transducer, Philips, Amsterdam, the Netherlands) was inserted, and images were acquired on the Philips i33 ultrasound machine (Philips, Amsterdam, the Netherlands).

Step 2: Placement of steerable sheath

A bidirectional steerable guiding sheath (Agilis™ EPI Steerable Sheath, 8.5F, St. Jude Medical, Minnetonka, MN, USA, Or DESTINO™ Reach 8.5F ID, usable length 77 cm, curve 17 mm, Oscor®, Florida, USA) was introduced over an extra-stiff guide wire (Lunderquist®, 0.035″/260 cm, Cook Medical, Bjaeverskov, Denmark) through the left carotid artery.

The aortic arch of pigs differs in anatomy when compared to humans. There are two branch arteries arising from the aortic arch, first, the brachiocephalic trunk, which involves both common carotid arteries as well as the right subclavian artery, and second, the left subclavian artery (28). Although either common carotid artery arises from the brachiocephalic trunk, introducing the steerable sheath through the left carotid artery appears to be favorable in targeting the NCC or RCC of the aortic valve.

Positioning of the sheath was verified with TEE and ICE, as well as fluoroscopically (Figures 2A–C).

Step 3: Piercing of the aortic valve leaflet

After targeting the NCC or RCC, respectively, under the guidance of transesophageal and intracardiac echocardiography as well as fluoroscopy, the leaflet hinge was pierced with a stiff-end of a coronary guide wire (IRON MAN Guide Wire, 0.014″ 190 cm, Abbott Vascular, Santa Clara CA, USA) (Figures 2C,D). To improve the visibility of the guide wire in the echo image, the wire can be roughened with sandpaper. An apparent septal bulge or a septal muscular shelf can be found in pigs just beneath the RCC and is easily pierced accidentally (Figures 3A,B). Piercing the septal bulge will direct the guide wire toward the right ventricle and if unnoticed the created defect will cause an aorto-right-ventricular fistula (Figures 3C,D). After verifying the guide wire position in the left ventricle, the leaflet puncture site was then dilated with a 5-mm PTCA balloon (NC Emerge MONORAIL™ PTCA Dilation Balloon 5 × 12 mm, Boston Scientific Corporation, Marlborough, MA, USA). The balloon should be flossed multiple times in its inflated state through the leaflet to ensure sufficient defect size.

Verification of PVL

Doppler echography was used for the initial assessment of PVL presence and severity (Figure 4A). The width of the jet is thereby measured in relation to the left ventricular outflow tract (LVOT) diameter. A jet width of minimally 25% to maximally 65% of the LVOT is aimed for, as this is considered mild-to-moderate aortic regurgitation by the ASE guidelines on Aortic Regurgitation (29). An aortography can additionally be performed for periprocedural densitometric quantification of PVL (Figure 4B). The final quantification of PVL was done by post-processing particle tracking analysis on 4D Flow MRI datasets.

Challenging LV performance

Aortic valve regurgitation causes an increase in end-diastolic pressure and volume in the left ventricle and an increase in the afterload (30). Dobutamine is a pharmacologic substance alternatively used instead of vasodilators, to induce cardiac stress (31). Dobutamine has a positive inotropic effect leading to an increase in cardiac output by selectively augmenting stroke volume and by a reflex decrease in total peripheral vascular resistance (32). Dobutamine is used clinically as a racemic mixture, whereby one of the stereoisomers has a strong agonistic adrenergic effect on α1 and a weaker effect on β1 and β2 activity, the other stereoisomer predominantly stimulates β1 and β2 adrenoreceptors and exhibits α1 antagonist activity (33). Thus, causing a null α1-mediated effect on the vasculature, a β2-induced increase in heart rate, and a positive inotropic effect mediated by all three receptors (33).

In this study, a dobutamine stress test was performed at baseline, after induction of PVL, and during MRI flow measurements. Dobutamine (Dobutrex, Teva Pharma AG, Basel, Switzerland; 0.5 mg/ml) was administered over a continuous pump infusion intravenously to effect. A 30% increase in heart rate was targeted and maintained over 10 min (PV loop) or for the duration of the MRI flow acquisition.

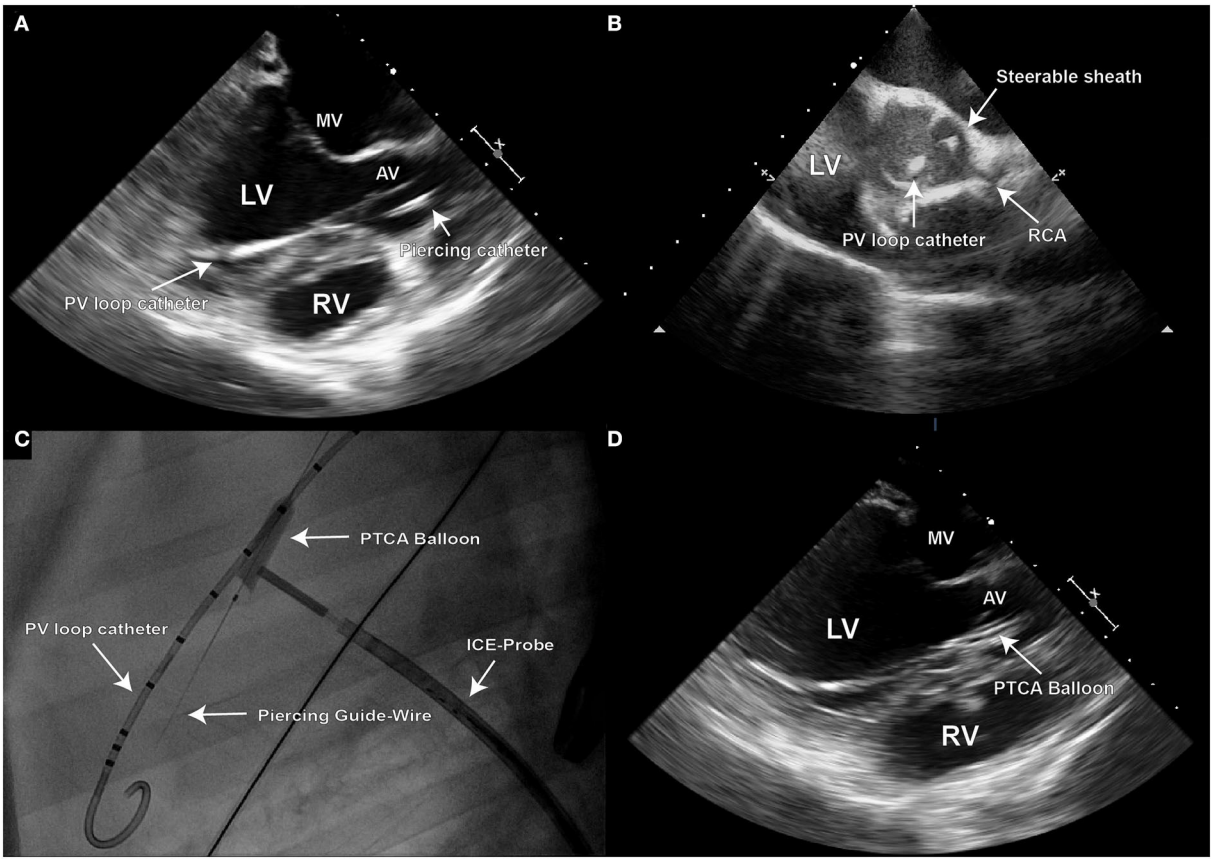

FIGURE 2
Due to the 2D character of echocardiographic imaging, two distinct perpendicular projections (long and short axis) are necessary for precise procedural navigation; **(A)** Transesophageal (TEE) long axis echo image demonstrating the final position of the steerable sheath on target for creation of the defect at the leaflet hinge point in the right coronary cusp (RCC) of the aortic valve; **(B)** Once such position is reached, intra-cardiac echo should be used to confirm the position in the short axis image; **(C)** Fluoroscopy is used to visualize the piercing guide wire during its positioning, and for control of the PTCA balloon inflation; **(D)** Inflated PTCA balloon used for defect dilation can be also visualized in TEE long axis view.

Phenylephrine is a direct-acting sympathomimetic amine that functions as an α1-adrenergic agonist. The described α1-adrenergic effects are thought to cause venoconstriction leading to a temporarily increased preload and to a larger extent arterial constriction which will increase systemic vascular resistance and afterload (34). In pigs, the administration of phenylephrine is associated with an increase in systemic arterial blood pressure, stroke volume, and cardiac output with no changes in heart rate. A preload-enhancing effect was observed in low-dose phenylephrine administration while higher doses appeared to increase contractility in a load-independent manner (35). In the presented study, a phenylephrine challenge was also performed at baseline, after induction of PVL, and during MRI flow measurements. Phenylephrine (Neo-Synephrine HCl, Ospedialia AG, Hüneberg, Switzerland, 0.1 mg/ml) was also administered over a continuous pump infusion intravenously to effect. This time a 30% increase in mean arterial pressure was targeted and maintained for over 10 min (PV loop) or the duration of the MRI flow acquisition, respectively.

Magnetic resonance imaging

Due to animal size and weight, MR imaging was performed on a clinical 3T system. The animals were placed in the right lateral position. During the measurements, the animals should be mechanically ventilated and blood pressure as well as endtidal CO_2 ($etCO_2$) should be monitored. Ventilator and monitoring equipment is commonly placed outside the Faraday's cage, therefore, $etCO_2$ monitoring is performed *via* a 14-m Heidelberger line and for mechanical ventilation, approximately 2 m × 12 m hoses are needed.

All imaging is commonly performed during ventilated breathing and cardiac synchronization by a pulse oximetry unit clipped to the animal's tail.

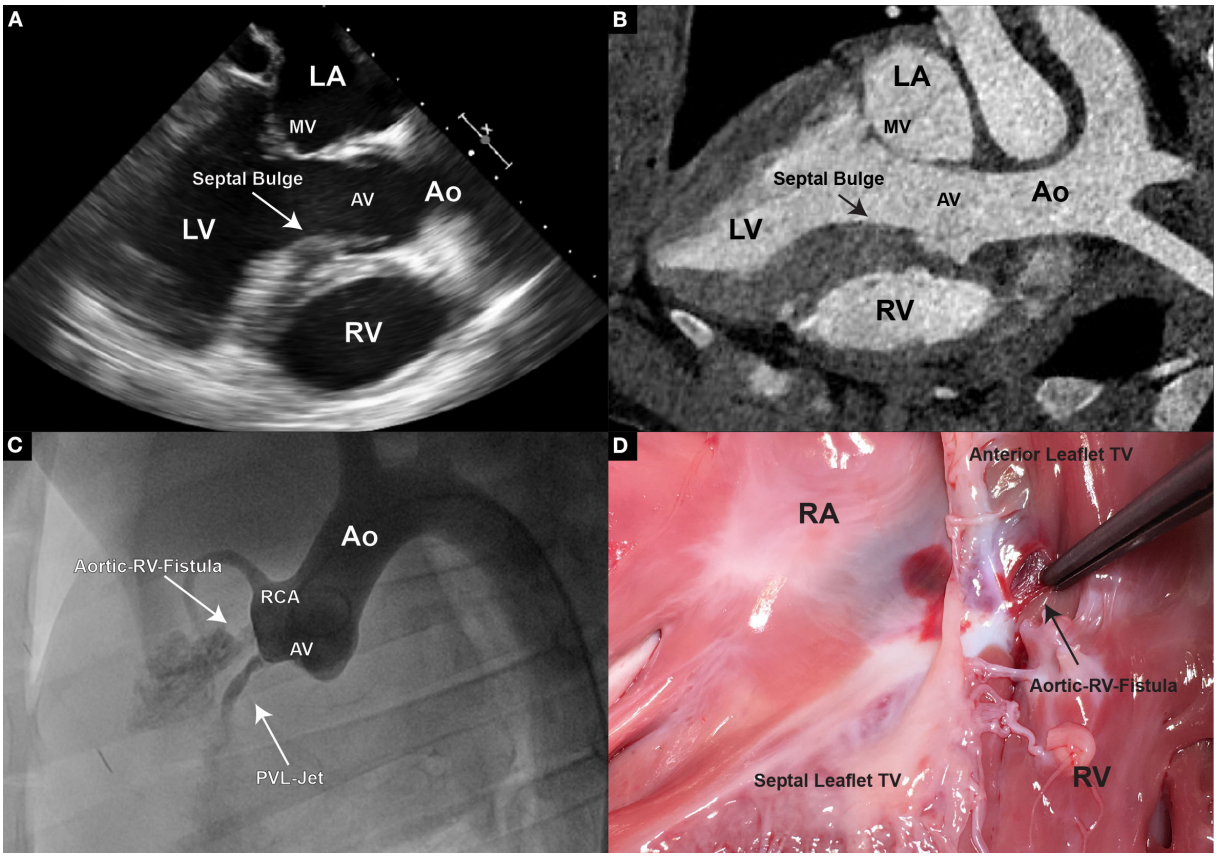

FIGURE 3
(A) In TEE, pigs display a unique feature of thickened septal wall. Especially the portion directly beneath the aortic valve, corresponding to the location of the RCC. Thickening of this region becomes prominent, especially during end-systole and early diastole; **(B)** In CT however, usually only general thickening of the septal wall can be observed, and often no prominent "bulge" is detectable; **(C)** An aortogram is performed following an erroneous piercing in the RCC region. A direct flow of contrast to the right ventricle could be observed demonstrating an aorto-right ventricular communication; **(D)** Upon pathological examination a fistula connecting the aortic root and the right ventricle was found.

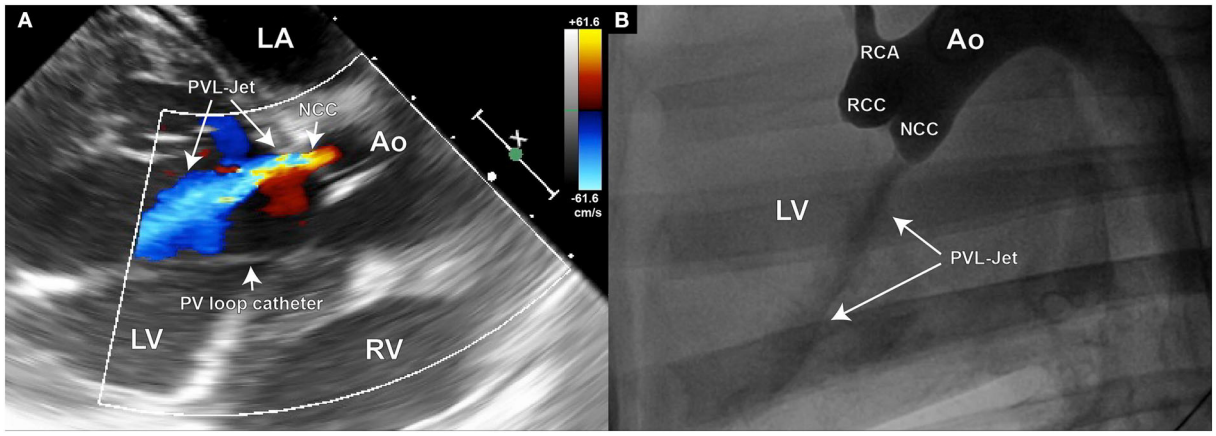

FIGURE 4
Echocardiography and aortography can be used for verification of the aortic valve defect; **(A)** Color Doppler image of the aortic insufficiency jet created in the NCC region of the aortic valve; **(B)** Aortographic image of the same animal in latero-lateral position also demonstrating the existence of the regurgitant jet. Such images can later be used for densitometric quantification of the regurgitant volume.

Functional imaging consisted of clinically used balanced steady-state free precession imaging in two-, three-, and four-chamber views as well as in short axis view covering the entire left ventricle. Imaging parameters were as follows: Field of view: 300 × 300 × 96 mm, spatial resolution 2 × 2 mm^2, slice thickness 8 mm, TR/TE 2.7 ms/1.35 ms, retrospective triggering, temporal resolution 31 ms, and under sampling factor 2.

The 4D flow imaging is performed using a sparsely sampled pseudo-spiral Cartesian 3D sampling pattern using golden angle increments (36, 37). The frequency encoding direction is aligned to the left-right direction in order to capture chest wall motion and the imaging volume is planned parallel to the four-chamber view. Imaging parameters were as follows: FOV 300 × 410 × 90 mm, spatial resolution 2.5 × 2.5 × 2.5 mm, excitations per shot 5, acquired temporal resolution 21 ms, TR/TE 3.9/2.2 ms−4.2/2.5 ms. To estimate the maximal velocity expected and adjust the velocity encoding strength (venc) a quick 2D through-plane velocity encoded scan was performed at three slice positions: distal, within, and proximal of the aortic valve. The applied venc's for 4D flow imaging in our setting were: 140–180 cm/s (baseline), 150–180 cm/s (Phenylephrine), and 180–280 cm/s (Dobutamine).

Local low-rank image reconstruction can be performed offline within the MRecon framework (GyroTools LLC, Zurich, Switzerland) incorporating the Berkeley Advanced Reconstruction Toolbox (BART) (36, 37). Two breathing motion states should be reconstructed to minimize breathing artifacts with an under-sampling factor of approximately six each.

Euthanasia and gross pathology

At the end of the study, pigs were fully heparinized (300 IU/kg) and euthanized under general anesthesia by administering an overdose of sodium pentobarbital (Eskonarkon®ad.us.vet., Streuli Pharma AG, Uznach, Switzerland;75 mg/kg body weight) intravenously. The heart was fully excised through a sternotomy and the aortic arch opened longitudinally. Leaflet defect size, location, and further injury to the LVOT or endocardial tissue are optically assessed and documented (Figures 5A,B).

(Anticipated) results

Creation of precisely placed aortic PVL defects with defined size is possible

To model the PVL of the aortic valve, the defect needs to be placed at the hinge point between the leaflet and the valvular annulus. Care must be taken for the defects not to be placed within the leaflet tissue, as this would not mimic the clinical situation. In our study, the defect-target areas were set at the hinge points of either the right coronary cusp (RCC) or the non-coronary cusp (NCC) of the aortic valve, respectively, as they represent the major predilection sites for PVLs in the clinic. In the reported six animals, three NCC and three RCC defects were targeted and successfully created using the described method. It is worth noting that intraprocedural imaging and procedural guidance were more challenging for the RCC defects, leading to longer procedural duration in this group. Immediately following the defect creation, resulting aortic regurgitant jets could be observed in TEE in all six animals (Figures 6A–F). However, due to the anatomical position of jet origin and their trajectory in the LV, NCC regurgitant jets could be fully visualized whereas it was only partially possible for the RCC jets (Figures 6A–C). Moreover, the postmortem analysis showed that 3/3 NCC and 2/3 RCC defects were precisely placed within the narrow hinge region in the middle of the valve leaflet. Due to an erroneous puncture in 1/3 RCC that created an aorto-right ventricular fistula (Figures 3C,D) the RCC target location was slightly moved laterally and the defect was placed 5 mm lateral from the middle point. Yet, all animals remained hemodynamically stable after defect creation, and during the subsequent measurements.

Stable positioning of the PV loop catheter enables measurements of the acute effects of PVL jets on ventricular work and direct comparison to baseline state

The fact that severe PVL and/or aortic insufficiency has a negative effect on patient survival and quality of life has been widely reported. However, the impact of mild-to-moderate jets is less clear and patients display a wide range of symptoms. It is important to understand what impact these jets might have on left ventricular work parameters. However, this is only possible if the PV loop catheter is able to record closely comparable signals before and after the defect creation and if the hemodynamic parameters (such as arterial blood pressure, heart rate, and cardiac contractility) remain within very narrow margins. PV loop catheter removal during the defect creation procedure would make this comparison almost impossible (Figure 7A). To avoid catheter removal, our initial approach was the transseptal placement of the PV loop catheter in the LV. However, signals obtained by such an approach were of insufficient quality and the catheter could not be held in a stable position, leading to strongly variable output. Consequently, we developed a method of placing the PV loop catheter in the aortic valve commissure between LCC and RCC. In this position, the catheter remained stable even during the transcatheter PVL creation. Hence, a direct comparison between the healthy (baseline) and PVL state could be made (Figure 7B). More importantly, PV loop catheter position and the signal remained stable during the

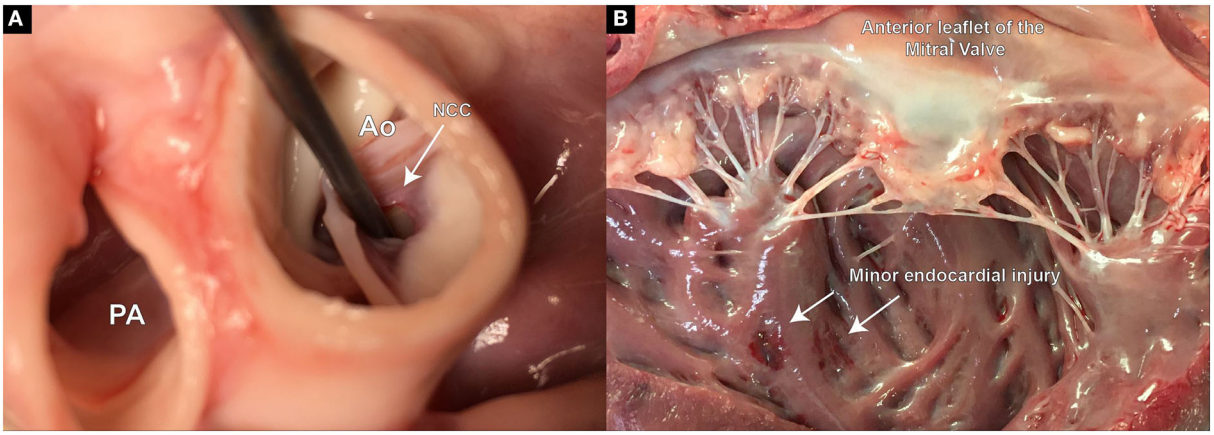

FIGURE 5
Postmortem examination of defect size, location, and potential extra-valvular injuries created during the procedure. **(A)** Demonstrates the defect precisely placed at the hinge point of the aortic leaflet in the RCC region; **(B)** Slight injury on the endocardial surface of the left ventricle, most likely caused during the insertion of the piercing guide wire.

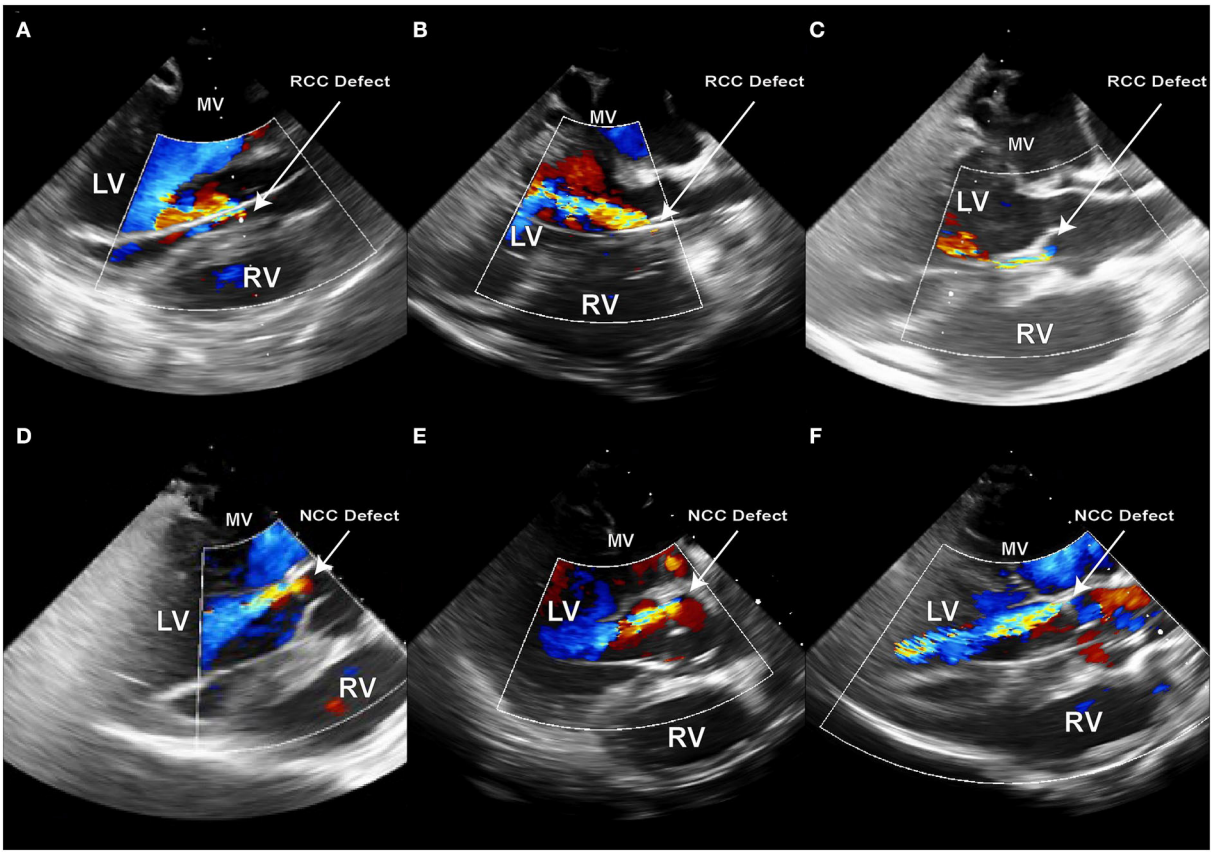

FIGURE 6
Echocardiography immediately after the creation of the PVL defect in sx consecutive animals. **(A–C)** Defects created in the RCC annular region; **(D–F)** Defects created in NCC annular region; PVL jet originating from the NCC region have a trajectory along the anterior leaflet of the mitral valve and can be fully visualized along their path in the LV. RCC jets on the other hand either flow along the septum or at a steep angle across the LV.

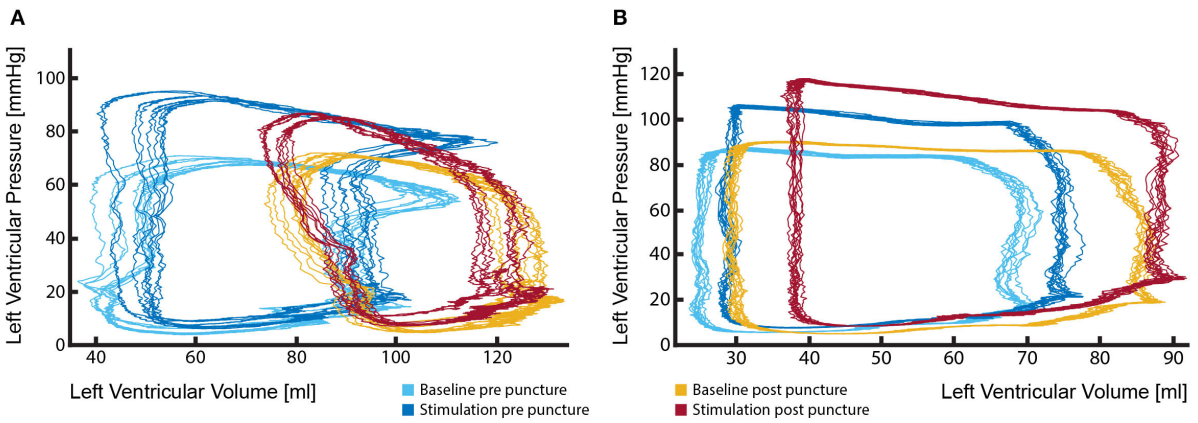

FIGURE 7
Stable position of the PV loop catheter during the entire procedure is fundamental for the evaluation of the effects of aortic regurgitant jets on left ventricular performance. **(A)** Marked change in PV loop curves following the removal and reinsertion of the catheter after the defect creation. Such changes render the comparison of the LV performance between the healthy state (light and dark blue loops) and aortic insufficiency state (red and yellow loops) particularly challenging and potentially misleading; **(B)** By keeping the catheter in a stable position during the entire procedure reliable measurements could be performed, delineating effects that aortic regurgitation causes to LV performance (light blue vs. yellow loops). Furthermore, investigations under pharmacologically changed hemodynamic conditions are possible (dark blue vs. red loops).

whole study, even throughout the drug-induced hemodynamic changes (Figure 7B).

Drug-induced changes in afterload and heart rate enable the study of the aortic PVL under clinically relevant conditions

Increased afterload markedly contributes to the severity of PVL as it aggravates aortic valve regurgitation. In an experimental setting, phenylephrine, as an α1-adrenergic agonist, can be used to induce peripheral arterial constriction, which will increase systemic vascular resistance and afterload. The direct effect of increased vascular resistance on regurgitation volume can be assessed and correlated.

An increased heart rate in patients with aortic valve regurgitation has previously been found to decrease regurgitant flow per stroke and per unit time (38) and a reduction in left ventricular end-diastolic pressure (LVEDP) (39). In a previous study, dobutamine in healthy pigs has shown to increase heart rate and ejection fraction, with a decrease in left ventricular end-diastolic volume and end-systolic volume, and no change in stroke volume (40). Dobutamine has furthermore shown to change the intra-cardiac blood flow pattern in healthy pigs (40).

The effect of dobutamine seemingly counteracting aortic valve regurgitation-induced increase in LVEDP and afterload on cardiovascular physiology and intra-cardiac blood flow pattern. It thereby examines important aspects of the clinical situation in patients, in which aortic valve regurgitation may manifest in an increasing afterload mitigating arterial hypertension or an increased heart rate induced by new onset tachycardiac atrial fibrillation. The latter is present in around 5% of transcatheter valve implantation and in a remarkable 40% of surgical aortic valve replacements (1). Both clinical conditions are proven cardiovascular risk factors by themselves and may potentially have a negative synergistic effect on the increased mortality and morbidity induced by PVL.

Echocardiography and densitometry provide a reliable solution for experimental assessment of PVL severity in a porcine model

Although echocardiography is challenging in the porcine model, with moderate technique adaptations most of the interventional-relevant cardiac structures can be readily visualized (23). However, providing echocardiographic windows appropriate for Doppler flow assessments is much more challenging. Moreover, PVL jets have a distinct trajectory within the 3D space of the LV. Due to a limited echo–window in TEE, it is often impossible to follow the jet in its full length. In our study, this was particularly challenging in the RCC group, where already within the LVOT the jet would exit the echo plane (Figures 6A–C). However, for severity assessment of aortic PVL the width of the jet within the LVOT is often used as a reliable parameter in the clinic (41, 42). Such measurements are reproducibly achievable by TEE in pigs and could demonstrate

that 6/6 defects created have caused mild-to-moderate aortic regurgitation. On the other hand, densitometry is much less sensitive, albeit not completely insensitive, to projection angles and imaging windows. In contrast to humans, the best projection for densitometric imaging of aortic insufficiency is a latero-lateral projection. Care has to be taken that no overlap of cardiac and aortic structures is imaged and the scapulae are not in the frame. Furthermore, the high volume (20 ml in 1.5 s) contrast agent injection in the aortic root required for the densitometric analysis could lead to a short increase in the local aortic pressure. As the difference in aortic and LV diastolic pressures is the driving force behind the aortic regurgitation, such pressure increase on the aortic side exactly at the time point of evaluation could potentially lead to PVL overestimation. Although a clear correlation between the echocardiographic and densitometric regurgitant volume assessment has been shown in patients (43), there are currently no data from animal trials.

The 4D flow MRI delivers answers to correlate disturbed ventricular blood flow patterns and potential adverse remodeling

Diastolic intraventricular blood flow acquired with 4D MRI has shown to be altered in pigs with mild-to-moderate PVL in a defect site (NCC vs. RCC) dependent manner (3) as well as under dobutamine stress alone when compared to healthy pigs (40). Deviations from physiologic diastolic blood flow are described to result in an increased energy dissipation within the LV (44). The effect of pharmacologically increased afterload or heart rate on intra-cardiac flow patterns in 4D MRI can give further insights into kinetic energy changes within the left ventricular blood pool in mild-to-moderate PVL.

Discussion

Paravalvular regurgitation or leak (PVL) is a complication associated with transcatheter valve replacements and causes turbulent blood flow below the respective valve with varied clinical consequences (42). Porcine models for the study of the effects of altered blood flow and hemodynamics on cardiac health after induction of PVL are of great interest. However, hemodynamic studies are easily biased by insufficient considerations of confounding factors. Aside from selecting pigs of appropriate size and weight, the health status can have a significant impact on cardiovascular and hemodynamic properties and should be assessed prior to animal purchase. On commercial farms, pigs are often subjected to handling practices causing acute stress (45). The major pathways activated by stressors are the hypothalamic–pituitary–adrenal (HPA) axis and the sympathetic nervous system (46). Stress-free handling of pigs used for hemodynamic studies is therefore essential. An appropriate acclimatization time for the animals at a new facility should be granted as during transportation and after stabling, pigs are confronted with a variety of stressors leading to stress-induced changes in the cardiovascular, endocrine, immune, and reproductive systems (47–49). Transporting and housing pigs in familiar groups can attenuate social stress (50). To prevent heat or cold stress in pigs, it is critical to base housing temperature on the energy content of the diet, the pig's growth status, and group housing (51). Utilizing stressed animals before their physiological status normalizes can have considerable and unintended effects on cardiovascular research results (49). While primary mediators of stress (e.g., catecholamines and glucocorticoids) will return to physiological values within 24 h, changes in the immune and endocrine systems may take up to 7 days to normalize (49). The diet changes should be induced gradually during the time of acclimatization. Animals displaying diarrhea should be excluded from any study as diarrhea contributes to an increased loss of electrolytes and water over the bowel lumen (52) causing a disruption in homeostasis and acid-base balance. These changes have been shown to affect cardiac contractility and rhythm with a potentially fatal outcome (53, 54). Studies in rats showed osmotic diarrhea, often accompanied by a reduction in food intake, to cause a reduction in heart weight and protein content by reduced protein synthesis (55). Various anesthetic protocols are used in laboratory pigs, each having its advantages and disadvantages. The requirements for the anesthetic protocol are particularly high when conducting hemodynamic studies. Adequate intramuscular sedation is commonly required in pigs, for safe handling and to place an intravenous catheter in the auricular vein for induction of general anesthesia. Dissociative anesthetic drugs like ketamine and tiletamine are thereby often combined with sedative agents like azaperone, midazolam, zolazepam or α-2 agonists, such as detomidine, medetomidine or dexmedetomidine (56–59). As α-2 agonists are described to induce adverse cardiovascular effects such as bradycardia, increased systemic vascular resistance, reduced cardiac output and oxygen delivery (60, 61), they are less suitable for cardiovascular research. Anesthesia can be maintained with inhalation agents or intravenous drugs (TIVA), or a combination of both. Isoflurane and other volatile anesthetics have dose-dependent effects on the hemodynamic and respiratory function which can be attenuated when combined with partially intravenous anesthesia and analgesia (PIVA) (62, 63). Anecdotally, the ventricular fibrillation (VF) threshold in pigs is markedly lower than in humans. One plausible reason is the Purkinje system, which is located transmurally in pigs and subendocardial in humans (64). With pigs being more prone to VF and other cardiac arrhythmias during cardiac interventions, antiarrhythmic agents are an integral part of a successful anesthetic protocol. Amiodarone is a potent antiarrhythmic drug successfully used in the treatment

of ventricular and supraventricular arrhythmias in pigs (65, 66). However, a study in dogs showed a dose-related decrease in both coronary and systemic vascular resistance, as well as a decrease in cardiac contractility after the administration of amiodarone (67). Hemodynamic side effects resulting in a decreased aortic (systolic, diastolic, and mean) and left ventricular (systolic and end-diastolic) pressure are also described in humans (68). The hemodynamic effect of amiodarone as a potent antiarrhythmic drug in pigs should therefore be taken into consideration. Porcine models of aortic PVL are commonly created by the implantation of a prosthetic valve (TAVI) (4). Prosthetic aortic valves can thereby be implanted either in an antegrade matter trans-apically through a subxiphoid access or mini-thoracotomy in the 6th intercostal space (69) or retrograde through a percutaneous access sheath in the femoral artery (70). Percutaneous approaches are often hampered by the need for large access sheaths increasing the risk for arterial dissection and perforation (71). Transapical approaches on the other hand require the placement of a large access sheath through the left ventricular apex. The puncture site is closed by a purse-string suture after successful valve implantation, often causing apical regional wall motion abnormalities with an overall decrease in left ventricular function due to myocardial injury (72). Porcine TAVI-induced PVL models are therefore impractical for hemodynamic studies. Furthermore, although there is no risk for prosthetic valve movement or dislodgement using an MR system operating at 1.5 T or less, the presence of an artifact may affect the diagnostic imaging quality and 4D flow assessment through the prosthetic valve (73). The described minimally invasive and reproducible porcine model is therefore ideal for a detailed investigation of hemodynamic effects and the short-term impact caused by mild-to-moderate PVL in patients. Despite a high success rate (6/6) in creating mild-to-moderate aortic regurgitation, specifically targeting leaflet hinge points, especially in the RCC region remains somewhat challenging and not completely devoid of complications. Where the mid-points of the NCC leaflet hinge are clearly visible and easily reachable with the described method and equipment, setting of RCC defects requires adaptations in intra-procedural imaging as well as interventional technique. Moreover, the unique porcine feature of the muscular septal shelf (septal bulge) positioned just beneath the RCC aortic leaflet could be the cause of complications if erroneously pierced (21). In our study, this occurred in one-third RCC targeted defects. Furthermore, effects of such a structure on the trajectory and path of the PVL jet originating from RCC can currently not be excluded and have to be considered as a limitation to the translatability of the results. Yet, due to the minimally invasive nature of the PVL defect creation technique (the procedure requires one femoral vein and two arterial accesses) the model described here potentially offers a viable platform for long-term investigation of cardiac remodeling and other adverse effects caused by aortic PVL. In accordance to the 3R principles, such model would represent a substantial refinement in comparison to the surgical or even transcatheter implantation of a defective valve (4). Moreover, post-operative manipulations necessary for the administration of anticoagulation therapy following valve implantations are not required in our model as there is no thrombogenic foreign material. As the PVL orifices represent areas of high-velocity flow, it is not expected that they would spontaneously heal in our model. However, such aspects as well as the induction and progression of adverse cardiac remodeling need to be carefully evaluated in studies specifically designed for that purpose. Pressure–volume loops (PV loops) are the gold standard for real-time load-dependent and load-independent measures of the left ventricular systolic and diastolic function. A practical guide on PV loop measurements in pigs has recently been published (27). However, PV loop measurements are easily disturbed through further interventions, such as aortic valve leaflet piercing. To avoid interference at the aortic valve and to avoid moving the PV loop catheter between measurements, transseptal placement of the PVL catheter was considered. Transseptal puncture was performed under ICE guidance and verified by left atriography. However, with the left atrial height being much lower in pigs than in humans (74) and the porcine fossa ovalis being both deeper and more superiorly positioned, trans-septal placement of the PV loop catheter leads to a lateral displacement of the posterior leaflet of the mitral valve, causing the catheter to extensively move with the opening and closing of the mitral valve.

Further consideration when conducting hemodynamic studies in pigs has to be given to an optimized intra-operative fluid management, which is essential to maintain intravascular volume and hence cardiac preload and cardiac output. Longlasting anesthetic procedures tend to cause hypovolemia due to ongoing losses through mechanical ventilation and urinary output. Additionally, blood loss through the access sheath and catheters, which is further aggravated due to anticoagulation therapy, has to be accounted for. Intravascular volume status should be assessed and compensated throughout the study by combining laboratory parameters, fluid administration, and urine output measurements with monitoring of central venous pressure and cardiac output (75).

Despite taking into consideration all the described dos and don'ts in establishing a porcine model for PVL, substantial inter-individual variability in hemodynamic compensation to PVL in pigs is to be expected. It is all the more important to have a standardized and reproducible model of PVL to exclude procedural bias.

Data availability statement

The original contributions presented in the study are included in the article/supplementary

material, further inquiries can be directed to the corresponding author.

Ethics statement

The animal study was reviewed and approved by Cantonal Veterinary Office Zurich, Switzerland (ZH213/2019).

Author contributions

NC: conceptualization, study design, development of the animal model, surgical procedure, animal handling, preparation, and review of the manuscript. MW, LG, and MKo: development of animal model, surgical procedure, and preparation of the manuscript. NT, MH, AL, and TS: animal handling and anesthesia. MKu: study design and echocardiographic imaging analysis. CS: 4D MRI protocol and imaging procedure and preparation of the manuscript. VF and ME: data interpretation and critical review of the manuscript. All authors contributed to the article and approved the submitted version.

Funding

This work was supported by a research grant from the Swiss Heart Foundation and was performed within the framework of the ETHeart initiative. Open access funding provided by ETH Zurich.

Acknowledgments

The authors would like to thank Prof. Margarete Arras, Mrs. Flora Nicholls, and the animal caretakers of the Central Biological Laboratory for their valuable support in animal housing.

Conflict of interest

The authors declare that the research was conducted in the absence of any commercial or financial relationships that could be construed as a potential conflict of interest.

Publisher's note

References

1. Mack MJ, Leon MB, Thourani VH, Makkar R, Kodali SK, Russo M, et al. Transcatheter aortic-valve replacement with a balloon-expandable valve in low-risk patients. *N Engl J Med.* (2019) 380:1695–705. doi: 10.1056/NEJMoa1814052

2. Sponga S, Perron J, Dagenais F, Mohammadi S, Baillot R, Doyle D, et al. Impact of residual regurgitation after aortic valve replacement. *Eur J Cardiothorac Surg.* (2012) 42:486–92. doi: 10.1093/ejcts/ezs083

3. Cesarovic N, Weisskopf M, Kron M, Glaus L, Peper ES, Buoso S, et al. Septaly oriented mild aortic regurgitant jets negatively influence left ventricular blood flow-insights from 4D flow MRI animal study. *Front Cardiovasc Med.* (2021) 8:711099. doi: 10.3389/fcvm.2021.711099

4. Rosa B, Machaidze Z, Mencattelli M, Manjila S, Shin B, Price K, et al. Cardioscopically guided beating heart surgery: paravalvular leak repair. *Ann Thorac Surg.* (2017) 104:1074–9. doi: 10.1016/j.athoracsur.2017.03.028

5. Bunck AC, Juttner A, Kroger JR, Burg MC, Kugel H, Niederstadt T, et al. 4D phase contrast flow imaging for in-stent flow visualization and assessment of stent patency in peripheral vascular stents–a phantom study. *Eur J Radiol.* (2012) 81:e929–37. doi: 10.1016/j.ejrad.2012.05.032

6. Kirk RGW. Recovering the principles of humane experimental technique: the 3Rs and the human essence of animal research. *Sci Technol Human Values.* (2018) 43:622–48. doi: 10.1177/0162243917726579

7. Yi GH, Cheng Y, Aboodi MS, Farnan R, Kar S, Burkhoff D, et al. Safety and feasibility of percutaneous delivery of a novel circulatory assist device (CircuLite(R) SYNERGY(R)) in the swine model. *EuroIntervention.* (2013) 9:259–68. doi: 10.4244/EIJV9I2A42

8. Monreal G, Sherwood LC, Sobieski MA, Giridharan GA, Slaughter MS, Koenig SC. Large animal models for left ventricular assist device research and development. *ASAIO J.* (2014) 60:2–8. doi: 10.1097/MAT.0000000000000005

9. Smerup M, Pedersen TF, Nyboe C, Funder JA, Christensen TD, Nielsen SL, et al. A long-term porcine model for evaluation of prosthetic heart valves. *Heart Surg Forum.* (2004) 7:E259–64. doi: 10.1532/HSF98.20041015

10. Opriessnig T, Janke BH, Halbur PG. Cardiovascular lesions in pigs naturally or experimentally infected with porcine circovirus type 2. *J Comp Pathol.* (2006) 134:105–10. doi: 10.1016/j.jcpa.2005.06.007

11. Brewer LA, Lwamba HC, Murtaugh MP, Palmenberg AC, Brown C, Njenga MK. Porcine encephalomyocarditis virus persists in pig myocardium and infects human myocardial cells. *J Virol.* (2001) 75:11621–9. doi: 10.1128/JVI.75.23.11621-11629.2001

12. Neil DH, McKay KA, L'Ecuyer C, Corner AH. Glasser's disease of swine produced by the intracheal inoculation of haemophilus suis. *Can J Comp Med.* (1969) 33:187–93.

13. Jensen HE, Gyllensten J, Hofman C, Leifsson PS, Agerholm JS, Boye M, et al. Histologic and bacteriologic findings in valvular endocarditis of slaughter-age pigs. *J Vet Diagn Invest.* (2010) 22:921–7. doi: 10.1177/104063871002200611

14. Pallares FJ, Yaeger MJ, Janke BH, Fernandez G, Halbur PG. Vitamin E and selenium concentrations in livers of pigs diagnosed with mulberry heart disease. *J Vet Diagn Invest.* (2002) 14:412–4. doi: 10.1177/104063870201400509

15. Shen H, Thomas PR, Ensley SM, Kim WI, Loynachan AT, Halbur PG, et al. Vitamin E and selenium levels are within normal range in pigs diagnosed with mulberry heart disease and evidence for viral involvement in the syndrome is lacking. *Transbound Emerg Dis.* (2011) 58:483–91. doi: 10.1111/j.1865-1682.2011.01224.x

16. Lelovas PP, Kostomitsopoulos NG, Xanthos TT. A comparative anatomic and physiologic overview of the porcine heart. *J Am Assoc Lab Anim Sci.* (2014) 53:432–8.

17. Crick SJ, Sheppard MN, Ho SY, Gebstein L, Anderson RH. Anatomy of the pig heart: comparisons with normal human cardiac structure. *J Anat*. (1998) 193 (Pt 1):105–19. doi: 10.1046/j.1469-7580.1998.19310105.x

18. Hughes HC. Swine in cardiovascular research. *Lab Anim Sci.* (1986) 36:348–50.

19. Barbanti M, Yang TH, Rodes Cabau J, Tamburino C, Wood DA, Jilaihawi H, et al. Anatomical and procedural features associated with aortic root rupture during balloon-expandable transcatheter aortic valve replacement. *Circulation.* (2013) 128:244–53. doi: 10.1161/CIRCULATIONAHA.113.002947

20. Ribeiro HB, Nombela-Franco L, Urena M, Mok M, Pasian S, Doyle D, et al. Coronary obstruction following transcatheter aortic valve implantation: a systematic review. *JACC Cardiovasc Interv.* (2013) 6:452–61. doi: 10.1016/j.jcin.2012.11.014

21. Benhassen LL, Ropcke DM, Lading T, Skov JK, Bechsgaard T, Skov SN, et al. Asymmetric dynamics of the native aortic annulus evaluated by force transducer and sonomicrometry in a porcine model. *Cardiovasc Eng Technol.* (2019) 10:482–9. doi: 10.1007/s13239-019-00418-1

22. Kerut EK, Valina CM, Luka T, Pinkernell K, Delafontaine P, Alt EU. Technique and imaging for transthoracic echocardiography of the laboratory pig. *Echocardiography.* (2004) 21:439–42. doi: 10.1111/j.0742-2822.2004.04003.x

23. Sundermann SH, Cesarovic N, Falk V, Bettex D. Two- and three-dimensional transoesophageal echocardiography in large swine used as model for transcatheter heart valve therapies: standard planes and values. *Interact Cardiovasc Thorac Surg.* (2016) 22:580–6. doi: 10.1093/icvts/ivv381

24. Billig S, Zayat R, Ebeling A, Steffen H, Nix C, Hatam N, et al. Transesophageal echocardiography in swine: evaluation of left and right ventricular structure, function and myocardial work. *Int J Cardiovasc Imaging.* (2021) 37:835–46. doi: 10.1007/s10554-020-02053-7

25. Naqvi TZ, Zarbatany D, Molloy MD, Logan J, Buchbinder M. Intracardiac echocardiography for percutaneous mitral valve repair in a swine model. *J Am Soc Echocardiogr.* (2006) 19:147–53. doi: 10.1016/j.echo.2005.09.008

26. Burkhoff D, Mirsky I, Suga H. Assessment of systolic and diastolic ventricular properties via pressure-volume analysis: a guide for clinical, translational, and basic researchers. *Am J Physiol Heart Circ Physiol.* (2005) 289:H501–12. doi: 10.1152/ajpheart.00138.2005

27. Stonko DP, Edwards J, Abdou H, Elansary NN, Lang E, Savidge SG, et al. A technical and data analytic approach to pressure-volume loops over numerous cardiac cycles. *JVS Vasc Sci.* (2022) 3:73–84. doi: 10.1016/j.jvssci.2021.12.003

28. Lin C, Wang L, Lu Q, Li C, Jing Z. Endovascular repair of the aortic arch in pigs by improved double-branched stent grafts. *Ann R Coll Surg Engl.* (2013) 95:134–9. doi: 10.1308/003588413X13511609955814

29. Zoghbi WA, Adams D, Bonow RO, Enriquez-Sarano M, Foster E, Grayburn PA, et al. Recommendations for noninvasive evaluation of native valvular regurgitation: a Report from the American Society of Echocardiography Developed in Collaboration with the Society for Cardiovascular Magnetic Resonance. *J Am Soc Echocardiogr.* (2017) 30:303–71. doi: 10.1016/j.echo.2017.01.007

30. Maurer G. Aortic regurgitation. *Heart.* (2006) 92:994–1000. doi: 10.1136/hrt.2004.042614

31. Lak HM, Ranka S, Goyal A. *Pharmacologic Stress Testing.* Treasure Island (FL): StatPearls. (2022).

32. Ruffolo RR Jr. The pharmacology of dobutamine. *Am J Med Sci.* (1987) 294:244–8. doi: 10.1097/00000441-198710000-00005

33. Dubin A, Lattanzio B, Gatti L. The spectrum of cardiovascular effects of dobutamine - from healthy subjects to septic shock patients. *Rev Bras Ter Intensiva.* (2017) 29:490–8. doi: 10.5935/0103-507X.20170068

34. Richards E, Lopez MJ, Maani CV. *Phenylephrine*. StatPearls. Treasure Island (FL): StatPearls Publishing Copyright © 2022, StatPearls Publishing LLC. (2022).

35. Wodack KH, Graessler MF, Nishimoto SA, Behem CR, Pinnschmidt HO, Punke MA, et al. Assessment of central hemodynamic effects of phenylephrine: an animal experiment. *J Clin Monit Comput.* (2019) 33:377–84. doi: 10.1007/s10877-018-0204-6

36. Walheim J, Dillinger H, Gotschy A, Kozerke S. 5D Flow tensor MRI to efficiently map reynolds stresses of aortic blood flow *in-vivo*. *Sci Rep.* (2019) 9:18794. doi: 10.1038/s41598-019-55353-x

37. Walheim J, Dillinger H, Kozerke S. Multipoint 5D flow cardiovascular magnetic resonance - accelerated cardiac- and respiratory-motion resolved mapping of mean and turbulent velocities. *J Cardiovasc Magn Reson.* (2019) 21:42. doi: 10.1186/s12968-019-0549-0

38. Warner HR, Toronto AF. Effect of heart rate on aortic insufficiency as measured by a dye-dilution technique. *Circ Res.* (1961) 9:413–7. doi: 10.1161/01.RES.9.2.413

39. Judge TP, Kennedy JW, Bennett LJ, Wills RE, Murray JA, Blackmon JR. Quantitative hemodynamic effects of heart rate in aortic regurgitation. *Circulation.* (1971) 44:355–67. doi: 10.1161/01.CIR.44.3.355

40. Cesarovic N, Busch J, Lipiski M, Fuetterer M, Fleischmann T, Born S, et al. Left ventricular blood flow patterns at rest and under dobutamine stress in healthy pigs. *NMR Biomed.* (2019) 32:e4022. doi: 10.1002/nbm.4022

41. Fanous EJ, Mukku RB, Dave P, Aksoy O, Yang EH, Benharash P, et al. Paravalvular leak assessment: challenges in assessing severity and interventional approaches. *Curr Cardiol Rep.* (2020) 22:166. doi: 10.1007/s11886-020-01418-7

42. Pinheiro CP, Rezek D, Costa EP, Carvalho ES, Moscoso FA, Taborga PR, et al. Paravalvular regurgitation: clinical outcomes in surgical and percutaneous treatments. *Arq Bras Cardiol.* (2016) 107:55–62. doi: 10.5935/abc.20160086

43. Schultz CJ, Slots TL, Yong G, Aben JP, Van Mieghem N, Swaans M, et al. An objective and reproducible method for quantification of aortic regurgitation after TAVI. *EuroIntervention.* (2014) 10:355–63. doi: 10.4244/EIJY14M05_06

44. Stugaard M, Koriyama H, Katsuki K, Masuda K, Asanuma T, Takeda Y, et al. Energy loss in the left ventricle obtained by vector flow mapping as a new quantitative measure of severity of aortic regurgitation: a combined experimental and clinical study. *Eur Heart J Cardiovasc Imaging.* (2015) 16:723–30. doi: 10.1093/ehjci/jev035

45. Martinez-Miro S, Tecles F, Ramon M, Escribano D, Hernandez F, Madrid J, et al. Causes, consequences and biomarkers of stress in swine: an update. *BMC Vet Res.* (2016) 12:171. doi: 10.1186/s12917-016-0791-8

46. Won E, Kim YK. Stress, the autonomic nervous system, and the immune-kynurenine pathway in the etiology of depression. *Curr Neuropharmacol.* (2016) 14:665–73. doi: 10.2174/1570159X14666151208113006

47. Seidler T, Alter T, Krüger M, Fehlhaber K. Transport stress–consequences for bacterial translocation, endogenous contamination and bactericidal activity of serum of slaughter pigs. *Berl Munch Tierarztl Wochenschr.* (2001) 114:375–7. doi: 10.31274/safepork-180809-1163

48. Zucker BA, Kruger M. Effect of transport stress on the content of endotoxin in blood of slaughter pigs. *Berl Munch Tierarztl Wochenschr.* (1998) 111:208–10.

49. Obernier JA, Baldwin RL. Establishing an appropriate period of acclimatization following transportation of laboratory animals. *ILAR J.* (2006) 47:364–9. doi: 10.1093/ilar.47.4.364

50. Otten W, Puppe B, Kanitz E, Schon PC, Stabenow B. Physiological and behavioral effects of different success during social confrontation in pigs with prior dominance experience. *Physiol Behav.* (2002) 75:127–33. doi: 10.1016/S0031-9384(01)00630-8

51. Quiniou N, Noblet J, van Milgen J, Dubois S. Modelling heat production and energy balance in group-housed growing pigs exposed to low or high ambient temperatures. *Br J Nutr.* (2001) 85:97–106. doi: 10.1079/BJN2000217

52. Shah GS, Das BK, Kumar S, Singh MK, Bhandari GP. Acid base and electrolyte disturbance in diarrhoea. *Kathmandu Univ Med J (KUMJ).* (2007) 5:60–2.

53. Frustaci A, Pennestrì, Scoppetta C. Myocardial damage due to hypokalaemia and hypophosphataemia. *Postgrad Med J.* (1984) 60:679–81. doi: 10.1136/pgmj.60.708.679

54. Kane MG, Luby JP, Krejs GJ. Intestinal secretion as a cause of hypokalemia and cardiac arrest in a patient with strongyloidiasis. *Dig Dis Sci.* (1984) 29:768–72. doi: 10.1007/BF01312953

55. Hunter RJ, Patel VB, Miell JP, Wong HJ, Marway JS, Richardson PJ, et al. Diarrhea reduces the rates of cardiac protein synthesis in myofibrillar protein fractions in rats in vivo. *J Nutr.* (2001) 131:1513–9. doi: 10.1093/jn/131.5.1513

56. Heinonen ML, Raekallio MR, Oliviero C, Ahokas S, Peltoniemi OA. Comparison of azaperone-detomidine-butorphanol-ketamine and azaperone-tiletamine-zolazepam for anaesthesia in piglets. *Vet Anaesth Analg.* (2009) 36:151–7. doi: 10.1111/j.1467-2995.2008.00443.x

57. Santos M, Bertran de Lis BT, Tendillo FJ. Effects of intramuscular dexmedetomidine in combination with ketamine or alfaxalone in swine. *Vet Anaesth Analg.* (2016) 43:81–5. doi: 10.1111/vaa.12259

58. Sakaguchi M, Nishimura R, Sasaki N, Ishiguro T, Tamura H, Takeuchi A. Anesthesia induced in pigs by use of a combination of medetomidine, butorphanol, and ketamine and its reversal by administration of atipamezole. *Am J Vet Res.* (1996) 57:529–34.

59. Lee JY, Kim MC. Anesthesia of growing pigs with tiletamine-zolazepam and reversal with flumazenil. *J Vet Med Sci.* (2012) 74:335–9. doi: 10.1292/jvms.10-0501

60. Vainio OM, Bloor BC, Kim C. Cardiovascular effects of a ketamine-medetomidine combination that produces deep sedation in Yucatan mini swine. *Lab Anim Sci.* (1992) 42:582–8.

61. Tendillo FJ, Mascias A, Santos M, Segura IA, San Roman F, Castillo-Olivares JL. Cardiopulmonary and analgesic effects of xylazine, detomidine, medetomidine, and the antagonist atipamezole in isoflurane-anesthetized swine. *Lab Anim Sci.* (1996) 46:215–9.

62. Duval JD, Pang JM, Boysen SR, Caulkett NA. Cardiopulmonary effects of a partial intravenous anesthesia technique for laboratory swine. *J Am Assoc Lab Anim Sci.* (2018) 57:376–81. doi: 10.30802/AALAS-JAALAS-17-000164

63. Lervik A, Raszplewicz J, Ranheim B, Solbak S, Toverud SF, Haga HA. Dexmedetomidine or fentanyl? Cardiovascular stability and analgesia during propofol-ketamine total intravenous anaesthesia in experimental pigs. *Vet Anaesth Analg.* (2018) 45:295–308. doi: 10.1016/j.vaa.2017.08.012

64. Glomset DJ, Glomset AT. A morphologic study of the cardiac conduction system in ungulates, dog, and man: Part II: The purkinje system. *Am Heart J.* (1940) 20:677–701. doi: 10.1016/S0002-8703(40)90530-0

65. Gill J, Heel RC, Fitton A. Amiodarone. An overview of its pharmacological properties, and review of its therapeutic use in cardiac arrhythmias. *Drugs.* (1992) 43:69–110. doi: 10.2165/00003495-199243010-00007

66. Sattler SM, Lubberding AF, Skibsbye L, Jabbari R, Wakili R, Jespersen T, et al. Amiodarone treatment in the early phase of acute myocardial infarction protects against ventricular fibrillation in a porcine model. *J Cardiovasc Transl Res.* (2019) 12:321–30. doi: 10.1007/s12265-018-9861-6

67. Singh BN, Jewitt DE, Downey JM, Kirk ES, Sonnenblick EH. Effects of amiodarone and L8040, novel antianginal and antiarrhythmic drugs, on cardiac and coronary haemodynamics and on cardiac intracellular potentials. *Clin Exp Pharmacol Physiol.* (1976) 3:427–42. doi: 10.1111/j.1440-1681.1976.tb00620.x

68. Cote P, Bourassa MG, Delaye J, Janin A, Froment R, David P. Effects of amiodarone on cardiac and coronary hemodynamics and on myocardial metabolism in patients with coronary artery disease. *Circulation.* (1979) 59:1165–72. doi: 10.1161/01.CIR.59.6.1165

69. Huber CH, Cohn LH, von Segesser LK. Direct-access valve replacement a novel approach for off-pump valve implantation using valved stents. *J Am Coll Cardiol.* (2005) 46:366–70. doi: 10.1016/j.jacc.2005.04.028

70. Ferrari M, Figulla HR, Schlosser M, Tenner I, Frerichs I, Damm C, et al. Transarterial aortic valve replacement with a self expanding stent in pigs. *Heart.* (2004) 90:1326–31. doi: 10.1136/hrt.2003.028951

71. Masson JB, Kovac J, Schuler G, Ye J, Cheung A, Kapadia S, et al. Transcatheter aortic valve implantation: review of the nature, management, and avoidance of procedural complications. *JACC Cardiovasc Interv.* (2009) 2:811–20. doi: 10.1016/j.jcin.2009.07.005

72. Barbash IM, Dvir D, Ben-Dor I, Corso PJ, Goldstein SA, Wang Z, et al. Impact of transapical aortic valve replacement on apical wall motion. *J Am Soc Echocardiogr.* (2013) 26:255–60. doi: 10.1016/j.echo.2012.11.003

73. Edwards MB, Taylor KM, Shellock FG. Prosthetic heart valves: evaluation of magnetic field interactions, heating, and artifacts at 1.5 T. *J Magn Reson Imaging.* (2000) 12:363–9. doi: 10.1002/1522-2586(200008)12:2<363::aid-jmri21>3.0.co;2-3

74. Lipiski M, Eberhard M, Fleischmann T, Halvachizadeh S, Kolb B, Maisano F, et al. Computed Tomography-based evaluation of porcine cardiac dimensions to assist in pre-study planning and optimized model selection for pre-clinical research. *Sci Rep.* (2020) 10:6020. doi: 10.1038/s41598-020-63044-1

75. Kalantari K, Chang JN, Ronco C, Rosner MH. Assessment of intravascular volume status and volume responsiveness in critically ill patients. *Kidney Int.* (2013) 83:1017–28. doi: 10.1038/ki.2012.424

frontiers | Frontiers in Veterinary Science

TYPE Original Research
PUBLISHED 14 October 2022
DOI 10.3389/fvets.2022.965316

OPEN ACCESS

EDITED BY
Abirami Kugadas,
Takeda, United States

REVIEWED BY
Ellie Jordan Putz,
Agricultural Research Service (USDA), United States
Kris Helke,
Medical University of South Carolina, United States

*CORRESPONDENCE
Jorge A. Piedrahita
japiedra@ncsu.edu

†These authors have contributed equally to this work

SPECIALTY SECTION
This article was submitted to Comparative and Clinical Medicine, a section of the journal Frontiers in Veterinary Science

RECEIVED 09 June 2022
ACCEPTED 20 September 2022
PUBLISHED 14 October 2022

CITATION
Sper RB, Proctor J, Lascina O, Guo L, Polkoff K, Kaeser T, Simpson S, Borst L, Gleason K, Zhang X, Collins B, Murphy Y, Platt JL and Piedrahita JA (2022) Allogeneic and xenogeneic lymphoid reconstitution in a *RAG2*$^{-/-}$*IL2RG*$^{y/-}$ severe combined immunodeficient pig: A preclinical model for intrauterine hematopoietic transplantation.
Front. Vet. Sci. 9:965316.
doi: 10.3389/fvets.2022.965316

Allogeneic and xenogeneic lymphoid reconstitution in a *RAG2*$^{-/-}$*IL2RG*$^{y/-}$ severe combined immunodeficient pig: A preclinical model for intrauterine hematopoietic transplantation

Renan B. Sper[1,2†], Jessica Proctor[1,2†], Odessa Lascina[2†], Ling Guo[1,2†], Kathryn Polkoff[1,2], Tobias Kaeser[1,3], Sean Simpson[1,2], Luke Borst[1,3], Katherine Gleason[1,2], Xia Zhang[1,2], Bruce Collins[1,2], Yanet Murphy[2], Jeffrey L. Platt[4] and Jorge A. Piedrahita[1,2*]

[1]Comparative Medicine Institute, North Carolina State University, Raleigh, NC, United States, [2]Department of Molecular Biomedical Sciences, College of Veterinary Medicine, North Carolina State University, Raleigh, NC, United States, [3]Department of Population Health and Pathobiology, College of Veterinary Medicine, North Carolina State University, Raleigh, NC, United States, [4]Department of Surgery and Microbiology and Immunology, University of Michigan Health System, Ann Arbor, MI, United States

Mice with severe combined immunodeficiency are commonly used as hosts of human cells. Size, longevity, and physiology, however, limit the extent to which immunodeficient mice can model human systems. To address these limitations, we generated *RAG2*$^{-/-}$ *IL2RG*$^{y/-}$ immunodeficient pigs and demonstrate successful engraftment of SLA mismatched allogeneic D42 fetal liver cells, tagged with pH2B-eGFP, and human CD34^{+} hematopoietic stem cells after *in utero* cell transplantation. Following intrauterine injection at day 42–45 of gestation, fetuses were allowed to gestate to term and analyzed postnatally for the presence of pig (allogeneic) and human (xenogeneic) B cells, *T*-cells and NK cells in peripheral blood and other lymphoid tissues. Engraftment of allogeneic hematopoietic cells was detected based on co-expression of pH2B-eGFP and various markers of differentiation. Analysis of spleen revealed robust generation and engraftment of pH2B-eGFP mature B cells (and IgH recombination) and mature *T*-cells (and *TCR-β* recombination), T helper (CD3^{+}CD4^{+}) and T cytotoxic (CD3^{+}CD8^{+}) cells. The thymus revealed engraftment of pH2B-eGFP double negative precursors (CD4^{-}CD8^{-}) as well as double positive (CD4^{+}, CD8^{+}) precursors and single positive *T*-cells. After intrauterine administration of human CD34^{+} hematopoietic stem cells, analysis of peripheral blood and lymphoid tissues revealed the presence of human *T*-cells (CD3^{+}CD4^{+} and CD3^{+}CD8^{+}) but no detectable B cells or NK cells. The frequency of human CD45^{+} cells in the circulation decreased

rapidly and were undetectable within 2 weeks of age. The frequency of human CD45$^+$ cells in the spleen also decreased rapidly, becoming undetectable at 3 weeks. In contrast, human CD45$^+$CD3$^+$ *T*-cells comprised >70% of cells in the pig thymus at birth and persisted at the same frequency at 3 weeks. Most human CD3$^+$ cells in the pig's thymus expressed CD4 or CD8, but few cells were double positive (CD4$^+$ CD8$^+$). In addition, human CD3$^+$ cells in the pig thymus contained human *T*-cell excision circles (TREC), suggesting *de novo* development. Our data shows that the pig thymus provides a microenvironment conducive to engraftment, survival and development of human *T*-cells and provide evidence that the developing *T*-cell compartment can be populated to a significant extent by human cells in large animals.

KEYWORDS

severe combined immunodeficiency, pig, xenotransplantation, allotransplantation, hematopoietic, RAG2, IL2RG, transgenic

Introduction

Severe combined immunodeficient (SCID) mouse models have allowed researchers to answer fundamental questions related to immune system development and function and have served as crucial bridging models in the field of stem cell transplantation, leading to new discoveries with potential pre-clinical application in human medicine (1–3). Commonly used SCID mice models include non-obese diabetic/SCID mice, NODShi.Cg-*Prkdc*^{SCID}*Il2RG*^{tm1Sug} and C;129S4*RAG-2*^{tm1Flv}*IL2RG*^{tm1Flv} (4). All these models harbor multiple genetic modifications abolishing adaptive immunity development, facilitating engraftment of human cells of different lineages. Of these genes, *RAG1, RAG2,* and *ILR2RG,* play a key role in *T*-cell, B cell and Natural Killer (NK) cell development and/or survival. The RAG1 and RAG2 proteins catalyze recombination of B cell receptor (BCR) and *T*-cell receptor (TCR) genes, and inactivation of *RAG1* or *RAG2* leads to a lack of mature B cells and *T*-cells (5). Inactivation of *RAG1* or *RAG2* leads to severe combined immunodeficiency (SCID). *IL2RG*, located on the X chromosome, encodes a subunit of the IL-2 receptor, also present in the IL-4, IL-7, IL-9, IL-15, and IL-21 receptors (6). The result of *IL2RG* inactivation is broadly impaired cytokine signaling, leading to aberrant *T*-cell thymic development, lack or reduced thymus and peripheral lymph node development, and lack of IL-15 NK cell-mediated differentiation (7). Combined, these *IL2RG*$^{-/-}$ characteristics lead to XSCID syndrome (8). In mice inactivation of *IL2RG* and *RAG1* or *RAG2* leads to profound immunodeficiency and allows engraftment of human hematopoietic stem cells (3). Of note, other SCID syndromes may be caused by adenosine deaminase (ADA) deficiency, or Janus kinase 3 (Jak3) deficiency (9).

Despite the fundamental role of SCID mice models, certain limitations exist such as species-specific differences at the anatomical and physiological scale. Pigs resemble humans in terms of organ size, life span, anatomical, and physiological characteristics. Thus, they are considered as important laboratory animal models for biomedical research, especially for tissue engineering and human organ transplantation involving xenograft procedures (10). SCID pigs can be potentially important research tools to facilitate long-term follow-up studies of immune responses, xenotransplantation, stem cells, and cancer over clinically relevant time frames. Furthermore, SCID pigs can play a key role in assessing the safety of stem cell therapies, or the effects of surgery and radiation therapy in transplanted tumors, thus constituting an important preclinical model. Within the last decade there have been numerous SCID pig models created, including *IL2RG* knockout (11–15), *RAG1* and or *RAG2* knockout (16–19), as well as double gene knockouts of *IL2RG*, *RAG*, or *ARTEMIS* (20–22), resulting in a range of translational research models, including models of infection with human norovirus (20), human iPSC engraftment (17), tumor melanoma cell engraftment (11), and allogeneic hematopoietic lineage engraftment (15, 17). Only one group to date has shown human *T*-cell restricted xenogeneic engraftment in a *IL2RG*/*ART* null SCID pig (22). Our results confirm and extend those observations using a different double mutant genetic background, the *RAG2*$^{-/-}$*IL2RG*$^{y/-}$. From heretofore, we will refer to this line as the *DKO* line. Using the *DKO* line we demonstrate significant allogeneic and xenogeneic engraftment following *in utero* transplantation of pig H2B-GFP tagged fetal liver cells or human CD34$^+$ cells, respectively.

Materials and methods

Ethics statement

This study was carried out in strict accordance with the recommendations in the Guide for the Care and Use of Laboratory Animals of the National Institutes of Health. The

animals used in this study were obtained from a university-owned herd, and all animal procedures were approved by the Institutional Animal Care and Use Committee of North Carolina State University (Raleigh, NC). Animals were sacrificed by one of two methods, intravenous injection of sodium pentobarbital, or penetrating captive bolt euthanasia followed by jugular exsanguination. Both methods meet the recommended guidelines of the American Veterinary Medical Association for euthanasia in pigs. All surgeries were performed under isoflurane anesthesia, and a post-surgical regimen of bupivacaine, Banamine-S was administered to minimize pain. Xenotransplantation procedure and management of xenografted pigs was performed at an approved facility within the College of Veterinary Medicine under proper guidelines in accordance with IACUC protocols. All human samples were obtained from healthy donors under an approved IRB to the University of Michigan and shipped to North Carolina State University without any identifying information.

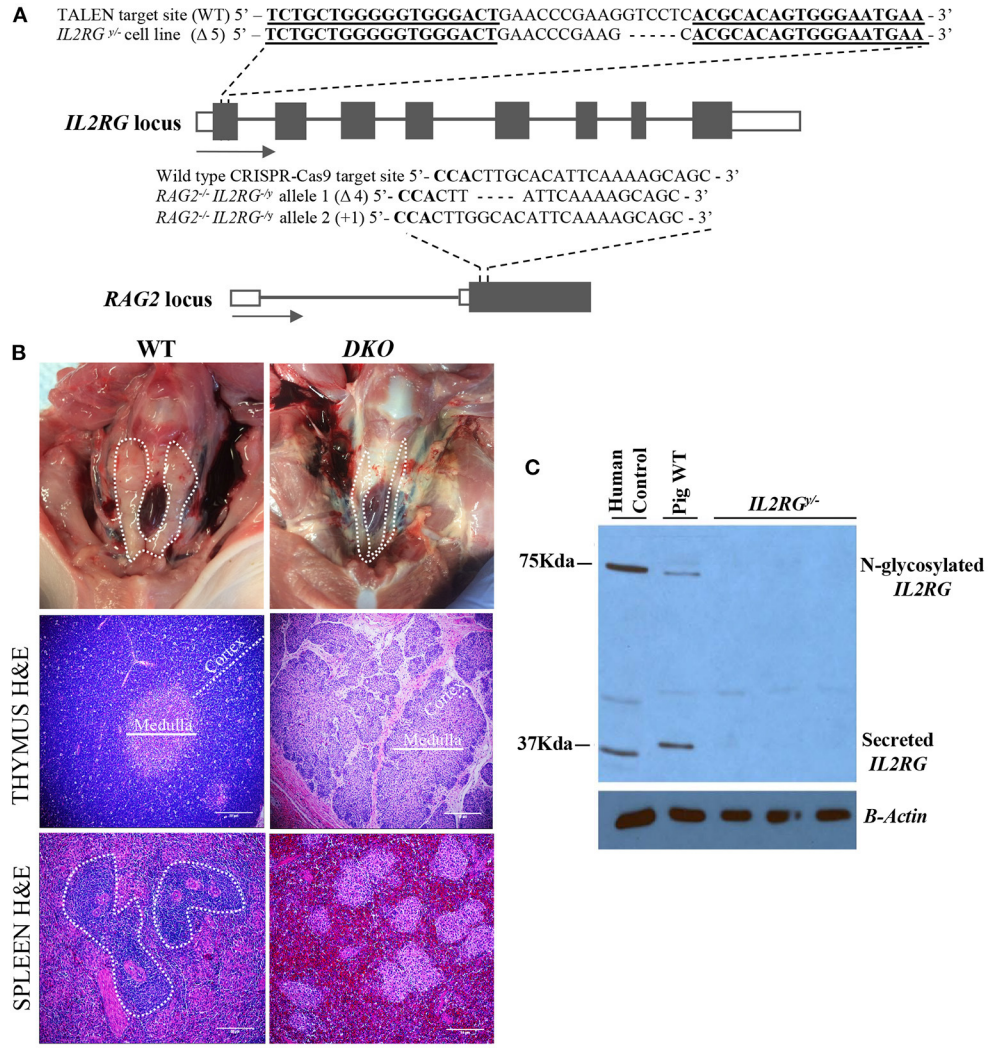

FIGURE 1
Genotype and initial characterization of *DKO* pigs. **(A)** DNA sequencing of the *IL2RG* and *RAG2* locus target regions detected from *DKO* pigs. Wild type (WT) sequence is shown as a reference. TALEN binding sites are represented by bold and underlined sequences, while bold sequences represent the PAM sequence. **(B)** Thymus (cervical region) from wild-type pigs could be easily visualized (dotted contour white line) while in age-matched *DKO* pigs it was nearly undetectable. H&E microscopic (20x magnification) evaluation of the *DKO* thymus revealed a poorly developed thymus lacking proper cortex (white dotted line), Medulla is also indicated (solid white line). The spleen of wild type age-matched pigs had visible germinal centers (dotted contour white line) while the spleen of *DKO* pigs did not. **(C)** Western blot for *IL2RG* using wild type (WT) and mutant pig heart tissue lysates obtained from $IL2RG^{y/-}$ pig fetuses. Human peripheral blood served as human positive control.

Generation of *DKO* porcine fetal fibroblast line

All gene edits were carried out in fetal fibroblasts obtained from D30 fetuses collected from three-way Yorkshire × Landrace × Duroc crossbred animals from the Swine Educational Unit at North Carolina State University as previously described (23). Initially, an *IL2RG*$^{y/-}$ fetal fibroblast line was generated using TALENs (Supplementary Figures 1A,B). This cell line was selected for further targeting of the *RAG2* locus *via* CRISPR-Cas9 using custom-designed *gRNAs* targeting exon 2 and a hygromycin reporter plasmid containing the *RAG2* CRISPR-Cas9 target sequence (Supplementary Figures 1C–E). This reporter plasmid consists of a red fluorescent protein (RFP) gene as a transfection control, and an out-of-frame hygromycin gene fused to GFP. Gene editing after cleavage of the *RAG2* target results in correction of the out-of-frame fusion hygromycin and GFP gene allowing for both hygromycin selection using 2 mg/ml for 48 h, or and separation of cell by FACS based on GFP expression to enrich for *RAG2* mutants. Following hygromycin and GFP selection/enrichment, single cell clonal colonies were generated by seeding at limiting dilutions, and screening performed by PCR followed restriction enzyme digestion using a *HpyCH4V* restriction site overlapping the gRNA target site (Supplementary Figure 1F). Genomic DNA from single cell colonies were isolated, primers designed to amplify a 190 bp amplicon containing the restriction site, followed by *HpyCH4V* digestion and DNA sequencing of the *RAG2* locus target site. A colony containing biallelic mutations of one bp insertion in one allele, and a four base pair deletion in the other allele, was used to generate the *DKO* transgenic pigs *via* SCNT (Figure 1A).

Generation of *DKO* pigs *via* somatic cell nuclear transfer

DKO pregnancies were generated *via* SCNT as previously described (24). All chemicals were purchased from Sigma (St. Louis, MO) unless otherwise specified. Oocytes from mixed commercial breed sows were collected from local slaughterhouses. Cumulus cells were removed from the oocyte by vortex for 5 min in 0.1% bovine testicular hyaluronidase. Oocytes were incubated in manipulation media (Ca-free NCSU-23 with 5% FBS) containing 5 μg/mL bisbenzimide and 7.5 μg/mL cytochalasin B for 5 min. Following the incubation period, oocytes were enucleated by removing the first polar body and metaphase II plate. Single cells were injected and fused to each enucleated oocyte. Fusion/activation was induced by two DC pulses of 140V for 40 μsec in 280 mM mannitol, 0.001 mM $CaCl_2$, and 0.05 mM $MgCl_2$. After fusion/activation, oocytes were placed back in NCSU-23 medium with 0.4% BSA and cultured at 38.5°C, 5% CO_2 in a humidified atmosphere for less than an hour, before being surgically transferred into a synchronized recipient.

Genotyping of *DKO* Double Knock-out (*DKO*) Pigs

For the *IL2RG* genotyping gDNA was isolated from porcine fetal fibroblast colonies and generated pigs and the primers 5′ CCACTGGAGTTTTTCATTTTGATG 3′ and 5′ ATCCGAAA AGCTCATTATTTGGTGT 3′ used to amplify the TALEN binding site and flanking region (∼1 Kb) under the following conditions 98°C for 1 min; 35 cycles (98°C for 10 s, 64.5°C for 10 s, 72°C for 15 s), 72°C for 1 min. Restriction digest with *AvaII* was performed to detect mono allelic indels of the *IL2RG* locus. For *RAG2* genotyping gDNA was isolated from porcine fetal fibroblast colonies and generated pigs and the primers 5′ CCACTGGAGTTTTTCATTTTGATG 3′ and 5′ ATCCGAAA GCTCATTATTTGGTGT 3′ used to amplify the CRISPR-Cas9 binding site and flanking region (190 bp) under the following conditions 98°C for 1 min; 35 cycles (98°C for 10 s, 64.5°C for 10 s, 72°C for 10 s), 72°C for 1 min. Restriction digest with *HypCH4V* was performed to detect mono and biallelic indels of the *RAG2* locus.

Allogeneic transfer donors: Swine Leukocyte Antigen (SLA) Matching of PH2B-EGFP donors and *DKO* recipient cell line and isolation of liver hematopoietic stem cells

To ensure that the allogeneic transplants were done across different swine leukocyte antigen complex (SLA) haplotypes, both the pH2B-eGFP D42 fetal liver donor cells derived from a gene edited line we previously generated that contains the pH2B-GFP under the ACTB promoter (25), and the recipient *DKO* line were typed *via* a previously described PCR assay using site specific primers (PCR-ssp) (26–28). The assay included primers specific for identification of pig MHC-I pig loci *SLA-1, SLA-2* and *SLA-3*, and MHC-II pig loci *DRB1*, *DQB1* and *DQA* (Supplementary Figures 2A,B), therefore testing the pig *SLA* analogues to classical *HLA* regulating the success of hematopoietic stem cell transplantation.

Allogeneic hematopoietic stem cells were obtained from fetal livers. Midgestational fetal liver cells are known to be enriched for hematopoietic stem cells and are routinely used in mouse models of *in utero* hematopoietic stem cell transplantation (29, 30). Forty-two days pH2B-eGFP fetal liver cells were isolated using a previous reported protocol (31). Briefly, D42 pH2B-eGFP fetal male livers (3 separate donors) were minced, digested

in liver digestion media (Gibco #17703034), and washed with Iscove Modified Dulbecco's Media (Gibco #12440053). Fetal liver parenchymal and hematopoietic stem cells were separated by density centrifugation and the cell fraction enriched for hematopoietic stem cells cryopreserved in Hanks' Balanced Salt Solution (HBSS) containing 5% DMSO, 0.3 M Sucrose and no calcium/magnesium.

Xenogenetic transfer donors: Immunomagnetic selection of CD34 + cells

Peripheral blood mobilized stem cells (PBMC) from two unrelated male adult donors were utilized as the source of stem cells. Hematopoietic stem cell mobilization was achieved by conducting standard mobilization treatment with G-CSF, followed by peripheral blood harvest and cryopreservation. Each cryopreserved bag contained ∼50 ml per bag. A total of four bags were used per pregnancy. Frozen peripheral blood containing mobilized hematopoietic stem cells were thawed and washed in autoMACS Rinsing Solution (Miltenyibiotec #130-091-222) containing MACS BSA Stock Solution (#130-091-376) at 1:20 dilution. Mononuclear cells were isolated *via* centrifugation in Ficoll-Paque PLUS (GE Healthcare #71-7167-00 AG), yielding ∼600 million PBMCs containing mobilized HSCs. Mononuclear cells were incubated with CD34 MicroBead Kit—UltraPure (Miltenyibiotec #130-100-453), and $CD34^+$ human cells isolated with a magnetic system described previously. Purification to 97.7% was confirmed *via* flow cytometry (Supplementary Figure 2C). Sexing of donor cells were done by PCR using the X linked ALT1 gene (5′-CCCTGATGAAGAACTTGTATCTC-−3′ and 5′- GAAATTA CACACATAGGTGGCACT- 3′), and the human SRY from the Y chromosome (5′-CATGAACGCATTCATCGTGTGGTC-3′ and 5′-CTGCGGGAAGCAAACTGCAATTCTT-3′). PCR conditions were 98°C for 1 min; 35 cycles (98°C for 10 s, 58°C for 10 s, 72°C for 8 s), 72°C for 1 min (Supplementary Figure 2D).

In utero hematopoietic transplantation of PH2B-EGFP pig fetal liver hematopoietic stem cells or CD34 + cell transplantation

Allo and Xenotransplantation procedures and management of allografted and xenografted pigs was performed at an approved facility within the College of Veterinary Medicine under proper guidelines in concordance with IACUC protocols. At D42 of gestation a wildtype sow carrying a transgenic *DKO* pregnancy was prepared for surgery. pH2B-eGFP fetal liver cells were thawed and ran through a live dead magnetic isolation system (Miltenyibiotec #130-090-101) using LS Columns (Miltenyibiotec #130-042-401) placed in a QuadroMACS Separator (Miltenyibiotec #130-090-976). In utero transfer were carried out essentially as described (22) with the exception that the cells were injected intra-hepatically, not intraperitoneally, *via* ultrasound guided (Aloka) procedure, using a PAN chiba (25 gauge × 6 cm) cytological aspirating needle (Gallini Medical Devices ref #PA25-6). First, each fetus was located with the ultrasound and scanned from cranial to caudal direction until the hyperechoic liver structure and central vein (hypoechoic) was identified caudally to the thoracic cavity. The probe was held in position and the PAN chiba needle inserted through the uterine wall until it could be identified in the ultrasound. One uterine horn was scanned at a time, from the tip of the uterine horn (next to the ovary) all the way down to the uterine horn bifurcation. Per fetus, a total of 30 ul of saline cell suspension was slowly injected. Deposition of cell suspension solution was visible in the ultrasound screen, followed by retraction of the needle while maintaining contact ultrasound visualization of the liver.

For allogeneic engraftment, 3 *DKO* fetuses from one pregnancy received 3.5×10^6 fetal liver hematopoietic stem cells isolated from D42 pH2B-eGFP fetal liver donors (1 unique donor per *DKO* recipient). For xenogeneic engraftment with human hematopoietic stem cells, 7×10^6 viable human $CD34^+$ cells/fetus were transplanted *via* intra-hepatic ultrasound-guided fetal injection into *DKO* D42 fetuses. Fetuses from two pregnant gilts were injected with cells from two independent male human donors and resulted in three and four viable pigs at term (total n = 7 viable term pigs). Non-injected $RAG2^{-/-}IL2RG^{y/-}$ ($n = 3$) and injected wild type $RAG\text{-}2^{+/+}IL2RG^{+/y}$ ($n = 2$) served as controls. ($CD34^+$ enrichment and donor sexing data are presented in (Supplementary Figures 2C,D). A timeline schematic of all *in vivo* procedures and sample harvests performed is provided in Supplementary Figure 3.

Histological and immunofluorescence analyses

DKO and aged matched wild type controls pigs were euthanized, and lymphoid organs isolated. Age of euthanasia ranged from 1 day to 3 weeks and are stated in each figure legend. For hematoxylin and eosin (H&E) and immunohistochemistry staining, the thymus and spleen were fixed in 10% neutral buffer formalin for 24 h, followed by 70% ethanol for 24 h. For immunofluorescence analysis, fresh tissue samples were placed in 30% sucrose at 5°C overnight, followed by OCT embedding and freezing. For IHC analysis of paraffin embedded tissues of non-injected *DKO* pigs, samples were stained with mouse anti-human CD79α unconjugated (BioRad/AbDSerotec

#MAC2538), anti-human CD3 (Dako #A0452), and rabbit anti-human CD335 (BIOSS #bs-10027R). For detection of human cells fresh OCT embedded thymus and spleen were immunostained with mouse anti-human CD45 FITC labeled (BD #555482). Cell numbers were obtained *via* ImageJ processing and analysis and expressed as the number of cells/higher power field (40x magnification). At least three images were acquired and analyzed.

Flow cytometry

Peripheral blood (PB) collected into EDTA containing tubes and single-cell suspension from thymus and spleen from *DKO* pigs were processed and prepared for antibody staining immediately after collection. A total of 1×10^6 cells were stained per sample. For detection of pig cells, we used the following antibodies. For *T*-cells, mouse anti pig CD3 epsilon Alexa Fluor 405 labeled (Novus #NBP1-28225AF405), mouse anti pig CD8 PE labeled (BD #559584) and mouse anti pig CD4 PE-Cy7 labeled (BD #561473). For detection of pig B cells mouse anti human CD79α Alexa Fluor 647 Labeled (BioRad/AbDSerotec #MCA2538A647) using LEUCOPERM kit (BioRad/AbDSerotec #BUF09) for intracellular staining. For detection of pig NK cells, mouse anti pig CD335 (BioRad/AbDSerotec #MCA5972GA) conjugated with APC-Cy7 with the kit LN#131PACCY7 (BioRad/AbDSerotec). Samples were incubated for 1h at 5°C in staining buffer (BD #554657), followed by red blood lysis and fixation with lysing solution (BD #349202) and washing. All flow data was gated and displayed as a percentage of gated mononuclear cells. For the detection of human lymphocytes from peripheral blood, thymus, spleen of xenografted pigs were stained with mouse anti-human CD45-PE-CF594 (BD #562279), for *T*-cell detection, mouse anti-human CD3 PE labeled (BD #555333), mouse anti-human CD8 APC labeled (BD #340584) and mouse anti-human CD4 FITC labeled (BD #561842) were used. For detection of human B cells, mouse anti-human CD19 FITC labeled (BD #564456), for human NK cells mouse anti-human CD335 FITC labeled (BD #564536). We conducted a series of flow cytometry antibody cross reactivity studies by mixing human and pig hematopoietic cells, showing no cross reactivity, as well as staining non-injected *DKO* pigs as negative controls. Flow cytometry analysis was performed with Flow Jow software. Gating strategy was applied to remove dead cells and debris, followed by a single cell gate, followed by a mononuclear cell gate and analysis of the markers of cells of interest. *T*-cell subsets were analyzed by gating of $CD3^+$ cells.

PCR assay for detection of pig V(D)J rearranged IgH and TCR-β locus

Genomic DNA was isolated from peripheral blood mononuclear cells, thymus and spleen. The previous reported primers (32, 33) D1J1-F and D1J1-R were used it to identify D-J rearrangement of the *TCR-β* locus in peripheral blood and thymus of *DKO* pigs with Phire Hot Start II DNA Polymerase (Thermofisher #F122L) under the following conditions, 98°C for 1 min; 35 cycles (98°C for 10 s, 68°C for 10 s, 72°C for 30 s), 72°C for 1 min. *IgH* rearrangement was detected by PCR utilizing the previous reported primers FR1 and JH (rearranged *IgH*) and D4-F and J3-R (germinal control) (18) with Phire Hot Start II DNA Polymerase under the following conditions 98°C for 1 min; 35 cycles (98°C for 10 s, 62.5°C for 10 s, 72°C for 30 s), 72°C for 1 min.

PCR assay for detection of VαJα human TREC recombination

To demonstrate human TCR rearrangement in the thymus of xenografted pigs, previous reported primers (32, 33) were used to amplify the *δRec-ΨJα* segment of the human coding joint *T*-cell receptor excision circle (*VαJα* TREC). This extrachromosomal DNA circle indicates proper *δRec-ΨJα* recombination. Amplification of the *IL2RG* locus was used as control for DNA loading. Ten ng of gDNA from thymus and blood were used as templates, thymus of a *DKO* non-injected pig served as negative control, while gDNA from donor cells used for xenoengraftment was used as positive control. Forward and reverse primers were 5′ CTAATAATAAGATCCTCAAGGGTCGAGACTGTC 3′ and 5′ CCTGTTTGTTAAGGCACATTAGAATCTCTCACTG 3′. PCR conditions for *VαJα* TREC were 98°C for 1 min; 35 cycles (98°C for 10 s, 69°C for 10 s, 72°C for 15 s), 72°C for 1 min.

Statistical analysis

Statistical analysis and graphs were generated in GraphPad Prism 8. Data comparison between two groups was performed *via* two-tailed unpaired t-test with a significance value of 0.05. Multiple group analysis was performed *via* analysis of variance (ANOVA) with Tukey's multiple comparisons test with a significance value of 0.05.

Results

Generation of *DKO* gene-edited pigs

The *IL2RG* pig locus was targeted with custom-designed TALENs assembled *via* FLASH system (34). This cell line harbors a 5 base pair deletion of exon 1 of the *IL2RG* locus (Figure 1A). Targeted cells were used for SCNT to generate

IL2RG null D42 fetuses, and lack of IL2RG protein was confirmed by Western blot (Figure 1C). These fibroblasts were then used to inactivate the *RAG2* gene. A high targeting efficiency, with indel frequency reaching 79% (51% monoallelic and 28% monoallelic) was obtained (Supplementary Figure 1G). Four homozygous and two heterozygous colonies were submitted for DNA sequencing, revealing deletion, point mutations and insertions (Supplementary Figure 4). Sequencing analysis of one colony (#29) revealed biallelic mutations of 4 base pair deletion from one allele and a 1 base pair insertion in the other allele. In silico analysis of both allelic mutations predicted multiple premature stop codons immediately downstream of the CRISPR-Cas9 binding site, leading to lack of RAG2 protein expression. This colony, therefore, was selected as the SCNT donor to generate *DKO* transgenic pigs. A total of 291 (*DKO*) reconstructed embryos were transferred and 2 pregnancies carried to term, generating five *DKO* transgenic pigs that were used for initial analysis, with 1 pig dying at birth resulting in 4 DKO pigs used for phenotype characterization. For xenogeneic engraftment, additional pregnancies were generated, and fetuses injected at D42 of gestation with human CD34 cells.

Lymphoid lineage analysis of non-engrafted pigs

Analysis of lymphoid lineage of peripheral blood cells from age-matched *DKO* ($n = 4$) pigs was performed *via* flow cytometry at 1 week of age with antibodies specific for pig CD3, CD4, CD8, CD79α and NKp46 (CD335). *DKO* pigs had a marked reduction (% gated mononuclear cells) of CD79α $^+$ cells compared to controls ($p < 0.0001$) (Figures 2A,B). Analysis of *T*-cells populations in peripheral blood *via* expression of CD3 $^+$ CD4 $^+$ and CD3 $^+$ CD8 $^+$ revealed that *DKO* pigs had reduced levels of CD3$^+$CD4 $^+$ *T*-cells ($p < 0.0001$) and CD3$^+$CD8$^+$ *T*-cells ($p < 0.0001$) (Figures 2A,B). Next, we studied peripheral blood levels of NK cells *via* flow cytometric analysis using the marker NKp46 (CD335) (35). *DKO* pigs had a marked reduction in levels of CD335$^+$ cells in peripheral blood (∼0.8%), however, this was not significantly different from WT (∼2.95%) ($p = 0.1575$) (Figures 2A,B).

Histopathological analysis of the spleen of *DKO* pigs showed was devoid germinal centers (Figure 1B). No macroscopically visible lymph nodes were detected in *DKO* pigs, likely a consequence of *IL2RG* inactivation. Spleen IHC for CD79α showed a marked reduction of CD79α $^+$ cell in *DKO* ($p = 0.0009$) (Figures 2C,D). Similarly, there was a marked reduction of CD3 $^+$ cell and CD335 in *DKO* pigs ($p < 0.0001$ and $p = 0.0066$, respectively) (Figures 2C,D). The thymus of *DKO* pigs was poorly developed, lacking proper cortical zone development (Figure 1C) and exhibited a marked reduction of CD3$^+$ cells ($p < 0.0001$) (Figures 2C,D). These observations are in concordance with previous reports (20).

Analysis of RAG2 activity using PCR assays to detect molecular *V(D)J IgH* rearranged locus of B cells in the spleen and *D-J TCR-β* in the thymus showed that rearranged loci could be detected in the control animals but not in *DKO* pigs (Supplementary Figure 5). Together these results extend previous phenotypic analysis of *DKO* deficient pigs (20) and confirm that *DKO* pigs display a severe combined immunodeficient phenotype.

SLA typing of donor cells and host *DKO* line

SLA typing of donor and recipients demonstrated transplants to be bidirectional mismatches (0/8) for donor 1 and 2, with only one allele being shared (*SLA-3 03xx*) and mostly unidirectional mismatch (0/8) for donor 3 with 7 alleles being common shared (*SLA-1 04xx, SLA-2 04xx, SLA-3 03xx, 04xx, DRB1-07xx, DQB1 02xx, 09xx*). Only one perfect haplotype match was observed for *DQA* between donor 3 and recipients. Therefore, all donors were classified as poor hematopoietic stem cells donors (Supplementary Figures 2A,B).

Allogeneic PH2B-EGFP lymphoid cells in lymphoid tissue of *DKO* allografted pigs

The pH2B-eGFP positive donor cells could be identified and overlapped with CD3$^+$ cells as demonstrated by immunofluorescence analysis of allograted thymus at 1 week of age, while absent from aged matched wild type spleen and non-injected *DKO* pigs (Figure 3A). Additionally, allogeneic *T*-cell engraftment was confirmed *via* flow cytometry detection of pH2B-eGFP and staining the thymus of a *DKO* pig for CD3, CD4 and CD8. The pH2B-eGFP positive cells were easily identified (Figure 3B) and supported identification of engraftment of basic *T*-cell phenotypes in all three *DKO* pigs receiving each a different donor haplotype (Figures 3B–F). In contrast, pH2B-eGFP positive cells were absent from the thymus of aged-matched non-injected *DKO* pigs (Figure 3A). In addition, TCR-β rearrangement was detected in the thymus of allografted pigs (Figure 3G). The pH2B-eGFP positive donor cells could also be identified and overlapped with CD79α$^+$ cells in the spleen (Figure 4A). Flow cytometry analysis of allografted *DKO* pigs spleen at 1 week of age showed >90% GFP$^+$ CD79α$^+$ cells (Figures 4B,C). As

10.3389/fvets.2022.965316

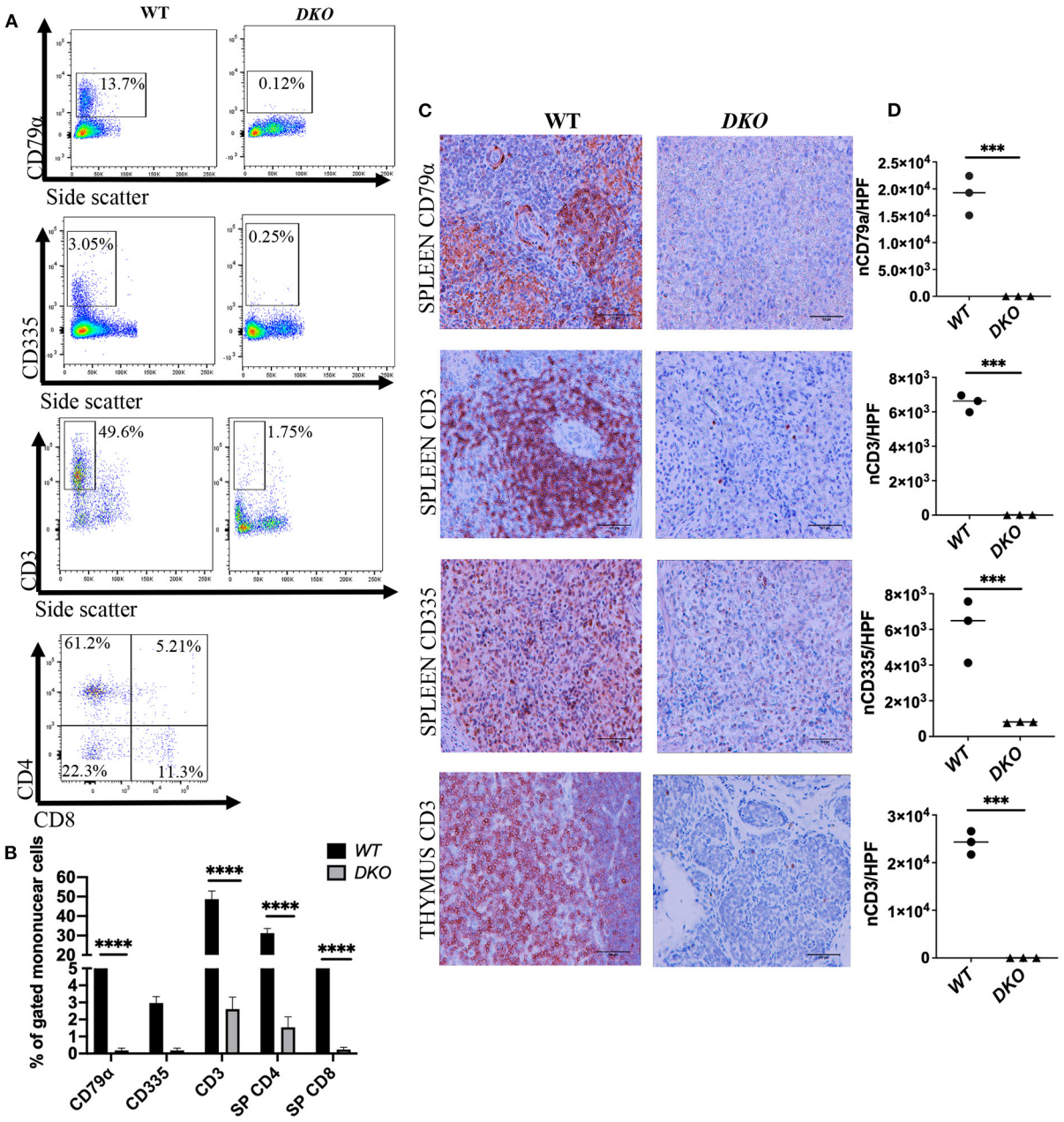

FIGURE 2
Lymphoid cell analysis of peripheral blood and lymphoid tissue from immunodeficient *DKO* pigs. **(A)** Representative peripheral blood flow cytometry analysis showing CD79α$^+$ cells, CD335$^+$ cells, CD3$^+$ CD4$^+$ cells and CD3$^+$ CD8$^+$ cells for wild type ($n = 3$) and *DKO* ($n = 4$) pigs at 1 week of age. CD79α$^+$, CD335$^+$, CD3$^+$ CD4$^+$, and CD3$^+$ CD8$^+$ are nearly undetectable in the peripheral blood of *DKO* pigs. **(B)** Histogram plot with bar of percentage from gated mononuclear cells for CD79α$^+$, CD335$^+$, CD3$^+$, CD3$^+$ CD4$^+$ and CD3$^+$ CD8$^+$ cells. Data represents mean, bars indicate standard deviation, and adjusted *p* values are represented for Tukey's multiple comparisons tests one-way ANOVA with a significance value of 0.05. **(C)** Representative immunohistochemistry (40x magnification) showing spleen staining for CD79α $^+$ (B cells), CD335$^+$ (NK cells), and spleen and thymus staining for CD3 (*T*-cells) for wild type ($n = 3$) and *DKO* ($n = 3$) pigs at 3 weeks of age. **(D)** scatter plot with individual values for the number of CD79α$^+$ (spleen), CD335$^+$ (spleen) and CD3$^+$ (thymus and spleen) cells per high power field microscopy. CD79α$^+$, CD335$^+$, and CD3$^+$ cells are nearly absent in the spleen, and CD3$^+$ cells are nearly absent in the thymus of *DKO* pigs. Line represents the mean, and adjusted *p* values are represented for unpaired two-sample *t*-test with a significance value of $P < 0.05$. ***$P < 0.001$, ****$P < 0.0001$.

expected, *IgH* rearrangement was detected in the spleen of wild type and allografted pigs, while absent in *DKO* pigs (Figure 4D). Together, these results demonstrated that *in utero* allogeneic stem cell transplantation can be used successfully to establish lymphoid allogeneic engraftment in *DKO* pigs.

10.3389/fvets.2022.965316

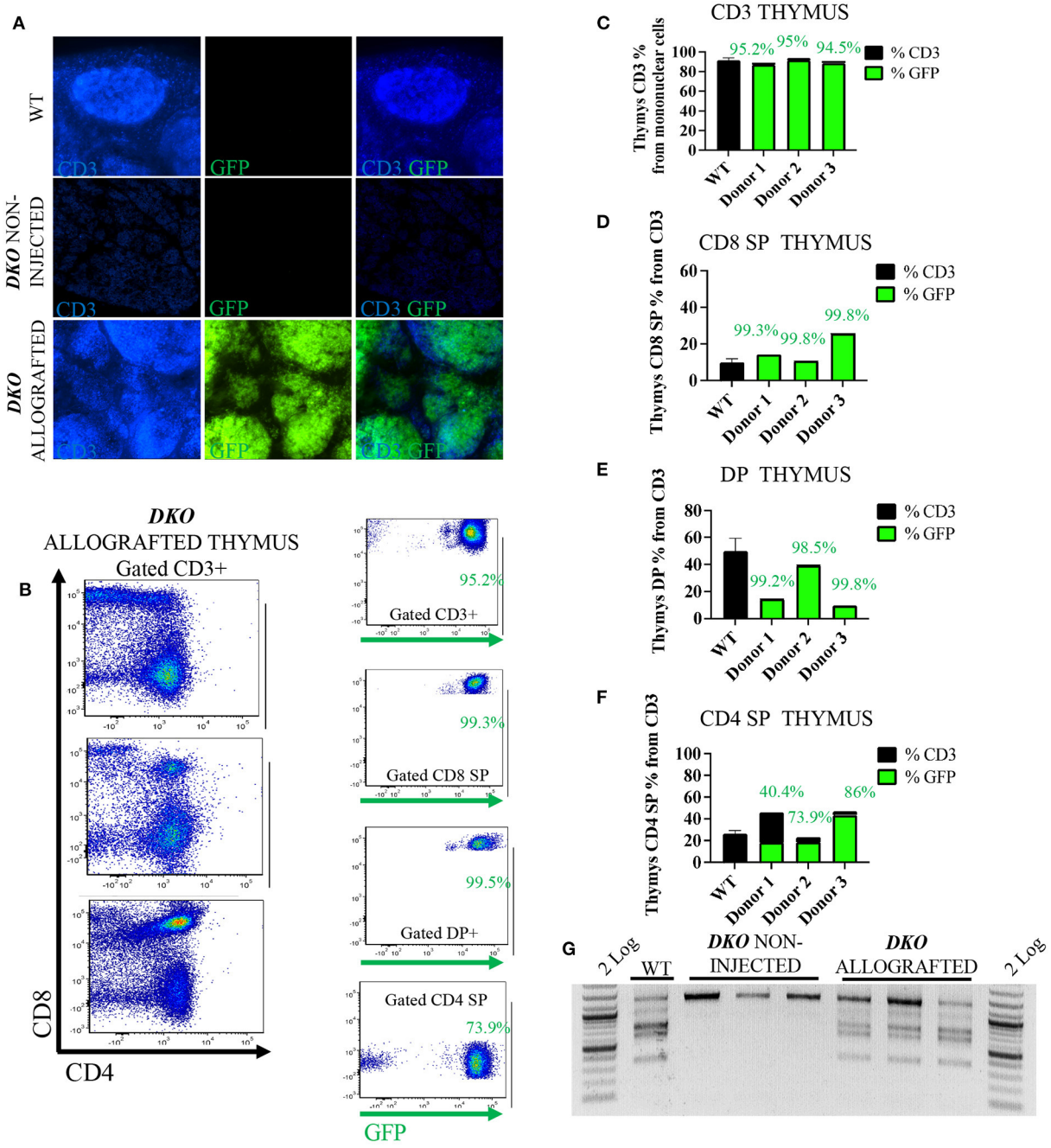

FIGURE 3
In utero allogeneic transplantation of pH2B-eGFP fetal liver cells restored *T*-cells and *TCR-β* recombination in the thymus of 1-week-old *DKO* pigs. **(A)** Immunofluorescence staining (20x magnification) for CD3 (blue), and pH2B-eGFP (GFP-green). Wild-type thymus contains CD3 positive cells, but not pH2B-eGFP (GFP) positive cells. Thymus of non-injected *DKO* pigs is negative for both CD3 and pH2B-eGFP cells. The thymus of allografted *DKO* pigs contains CD3 cells, all overlapping with pH2B-GFP positive cells. **(B)** flow cytometry plots from the thymi of three allografted *DKO* pigs, showing expression of CD4 and CD8 (gated on $CD3^+$ cells). Also shown are representative plots of GFP^+ $CD3^+$, $CD3^+CD8^+$, $CD3^+CD4^+CD8^+$ (DP) and $CD3^+CD4^+$ cells. **(C–F)** Histogram showing thymic percentage and chimerism of $CD3^+$ cells **(C)**, $CD3^+CD8^+$ cells **(D)**, DP cells **(E)** and $CD3^+CD4^+$ cells **(F)** from thymi of all three *DKO* allografted pigs, while a wild type ($n = 3$) serves as positive control. The green histogram represents the levels of pH2B-eGFP chimerism, indicating the percentage of allograft donor-origin cells from the respective population. **(G)** PCR assay for the identification of rearranged *TCR-β* locus from thymus gDNA. Non-injected *DKO* pig thymus served as a negative control and a wild type as the positive control. All three allografted pig thymi display rearranged *TCR-β* locus.

10.3389/fvets.2022.965316

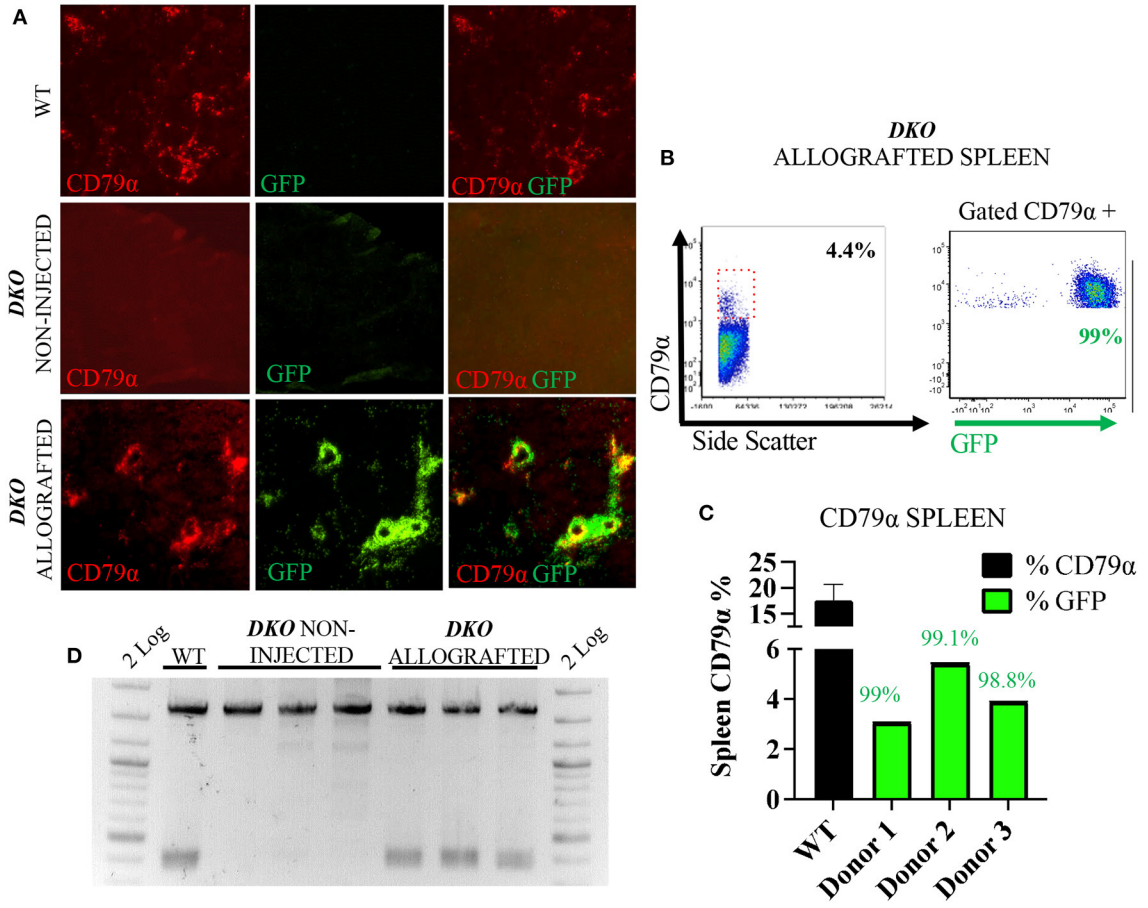

FIGURE 4
In utero allogeneic transplantation of pH2B-eGFP fetal liver cells restored B cells and *IgH* recombination in the spleen of 1-week-old *DKO* pigs. **(A)** Immunofluorescence staining (20x magnification) for CD79α (red), and pH2B-eGFP (GFP-green). Overlay images are also represented. Wild-type spleen contains CD79α+ cells, but not pH2B-eGFP positive cells. Spleen of non-injected *DKO* pigs is negative for both CD79α+ and pH2B-eGFP cells. The spleen of allografted *DKO* pigs contains CD79α+ cells, all overlapping with pH2B-eGFP cells. **(B)** Representative flow cytometry plot from *DKO* allografted spleen showing expression of CD79α. A red box indicates the CD79α positive cells within the spleen. Representative flow cytometry of gated CD79α+ cells expressing pH2B-eGFP is also shown. **(C)** Histogram showing the percentage of CD79α+ cells from the spleen of all three *DKO* allografted pigs, while wild type ($n = 3$) serves as a positive control. Green histogram represents the levels of pH2B-eGFP chimerism, indicating the percentage of allograft donor-origin cells in the CD79α+ population. **(D)** PCR assay for the identification of rearranged *IgH* locus from spleen gDNA. Non-injected *DKO* spleen serve as negative controls, and a wild type as a positive control. All three allografted piglets display *IgH* rearranged locus.

Human lymphoid cells in cord and peripheral blood from Xenografted *DKO* pigs

Next, we investigated if *DKO* pigs could engraft with human hematopoietic stem cells using the same transplantation method with higher total cell dose/fetus. Cord blood was collected from control and xenografted *DKO* pigs at birth and analyzed *via* flow cytometry. Human peripheral blood ($n = 3$) was used as a reference. *DKO* non-injected ($n = 4$) and wild type pigs served as negative controls. Of the seven *DKO* fetuses injected with human hematopoietic stem cells, four had a detectable (>1.0%) population of human $CD45^+$ cells at birth, with percentages differing statistically from *DKO* non- injected ($n = 3$) ($p = 0.0128$) (Figures 5A, 6A). Engraftment ranged from 3 to 4%. Human CD3 staining showed detectable human $CD3^+$ cell percentages that did not differ statistically ($p = 0.14$) from *DKO* non-injected levels, although it differed on cell number/100 ul of blood ($p = 0.0261$) (Figures 5B, 6B). Phenotypic characterization of human CD3 cells revealed the presence of human double negative, hDP ($CD3^+CD4^+CD8^+$) and human single positive *T*-cells, (hCD4 SP ($CD3^+CD4^+CD8$-), hCD8 SP ($CD3^+$ CD4-$CD8^+$) (Figures 5C, 6C–F). When compared to human adult peripheral blood, xenografted pigs had higher percentages of hCD8 SP and hDN *T*-cells compared to adult human peripheral blood ($p = 0.0103$ and $p = 0.0015$, respectively) (Figures 5C,

10.3389/fvets.2022.965316

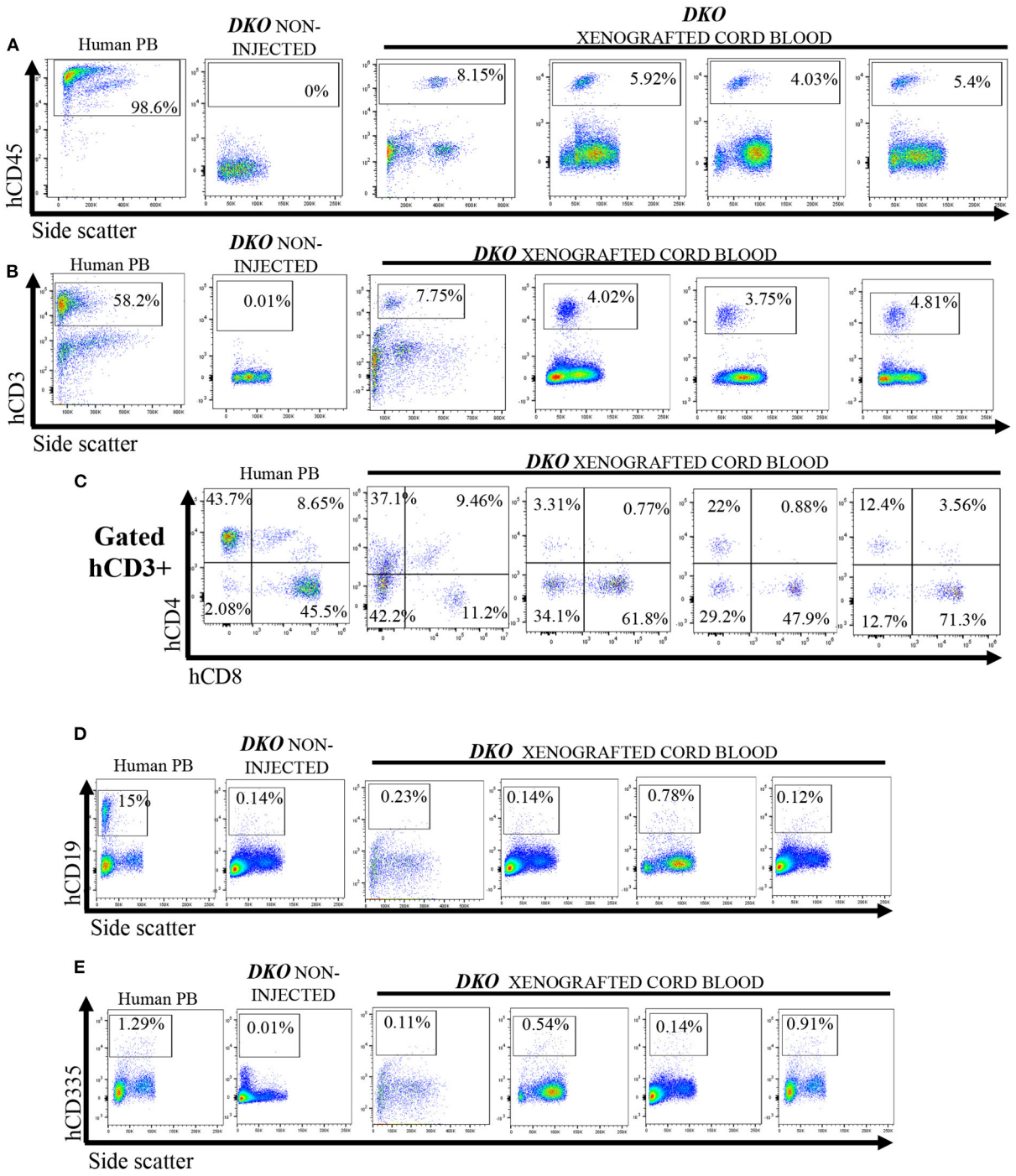

FIGURE 5
Cord blood flow cytometry analysis for human *T*-cells, B cell and NK cells from non-injected and xenografted *DKO* pigs. Flow cytometry analysis for human lymphoid cells in cord blood from xenografted pigs ($n = 4$). Peripheral human blood served as positive controls, while non-injected *DKO* pigs ($n = 4$) served as negative controls. All xenografted pigs ($n = 4$) showed; **(A)** A distinct hCD45 population of circulating mononuclear cells. **(B)** A hCD3 population of circulating cells with similar percentages as hCD45 cells. **(C)** Expression of hCD4 and hCD8 among $hCD3^+$ cells, presence of SP hCD4 and SP hCD8, DN and DP. **(D)** Xenografted *DKO* pigs showed nearly undetectable levels of hCD19 (B-cells) and a small but significant ($P < 0.05$) presence of hCD335 **(E)** cells when compared to non-injected *DKO* pigs. Only one representative non-injected animal and human peripheral blood (PB) sample is shown.

10.3389/fvets.2022.965316

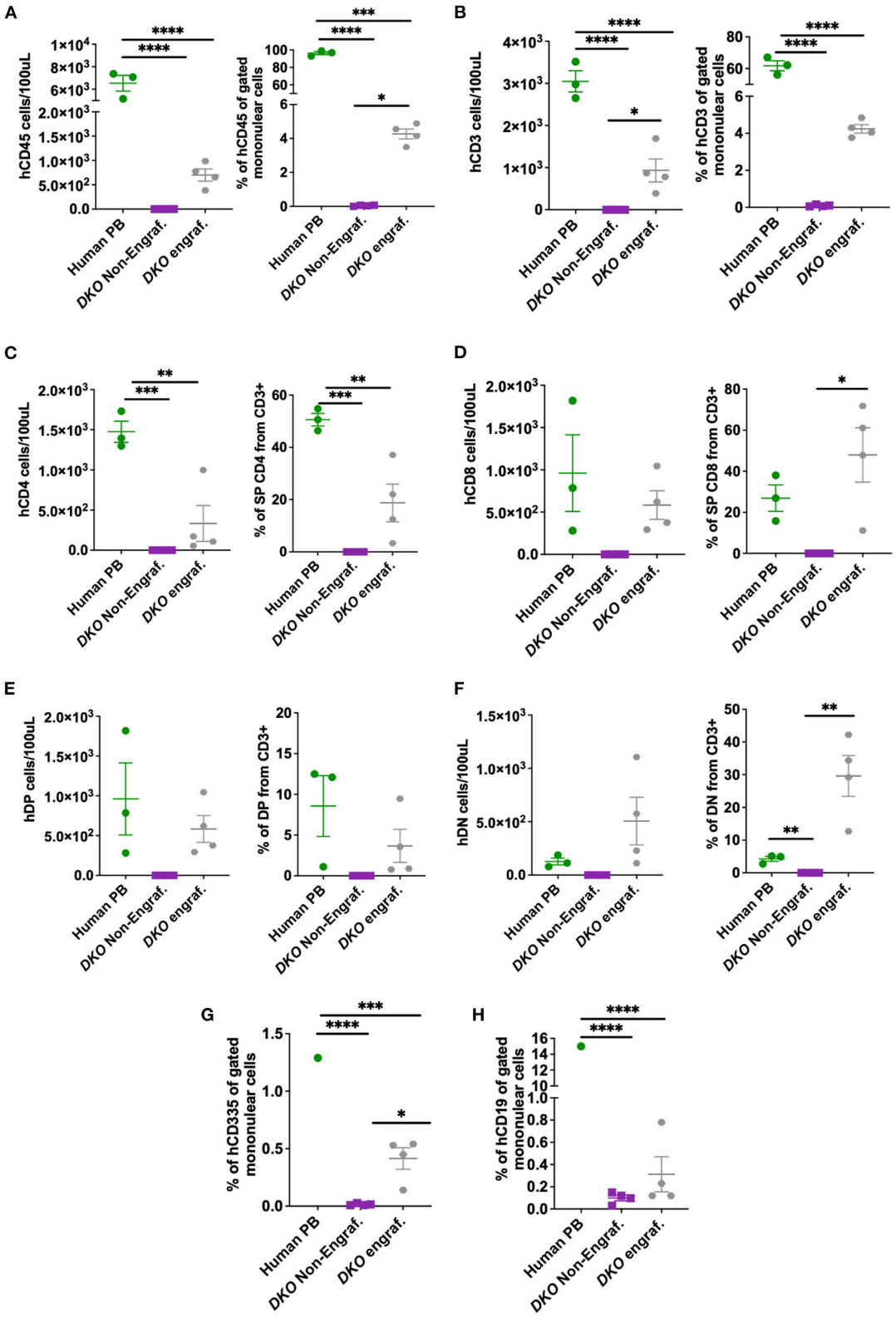

FIGURE 6
Cell number and percentage quantification of cord blood flow cytometry data from *DKO* xenografted pigs. **(A–F)** Scatter plot showing number of human cells/100 μL and percentage from mononuclear cell (from $CD3^+$ for T subsets) or pig cord blood for human CD45, human CD3, human CD4, human CD8, human double positive (hDP) and human double negative (hDN) *T*-cells. Human blood served as positive control while the blood of non-injected *DKO* pigs served as a negative control. The line represents the mean, and adjusted *p* values are represented for Tukey's multiple comparisons tests one-way ANOVA with a significance value of $P < 0.05$. **(G,H)** Scatter plot showing human CD335 and CD19 percentage from mononuclear cells. *$P < 0.05$, **$P < 0.01$, ***$P < 0.001$, ****$P < 0.0001$.

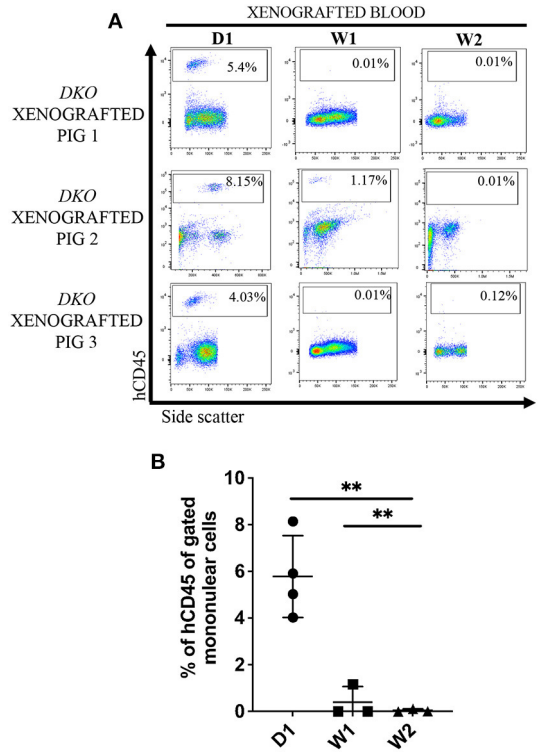

FIGURE 7
Postnatal clearance of human cells from the peripheral circulation in *DKO* xenografted pigs. **(A)** Flow cytometry analysis of peripheral blood and bone marrow for human CD45$^+$ cells at birth ($n = 1$), 1 week ($n = 1$), and 2 weeks ($n = 1$) of age of three *DKO* xenografted pigs. While significant hCD45 cells were detectable at birth they reached nearly undetectable levels between 1 and 2 weeks of life. **(B)** Scatter plot showing the data presented in **(A)**. Data represent individual values for the percentage of human CD45 from mononuclear cells, line represents the mean, and adjusted *p* values are represented for Tukey's multiple comparisons tests one-way ANOVA with a significance value of 0.05. *$P < 0.01$.

6C–F). Interestingly, cord blood of *DKO* pigs showed detectable (different from *DKO* non-engrafted, $p = 0.0127$) levels of human NK cells (CD335), while having nearly undetectable levels of human B cells (CD19$^+$). Taken together, these results suggest *DKO* pigs sustain restricted human *T*-cell lineage engraftment after *in utero* hematopoietic stem cell transplantation.

Next, we set out to investigate the sustained presence of human lymphoid cells in peripheral blood of *DKO* pigs up to 3 weeks post birth. Peripheral blood from xenografted *DKO* pigs collected at 1 week ($n = 3$) and 2 weeks ($n = 3$) of age contained a detectable but decreasing frequency of human CD45$^+$ cells (mean of 0.39% at 1 week and 0.12%, at 2 weeks) being nearly undetectable by 2 weeks of age ($p = 0.0011$) (Figures 7A,B). These results suggest the presence of a post-natal barrier to persistence and/or expansion of human hematopoietic cells.

Analysis of thymi from xenografted *DKO* pigs

Next, we examined the thymi of xenografted *DKO* pigs for the presence of human leukocytes. While histological analysis of xenografted *DKO* thymi showed poorly developed cortical zones and large medullary regions (Figures 8A,B), human CD45 staining confirmed the robust presence of human cells (Figure 8C). *T*-cell phenotype frequencies (hCD3, hCD4, hCD8, hDN and hDP) of xenografted thymi was compared to thymi of age-matched wild type pigs using pig specific antibodies (pCD3, pCD4, pCD8, pDN and pDP). Human CD3$^+$ cells were detected at high frequencies at all-time points analyzed (Figure 9A). No differences were seen in frequencies of xenografted human hCD4 SP and hCD8 SP *T*-cells when compared to wild type pig CD4 SP ($p = 0.11$) and pig CD8 SP cytotoxic *T*-cells ($p = 0.22$) (Figures 9B–D). Xenografted pigs, however, displayed decreased frequencies of hDN *T*-cells compared to wild type pig DN *T*-cells ($p = 0.02$) as well as decreased frequencies of hDP double positive *T*-cells compared to wild type pig DP double negative *T*-cells ($p = 0.0002$) (Figures 9B,E,F).

To demonstrate that the thymi of xenografted *DKO* pigs can sustain human *T*-cell thymopoiesis, we examined for the presence of *T*-cell receptor excision circles (TREC) in the thymus at day 1 ($n = 1$), week 2 ($n = 1$), week 3 ($n = 1$), and cord blood ($n = 3$). Human TRECs were not detected in cord blood of xenografted *DKO* pigs ($n = 3$), even though these animals contained significant numbers of human *T*-cells at birth. However, human TRECs were detected in the thymus of xenografted *DKO* pigs at all stages examined.

Spleen and bone marrow analysis of Xenografted *DKO* pigs

Since human *T*-cell development clearly occurred in the newborn thymus but human *T*-cells were scarce in the periphery of *DKO* pigs, we further asked whether xenograft persistence could be lymphoid tissue dependent. To answer this question, we studied the spleen and bone marrow of xenografted TKO for the presence of human CD45$^+$, CD3$^+$ (and co-expression of CD4 and CD8), human CD19$^+$ and CD335$^+$ cells. Human CD45$^+$ and CD3$^+$ cells were present in the spleen and bone marrow at birth, but human CD19$^+$ and human CD335$^+$ were nearly undetectable. Similarly, to peripheral blood analysis, the number of human *T*-cells in the spleen and bone marrow decreased after birth (Figures 10A,B). Lastly, we decided to demonstrate that human CD45$^+$ cells were present in the spleen *via* immunofluorescence. As expected, human CD45$^+$ cells were present in the spleen of xenografted *DKO* at day 1 but absent in the spleen of xenografted *DKO* at week 2. When compared to aged-matched WT spleen stained with

10.3389/fvets.2022.965316

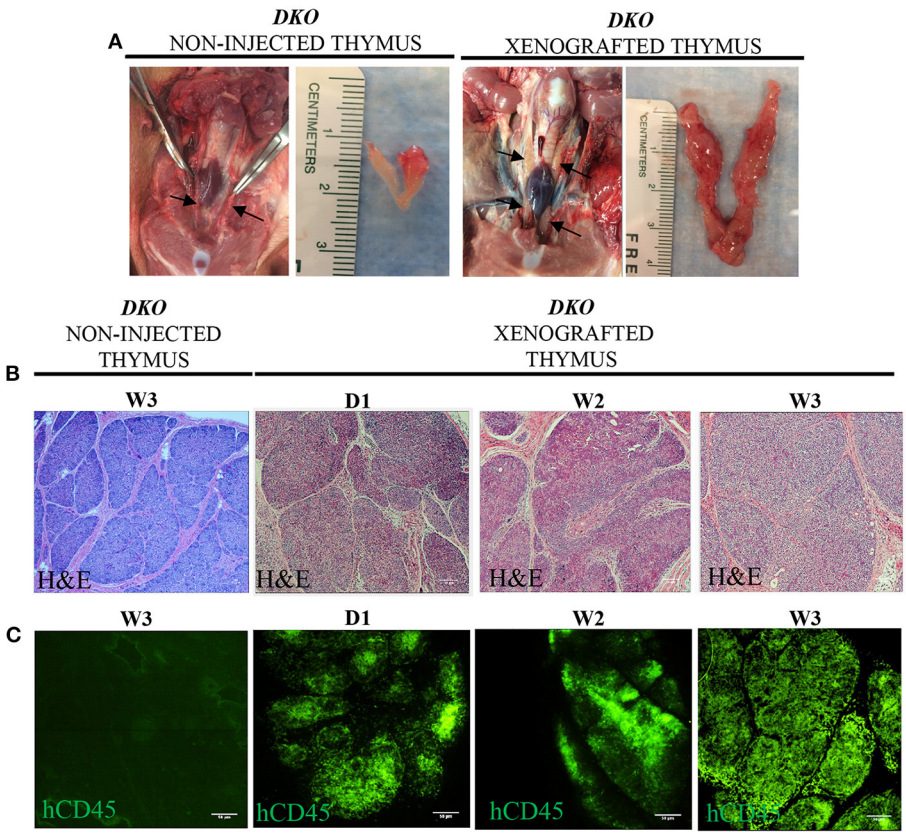

FIGURE 8
Macroscopic, microscopic and human CD45 immunofluorescence staining in the thymi of xenografted *DKO* pigs. **(A)** Representative macroscopic anatomy images of the thymus of non-injected and xenografted pigs. The xenografted thymus was noticeably expanded and larger than the non-injected thymus. **(B)** H&E histological structure (20x magnification) of thymi from non-injected pigs at 3 weeks and the thymi of three xenografted pigs at birth ($n = 1$), two ($n = 1$), and 3 weeks ($n = 1$) of age. **(C)** Immunofluorescence staining for human CD45$^+$ cells with FITC conjugated antibodies is also shown. Non-injected thymus served as a negative control, showing no cross-reactivity.

pCD45, pCD45 staining showed an expected multifocal pattern resembling lymphoid structure. In contrast, hCD45 staining in the spleen of xenografted *DKO* pig at day 1 displays a different pattern, with human CD45 cells surrounding areas that resemble large vascular structures (Fiugre 10C). Taken together, these results suggest the presence of post-natal barriers present in lymphoid tissues (other than the thymus) impeding persistent survival of human cells in xenografted *DKO* pigs.

Discussion

Human hematopoietic stem cells have been introduced into mature and fetal pigs, but engraftment in immunocompetent pigs has been so low that it could only be detected by PCR or by *in situ* detection of human Alu sequences (33). Previously we used *in utero* hematopoietic stem cell transplantation of human *T*-cell-depleted bone marrow and umbilical cord blood into wild type pig fetuses, leading to low human *T*-cells present in peripheral blood with a marked decline in chimerism within 1 week from birth (33). One report showed presence of human cells using flow cytometric analysis (36) and identified human cells in the thymus (1.6% hCD45) and bone marrow (1.1% hCD45) of a fetus injected with human CD34$^+$ cells at D35 of gestation and collected at D90 of gestation. Peripheral blood levels of human CD45 at birth were 0.58% and there was no evidence of B cell or NK cells. Collectively these reports demonstrate that, while immunocompetent pigs can sustain human lymphoid lineage engraftment after *in utero* hematopoietic stem cell transplantation, the level of engraftment is too low to be of practical use. Suzuki et al. (15) described successful allogeneic postnatal bone marrow transplantation of *IL2RG* knock-out pigs. In this study, successful engraftment was established with and without conditioning, resulting in variable T, NK and B cell engraftment, and consequently, increased lifespan of certain animals when compared to non-injected controls.

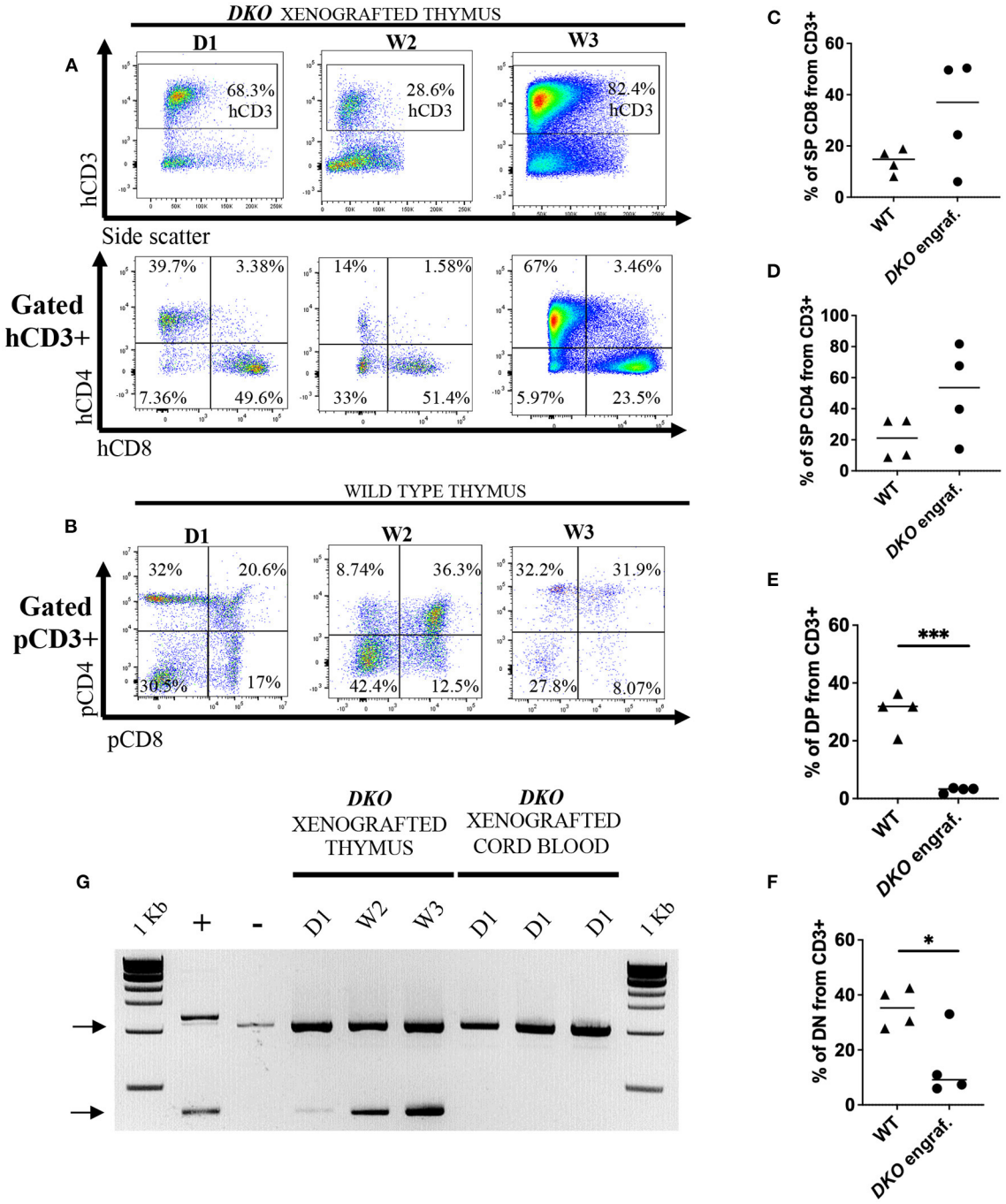

FIGURE 9
Sustained human engraftment of the thymus in *DKO* xenografted pigs. **(A)** Flow cytometry analysis from xenografted *DKO* pig thymi for hCD3, hCD4 and hCD8 from birth to 3 weeks of age. In contrast to peripheral blood and spleen, where human cells were undetectable by 2 weeks of age, in the thymus, robust engraftment could still be detected at 3 weeks of age. There were no changes in the distribution of SP hCD4, SP hCD8 with age. **(B)** Flow cytometry plots of wild-type pig thymi showing pig CD4 and pig CD8 expression in age-matched wild-type pig thymi. **(C–F)** Scatter plot with individual values for percentages (from $CD3^+$) of pig (WT) and human (xenografted) $CD3^+$ $CD8^+$ **(C)**, $CD3^+$ $CD4^+$ **(D)**, DP **(E)** and DN **(F)** from wild type and xenografted thymi, respectively. Line represents the mean, and adjusted *p* values are represented for unpaired two-sample t-test with a significance value of 0.05. **(G)** PCR assay with human primers specific for identification of human TREC (~400 bp). Pig *IL2RG* amplicon served as internal primer control (~1 Kb) (Top black arrow). Each PCR reaction contains 50 ng of gDNA. Human peripheral blood mobilized stem cells gDNA served as positive control (+), while gDNA from the thymus of a non-injected *DKO* pig served as negative control (–). Samples tested include thymus from xenografted pigs (birth, 2 weeks, and 3 weeks), and gDNA from cord blood of xenografted *DKO* pigs at birth (when human cells were detected *via* flow cytometry).

10.3389/fvets.2022.965316

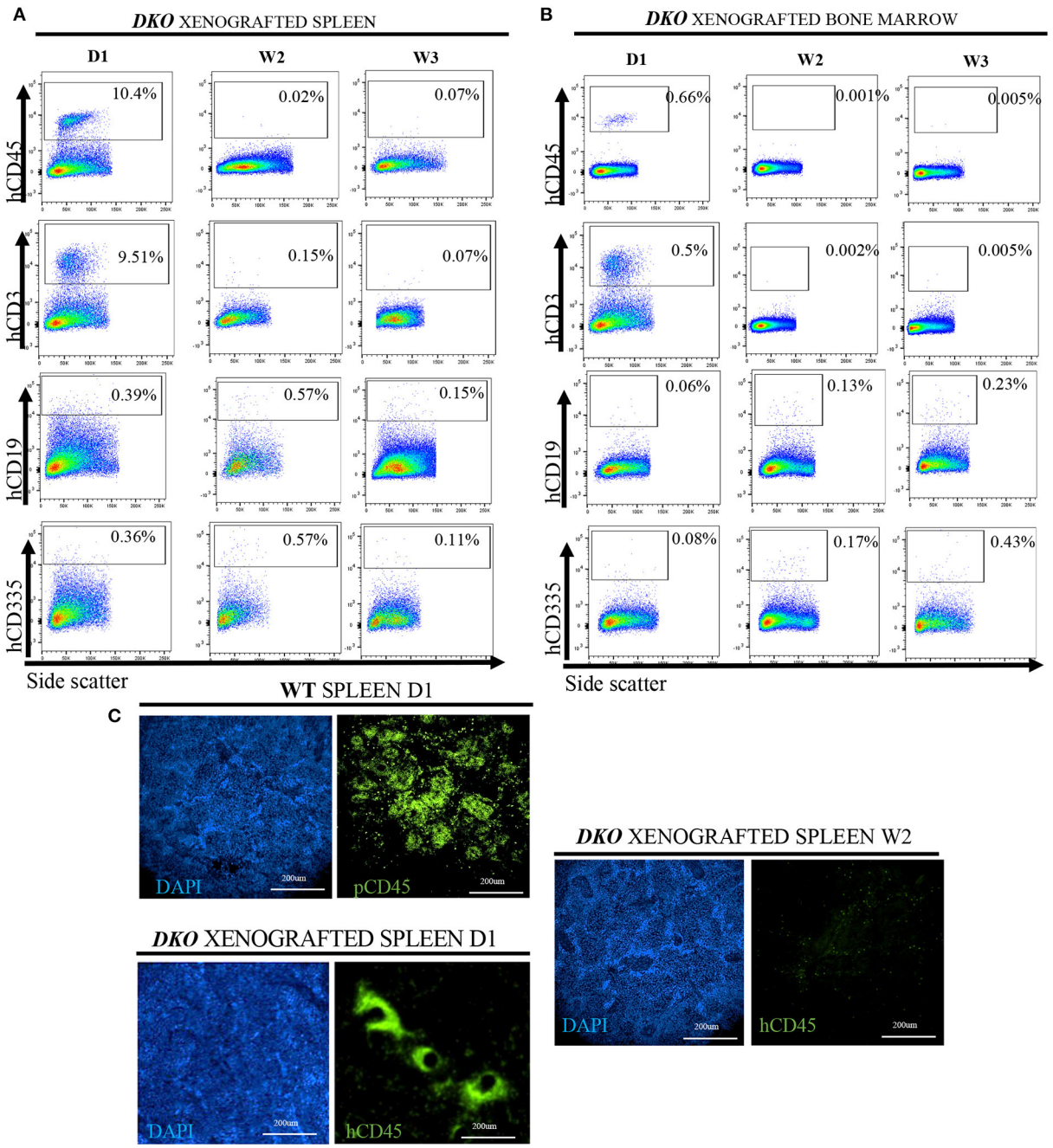

FIGURE 10
Postnatal clearance of human cells from the spleen and bone marrow of xenografted *DKO* pigs. Flow cytometry analysis for the presence of human CD45$^+$, human CD3$^+$, human CD19$^+$ and human CD335 (versus side scatter) in the spleen **(A)** or bone marrow **(B)** of xenografted *DKO* pigs from birth to 3 weeks of age. Human CD45$^+$ and human CD3$^+$ cells were identified in the bone marrow and spleen of a *DKO* pig at birth but became undetectable between 2 and 3 weeks of age. Few, if any, hCD19 or hCD335 were detected at any stage of analysis. These data parallels that seen in circulating cells. **(C)** Detection and the overall organization of CD45+ cells in the spleen (20x magnification) of WT (pCD45) ($n = 1$) and xenografted *DKO* (hCD45) ($n = 1$) at day 1, and week 2 ($n = 1$). Human CD45$^+$ cells were detected at day 1 but not at week 2 in *DKO* xenografted pigs, consistent with the clearance observed *via* flow cytometry. Immune-competent WT pig spleen staining with pig-specific CD45 antibodies showed multifocal distribution of pig CD45, as expected. In contrast, xenografted *DKO* day 1 spleen showed a different pattern, with human CD45 cells surrounding areas that resemble large vascular structures.

A separate study continues the steps of developing immunodeficient pigs for allogeneic and xenogeneic transplantation studies. Lee et al. (17) generated and characterized a *RAG2* deficient transgenic pig model, and demonstrated successful engraftment of human iPSC and allogeneic trophoblast stem cells. A *DKO* pig model has been described by Lei et al. (20) using direct injection of CRISPR/Cas9 system in developing embryos; no stem transplantation studies were performed. Importantly the immunodeficient phenotype or the *DKO* model described here is consistent with the results of Lei et al. (20) showing marked reduction in peripheral blood B, T and NK cells, while also showing poor lymphoid tissue development. To our knowledge, this is the first report carrying out allogeneic and xenogeneic stem cells *in utero* transplantation in a IL2RG/RAG2 *DKO* pig model.

Using gene-edited pigs lacking *IL2RG* and *ART*, Boettcher et al. (22) demonstrated successful establishment of an immunodeficient phenotype, with main lymphoid cells nearly undetectable in peripheral blood and lymphoid tissue, resembling the model reported by Lei et al. (20) and our group. Boettcher et al. (22) further carried out post-natal allogeneic SLA matched bone marrow transplantation, as well as *in utero* hematopoietic stem cell xenotransplantation. Using SLA matched bone marrow (female donor, 4y) and intravenous infusion into a 5 days old male *IL2RG*/*ART* null piglet, they reported successful allogeneic engraftment of T and NK cells but limited to no B cell engraftment. Overall chimerism was monitored and maintained for at least 4 months. Major differences with the present hematopoietic allogeneic transplantation study include (a) *DKO* vs. *ART* $^{-/-}$*IL2RG* $^{y/-}$; (b) SLA mismatched vs. SLA matched; and (c) postnatal bone marrow donor HSC vs. fetal liver HSCs.

In the *DKO* background, our results show sustained allogeneic engraftment of SLA mismatched pH2B-eGFP-tagged fetal liver mononuclear cells containing hematopoietic stem cells. There are seven classical class I genes and three non-classical class I genes mapped to the SLA complex. The constitutively expressed classical *SLA* class I genes are *SLA-1*, *SLA-2* and *SLA-3*, while the rest are pseudogenes. SLA class II loci in the pig include *DRB1*, *DQA, DQB1, DOB1, DMB, DMA, and DOA* (28). In humans, histocompatibility testing between unrelated donors and recipients prior to hematopoietic stem cell transplantation is performed for five loci: *HLA-A, -B, -C, -DRB1*, and *DQB1*. Optimal transplantations are defined as 10/10, a perfect match between the critical 5 *HLA* locus cited above between donor and recipient. 8/8 refers to high-resolution matching at four of the loci. Minimum requirements for adult bone marrow and peripheral blood mobilized cells transplantation are 6 of 8 loci matches for *HLA-A, -B, -C* and *DRB1* (37). In addition, the presence of donor antigens or alleles not shared by the recipient determines host vs. graft allorecognition, while the presence of recipient alleles or antigens not shared by the donor determines graft vs. host allorecognition, both individual scenarios are classified as unidirectional mismatch and may lead to failure of engraftment (38). In addition, both scenarios may occur simultaneously between a single donor and recipient (each one having an allele that the other one does not have), leading to a bidirectional mismatch and failure of engraftment (38). All three cell donors were classified as poor donors, since a perfect match was not observed for SLA-1, 2, 3 and DRB1 and DQB1. The lack of B cell, CD8 SP and DP cells in *DKO* pigs allowed substantial engraftment of these lineages (Figures 3, 4). Variable mix of host and donor cells was observed within the CD4 SP cell population (Figure 3F). We further demonstrated that rearranged *IgH* and *TCR-β* could be detected post transplantation in the spleen and thymus of allografted pigs, respectively. Taken together, these data reflect the immunodeficient phenotype of the *DKO* pig model, and its ability to engraft with SLA-mismatched allogeneic cells, while also highlighting the utility of the pH2B-eGFP model. Further, an in-utero stem cell transplantation approach may take advantage of the tolerant immunologically privileged status of the fetus and represents an alternative large animal model for *in utero* clinical therapies of immunodeficiency disorders (39). It is also important to note the limitations of our allogeneic studies as due to technical difficulties, we were not able to investigate allogeneic engraftment in peripheral blood nor did we examine myeloid or sustained long-term engraftment.

Notable, similar to our transplantation study, Boettcehr et al. (22) also reported *in utero* cord blood derived human CD34^{+} stem cell transplantation in *IL2RG* $^{-/-}$*ART* $^{-/-}$ fetuses. They reported a total of three piglets, one euthanized at birth and two euthanized at day 1, with only two showing any significant engraftment and the third low to no engraftment (<1%). Thus, their results are based on two observations. Their approach differs not only in the mutant genetic background used but also on the source of human hematopoietic cells. While we used CD34^{+} enriched from peripheral blood of normal donors, Boettcher et al. (22) used in vitro cultured and expanded CD34 cells. They also report a smaller number of xenografted animals (2 vs. 4) and the longer period the examined engraftment was one day vs. 3 weeks in this report. However, similar to our results, they reported that the two engrafted piglets displayed evidence of human CD45^{+} cell engraftment in peripheral blood and lymphoid organs. Human CD45^{+} cells were predominantly CD3^{+} cells, with one animal displaying human *T*-cell levels of 63% in the thymus.

Using the *DKO* mutant genetic background, we confirm and extend these observations and demonstrate that *in utero* hematopoietic stem cell transplantation of peripheral blood mobilized human CD34^{+} cells into *DKO* pig fetuses result in never before reported levels of engraftment ranging from 80% at week 3 (thymus) (Figure 9) to 8% (cord blood) (Figures 5, 6). To our knowledge, this is the highest human hematopoietic engraftment achieved in a pig model. While

significant engraftment with human cells was detected, the pattern of engraftment varied from that seen in an immune-competent human or wild-type pigs. In the xenografted pigs, T-cells were identified in blood, spleen and thymus at birth. In contrast, B and NK cell production was minimal, if any. In addition, examination of CD4 and CD8 populations revealed a shift when compared with human or immunocompetent pigs. As shown in Figures 5, 6, there was a significant increase in peripheral blood DN CD4 CD8 cells in the xenografted animals compared to normal human peripheral blood. In the thymus, in contrast, the opposite was true, with the xenografted thymus having a low population of DN and DP *T*-cells compared to wild type thymus (Figure 9). This could reflect hastened maturation or uncoordinated early development.

TRECs are generated during V(D)J gene recombination, a process responsible for the diversity of *T*-cell antigen receptor (TCR) repertoire. This complex end-to-end fusion of gene segments is mediated by recombination-activating genes *RAG1/2* that recognize "heptamer–spacer–nonamer" recombination signal sequences (RSSs) flanking each V, D and J gene segment. Generation of a coding TCR chain results in the excision of extrachromosomal DNA circles (TREC). Therefore, its identification correlates with *T*-cell differentiation (33, 40). We selected previously reported human-specific primers capable of detecting *TCRδ* to *TCRα* recombination ($\delta Rec\text{-}\Psi J\alpha$), since $\delta Rec\text{-}\Psi J\alpha$ represents ∼67% of recombination events (41, 42). All the thymi from xenografted animals showed the presence of TRECs. As duplication of TREC circles within replicating mature *T*-cells does not occur (43), the presence of human TREC suggests the pig thymus can sustain de novo human *T*-cell thymopoiesis. Together these results indicate that while the thymus of *DKO* pigs accept *T*-cell precursor cells and support development of phenotypically mature *T*-cells, mature *T*-cells are either not released from the thymus or are released but rapidly cleared in the periphery. Further, by contrasting the results to peripheral blood human leukocyte clearance, it may suggest that the *DKO* thymus is an immunological safe niche for the presence of human leukocytes.

It should be noted that the xenografted profile of *DKO* pig differs considerably from the $RAG2^{-/-}Il2RG^{y/-}$ mouse. While in the *DKO* pig, the engraftment is essentially T-cell driven in all tissues examined, in mice, B-cells predominate over T-cells (2-3X higher), and in the thymus, the T- cell population is dominated by double positive cells (>70%). This is drastically different in the *DKO* pig with SP CD4 and SP CD8 being the two main T-cell populations seen in thymus at all stages examined. Although the thymi of xenografted *DKO* pigs displayed lower frequencies of DP and DN *T*-cells when compared to age matched wild type pig thymus, detection of human TREC is suggestive that human *T*-cell development can proceed to the generation of human T-cells (or at least initiate to that stage). The mouse thymus does not support maturation of human T-cells and requires the presence of human or pig fetal thymic tissue (44, 45). Our observations confirm human T-cell development in a pig thymus (45).

Also, the xenogeneic transfers used enriched CD34 cells and allogeneic transfers utilized fetal liver cells as a source of hematopoietic stem cells as reliable pig CD34 antibodies are not available. Notwithstanding this donor source difference, the data shows that allogeneic $CD34^+$ can generate all lymphoid lineages while xenogeneic HSC can only generate T-cells. Thus, the lack of B-cells in the *DKO* pig suggests that the cytokines responsible for controlling proliferation and/or differentiation of $CD34^+$ HSC into B or NK cells are incompatible between pigs and humans. In mice, some of these deficiencies have been overcome by the humanized MISTRG mice that express the human factors M-CSF, IL-3, SIRP-a, GM-CSF and TPO (46). This strain yields significantly higher engraftment of human bone marrow cells and produces more functional NK cells, T and B cells. We feel that a similar approach will also improve the development of B and NK cells in the *DKO* pig. It is also important to note the limitations of our xenogeneic studies, as our study did not examined for the presence of human myeloid and RBC cells, human bone marrow $CD34^+$ in pigs bone marrow, testing of different sources of human $CD34^+$ cells (cord blood, bone marrow), or presence of human T regulatory cells in the thymi of xenografted pigs.

An additional issue in the *DKO* pig is the rapid clearance of human cells from peripheral blood and spleen soon after birth, suggesting non-lymphoid barriers to human engraftment. The one exception was the thymus capable of sustaining never reported before levels of human CD3 engraftment (up to 82.4% at 3 weeks). The reason for this clearance remains unexplained but could be due to incompatibilities between SIRP-α and CD47. Incompatibility between CD47 and SIRP-a results in phagocytosis of donor cells by host macrophages. Expression of human SIRP-α in immunodeficient mice abolishes this incompatibility and results in higher human cell engraftment and mobilization (47). In addition, it has been shown that pig CD47 does not interact with human SIRP-α (48) and others have shown that expression of human CD47 in pig cells increases engraftment in a mouse model of pig-to-human transplantation (49). Boettcher et al. (50), however, has shown that there is at least partial binding between the two molecules with an increase in phagocytosis on human cells by pig monocytes from 5% in controls to 20% when using antibodies that block the CD47 and SIRP-α interaction. We are now examining this in more detail to determine the role of CD47-SIRP-α incompatibility in the rapid clearance of human cells in the xenografted *DKO* pigs.

In conclusion, while hematopoietic engraftment in an immunodeficient pig has been reported before using a *IL2RG/ART* null pig (22), this is, to our knowledge, the first report that demonstrates prolonged engraftment (3 weeks vs. one day), rapid clearance of human cells postnatally, and the presence of human TRECs supporting de novo T-cell development in the thymus. In addition, we present

novel data not previously reported in either allogeneic or xenogeneic transplantation in a *RAG/IL2RG* null (*DKO*) pig. This model can be used for understanding the limitations of *in utero* hematopoietic stem cell transplantation of human $CD34^+$ cell engraftment, and also as a first step toward improving transplantation of human stem cells from different tissues/sources for generation of chimeric human tissues and organs for xenotransplantation applications in a large animal model.

Data availability statement

The original contributions presented in the study are included in the article/Supplementary material, further inquiries can be directed to the corresponding author.

Ethics statement

This study was carried out in strict accordance with the recommendations in the Guide for the Care and Use of Laboratory Animals of the National Institutes of Health. The animals used in this study were obtained from a university-owned herd, and all animal procedures were approved by the Institutional Animal Care and Use Committee of North Carolina State University (Raleigh, NC).

Author contributions

RS and JAP: conception and design, acquisition of data, analysis and interpretation of data, and drafting of manuscript. OL, JP, TK, and KP: conception and design, acquisition of data, analysis, and interpretation of data. LG: conception and design and acquisition of data. LB: analysis and interpretation of data. SS, KG, XZ, BC, YM, and JLP: acquisition of data. JLP: conception and design, interpretation of data, and drafting of manuscript. All authors contributed to the article and approved the submitted version.

Funding

Funding provided by NIH grants R01-OD023138 and R01HL051587 to JAP and JLP.

Acknowledgments

We are thankful for the support and hard work of the North Carolina State University Lab Animal Resources, Veterinary Services, and Flow Cytometry Core Facility.

Conflict of interest

The authors declare that the research was conducted in the absence of any commercial or financial relationships that could be construed as a potential conflict of interest.

Publisher's note

Supplementary material

The Supplementary Material for this article can be found online at: https://www.frontiersin.org/articles/10.3389/fvets.2022.965316/full#supplementary-material

SUPPLEMENTARY FIGURE 1
Enrichment systems for *IL2RG* and *RAG2* genome targeting in somatic cell porcine fetal fibroblast. **(A)** Schematic representation of nuclease reported vectors (pSSA) for modification of *IL2RG*. *IL2RG* TALEN reported vector contains GFP gene split into two inactive fragments containing overlapping homologies with the TALEN site between them flanked by *NheI* and *EcoRI* restriction sites. In cells, cleavage at the TALEN site will initiate single strand annealing and generate an active GFP gene. **(B)** Fluorescence activated cell sorting analysis to enrich for *IL2RG* edited fetal fibroblast lines. Negative controls group include no vector (−) and pSSA only, while pMAX served as GFP control (+), GFP+ cells from pSSA + *IL2RG* TALEN group (4.2%) were sorted for generation of single cell colonies. *IL2RG*$^{-/y}$ cells were screened and selected for a second round of somatic cell nuclear transfer, followed by fetal fibroblast isolation and subsequent *RAG2* editing. **(C)** Schematic representation of reporter plasmid used for enrichment of *RAG2* modification, containing CMV promoter, RPF, *RAG2* CRISPR-Cas9 gRNA target binding site (flanked by *EcoRI* and *BamHI*) followed by 2A peptide and hygromycin fused with GFP. Cells were treated with 2 mg/ml hygromycin for 48 h, 48 h post-transfection. **(D)** Schematic representation of the *RAG2* pig locus, the red line indicates the CRISPR-Cas9 binding site, arrows indicate primers used for PCR, the amplicon contains 3 *HpyCH4V* restriction sites used for screening. **(E)** Fluorescence microscopy of *IL2RG*$^{-/y}$ cell line 48 h post-transfection showing reported alone transfected cells to only express RFP (texas red channel) (transfection control), while few cells transfected with *RAG2* CRISPR-Cas9 and reporter co-expresses RFP and GFP, indicating reporter activity. **(F)** Single cell colony PCR and *HpyCH4V* assay for detection *DKO* cells lines. Wild type (WT) PCR amplicons digested and undigested with *HpyCH4V* served as controls. The presence of three bands indicates heterozygous lines for *RAG2*, while the presence of two bands in conjunction with the disappearance of the 190 bp band indicates homozygous lines. Colonies selected for sequencing are indicated. **(G)** Overall targeting efficiency of the pig *RAG2* locus, indicating total indels frequency (79%), heterozygous (51%) and homozygous (28%).

SUPPLEMENTARY FIGURE 2
Haplotype characterization of pH2B-eGFP pig donors and DKO line, and human hematopoietic stem cell selection and sex determination. **(A)** Haplotype PCR gels for *DKO* line, and pH2B-eGFP fetal liver donors 1, 2, and 3 used for *in utero* allogeneic transplants. Red boxes indicate the

MHC-I (SLA-1, SLA-2, SLA-3) and MHC-II (DRB1, DQB-1, and DQA) PCR reactions with different primers. A Positive internal control primer (porcine a-actin gene, 516 bp) is present in all reactions. Each well also contains 1 pair of primers specific for the multicopy alleles for each sub-haplotype group. The presence of a smaller band indicates a positive signal for the corresponding allele. **(B)** Summary of the findings obtained by PCR. Donors were found to be mostly different MHC-I and MHC-II overall haplotypes. **(C)** Flow cytometry analysis of donor A CD34 + cells utilized for *in utero* xenogeneic transplants. Peripheral blood mobilized stem cells were stained with anti-human CD34 antibodies prior to magnetic isolation (pre CD34 enrichment) and after purification in magnetic columns (post CD34 enrichment), revealing a 97.7% enrichment of CD34+ cells. **(D)** PCR assay for detection of X and Y chromosomes from donor A and donor B human cells. A set of primers were used to amplify the human X and Y chromosome, with male (M) and female (Y) templates serving as gender controls. Donor cells were found + for X and Y chromosomes, revealing donor A and B be of the male sex.

SUPPLEMENTARY FIGURE 3
Timeline schematic of all *in vivo* procedures and sample harvests performed.

SUPPLEMENTARY FIGURE 4
DNA sequence of single cell colonies generated by nucleofection of *IL2RG* targeting TALENs and *RAG2* targeting CRISPR-Cas9. DNA sequencing of target region detected from selected single cell *IL2RG*$^{-/y}$ (TALEN) colonies. Also shown is a list of *RAG2* mutations (homozygous and heterozygous) identified in *DKO* cell lines (generated on the *IL2RG* background). TALEN binding sites are represented for bold and underline sequences, while bold sequences represent PAM sequence. Allelic status is also shown.

SUPPLEMENTARY FIGURE 5
Evidence of loss of rearranged *TCR-β* locus in the thymus and *IgH* locus in the spleen of *DKO* pigs. **(A)** Detection of *D-J TCR-β* locus rearrangement in thymus gDNA. A germinal band is present in all samples (~1,500 bp), while the presence of bands smaller than 750 bp (indicated by black arrow) indicates rearranged *TCR-β* locus. This band is present in the thymus of wild-type pigs and absent in the thymus of *DKO* pigs. **(B)** Detection of V(D)J *IgH* locus rearrangement in spleen gDNA. A germinal band is present in all samples (~1,500 bp), while the presence of a 500 bp (indicated by black arrow) indicates rearranged *IgH* locus. This band is present in the spleen of wild-type and absent in the spleen of *DKO* pigs. This indicates the lack of *RAG2* activity.

References

1. Greiner DL, Hesselton RA, Shultz LD, SCID. Mouse models of human stem cell engraftment. *Stem Cells.* (1998) 16:166–77. doi: 10.1002/stem.160166

2. Shultz LD, Ishikawa F, Greiner DL. Humanized mice in translational biomedical research. *Nat Rev Immunol.* (2007) 7:118–30. doi: 10.1038/nri2017

3. Stripecke R, Münz C, Schuringa JJ, Bissig K-D, Soper B, Meeham T, et al. Innovations, challenges, and minimal information for standardization of humanized mice. *EMBO Mol Med.* (2020) 12:e8662. doi: 10.15252/emmm.201708662

4. Shultz LD, Brehm MA, Garcia-Martinez JV, Greiner DL. Humanized mice for immune system investigation: progress, promise and challenges. *Nat Rev Immunol.* (2012) 12:786–98. doi: 10.1038/nri3311

5. McBlane JF, van Gent DC, Ramsden DA, Romeo C, Cuomo CA, Gellert M, et al. Cleavage at a V(D)J recombination signal requires only RAG1 and RAG2 proteins and occurs in two steps. *Cell.* (1995) 83:387–95. doi: 10.1016/0092-8674(95)90116-7

6. Sugamura K, Asao H, Kondo M, Tanaka N, Ishii N, Ohbo K, et al. The interleukin-2 receptor gamma chain: its role in the multiple cytokine receptor complexes and *T*-cell development in XSCID. *Annu Rev Immunol.* (1996) 14:179–205. doi: 10.1146/annurev.immunol.14.1.179

7. Cao X, Shores EW, Hu-Li J, Anver MR, Kelsall BL, Russell SM, et al. Defective lymphoid development in mice lacking expression of the common cytokine receptor gamma chain. *Immunity.* (1995) 2:223–38. doi: 10.1016/1074-7613(95)90047-0

8. Noguchi M, Yi H, Rosenblatt HM, Filipovich AH, Adelstein S, Modi WS, et al. Interleukin-2 receptor gamma chain mutation results in X-linked severe combined immunodeficiency in humans. *Cell.* (1993) 73:147–57. doi: 10.1016/0092-8674(93)90167-O

9. Buckley RH, Schiff RI, Schiff SE, Markert ML, Williams LW, Harville TO, et al. Human severe combined immunodeficiency: genetic, phenotypic, and functional diversity in one hundred eight infants. *J Pediatr.* (1997) 130:378–87. doi: 10.1016/S0022-3476(97)70199-9

10. Niemann H, Petersen B. The production of multi-transgenic pigs: update and perspectives for xenotransplantation. *Transgenic Res.* (2016) 25:361–74. doi: 10.1007/s11248-016-9934-8

11. Ren J, Yu D, Fu R, An P, Sun R, Wang Z, et al. *IL2RG* -deficient minipigs generated *via* CRISPR/Cas9 technology support the growth of human melanoma-derived tumours. *Cell Proliferation.* (2020) 53:12863. doi: 10.1111/cpr.12863

12. Hara H, Shibata H, Nakano K, Abe T, Uosaki H, Ohnuki T, et al. Production and rearing of germ-free X-SCID pigs. *Exp Anim.* (2018) 67:139–46. doi: 10.1538/expanim.17-0095

13. Kang J-T, Cho B, Ryu J, Ray C, Lee E-J, Yun Y-J, et al. Biallelic modification of IL2RG leads to severe combined immunodeficiency in pigs. *Reproduct Biol Endocrinol.* (2016) 14:5. doi: 10.1186/s12958-016-0206-5

14. Watanabe M, Nakano K, Matsunari H, Matsuda T, Maehara M, Kanai T, et al. Generation of interleukin-2 receptor gamma gene knockout pigs from somatic cells genetically modified by zinc finger nuclease-encoding mRNA. *PLoS One.* (2013) 8:e76478. doi: 10.1371/journal.pone.0076478

15. Suzuki S, Iwamoto M, Saito Y, Fuchimoto D, Sembon S, Suzuki M, et al. Il2rg gene-targeted severe combined immunodeficiency pigs. *Cell Stem Cell.* (2012) 10:753–8. doi: 10.1016/j.stem.2012.04.021

16. Suzuki S, Iwamoto M, Hashimoto M, Suzuki M, Nakai M, Fuchimoto D, et al. Generation and characterization of RAG2 knockout pigs as animal model for severe combined immunodeficiency. *Vet Immunol Immunopathol.* (2016) 178:37–49. doi: 10.1016/j.vetimm.2016.06.011

17. Lee K, Kwon D-N, Ezashi T, Choi Y-J, Park C, Ericsson AC, et al. Engraftment of human iPS cells and allogeneic porcine cells into pigs with inactivated RAG2 and accompanying severe combined immunodeficiency. *Proc Natl Acad Sci U S A.* (2014) 111:7260–5. doi: 10.1073/pnas.1406376111

18. Huang J, Guo X, Fan N, Song J, Zhao B, Ouyang Z, et al. RAG1/2 knockout pigs with severe combined immunodeficiency. *J Immunol.* (2014) 193:1496–503. doi: 10.4049/jimmunol.1400915

19. Ito T, Sendai Y, Yamazaki S, Seki-Soma M, Hirose K, Watanabe M, et al. Generation of recombination activating gene-1-deficient neonatal piglets: a model of T and B cell deficient severe combined immune deficiency. *PLoS One.* (2014) 9:e113833. doi: 10.1371/journal.pone.0113833

20. Lei S, Ryu J, Wen K, Twitchell E, Bui T, Ramesh A, et al. Increased and prolonged human norovirus infection in RAG2/IL2RG deficient gnotobiotic pigs with severe combined immunodeficiency. *Sci Rep.* (2016) 6:25222. doi: 10.1038/srep25222

21. Boettcher AN, Cino-Ozuna AG, Solanki Y, Wiarda JE, Putz E, Owens JL, et al. CD3ε+ Cells in pigs with severe combined immunodeficiency due to defects in ARTEMIS. *Front Immunol.* (2020) 11:510. doi: 10.3389/fimmu.2020.00510

22. Boettcher AN Li Y, Ahrens AP, Kiupel M, Byrne KA, Loving CL, et al. Novel engraftment and *T*-cell differentiation of human hematopoietic cells in ART -/– IL2RG -/Y SCID pigs. *Front Immunol.* (2020) 11:100. doi: 10.3389/fimmu.2020.00100

23. Estrada J, Sommer J, Collins B, Mir B, Martin A, York A, et al. Swine generated by somatic cell nuclear transfer have increased incidence of intrauterine growth restriction (IUGR). *Cloning Stem Cells.* (2007) 9:229–36. doi: 10.1089/clo.2006.0079

24. Walker SC, Shin T, Zaunbrecher GM, Romano JE, Johnson GA, Bazer FW, et al. A highly efficient method for porcine cloning by nuclear

transfer using in vitro-matured oocytes. *Cloning Stem Cells.* (2002) 4:105–12. doi: 10.1089/153623002320253283

25. Sper RB, Koh S, Zhang X, Simpson S, Collins B, Sommer J, et al. Generation of a stable transgenic swine model expressing a porcine Histone 2B-eGFP fusion protein for cell tracking and chromosome dynamics studies. *PLoS One.* (2017) 12:e0169242. doi: 10.1371/journal.pone.0169242

26. Ho C-S, Martens GW, Amoss MS, Gomez-Raya L, Beattie CW, Smith DM. Swine leukocyte antigen (SLA) diversity in sinclair and hanford swine. *Develop Comparat Immunol.* (2010) 34:250–7. doi: 10.1016/j.dci.2009.09.006

27. Yeom S-C, Park C-G, Byeong-Chun LEE, Wang-Jae LEE, SLA. typing using the PCR-SSP method and establishment of the SLA homozygote line in pedigreed SNU miniature pigs. *Anim Sci J.* (2010) 81:158–64. doi: 10.1111/j.1740-0929.2009.00727.x

28. Gao C, Jiang Q, Guo D, Liu J, Han L, Qu L. Characterization of swine leukocyte antigen (SLA) polymorphism by sequence-based and PCR-SSP methods in Chinese Bama miniature pigs. *Dev Comp Immunol.* (2014) 45:87–96. doi: 10.1016/j.dci.2014.02.006

29. Nguyen Q-H, Witt RG, Wang B, Eikani C, Shea J, Smith LK, et al. Tolerance induction and microglial engraftment after fetal therapy without conditioning in mice with Mucopolysaccharidosis type VII. *Sci Transl Med.* (2020) 12:eaay8980. doi: 10.1126/scitranslmed.aay8980

30. Witt RG, Wang B, Nguyen Q-H, Eikani C, Mattis AN, MacKenzie TC. Depletion of murine fetal hematopoietic stem cells with c-Kit receptor and CD47 blockade improves neonatal engraftment. *Blood Adv.* (2018) 2:3602–7. doi: 10.1182/bloodadvances.2018022020

31. Bility MT, Zhang L, Washburn ML, Curtis TA, Kovalev GI, Su L. Generation of a humanized mouse model with both human immune system and liver cells to model hepatitis C virus infection and liver immunopathogenesis. *Nat Protoc.* (2012) 7:1608–17. doi: 10.1038/nprot.2012.083

32. Zhang L, Lewin SR, Markowitz M, Lin HH, Skulsky E, Karanicolas R, et al. Measuring recent thymic emigrants in blood of normal and HIV-1-infected individuals before and after effective therapy. *J Exp Med.* (1999) 190:725–32. doi: 10.1084/jem.190.5.725

33. Ogle BM, Knudsen BE, Nishitai R, Ogata K, Platt JL. Toward development and production of human *T*-cells in swine for potential use in adoptive *T*-cell immunotherapy. *Tissue Eng Part A.* (2009) 15:1031–40. doi: 10.1089/ten.tea.2008.0117

34. Reyon D, Tsai SQ, Khayter C, Foden JA, Sander JD, Joung JK, et al. assembly of TALENs for high-throughput genome editing. *Nat Biotechnol.* (2012) 30:460–5. doi: 10.1038/nbt.2170

35. Sivori S, Pende D, Bottino C, Marcenaro E, Pessino A, Biassoni R, et al. NKp46 is the major triggering receptor involved in the natural cytotoxicity of fresh or cultured human NK cells. *Correlation between surface density of NKp46 and natural cytotoxicity against autologous, allogeneic or xenogeneic target cells. Eur J Immunol.* (1999) 29:1656–66.

36. Fujiki Y, Fukawa K, Kameyama K, Kudo O, Onodera M, Nakamura Y, et al. Successful multilineage engraftment of human cord blood cells in pigs after *in utero* transplantation. *Transplantation.* (2003) 75:916–22. doi: 10.1097/01.TP.0000057243.12110.7C

37. Woolfrey T, Müller S, Spellman D. *National marrow donor program HLA matching guidelines for unrelated adult donor hematopoietic cell transplants. Transplantation*. (20088. 14, 45–53. Available online at: https://www.astctjournal.org/article/S1083-8791(08)00274-7/abstract

38. Petersdorf EW. HLA: mismatching in transplantation. *Blood.* (2015) 125:1058–9. doi: 10.1182/blood-2014-12-619015

39. Magnani A, Jouannic J-M, Rosain J, Gabrion A, Touzot F, Roudaut C, et al. Successful *in utero* stem cell transplantation in X-linked severe combined immunodeficiency. *Blood Adv.* (2019) 3:237–41. doi: 10.1182/bloodadvances.2018023176

40. Liu J, Hill BJ, Darko S, Song K, Quigley MF, Asher TE, et al. The peripheral differentiation of human natural killer *T*-cells. *Immunol Cell Biol.* (2019) 97:586–96. doi: 10.1111/imcb.12248

41. van der Weerd K, Dik WA, Schrijver B, Bogers AJJC, Maat APWM, van Nederveen FH, et al. Combined TCRG and TCRA TREC analysis reveals increased peripheral T-lymphocyte but constant intra-thymic proliferative history upon ageing. *Mol Immunol.* (2013) 53:302–12. doi: 10.1016/j.molimm.2012.08.019

42. Diaz M, Douek DC, Valdez H, Hill BJ, Peterson D, Sanne I, et al. *T*-cells containing *T*-cell receptor excision circles are inversely related to HIV replication and are selectively and rapidly released into circulation with antiretroviral treatment. *AIDS.* (2003) 17:1145–9. doi: 10.1097/00002030-200305230-00005

43. Livak F, Schatz DG. T-cell receptor alpha locus V(D)J recombination by-products are abundant in thymocytes and mature *T*-cells. *Mol Cell Biol.* (1996) 16:609–18. doi: 10.1128/MCB.16.2.609

44. Li Y, Teteloshvili N, Tan S, Rao S, Han A, Yang Y-G, et al. Humanized Mice Reveal New Insights Into the Thymic Selection of Human Autoreactive CD8+ *T*-cells. *Front Immunol.* (2019) 10:63. doi: 10.3389/fimmu.2019.00063

45. Kalscheuer H, Onoe T, Dahmani A, Li H-W, Hölzl M, Yamada K, et al. Xenograft tolerance and immune function of human *T*-cells developing in pig thymus xenografts. *J Immunol.* (2014) 192:3442–50. doi: 10.4049/jimmunol.1302886

46. Radtke S, Chan Y-Y, Sippel TR, Kiem H-P, Rongvaux A. MISTRG mice support engraftment and assessment of nonhuman primate hematopoietic stem and progenitor cells. *Exp Hematol.* (2019) 70:31–41. doi: 10.1016/j.exphem.2018.12.003

47. Strowig D, Rongvaux T, Rathinam A. Transgenic expression of human signal regulatory protein alpha in $Rag2^{-/-}$ $\gamma c^{-/-}$ mice improves engraftment of human hematopoietic cells in humanized mice. *Proc Estonian Acad Sci Biol Ecol.* (2011) 108, 13218–13223. doi: 10.1073/pnas.1109769108

48. Ide K, Ohdan H, Ahara H, Asahara T. Human CD47 on porcine antigen presenting cells have a possibility of preventing T-cell mediated xenograft rejection through inhibitory signaling to SIRP Alpha. *Transplantation.* (2008) 86:238–9. doi: 10.1097/01.tp.0000332060.51861.eb

49. Tena A, Kurtz J, Leonard DA, Dobrinsky JR, Terlouw SL, Mtango N, et al. Transgenic expression of human CD47 markedly increases engraftment in a murine model of pig-to-human hematopoietic cell transplantation. *Am J Transplant.* (2014) 14:2713–22. doi: 10.1111/ajt.12918

50. Boettcher AN, Cunnick JE, Powell EJ, Egner TK, Charley SE, Loving CL, et al. Porcine signal regulatory protein alpha binds to human CD47 to inhibit phagocytosis: Implications for human hematopoietic stem cell transplantation into severe combined immunodeficient pigs. *Xenotransplantation.* (2019) 26:e12466. doi: 10.1111/xen.12466

frontiers | Frontiers in Veterinary Science

TYPE Brief Research Report
PUBLISHED 24 October 2022
DOI 10.3389/fvets.2022.919454

OPEN ACCESS

EDITED BY
Gerd Heusch,
University of
Duisburg-Essen, Germany

REVIEWED BY
Oiva Jouko Arvola,
University of Helsinki, Finland
Petra Kleinbongard,
Essen University Hospital, Germany

*CORRESPONDENCE
Montserrat Rigol
mrigol@recerca.clinic.cat

†These authors have contributed equally to this work and share first authorship

SPECIALTY SECTION
This article was submitted to Comparative and Clinical Medicine, a section of the journal Frontiers in Veterinary Science

RECEIVED 13 April 2022
ACCEPTED 30 September 2022
PUBLISHED 24 October 2022

CITATION
Solanes N, Bobi J, Arrieta M, Jimenez FR, Palacios C, Rodríguez JJ, Roqué M, Galán-Arriola C, Ibañez B, Freixa X, García-Álvarez A, Sabaté M and Rigol M (2022) An open secret in porcine acute myocardial infarction models: The relevance of anaesthetic regime and breed in ischaemic outcomes. *Front. Vet. Sci.* 9:919454. doi: 10.3389/fvets.2022.919454

An open secret in porcine acute myocardial infarction models: The relevance of anaesthetic regime and breed in ischaemic outcomes

Núria Solanes[1†], Joaquim Bobi[1,2†], Marta Arrieta[1], Francisco Rafael Jimenez[1], Carmen Palacios[1], Juan José Rodríguez[1], Mercè Roqué[1], Carlos Galán-Arriola[3], Borja Ibañez[3], Xavier Freixa[1], Ana García-Álvarez[1], Manel Sabaté[1] and Montserrat Rigol[1,4]*

[1]Hospital Clínic, Institut d'Investigacions Biomédiques August Pi i Sunyer (IDIBAPS) and Cardiology Department, Institut Clínic Cardiovascular, Universitat de Barcelona, Barcelona, Spain, [2]Experimental Cardiology Department, Erasmus MC University Medical Centre, Rotterdam, Netherlands, [3]Centro Nacional de Investigaciones Cardiovasculares Carlos III, CIBER de enfermedades cardiovasculares (CIBERCV), IIS- Fundación Jiménez Díaz Hospital, Madrid, Spain, [4]Bioresearch and Veterinary Services, The University of Edinburgh, Edinburgh, United Kingdom

Large animal models of acute myocardial infarction (AMI) play a crucial role in translating novel therapeutic approaches to patients as denoted by their use in the right-before-human testing platform. At present, the porcine model of AMI is used most frequently as it mimics the human condition and its anatomopathological features accurately. We want to describe to, and share with, the translational research community our experience of how different anaesthetic protocols (sevoflurane, midazolam, ketamine+xylazine+midazolam, and propofol) and pig breeds [Large White and Landrace x Large White (LLW)] can dramatically modify the outcomes of a well-established porcine model of closed-chest AMI. Our group has extensive experience with the porcine model of reperfused AMI and, over time, we reduced the time of ischaemia used to induce the disease from 90 to 50 min to increase the salvageable myocardium for cardioprotection studies. For logistical reasons, we changed both the anaesthetic protocol and the pig breed used, but these resulted in a dramatic reduction in the size of the myocardial infarct, to almost zero in some cases (sevoflurane, 50-min ischaemia, LLW, 2.4 ± 3.9% infarct size), and the cardiac function was preserved. Therefore, we had to re-validate the model by returning to 90 min of ischaemia. Here, we report the differences in infarct size and cardiac function, measured by different modalities, for each combination of anaesthetic protocol and pig breed we have used. Furthermore, we discuss these combinations and the limited literature pertaining to how these two factors influence cardiac function and infarct size in the porcine model of AMI.

KEYWORDS

myocardial infarction, anaesthesia, pig breed, porcine models, translational research

Introduction

Acute myocardial infarction (AMI) and subsequent heart failure have been a leading cause of mortality and morbidity worldwide in the last decades (1). To address this, effective translation of novel therapeutic options to patients is crucial and multiple different expert recommendations have emphasized the key role of large-animal models of AMI as a right-before-patient test platform (2).

Presently, the swine (*Sus scrofa domestica*) is one of, if not, the most used large-animal model of AMI, primarily due to the significant anatomical similarities between pig and human hearts including their coronary vascular systems, for example minimal to absent collateral circulation (3). Due to these similarities, myocardial ischaemia/reperfusion in porcine models reproduces the pathophysiologic mechanisms of human acute ST-elevation myocardial infarction so accurately (3, 4) that the porcine model of AMI is used in research centers worldwide.

The basic concept behind the AMI model is to induce the lesion by occluding a coronary artery followed (or not) by reperfusion. Despite this basic concept, there are variations in the methodologies employed by different research groups/centers due to the specific purpose of the model and the expertise and limitations of each research group/center. Consequently, this has led to a number of porcine AMI models, each with slight variations and all at the expense of a standardized methodology, which hampers comparison between data from different groups and limits data pooling. Unfortunately, some of these variations in methodology have an influence on the outcome of ischaemia, resulting in a variable range of areas of necrosis (minimal to large myocardial infarctions). One influential factor is the anaesthetic protocol (5, 6), as some anaesthetics have cardioprotective properties (7). For example, the use of sevoflurane in human patients undergoing coronary artery bypass surgery has been linked to a reduction in the severity of the ischaemic insult. In pigs, some studies have also described cardioprotective effects associated with inhaled anaesthesia (8, 9) but it is not clear how consistent this protection is depending on the ischaemia duration induced by different methodologies. Less is known about the influence of different pig breeds, or familial lineages within a breed, on the susceptibility of the myocardium to ischaemia. Overall, the influence of the anaesthetic protocol and other variables, such as pig breed or age, on the extent and severity of the resultant ischaemia induced in porcine models of AMI is poorly described in the literature. This variation between methodologies is a topic of active discussion among translational scientists, despite a limited general interest in reporting failed pilot studies or negative results.

Here, we describe and share with the translational research community, our group's experience of how different porcine anaesthetic protocols and breeds can dramatically modify the severity of the resultant infarct in a well-established swine model of closed-chest AMI.

Materials and methods

Study groups

We compared pilot data (study A) with historical data generated by our group [studies B (10), C (11), and D (12) see below]. This study has been approved prior to its initiation, according to the European (2010/63/EU) and Spanish (RD 53/2013) regulations, by the Ethics Committee on Animal Experimentation of the Center for Comparative Medicine and Bioimage (CMCiB) and by *Generalitat de Catalunya* (reference 10802). All protocols used in this study comply with the principles of the 3Rs to prioritize animal welfare. All animal experimentation from study A was developed at the Centre for Comparative Medicine and Bioimage (CMCiB) of the Germans Trias i Pujol Research Institute (IGTP) (reference B9900005), Barcelona, Spain.

Study A was comprised of twenty Landrace x Large White female pigs (33.1 ± 2 kg; 3–4 months old) that underwent a reperfused AMI after different occlusion durations of the left anterior descending (LAD) coronary artery and under different anaesthetic regimens. Sub-groups were defined as the following: sub-group SEVO-50, anaesthesia maintained by inhalation with sevoflurane (0.6–3%) and 50 min of LAD coronary artery occlusion ($n = 10$); sub-group MIDA-50, anaesthesia maintained with intravenous (IV) midazolam (2–2.5 mg/kg/hour) and 50 min of LAD coronary artery occlusion ($n = 1$); sub-group MIDA-90, anaesthesia maintained with IV midazolam (2–2.5 mg/kg/hour) and 90 min of LAD coronary artery occlusion ($n = 9$) (Table 1, Study A).

Study A

The animals were acclimated for a minimum of 7 days and a maximum of 15 days in the research facilities prior to any procedures. A light–dark cycle of 12 h (with natural light through the glass, which guaranteed 12 h of light supplemented by artificial light if necessary), an ambient temperature of between 16 and 24°C, relative humidity between 30 and 70%, 15–20 air renewals per hour, and twice-daily feeding cycles along with *ad libitum* drinking water were provided for all animals.

The temperature was monitored using a rectal probe throughout the experimental procedure of AMI induction until the animal recovered from anaesthesia.

Reperfused AMI procedure

Pre-medication of all the animals was comprised of intramuscular (IM) injection of ketamine (6 mg/kg), xylazine (4 mg/kg), and midazolam (0.16 mg/kg), and propofol (1–2 mg/kg) was administered intravenously for induction of

TABLE 1 Pig breed, ischaemia time, anaesthetic regimens, and echocardiography or CMR results from the present study and previous publications of our research team.

	Study A – 2020/2021			Historical data		
	SEVO – 50	**MIDA – 50**	**MIDA – 90**	**Study B – 2017 (9)**	**Study C – 2014 (10)**	**Study D – 2010 (11)**
Pig breed	Landrace x Large White	Landrace x Large White	Landrace x Large White	Large White	Landrace x Large White	Landrace x Large White
Occlusion duration (min)	50	50	90	50	90	90
Pre-medication	KXM (6; 4; 0.16 mg/Kg, respectively)	KXM (6; 4; 0.16 mg/Kg, respectively)	KXM (6; 4; 0.16 mg/Kg, respectively)	KXM (20; 2; 0.5 mg/Kg, respectively)	Azaperone (2 mg/kg)	Azaperone (2 mg/kg)
Anaesthesia (induction)	Propofol (1–2 mg/kg)	Propofol (1–2 mg/kg)	Propofol (1–2 mg/kg)	_____	Sodium thiopental (30 mg/kg)	Sodium thiopental (30 mg/kg)
Anaesthesia (maintenance)	Sevoflurane (0.6–3 %) + Fentanyl (0.005–0.01 mg/kg/h)	Midazolam (2–2.5 mg/Kg/h) + Fentanyl (0.005–0.01 mg/kg/h)	Midazolam (2–2.5 mg/Kg/h) + Fentanyl (0.005–0.01 mg/kg/h)	KXM (2; 0.2; 0.2 mg/kg/h; respectively) + Fentanyl (0.007 mg/kg/h)	Propofol (10 mg/kg/min) + Fentanyl (0.025 mg/kg/h)	Propofol (10 mg/kg/min) + Fentanyl (0.025 mg/kg/h)
Animals* (sample size)	$n = 9$	$n = 1$	$n = 9$	$n = 7$	G15 min $n = 6$ G7d $n = 6$	Gic $n = 4$ Gte $n = 4$
LV function (method)	CMR	CMR	CMR	CMR	Intracardiac echocardiogram	Intracardiac echocardiogram
LV function (time points, days post-AMI)	90, 150	15	60, 120	7, 60	7, 21	7, 21
LVEDV (ml)	T90, 102.9 ± 15.5 T150, 129.7 ± 15.9	T15, 106.8	T60, 125 ± 14.1 T120, 156.2 ± 26.8	T7, 133.2 ± 17.0 T60, 201.3 ± 37.3	G15 min-T7, N/A G7d-T7, 30.4 ± 20.4 G15 min-T21, 46.3 ± 5 G7d-T21, 30.8 ± 22.7	G1-T7, 29.3 ± 0.6 G2-T7, 32.4 ± 4 G1-T21, 27.3 ± 3.9 G2-T21, 34.1 ± 5.9
LVESV (ml)	T90, 46.4 ± 9.3 T150, 63.2 ± 10	T15, 56.3	T60, 76.6 ± 14.4 T120, 96.1 ± 18.1	T7, 80.3 ± 16.9 T60, 126.5 ± 35.8	G15 min-T7, N/A G7d-T7, 14.3 ± 9.3 G15 min-T21, 22.3 ± 3.9 G7d-T21, 15.5 ± 11.8	G1-T7, 16.0 ± 0.2 G2-T7, 16.0 ± 0.2 G1-T21, 13.8 ± 1.3 G2-T21, 16.6 ± 3.2
LVEF (%)	T90, 54.7 ± 6.6 T150, 51.4 ± 3.2	T15, 47.2	T60, 39.1 ± 5.3 T120, 38.5 ± 3.4	T7, 40.2 ± 5.2 T60, 37.9 ± 6.3	G15 min-T7, N/A G7d-T7, 52 ± 3 G15 min-T21, 51 ± 9 G7d-T21, 52 ± 7	G1-T7, 45 ± 1 G2-T7, 50 ± 5 G1-T21, 49 ± 2 G2-T21, 51 ± 8
Infarct size (method)	CMR	CMR	CMR	CMR	Morphometry	Morphometry
Infarct size (% LV)	T90, 2.4 ± 3.9 T150, 1.8 ± 3.4	T15, 0	T60, 16.4 ± 4.6 T120, 15.7 ± 3.2	T7, 30.8 ± 5.5 T60, 19.1 ± 4.3	G15 min-T7, N/A G7d-T7, N/A G15 min-T21, 24 ± 4 G7d-T21, 21 ± 3	G1-T7, N/A G2-T7, N/A G1-T21, 19 ± 10 G2-T21, 22 ± 12

Values are represented as mean ± SD. SEVO, sevoflurane; MIDA, midazolam; AMI, acute myocardial infarction; CMR, cardiac magnetic resonance imaging; LV, left ventricle; LVEDV, left ventricular end-diastolic volume; LVEF, left ventricular ejection fraction; LVESV, left ventricular end-systolic volume; KXM, ketamine + xylazine + midazolam; N/A, non-applicable. G15min, group of control animals with vehicle administration 15 min after AMI induction; G7d, group of control animals with vehicle administration 7 days after AMI induction; Gic, group of control animals with intracoronary vehicle administration after AMI induction; Gte, group of control animals with transendocardial vehicle administration after AMI induction; * animals that survived AMI induction.

anaesthesia. Anaesthesia was maintained with either sevoflurane (between 1.5 and 2.5 % but occasionally, to maintain stable hemodynamics with the required plane of anaesthesia, it was reduced to 0.6 % or raised to 3 %) or midazolam (2.0–2.5 mg/kg/h) depending on the study group (see above). An infusion of IV fentanyl (0.005–0.01 mg/kg/hour) during the procedure and buprenorphine (0.01 mg/kg, IM) toward the end of anaesthesia, to provide analgesia, were administered. Animals were orotracheally intubated, and mechanical ventilation was maintained during induction of AMI.

Following intubation, animals were mechanically ventilated (WATO EX-35). Ventilatory parameters were initially set as follows: volume-control, tidal volume 10 ml/kg, inspiratory fraction of oxygen 0.45, positive end-expiratory pressure 3 cm H_2O, and respiratory rate adjusted to maintain $PaCO_2$ within the physiologic range (35–45 mmHg).

Saline was administered intravenously at 10 ml/kg/hour and adjusted to maintain arterial pressure within normal values.

During the AMI induction procedure, attempts were made to maintain heart rate and mean arterial pressure between the ranges of 60–100 bpm and 60–70 mmHg, respectively, whilst maintaining an adequate plane of anaesthesia. However, it should be noted that blood pressure was monitored using a pressure cuff, the values of which are considered to be 10–15 mmHg lower compared to those obtained by using sensors placed in more invasive locations.

Briefly, the procedure consisted of percutaneous catheterization, *via* the femoral artery, of the LAD coronary artery, in which a balloon catheter was advanced, under fluoroscopic guidance, and inflated after the first diagonal branch, for 50 min or 90 min, followed by reperfusion for 15 min under anaesthesia prior to recovery. During coronary catheterization, appropriate anticoagulation was provided (an initial IV bolus of 3,000 IU heparin followed by boluses of 1,000 IU every 30 min). The day before induction of AMI, all animals received a loading dose of clopidogrel (150 mg/animal, PO) as an antithrombotic and this was continued for 2 days after the induction of AMI (clopidogrel 75 mg/animal/day, PO). During ischaemia, a continuous infusion of lidocaine (50 μg/kg/min, IV; sub-groups SEVO-50 and MIDA-50) or amiodarone (5.5 mg/kg/h, IV; sub-group MIDA-90) was administered to prevent malignant ventricular arrhythmias.

During follow-up, animals were monitored daily by a technician and weekly by a named veterinary surgeon. Animals were weighed weekly, and weight lost was monitored closely.

Infarct outcomes by cardiac imaging and histology

Infarct size and left ventricle function were studied by cardiac magnetic resonance (CMR) imaging at the following time points: sub-group SEVO-50 at 90 and 150 days post-procedure, sub-group MIDA-50 at 15 days post-procedure, and sub-group MIDA-90 at 60 and 120 days post-procedure. CMR imaging was performed with a Vantage Galan 3.0 Tesla magnet (Canon Medical Systems Corporation, Tokyo, Japan), and each study consisted of a cine steady-state free-precision sequence to assess biventricular volumes and ejection fraction, and a late gadolinium-enhanced (LGE) sequence to determine infarct size. Images were analyzed by two independent, blinded investigators and processed with analysis software (QMass. Medis, Leiden, The Netherlands) as described previously (10).

After the last imaging time point animals were euthanized with an overdose of IV pentobarbital and hearts were collected for further detailed analyses. Briefly, the hearts and transverse slices were photographed to record gross lesions. Representative samples of the anterior wall of the left ventricle were collected from healthy and fibrotic areas (macroscopically pale areas), placed into fixative (10% buffered formalin), and processed by routine histological methods for the examination of haematoxylin and eosin (H&E)-stained tissue sections.

Study groups B, C, and D

The results from study A were compared with control animals (with AMI and vehicle administration) from our previous research, studies B (10), C (11), and D (12). All animals were the same age, sex, and weight as those in study A at the beginning of the study. The procedure used to induce a reperfused AMI was the same in all the studies but used different times of duration of occlusion and different anaesthetic protocols depending on the aim of the study and the research center where the study was performed (Table 1). In summary, in study B we occluded the LAD coronary artery for 50 min and the anaesthetic protocol consisted of a combination of ketamine, xylazine, and midazolam (2.0, 0.2, and 0.2 mg/kg/h, respectively, IV) to induce and maintain general anaesthesia, and in studies C and D the LAD coronary artery was occluded for 90 min and anaesthesia was induced with sodium thiopental (30 mg/kg) and maintained with propofol (10 mg/kg/min, IV). In all studies, analgesia was provided by continuous infusion of fentanyl (0.005–0.025 mg/kg/h, IV) during the procedure.

Results

AMI procedure mortality

Studies A, B, C, and D had 5, 12.5, 8, and 32% AMI-related mortality, respectively, due to irreversible ventricular fibrillation during AMI induction. The rest of the animals completed the whole study as planned.

Study A. Temperature and haemodynamic data

Temperatures remained within the range of 36.5 ± 0.4°C in the SEVO-50 sub-group, 37.5 ± 0.1°C in the MIDA-50 sub-group, and 36.6 ± 0.3°C in the MIDA-90 sub-group. These temperature ranges were considered acceptable for anaesthetized pigs.

TABLE 2 Mortality, events, and inotrope administration during AMI induction.

	Study A – 2020/2021		
	SEVO – 50	MIDA – 50	MIDA – 90
Mortality	1/10	0/1	0/9
Asystole and/or ventricular fibrillation	6/9	1/1	4/9
Atropine administration	3/9	0/1	2/9
Adrenaline administration	3/9	1/1	0/9
Noradrenaline administration	1/9	1/1	0/9

Values are represented as number of animals/number of total animals. SEVO, sevoflurane; MIDA, midazolam.

The mean heart rate during ischaemia time (minutes of anterior descending coronary occlusion) in the SEVO-50 sub-group was 74.5 ± 9.3bpm, in the MIDA-50 sub-group it was 91.5 ± 2.1 bpm, and in the MIDA-90 sub-group it was 58.6 ± 7.5 bpm.

The mean arterial pressure during 50 or 90 min of ischaemia (anterior descending coronary artery occlusion) was 48.6 ± 10.9 mmHg in the SEVO-50 sub-group, 64 ± 8.5 mmHg in the MIDA-50 sub-group, and 47.7 ± 7 mmHg in the MIDA 90 sub-group.

The need for inotropes and events as asystole and ventricular fibrillation during ischaemia can be found in Table 2.

Cardiac function and infarct size

The CMR imaging results are summarized in Table 1. Animals from Study A sub-group SEVO-50 maintained their left ventricular ejection fractions (LVEF) within the normal range at both time points examined (54.7 ± 6.6% at 90 days and 51.4 ± 3.2% at 150 days post-procedure). Animals from Study A sub-group MIDA-90 had a reduced LVEF at both follow-up time points (39.1 ± 5.3% at 60 days and 38.5 ± 3.4% at 120 days post-procedure). The single animal in Study A sub-group MIDA-50 anaesthetized with midazolam and subjected to 50 min of ischaemia showed an LVEF of (47.2%) at 15 days post-procedure.

In agreement with the above LVEF results, animals from sub-group MIDA-90 had a significant area of LGE+ myocardium (infarcted) in the left ventricle (16.4 ± 4.6% at 60 days and 15.7 ± 3.2% at 120 days post-procedure). Conversely, animals in sub-group SEVO-50 that were maintained under anaesthesia with sevoflurane and had the LAD coronary artery occluded for 50 min displayed very limited areas of myocardial infarction (2.4 ± 3.9% at 90 days and 1.8 ± 3.4% at 150 days post-procedure). In the single animal in sub-group MIDA-50 subjected to 50-min LAD coronary artery occlusion but anaesthetized with midazolam, no infarcted tissue was detectable by CMR imaging at 15 days post-procedure. Figures 1A–C displays late gadolinium CMR images showing the differences in size of infarcts in each sub-group.

Macroscopic and microscopic myocardial remodeling

Macroscopic evaluation of sub-group SEVO-50 hearts revealed, in six of nine animals, several small (~0.5–1.0 cm^2) irregularly shaped fibrotic foci devoid of transmural extension into the interventricular septum and/or the anterior or lateral wall of the left ventricle. Three of the six animals with small areas of fibrosis did not show any LGE+ tissue in CMR imaging studies (Figure 1D). The three remaining hearts in this sub-group were devoid of any gross lesions. The single MIDA-50 animal had only one small focus of fibrosis in the anterior wall of the left ventricle (Figure 1E). All animals from sub-group MIDA-90 had variably sized foci of transmural myocardial infarction (pale fibrotic areas with thinning of the wall in some areas) involving areas of the septum, and anterior and lateral walls of the left ventricle from the apex to the base of the heart (Figure 1F).

Microscopic evaluation of all representative samples obtained from fibrotic foci showed deficits in the myocardium, presumably previously necrotic cardiomyocytes, replaced by fibrosis, and surrounded by very small numbers necrotic cardiomyocytes and inflammatory cells and variable amounts of neovascularization (Figure 1).

Discussion

The novel data from our present study (Study A) along with our previous studies (B, C, and D) in a porcine model of induced AMI with respect to the induced myocardial infarction (as detected by CMR imaging, and macroscopic and microscopic evaluations) and subsequent LVEF show notable variations in the outcomes influenced by the anaesthetic protocol, duration of occlusion of LAD coronary artery, and breed of pig. For example, when subjecting a Landrace x Large White pig to 50-min LAD coronary artery occlusion using sevoflurane to maintain general anaesthesia, this resulted in minimal / non-detectable myocardial damage.

The cardioprotective potential of some anaesthetic agents, mainly gaseous, against ischaemic injury has been reported previously (5, 9, 13). However, the effectiveness of the protection of anaesthesia may be influenced depending on whether the protective agent is given before, during, or after induction of ischaemia or a combination of them. The present study addresses the effects of different anaesthetics agents used for maintaining general anaesthesia during the induction of

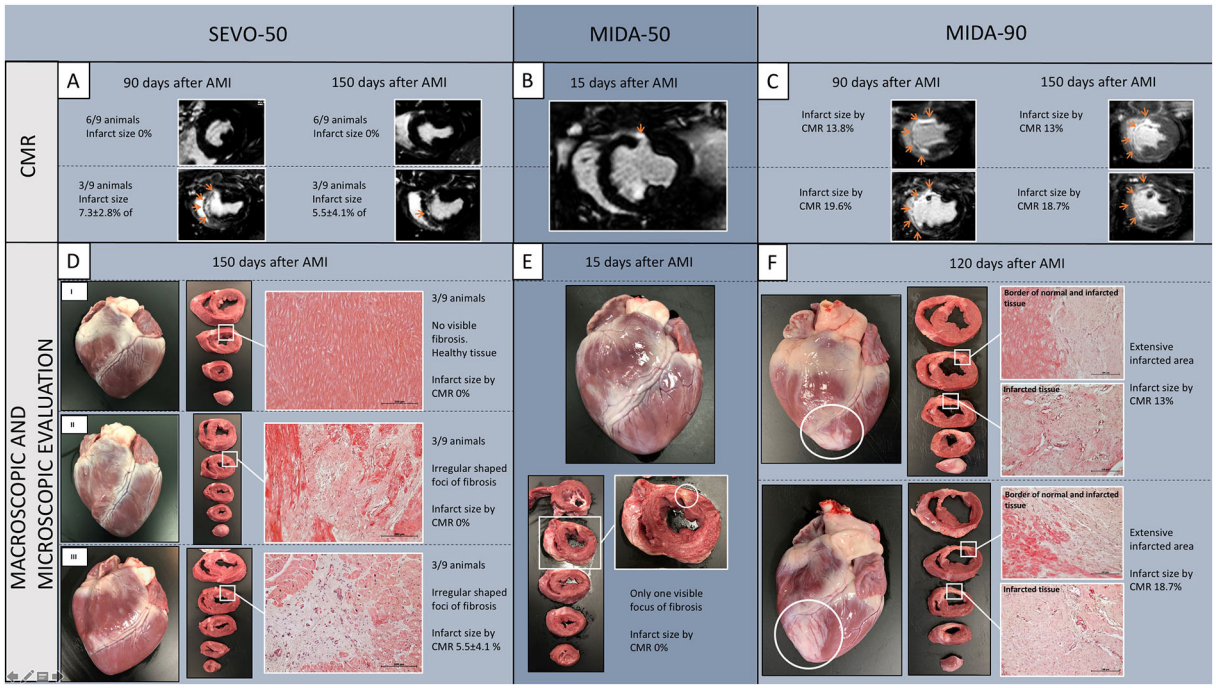

FIGURE 1
Late gadolinium-enhanced CMR representative images from Study A, sub-group SEVO-50 **(A)**, the single MIDA-50 animal **(B)**, and sub-group MIDA-90 **(C)**. CMR analysis showed infarcts were significantly smaller in sub-groups SEVO-50 and MIDA-50 compared to sub-group MIDA-90. Arrows depict late gadolinium-enhanced infarcted myocardium. **(D)** Macroscopic view of the anterior wall of the heart and transverse slices from apex to base showing an example of myocardial integrity devoid of any fibrotic areas (DI), an example of small areas of fibrosis (white box) with 0% of infarct size documented by CMR (DII), and an example of visible small areas of fibrosis with 5.1% (7.3 ± 2.8%, group SEVO-50, $n = 3$) of infarct size documented by CMR (DIII). **(E)** Small area of fibrosis visible in the fourth transverse heart slice in the single MIDA-50 animal. **(F)** Examples of extensive transmural infarction resulting in fibrosis. Representative histological sections were stained by haematoxylin and eosin (Original magnification 100x). SEVO, sevoflurane; MIDA, midazolam; AMI, acute myocardial infarction; CMR, cardiac magnetic resonance.

myocardial ischaemia and the early phase of reperfusion. Several mechanisms have been proposed for the cardioprotective effects attributed to volatile anaesthetics such as the reduction in myocardial oxygen demand (in part attributed to reduced cardiac work) and better maintenance of energy stores or activation of pro-survival pathways, among others (13–16). However, the extent of this protective effect remains unclear. For this reason, the duration of ischaemia is critical to assess the potential cardioprotection by any anaesthetic agent. In a previous study from our group, 50-min LAD coronary artery occlusion/reperfusion resulted in a myocardial infarct and resultant fibrosis of ≈20% of the left ventricle at 60 days post-procedure (10) when using a combination of ketamine, midazolam, and xylazine (+ fentanyl) to maintain general anaesthesia. However, in Study A, the same occlusion protocol with sevoflurane resulted in minimal to no myocardial injury (2.4 ± 3.9% at 90 days) and normal left ventricle function. This protective effect is similar to that observed by Larsen et al. (17) in a similar porcine model of reperfused AMI (45-min occlusion of LAD coronary artery) that resulted in a 68% reduction in the infarct size when using sevoflurane to maintain general anaesthesia compared to pentobarbital (a non-cardioprotective anaesthetic agent). The 50-min occlusion of the LAD coronary artery in the single animal receiving midazolam, a benzodiazepine, to maintain general anaesthesia did not result in infarcted myocardium despite midazolam not being considered cardioprotective. However, activation of a benzodiazepine receptor protects the myocardium against ischaemia–reperfusion in rats (18), and this could partially explain our results. Another possible explanation for the lack of infarcted myocardium in the MIDA-50 mins occlusion animal is that the anaesthetic protocols used by our research group always combine the maintenance anaesthetic agent with a continuous infusion of an opioid (fentanyl) to alleviate intraprocedural pain which reduces the dose of anaesthesia required. Opioids can reduce myocardial injury associated with ischaemia and reperfusion, hypothetically *via* both cardiac and extra-cardiac activation of opioid receptors (19). However, this seems contrary to our previous results (10) of the same 50-min occlusion (+ reperfusion) procedure using midazolam in combination with ketamine and xylazine that included the same dose of fentanyl, yet resulted in clear irreversible myocardial damage.

The different outcomes between both anaesthetic protocols could be explained by the dose of midazolam used as it was more than 10 times greater in study A. This could result in more efficient synergistic cardioprotective effects of midazolam and fentanyl in 50-min occlusion.

Another possible confounding factor is that the protocol using ketamine, midazolam, and xylazine (+ fentanyl) has only been used in Study B, which was performed in animals with a slightly different genetic background, pure Large White pigs instead of Large White x Landrace, and so a potential effect of breed cannot be discounted. In our experience, the most common farm swine breeds used for cardiovascular research in Europe include Landrace, Large White, Yorkshire, and Duroc, and their crosses. However, there are no studies directly comparing the effects of those genetic backgrounds on the outcomes of myocardial ischaemia.

We are aware that caution should be taken when comparing the combination of midazolam with a 50-min of occlusion of the LAD coronary artery and a different breed because there is only one animal in this group. The decision not to increase the number of animals in this protocol was motivated by the lack of induction of myocardial infarct, despite angiographically complete occlusion of the coronary artery, and the main goal of these pilot experiments was to establish a significant myocardial scar at 90 days post-induction that was to be treated with a novel regenerative therapeutic agent. Therefore, to avoid futile use of more animals, we decided not to continue with this protocol but studies of more animals would be required to confirm or refute the above-mentioned hypothesis.

The protocol that resulted in the desired infarct size was 90-min occlusion using midazolam (+ fentanyl) to maintain general anaesthesia. This was similar to our previous studies using 90 min of occlusion with propofol (+ fentanyl) (12), although a direct comparison of the infarct sizes is challenging due to the different methods used to determine them. The scar size at long-term follow-up was also similar to that obtained with ketamine, midazolam, and xylazine (+ fentanyl) with a 50-min occlusion in Large White pigs. Although xylazine (α-2 agonist) and midazolam (benzodiazepine) potentially have cardioprotective features, in this case, the combination of different anaesthetic agents allowed us to significantly reduce the dose of all the components, resulting in a hypothetically non-cardioprotective anaesthetic protocol.

This study has several limitations. First, we used juvenile pigs in all the studies due to logistic and methodologic reasons (manageable body size/weight of young animals) and budget limitations (high costs of adult minipigs). Myocardial infarction in humans is mainly a disease of the adult patient. Considerations should be taken when interpreting the results of AMI in young swine subjects as it might not completely mimic the pathology of adult subjects. Another limitation is that we only included female subjects in our study with the aim to be able to compare the outcomes with our previous works, with only female animals included. Current recommendations for animal research stress the need to use both female and male subjects in preclinical research for a more accurate translation to general human population. In the case of myocardial infarction, the effect of sex has been studied and it has been reported that the myocardium from females might be more protected against ischaemia, compared to males, but with worse myocardial remodeling (20, 21). Nevertheless, regarding preclinical research, a recent study shows that there are no differences in terms of infarct size and cardioprotection potential between female and male Göttingen minipigs (22). It was not designed to compare the effects of different anaesthetics on the outcome of induced AMI, and therefore, direct comparisons and statistical analyses are limited. Furthermore, we also discuss historical data of experiments performed by the same research group but in different research facilities, and therefore, changes in the equipment, housing, and general care of the animals may be confounding factors. Despite these limitations, we, as translational researchers, consider that these results are useful to avoid the use of animals in experiments that will fail to produce the AMI required for studies. The use of anaesthetic agents with faster recovery profiles, such as sevoflurane or desflurane, in preclinical research is encouraged to refine post-operative care and reduce anaesthesia-associated complications during weaning from mechanical ventilation because these are anaesthetic agents commonly used in clinical practice (23), which facilitates translation. However, based on our results and experience, and evidence from the literature, careful consideration should be taken when using the porcine model of reperfused AMI studies that have short durations of coronary occlusion and anaesthetic agents with potential cardioprotective features, such as sevoflurane. In addition, preclinical researchers should always be aware that each breed/lineage is endowed with specific features, namely cardiac sensibility/resistance to ischaemia.

Data availability statement

The original contributions presented in the study are included in the article/supplementary material, further inquiries can be directed to the corresponding authors.

Ethics statement

The animal study was reviewed and approved by Ethics Committee on Animal Experimentation of the Centre for Comparative Medicine and Bioimage (CMCiB) and by Generalitat de Catalunya (reference 10802).

Author contributions

NS, JB, MA, FJ, CP, JR, MR, CG-A, XF, AG-A, MS, and MR performed the experimental works. NS, JB, and MR wrote the

manuscript. BI, XF, MS, and MR provided funding. All authors reviewed and approved the published version of the manuscript.

Funding

This research was funded by a grant (PI18/00277) from Instituto de Salud Carlos III (ISCIII), Spain—Fondo Europeo de Desarrollo Regional (FEDER). FJ is the recipient of the Ayudas para la formación de profesorado Universitario (FPU19/04925) grant from the Spanish Ministry of Science and Innovation. IDIBAPS belongs to the CERCA Programme and receives partial funding from the Generalitat de Catalunya.

Acknowledgments

We thank Mark Dagleish for English editing and CMCiB staff for their technical assistance in the animal procedures. This work was partially developed at the Center de Recerca Biomèdica Cellex, Barcelona.

Conflict of interest

The authors declare that the research was conducted in the absence of any commercial or financial relationships that could be construed as a potential conflict of interest.

Publisher's note

All claims expressed in this article are solely those of the authors and do not necessarily represent those of their affiliated organizations, or those of the publisher, the editors and the reviewers. Any product that may be evaluated in this article, or claim that may be made by its manufacturer, is not guaranteed or endorsed by the publisher.

References

1. Roth GA, Mensah GA, Johnson CO, Addolorato G, Ammirati E, Baddour LM, et al. Global burden of cardiovascular diseases and risk factors, 1990–2019: update from the GBD 2019 study. *J Am Coll Cardiol.* (2020) 76:2982–3021. doi: 10.1016/j.jacc.2020.11.010

2. Lecour S, Andreadou I, Bøtker HE, Davidson SM, Heusch G, Ruiz-Meana M, et al. IMproving preclinical assessment of cardioprotective therapies (IMPACT) criteria: guidelines of the EU-cardioprotection cost action. *Basic Res Cardiol.* (2021) 116:5. doi: 10.1007/s00395-021-00893-5

3. Lindsey ML, Bolli R, Canty JM, Du XJ, Frangogiannis NG, Frantz S, et al. Guidelines for experimental models of myocardial ischemia and infarction. *Am J Physiol - Hear Circ Physiol.* (2018) 314:H812–38. doi: 10.1152/ajpheart.00335.2017

4. Heusch G, Skyschally A, Schulz R. The in-situ pig heart with regional ischemia/reperfusion - ready for translation. *J Mol Cell Cardiol.* (2011) 50:951–63. doi: 10.1016/j.yjmcc.2011.02.016

5. Cobo AA, Margallo FMS, Díaz CB, Blázquez VB, Bueno IG, Crisóstomo V. Anesthesia protocols used to create ischemia reperfusion myocardial infarcts in swine. *J Am Assoc Lab Anim Sci.* (2020) 59:478–87. doi: 10.30802/AALAS-JAALAS-19-000137

6. Bøtker HE, Hausenloy D, Andreadou I, Antonucci S, Boengler K, Davidson SM, et al. Practical guidelines for rigor and reproducibility in preclinical and clinical studies on cardioprotection. *Basic Res Cardiol.* (2018) 113:39. doi: 10.1007/s00395-018-0696-8

7. Weber NC, Schlack W. The concept of anaesthetic-induced cardioprotection: mechanisms of action. *Best Pract Res Clin Anaesthesiol.* (2005) 19:429–43. doi: 10.1016/j.bpa.2005.02.003

8. Weber NC, Schlack W. Inhalational anaesthetics and cardioprotection. *Handb Exp Pharmacol.* (2008) 182:187–207. doi: 10.1007/978-3-540-74806-9_9

9. Redel A, Stumpner J, Tischer-Zeitz T, Lange M, Smul TM, Lotz C, et al. Comparison of isoflurane-, sevoflurane-, and desflurane-induced pre- and postconditioning against myocardial infarction in mice in vivo. *Exp Biol Med.* (2009) 234:1186–91. doi: 10.3181/0902-RM-58

10. Bobi J, Solanes N, Fernández-Jiménez R, Galán-Arriola C, Dantas AP, Fernández-Friera L, et al. Intracoronary administration of allogeneic adipose tissue–derived mesenchymal stem cells improves myocardial perfusion but not left ventricle function, in a translational model of acute myocardial infarction. *J Am Heart Assoc.* (2017) 6:1–18. doi: 10.1161/JAHA.117.005771

11. Rigol M, Solanes N, Roura S, Roqué M, Novensà L, Dantas AP, et al. Allogeneic adipose stem cell therapy in acute myocardial infarction. *Eur J Clin Invest.* (2014) 44:83–92. doi: 10.1111/eci.12195

12. Rigol M, Solanes N, Farré J, Roura S, Roqué M, Berruezo A, et al. Effects of adipose tissue-derived stem cell therapy after myocardial infarction: impact of the route of administration. *J Card Fail.* (2010) 16:357–66. doi: 10.1016/j.cardfail.2009.12.006

13. Lin S, Neelankavil J, Wang Y. Cardioprotective effect of anesthetics: translating science to practice. *J Cardiothorac Vasc Anesth.* (2021) 35:730–40. doi: 10.1053/j.jvca.2020.09.113

14. Qiao S. gang, Sun Y, Sun B, Wang A, Qiu J, Hong L, et al. Sevoflurane postconditioning protects against myocardial ischemia/reperfusion injury by restoring autophagic flux via an NO-dependent mechanism. *Acta Pharmacol Sin.* (2019) 40:35–45. doi: 10.1038/s41401-018-0066-y

15. Xie H, Zhang J, Zhu J, Liu L, Rebecchi M, Hu S, et al. Sevoflurane post-conditioning protects isolated rat hearts against ischemia-reperfusion injury via activation of the ERK1/2 pathway. *Acta Pharmacol Sin.* (2014) 35:1504–13. doi: 10.1038/aps.2014.78

16. Hong L, Sun Y, An JZ, Wang C, Qiao SG. Sevoflurane preconditioning confers delayed cardioprotection by upregulating AMP-activated protein kinase levels to restore autophagic flux in ischemia-reperfusion rat hearts. *Med Sci Monit.* (2020) 26:1–12. doi: 10.12659/MSM.922176

17. Larsen JR, Aagaard S, Lie RH, Sloth E, Hasenkam JM. Sevoflurane improves myocardial ischaemic tolerance in a closed-chest porcine model. *Acta Anaesthesiol Scand.* (2008) 52:1400–10. doi: 10.1111/j.1399-6576.2008.01755.x

18. Obame FN, Zini R, Souktani R, Berdeaux A, Morin D. Peripheral benzodiazepine receptor-induced myocardial protection is mediated by inhibition of mitochondrial membrane permeabilization. *J Pharmacol Exp Ther.* (2007) 323:336–45. doi: 10.1124/jpet.107.124255

19. Tanaka K, Kersten J, Riess M. Opioid-induced cardioprotection. *Curr Pharm Des.* (2014) 20:5696–705. doi: 10.2174/1381612820666140204120311

20. Schüpke S, Mehilli J. Less myocardial scar but greater propensity for heart failure: Another gender paradox in myocardial infarction. *Eur Heart J.* (2017) 38:1664–5. doi: 10.1093/eurheartj/ehx230

21. Dekleva M, Lazic JS. Sex differences in left ventricular remodelling and heart failure development. *Biomed Res Clin Prac.* (2021) 6:1–5. doi: 10.15761/BRCP.1000225

22. Kleinbongard P, Lieder H, Skyschally A, Heusch G. No sex-related differences in infarct size, no-reflow, and protection by ischaemic pre-conditioning in Göttingen minipigs. *Cardiovasc Res.* (2022) 5:1–10. doi: 10.1093/cvr/cvac062

23. Skyschally A, Kleinbongard P, Lieder H, Gedik N, Stoian L, Amanakis G, et al. Novel mechanisms of myocardial ischemia, ischemia-reperfusion, and protection by myocardial conditioning. *Am J Physiol Heart Circ Physiol.* (2018) 315:H159–72. doi: 10.1152/ajpheart.00152

Frontiers in Veterinary Science

Transforms how we investigate and improve animal health

The third most-cited veterinary science journal, bridging animal and human health with a comparative approach to medical challenges. It explores innovative biotechnology and therapy for improved health outcomes.

Discover the latest Research Topics

See more →

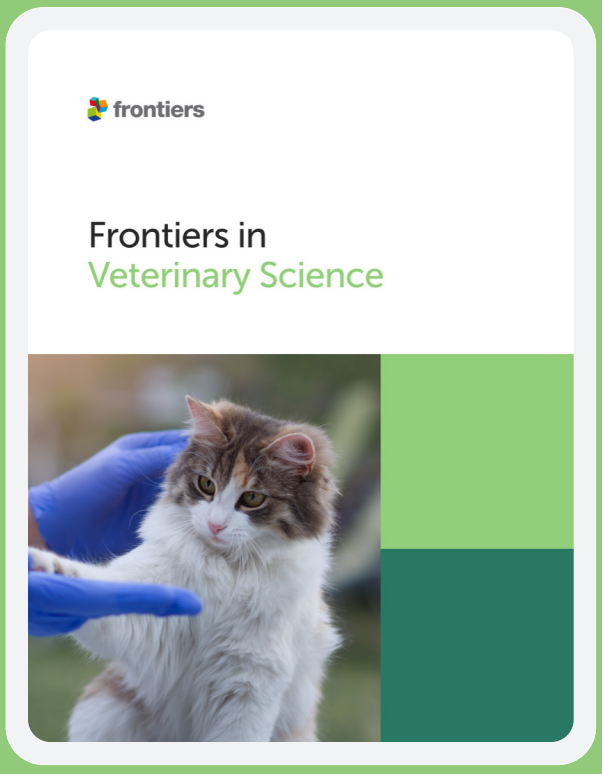

Frontiers

Avenue du Tribunal-Fédéral 34
1005 Lausanne, Switzerland
frontiersin.org

Contact us

+41 (0)21 510 17 00
frontiersin.org/about/contact